Post-Synthetic Modification of Metal-Organic Frameworks

Keenan, Luke

Award date:
2014

Awarding institution:
University of Bath

Post-Synthetic Modification of Metal-Organic Frameworks

Luke Lawrence Keenan

A thesis submitted for the degree of Doctor of Philosophy

University of Bath
Department of Chemistry

May 2014

For Sarah, Maria, Rob, Christine and Sean.

i. Table of Contents

ii. Acknowledgements

The author thanks Dr Andrew Burrows, Dr Mary Mahon, Dr Laura Fisher, Dr Anna Warren, Viorica Sebestyen, Dr Dongmei Jiang, Diamond Light Source for access to beamline I11 (Dr Chiu Tang for assistance with the high resolution powder X-ray diffraction measurements), beamline I19 (Dr Mark Warren and Dr Harriott Nowell for assistance with X-ray diffraction experiments), Dr John Lowe for assistance with NMR measurements, Alan Carver for help with elemental analysis and the EPSRC for financial support.

iii. Declaration of Work Done in Conjunction with Others

I declare that work carried out in Chapter 3 entitled "PSM of MIL-101(Cr)-NH_2 *via* a Diazonium Intermediate" was carried out in conjunction with Dr. Dongmei Jiang.

iv. Abstract

Post-synthetic modification (PSM) of metal-organic frameworks (MOFs) has increased in importance in the last decade, as a pathway to access more complex surfaces in the pores and channels of porous coordination polymers. This thesis will describe new examples of tandem PSM processes leading to new functionalised MOFs that are inaccessible by direct synthesis.

Chapter 1 introduces metal-organic frameworks (MOFs) and reviews the literature ranging from the basic building blocks to 3-D infinite networks. Post-synthetic modification (PSM) is introduced and a review of recent literature given. The aims of this report are also detailed at the close of the chapter.

Chapter 2 contains an investigation into the conversion of primary amino to secondary amino groups in the pores of MOFs *via* a tandem PSM reaction. The pendent amino groups of $[Zn_4O(BDC\text{-}NH_2)_3]$ (IRMOF-3) and $[Cr_3O(OH)(OH_2)_2(BDC)_3]$ (MIL-101(Cr)-NH_2) were modified to produce secondary amino functionalised groups protruding into the void space. Several crystal structures are described including two obtained for the products of the PSM reaction on IRMOF-3. Nitrogen and carbon dioxide absorption was carried and high selectivity for CO_2 over N_2 was observed.

Chapter 3 describes a new hydrothermal synthetic method of MIL-101(Cr)-NH_2 and the modification, post-synthesis, to form halo- and azo dye-functionalised pore surfaces by a tandem diazotisation reaction. Quantitative yields are reported for the conversion to the halogenated frameworks inaccessible by direct synthesis with the analogous dicarboxylic acid. Gas adsorption studies demonstrated increased selectivity for CO_2 over N_2.

Chapter 4 details the synthesis of new MOFs, with the potential for PSM, and crystallographic information is supplied for each new extended structure. The linkers, based on isophthalic acid, (1,3-benzenedicarboxylic acid) functionalised at the 5- position, were investigated with a range of metal salts and the resulting frameworks exposed to PSM reaction conditions where appropriate. By using a mixed ligand stoichiometry in the MOF synthesis reaction, 4,4'-bipy and BPDC have been incorporated into new extended frameworks. A new, simpler, synthetic route to the amino functionalised honeycomb framework $[Zn_4(BDC\text{-}NH_2)_3(NO_3)_2(H_2O)_2]$ (PNMOF-3) is also reported.

v. List of Abbreviations

ASU	Asymmetric unit
ATB	Adamantanetetrabenzoic acid
BDC	Benzene-1,4-dicarboxylate
bipy	2,2'-bipyradine
BPDC	[1,1'-biphenyl]-4,4'-dicarboxylate
BTB	4,4',4''-benzene-1,3,5-triyltribenzoate
BTC	Benzene-1,3,5-tricarboxylate
BTEC	Benzene-1,2,4,5-tetracarboxylate
dabco	1,4-Diazabicyclo[2.2.2]octane
ddn	1,12-Dodecanedinitrile
DOE	U.S. Department of Energy
DMF	*N*,*N*-Dimethylformamide
DMSO	Dimethyl sulfoxide
DMSO-d_6	Deuterated dimethyl sulfoxide
DPH	2,4-Dinitrophenylhydrazine
FT-IR	Fourier transform infra-red spectroscopy
AIP	5-Aminoisophthalate
AMIP	5-Acetamidoisophthalate
IIP	5-Iodoisophthalate
HPDC	4,5,9,10-Tetrahydropyrene-2,7-dicarboxylate
HRMS	High resolution mass spectrometry
IP	Benzene-1,3-dicarboxylate
MIL	Material of Institute Lavoisier
MOP	Metal-organic polymer
MOF	Metal-organic framework
NMR	Nuclear magnetic resonance
PCP	Porous coordination polymers
PDC	Pyrene-2,7-dicarboxylate
phen	1,10-Phenanthroline
POM	Polyoxometalates
PSM	Post-Synthetic Modification
py	Pyridine
pyz	Pyrazine
PXRD	Powder X-ray diffraction
SBU	Secondary building unit
TCNQ	Tetracyanoquinodimethane
TCPB	1,2,4,5-Tetrakis(4-carbonylphenyl)benzene
THF	Tetrahydrofuran
TGA	Thermogravimetric analysis
TPDC	[1,1':4',1"-terphenyl]-4,4"-dicarboxylate
UiO	University of Oslo
ZIF	Zeolitic imidazolate framework

1. Introduction

1.1. Metal-organic Frameworks: A Brief History

Metal-organic frameworks (MOFs) are a class of materials that consist of metal nodes, made up of metal cations, and organic linkers, which are usually rigid anions.[1] These linkers coordinate to the metals through electron pair donor sites e.g. carboxylate oxygen atoms or nitrogen atoms. The nodes and linkers can self-assemble to form 1-D chains, 2-D sheets and 3-D networks, Figure 1.1.[2] MOFs have attracted a lot of attention since their inception, firstly in the 1960s,[3] and then in the 1980s,[4, 5] due to their high surface areas and the ability to design their crystal architecture. The term metal-organic framework was not used for these materials until 1995; as before then they were considered a subset of coordination polymers.[4]

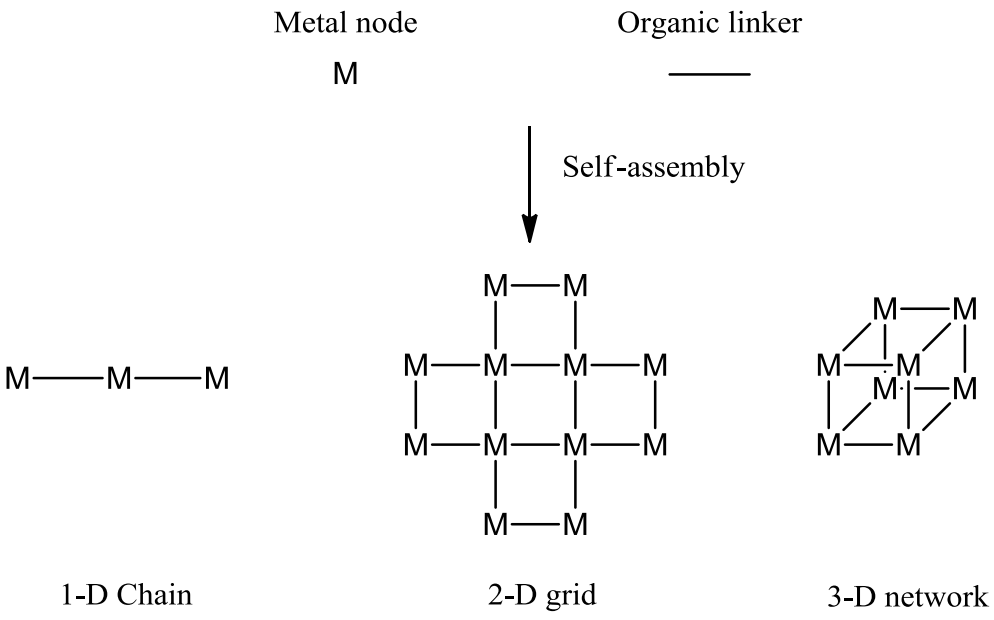

Figure 1.1. Self-assembly of nodes and linkers into three classes of MOF architectures.

Yaghi described the advantages of MOFs over other porous materials, such as zeolites, due to their "precise rational design from shape, size and functionalisation of pores" in a 1995 Nature report.[4] Since then, there has been an explosion in the number of groups investigating, and papers published, about MOFs, under the broader field of (porous) coordination polymers. The number of citations for coordination polymers was 204 in 1996 and 2745 in 2012.[5] Interestingly H. Kitagawa reports ~400 citations for 1996.[6] This highlights a controversy in naming these materials as different research groups use either

metal- organic framework (MOF), porous coordination polymer (PCP) or porous coordination network (PCN). This may reflect an absence of official nomenclature by IUPAC.[7] They have gone some way to rectify this by publishing new recommendations for the nomenclature of polymers, in 2012, that is a prerequisite for defining the nomenclature for coordination polymers, which MOFs are a subsection of.[8]

One of the first reported MOF structures, and rationale for its framework, came in 1989 by Robson and Hoskins. They demonstrated an extended 3-D networks with copper(II) and a tetrakis(4-cyanophenyl)methane rod-like connecting unit, Figure 1.2.[9]

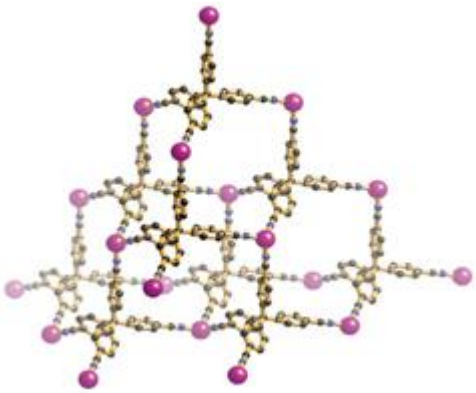

Figure 1.2. Framework of $[Cu(C(C_6H_4CN)_4)]$. Cu: purple, C: black, N: blue.[9]

They had the foresight to see the potential of the materials that they had prepared and listed their potentially interesting molecular sieve, ion-exchange and mechanical properties. Robson also goes on to say that, after appropriate functionalisation, the materials may be tailor-made for heterogeneous catalysis.[9]

One of the first dedicated MOF groups involved Yaghi and in 1995 he reported a cobalt(II) BTC (BTC = benzene-1,3,5-tricarboxylate) 2-D layered MOF, $[Co_3(BTC)_2(py)_6]\cdot 2py$ with the octahedral metal axial positions capped by pyridine (py) ligands.[4] It shows selectivity in the guest molecules that can be incorporated into the voids between the layers with pyridine and nitrobenzene. The guests interact through π-stacking with the BTC in the framework and they can be adsorbed and desorbed reversibly with retention of the framework, as witnessed by powder X-ray diffraction (PXRD) and FT-IR spectroscopy.[4]

It is useful to see some examples of how common basic building units can extend in each dimension. The secondary building unit (SBU) in a MOF is referred to when describing the arrangement of the metal nodes and coordination modes of incorporated linkers. Generally,

the overarching framework can be deduced by linking together SBUs from their points of extension. A common SBU consists of two metal cations bridged by four carboxylate anions, for example in the paddle wheel SBU of $[Zn_2(BDC)_2(OH_2)_2]\cdot 2DMF$, MOF-2, (BDC = 1,4-benzenedicarboxylate), Figure 1.3.[10] The $[Zn_2(O_2CR)_4]$ SBU nodes connect through the BDC ligands leading to an extended structure.

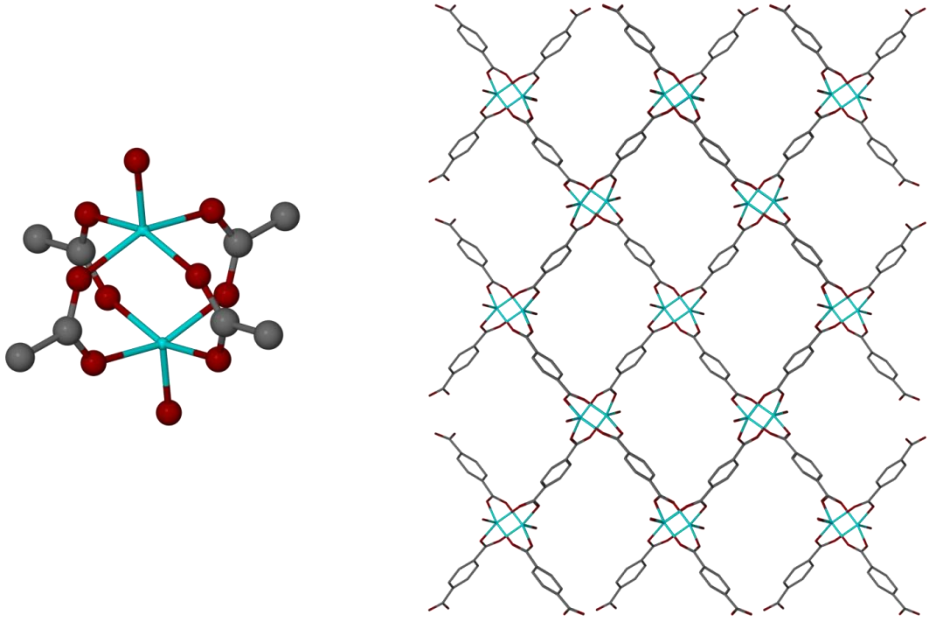

Figure 1.3. (left) $Zn_2(O_2CR)_4$ paddle wheel SBU. **(right)** Extended 2-D framework of MOF-2. Zn: blue, O: red, C: black. Axial solvent oxygens shown.[10]

The simplest way for SBUs to link together is by extending in one dimension. Examples of one-dimensional MOFs are chains, ladders and helices, Figure 1.4. There is a tendency to have less porosity in materials based on chain and ladder structures because the 1-D networks can often pack close together. In the 1-D MOF, $[Cd(BPDC)(phen)_2]$ (BPDC = 1,1'-biphenyl-4,4'-dicarboxylate, phen = 1,10-phenanthroline), the cadmium(II) ions are linked to each other by BPDC anions and capped with two chelating 1,10-phenanthroline per metal, Figure 1.4(a). The chains pack in the solid state due to van der Waals forces and π-stacking between adjacent aromatic moieties from different chains.[11]

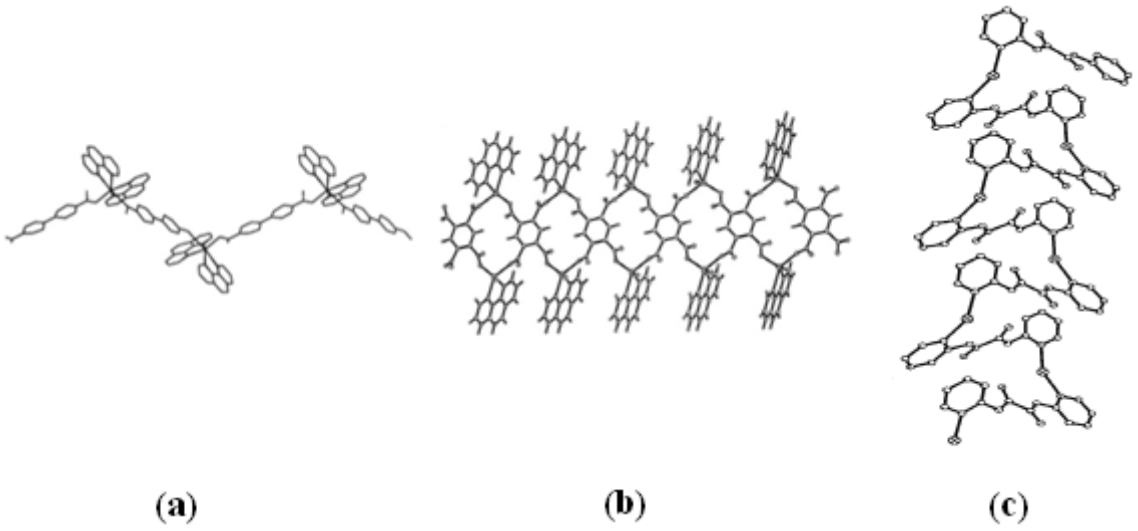

Figure 1.4. (a) Zig-zag chain of $[Cd(BPDC)(phen)_2]$,[11] **(b)** Ladder structure of $[Cd_2(BTEC)(phen)_2(H_2O)_2]$,[11] **(c)** One helical chain of [Ag(*N*,*N'*-di(2-pyridyl)oxamide)]$^+$[NO_3]$^-$.[12]

In the same publication by Qiu and co-workers, substituting BPDC for benzene-1,2,4,5-tetracarboxylate (BTEC), in the reaction, the framework that is formed is a one dimensional ladder-like structure, $[Cd_2(BTEC)(phen)_2(H_2O)_2]$, with carboxylate rungs and a [Cd(phen)] backbone, Figure 1.4(b).[11] The final example of a one-dimensional MOF is a helical framework. [Ag(*N*,*N*'-di(2-pyridyl)oxamide)]$^+$[NO_3]$^-$ forms helical chains held together by π-π interactions between pyridyl ligands. Neighbouring helices pack together by hydrogen bonding, Ag···O-C interactions and bridging nitrate anions, Figure 1.4(c).[12]

Two-dimensional MOFs commonly present as lamellar structures like those shown in Figure 1.5. For example, $[Zn_2(BDC)_2(DMF)_2]$, is a typical flat square-grid sheet (*c.f.* Figure 1.3) consisting of a paddle wheel SBU and with layers held together by van der Waals forces and π-stacking between organic groups in neighbouring layers, along with interactions between the framework and DMF in the pores, Figure 1.5(a).[13] A more complex example, building upon the zigzag chain, the corrugated sheet of [Cd(BDC)(phen)] (phen = 1,10-phenanthroline),[11] stacks together with DMF in small pockets between layers, Figure 1.5(b). In contrast to the aforementioned materials, the example of a two-dimensional MOF, $[Zn_3(BPDC)_3(DMF)_2]$,[13] forms hexagonal sheets that are held together by van der Waals forces, π-stacking and interactions with DMF, similar to those in the square-grid example of Figure 1.5(a).

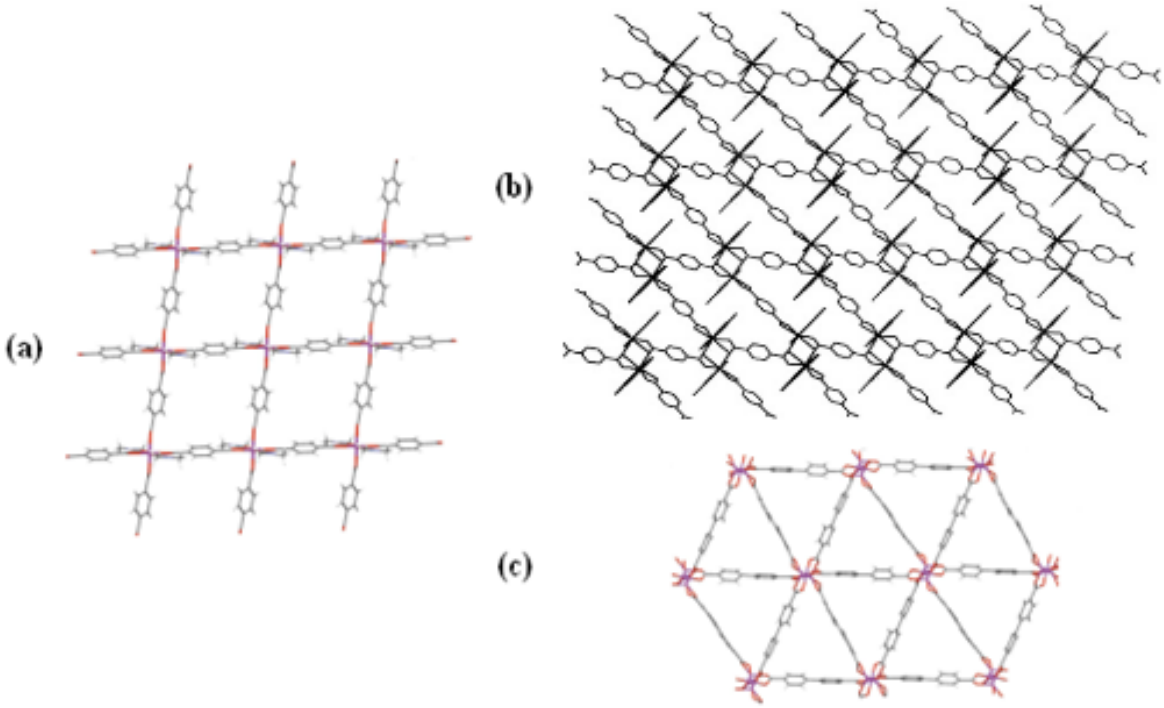

Figure 1.5. (a) 2-D square-grid layer of $[Zn_2(BDC)_2(DMF)_2]$.[13] **(b)** 2-D layer of [Cd(BDC)(phen)].[11] **(c)** 2-D hexagonal sheet of $[Zn_3(BPDC)_3(DMF)_2]$.[13]

Three-dimensional networks tend to have low crystal packing efficiency caused by the rigidity, shape and size of the linker. This can lead to a high percentage of the unit cell being empty space. The easiest 3-D framework to visualise is the octahedral net (Reticular Chemistry Structure Resource (RCSR) symbol **pcu-a**, also known as polycubane),[14] for which MOF-5, $[Zn_4O(BDC)_3]$, is a well known example, Figure 1.6(a).[15] The $[Zn_4O(O_2CR)_3]$ SBU extends in three dimensions through the carboxylate groups, of the BDC ligands, in all three dimensions. Channels are a typical feature of this framework type.

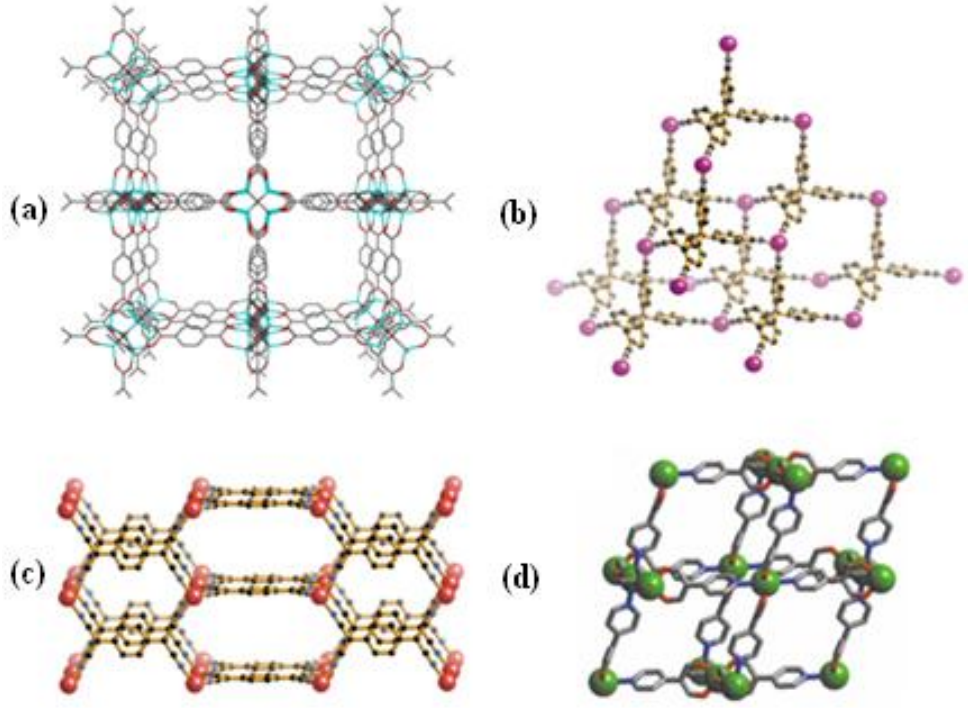

Figure 1.6. (a) 3-D octahedral net of MOF-5.[15] **(b)** Diamondoid net of $[Cu(C(C_6H_4CN)_4)]$.[16] **(c)** PtS net of $[Cu(TCNQ)]\cdot(Ph_3PMe)$.[16] **(d)** NbO cage of $[Cu(pyac)_2]\cdot 0.5EtOH\cdot 3H_2O$.[17] Guest molecules are omitted for clarity.

In contrast the diamond-like net (**dia**) is formed in $[Cu(C(C_6H_4CN)_4)]$.[16] Each node and linker exhibit tetrahedral coordination with large apertures between ligands, Figure 1.6(b). Frameworks that assemble from 4-coordinate square building units and 4-coordinate tetrahedral building units are designated PtS networks, for example, $[Ph_3PMe][Cu(TCNQ)]$ (TCNQ = tetracyanoquinodimethane), with $TCNQ^{2-}$ as a planar square linker and a Cu(I) ion as the tetrahedral node, Figure 1.6(c).[16] NbO type frameworks are related to octahedral nets, but with the corner and middle nodes removed. For example in $[Cu(pyac)_2]\cdot 0.5EtOH\cdot 3H_2O$, (Hpyac = 3-(4-pyridyl)pentane-2,4-dione), the cage contains pores linked to each other by smaller openings, Figure 1.6(d).[17]

1.2. The Design of MOF Architectures

1.2.1. Carboxylate Linkers

Some of the MOFs in the previous section were designed with the overall framework in mind before the ligands and metals were chosen. This section will address the design of MOFs. A range of carboxylic acids used in MOF syntheses are shown in Figure 1.7.

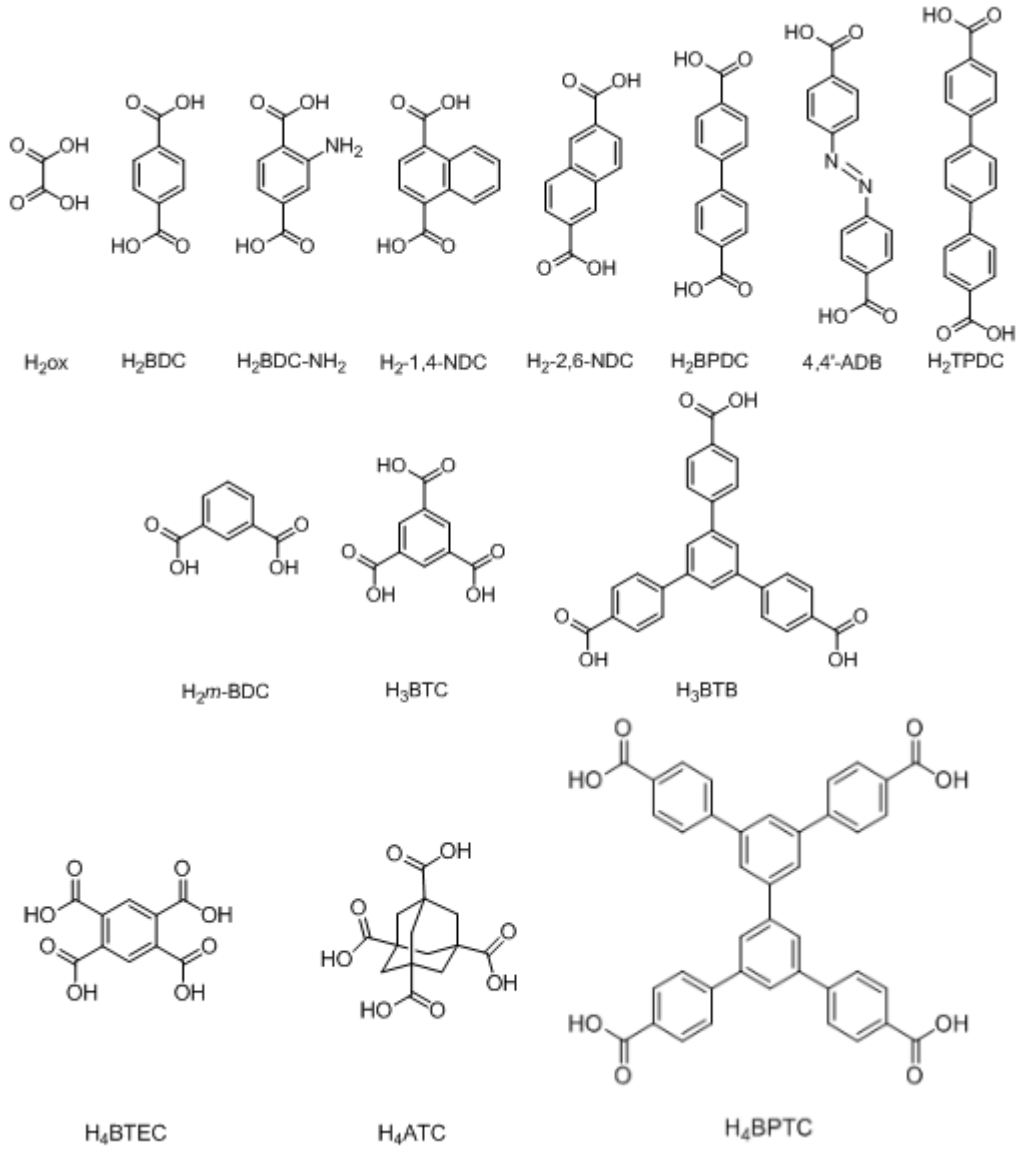

Figure 1.7. Range of carboxylic acids used in MOF synthesis.

An isoreticular series is made of similar overall framework topologies. In such a series the surface area can be proportional to the size of the ligand.[18] New design routes can be achieved using augmentation (increasing size) and decoration of ligands of MOFs that

have already been shown to produce porous (containing empty voids) materials, with an emphasis on open frameworks for maximum accessible surface area.

In 1999 the synthesis and structure of MOF-5 was reported by Yaghi and co-workers.[15] This was a watershed moment for the field. The synthetic conditions described vapour diffusion of triethylamine into a solution of zinc(II) nitrate and benzene-1,4-dicarboxylic acid (H_2BDC) in *N,N'*-dimethylformamide (DMF). Hydrogen peroxide (H_2O_2) was added to facilitate the formation of a central tetrahedral oxide evidenced from the single crystal data. MOF-5 has the formula $[Zn_4O(BDC)_3]$. The surface area, S_{BET} = 3800 m^2g^{-1} is a measure of porosity and is significantly higher (a factor of four) than zeolitic materials that came before, which made these types of materials so interesting for many applications. This synthetic method has been simplified in the ensuing years and a solvothermal route in *N-N'*-diethylformamide (DEF) is now routinely employed without the use of H_2O_2, and gives the product within 2 h,[19, 20] Scheme 1.1.[18]

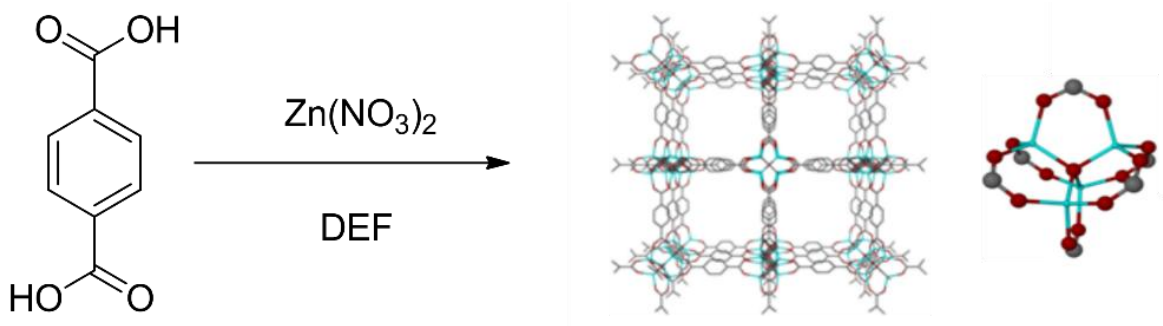

Scheme 1.1. MOF-5 Synthesis showing the framework (middle) and SBU (right). Zn = blue, C = black, O = red.[18]

Each node consists of four zinc(II) cations surrounding a tetrahedral oxide anion (μ_4-O^{2-}). This node is bound by six BDC carboxylates, making the SBU and the BDC ligands link nodes together to assemble an octahedral network, Scheme 1.1. The crystals can grow to millimetre scale and the free volume in the resulting framework is 79.2 %, after removal of the guest solvent molecules by activation, resulting in the low density of the crystals (0.61 gcm^{-3}).[18] Activation is the method by which the voids (*e.g.* 11.2 Å channels in MOF-5) of a material are emptied of guest solvent molecules, usually by heat and vacuum, present from a reaction. The dicarboxylate linkers can be systematically increased in size and functionality (augmentation and decoration respectively) resulting in a reticular series, Figure 1.8.[18]

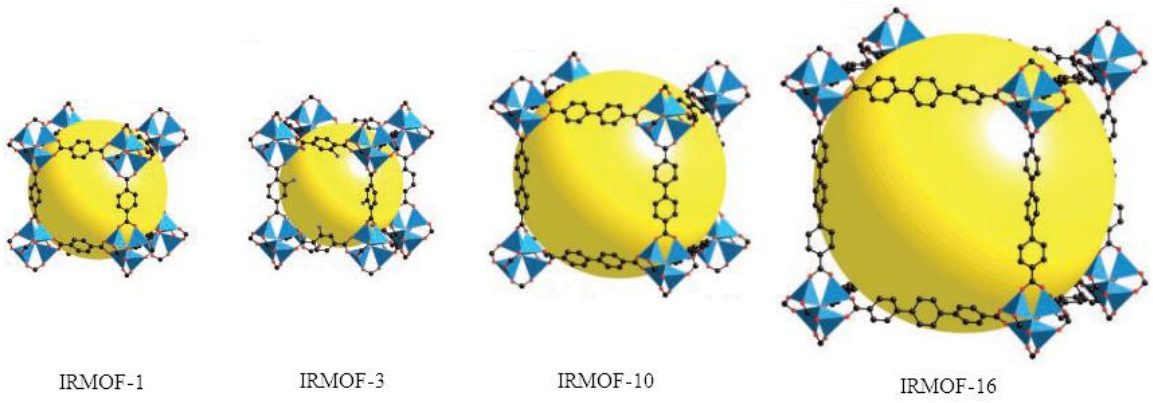

Figure 1.8. An isoreticular series of cubic IRMOFs showing augmentation and decoration.[18] Pores shown by yellow sphere.

The largest of these MOFs (IRMOF-16) has large voids (19.1 Å diameter) and low density, 0.21 gcm^{-3}.[18] The thermal stability of the IRMOF series is relatively high at ~450 °C, though this is low compared to other porous materials, such as zeolites.[19] What MOFs lack in thermal stability is compensated in surface area, IRMOF-3 (amino tagged MOF-5) has a surface area in the range, S_{BET} = 2400-2600 m^2g^{-1} depending on the method of activation.[20]

These materials have to be handled in a dry atmosphere because as the size of linker increases, moisture sensitivity increases. MOF-5 will decompose to the less porous framework material, $[Zn_3(OH)_2(BDC)_2]\cdot 2DEF$ (MOF-69C),[21] in less than one minute, in atmospheric humidity and in less than 10 seconds when placed in water (as the H_2O molecules break up the SBU by coordinating to the tetrahedral zinc ions).[22] These IRMOF materials are also unstable in acidic and basic environments for similar reasons: H^+ cations reprotonate carboxylate groups and OH^- anions coordinate to the metal ions.

The Férey group, at the Material Institute de Lavoisier, use the MIL acronym for their porous frameworks. An example is the 3-D MOF $[Cr_3(O)F(H_2O)_2(BDC)_3]\cdot nH_2O$ (where n is ~25), MIL-101(Cr).[23] The SBU has a μ_3-O oxide bridging three pseudo-octahedral Cr^{3+} ions, with six bridging BDCs and the final metal sites being taken up by two waters and a fluoride anion, Scheme 1.2.[23] The extended structure has two types of mesopores: the larger having hexagonal windows of ~14.5 Å by 16 Å into a 34 Å diameter pore; the smaller having pentagonal windows of ~12 Å width into a 24 Å diameter pore, Figure 1.9. There are also micropores present with an aperture of ~8.6 Å.[23] The MOF is stable in

aqueous acidic solution but can be digested by a base, such as NaOH. The BET surface area of 4100 m^2g^{-1} is considerably higher than the IRMOF series.

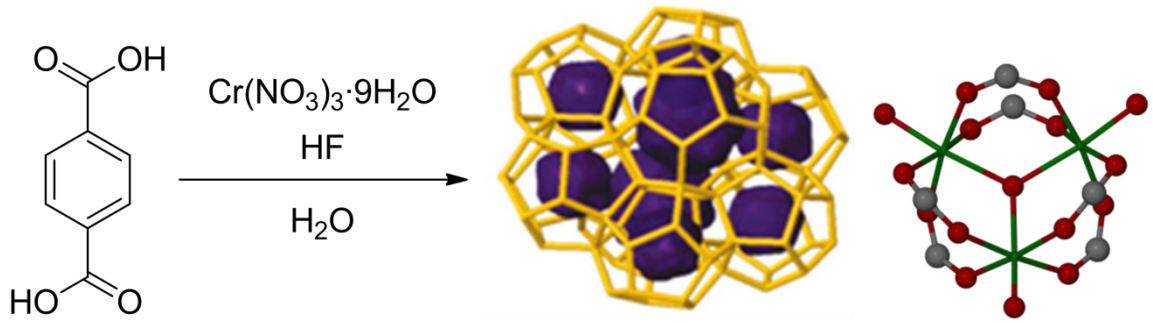

Scheme 1.2. MIL-101(Cr) synthesis, mesoporous framework and SBU. Cr: green, C: grey, O: red. Pores represented by purple polyhedra.[23]

MOFs stable in acid and/or base are much sought after in industry as they can withstand harsh conditions. One such example containing BDC is *$[Zr_6O_4(OH)_4(BDC)_6]$* (UiO-66, UiO = *Universitetet i Oslo)* reported by Cavka, Figure 1.9.[24] The framework's pore dimensions are 15.7 x 12.3 Å and result in a BET surface area of 1067 m^2g^{-1}. The $[Zr_6O_4(OH)_4]$ SBU is resistant to degradation by most acid and bases, with the exception of those containing a fluoride, and it has the added benefit of decomposing at 540 °C. These attributes increase the potential applications for use in aqueous conditions, of varying pH, and at a high temperature.

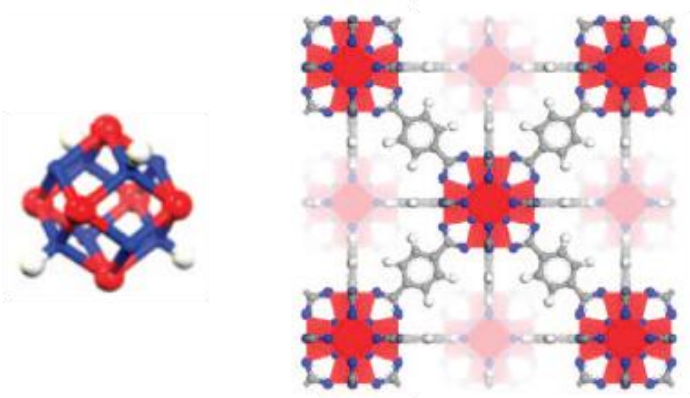

Figure 1.9. (left) SBU and **(right)** framework of UiO-66. Zr: red, C:grey, O:blue, H:white.[24]

Exploring ligands other than BDC, such as the tricarboxylate BTC, $[Cu_3(BTC)_2(H_2O)_3]$ (HKUST-1, HKUST = Hong Kong University of Science and Technology) reported by Williams and co-workers in 1999.[25] The SBU is that of a Cu_2 paddle-wheel extending in three dimensions through four BTC ligands. Channels of 1 nm diameter exist down the [100] direction of the cubic unit cell, Figure 1.10(a). The axial water molecules are usually

a good indicator that a MOF is stable to water exposure; however HKUST-1 will decompose with prolonged water contact.

MOF-177, $[Zn_4O(BTB)_2]$ was reported by Matzger, from the assembly of BTB (benzene-1,3,5-tribenzoate) and the $[Zn_4O(O_2CR)]$ SBU.[26] In an attempt maximise the surface area, BTC was extended by the addition of an extra benzene ring in each arm of the ligand giving BTB (augmentation) and in the reaction with zinc nitrate results in pores of 10.8 Å, Figure 1.10(b), and a very large BET surface area of 4750 m^2g^{-1}.[26]

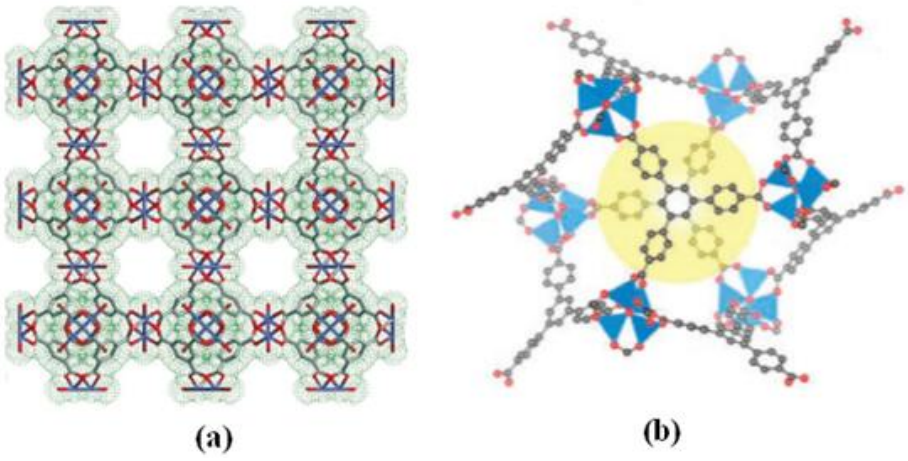

Figure 1.10. (a) View down channels of HKUST-1.[25] **(b)** Pore of MOF-177.[26] Cu: light blue, Zn: blue polyhedra, C:grey, O:red.

Tetracarboxylates have also been used in MOF synthesis, for example MOFs made in the University of Nottingham (NOTTs) have some of the largest BET surface areas for indium MOFs (NOTT-202a, S_{BET} = 2220 m^2g^{-1}). Schröder and co-workers showed that desolvating the framework of $[Me_2NH_2]_7[In_4(L)_7]\cdot 48DMF\cdot 40H_2O$, (NOTT-202, L = biphenyl-3,3',5,5'-tetra-(phenyl-4-carboxylate)) undergoes a structural change to form NOTT-202a. This new MOF, formed by a simple PSM, consists of four large tetracarboxlyate ligands surrounding a 7-coordinate indium(III) centre, with dimethylammonium counter-cations in the channels. Rhombic channels running along the crystallographic *b*-axis measure 9.0 x 9.0 Å, Figure 1.11(a).[27]

MOFs containing calix[4]arenes are an interesting class of compounds because of the ability to have frameworks with intrinsic and extrinsic pores.[28] The bowl of the calixarene has intrinsic porosity and the pores of the framework give the potential for forming extrinsic pores. Burrows *et al*. reported the calix[4]arene based MOF,

$[Cu_2(caldc)_2(DMF)_2]$, (caldc = calix[4]arene dicarboxylate). The 2-D sheets are shown in Figure 1.11(b) and illustrate the hourglass shaped pores.[28]

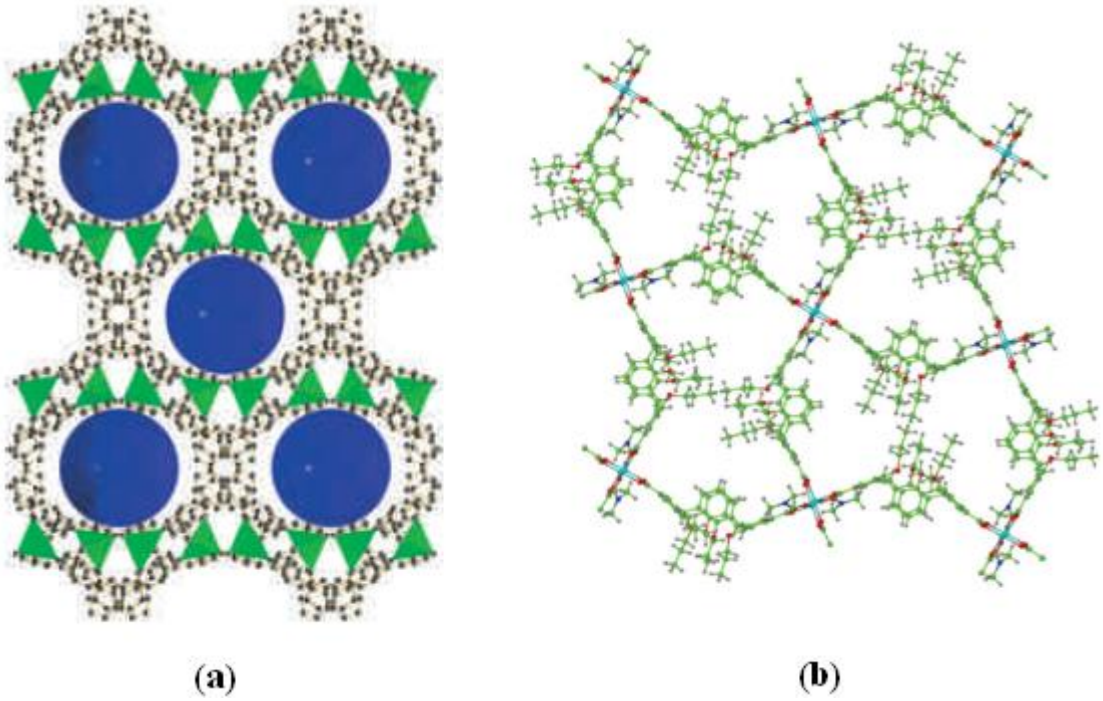

Figure 1.11. (a) View along channels (blue circles) of NOTT-202a. In: green, O: red, C: grey, H: grey.[27] **(b)** 2-D sheets of $[Cu_2(caldc)_2(DMF)_2]$, Cu: Blue, O: red, C: green, H: grey.[28]

To date, the calix[4]arene materials have not been successfully activated, by removal of DMF, however computational simulations suggest the bowls could favourably bind H_2. There have also been advances in this area with some mixed ligand thiacalix[4]arene and nitrogen pillaring ligand based MOFs, e.g. $[Co_2(TCTA)(bpy)]$, (TCTA = *p-tert*-butyl-thiacalix[4]arene tetraacetate), by Kim *et al.*[29]

The final example of MOFs consisting of carboxylate ligands pertain to combinations of linkers, specifically BTB (benzene-1,3,5-tribenzoate) and BDC. The stoichiometry of the reactants plays an important part in the growth of different MOFs from the same constituent ligands. Matzger *et al*. reported that varying ratios of ligands can result in three different MOFs, of these phase-pure $[(Zn_4O)_3(BTB)_4(BDC)_3]$, (UMCM-1, University of Michigan Crystalline Material) is formed between reactant ratios of 1:1 and 2:3, BTB:BDC. MOF-177 is favoured with an excess of BTB and MOF-5 with an excess of BDC.[30]

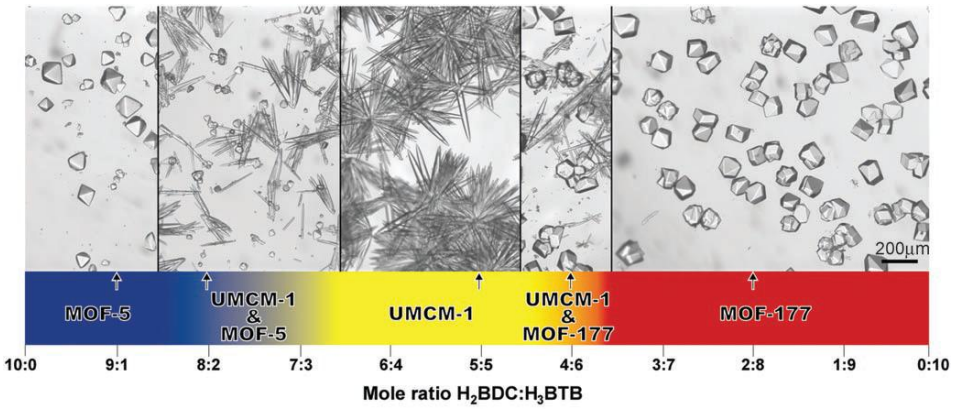

Figure 1.12. Crystalline products as a function of varying ligand ratios in the reaction between $Zn(NO)_3 \cdot 4H_2O$, H_2BDC and H_2BTB, in DEF at 85 °C for 48 h.[30]

UMCM-1 has the $[Zn_4O(O_2CR)]$ SBU, Figure 1.13(a), nine of which form a pore of diameter 1.6 nm, Figure 1.13(b), when the BTB linkers are incorporated. Six of those cages surround a hexagonal 1-D channel of maximum width 3.2 nm, Figure 1.13(c). This leads to a very open framework with S_{BET} = 4160 m^2g^{-1}, the largest recorded for a MOF when reported in 2008.[30] This framework is very tolerant of incorporating a 2-substituted BDC ligand instead of BDC during MOF formation and the resulting functionalised MOF is susceptible to PSM reactions.[31]

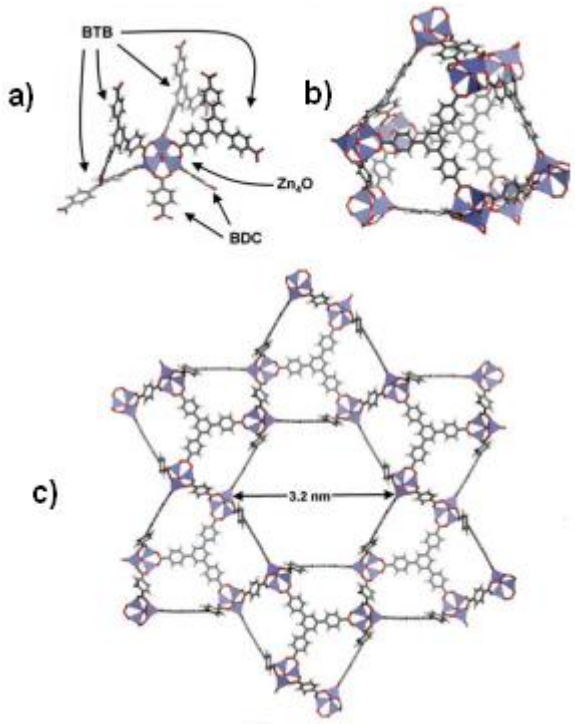

Figure 1.13. (a) BTB linkers surrounding the node of UMCM-1, **(b)** Smaller pore encased by nine SBUs, **(c)** View down larger 1-D channel.[30]

1.2.2. Nitrogen-donor linkers

The most common N-donor linkers utilised in MOF formation are heterocycles e.g. pyrazine (pyz). Similarly to carboxylates they are rigid, due to aromaticity, which means that they can be deployed in rational synthesis. The most common N-donor linkers used in MOF syntheses are summarised in Figure 1.14.

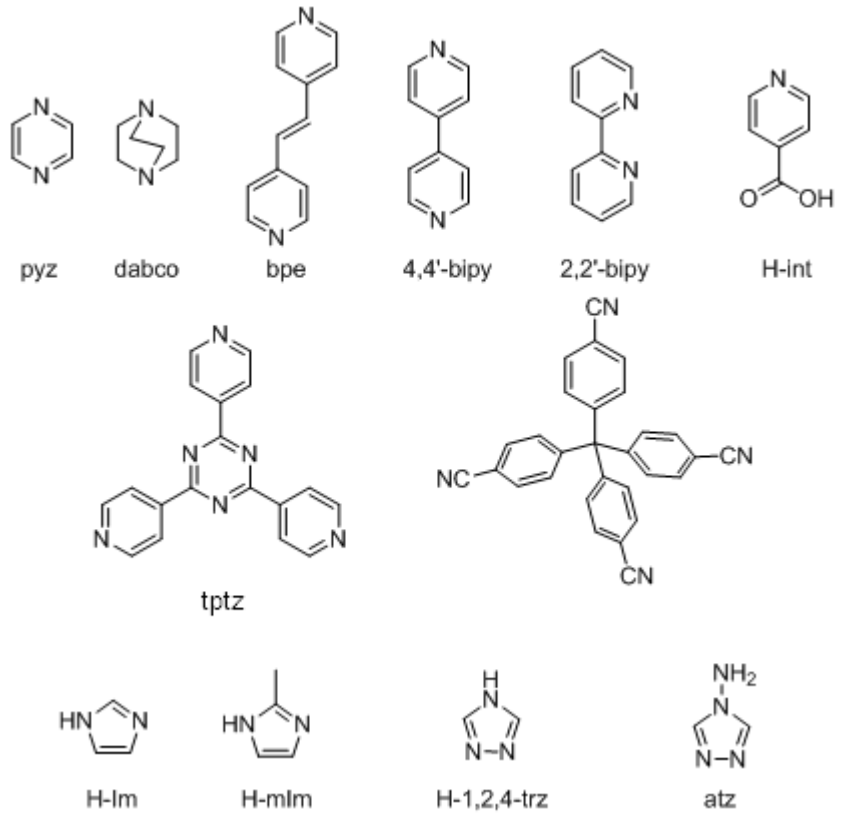

Figure 1.14. A selection of nitrogen-donor linkers

$[Zn_2(BDC)_2(dabco)]$, DMOF-1 (dabco-MOF-1), is based on a 2-D square grid $[M_2(L)_2]$ sheet with the bridging *N,N'*-donor ligand, 1,4-diazobicyclo[2.2.2.]octane (dabco),) bridging the nodes of adjacent sheets into a 3-D framework, Figure 1.15(a).[32] This is an example from Kim's group of designing MOFs through mixing pillaring ligands, and carboxylates based on predictable SBUs of certain metals. The N-donor linker dabco was chosen because it is more basic than pyrazine and has a greater chance of holding the sheets together. One dimensional channels (7.5 Å diameter) run down the crystallographic *c*-axis interlinked in three dimensions by windows of ~4 Å, yielding a surface area of 1450 m^2g^{-1}.

A series of structures from Kitagawa, including [Zn(IP)(bipy)] (CID-1, CID = coordination polymer with interdigitated structure) incorporates 4,4'-bipyridine (bipy) and isophthalate (IP = 1,3-BDC) linkers, Figure 1.15(b).[32] The arene rings point into the pores of adjacent sheets and this 2-D interdigitated structure allows for reversible breathing when absorbing guest molecules. The pores open more at higher concentration of guest molecules, shown by a two step MeOH adsorption isotherm.[33]

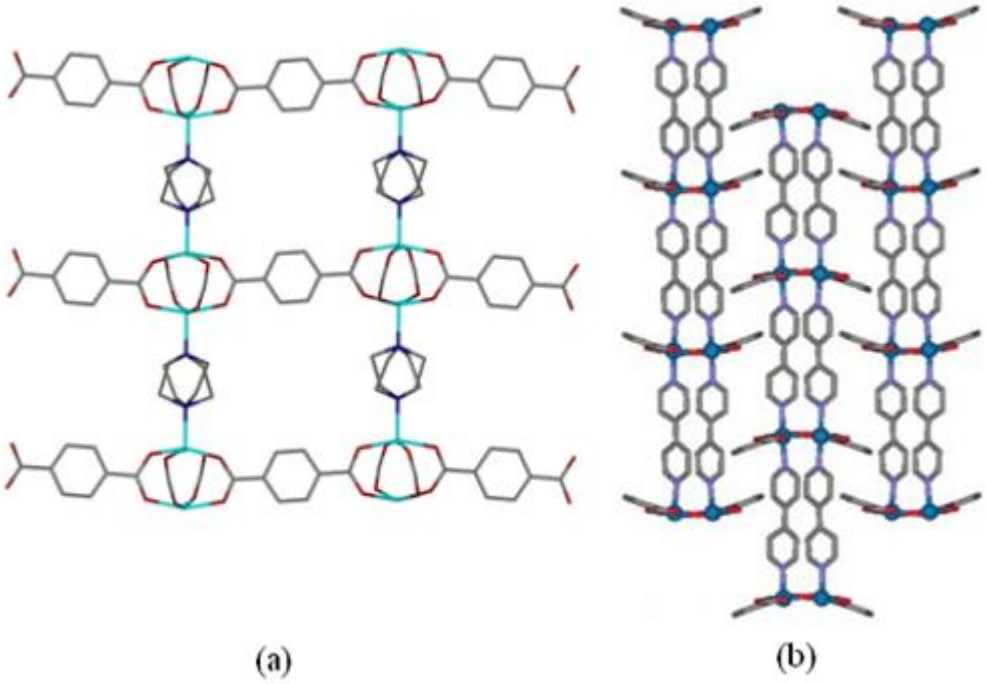

Figure 1.15. (a) View along *a*-axis of DMOF-1 showing the 4 Å windows.[34] **(b)** View along *a*-axis of CID-1. Zn: light blue, N: dark blue, C: grey, O: red. H atoms and solvent omitted.[32]

The main class of anionic nitrogen based MOFs is undoubtedly zeolitic imidazolate frameworks (ZIFs). They have a slightly different genesis to MOFs in that there is precedence in the early 1980s, with Cucurbital.[35] A well utilised and reported example is $[Zn(mIm)_2]$ (ZIF-8, mIm = methyl imidazolate). Yaghi reported the extended structure using 2-methyl imidazolate (mIm) as the organic linker.[36] A simple tetrahedral zinc centre coordinated to four imidazolates forms a 3-D network with pores of diameter 11.6 Å and pore apertures of width 3.4 Å, resulting in S_{BET} = 1630 m^2g^{-1}, Scheme 1.3. The major advantage of these structures over the open framework carboxylates is that ZIFs are stable in water and can be activated and retain crystallinity when exposed to the atmosphere, which explains the interest in these systems for industrial applications.[37]

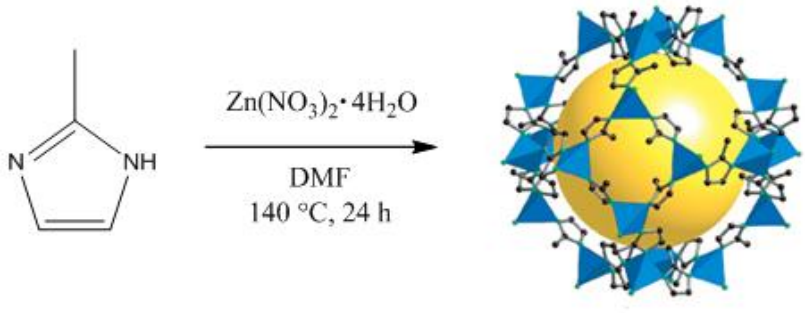

Scheme 1.3. Synthetic conditions for ZIF-8 from H-mIm. Zn: blue, C: black. Yellow sphere, of diameter 11.6 Å, represents the pore.[36]

Other than purely nitrogen-linker based MOFs, O and N-donor atoms can be part of the same ligand. The MOF $[Cu(int)_2]\cdot DMF$ (int = isonicotinate) was reported by Chen *et al.*[38] The framework has Cu(II) ions running along the *a*-axis, bridged by carboxylate groups, Figure 1.16. N-donor atoms from the ligands cap the distorted square pyramidal Cu(II) atoms, forming 3-D channels of width 10 x 11 Å. The material was synthesised solvothermally in DMF, from $Cu(NO_3)_2$ and int, after 5 days reaction time.

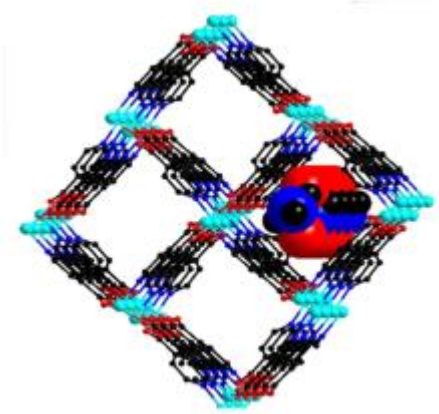

Figure 1.16. View down the channels of $[Cu(int)_2]\cdot DMF$. Cu: light blue, C: black, O: red, N: dark blue. DMF shown by space filling model.[38]

It is clear that ZIFs are generally more stable than carboxylate MOFs with respect to hydro stability and industrial research is more interested in this property of the material, but MOFs have the largest reported surface areas at this time so are still relevant for many applications.

1.2.3. Phosphonate linkers

It is not just carboxylates that can bridge metal ions and form SBUs. Phosphonates can form interesting extended frameworks and a selection of linkers is given in Figure 1.17.

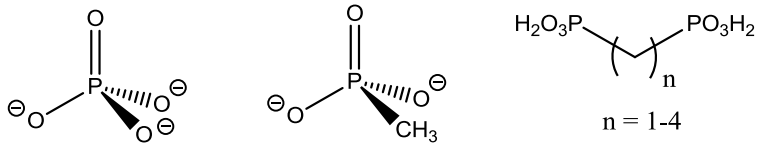

Figure 1.17. Selection of phosphonates and phosphinic acids used in MOF synthesis.

Phosphonates can emulate the Zn_4O SBU as seen in the case of the MOF, $[Na_3][Zn_4O(PO_4)_3]\cdot 6H_2O$, by Harrison and co-workers, Figure 1.18.[39] The framework topology is similar to MOF-5 but with counter-cations in the channels coordinated to the phosphonate groups. Analogous structures were made with other Group 1 metals: Li, K, Rb and Cs, as counter-cations; and also with arsenates instead of phosphonates.

MIL-48 reported by Férey and co-workers has the formula $[Na][Zn_2(OH)(O_3P\text{-}CH_2\text{-}PO_3)]\cdot 1.5H_2O$.[40] This diphosphonate contains two different SBUs. The first is a chain of ZnO_4 tetrahedra and the second is a mixed hexameric column, consisting of two ZnO_4 tetrahedra and two methylenediphosphonate groups. Therefore the overall 3-D architecture has channels that encapsulate Na^+ cations and water molecules. It was synthesised hydrothermally in the presence of NaOH, Figure 1.18(b).

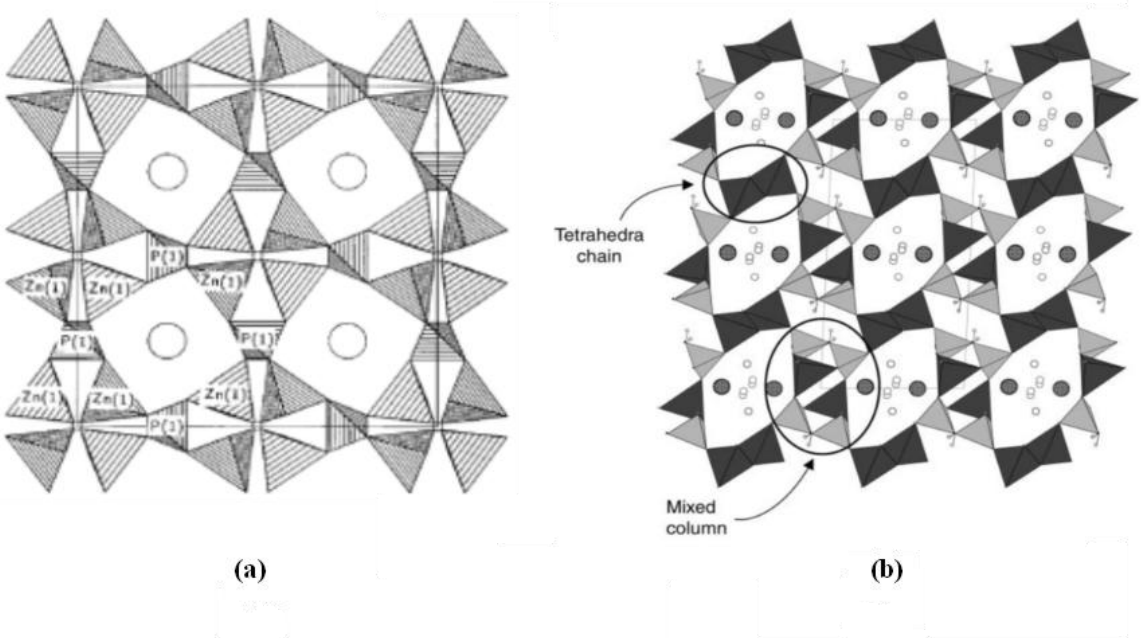

Figure 1.18. (a) $[Na_3Zn_4O(PO_4)_3]\cdot 6H_2O$.[39] **(b)** MIL-48 view down chain SBUs.[40]

1.3. Interpenetration

As the pore volume of a MOF increases so does the chance of interpenetration, or catenation (depending on the framework symmetry). This is where one or more independent entangled frameworks are present and though there are no formal interactions between them they cannot be separated without bond breaking. Interpenetration occurs during self-assembly because the pores are large enough to accommodate one or more ligand moieties. Porosity is generally reduced by interpenetration, which range from 2-fold to 12-fold.[6] (SBUs of independent frameworks can also be held in close proximity with no interactions between them and this can have applications in nanowire formation from MOF precursors).[41]

Compounds of the IRMOF series reported by Yaghi *et al.* that are doubly interpenetrated consist of the longer length ligands: 1,1'-biphenyl-4,4'-dicarboxylate, (BPDC) IRMOF-9; 4,5,9,10-tetrahydropyrene-2,7-dicarboxylate, (HPDC) IRMOF-11; pyrene-2,7-dicarboxylate, (PDC) IRMOF-13; and [1,1':4',1''-terphenyl]-4,4''-dicarboxylate, (TPDC) IRMOF-15. They reported that the non-interpenetrated structures can be accessed by simply repeating the reaction in more dilute conditions.[18] Catenation can also be overcome by using template effects, for example using a larger molecule solvent. In the case of UMCM-1, DMF yielded no framework or crystals of any kind, whereas DEF gave the porous framework.[30]

Frameworks that often interpenetrate are the PIZOF series.[42] They are zirconium based MOFs that have the UiO SBU, $[Zr_6O_4(OH)_4(O_2CR)_6]$, but rather than BDC, PIZOFs consist of elongated ligands consisting of three phenyl groups, linearly 1,4-connected by ethyne groups. PIZOF-2 has the formula $[Zr_6O_4(OH)_4(L)_6]$, L= 4,4'-((2,5-dimethoxy-1,4-phenylene)bis(ethyne-2,1-diyl))dibenzoate. The ligand in this system is long enough, and the voids large enough, to allow extra ligands in and accommodate a secondary tetrahedral framework, shown in Figure 1.19.[42]

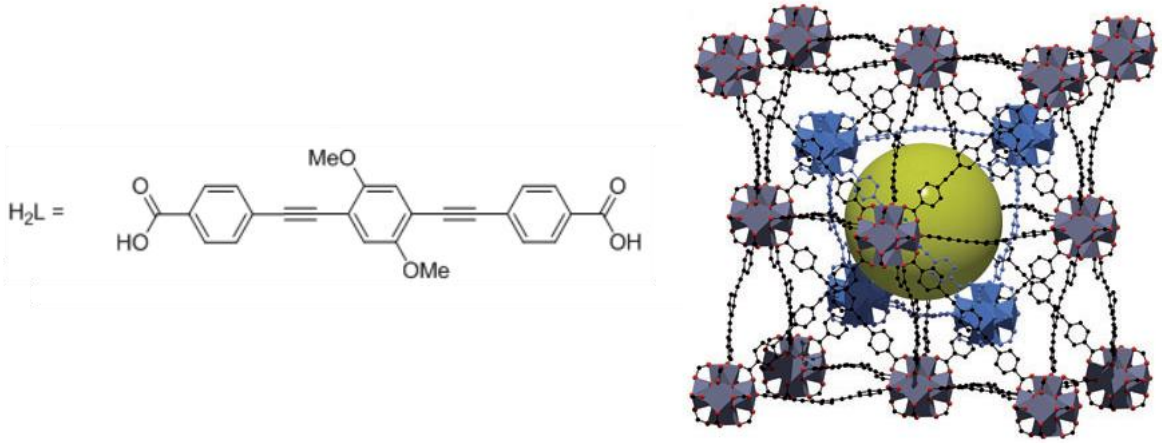

Figure 1.19. (left) Large linker H_2L, R^1,R^2 = OMe. **(right)** Interpenetrated structure of PIZOF-2. Zr: blue and grey polyhedra, C: black and blue, O: red. Yellow sphere represents tetrahedral shaped pore of diameter 19 Å.[42]

One of the most interpenetrated structures reported so far has been a ten-fold interpenetrated MOF of $[Ag(ddn)_2]\cdot NO_3$ (ddn = 1,12-dodecanedinitrile). This MOF is based on a very large adamantanoid cage structure, as shown in Figure 1.20.[43]

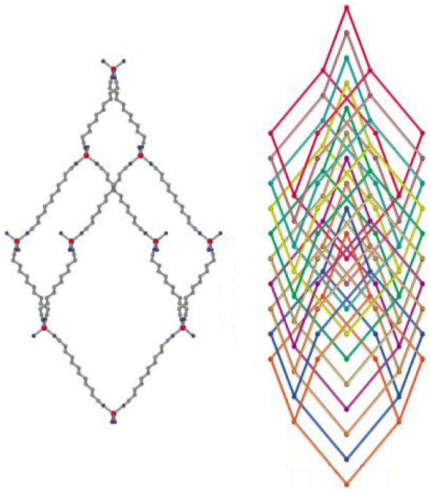

Figure 1.20. (left) One adamantanoid cage. (Ag: red, N: blue, C: grey). **(right)** Schematic representation of the ten-fold interpenetrated structure.[43]

1.4. Synthesis of MOFs

1.4.1. Synthetic Methods

The earliest methods for synthesising MOFs were simple solvothermal or hydrothermal processes with sometimes breathtaking results. These approaches are still the main-stay of synthetic methods since their adoption from the synthesis of zeolites.[44] In a typical experiment a metal salt and a carboxylic acid are dissolved together, sealed and placed in an oven until the reaction is complete. DMF is a good solvent because of its large solubility range and high boiling point, as well as its ability to act as a weak base to deprotonate the carboxylic acids. When the reaction has gone to completion, the products crystallise from the mother liquor.

The merits of solvothermal methods over more complex methods include large crystal size, easy scalability and the availability of high throughput methods. The option of using microwave assistance is available to augment the reaction. Disadvantages can include long reaction times, low percentage yields, high temperatures needed, and the use of toxic solvents (*e.g.* DMF).[45]

Microwave-assisted synthesis can speed up reaction times but generally yield very small crystals. Lin and co-workers used this method to synthesise MIL-101(Fe) in DMF at 150 °C. They obtained a modest yield of 20 % and particle sizes of ~200 nm. In trying to make the amino functionalised analogue structure they could only get incorporations of less than 20 mol % amino groups.[46] MOF-5, has also been synthesised with microwave assistance at 95 °C for 9 minutes,[47] with a powder X-ray diffraction pattern as good as solvothermal methods but with particle sizes of ~5-25 μm (compared to the solvothermal route of ~500 μm).

Vapour diffusion is a synthetic technique that involves dissolving a metal source and ligand in solvent, *i.e.* DMF, and placing this in an open container surrounded by a solution of volatile base, such as triethylamine. The base then diffuses into the reaction mixture, thus increasing the acidic ligand:conjugate base ratio by deprotonation, thereby facilitating MOF growth. This room temperature strategy can help form large crystals due to slow reaction times, Figure 1.21(a).[48]

An example of a MOF synthesis using vapour diffusion, by Wu and co-workers, is in the synthesis of [Pb(1,4-NDC)(DMF)].[48] $Pb(NO_3)_2$ and H_2-1,4-NDC (naphthalene

dicarboxylate) were dissolved in DMF in one container and triethylamine (TEA) was dissolved in DMF in a separate container. Slow diffusion of TEA into the solution with the metal and ligand gave slow growth of the MOF product, Figure 1.21(b).

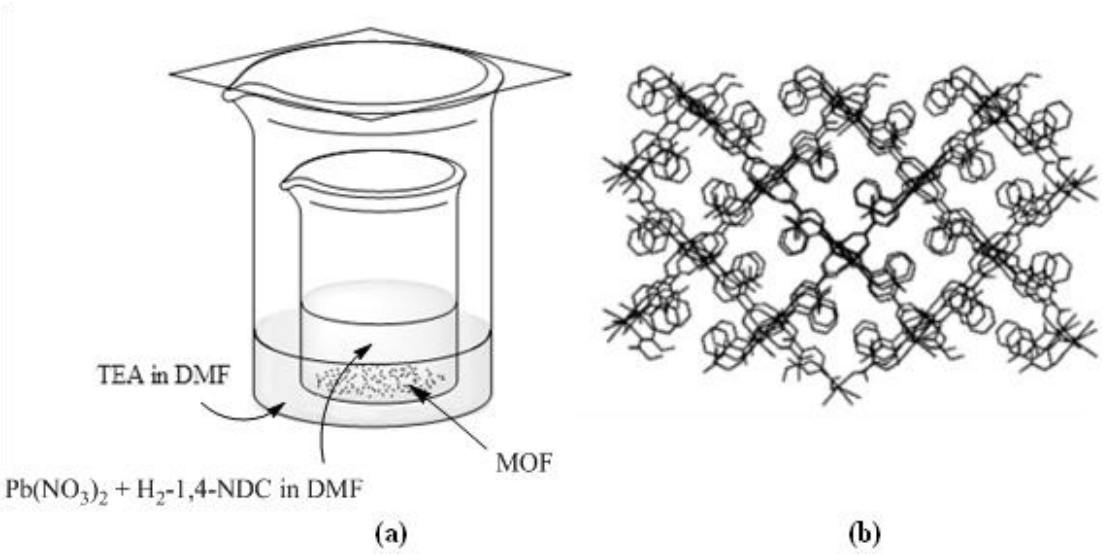

Figure 1.21. (a) A general vapour diffusion setup **(b)** 2-D sheet of [Pb(1,4-NDC)(DMF)] view down *a*-axis.[48]

Gel crystallisation involves adding a gelling agent to a MOF reaction mixture to reduce the rate of diffusion and therefore the rate of framework formation. The MOF $[Ba_2(O_3P(CH_2)_3PO_3)]\cdot 3H_2O$ was made using this technique by Tuikka *et al*.[49] Initially, the metal salt, barium(II) chloride, was dissolved in water in a test tube. A gelling agent (tetramethoxysilane) was then added to this solution and the mixture shaken until it was homogenous. Then the solution was allowed to gel and an aqueous solution of ethanediphosphonic acid was layered on top of this gel and left for three weeks. This technique is sufficiently slow to garner large crystals, however long reaction times and extra separation steps, of products from gel layers, have to be negotiated.

The toxicity of solvents used in MOF reactions is a concern that some synthetic methods try to address. The most effective way of reducing solvent toxicity is by removing it. Mechanosynthesis, or milling, is being utilised by the James group as a fast, scalable and potentially non-toxic way of synthesising MOFs.[50] Ball bearings are added to a stainless steel vessel along with the reagents and only stoichiometric amounts of liquid. The whole vessel is sealed and shaken effectively grinding the reagents together, allowing MOF formation. A typical liquid assisted grinding reaction would run at 30 Hz for 20 minutes.[50]

This is a very aggressive technique so, generally, the products made from this method are micro- to nano-crystalline, at room temperature and in a shorter time.

Sonochemical synthesis is carried out by exposing a reaction mixture to 20 kHz-10 MHz ultrasound waves and can be beneficial for several reasons. No extra heat is required for the system, reactions can be completed in a shorter timeframe (*i.e.* not left overnight) and the crystalline product can have narrower size distributions, which are particularly useful for applications in membrane coating.[51, 52]

Sonochemical synthesis is a useful method for making nano-sized (<100 nm) crystals. This is a consequence of the instantaneous formation, of crystals, in local solvent cavity hot spots that have very short lifetimes (~ms) and size (in the order of tens of microns).[53] Effective temperatures can reach 5000 K and pressures of 1000 bar, by a process called cavitation.[53] This is where bubbles form, grow and collapse. MOF-5,[54] MOF-177,[54] and HKUST-1 have all been produced sonochemically at room temperature.[55] In 2013, Fard *et al.* produced the 2D MOF $[Pb_2(N_3)(NO_3)L_2]$, (L = 8-hydroxyquinolate), in water using sono chemistry. The resulting crystals were nano-scale and could be converted to nano-PbO particles, Figure 1.22, by heating to 400 °C by a process called calcination.[56]

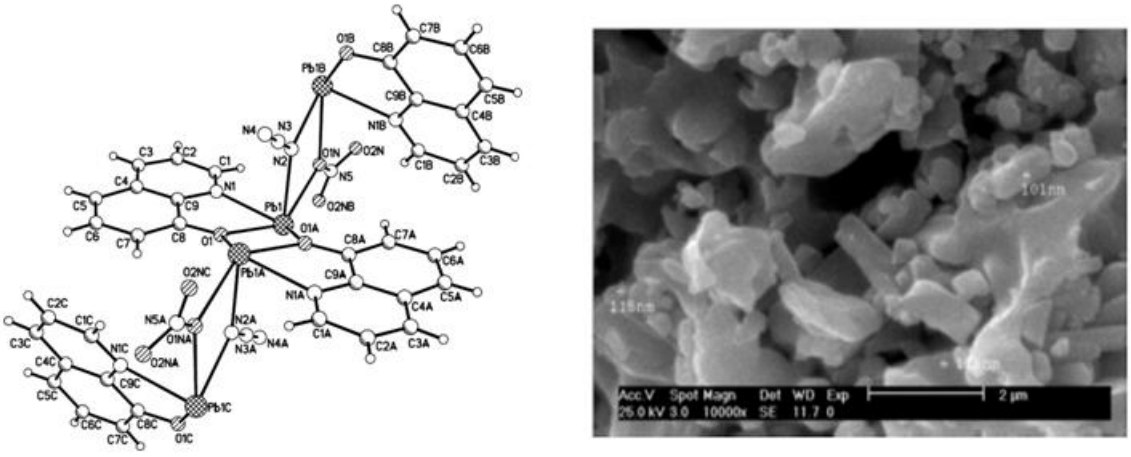

Figure 1.22. (left) Metal coordination in $[Pb_2(\mu_2\text{-}N_3)(\mu_2\text{-}NO_3)L_2]$, **(right)** SEM of $[Pb_2(\mu\text{-}N_3)(\mu\text{-}NO_3)L_2]$ nano-crystals.[56]

Electrochemical synthesis of MOFs offers an alternative means of synthesis that does not require the addition of an external heat source, but it can be expensive to run on an industrial scale. This approach works by forming ions of the reagents in solution, therefore replacing the need for a base. Electrochemical methods are well suited to the formation of

MOF membranes because of the inherent even coverage achieved on scaffolds, due to the even deposition of the MOF product. Joaristi and co-workers used this method to make HKUST-1 on a copper mesh by directed nucleation, Figure 1.23,[57] onto an anode surface in a EtOH:H_2O solution. The copper scaffold reacts with anions from the bulk, therefore no metal salt is needed with quantitative consumption of the linker. This is interesting as directed nucleation is useful for continuous, fast synthesis at room temperature. Disadvantages of this method include, detachment of copper from the anodic scaffold and loss of film at the vertices of the scaffold.[57]

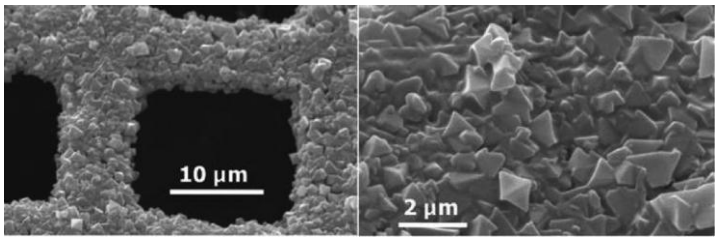

Figure 1.23. SEM of HKUST-1 on copper mesh.[57]

1.4.2. MOF Formation and Nucleation

The means by which MOFs nucleate in solution has been investigated to find better conditions for growth. Whittingham postulated a mechanism for the initial stages of MOF aggregation.[58] A soluble molecular complex first forms when the reagents are dissolved, then the metal aqua-ligand acid groups align *via* hydrogen-bonding, and subsequently the SBU forms through condensation processes. Supramolecular interactions also dictate orientation and optimum crystal packing, along with solvent, temperature and any templating effects by solvent or other organic additives.[58]

The syntheses of MOFs are typically carried out in under the saturation for the solvent in use. In a MOF formation solution, random fluctuations in concentration lead to sufficiently large nuclei for homogenous growth and, depending on the density of the crystals, these collect on the bottom of the vessel or rise to the surface of the solvent. Heterogeneous growth can occur at the walls of the vessel, at the liquid/liquid, liquid/gas surface interface and on micro- and nano-particles present in most solutions *e.g*. already formed crystals, dust, impurities and defects in the reaction vessel.[59]

Atomic force microscopy, AFM, provides a method of investigating how MOFs grow *in situ*. Attfield and co-workers showed a predominantly two-dimensional birth-and-spread growth mode, interspersed with spiral growth modes, for MOF-5, Figure 1.24,[60] with each

step being either 0.7nm (BDC) or 1.2nm (Zn_4O and BDC). Similarly HKUST-1 exhibits a spiral growth mechanism.[61]

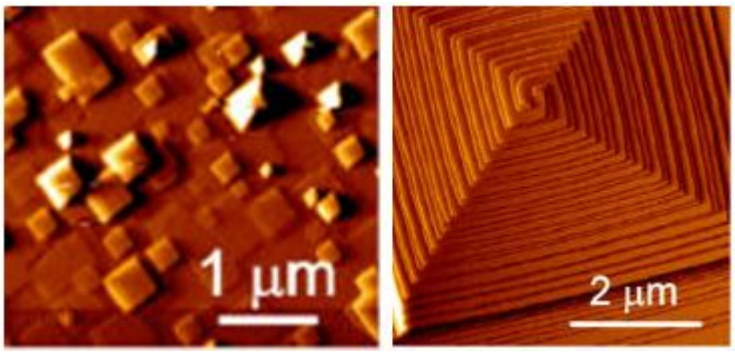

Figure 1.24. **(left)** AFM of MOF-5 showing 2-D heterogeneous nucleation on larger crystals. **(right)** AFM showing MOF-5 spiral growth.[60]

A secondary method to investigate how MOFs grow *in situ* is by PXRD, using high intensity X-rays at a synchrotron. Millange and co-workers showed the early stages of nucleation in MOF-14,[62] a $[Cu_3(BTB)_2]$ interpenetrated network, and HKUST-1, $[Cu_3(BTC)_2]$. For this analysis they utilised *in situ* EDXRD (energy dispersive X-ray diffraction) with time dependent measurements.[63] MOF-14 takes three hours to form a phase pure sample, with nucleation occurring throughout the reaction even after large crystals are present. This is shown in the diffraction pattern in Figure 1.25. Activation energies of nucleation were calculated by Arrhenius analysis and showed MOF-14 to have a higher barrier to nucleation than HKUST-1 which is believed to be due to the interpenetrated nature of MOF-14.[63]

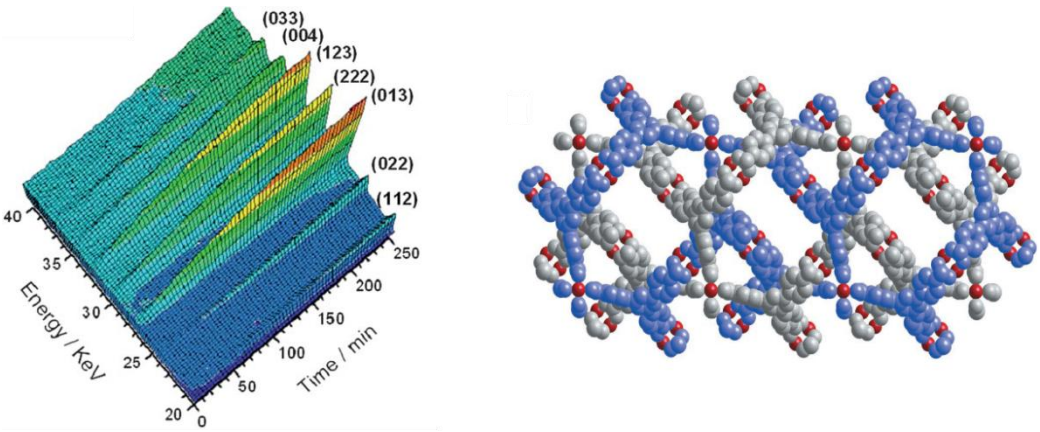

Figure 1.25. (left) time resolved EDXRD[63] of **(right)** MOF-14 growth.[62] C: grey and blue (for two separate catenated frameworks), Cu: red.

Understanding nucleation processes for a given system leads to understanding how to control the rate of crystallisation and polymorphism depending on the synthetic method and conditions. For the MOF system $[Zn_2(BDC)_2(dabco)]$, there are two phases that can form in a solvothermal reaction: tetragonal (typical square building blocks) and trigonal (triangular building blocks). Kitagawa *et al.* controlled the phase of the MOF produced by cooling the system down, at the beginning the reaction, to isolate the triangular building blocks of the trigonal framework. The hexagonal crystals of $[Zn_2(BDC)_2(dabco)]$ were separated by filtration after 30 minutes, instead of leaving the reaction mixture at high temperature, 120 °C for 48 h, to obtain the tetragonal MOF.[64]

Nucleation can also be controlled by seeding. This method can be as simple as adding small crystals of a MOF into the reaction mixture at the beginning, thus accelerating the heterogeneous nucleation and extending the crystal in a core-shell synthesis.[65] Adding in new ligands and metal salts can lead to growth on existing crystals to effectively build up layers of different composition. This is the concept on which growing HKUST-1 on pretreated surfaces or scaffolds, such as a copper mesh (section 1.4.1), relies on.[57]

More sophisticated methods of seeding have been reported by Falcaro *et al.* in 2011.[66] They used a phosphate based surfactant Pluronic F-127, which aggregates to form desert rose microparticles (DRMs, α-hopeite microparticles), as a suspension to seed the growth of MOF-5 crystals *in situ* and on substrates such as alumina (Al_2O_3).

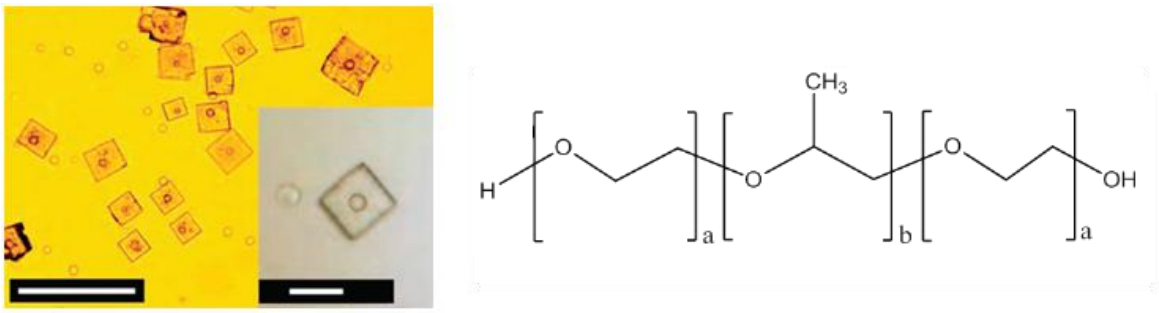

Figure 1.26. (left) DRM seeded MOF-5. 200µm scale bar and inset scale bar 50µm.[66] **(right)** Pluronic F-127, a~106, b~70.[67]

1.4.3. Modulated Crystal Synthesis

An additive can help when attempting to manipulate crystal size. Benzoic acids or acetic acids can slow down crystallisation, by competing with dicarboxylate ligands, for metal sites thus modulating crystal growth. Schaake and co-workers showed this with IRMOF-3

and the UiO series by adding benzoic acid to the reaction mixture in varying stoichiometries. Figure 1.27 shows the PXRD patterns of UiO-66, $[Zr_6O_4(OH)_4(BDC)_{12}]$, illustrating an increased crystal size with increased benzoic acid concentration, with crystal sizes in the range 10-200 nm.[68]

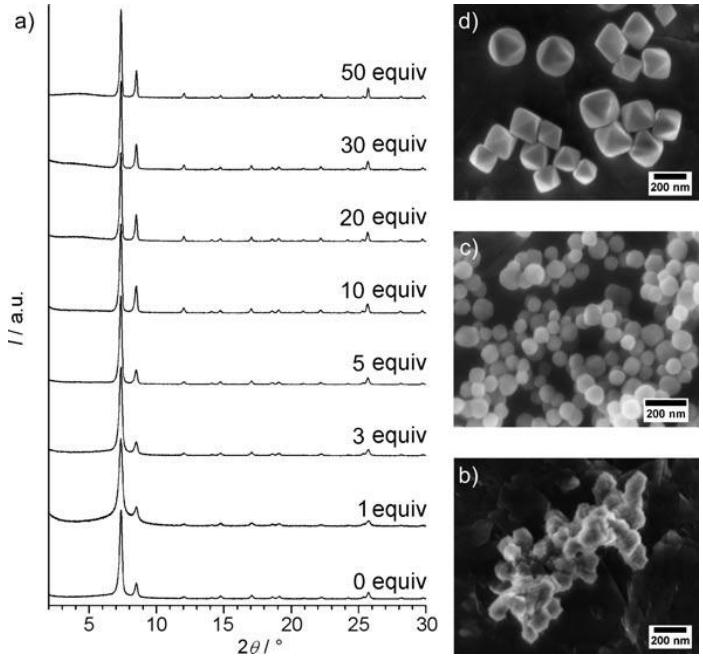

Figure 1.27. (a) PXRD of UiO-66 as a function of benzoic acid equivalents. SEM of crystal products with **(b)** 0 eq., **(c)** 10 eq. and **(d)** 30 eq. [68]

Kitagawa *et al.* used modulators with HKUST-1.[69] The morphology of the crystalline product was influenced by altering concentrations of lauric acid (*n*-dodecanoic acid) in a microwave assisted, solvothermal reaction. Directed growth in the [100] or [111] directions lead to cube, cuboctahedral or octahedral crystals on a sliding scale and SEMs of the crystal morphologies are shown in Figure 1.28.[69]

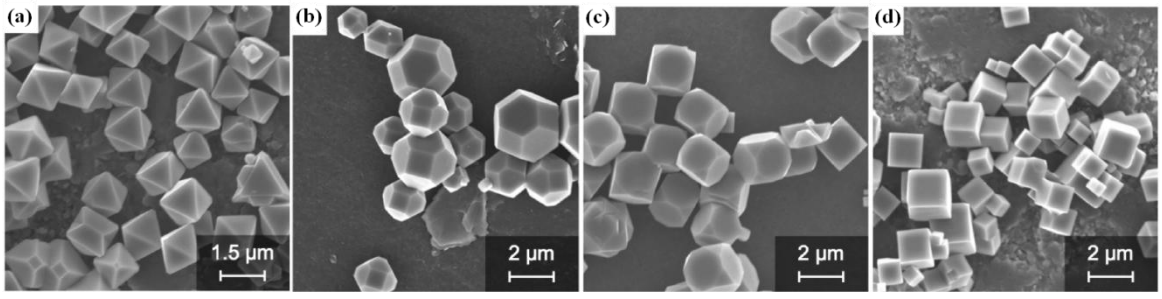

Figure 1.28. SEMs of HKUST-1 products as a function of lauric acid equivalents: **(a)** 50 eq. ([111] growth) **(b)** 75 eq. **(c)** 100 eq. **(d)** 125 eq. ([100] growth).[69]

1.5. Porous Frameworks

The main structure-property relationship that is created from the low density and large voids in porous MOFs, is the surface area per gram. Pores or voids come in many shapes and sizes but are generally classed as micro- or mesopores. The definition of a micropore is any void less than 2 nm and a mesopore is 2-50 nm in diameter with anything larger macroporous.[70]

Guest molecules, such as DMF or H_2O, are sometimes an integral part of the structure by occupying voids and channels preventing structural collapse. They can act as templates for framework formation and the ligands interact with the solvent molecules during nucleation and crystal growth. Activation by removing the guest solvent molecules with heat and vacuum, or exchanging the guests with a solvent or gas that does not interact in the same way, may break down the long range order of the crystals. The pores can collapse and the whole crystal structure may become amorphous.[71]

MOFs whose framework is kept open by guest molecules has been demonstrated by Kitagawa *et al.*, in the example of $[Cu_2(dmcapz)_2(OH_2)]\cdot 1.5DMF$, (dmcapz = 3,5-dimethyl-4-carboxypyrazolate). This structure contains a bridging water molecule anchoring two Cu(I) centres together. When this is removed, the crystals turn sky blue and the PXRD peaks shift considerably, representing a change in structure.[72] This can also be monitored by thermogravametric analysis (TGA). In the report the authors demonstrate a significant weight loss (~30 % owing to the DMF and H_2O molecules) up to 120 °C and framework decomposition above 300 °C, shown in Figure 1.29.[72]

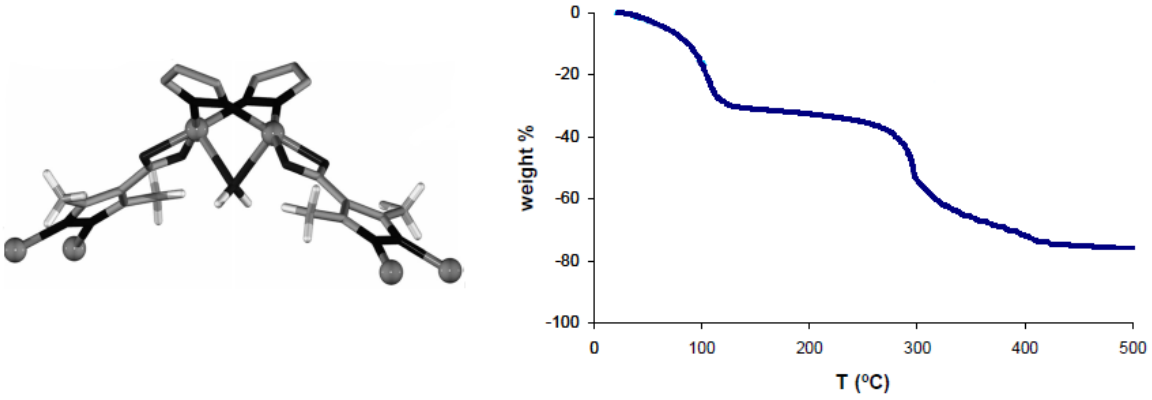

Figure 1.29. (left) Coordination around metal centres of $[Cu_2(dmcapz)_2(OH_2)]\cdot 1.5DMF$. Cu: Grey, O: dark grey, N: black, C: grey and H: white rods. **(right)** TGA trace showing activated MOF by a plateau centred around 200 °C.[72]

1.5.1. Activating MOFs

To make use of the high porosity of MOFs, the pores or channels need to be emptied. This is done by activating the material, a schematic representation of which is shown in Scheme 1.4. It takes more energy (a higher temperature and stronger vacuum) to remove a less volatile guest, for example DMF is harder to remove than $CHCl_3$. Exchanging a high boiling point solvent with a lower boiling one (that also has less interaction with the framework) can allow less aggressive techniques (*i.e.* lower heat and vacuum to be used) to activate a MOF. Activation affects sorption capacity for all gas types, but handling the materials becomes an issue with sensitivity to water generally increasing as the metal sites, contained in SBUs, are exposed.

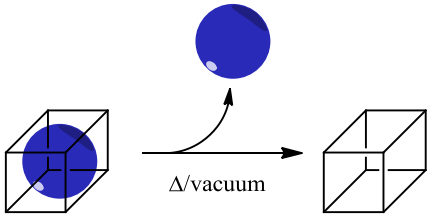

Scheme 1.4. Activation of a 3-D MOF. Blue sphere represents solvent guest molecules.

An activated sample, in which the framework structure has been retained, is evidenced by the presence of a plateau in the TGA and retention of peak positions in the PXRD pattern. Activation may be unsuccessful if the DMF is integral to the structure. This may manifest as an absence of a plateau in the TGA plot, for example in the MOF [Mn(AIP)(DMF)], (CPO-9, AIP = 5-aminoisophthalate), Figure 1.30.[73]

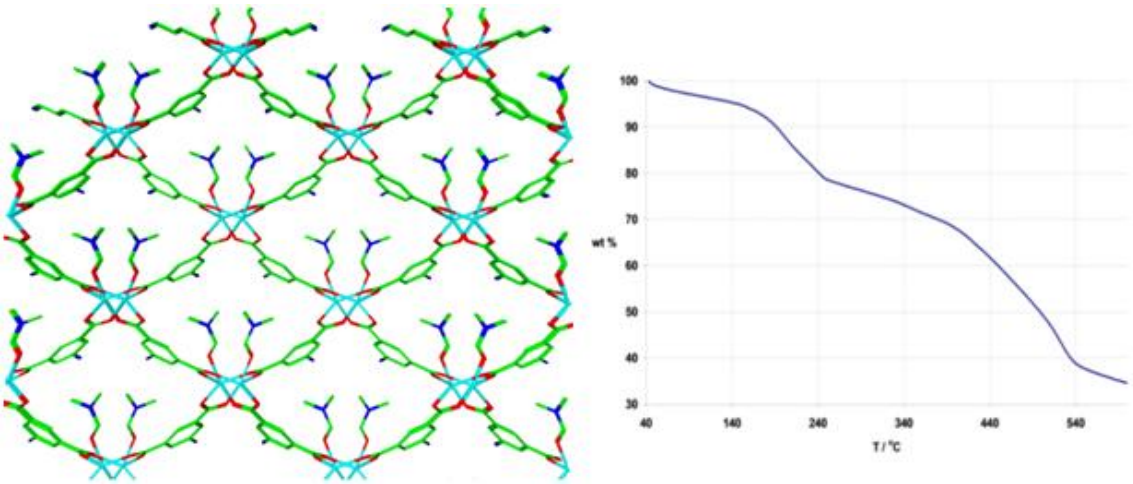

Figure 1.30. (left) View of the network of CPO-9, showing DMF bound to the framework. Zn: light blue, O: red, C: green, N: dark blue.[73] **(right)** TGA of CPO-9 showing no plateau region.

Aggressive or hard techniques use heat and vacuum for long periods of time. 150 °C under vacuum for 24 h are the typical activation conditions for the IRMOF series.[18] The general rule to follow is that the activation temperature is dependent on the boiling point of the guest species (153 °C for DMF).

These hard activations often break down crystallinity and can lead to negligible surface areas. Figure 1.31 shows HKUST-1 before and after decomposition and shows opaque, mottled, crystals.[74] The BET surface area diminishes with crystallinity and this is especially true for the IRMOF series.

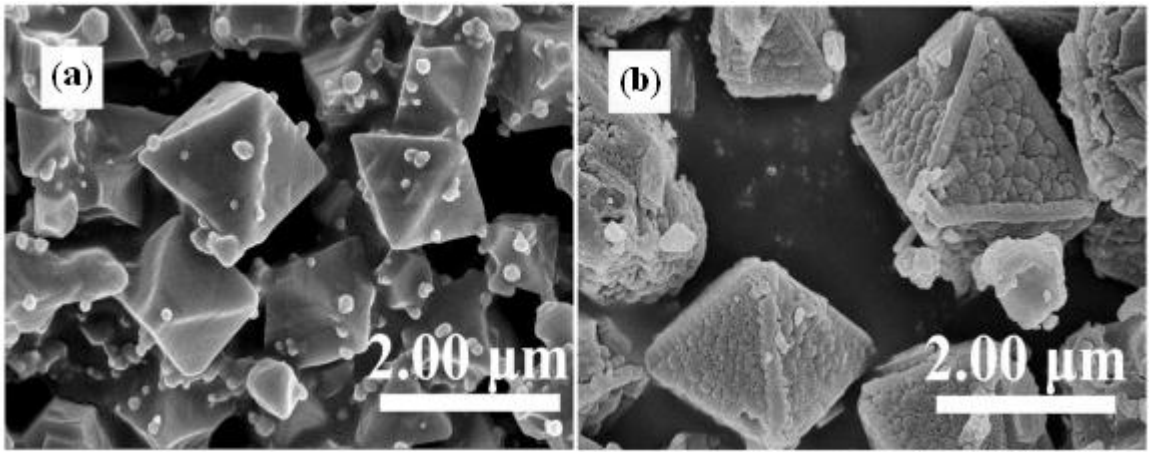

Figure 1.31. SEM of HKUST-1 crystals **(a)** freshly synthesised, **(b)** and decomposed.[74]

A soft or mild method of activation is to flow nitrogen gas, over the MOF evaporating the guest solvent, but with a low heat and no vacuum so crystallinity is retained. Progressing one stage further is to use supercritical carbon dioxide, ScD.

ScD can act as a mild activating agent and has been shown to give high surface areas, for the same MOF system, over other activation methods. It combines guest exchange with soft evaporation and also ensures complete activation, *i.e.* no solvent left behind, because above the critical point no phase boundaries exist and capillary forces are lessened between the CO_2 molecules. Hupp and co-workers used SCD on the IRMOF series and MOFs comprising of larger dicarboxylates.[75] The MOFs were first solvent exchanged with EtOH. The EtOH soaked MOFs were placed in a dryer with $CO_{2(l)}$ then taken above the critical point (31 °C, 73 atm) for 30 minutes. Finally the chamber temperature was slowly vented over 18 h. The BET surface area of the extremely moisture sensitive IRMOF-16 was quadrupled (470 m^2g^{-1} to 1910 m^2g^{-1}) using SCD as the means of activation.[76]

Lin and co-workers exchanged the included solvent with benzene then removed this by freeze-drying in the copper tetracarboxlyate MOF, $[Cu_2(L^1)(H_2O)_2]\cdot 6DEF\cdot 2H_2O$ (L^1 = methanetetra-*p*-benzoate).[77] They hypothesise capillary forces arising from the surface tension between solvent molecules being removed can destroy crystallinity and, hence, reduce the surface area. The framework has open channels along all three crystallographic axes allowing for soft activation because the guests can easily diffuse throughout the MOF. The benzene was removed by sublimation after three freeze-thaw cycles at 0 °C, tripling the BET surface area in this system.[77]

1.5.2. Gas Adsorption and Storage

The main technique for measuring the surface area of a MOF is by measuring nitrogen adsorption isotherms to give the BET surface area. MOFs with pores larger than ~5 Å are commonly assessed using $N_{2(l)}$, at 77 K, for measurements because of its inert nature and reversible physisorption capability.[78]

There are six IUPAC recognised isotherm types, summarised in Figure 1.32.[78] Type I is typical of microporous materials which exhibit most adsorption below partial pressure p/p^0 0.1. Type II is observed in non-porous and macroporous materials with weak adsorbant-adsorbate interactions. Type III is common in non-porous materials with low absolute amount of loading and very weak adsorbant-adsorbate interactions where the fluid-fluid interactions are stronger than those between the fluid and solid. A Type IV isotherm is observed in meso- or macroporous materials and exhibits a hysteresis loop. Adsorption follows the same pathway as type II, but desorption is delayed at higher p/p^0, due to capillary condensation or multilayering of adsorbate. Type V isotherms also have a hysteresis loop but have weaker adsorbant-adsorbate interactions than type IV. Type VI, only seen in macroporous materials, has a stepwise layer upon layer adsorption. The steps arising after one layer of adsorbate is completed before moving on to the next layer.[6, 78, 79]

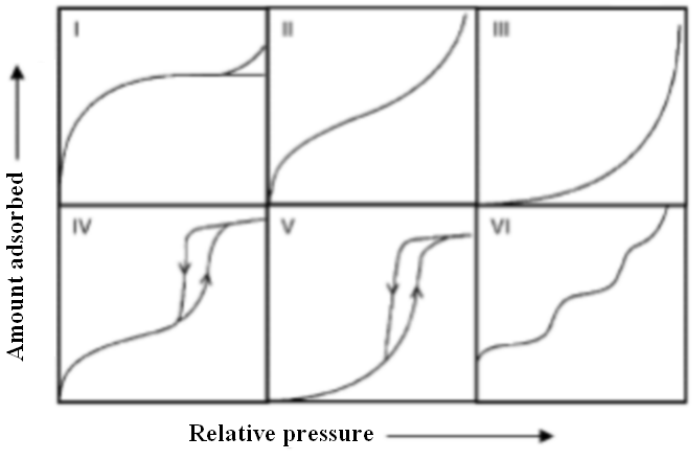

Figure 1.32. Adsorption isotherm classifications by IUPAC.[78]

Yaghi and co-workers summarised micro- meso- and macropores elegantly, in a study on MOF-5, Figure 1.33.[80] Microporosity is observed in a standard MOF-5 crystal. "Spongy" MOF-5, spng-MOF-5, is made by adding 4-(dodecyloxy)benzoic acid (DBA) to the reaction mixture in stoichiometric amounts, and exhibits meso- and macro-pores in the range 10-100nm. Growing a layer of standard MOF-5 on top of spng-MOF-5 yields a pomegranate-like crystal, pmg-MOF-5, with overall porosity somewhere between the two *i.e.* mesoporous.[80] This leads to CO_2 adsorption that has a hysteresis loop at $p/p^0 = 0.2$, which is a property not seen in the original MOF-5.[80]

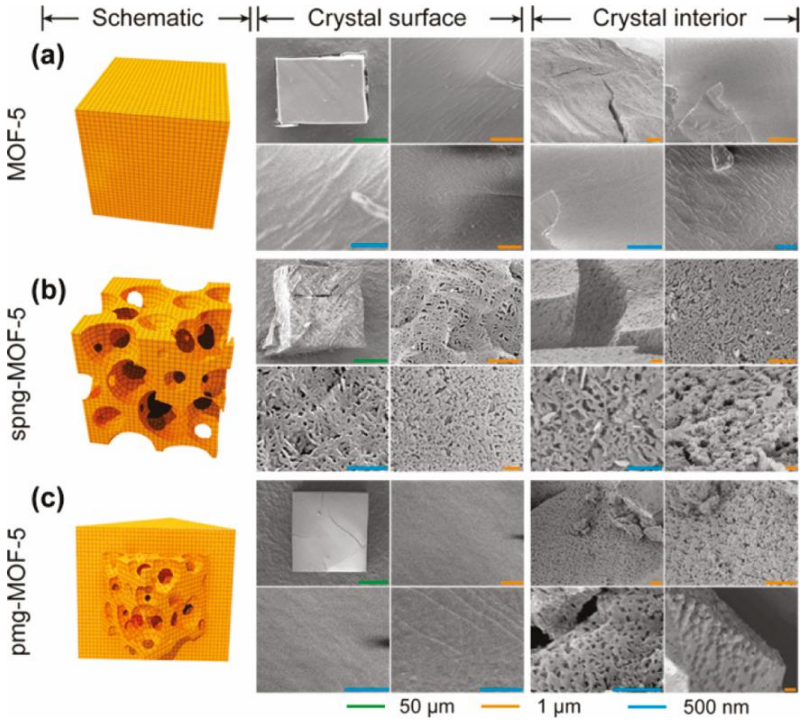

Figure 1.33. (left) Diagrammatic representation of pores structures observed in the SEM **(right)**.[80]

The U.S. Department of Energy (DOE) has set material targets for the storage of certain gases: CO_2 capture needs to be 90 % efficient,[81] H_2 5.5 wt% 2015, 40 g/L for 2015 and 70g/L for 2050 ,[82, 83] and CH_4 180 cm^3 (STP) cm^{-3} at 298 K and 35 bar.[84] The hydrogen storage target is the only one yet to be realised. This is a complicated area as each target requires different temperature and pressure depending on application and is constantly being updated. Some groups specifically aim for the targets and design MOF systems especially, and others' systems realise some targets by serendipity. For use in commercial applications MOFs are assessed on volumetric capacity (the volume of gas adsorbed per volume of adsorbent) and gravimetric capacity (the weight % of gas adsorbed).[78]

Carbon capture and storage (CCS) is a topic of interest in the current-climate change debate and MOFs are seriously considered by material scientists, especially for industrial processes such as power stations, which now must capture 90 % of produced CO_2.[81] Properties that favour CO_2 adsorption generally consist of two-stages,[85] and adsorption displaying hysteresis, seen in mesoporous structures and networks containing amino and alkynyl groups that strengthen CO_2-framework interactions. MOF-polymer composites also open many avenues for tuning gas storage performance.[86-88]

The linker in IRMOF-3, BDC-NH_2, has been simulated interacting with CO_2 computationally using Grand Canonical Monte Carlo (GCMC) calculated adsorption energies, by Vitillo and co-workers. Figure 1.34(a) shows the optimised interaction site of CO_2 with BDC-NH_2 adjacent to the amino group.[87] Interactions of $CO_{2(g)}$ molecules and the amino groups, in the pores of the amino triazolate based MOF, $[Zn_2(atz)_2(ox)]$, (where atz = 3-amino-1,2,4-triazolate, ox = oxalate), are shown in Figure 1.34(b), to be heavily influenced by the amino groups.[89]

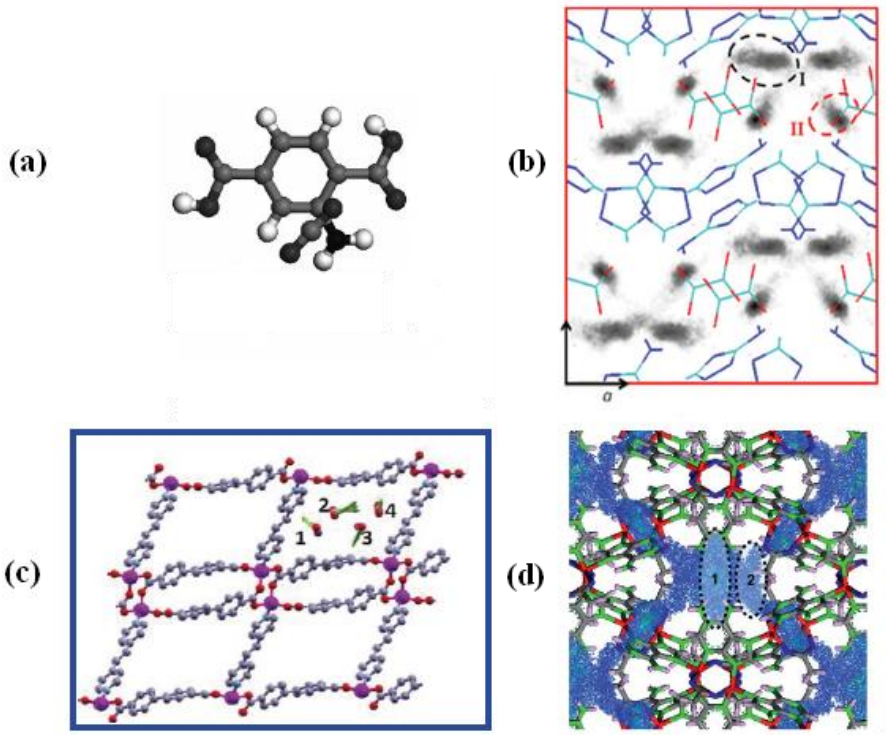

Figure 1.34. Simulated CO_2 adsorption sites: **(a)** on $H_2BDC\text{-}NH_2$;[87] **(b)** in the pores of $[Zn_2(atz)_2(ox)]$;[90] **(c)** in the channels of $[Zn_2(BPDC)_2(bpee)]$;[89] **(d)** potential energy map of CO_2 at 1 x 10^{-2} bar in the channels of $[Cu_2(ade)_2(acetate)_2]$.[91]

Nijem *et al.* calculated adsorption site preference in the BPDC based MOF $[Zn_2(BPDC)_2(bpee)]$, where bpee = 1,2-bis(4-pyridyl)ethylene, using Density Functional Theory, DFT, methods. The adsorption sites 1 and 4 have the lowest energy and therefore are most favoured, Figure 1.34(c).[90] Visualisations of CO_2 adsorption in the channels of the metal-biomolecule framework (BioMOF), $[Cu_2(ade)_2(acetate)_2]$ (ade = adeninate), illustrate specific avenues where the gas molecules permeate through the structure, as well as pore size distribution of sites 1 and 2, Figure 1.34(d).[91] These computational analyses are important to aid in the design of more targeted adsorption materials.

1.6. Post-synthetic Modification

Post-synthetic modification (PSM) is a single-crystal to single-crystal transformation and is a process involving conversion of pendent groups at the surface or in the pores of MOFs, to change the physical or chemical properties. This can be achieved *via* chemical reaction, adsorption, ligand or metal exchange, light and pressure stimuli. Often, PSM gives access to MOFs not available by direct synthesis. Direct synthesis does not always afford the correct topology, therefore, more control is gained from using tagged ligands, with robust

functionality and with simple modification pathways in mind.[92] Scheme 1.5 summarises the fundamentals of PSM.[1]

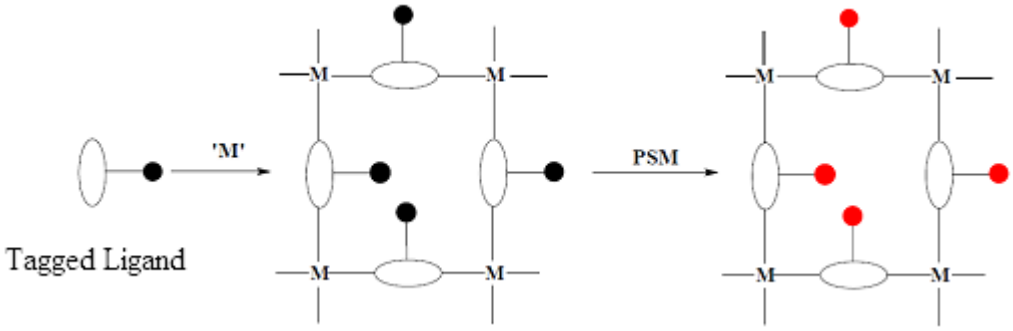

Scheme 1.5. Representation of a post-synthetic modification strategy for MOFs.[1]

PSM is a useful technique because it avoids the scenario of functional groups binding to the metal ions, as well as carboxylate groups, during initial framework construction. For most applications the metal component is only needed in the SBU.

For a PSM to be successful the product must retain crystallinity with the framework still intact. This is diagnosed by a combination of X-ray diffraction, BET surface area and ideally, scanning electron microscopy (SEM) or transmission electron microscopy (TEM). There should be no dissolution and recrystalisation to form the modified MOF by the direct synthesis with modified ligand. Proton (^{1}H) NMR is also useful for to evidence the percentage conversion, by digesting the framework into its constituent ligands by an acid or base. This technique is favoured over solid state NMR to avoid broad peaks, reducing the accuracy of measuring the degree of conversion. Some reactions on crystals proceed with a colour change in the MOF indicating a modification has occurred.[1]

1.6.1. Solvent PSM

One of the first examples of PSM was reported by Lee in 1995 using a silver triflate MOF, with a large tribenzonitrile ligand, $[Ag(L)(CF_3SO_3)]\cdot 2C_6H_6$ (L = 3,3',3''-(benzene-1,3,5-triyltris(ethyne-2,1-diyl))tribenzonitrile). The mother liquor, benzene, was incorporated into channels during the reaction and was removed by heating to 145 °C and subsequently reabsorbed over ~60 h by soaking in benzene, Figure 1.35(a).[93]

This simple solvent exchange is fundamental to PSM chemistry. The Lin group also explored solvent exchange on the MOF, $[Cd(L)_2(ClO_4)_2]\cdot 11EtOH\cdot 6H_2O$ (L = (*S*)-2,2'-diethoxy-1,1'-binaphthyl-6,6'-bis(4-vinylpyridine)). Ethanol was reversibly exchanged

with benzene, in chiral 1-D hexagonal channels, and the crystallinity monitored by single crystal X-ray diffraction. They speculate this MOF has good potential for heterogeneous asymmetric catalysis, as the structure can be maintained after solvent exchange, Figure 1.35(b).[94, 95]

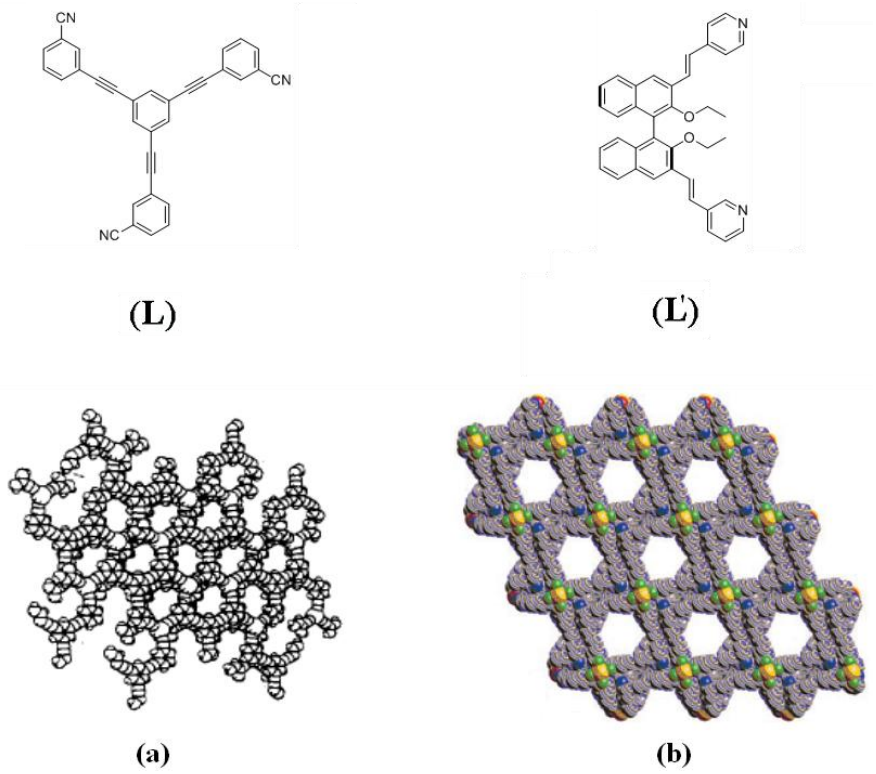

Figure 1.35. Solvent exchange sites. View down channels of **(a)** $[Ag(L)(CF_3SO_3)]$[93] and **(b)** $[Cd(L')_2(ClO_4)_2]$ with associated ligands L and L' respectively.[94, 95]

1.6.2. Pioneering Amino Tag Group PSM Reactions

IRMOF-3, Figure 1.36, the amino derivative of IRMOF-1 (IRMOF-3 linker = 2-amino-1,4-benzenedicarboxylate, BDC-NH_2) has been extensively studied because of its simple synthesis, porous crystalline network and variety of possible reactions with the amino tag group.[18]

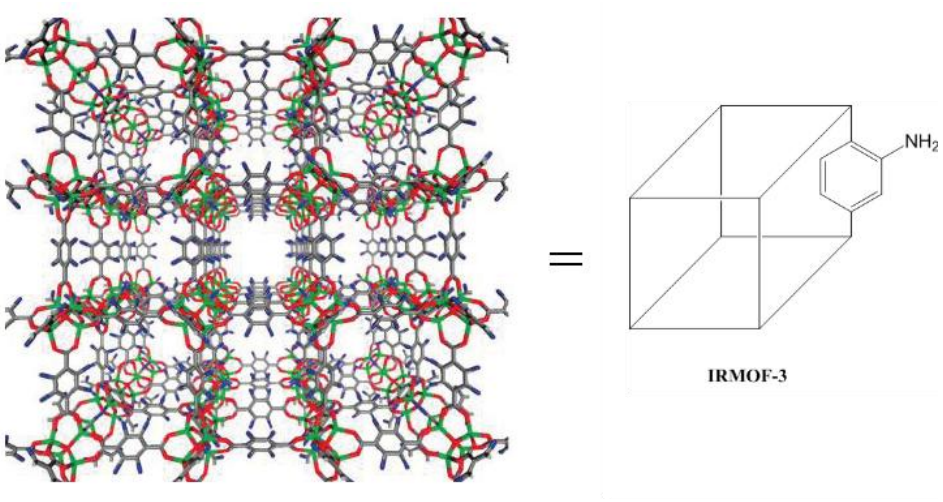

Figure 1.36. (left) Packing of IRMOF-3 with disordered NH_2 groups shown (Zn: green, C: grey, O: red, N: blue),[18] **(right)** Schematic representation of IRMOF-3.[20]

Wang and Cohen reported making amide tagged IRMOF-3, IRMOF-3-AM, from reacting IRMOF-3 with a variety of anhydrides.[20] PSM on IRMOF-3 has been carried out by Cohen *et al.* with acetic anhydride derivatives, succinic anhydride and chiral anhydrides to make amide, carboxylic acid, and chiral containing groups respectively, that protrude into MOF pores. These covalent PSMs are summarised in Scheme 1.6.[20] The percentage conversion of amino groups to amide groups range from 97 % (IRMOF-3-AM2) to 11 % (IRMOF-3-AM19) after five days reaction time. As the chain length increases, above n = 6, the conversion lessens.

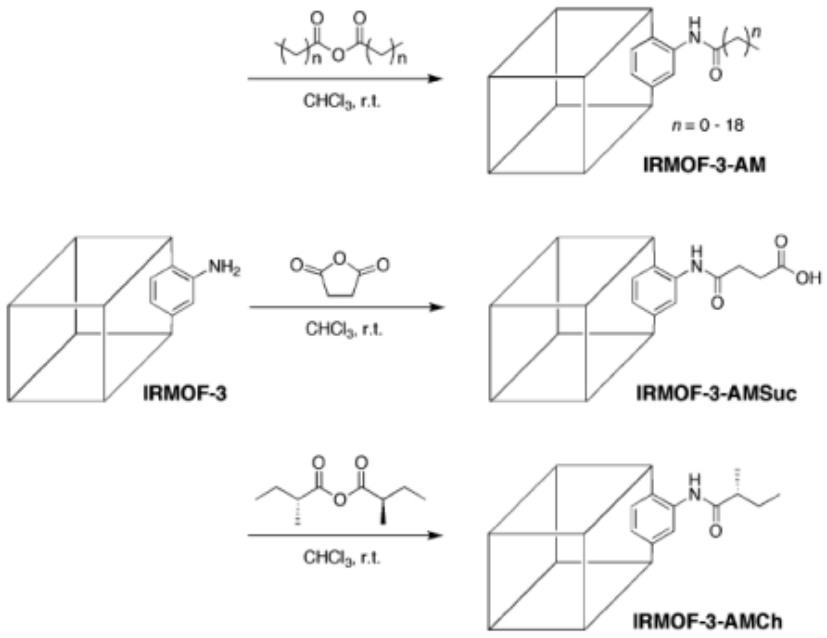

Scheme 1.6. PSM of IRMOF-3 with various anhydrides. Amino tags converted to amides.[20]

1.7. Covalent PSM: Functional Group Conversion

The following review will mainly address covalent PSM, the changing of functionality of pendent groups incorporated into the framework by covalent mechanisms. There are other types available that are not discussed herein i.e. dative PSM,[96] PSM of SBUs,[97] guest molecule inclusion by physisorption i.e. for drug delivery[98] or nanoparticles inclusion,[99] photo-PSM,[100] pressure modification,[101] self-sacrifice of MOFs[102] and the post-synthetic exchange (PSE) of ligands and metals.[103]

New MOFs with functional groups covalently bound to the pore surface are sought after due to their robustness, design ability and ease of synthesis. An example of the many different functional groups available for inclusion in MOFs was demonstrated by Yaghi *et al.* who reported a multivariate MOF (MTV-MOF) series. They combined two to eight functionalities in the MOF-5 based framework, summarised in Figure 1.37, by direct synthesis illustrating the tolerance of the system to varied tag groups.[104]

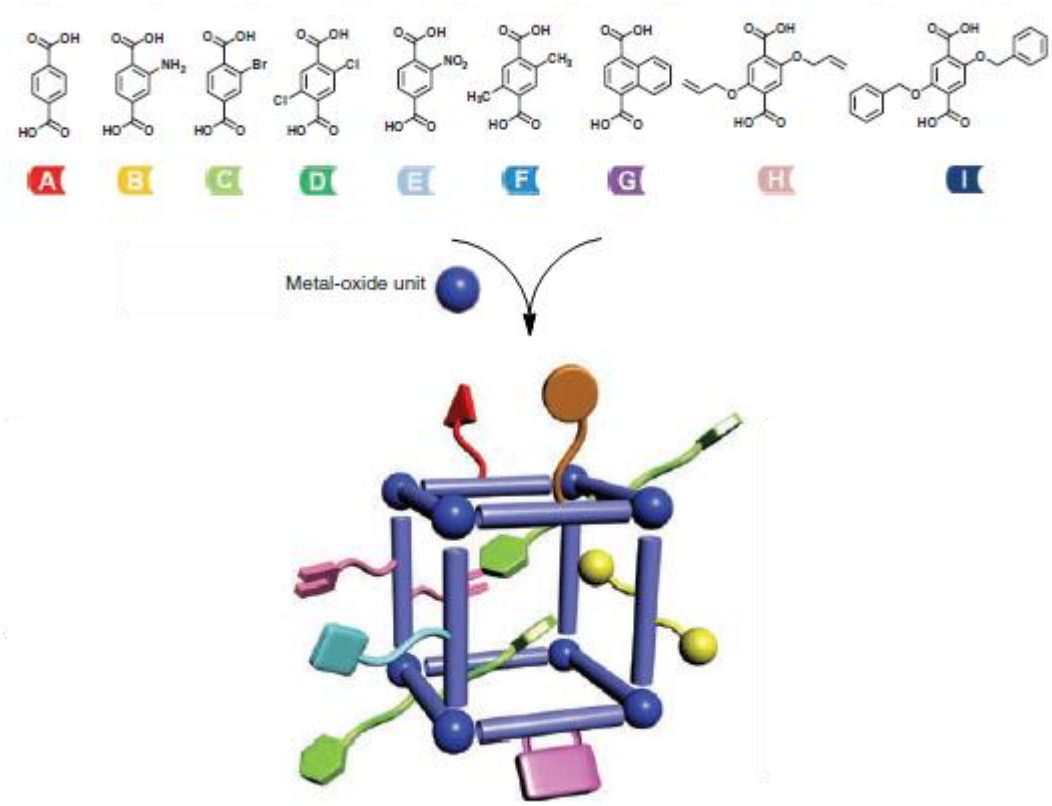

Figure 1.37. Schematic representation of the MTV-MOF-5 series with up to eight functionalities incorporated.

1.7.1. Conversion of Amines to Amides and Ureas

Cohen and co-workers led the way in the conversions of IRMOF-3 with anhydrides to form amides (summarised previously in Scheme 1.6).[20] This method of PSM by soaking in anhydride for 3 days, was not isolated to one MOF system as they went on to have the same success with UMCM-1-NH_2 and DMOF-1-NH_2, with the same scope of reactants as the IRMOF-3-AM PSM series, Scheme 1.7.[31]

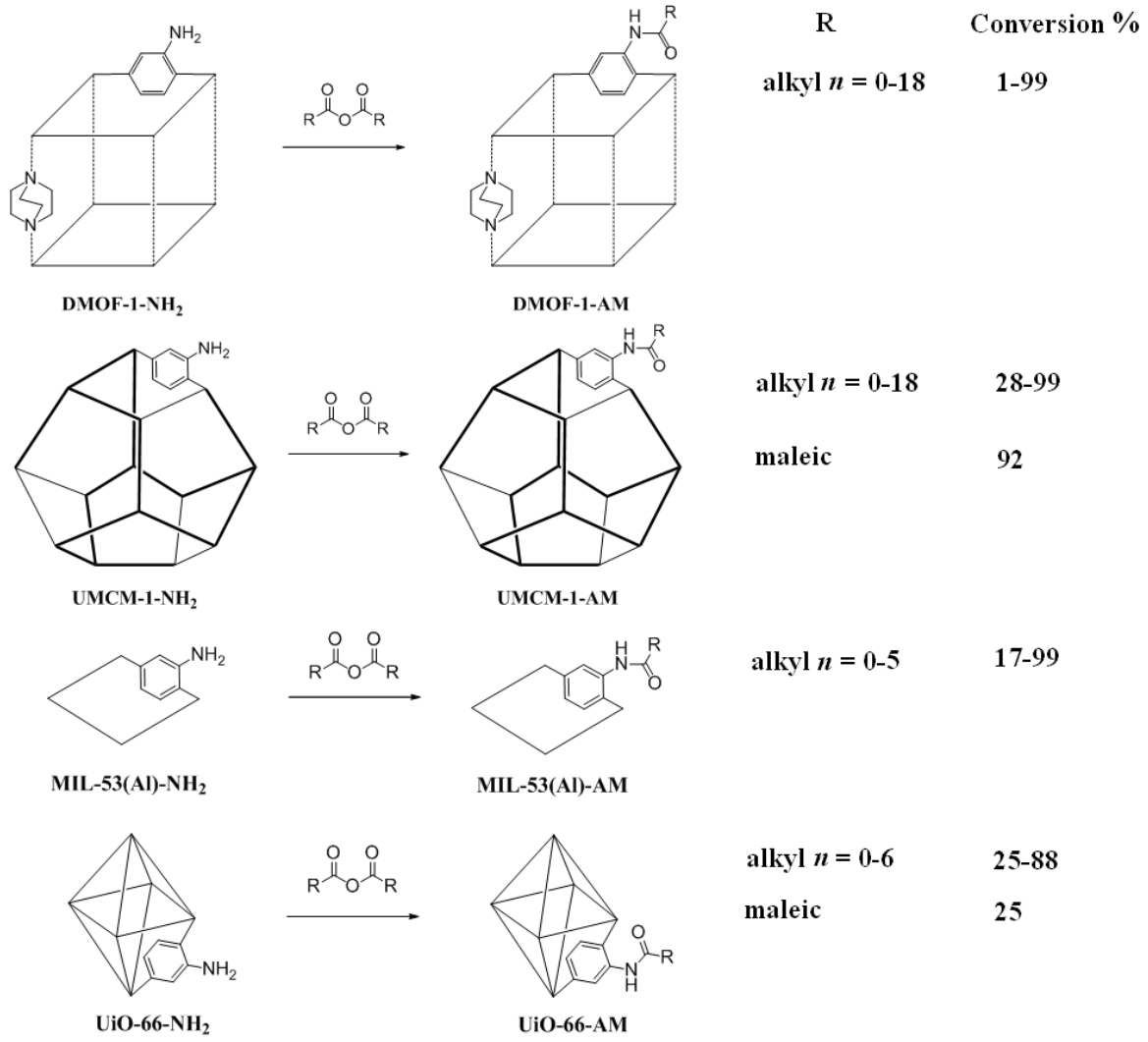

Scheme 1.7. Schematic representation of the PSM of various MOFs showing amino tag group conversion to amide groups by anhydride reagents. R = alkyl, cyclic.[20, 31, 105]

UMCM-1-NH_2 performs better than IRMOF-3 at longer chain lengths (*n*) with conversions in the range 99 % (UMCM-1-AM-1, *n* = 0) to 28 % (UMCM-1-AM-19, *n* = 18). This is expected with larger diameter pores (32 Å) and larger diameter pore apertures (30 Å) compared with a 7.6 Å channel in the case of IRMOF-3. Cao and co-workers reported, in

2012, the PSM of UMCM-1-NH_2 with maleic anhydride converting 92 % of amino tags to carboxylic acid functionalised tags.[105]

DMOF-1 has a smaller pore and a 5.7 Å pore aperture diameter displaying reduced conversion with the same anhydrides, compared to IRMOF-3. PSM product conversion of DMOF-1-NH_2 to the amido tagged DMOF-1-AM-1, n = 0 is still quantitative at ~99 %, but DMOF-1-AM-13 (n = 12) is 11 % and there is effectively no conversion of amino groups in the case of DMOF-1-AM-19.[31]

Cohen *et al.* also reported limited success of the PSM of MIL-53(Al)-NH_2 with linear alkyl anhydrides, up to n = 6, and assessed the hydrophobicity of the framework's voids.[106] In an investigation by Férey *et al.*, 100 % conversion was reported with formic acid on the same MOF using ^{15}N MAS NMR and elemental analysis as complementary techniques to estimate the degree of conversion.[107]

Recently Cohen *et al.* have reported the PSM of UiO-66-NH_2 with a small range of alkyl and cyclic anhydrides with varying degrees of success depending on the size of the reactant.[108] UiO-66-NH_2 is a very robust MOF and its exceptional stability coupled with functionality in the pores bodes well for many industrial applications. Amino to amide conversion proceeds using the same PSM method but conversion is slightly less than observed IRMOF-3 due to its bulky SBU. From 88 % conversion in the case of UiO-66-AM-1, conversion tails off to 25 % for UiO-66-AM-7.

A PSM reaction on the framework of [Cu_3(BTC-NH_2)$_2$], HKUST-1-NH_2, with acetic anhydride was reported by Fröba *et al*. The PSM product had 70% conversion to an acetamido functionality and a high BET surface area of 1900 m^2g^{-1}. This is higher than expected considering the framework is mildly water and acid sensitive accompanied with an acetic acid by-product from the PSM reaction.[109]

Burrows and co-workers reported a quantitative (>99 %) conversion for the PSM on [Zn_4O(BPDC-NH_2)$_3$] with ferrocene anhydride, shown in Scheme 1.8.[110] UMCM-1-NH_2 (17-31 % conversion), IRMOF-3 (5 % conversion), and MIL-53(Al)-NH_2 (conversion could not be reliably calculated) were also tried.[110]

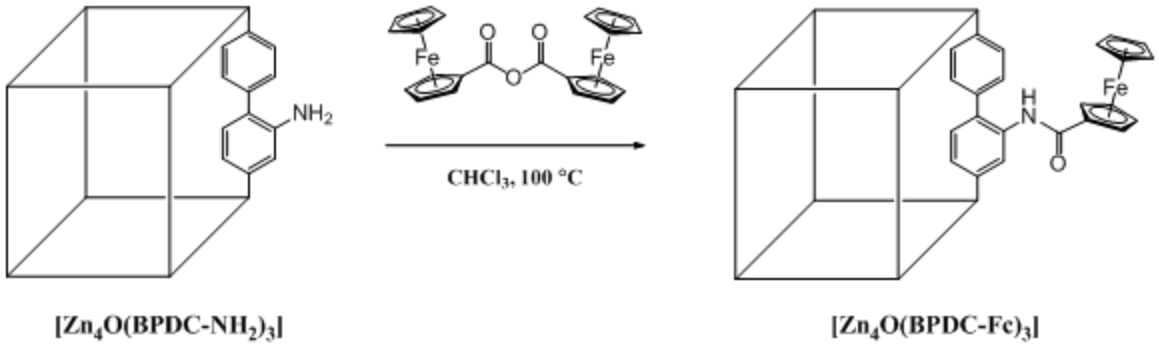

Scheme 1.8. PSM of $[Zn_4O(BPDC\text{-}NH_2)_3]$ with ferrocene anhydride giving 25 % conversion.[110]

Farrusseng *et al.* reporting modifying amino groups in the MOF, $[ZnF(TAZ\text{-}2NH_2)]$ ($2NH_2TAZ$ = 3,5-diamino-1,2,4-triazolate) with acyl chloride reagents to form amide groups The 4.7 Å diameter channel is very small so a conversion of 60 % with no loss of crystallinity achieved is surprising (confirmed by microanalysis based on N and C contents). $[ZnF(TAZ\text{-}2NH_2)]$ and IRMOF-3 (7.6 Å diameter channel gives ~60 % conversion by ^{1}H NMR but loss in crystallinity) yield the PSM product with a pyridine amide tag (nicotinoyl group) by acylation with nicotinoyl chloride, Scheme 1.9.[111]

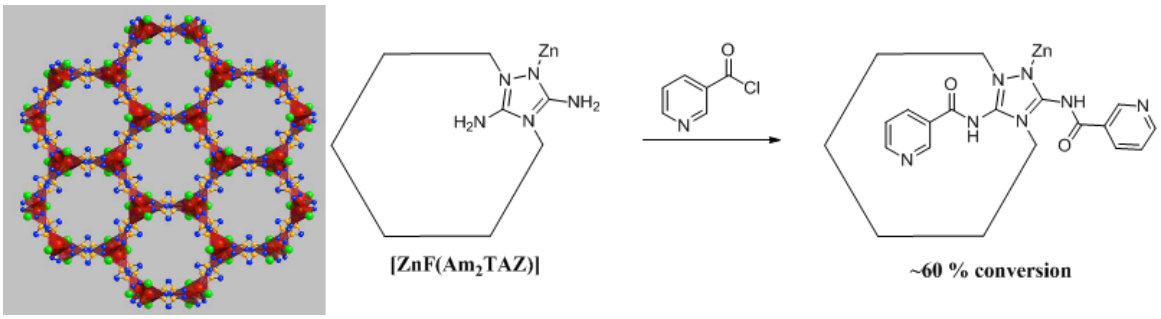

Scheme 1.9. PSM of amino groups of $[ZnF(Am_2TAZ)]$ to nicotinoyl groups.[111, 112]

Tandem PSM is the act of modifying an already modified framework *i.e.* exposing a MOF to two separate PSM reaction conditions in tandem. Cohen and co-workers report diphosgene and thiophosgene used as reagents in a MIL-53(Al)-NH_2 series to functionalise the MOF with isocyanates and isothiocyanates with conversion ~90 %.[113] To overcome the chemical stability of the MOF, digestion in HF/DMSO-d_6 had to be carried out to calculate the conversion by ^{1}H NMR, Scheme 1.10(*i*). Further reactions with amines or alcohols lead to MOF functionalised with urea and carbamate groups (Scheme 1.10(*ii*) and (*iii*)).[114]

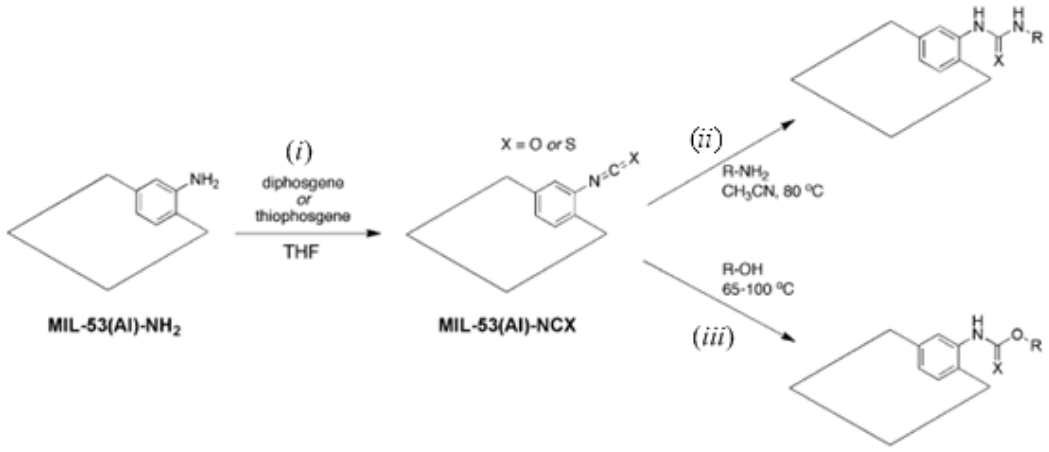

Scheme 1.10. Tandem PSM of MIL-53(Al)-NH_2 amino groups primarily to (*i*) isocyanates and isothiocyanates and (*ii*) urea and thiourea (*iii*) carbamate and thiocarbamate.[114]

Another way to gain access to urea functionalised materials is by using a trimethylsilyl isocyanate (TMS-NCO) PSM. Cohen *et al.* reported IRMOF-3 amine groups modified with TMS-NCO and trace water.[115] Water present in the reaction mixture forces the cleavage of the trimethylsilyl group yielding the urea product, IRMOF-3-UR0, *via* a trimethylsilyl urea intermediate. The achieved conversion was 99 % and they reported 71 % and 51 % conversions for ethyl- and pentyl-isocyanate summarised in Scheme 1.11.[116]

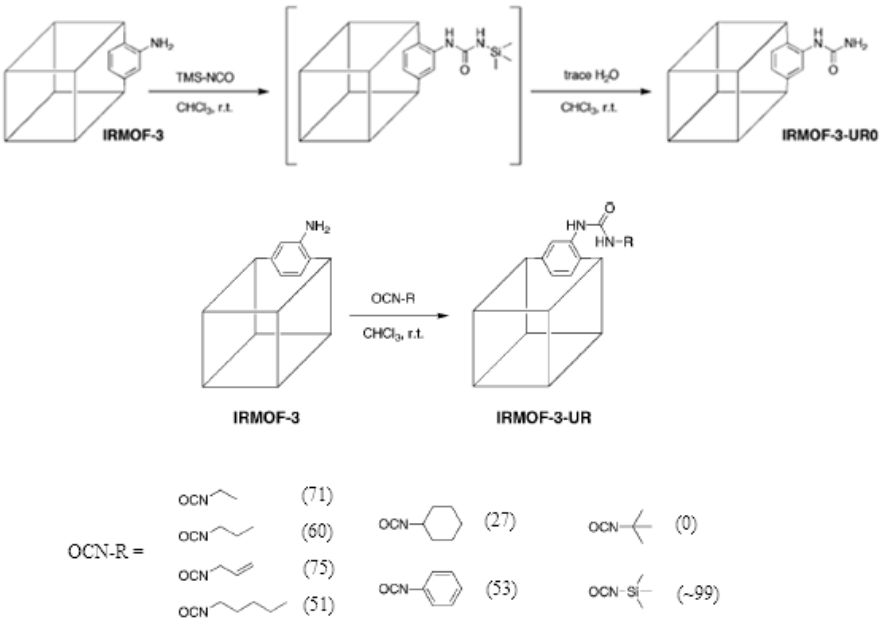

Scheme 1.11. Modification of IRMOF-3 amine groups to urea groups with NCO-R. Conversion percentages given in brackets.[116]

PSM is not limited to just tag groups in a framework. If the MOF is stable in an aqueous acidic solution then nitration is an option to add functionality to a benzene backboned MOF. Nitration of MIL-101(Cr) was reported by Stock *et al.* and in three steps groups were converted from nitro to amine to urea in near quantitative conversions during every reaction step, Scheme 1.12.[117] This approach to yield the amino tagged MIL-101(Cr) afforded better crystal quality than direct hydrothermal synthesis of MIL-101(Cr)-NH_2,[118] and is highlighted in the SEM, PXRD and BET surface area values.

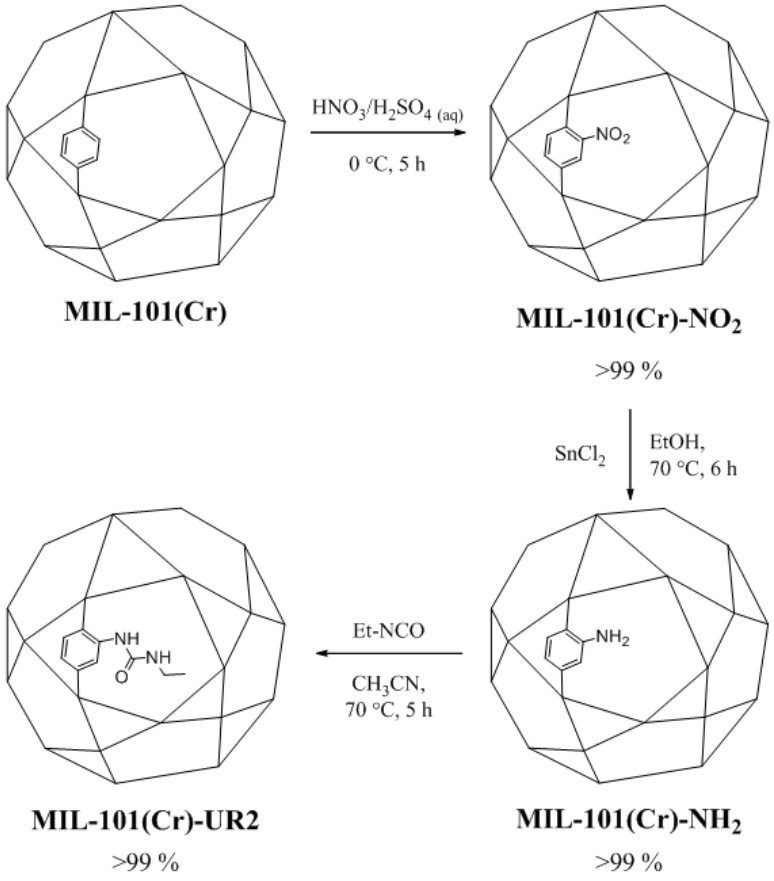

Scheme 1.12. Representation of nitration of MIL-101(Cr), reduction of nitro to amino group in the pores and subsequent PSM to urea functionalised MOF.[117]

1.7.2. Conversion of Amines to Imines

Rosseinsky and co-workers prepared the modification of IRMOF-3 with salicylaldehyde, in 2008, to form imine moieties, functionalised with alcohol groups, available for metal coordination.[119] They reported a tandem PSM, for IRMOF-3, soaked in a toluene solution and excess salicylaldehyde, for 7 days, yielded the PSM product, IRMOF-3$sal_{0.4}$ (40 % conversion to imine) The PSM reaction is summarised in Scheme 1.13 and corresponds to a conversion of ~13 % of the amino groups. Further modification with $VO(acac)_2$ gave

quantitative conversion to IRMOF-3-$V_{sal0.4}$ (100 % conversion in the second PSM) with each salicylaldehyde moiety binding a vanadium centre.[119]

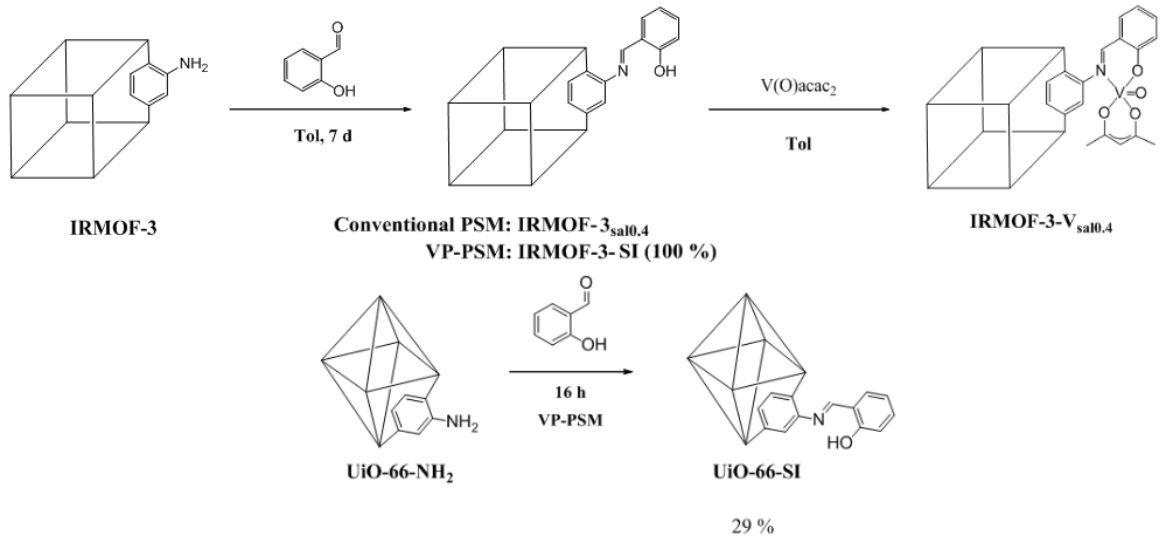

Scheme 1.13. Schematic representation of **(top)** IRMOF-3 conversion of amino to nicotinoyl groups. **(bottom)** UiO-66-NH_2 to salicylimino tagged framework.[119, 120]

Vapour phase PSM by van Bokhoven and co-workers using salicylaldehyde also resulted in an imine functionalised IRMOF-3. They reported adding by vapour phase $VO(acac)_2$ to bind metal sites into the pores of MIXMOF-5 (10 % amino groups incorporated in MOF-5) in quantitative conversions and UiO-66-NH_2 (29 % conversion) to the salicylimino functionalised material, UiO-66-SI. The advantages of VP-PSM over PSM carried out in solution are higher conversion and shorter reaction times. The disadvantage of this PSM method is exposing the pores to side products (acids and water) highlighted by the framework degradation of IRMOF-3 with anhydrides in VP-PSM.[120]

Tandem-PSMs are useful because they can occur in a one-pot synthesis. PSM of MIL-101(Fe)-NH_2 with 2-pyridine carboxaldehyde and $NiCl_2$ in a one-pot reaction gave ~30% conversion of amino groups to pyridine imino groups, Scheme 1.14.[121] Nickel centres are introduced as catalytic sites into the pores coordinating to the imino nitrogen atom and pyridine nitrogen atom. The nickel complex is made first to stop any competition with aldehyde reactant for amine groups. Applications for heterogeneous catalysis are the main uses for this type of PSM because of easy separation and reuse. In this case oligermisation of ethylene (15 Bar) with a co-catalyst, $AlClEt_2$, at 10^oC in heptane was reported by Canivet and Farrusseng. One equivalent of nickel functionalised MOF yields 10 % conversion to oligermisation product and three equivalents yields 30 % conversion.[121]

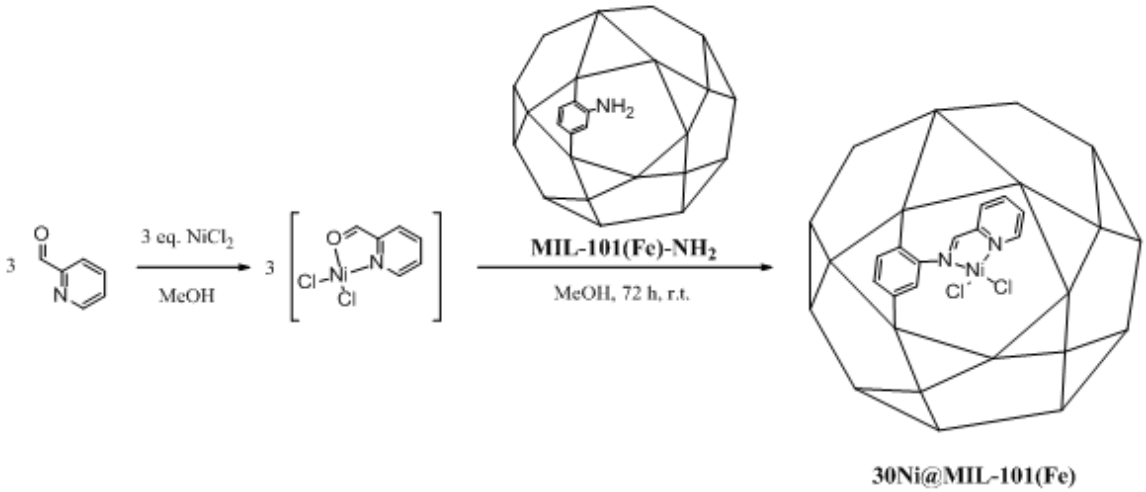

Scheme 1.14. Representation of 30 % nickel functionalised MOF PSM product from MIL-101(Fe)-NH_2 reacted with pyridine carboxaldehyde and $NiCl_2$ in methanol.[121]

A simpler one step example of amino to imino functional group conversion was reported by Ahn *et al.* IRMOF-3 and [$Mn(acac)_2$] are reacted, in one step, to tag the MOF by imino groups and simultaneously coordinating a manganese centre to it Scheme 1.15.[122] X-ray photon-electron spectroscopy (XPS) shows different manganese environments in the product and starting material, ICP-MS revealed approximately 10 % complexation of amino groups. The product material has been used as a heterogeneous catalyst for epoxidation of alkenes.[122]

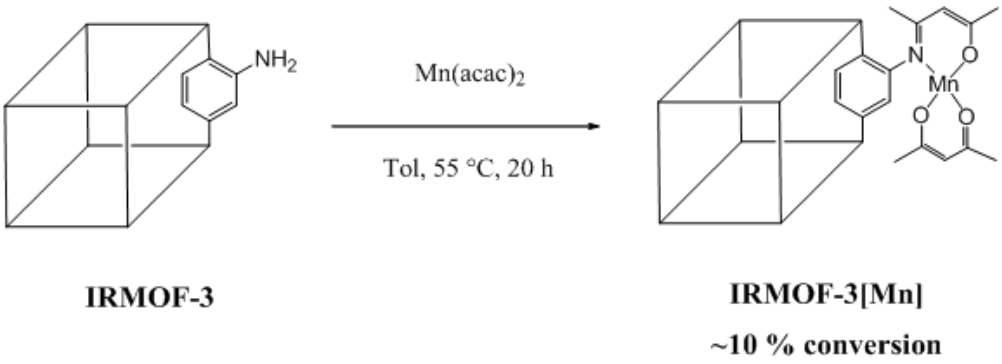

Scheme 1.15. Representation of PSM of IRMOF-3 with $Mn(acac)_2$ to form catalytic Mn centres in the pores of the MOF, in one-step.[122]

In a reversal of roles the aldehyde can be a part of the MOF as in the case of ZIF-90 (isostructural to ZIF-8 but with an aldehyde tag group) reported by Morris and Yaghi. They used a MOF with aldehyde tagged linkers and reduced these to alcohol groups with sodium borohydride in approximately 80 % conversion. In addition they reacted this MOF

with 2-aminoethanol to obtain the imino alcohol functionalised ZIF-92, with quantitative conversion, Scheme 1.16.[123]

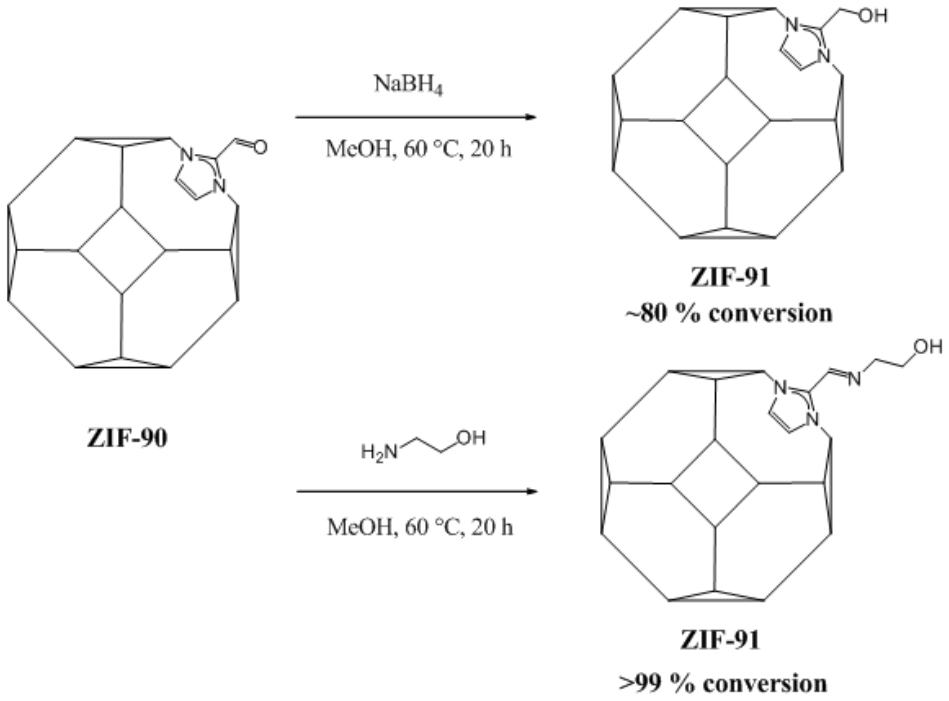

Scheme 1.16. Representation of PSM products from reaction of ZIF-90 with **(top)** sodium borohydride and **(bottom)** 2-aminoethanol.[123]

Also using ZIF-90, this time as a material to be immobilised onto a framework, Cao *et al.* made ZIF molecular sieves using an imine condensation PSM. Alumina (Al_2O_3) sieves were functionalised with amine groups and then reacted with ZIF-90 to form a membrane on the sieves, Scheme 1.17. The 20 μm ZIF-90 membrane is crack free and has aldehyde tags projecting outwards resulting in a selective membrane to allow only H_2 to pass in a mixed gas system of H_2/CH_4.[124]

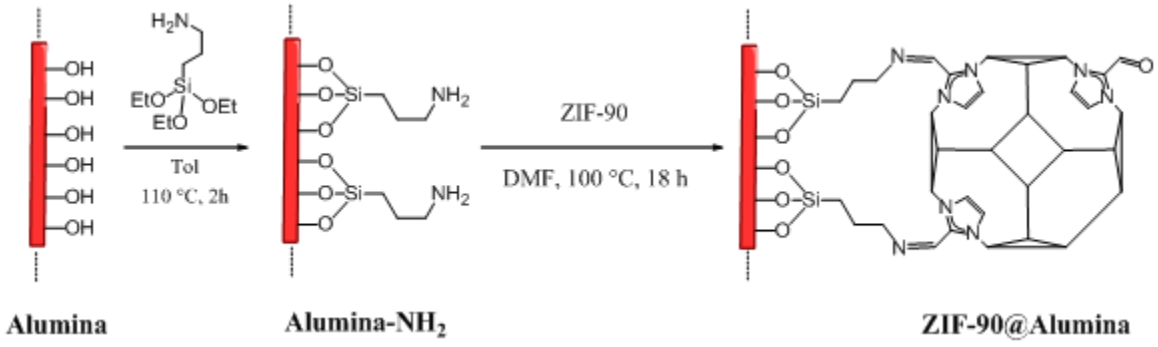

Scheme 1.17. Representation of MOF membrane formation on alumina sieves by covalent PSM of ZIF-90.[124]

1.7.3. Amine conversion to alternative groups

An interesting and complex example of PSM uses Sharpless click chemistry (click reactions on acetylene groups using azide derivatives and a Cu(I) catalyst) and was reported by Hupp *et al*.[125, 126] Scheme 1.19 shows the functionalisation of a custom made paddle-wheel MOF, $[Zn_2(NDC)_2(L^1)]$ (L^1 = 3-[(trimethylsilyl)ethynyl]-4-[2-(4-pyridinyl)ethenyl]pyridine), for this reaction. The MOF was synthesised by combining trimethylsilane tagged 1,2-di(pyridin-4-yl)ethene, pillaring, ligands and 1,2,4,5-tetrakis(4-carbonylphenyl)benzene, TCPB, with zinc(II)nitrate in DMF at 80 ºC for 24 h. The first MOF made (yellow in Scheme 1.18) has its pores deprotected by F^- ions (green) and subsequent click reaction to add RN_3 across the triple bond of the acetylene groups (blue). This was further developed by functionalising the surface with a different azide than the internal pores. This was achieved by carrying out the first deprotection step with the MOF soaked in chloroform, so the hydrophilic KF would not enter the pores. The surface was then deprotected so that the first click reaction proceeds only on the surface. The interior was then deprotected with a hydrophobic tetraethylammonium fluoride (TEAF) in THF solution. Then the next click reaction proceeded with a different azide.[126]

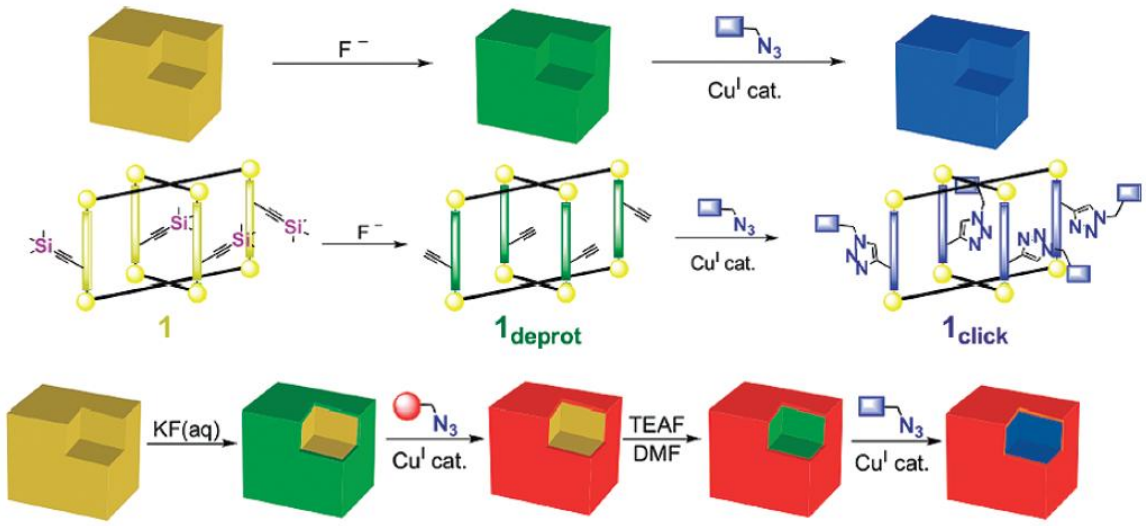

Scheme 1.18. Representation of internal/external functionalisation of $[Zn(NDC)_2(L^1)]$.[126]

Farruseng *et al.* also reported click chemistry on DMOF-1-NH_2. The azide is formed by reacting the amino groups with tBuONO/$TMSN_3$ followed by a click reaction with phenylacetylene to form $[Zn_2(L)_{1.8}(BDC\text{-}N_3)_{0.2}(dabco)]$ (DMOF-fun, L = BDC-phenyltriazoyl).[127] Conversion is 90 % and is seemingly unaffected by very small pores potentially reducing penetration of the acetylene and copper catalyst. In the same report

they repeated this PSM procedure with MIL-68(In)-NH_2 converting amino groups to N_3 groups (by tBuONO/$TMSN_3$, in a 90 % conversion) then further reacted with phenylacetylene to form the click reaction product MIL-68(In)-Fun with 90 % conversion.[127]

The PSM of IRMOF-3 with cyanuric chloride was reported by Jeong and co-workers and the products showed micro/meso pores and macroscopic trenches. The conversion of amine groups to cyanuric groups was 25 %, Scheme 1.19(top).[128] The trenches also had the effect of the surface area being reduced to 25 % of the starting material. Triethylamine acts a proton sink so the HCl produced from the PSM does not have time to decompose the framework. However this method is not fully effective as etching, from the by-products of the reaction, produces 4 nm mesopores (Scheme 1.19(bottom). This results in an overall reduction in the BET surface area and the material exhibits N_2 adsorption hysteresis at 77 K. The MOF PSM product was analysed by X-ray photoelectron spectroscopy with data obtained for crushed and intact samples, which showed difference in intensities in the nitrogen peaks at ~400 eV. The authors attributed these observations to the modified groups being more concentrated at the extremities of the crystals.[128]

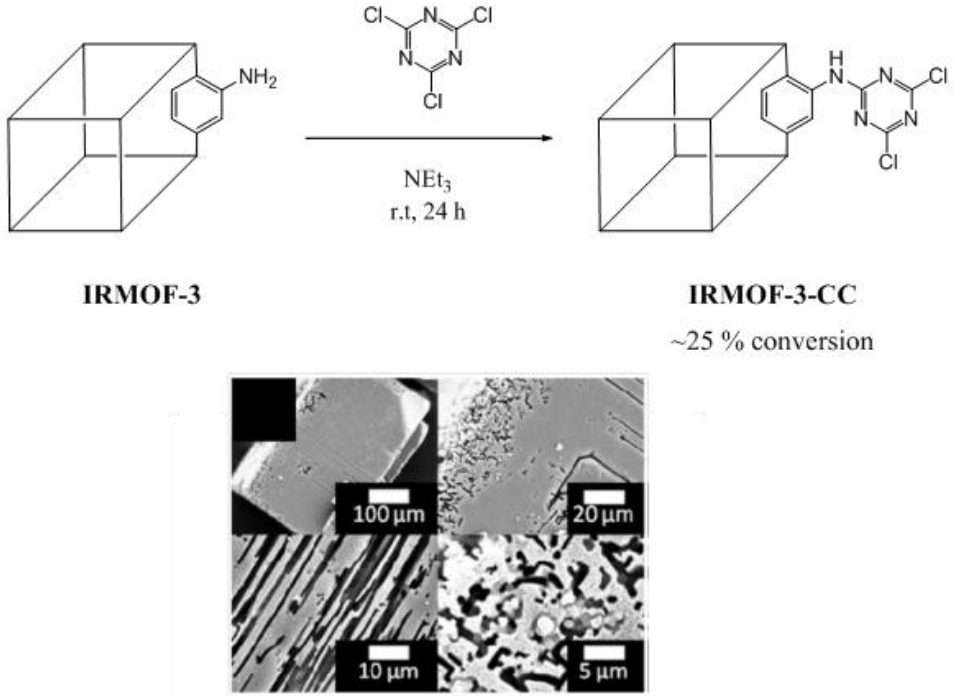

Scheme 1.19. (top) Schematic representation of the PSM of IRMOF-3 with cyanuric chloride (CC). **(bottom)** SEM of IRMOF-3-CC etched crystals.[128]

Cohen and co-workers reported a covalent PSM on UMCM-1-NH_2 and IRMOF-3 with nitrogen monoxide gas (NO) to yield a "NONOate" (-NHN=ONHOH) tagged MOF, Scheme 1.20.[129] The conversion was estimated by TGA weight losses (converted groups confirmed by FT-IR) and showed a ~86 % conversion to UMCM-1-NONO and a ~44 % conversion to IRMOF-3-NONO. There is secondary NO release from the NONOate group over time and they report that UMCM-1-NONO releases 0.1 ± 0.01 mmol NO g^{-1}. This is an interesting example of covalently storing gas, in a MOF, albeit with a lack on control of release in this case.[129]

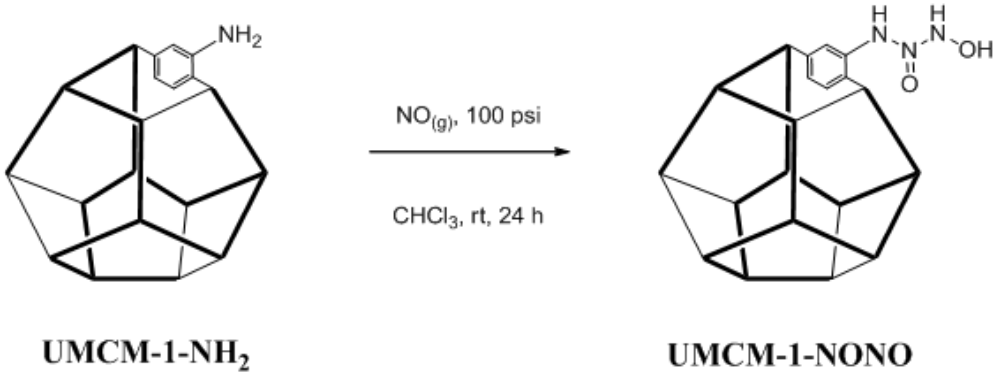

Scheme 1.20. Representation of the PSM reaction of UMCM-1-NH_2 to UMCM-1-NONO with $NO_{(g)}$.[129]

Ring opening reactions with NH_2 as a nucleophilic reactant were reported by Yaghi *et al.* on IRMOF-3 with a sultone, giving 57 % conversion to IRMOF-3b and with aziridine, to from the primary amine tagged, IRMOF-3c, with 36 % conversion, including some secondary addition on the same tag.[130] MIL-53(Al)-NH_2 undergoes PSM to ring open maleic anhydride with 43 % conversion to the maleic acid functionalised MOF, Scheme 1.21.[131] MOFs modified with cyclic anhydrides have been mentioned in section 1.6.

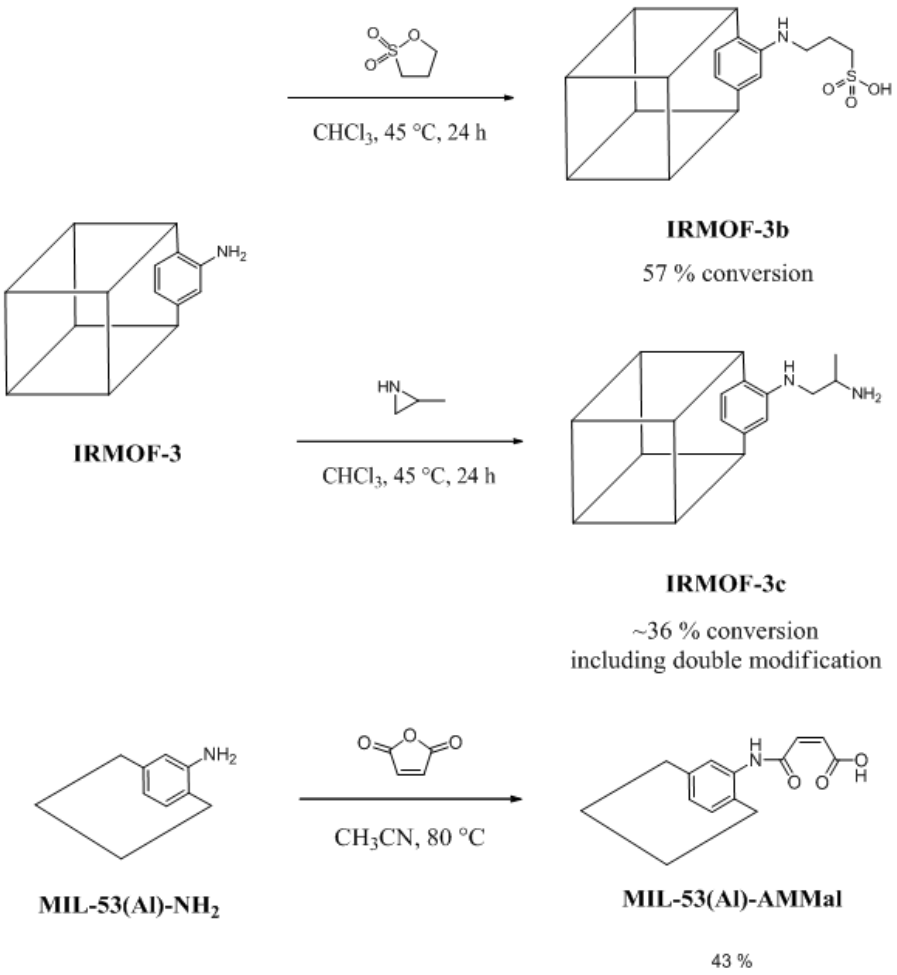

Scheme 1.21. Cycloaddition PSMs of IRMOF-3 and MIL-53(Al)-NH_2.[130, 131]

Diels-Alder reactions on the alkenyl groups of amide tagged IRMOF-3 and UMCM-1-NH_2 was reported by Cohen and co-workers. Initially the amino tags were reacted with pent-4-enoic anhydride in quantitative conversions. Then the dieneophile reacted with the diene, dimethyl-1,2,4,5-tetrazine-3,6-carboxylate (DTC), and was coupled by a Diels-Alder mechanism to the pendent alkene group with a release of $N_{2(g)}$. A MIXMOF-5 system was needed to be able to get quantitative conversion in IRMOF-3 system which entails making a partially amino functionalised MOF-5 for PSM, Scheme 1.22(top). This suggests that decreased pore size by reactant and product blocking decreases conversion in the PSM reaction.[132]

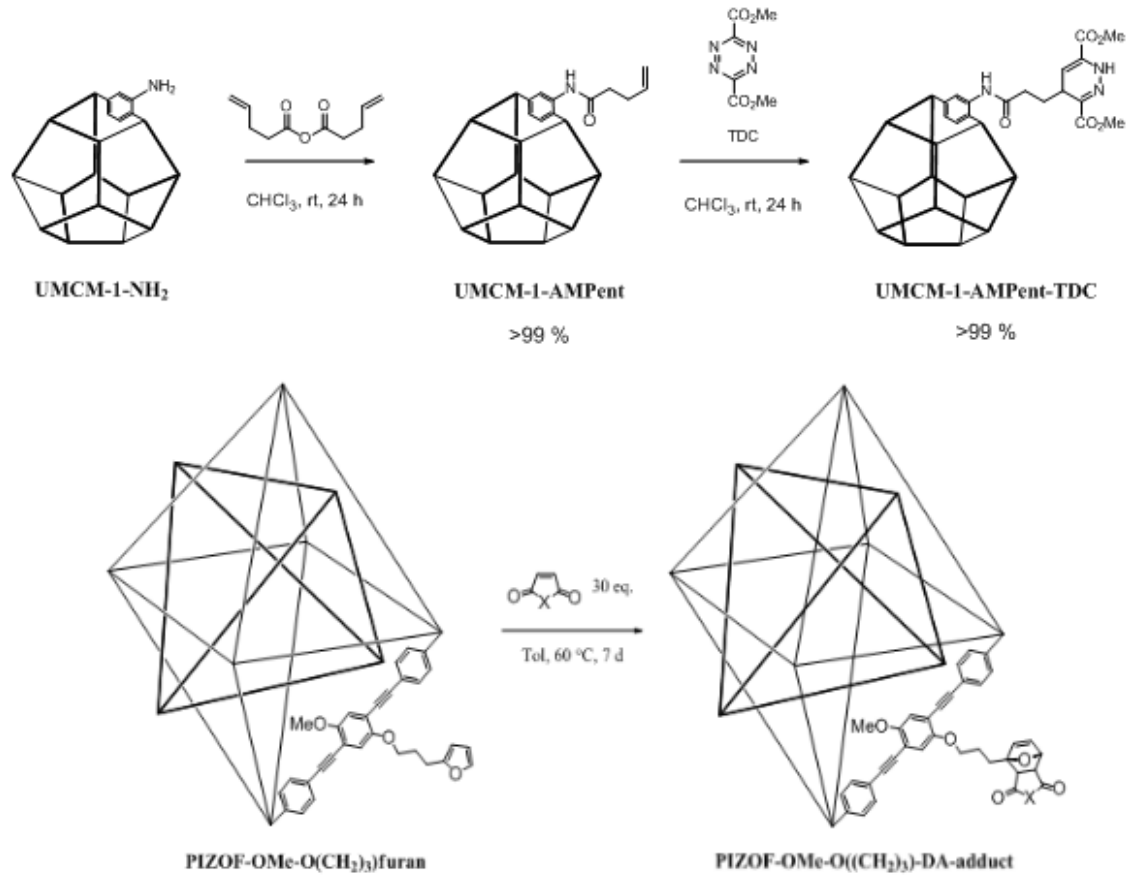

Scheme 1.22. Representation of the Diels-Alder PSM of (top) UMCM-1-NH_2 with pent-4-enoic anhydride followed by DTC and furan tagged PIZOF with an unsaturated cyclic anhydride. X = NH, NMe or NPh.[132, 133]

Godt *et al.* reported Diels-Alder PSMs on a furan tagged PIZOF system, PIZOF-OMe-O($(CH_2)_3$)furan with 1X-1*H*-pyrrole-2,5-dione in >99 % conversion (X = NH and NMe) and 89 % conversion (X = NPh). The MOF system formed is summarised in Scheme 1.22(bottom).[133] This PSM gives the MOF a lot of functionality, however the reaction does need lots of equivalents (thirty) of pyrrole-2,5-dione and a long reaction time of seven days.

1.7.4. PSM with Alternative Functionalised MOF Tags

Aldehyde groups have also been incorporated into MOF frameworks. Yaghi *et al.* reported that the aldehyde tagged ZIF, ZIF-90, had its pendent groups converted to OH moieties (by $NaBH_4$) and a separate imine condensation with ethylenediamine to functionalise the MOF with pendent alcohol.[123]

Burrows *et al.* synthesised a 2-aldehydo derivative of H_2BPDC: H_2BPDC-CHO. This was reacted with $Zn(NO_3)_2{\cdot}6H_2O$ in DMF to form the MOF, $[Zn_4O(BPDC\text{-}CHO)_3]$, exhibiting two-fold interpenetration, similar to the overall architecture of IRMOF-9 but with a subtly different SBU.[1] The free aldehyde groups, disordered over four sites of the linker, were reacted with 2,4-dinitrophenylhydrazine (DPH) to form the expected hydrazone, $[Zn_4O(OH_2)_2(BPDC\text{-}CHO)_{1.2}(BPDC\text{-}DPH)_{1.8}]$, at room temperature, in a ~60 % conversion, with a colour change from colourless to orange, Scheme 1.23. Evidence of the conversion of the tag groups was also observed in the single-crystal X-ray diffraction analysis shown by electron density present in the pores of a F_c-F_o plot.[1]

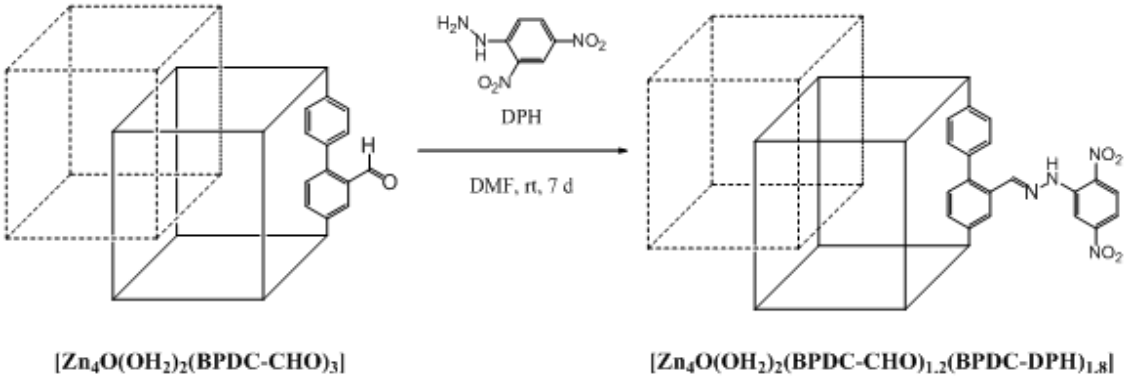

Scheme 1.23. Representation of the PSM reaction of aldehyde groups in $[Zn_4O(OH_2)_2(BPDC\text{-}CHO)_3]$ with DPH.[1]

The aldehyde tagged MOF SIM-1, $[Zn(mIm\text{-}CHO)_2]$ (mIm-CHO = aldehyde methyl imidazolate) is isostructural to ZIF-90 but the tags are on the opposite side of the linker. Farrusseng and co-workers modified the aldehyde groups by reacting with the long chain alkyl amine, dodecylamine, forming a sterically hindered imine, Scheme 1.24.[134] Due to the large nature of the amine reactant conversion of only 22 %, of aldehyde to imino groups, was achieved. However, this has the effect of coating the MOF with a hydrophobic shell and therefore protects it from hydrolysis by water or acid. The alkyl imino tagged PSM product SIM-2(C_{12}) was used as a catalyst for the addition of malononitrile to benzaldehyde in a Knoevenagel catalysis with 80 % conversion to product in four hours at room temperature, with 1 mol% loading. SIM-2(C_{12}) is significantly more catalytically active than the starting materials with conversions of SIM-1 (inactive 3 %) and dodecylamine less active (65 %).

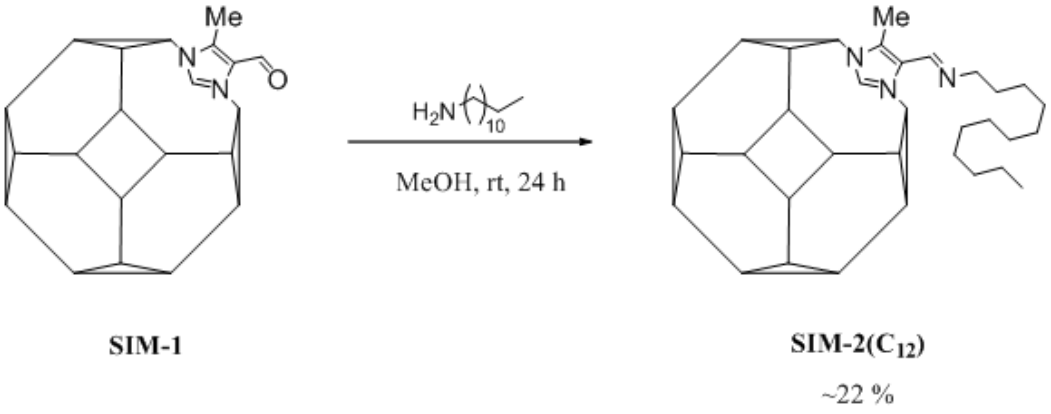

Scheme 1.24. Representation of the synthesis of SIM-2(C_{12}) by the PSM of SIM-1 with dodecylamine.[134]

Hydroxyl moieties on MOFs have been reported by Hupp and co-workers on the non-interpenetrated, zinc paddle wheel MOF, [Zn_2(TCPB)(DPG)]. (TCPB = 1,2,4,5-tetrakis(4-carboxyphenyl)-benzene and DPG = *meso*-1,2-bis(4-pyridyl)-1,2-ethanediol). These hydroxyl tag groups undergo the conversion to carboxylic acid groups through amide condensation.[135] Hupp *et al.* report almost quantitative conversion from the dihydroxylated linkers to the carboxylic acid tagged linkers using the cyclic anhydride reagent dihydrofuran-2,5-dione, Scheme 1.25(*i*). Then a second PSM with an aqueous solution of $CuCl_2$ was reported to demonstrate the chelation ability of the MOF showing a reduction of Cu^{2+} concentration from 75 ppm to 50 ppm after four hour exposure, Scheme 1.25(*ii*). This was accompanied with a material colour change from pale yellow to blue-green.[135]

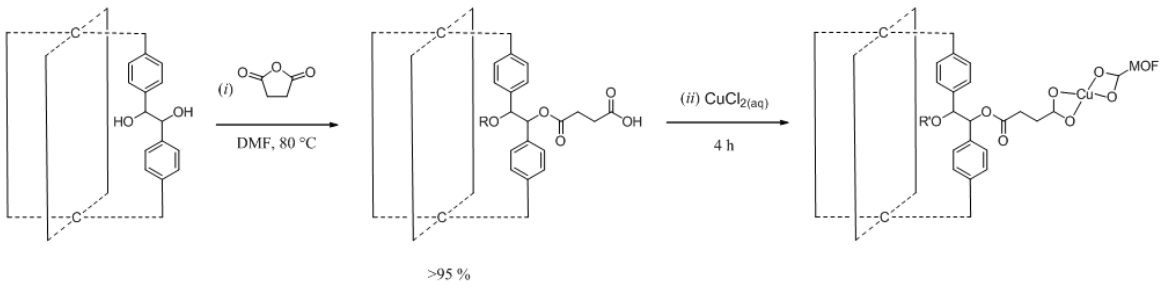

Scheme 1.25. Representation of a tandem PSM of [Zn_2(TCPB)(DPG)] by ***(i)*** ring opening of cyclic anhydride and ***(ii)*** chelation of Cu^{2+} reagent.[135] C = Aromatic backbone, R = carboxylic acid moiety, R' = chelated Cu^{2+} moiety.

An example of an allyloxy functionalised BPDC based MOF was reported by Richardson *et al.* with formula [$Zn_4O(L^1)_3(DMF)_2$], (L^1 = 2-(allyloxy)-[1,1'-biphenyl]-4,4'-

dicarboxylate).[136] This doubly interpenetrated network undergoes PSM by thermal stimulus resulting in a Claisen rearrangement. TG-DTA was used to see any exotherms in a plateau region to find the correct temperature for PSM without decomposition of the material. This is an example of a reagentless PSM. The first product formed at lower temperatures is $[Zn_4O(L^1)_{0.33}(L^2)_{2.47}(L^3)_{0.17}]$, ($L^2$ = 3-allyl-2-hydroxy-[1,1'-biphenyl]-4,4'-dicarboxylate, L^3 = 7-(4-carboxyphenyl)-2-methyl-2,3-dihydrobenzofuran-4-carboxylate), Scheme 1.26. The second product at higher temperatures is a cyclisation product $[Zn_4O(L^2)_{0.45}(L^3)_{2.55}]$ with no allyloxy groups present. This can also be obtained by heating the first PSM product for longer. It was found that crushed crystals get better PSM conversion by increasing the surface area of crystals exposed to heat.[136]

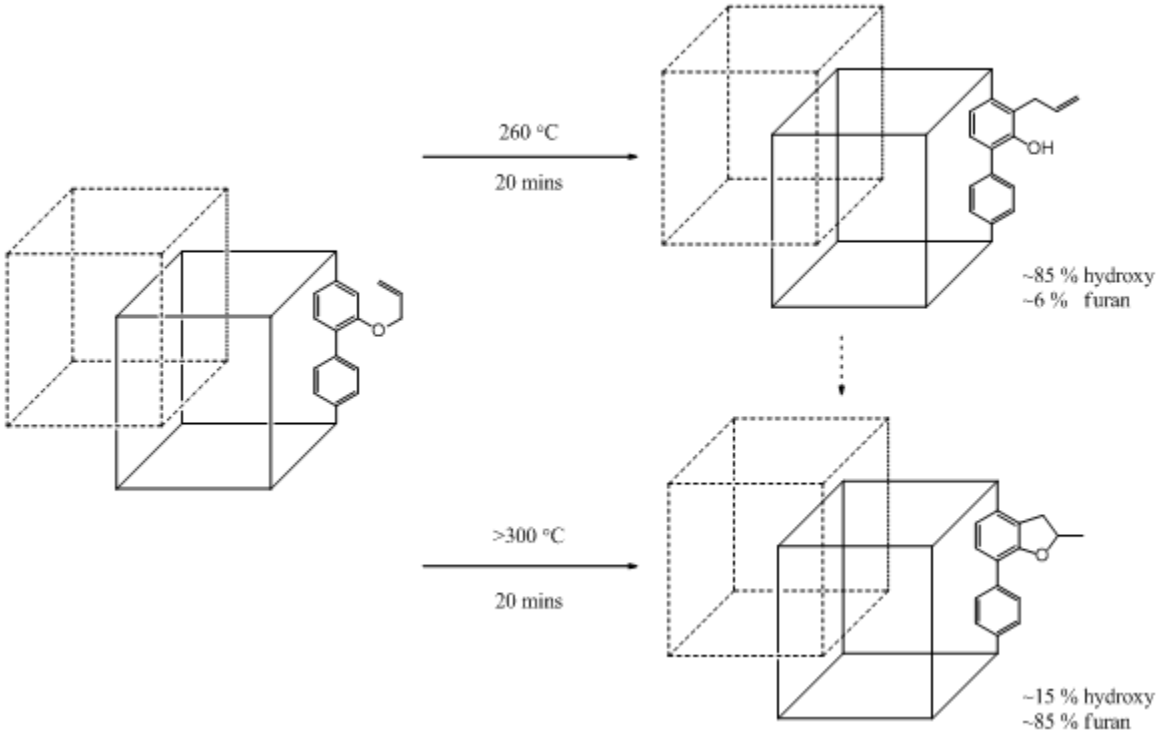

Scheme 1.26. Representation of the thermal PSM of $[Zn_4O(L^1)_3(DMF)_2]$, with the Claisen rearrangement **(top)** occurring before the ring closing reaction **(bottom)**.[136]

Dipyridyl linkers can be functionalised in the same fashion as carboxylate linkers. The following tandem PSM example, reported by Reiger and co-workers, summarises two PSM reactions and gives access to four functionalities in a MOF. The MOF they report has formula, $[Zn_2(TDC)_2\ (L^1)]$ and is based on a functionalised 4,4'-bipy and an accommodating dicarboxylate, 9,10-triptycenedicarboxylate (TDC). The MOF undergoes tandem PSM by double bond epoxidation, by dimethyldioxirane (DMDO), followed by

ring opening of the resulting epoxide tag by ethyl mercaptan, Scheme 1.27.[137] Conversion in the first step is quantitative with full epoxidation occurring after five hours (followed by kinetic investigations) whereas conversion with mercaptan plateaus at 50 % after five hours.

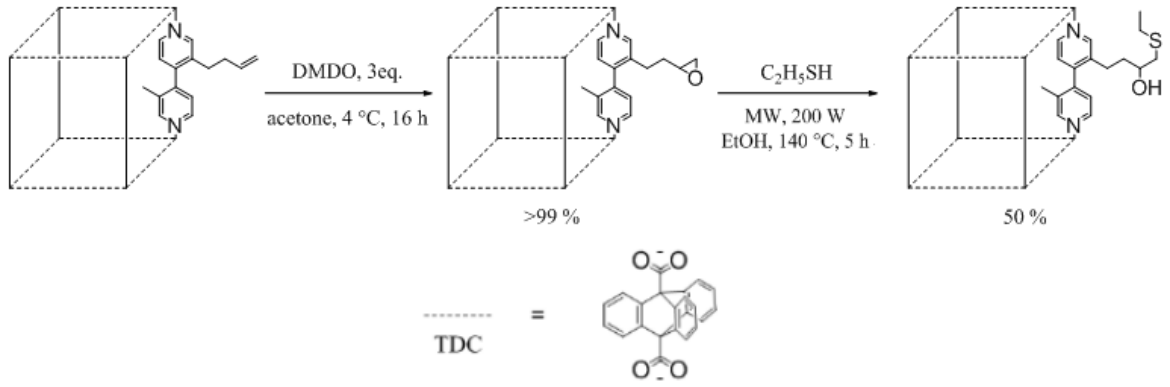

Scheme 1.27. Representation of a thioether tagged MOF formed by the PSM of alkenyl tag groups with DMDO, followed by ethyl mercaptan. Dashed linker represents TDC.[137]

Burrows *et al.* also used DMDO to perform PSM reactions on a sulphur tagged BPDC based MOF to yield a series of sulphone tagged MOFs.[138] $[Zn_4O(L^1)_3]$ to $[Zn_4O(L^6)_3]$ (L^1 = BPDC-sulphide, L^6 = BPDC-sulphone) was an example with quantitative conversion achieved in acetone at room temperature in only three hours, Scheme 1.28.[138]

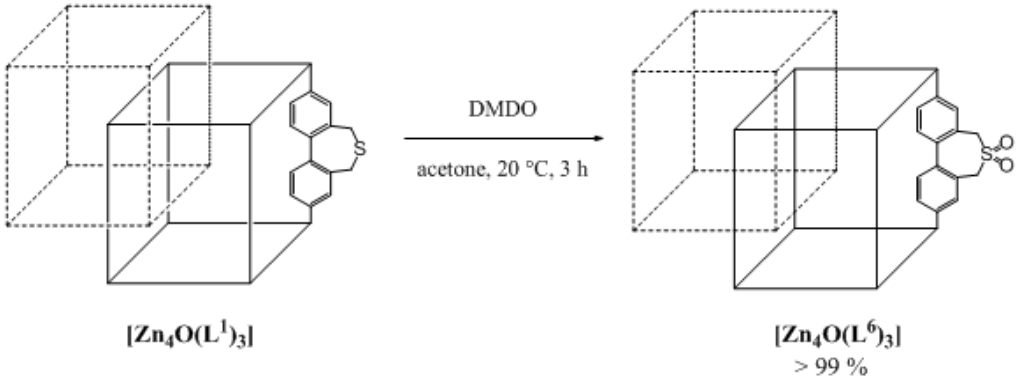

Scheme 1.28. Representation of the oxidative PSM of $[Zn_4O(L^1)_3]$ to $[Zn_4O(L^6)_3]$ by DMDO.[138]

Other types of PSM reactions on ethylene moieties have been reported, by Bauer and co-workers, with bromine.[139] They report the *trans*-stilbene based MOF, $[Zn_4O(SDC)_3]$ (SDC = *trans*-4,4′-stilbene dicarboxylate), bromonated to form the bromo tagged MOF $[Zn_4O(L)_3]$, (L = 4,4′-(1,2-dibromoethane-1,2-diyl)dibenzoate), with quantitative conversion to a *meso*- isomer and a pair of *rac*- isomers in the ratio of 4:1 in the PSM

product, summarised in Scheme 1.29.[139] This PSM is done on the backbone of the MOF rather than a pendent tag group and gives a different distribution of isomeric products compared with the same reaction in solution.

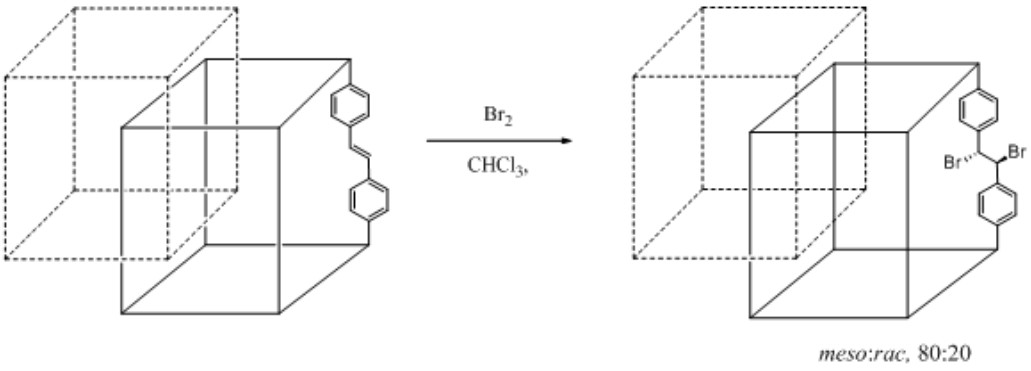

Scheme 1.29. Representation of the PSM of *trans*-stilbene MOF $[Zn_4O(SDC)_3]$ by exposure to bromine (major *meso*-isomer shown here).[139]

Microwave methods are useful for speeding up PSM reactions. Cohen and Kim demonstrated this with the cyanation of UiO-66-Br, reducing the synthetic time from 24 h to 10 minutes and doubling the conversion of bromo to cyano groups (from 43 % to 90 %) with zero detriment to crystallinity (Scheme 1.30).[140]

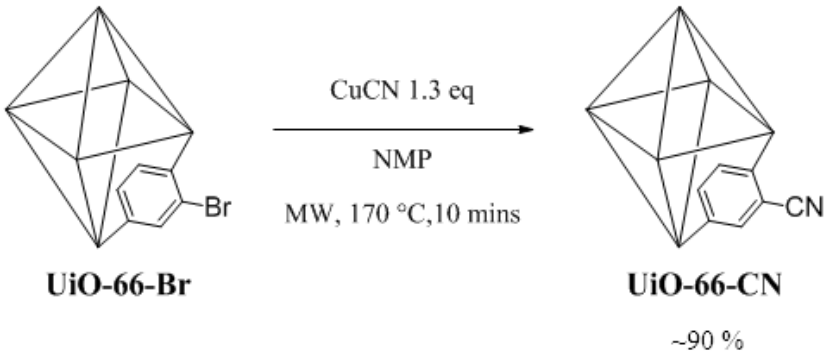

Scheme 1.30. Representation of the PSM of UiO-66-Br with CuCN with microwave assistance in *N*-methyl-2-pyrrolidone (NMP).[140]

1.8. Post-synthetic deprotection (PSD)

PSD is useful for synthesising functional MOFs such as ones which have groups with the propensity to complex metals in a direct synthesis. The process involves removing complexity in a MOF and producing larger voids. PSD is also referred to as protection-complexation-deprotection (PCD) in some reports.[141]

2,5-Dihydroxybenzenedicarboxylic acid (BDC-OH_2) was protected with acetic anhydride before a MOF formation reaction seen in a report by Kitagawa *et al.* in 2009.[141] [Zn(DACO-BDC)(bpy)] (DACO-BDC = 2,5-diacetoxyterephthalic acid) was synthesised for the ultimate goal of production of [Zn(BDC-OH_2)(bpy)] in a three step process to give free hydroxyl groups, Scheme 1.31. Usually these 4,4'-bipy and terephthalate systems form interpenetrated structures. This reaction approach inhibits interpenetration thanks to steric hindrance from the acetoxy protecting groups. PSD occurs slowly under the conditions of MOF formation in a one-pot process and in quantitative conversion.[141]

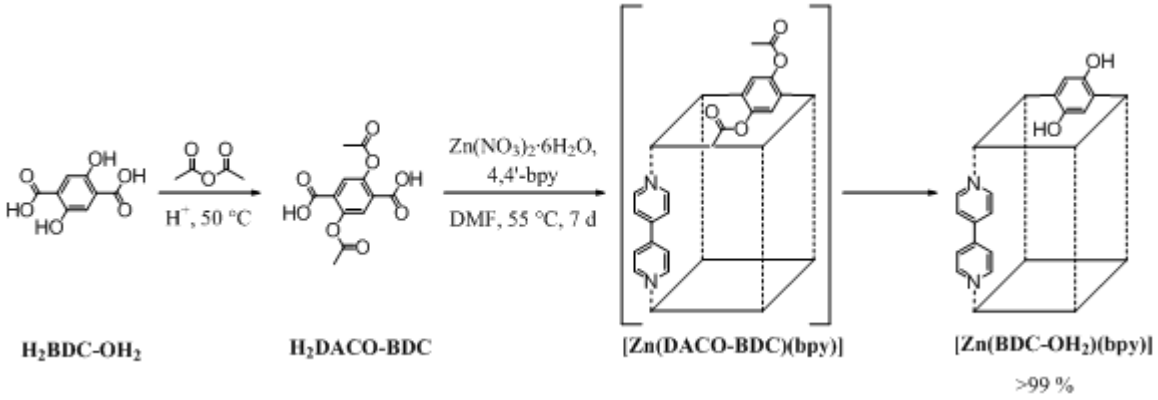

Scheme 1.31. PSD of acetoxy groups to hydroxyl groups in [Zn(DACO-BDC)(bpy)].[141]

Telfer *et al.* started using more conventional protecting group chemistry to synthesise amino-tagged, large pore, non-interpenetrated structures.[142] They protect the amine groups of H_2BPDC-NH_2 and proline functionalised H_2BPDC-Pro with Boc groups (*tert*-butyl carbamate) with the goal of deprotection *via* post-synthetic thermolysis.[143] TG-DTA data is used to find the temperature of deprotection before framework decomposition. Interpenetration is inhibited and the PSM expands the MOF cavities by unmasking the functional groups, Scheme 1.32.

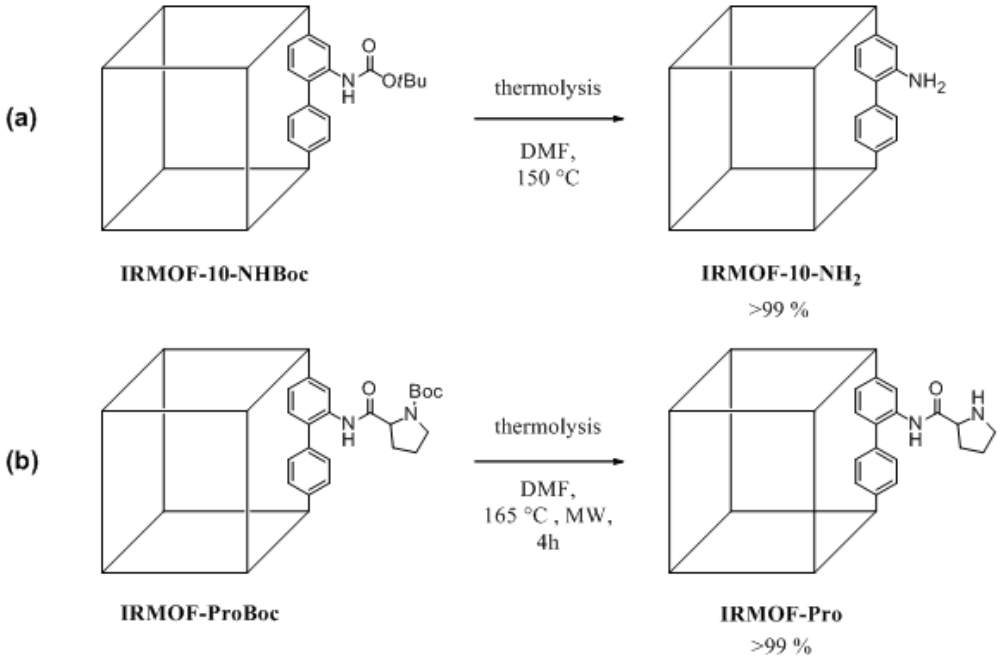

Scheme 1.32. PSD of the Boc tags to amine tags of (a) and (b) by thermolysis.[142, 143]

One advantage of PSM by thermolysis, compared with chemical deprotection, is an increased conversion of tag groups because there are no reactants diffusing in, blocking any products diffusing out. Pore collapse of IRMOF-9 at the surface (non-interpenetrated) can inhibit gas sorption but activation by supercritical CO_2 was reported by Telfer *et al.* to alleviate some of this problem.[144]

Farruseng *et al.* reported the PSM of MIL-68(In)-NH_2 with Fmoc amino acid moieties and then a secondary deprotection step yield the free amino acid tag groups on the MOF.[145] Proline Fmoc and alanine Fmoc protected tag groups were introduced *via* PSM with bromo-trispyrrolidinophosphonium hexafluorophosphate (PyBroP), in addition to 4-(dimethylamino)pyridine (DMAP), in chloroform. The deprotection was carried out with piperidine in DMF at room temperature in DMF for 30 minutes, Scheme 1.33.[145] This PSM method allows the anchoring of chiral, biological molecules to a MOF in relatively soft reaction conditions and ensures one molecule per hexagonal window due to the steric bulk of the protecting group.

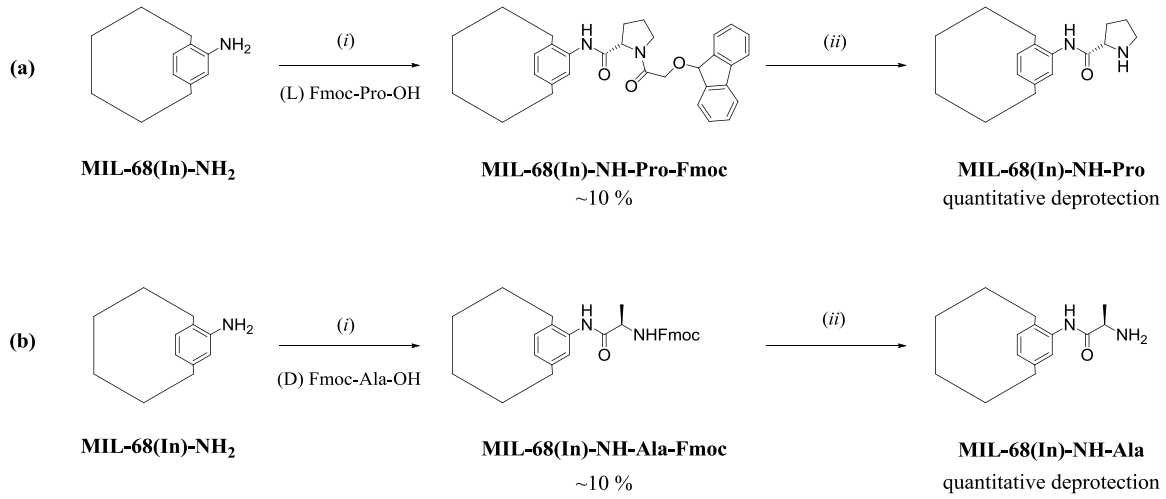

Scheme 1.33. Representation of PSM of MIL-68(In)-NH_2 (*i*) PyBroP,DMAP,$CHCl_3$ with **(a)** proline-Fmoc protected tag group and **(b)** alanine-Fmoc protected tag group, then PSD (*ii*) piperidine in DMF.[145]

1.9. Overall Limitations and Outlook for the Future

MOFs are made by reaction of a metal salt with a bridging ligand in a solvent such as DMF and can undergo modification, post-synthesis, to alter the chemical and physical properties of the MOF.

MOFs can be designed by selecting linkers with target architecture in mind. This can be done with computational aids. The surface areas of predicted MOFs can be screened and advances in this area have been reported by C. Wilmer, O. Farha and J. Hupp.[146] An analysis of a library (such as the MOFomics database)[147] can give predicted surface areas, which can reduce wasted time in the laboratory arising from trial and error.

Model systems can be made *in silico* where gas interacts with framework using density functional theory (DFT) calculations and Grand Canonical Monte Carlo Simulations.[148] It can also be used to show gas selectivity predictions e.g. alkyl groups are the best for methane adsorption[149] and CO_2 separation potential from structure property relationships.[150-152] Changing the functional groups in the model has been done on ZIF-8 for example by the Bux group finding discrepancies with experimental observations.[153]

One of the limitations of this modelling system is the assumption that the crystals are perfect, defect free and rigid. *In silico* modelling still has inaccuracies, for example permeance is very important even if the system shows high selectivity for a substrate and diffusivity is not well modelled at this time.

A limitation of MOFs mass production is scale up for the production in industry as high-throughput methods are still in their infant stages, such as spray-dry synthesis reported by Imaz *et al.* in 2012.[154] Prices are still very high but chemical companies such as Sigma-Aldrich are selling an ever expanding catalogue of MOFs e.g. ZIF-8 is sold as Basolite© Z1200.

The moisture sensitive MOFs are harder to commercialise. Hydrothermal stability of MOFs is a major stumbling block. The Willis group have calculated theoretical values of $\Delta E^{\ddagger}_{disp}$ (measure of hydrothermal stability): MOF-5 = 11.6 kcal/mol, HKUST-1 = 28.9, MIL-101(Cr)=35.8 and ZIF-8 = 55.7 (high stability).[155]

Exchanging the solvent in the pores of the framework with toluene, was found to alleviate some of the moisture sensitivity issues and allowed the MOF to be handled in a more humid environment than before, without the loss in crystallinity and hence, surface area.

The types of functional groups that have been incorporated onto MOF pore surfaces are usually small, simple moieties as space is usually limited inside framework voids. PSM has a wide scope for simple, small tag groups. Ligands with pendent groups i.e. -CHO, -OH, -OR, -SR, -X and -alkenyl can be incorporated into MOFs for use in PSM but depending on the system direct synthesis may not be viable.

There have been many reports of amide bond and urea formation but these groups are not robust enough in harsh conditions. Many MOFs are also not robust enough to tolerate the synthetic conditions with the acidic by-products sometimes hampering conversion due to a mandatory compromise between reaction time and crystallinity.

Other limitations of PSM occur because of blockages. Conversion is reduced when PSM reactants and by-products are diffusing in and out respectively slowing the process down. Also PSM tags can block the pores and channels in the MOF cutting off access further into the core of the crystals.

PSM can add functionality to a MOF or unmask protected groups on the pore surfaces. PSM reagents and tag roles in the reaction can be reversed so for every amine tag reacted with an aldehyde the opposite can also be true with aldehyde tags reacting in the same fashion. In the case of imine formation however the C=N double bond will shift one position depending which group is attached to the MOF.

MIXMOFs, reported by Fassureng and co-workers, are a class of MOFs with mixed functional ligands spread homogenously through the crystals.[156] These MIXMOF materials are interesting because they could overcome some limitations of PSM. The core of a MOF is much harder to modify because of blockages resulting from reactants diffusing in, products diffusing out and converted groups on the outer layers of the crystal. If the functional groups are spread throughout the MOF it may lead to increased conversions of functional groups because a smaller percentage are at the surface of a crystal.

One major target for the future of MOF synthesis and PSM (in gas storage) is to produce a system for reversible H_2 storage at room temperature and ambient conditions.[157] This has very interesting applications in the automobile industry and the energy sector.[158]

1.10. Aims and Objectives

The main aim of this study is to investigate new post-synthetic modification (PSM) reaction pathways on metal-organic frameworks (MOFs) and therefore to expand the number of available routes to prepare new functionalised frameworks, that are not available by direct synthesis. The method involves single crystal to single crystal transformations changing the functionality of the pore surfaces.

The effects of PSM reactions on the physical and chemical properties of the MOFs will be studied. Imino groups have been incorporated into MOFs previously but the reactions leading to them are chemically reversible, therefore the goal is to make an irreversible modification by converting a primary amine to a secondary amine tag group using aldehydes and a mild reducing agent.

The diazonium salt group has not been previously reported in MOF chemistry because most MOFs are unstable to the strongly acidic conditions that are needed to form this useful intermediate. Hence this PSM reaction is a good target to obtain a generic tool, for the MOF chemist, for use in acid stable systems, such as the MIL-101(Cr) topology.

There are only a few previously reported MOFs containing amino-isophthalate ligands suitable for PSM reactions. It is therefore necessary to synthesise a range of MOFs with different metal salts and tagged isophthalic acids for potential modification.

Characterisation by single crystal X-ray diffraction will be the main analytical technique to yield structural information of the new frameworks and to ideally monitor PSM conversion of tag groups.

1.11. References

[1] A. D. Burrows, C. G. Frost, M. F. Mahon, C. Richardson, *Angew. Chem., Int. Ed.,* **2008**, *47*, 8482.

[2] H. He, D. Collins, F. Dai, X. Zhao, G. Zhang, H. Ma, D. Sun, *Cryst. Growth Des.,* **2009**, *10*, 895.

[3] H. A. Goodwin, J. C. Bailar, *J. Am. Chem. Soc.,* **1961**, *83*, 2467.

[4] O. M. Yaghi, G. Li, H. Li, *Nature*, **1995**, *378*, 703.

[5] Web of Knowledge survey excluding all non chemistry or material science research areas. apps.webofknowledge.com

[6] S. Kitagawa, R. Kitaura, S. Noro, *Angew. Chem. Int. Ed.*, **2004**, *43*, 2334.

[7] S. R. Batten, N. R. Champness, X. M. Chen, J. Garcia-Martinez, S. Kitagawa, L. Ohrstrom, M. O'Keeffe, M. P. Suh, J. Reedijk, *CrystEngComm,* **2012**, *14*, 3001.

[8] R. C. Hiorns, R. J. Boucher, R. Duhlev, K. H. Hellwich, P. Hodge, A. D. Jenkins, R. G. Jones, J. Kahovec, G. Moad, C. K. Ober, D. W. Smith, R. F. T. Stepto, J. P. Vairon, J. Vohlídal, *Pure Appl. Chem.*, **2012**, *84*, 2167.

[9] B. F. Hoskins, R. Robson, *J. Am. Chem. Soc.*, **1989**, *111*, 5962.

[10] H. Li, M. Eddaoudi, T. L. Groy, O. M. Yaghi, *J. Am. Chem. Soc.,* **1998**, *120*, 8571.

[11] X. Shi, G. Zhu, X. Wang, G. Li, Q. Fang, G. Wu, G. Tian, M. Xue, X. Zhao, R. Wang, S. Qiu, *Cryst. Growth Des.*, **2005**, *5*, 207.

[12] Y. F. Hsu, J. D. Chen, *Eur. J. Inorg. Chem.*, **2004**, 1488.

[13] S. M. Hawxwell, H. Adams, L. Brammer, *Acta Crystallogr., Sect. B,* **2006**, *62*, 808.

[14] O. Delgado-Friedrichs, M. D. Foster, M. O'Keeffe, D. M. Proserpio, M. M. J. Treacy, O. M. Yaghi, *J. Solid State Chem.,* **2005**, *178*, 2533.

[15] H. Li, M. Eddaoudi, M. O'Keeffe, O. M. Yaghi, *Nature*, **1999**, *402*, 276.

[16] R. Robson, *Dalton Trans.,* **2008**, 5113.

[17] B. Chen, F. R. Fronczek, A. W. Maverick, *Chem. Commun.*, **2003**, 2166.

[18] M. Eddaoudi, J. Kim, N. Rosi, D. Vodak, J. Wachter, M. O'Keeffe, O. M. Yaghi, *Science*, **2002**, *295*, 469.

[19] G. Cruciani, *J. Phys. Chem. Solids*, **2006**, *67*, 1973.

[20] K. K. Tanabe, Z. Wang, S. M. Cohen, *J. Am. Chem. Soc.*, **2008**, *130*, 8508.

[21] N. L. Rosi, J. Kim, M. Eddaoudi, B. Chen, M. O'Keeffe, O. M. Yaghi, *J. Am. Chem. Soc.*, **2005**, *127*, 1504.

[22] S. J. Yang, C. R. Park, *Adv. Mater.*, **2012**, *24*, 4010.

[23] G. Férey, C. Mellot-Draznieks, C. Serre, F. Millange, J. Dutour, S. Surblé, I. Margiolaki, *Science*, **2005**, *309*, 2040.

[24] J. H. Cavka, S. Jakobsen, U. Olsbye, N. Guillou, C. Lamberti, S. Bordiga, K. P. Lillerud, *J. Am. Chem. Soc.*, **2008**, *130*, 13850.

[25] S. S. Y. Chui, S. M. F. Lo, J. P. H. Charmant, A. G. Orpen, I. D. Williams, *Science,* **1999**, *283*, 1148.

[26] H. K. Chae, D. Y. Siberio-Perez, J. Kim, Y. Go, M. Eddaoudi, A. J. Matzger, M. O'Keeffe, O. M. Yaghi, *Nature*, **2004**, *427*, 523.

[27] S. Yang, X. Lin, W. Lewis, M. Suyetin, E. Bichoutskaia, J. E. Parker, C. C. Tang, D. R. Allan, P. J. Rizkallah, P. Hubberstey, N. R. Champness, K. Mark Thomas, A. J. Blake, M. Schroder, *Nat. Mater.*, **2012**, *11*, 710.
[28] S. P. Bew, A. D. Burrows, T. Duren, M. F. Mahon, P. Z. Moghadam, V. M. Sebestyen, S. Thurston, *Chem. Commun.*, **2012**, *48*, 4824.
[29] K. Kim, S. Park, K. M. Park, S. S. Lee, *Cryst. Growth Des.*, **2011**, *11*, 4059.
[30] K. Koh, A. G. Wong-Foy, A. J. Matzger, *Angew. Chem., Int. Ed.*, **2008**, *47*, 677.
[31] Z. Wang, K. K. Tanabe, S. M. Cohen, *Inorg. Chem.*, **2008**, *48*, 296.
[32] S. Horike, D. Tanaka, K. Nakagawa, S. Kitagawa, *Chem. Commun.*, **2007**, 3395.
[33] D. Tanaka, A. Henke, K. Albrecht, M. Moeller, K. Nakagawa, S. Kitagawa, J. Groll, *Nat. Chem.*, **2010**, *2*, 410.
[34] D. N. Dybtsev, H. Chun, K. Kim, *Angew. Chem. Int. Ed.*, **2004**, *43*, 5033.
[35] W. A. Freeman, W. L. Mock, N. Y. Shih, *J. Am. Chem. Soc.*, **1981**, *103*, 7367.
[36] K. S. Park, Z. Ni, A. P. Coté, J. Y. Choi, R. Huang, F. J. Uribe-Romo, H. K. Chae, M. O'Keeffe, O. M. Yaghi, *Proc. Natl. Acad. Sci.*, **2006**, *103*, 10186.
[37] A. Phan, C. J. Doonan, F. J. Uribe-Romo, C. B. Knobler, M. O'Keeffe, O. M. Yaghi, *Acc. Chem. Res.*, **2009**, *43*, 58.
[38] T.-T. Lian, S.-M. Chen, *Inorg. Chem. Commun.*, **2011**, *18*, 8.
[39] W. T. A. Harrison, R. W. Broach, R. A. Bedard, T. E. Gier, X. Bu, G. D. Stucky, *Chem. Mater.*, **1996**, *8*, 691.
[40] K. Barthelet, C. Merlier, C. Serre, M. Riou-Cavellec, D. Riou, G. Ferey, *J. Mater. Chem.*, **2002**, *12*, 1132.
[41] B. W. Jacobs, R. J. T. Houk, M. R. Anstey, S. D. House, I. M. Robertson, A. A. Talin, M. D. Allendorf, *Chem. Sci.*, **2011**, *2*, 411.
[42] A. Schaate, P. Roy, T. Preuße, S. J. Lohmeier, A. Godt, P. Behrens, *Chem. Eur. J.*, **2011**, *17*, 9320.
[43] L. Carlucci, G. Ciani, D. M. Proserpio, S. Rizzato, *Chem. Eur. J.*, **2002**, *8*, 1519.
[44] C. S. Cundy, P. A. Cox, *Chem. Rev.*, **2003**, *103*, 663.
[45] N. Stock, S. Biswas, *Chem. Rev.*, **2012**, *112*, 933.
[46] S. Bauer, C. Serre, T. Devic, P. Horcajada, J. Marrot, G. Férey, N. Stock, *Inorg. Chem.*, **2008**, *47*, 7568.
[47] J. Y. Choi, J. Kim, S. H. Jhung, H. K. Kim, J.-S. Chang, H. K. Chae, *Bull. Korean Chem. Soc.*, **2006**, *27*, 1523
[48] R. F. Wu, T. L. Zhang, X. J. Qiao, J. G. Zhang, Y. H. Liu, *Chin. J. Inorg. Chem.*, **2006**, *22*, 1340.
[49] M. Tuikka, M. Haukka, M. Ahlgrén, *Solid State Sci.*, **2007**, *9*, 535.
[50] W. Yuan, J. O'Connor, S. L. James, *CrystEngComm*, **2010**, *12*, 3515.
[51] B. Seoane, J. M. Zamaro, C. Tellez, J. Coronas, *CrystEngComm*, **2012**, *14*, 3103.
[52] J. A. Thompson, K. W. Chapman, W. J. Koros, C. W. Jones, S. Nair, *Microporous Mesoporous Mater.*, **2012**, *158*, 292.
[53] J. H. Bang, K. S. Suslick, *Adv. Mater.*, **2010**, *22*, 1039.
[54] D. J. Tranchemontagne, J. R. Hunt, O. M. Yaghi, *Tetrahedron*, **2008**, *64*, 8553.
[55] M. Schlesinger, S. Schulze, M. Hietschold, M. Mehring, *Microporous Mesoporous Mater.*, **2010**, *132*, 121.
[56] M. J. S. Fard, F. Rastaghi, N. Ghanbari, *J. Mol. Struct.*, **2013**, *1032*, 133.
[57] A. Martinez Joaristi, J. Juan-Alcaniz, P. Serra-Crespo, F. Kapteijn, J. Gascon, *Cryst. Growth Des.*, **2012**, *12*, 3489.
[58] A. Ramanan, M. S. Whittingham, *Cryst. Growth Des.*, **2006**, *6*, 2419.

[59] R. Lacmann, A. Herden, C. Mayer, *Chem. Eng. Technol.*, **1999**, *22*, 279.
[60] P. Cubillas, M. W. Anderson, M. P. Attfield, *Chem. Eur. J.*, **2012**, *18*, 15406.
[61] M. Shoaee, M. W. Anderson, M. P. Attfield, *Angew. Chem., Int. Ed.*, **2008**, *47*, 8525.
[62] B. Chen, M. Eddaoudi, S. T. Hyde, M. O'Keeffe, O. M. Yaghi, *Science*, **2001**, *291*, 1021.
[63] F. Millange, R. El Osta, M. E. Medina, R. I. Walton, *CrystEngComm*, **2011**, *13*, 103.
[64] M. Kondo, Y. Takashima, J. Seo, S. Kitagawa, S. Furukawa, *CrystEngComm*, **2010**, *12*, 2350.
[65] K. Koh, A. G. Wong-Foy, A. J. Matzger, *Chem. Commun.*, **2009**, *0*, 6162.
[66] P. Falcaro, A. J. Hill, K. M. Nairn, J. Jasieniak, J. I. Mardel, T. J. Bastow, S. C. Mayo, M. Gimona, D. Gomez, H. J. Whitfield, R. Ricco, A. Patelli, B. Marmiroli, H. Amenitsch, T. Colson, L. Villanova, D. Buso, *Nat. Commun.*, **2011**, *2*, 8.
[67] B. M. El-Houssieny, H. M. Hamouda, *Drug Discov. Ther.*, **2010**, *4*, 33.
[68] A. Schaate, P. Roy, A. Godt, J. Lippke, F. Waltz, M. Wiebcke, P. Behrens, *Chem. Eur. J.*, **2011**, *17*, 6643.
[69] A. Umemura, S. Diring, S. Furukawa, H. Uehara, T. Tsuruoka, S. Kitagawa, *J. Am. Chem. Soc.*, **2011**, *133*, 15506.
[70] R. Krishna, *J. Phys. Chem. C*, **2009**, *113*, 19756.
[71] M. Maekawa, T. Tominaga, K. Sugimoto, T. Okubo, T. Kuroda-Sowa, M. Munakata, S. Kitagawa, *CrystEngComm*, **2012**, *14*, 1345.
[72] E. Quartapelle Procopio, T. Fukushima, E. Barea, J. A. R. Navarro, S. Horike, S. Kitagawa, *Chem. Eur. J.*, **2012**, *18*, 13117.
[73] K. O. Kongshaug, H. Fjellvåg, *Polyhedron*, **2007**, *26*, 5113.
[74] F. Wang, H. Guo, Y. Chai, Y. Li, C. Liu, *Microporous Mesoporous Mater.*, **2013**, *173*, 181.
[75] A. P. Nelson, O. K. Farha, K. L. Mulfort, J. T. Hupp, *J. Am. Chem. Soc.*, **2008**, *131*, 458.
[76] O. K. Farha, J. T. Hupp, *Acc. Chem. Res.*, **2010**, *43*, 1166.
[77] L. Ma, A. Jin, Z. Xie, W. Lin, *Angew. Chem., Int. Ed.*, **2009**, *48*, 9905.
[78] A. J. Fletcher, K. M. Thomas, M. J. Rosseinsky, *J. Solid State Chem.*, **2005**, *178*, 2491.
[79] S. Brunauer, L. S. Deming, W. E. Deming, E. Teller, *J. Am. Chem. Soc.*, **1940**, *62*, 1723.
[80] K. M. Choi, H. J. Jeon, J. K. Kang, O. M. Yaghi, *J. Am. Chem. Soc.*, **2011**, *133*, 11920.
[81] T. M. McDonald, W. R. Lee, J. A. Mason, B. M. Wiers, C. S. Hong, J. R. Long, *J. Am. Chem. Soc.*, **2012**, *134*, 7056.
[82] J. Sculley, D. Yuan, H. C. Zhou, *Energy Environ. Sci.*, **2011**, *4*, 2721.
[83] J. L. Mendoza-Cortes, W. A. Goddard, H. Furukawa, O. M. Yaghi, *J. Phys. Chem. Lett.*, **2012**, *3*, 2671.
[84] W. Zhou, *Chem. Rec.*, **2010**, *10*, 200.
[85] J. Seo, C. Bonneau, R. Matsuda, M. Takata, S. Kitagawa, *J. Am. Chem. Soc.*, **2011**, *133*, 9005.
[86] S. Choi, T. Watanabe, T. H. Bae, D. S. Sholl, C. W. Jones, *J. Phys. Chem. Lett.*, **2012**, *3*, 1136.
[87] J. G. Vitillo, M. Savonnet, G. Ricchiardi, S. Bordiga, *ChemSusChem*, **2011**, *4*, 1281.
[88] E. Stavitski, E. A. Pidko, S. Couck, T. Remy, E. J. M. Hensen, B. M. Weckhuysen, J. Denayer, J. Gascon, F. Kapteijn, *Langmuir*, **2011**, *27*, 3970.
[89] R. Vaidhyanathan, S. S. Iremonger, G. K. H. Shimizu, P. G. Boyd, S. Alavi, T. K. Woo, *Science*, **2010**, *330*, 650.
[90] N. Nijem, P. Thissen, Y. Yao, R. C. Longo, K. Roodenko, H. Wu, Y. Zhao, K. Cho, J. Li, D. C. Langreth, Y. J. Chabal, *J. Am. Chem. Soc.*, **2011**, *133*, 12849.

[91] S. Pérez-Yáñez, G. Beobide, O. Castillo, M. Fischer, F. Hoffmann, M. Fröba, J. Cepeda, A. Luque, *Eur. J. Inorg. Chem.*, **2012**, 5921.
[92] H. Furukawa, J. Kim, N. W. Ockwig, M. O'Keeffe, O. M. Yaghi, *J. Am. Chem. Soc.*, **2008**, *130*, 11650.
[93] D. Venkataraman, G. B. Gardner, S. Lee, J. S. Moore, *J. Am. Chem. Soc.*, **1995**, *117*, 11600.
[94] C.-D. Wu, W. Lin, *Angew. Chem., Int. Ed.*, **2005**, *44*, 1958.
[95] C.-D. Wu, W. Lin, *Inorg. Chem.*, **2005**, *44*, 1178.
[96] K. Leus, M. Vandichel, Y.-Y. Liu, I. Muylaert, J. Musschoot, S. Pyl, H. Vrielinck, F. Callens, G. B. Marin, C. Detavernier, P. V. Wiper, Y. Z. Khimyak, M. Waroquier, V. Van Speybroeck, P. Van Der Voort, *J. Catal.*, **2012**, *285*, 196.
[97] M. J. Ingleson, R. Heck, J. A. Gould, M. J. Rosseinsky, *Inorg. Chem.*, **2009**, *48*, 9986.
[98] P. Horcajada, C. Serre, M. Vallet-Regí, M. Sebban, F. Taulelle, G. Férey, *Angew. Chem., Int. Ed.*, **2006**, *45*, 5974.
[99] M. Müller, S. Turner, O. I. Lebedev, Y. Wang, G. van Tendeloo, R. A. Fischer, *Eur. J. Inorg. Chem.*, **2011**, *2011*, 1876.
[100] H. Sato, R. Matsuda, K. Sugimoto, M. Takata, S. Kitagawa, *Nat. Mater.*, **2010**, *9*, 661.
[101] A. J. Graham, D. R. Allan, A. Muszkiewicz, C. A. Morrison, S. A. Moggach, *Angew. Chem., Int. Ed.*, **2011**, *50*, 11138.
[102] S. Lim, K. Suh, Y. Kim, M. Yoon, H. Park, D. N. Dybtsev, K. Kim, *Chem. Commun.*, **2012**, *48*, 7447.
[103] H. Fei, J. F. Cahill, K. A. Prather, S. M. Cohen, *Inorg. Chem.*, **2013**, *52*, 4011.
[104] H. Deng, C. J. Doonan, H. Furukawa, R. B. Ferreira, J. Towne, C. B. Knobler, B. Wang, O. M. Yaghi, *Science*, **2010**, *327*, 846.
[105] Z. Xiang, S. Leng, D. Cao, *J. Phys. Chem. C*, **2012**, *116*, 10573.
[106] J. G. Nguyen, S. M. Cohen, *J. Am. Chem. Soc.*, **2010**, *132*, 4560.
[107] T. Ahnfeldt, D. Gunzelmann, T. Loiseau, D. Hirsemann, J. r. Senker, G. Férey, N. Stock, *Inorg. Chem.*, **2009**, *48*, 3057.
[108] S. J. Garibay, S. M. Cohen, *Chem. Commun.*, **2010**, *46*, 7700.
[109] K. Peikert, F. Hoffmann, M. Froba, *Chem. Commun.*, **2012**, *48*, 11196.
[110] J. E. Halls, A. Hernan-Gomez, A. D. Burrows, F. Marken, *Dalton Trans.*, **2012**, *41*, 1475.
[111] M. Savonnet, S. Aguado, U. Ravon, D. Bazer-Bachi, V. Lecocq, N. Bats, C. Pinel, D. Farrusseng, *Green Chem.*, **2009**, *11*, 1729.
[112] A. M. Goforth, C. Y. Su, R. Hipp, R. B. Macquart, M. D. Smith, H. C. zur Loye, *J. Solid State Chem.*, **2005**, *178*, 2511.
[113] C. Volkringer, S. M. Cohen, *Angew. Chem., Int. Ed.*, **2010**, *49*, 4644.
[114] K. K. Tanabe, S. M. Cohen, *Chem. Soc. Rev.*, **2011**, *40*, 498.
[115] E. Dugan, Z. Wang, M. Okamura, A. Medina, S. M. Cohen, *Chem. Commun.*, **2008**, *0*, 3366.
[116] S. J. Garibay, Z. Wang, K. K. Tanabe, S. M. Cohen, *Inorg. Chem.*, **2009**, *48*, 7341.
[117] S. Bernt, V. Guillerm, C. Serre, N. Stock, *Chem. Commun.*, **2011**, *47*, 2838.
[118] D. Jiang, L. L. Keenan, A. D. Burrows, K. J. Edler, *Chem. Commun.*, **2012**, *48*, 12053.
[119] M. J. Ingleson, J. Perez Barrio, J.-B. Guilbaud, Y. Z. Khimyak, M. J. Rosseinsky, *Chem. Commun.*, **2008**, 2680.
[120] M. Servalli, M. Ranocchiari, J. A. Van Bokhoven, *Chem. Commun.*, **2012**, *48*, 1904.
[121] J. Canivet, S. Aguado, Y. Schuurman, D. Farrusseng, *J. Am. Chem. Soc.*, **2013**, *135*, 4195.
[122] S. Bhattacharjee, D.-A. Yang, W.-S. Ahn, *Chem. Commun.*, **2011**, *47*, 3637.

[123] W. Morris, C. J. Doonan, H. Furukawa, R. Banerjee, O. M. Yaghi, *J. Am. Chem. Soc.*, **2008**, *130*, 12626.
[124] A. Huang, W. Dou, J. Caro, *J. Am. Chem. Soc.*, **2010**, *132*, 15562.
[125] T. Gadzikwa, G. Lu, C. L. Stern, S. R. Wilson, J. T. Hupp, S. T. Nguyen, *Chem. Commun.*, **2008**, *0*, 5493.
[126] M. Savonnet, D. Bazer-Bachi, N. Bats, J. Perez-Pellitero, E. Jeanneau, V. Lecocq, C. Pinel, D. Farrusseng, *J. Am. Chem. Soc.*, **2010**, *132*, 4518.
[127] M. Savonnet, D. Bazer-Bachi, N. Bats, J. Perez-Pellitero, E. Jeanneau, V. Lecocq, C. Pinel, D. Farrusseng, *J. Am. Chem. Soc.*, **2010**, *132*, 4518.
[128] Y. Yoo, H. K. Jeong, *Chem. Eng. J.*, **2012**, *181*, 740.
[129] J. G. Nguyen, K. K. Tanabe, S. M. Cohen, *CrystEngComm*, **2010**, *12*, 2335.
[130] D. Britt, C. Lee, F. J. Uribe-Romo, H. Furukawa, O. M. Yaghi, *Inorg. Chem.*, **2010**, *49*, 6387.
[131] S. J. Garibay, Z. Wang, S. M. Cohen, *Inorg. Chem.*, **2010**, *49*, 8086.
[132] C. Chen, C. A. Allen, S. M. Cohen, *Inorg. Chem.*, **2011**, *50*, 10534.
[133] P. Roy, A. Schaate, P. Behrens, A. Godt, *Chem. Eur. J.*, **2012**, *18*, 6979.
[134] J. Canivet, S. Aguado, C. Daniel, D. Farrusseng, *ChemCatChem*, **2011**, *3*, 675.
[135] T. Gadzikwa, O. K. Farha, K. L. Mulfort, J. T. Hupp, S. T. Nguyen, *Chem. Commun.*, **2009**, *0*, 3720.
[136] A. D. Burrows, S. O. Hunter, M. F. Mahon, C. Richardson, *Chem. Commun.*, **2013**, *49*, 990.
[137] K. Hindelang, S. I. Vagin, C. Anger, B. Rieger, *Chem. Commun.*, **2012**, *48*, 2888.
[138] A. D. Burrows, C. G. Frost, M. F. Mahon, C. Richardson, *Chem. Commun.*, **2009**, *0*, 4218.
[139] S. C. Jones, C. A. Bauer, *J. Am. Chem. Soc.*, **2009**, *131*, 12516.
[140] M. Kim, S. J. Garibay, S. M. Cohen, *Inorg. Chem.*, **2011**, *50*, 729.
[141] T. Yamada, H. Kitagawa, *J. Am. Chem. Soc.*, **2009**, *131*, 6312.
[142] R. K. Deshpande, J. L. Minnaar, S. G. Telfer, *Angew. Chem. Int. Ed.*, **2010**, *49*, 4598.
[143] D. J. Lun, G. I. N. Waterhouse, S. G. Telfer, *J. Am. Chem. Soc.*, **2011**, *133*, 5806.
[144] A. S. Gupta, R. K. Deshpande, L. Liu, G. I. N. Waterhouse, S. G. Telfer, *CrystEngComm*, **2012**, *14*, 5701.
[145] J. Canivet, S. Aguado, G. Bergeret, D. Farrusseng, *Chem. Commun.*, **2011**, *47*, 11650.
[146] C. E. Wilmer, M. Leaf, C. Y. Lee, O. K. Farha, B. G. Hauser, J. T. Hupp, R. Q. Snurr, *Nat. Chem.*, **2012**, *4*, 83.
[147] helios.princeton.edu/mofomics/
[148] P. L. Llewellyn, G. Maurin, T. Devic, S. Loera-Serna, N. Rosenbach, C. Serre, S. Bourrelly, P. Horcajada, Y. Filinchuk, G. Férey, *J. Am. Chem. Soc.*, **2008**, *130*, 12808.
[149] K. Sillar, J. Sauer, *J. Am. Chem. Soc.*, **2012**, *134*, 18354.
[150] C. E. Wilmer, O. K. Farha, Y.-S. Bae, J. T. Hupp, R. Q. Snurr, *Energy Environ. Sci.*, **2012**, *5*, 9849.
[151] J. K. Schnobrich, K. Koh, K. N. Sura, A. J. Matzger, *Langmuir*, **2010**, *26*, 5808.
[152] J.-R. Li, J. Sculley, H.-C. Zhou, *Chem. Rev.*, **2012**, *112*, 869.
[153] H. Bux, C. Chmelik, J. M. van Baten, R. Krishna, J. Caro, *Adv. Mater.*, **2010**, *22*, 4741.
[154] A. Carné-Sánchez, I. Imaz, M. Cano-Sarabia, D. Maspoch, *Nat. Chem.*, **2013**, *5*, 203.
[155] J. J. Low, A. I. Benin, P. Jakubczak, J. F. Abrahamian, S. A. Faheem, R. R. Willis, *J. Am. Chem. Soc.*, **2009**, *131*, 15834.
[156] T. Lescouet, E. Kockrick, G. Bergeret, M. Pera-Titus, S. Aguado, D. Farrusseng, *J. Mater. Chem.*, **2012**, *22*, 10287.

[157] N. Nijem, J.-F. Veyan, L. Kong, K. Li, S. Pramanik, Y. Zhao, J. Li, D. Langreth, Y. J. Chabal, *J. Am. Chem. Soc.*, **2010**, *132*, 1654.
[158] N. R. Champness, *Dalton Trans.*, **2011**, *40*, 10311.

2. *N*-alkylation of MOF Pore Surfaces by Post-Synthetic Modification

2.1. Introduction

Previously reported examples of amino group PSM reactions (Chap.1, section 1.7) to form imines and secondary amines, were carried out with the aldehyde tagged MOFs, SIM-1 and ZIF-91, and were reacted with primary amines, resulting in imino-alkyl chain products.[1] A report by Jeong *et al.* investigated the PSM of IRMOF-3 with cyanuric chloride forming a secondary amine, showing mesopore formation in the crystalline product.[2]

Kim *et al.*, in 2000, reported the use of an alkyl halide to modify the MOF $[Zn_3(\mu^3\text{-}O)(Htart)_6]\cdot 2H_3O\cdot 12H_2O$, (POST-1, tart = *D*-tartrate) and quantitatively converted the negatively charged framework to a positively charged framework, pyridine to alkyl-pyridinium, and turned off the basic catalysis that the starting material exhibited.[3] This was achieved by reacting POST-1 with CH_3I and $CH_3(CH_2)_5I$ resulting in *N*-alkylation of the pyridine groups protruding into the pores, summarised in Scheme 2.1. The product, POST-1-Me, displays enantioselective catalytic activity with respect to the transesterification of 2,4-dinitrophenyl acetate with ethanol.[3]

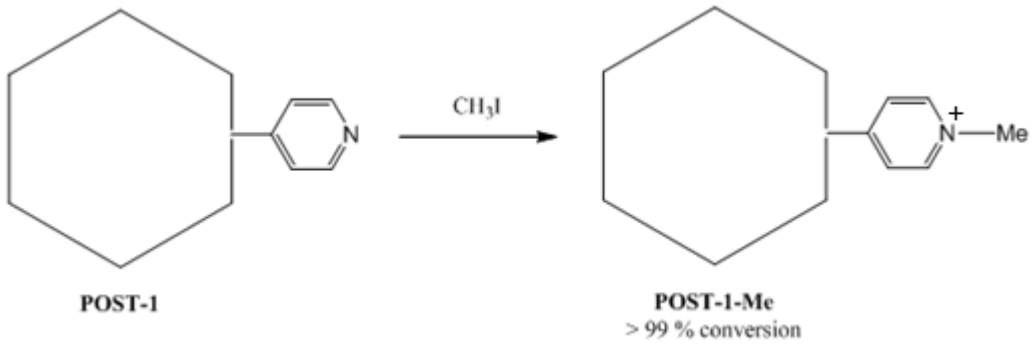

Scheme 2.1. Representation of the PSM of POST-1 with methyliodide.

The structure of POST-1 contains an octahedral Zn(II) trinuclear SBU that resembles the MIL topology reported by Ferév *et al.*, in 2005, with Cr^{3+} tricoordinate metal ions.[4]

Lin and co-workers demonstrated the nanoparticulate MOF, (NMOF, $[Fe_3\text{-}(\mu_3\text{-}O)Cl(H_2O)_2(BDC)_{2.48}(BDC\text{-}NH_2)_{0.52}]$, MIL-101(Fe)-$NH_2$, 17.4 mol% incorporation of amino groups), reaction with the organic fluorophore, 1,3,5,7-tetramethyl-4,4-difluoro-8-bromomethyl-4-bora-3*a*,4*a*-diaza-*s*-indacene, Br-BODIPY, to from a secondary amine as a

contrast agent for medical imaging.[5] They reported 20–40 % conversion, Scheme 2.2. This was the first reported iron(III) analogue of MIL-101(Cr) and an example of a secondary amine tagged MOF.

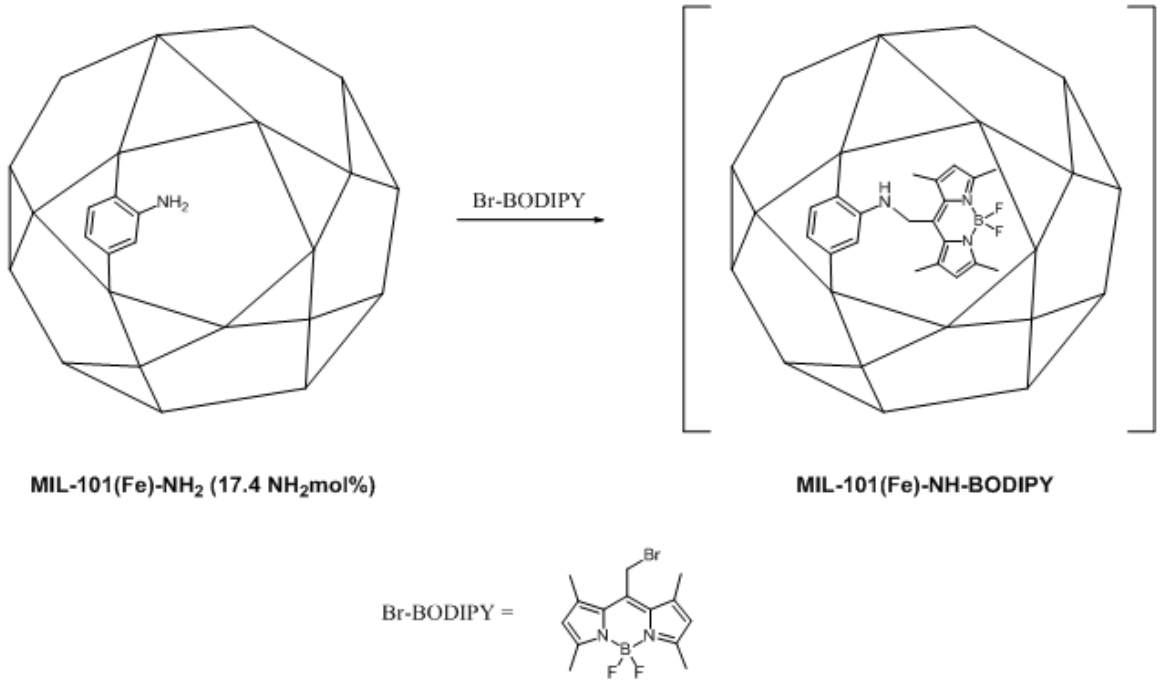

Scheme 2.2. Representation of the PSM of MIL-101(Fe)-NH_2 with Br-BODIPY to form a secondary amine functionalised MIL-101(Fe)-NH-BODIPY.[5]

Yaghi *et al.* reported the PSM of $[Zr_6O_4(OH)_4(BDC\text{-}NH_2)_4(BDC\text{-}NH_3^+Cl^-)_2]$, UiO-66-A, by exposure to ethanal. The only evidence of conversion, however, is solid-state ^{15}N NMR in support of their proposed reaction products UiO-66-B, Scheme 2.3.[6] The product distributions were altered by elongating the reaction time and lowering the reaction pressure, to favour of the aziridine functional group up to 56 % inclusion, UiO-66-C.

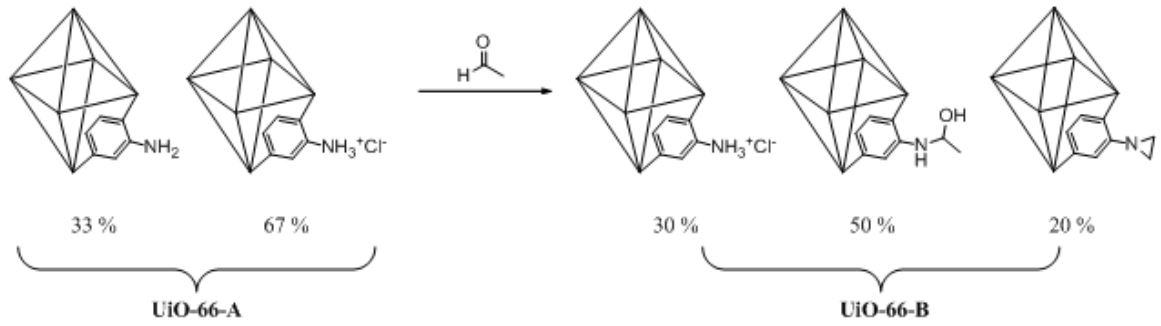

Scheme 2.3. Representation of the PSM of UiO-66-A with ethanal to form the hemiaminal and aziridine functionalised MOF, UiO-66-B.[6]

2.2. Reaction condition impact on the Secondary Amine Formation on the Pore Surface of IRMOF-3 by a Tandem Post-synthetic Modification.

2.2.1. Preliminary Investigation

IRMOF-3 was chosen as a candidate MOF for tandem PSM, due to large channels, ease of synthesis and the precedence for PSM studies on this MOF.[7] The main need was for a MOF with easily accessible amine groups protruding into its pores. Large channels are especially important for diffusion of reactants in, and by-products out. There are several PSMs on IRMOF-3 in the literature with which to compare the conversions. The stability of the framework is important with respect to the reactants as no acid or base can be involved without crystal degradation.

IRMOF-3 was synthesised according to a modified preparation by Cohen *et al.*[8] and washed with solvent (THF) for 3 days, with fresh solvent every 24 h. IRMOF-3 was then treated with the aldehydes, RCHO (R= Me, Et, Pr, *n*-C_7H_{15}), in THF at room temperature for 24 h, before adding $NaCNBH_3$ to the reaction mixture, which was then left for a further 48 h. The crystalline solid was then washed with fresh THF by decantation and subsequently washed and stored in toluene. The proposed condensation-reduction process is summarised in Scheme 2.4.

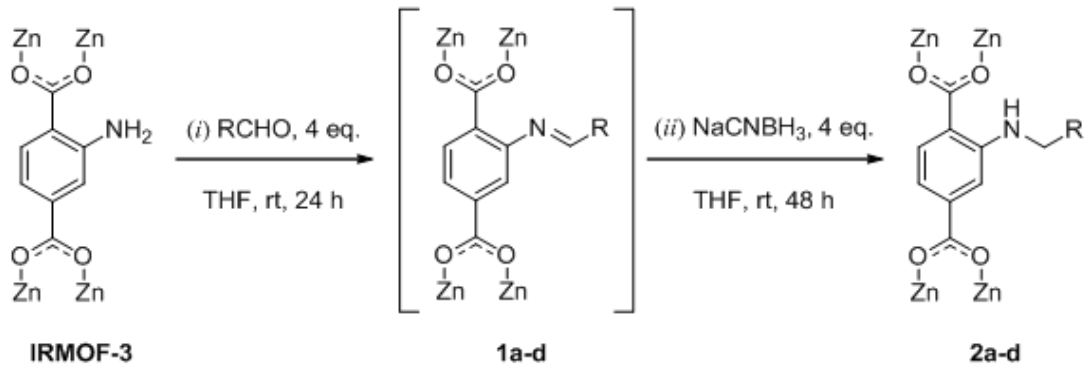

Scheme 2.4. General PSM procedure for the tandem PSM of IRMOF-3 with RCHO and $NaCNBH_3$. R = Me (**1a**, **2a**), Et (**1b, 2b**), Pr (**1c, 2c**), *n*-C_7H_{15} (**1d, 2d**).

2.2.2. Solvent Screening

Optimisation of the solvent system was found by carrying out the PSM reaction, between IRMOF-3 and excess acetaldehyde, in three different solvents (THF, DMF, $CHCl_3$) with excess $NaCNBH_3$, Table 2.1. THF was chosen because the conversion was slightly better

than in DMF and it gave the highest conversion of amino to ethylamino groups in the analogous dicarboxylic acid reactions (pre-synthetic modification on the free acid).

Solvent	IRMOF-3/%	IRMOF-3-Et/%
THF	67	33
DMF	69	31
$CHCl_3$	83	17

Table 2.1. Product distributions from the solvent screen for the PSM of IRMOF-3 with CH_3CHO.

The solvent in the IRMOF-3 framework was exchanged with each respective reaction solvent, prior to the PSM, to remove the DMF present from the MOF formation reaction, thereby enabling valid comparisons to be made. The PSM products were then washed by decantation over 3 days with fresh solvent replaced every 24 hours.

To assess the architectures of the MOF materials, post reaction, powder X-ray diffraction was used. The traces show no change in the bulk framework after PSM, evidenced by a lack of significant differences in the positions of the peaks, Figure 2.1.

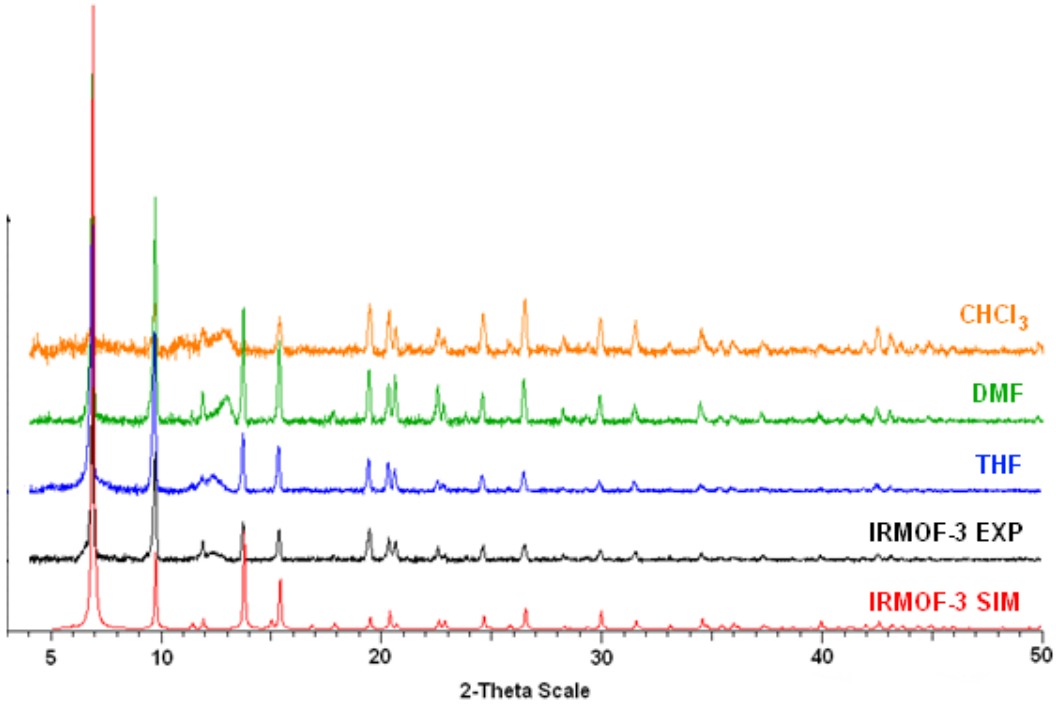

Figure 2.1. PXRD traces of PSM reaction products between IRMOF-3, MeCHO and $NaCHBH_3$, in THF (blue), DMF (green), $CHCl_3$ (orange). As synthesised IRMOF-3 (black). Simulated IRMOF-3 diffraction pattern from single crystal CCDC REFCODE = COJTOL (red).[8] The broad peaks at 12-13 (2θ) are attributed to the glass of the capillary tube.

The degree of *N*-alkylation was calculated from the ^{1}H NMR spectra of the digested MOFs. An acid digestion with DCl/D_2O in DMSO-d_6, was used to cleave the Zn-O bonds in the SBU and dissolve the protonated ligands. This gives sharper signals than solid-state NMR, therefore a more accurate interpretation and comparison of peak integrals is possible. The percentage modification of linkers is shown by an emergence of peaks in the aromatic region of the ^{1}H NMR spectrum (Figure 2.2) corresponding to the presence of H_2BDC-NH_2 and H_2BDC-NHR.

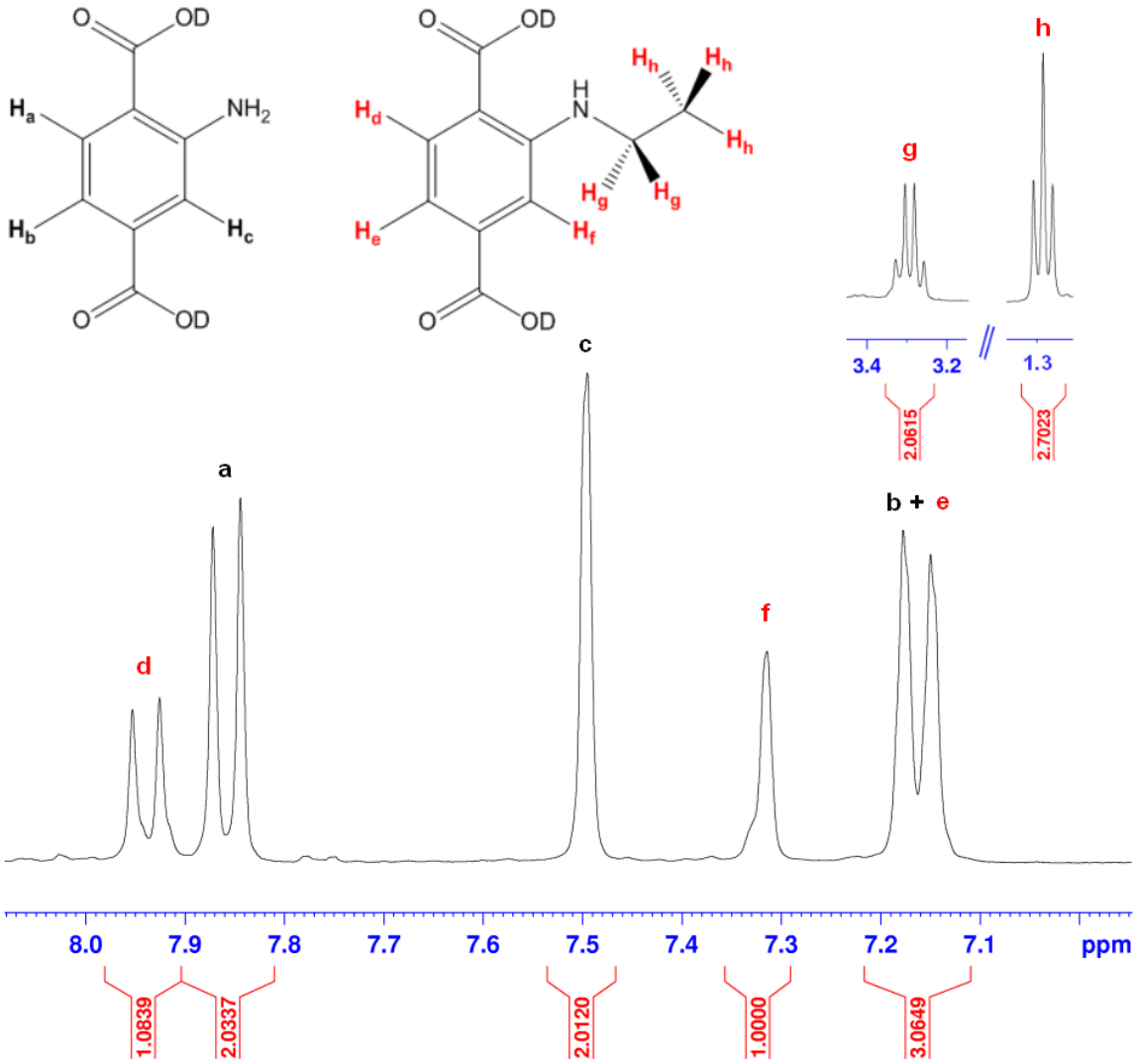

Figure 2.2. ^{1}H NMR for the digested crystals of **2a** (33% conversion) showing the aromatic region and (insert) the peaks in the aliphatic region. Integral of secondary amine peak, H_f, is calibrated to represent one hydrogen atom.

The change in shift of the aromatic protons in the starting material, H_a and H_c, compared with the PSM product, H_d and H_f (refer to Figure 2.2), is due to the change in environment after the addition of the alkyl chain, and allows conversion to be calculated. The aliphatic region shows the emergence of peaks corresponding to the alkyl amine chain. In the case of **2a,** the quartet (δ 3.3 ppm) representing two hydrogen atoms and the triplet (δ 1.3 ppm) representing three hydrogen atoms shows the C=N double bond, of imine **1a**, was successfully reduced to form a secondary amine.

2.2.3. Effect of Aldehyde Chain Length on Conversion

Increasing the aldehyde alkyl chain length, from n = 2 carbon atoms (ethanal) to 3 (propanal), 4 (butanal) and 8 (octanal) was investigated. The results, Table 2.2, show that as the length is increased, conversion decreases. This is a consequence of the blocking of pores from amine groups that have been converted to secondary amines in the extremities of the crystal inhibiting diffusion. In contrast to **2a**, the longer chains, **2b-d**, gave an additional by-product.

PSM Product	R	IRMOF-3 /%	By-product /%	Secondary amine/%
2a	Me	66	0	33
2b	Et	43	52	5
2c	Pr	61	31	8
2d	C_7H_{15}	81	10	9

Table 2.2. Conversion of IRMOF-3 to secondary amine functionalised MOF, at room temperature in THF after 72 h.

Using anhydrous THF as the sole solvent gave rise to a by-product seen in the ^{1}H NMR spectrum, for example in **2b**, Figure 2.3. In the above case of IRMOF-3 and propanal in the absence of a proton source a new ligand is present that is not seen from the digested product of the PSM reaction with ethanal. Signals at δ 7.08 and 7.41 ppm in the aromatic region and multiplets between 3.3 and 3.7 ppm were attributed to this compound. These signals were also present in the spectra of **2c** and **2d**. The PXRD data of the PSM products **2b-d** did not differ from the starting material, so the bulk cubic structure was not altered in this reaction. Attempts to identify and characterise this by-product were unsuccessful.

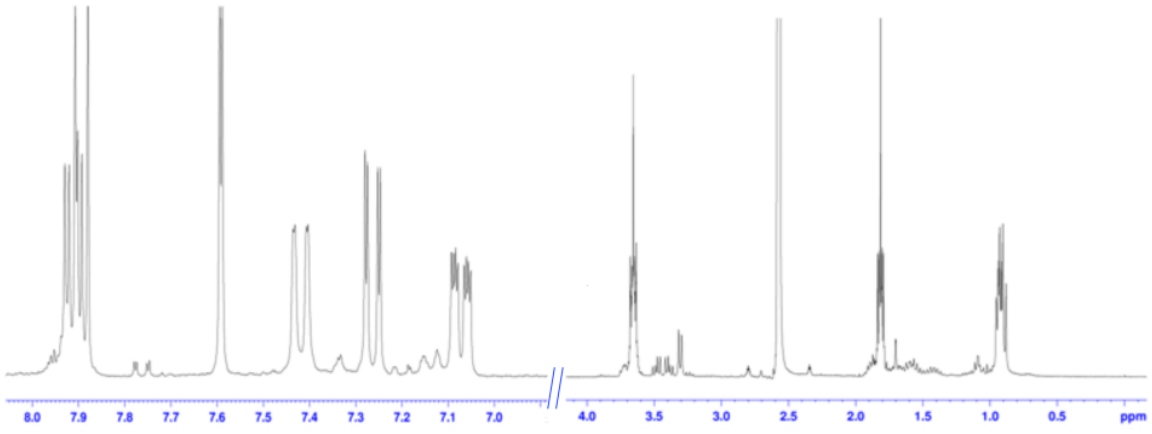

Figure 2.3. ^{1}H NMR spectrum of the digested PSM reaction product, **2b**, between IRMOF-3 and propanal, in THF at room temperature for 3 days.

There is precedence for an alternative PSM product from this reaction, in the 2011 report by Yaghi *et al.*, detailing the addition of ethanal to UiO-66-NH_2.[6] They report the PSM reaction initially forms a hemiaminal group, which then converts to an aziridine group over time. Yaghi reports a 56 % inclusion of the aziridine after 48 hours that is similar to the results presented here with IRMOF-3 *i.e.* 52 % conversion with propanal (an aldehyde one CH_2 unit longer) plus an additional 5 % secondary amino group. Therefore this could be the identity of the by-product but no conclusions can be drawn without further characterisation.

2.2.4. Optimising Reaction Time and $NaCNBH_3$ Equivalents

Increasing the reaction time for an additional three days gave no extra conversion to the unknown by-product or to the secondary amine; neither did introducing two further equivalents of $NaCNBH_3$. There was negligible conversion of amino groups after the aldehyde was left in solution for 24 h before addition of the borohydride (Table 2.3), and the overall framework remained intact from the PXRD (see appendix Figure 5.1. Therefore, it was rationalised that the maximised yield of product containing amino groups was attained within 72 hours.

The colour of IRMOF-3 becomes noticeably redder upon treatment with the aldehydes. This has been seen before in the investigation by van Bokhoven with salicylaldehyde to form the imino functionalised MOF, IRMOF-$3_{sal0.4}$.[9] However, there were no peaks attributed to the intermediate imine, **1a-d**, in the ^{1}H NMR spectra. It is likely that addition of acid to digest the MOF hydrolyses any imine back to H_2BDC-NH_2, therefore the imine

would not be distinguishable from the starting material in the ^{1}H NMR spectra. This means that conversions reported by ^{1}H NMR analysis herein assume no imine in the structure, hence, other techniques need to be used in conjunction, such as solid-state NMR measurements.

For this tandem PSM to be successful, two problems needed to be overcome: unwanted by-product formation and low conversion. Conversion was lower than some other PSMs in the literature, for example Cohen and co-worker's anhydride PSMs of equivalent chain lengths (quantitative conversions at $n < 5$ and $n < 9 = 46$ %).[8] This was thought to be due to blockage of the pores by insoluble boron side products such as $B(OH)_3$. To investigate this ^{11}B NMR spectroscopy was used to study digested samples of the PSM products of **2b**. A peak at δ 22 ppm present in the ^{11}B NMR spectra is consistent with the trigonal boron species $^{11}B(OMe)_2CN$ (δ 22-42 ppm),[10] Figure 2.4.

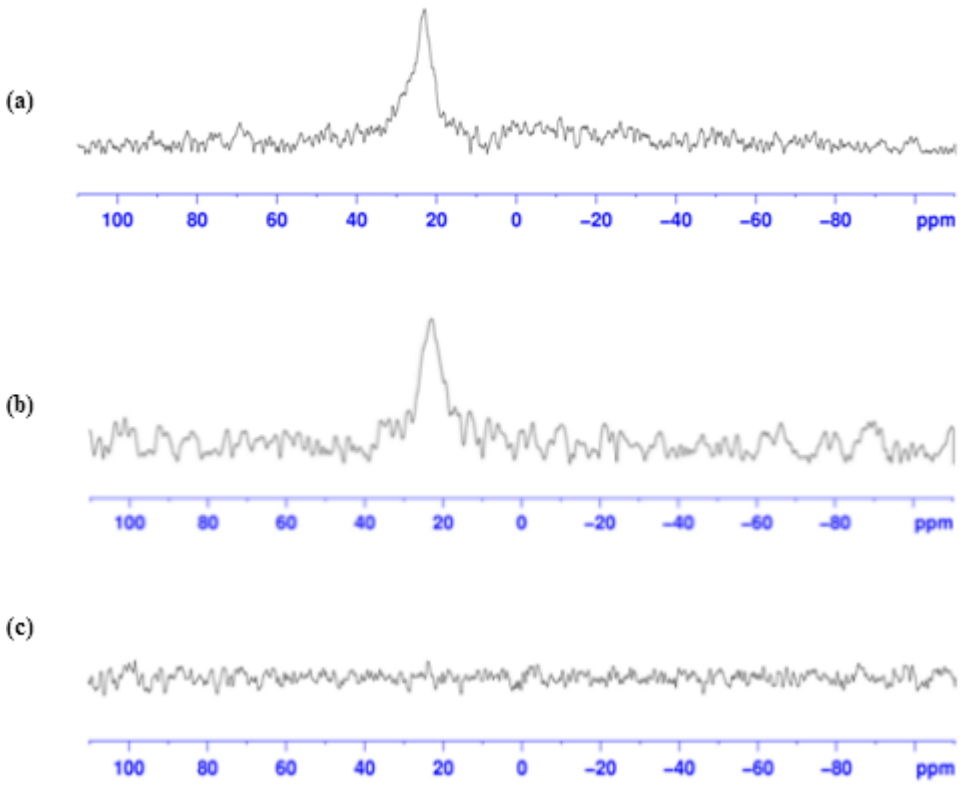

Figure 2.4. ^{11}B NMR spectra for the digested product from the reaction between IRMOF-3, EtCHO and $NaCNBH_3$ in (a) THF, (b) 15:1 THF:MeOH and (c) 1:1 THF:MeOH, showing the presence of a boron-containing side-product in (a) and (b).

2.2.5. Addition of Methanol to the PSM Reaction

MeOH was trialled as a co-solvent as there was precedence in the literature from the report of Yaghi *et al.* outlining $NaBH_4$ reduction of aldehyde to alcohol groups in ZIF-90.[11] The reaction between IRMOF-3, propanal and $NaCNBH_3$ was used as a test case and only the solvent system was varied. Increasing volume fractions of THF:MeOH (up to 1:1) reduced the relative amount of boron side products, in the PSM reaction product MOFs, as evidenced by the ^{11}B NMR spectra. There is also the unexpected benefit of inhibiting the formation of the unwanted by-products from the PSM reaction with aldehydes of chain lengths $n > 2$.

With a higher volume fraction of MeOH the crystals have visible fissures on their surface and the powder diffraction peak intensities are smaller, indicating a loss of crystallinity, however conversion to the secondary amine, **2b**, is increased (Table 2.4), perhaps because the reagents and products have more mobility through the crystal and can penetrate further into the crystal core.

THF:MeOH	IRMOF-3/%	By-product/%	IRMOF-3-Pr/%
1:0	43	52	5
15:1	55	3	42
1:1	36	4	60

Table 2.4. Percentage conversions of PSM products from the reaction between IRMOF-3, EtCHO and $NaCNBH_3$, in varying THF:MeOH ratios.

As the volume fraction of MeOH in the PSM reaction with propanal increases, the framework visibly degrades. The PXRD patterns are summarised in, Figure 2.5. Overall the bulk structure was confirmed not to change during the PSM reaction. The green trace (THF:MeOH, 1:1) exhibits an broad peak (after background subtraction) centred around 20 °(2θ) probably caused by an amorphous component in the sample perhaps related to the crystal degradation.

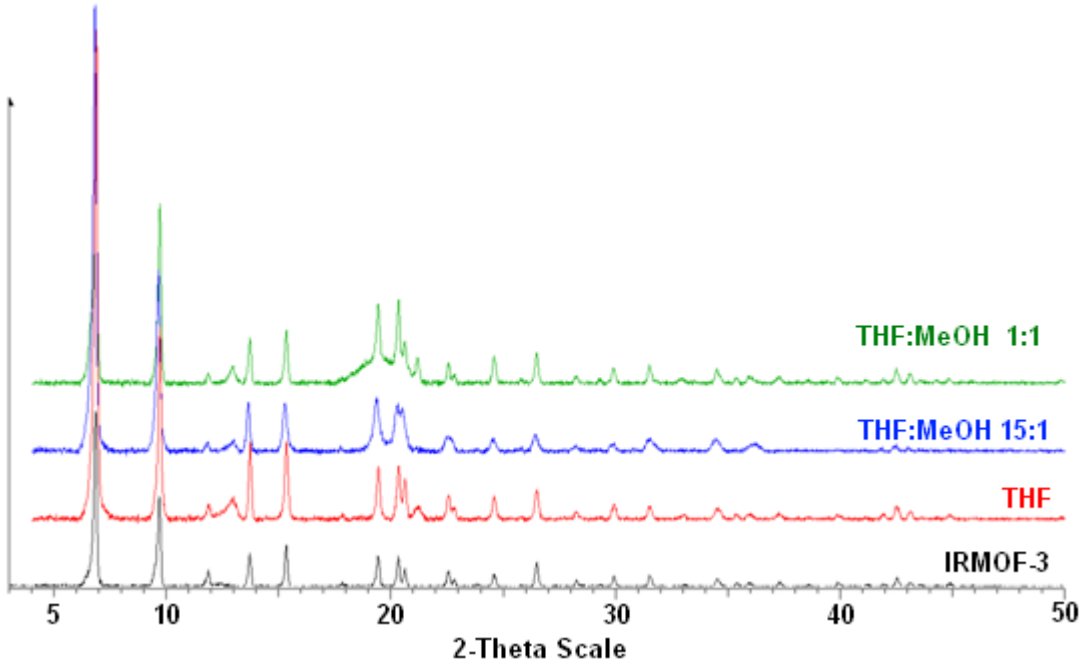

Figure 2.5. PXRD patterns of PSM products from the reaction between IRMOF-3, EtCHO and $NaCNBH_3$, carried out in various THF:MeOH ratios. The as-made IRMOF-3 is shown for comparison.

2.2.6. Temperature Variations

Increasing the temperature affords increased conversion, up to a maximum of 74% for **2a**, by increasing the rate of diffusion of reactants in and side-products out, Table 2.5. The degree of conversion of amino to alkyl-amino groups is greater at 50 °C than at room temperature, accompanied by a compromise in crystal quality shown by opaque, duller products. By-product formation seems to be unaffected or decreases as the temperature of the reaction increases, but a larger range of aldehyde results would be needed to make a firm conclusion on this relationship. The overall architecture of IRMOF-3 is retained in all cases from the PXRD data, (Appendix A, Figure 5.2).

PSM Product	**R**	**THF rt/%**	**THF 50 °C/%**	**THF/MeOH rt/%**	**THF/MeOH 50 °C/%**
2a	Me	(0) 33	(0) 66	(0) 49	(0) 74
2b	Et	(52) 5	(22) 3	(0) 42	(0) 69
2c	Pr	(31) 8	(30) 29	(0) 36	(0) 65
2d	C_7H_{15}	(10) 9	(9) 23	(0) 31	(0) 47

Table 2.5. Percentage conversions of IRMOF-3 to **2a-d** after 3 days, varying temperature and solvent (by-product % in brackets).

2.2.7. Varying the Hydride Source

Another variable to consider is the nature of the hydride source. Varying this shows that $NaCNBH_3$ is the only one, in this investigation, that gave any significant conversion from amino to alkyl-amino groups, summarised in Table 2.6. $NaBH_4$ gave negligible conversion as it may have all reacted with the free aldehyde in solution before reaching the imino groups in the MOF.

Hydride Source	IRMOF-3/%	Propylamino/%
$NaCNBH_3$	31	69
$NaBH_4$	98	2
$NaBH(OMe)_3$	>99	<1
$NaBH(OAc)_3$	92	8

Table 2.6. Percentage conversion from the reaction of IRMOF-3 and EtCHO, to **2b**, in THF:MeOH (15:1) at 50 °C for 72 h with a range of borohydrides.

Increasing the size of the groups on the borohydrides (acetoxy and methoxy) had a detrimental effect on conversion with neither yielding more than 8 %, this could be explained on steric grounds. The larger groups are too big and get blocked at the surface either because either the channels are too small for the reagent or initially the amino groups at the crystal extremities are converted and therefore block access to the amino groups in the interior of the crystals.

Solubility is a key variable; the acetoxy and methoxy borohydrides did not dissolve in the solvent system (THF:MeOH, 15:1) therefore could not deliver the hydride. Extra equivalents of hydride after the PSM reaction did not affect the tag group percentage distributions of the MOFs.

2.3. Scope of Tandem Post-Synthetic Modification

The optimised reaction scheme is summarised in Scheme 2.5. IRMOF-3 was reacted with the aldehyde RCHO (R = Me, Et, Pr, *n*-C_7H_{15}) in THF:MeOH (15:1) at 50 °C for 24 hours, before adding $NaCNBH_3$ to the reaction mixture. Hydrolysis of the borohydride with evolution of hydrogen gas occurred, so 10 minutes was allowed for H_2 production to cease, under a flow of N_2, also cooled in an ice bath to less than 5 °C. The mixture was then sealed and heated to 50 °C for 48 hours, with no stirring, so as not to break up the crystals. The crystalline product was washed with THF:MeOH (15:1). The resulting yellow-orange

crystals were then washed in toluene once per day for three days, keeping the material under toluene for storage to prevent water exposure.

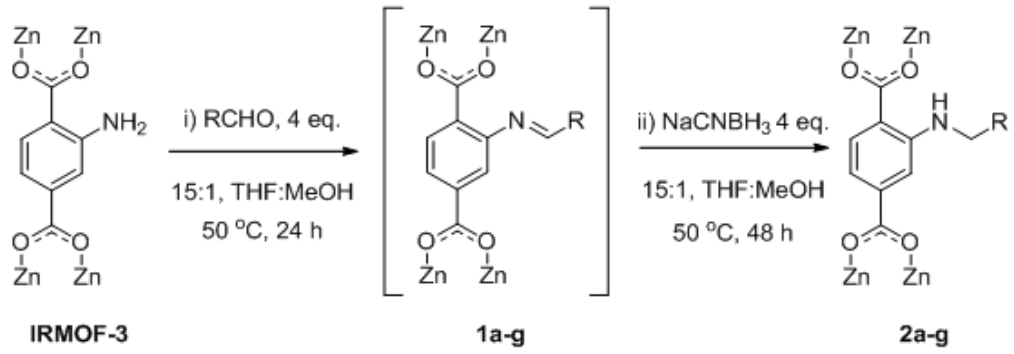

Scheme 2.5. General optimised PSM procedure. R = Me (**1a**, **2a**), Et (**1b**, **2b**), Pr (**1c**, **2c**), *n*-C_7H_{15} (**1d**, **2d**), C_6H_9 (**1e**, **2e**), Fc (**1f**, **2f**), C_6H_4SMe (**1g**, **2g**).

To investigate the scope of the reaction, these conditions were used with the functional aldehydes: 1,2,3,6-tetrahydrobenzaldehyde, ferrocenecarboxaldehyde, 2-methylthiobenzaldehyde, Figure 2.6. The results from the PSM reactions with these aldehydes, IRMOF-3 and $NaCNBH_3$ are summarised in Table 2.7. A further two aldehyde reagents were tried, 4-carboxyphenylbenzaldehyde and 2,3-dihydroxybenzaldehyde, but yielded non-crystalline solids, evidenced by powder X-ray diffraction, and are not discussed further.

Compound	**R**	**IRMOF-3-CH_2R /%**		**Av. IRMOF-3-CH_2R /%**	**S_{BET} (B2) /m^2g^{-1}**
		B1	**B2**		
2a	Me	79	69	74	749
2b	Et	69	69	69	943
2c	Pr	62	67	65	823
2d	*n*-C_7H_{15}	41	52	47	659
2e	C_6H_9	54	43	49	1004
2f	Fc	30	23	27	612
2g	C_6H_4SMe	25	24	25	672

Table 2.7. Conversions and surface areas of two independent PSM reactions B1 and B2: IRMOF-3 to secondary amino-functionalised MOFs, at 50 °C in THF-MeOH after 72 h.

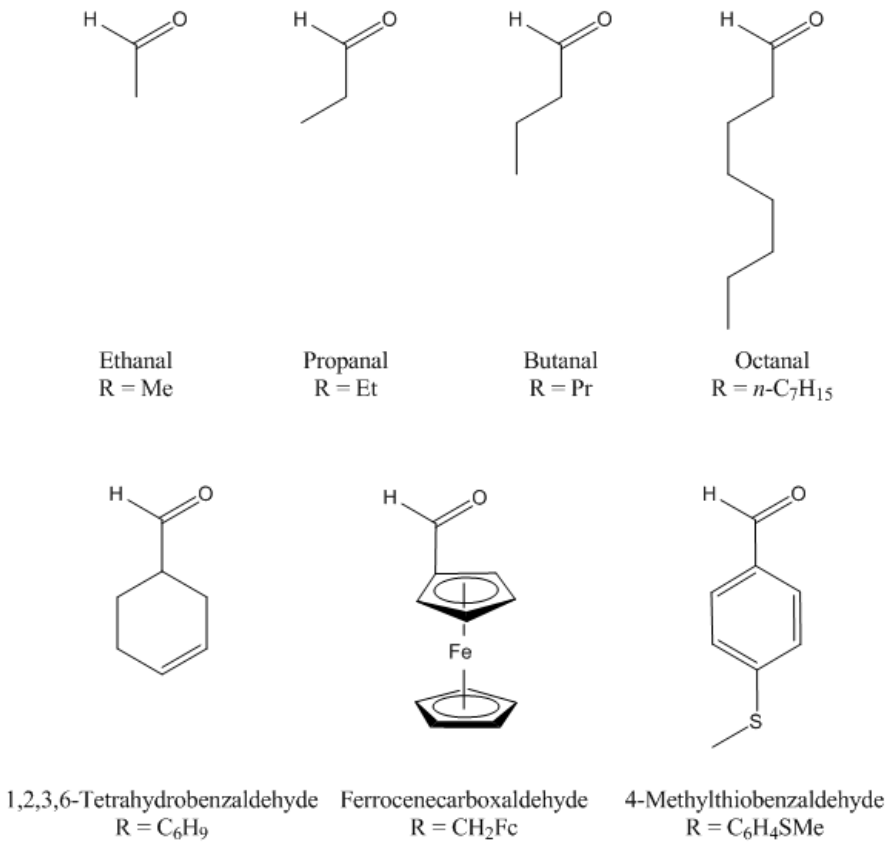

Figure 2.6. Structures of all the aldehydes successfully employed in this PSM investigation.

As the chain length increases from n = 2 (**2a**) to n = 8 (**2d**), the conversion decreases from 74 % to 47 % respectively, as expected. The difference between **2e** and **2g** is two non-hydrogen atoms (**2g** is longer) and this reduces the percentage of groups that can be converted in the framework, from 49 % to 25 %.

The powder X-ray diffraction data of **2a**-**g**, shown in Appendix A, (Figure 5.3 and Figure 5.4) confirms the overall framework to be unchanged from IRMOF-3 during the tandem PSM reaction. Visually the single crystal quality decreases as aldehyde chain length decreases, seen by an increased noise and broadening in the PXRD patterns.

This may be explained because the smaller, more volatile aldehydes penetrate deeper into the crystals, allowing for a higher conversion, however as the ethylamino groups are smaller, the borohydride is less impeded therefore leading to higher crystal degradation. Conversely the longer chains give more protection of the SBU from hydride anions and water molecules that reduce the crystallinity by attacking the $[Zn_4O(O_2CR)]$ Zn-O carboxylate bonds.

2.3.1. Tandem PSM of IRMOF-3 with Ethanal

From the ^{1}H NMR spectrum of the digested product of **2a**, Figure 2.7, the presence of a triplet at δ 1.29 ppm (integral: 3H), from the β-carbon to the nitrogen of H_2BDC-NHEt, showed a CH_3 group next to a neighbouring group of CH_2 (α-carbon) from the secondary amino-alkyl chain. Conversion was calculated by comparing the ratio of Ar-H doublets at δ 7.56 and 7.34 ppm for H_2BDC-NH_2 and H_2BDC-NHEt respectively. The average conversion was 74 % determined from two consistent, independent reactions, and gave the formula for **2a** as $[Zn_4O(BDC\text{-}NH_2)_{0.78}(BDC\text{-}NHEt)_{2.22}]$.

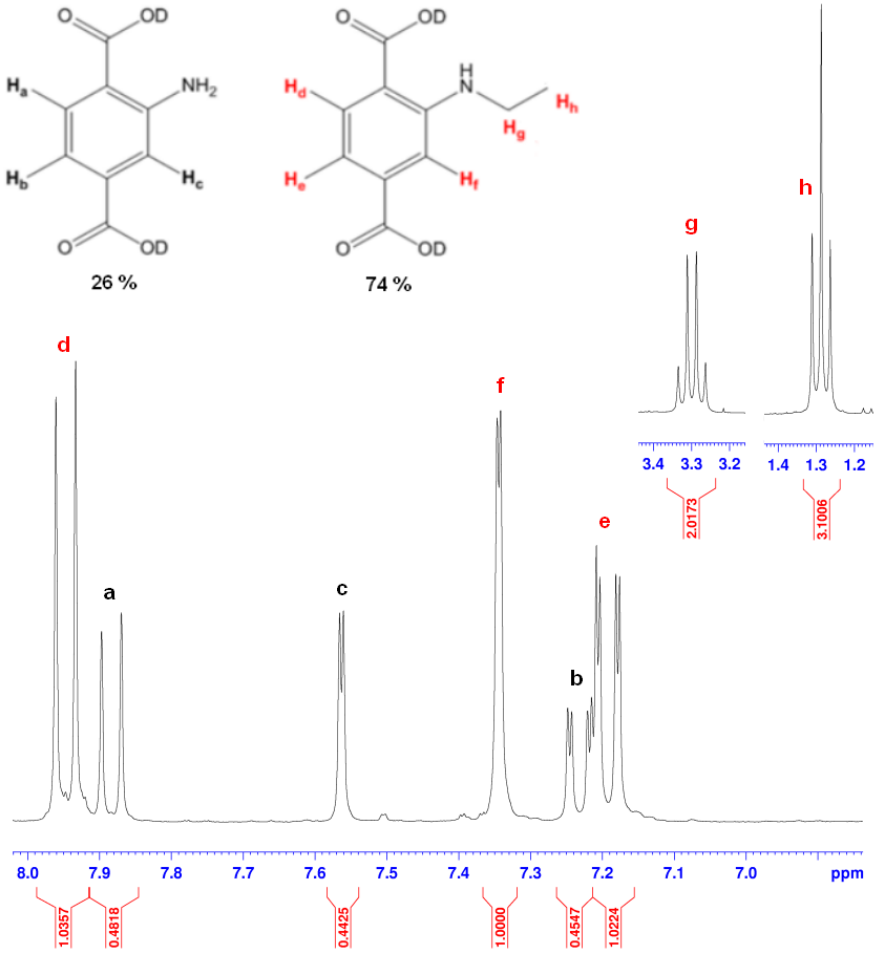

Figure 2.7. Aromatic and aliphatic (insert) regions of ^{1}H NMR spectrum of digested **2a** (inset). Tandem PSM product from the reaction between IRMOF-3, MeCHO, $NaCNBH_3$ in THF:MeOH (15:1) at 50 °C.

The negative ESI mass spectrum, of digested **2a**, confirms the presence of the singly deprotonated anion of H_2BDC-NHEt at *m/z* = 208.0646 (predicted $[M\text{-}H]^-$ = 208.0615).

This form of analysis can confirm the formation of the target linker and dismiss doubly *N*-alkylated linkers but was not used for quantifying conversion percentages.

The *in situ* FT-IR spectrum can be qualitatively used to gauge conversion by observing changes in the NH_2 (N-H stretch) peaks at high wavenumbers. This is one of the few techniques that can be carried out on the material without digestion. In the case of **2a** it shows a loss, or broadening, of both NH stretches compared to the starting material (3380 and 3500 cm^{-1}), Figure 2.8. The fingerprint region corresponds well with the starting framework but the expected N-H stretch at ~3380 cm^{-1} (seen in the dicarboxylic acid direct modification, Section 2.4) is not discernible. These data must be used in conjunction with other analytical methods, such as ^1H NMR spectroscopy, to determine the quantitative conversion and analyse fine structural features.

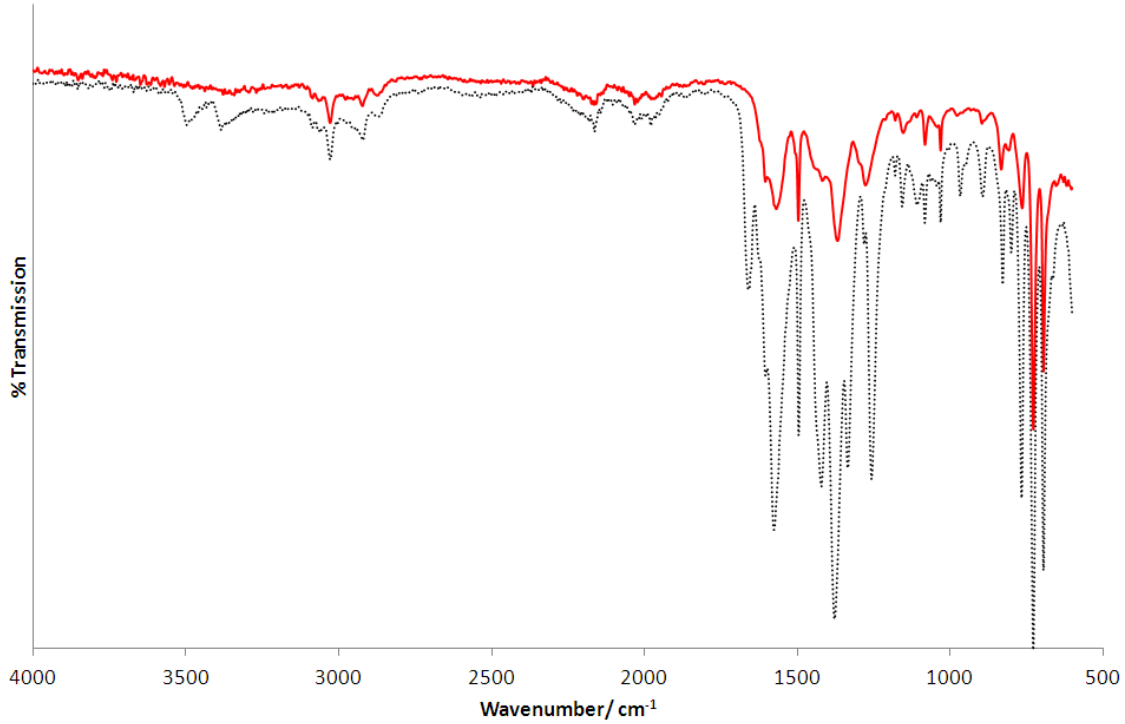

Figure 2.8. FT-IR spectrum of **2a** (red) and IRMOF-3 (black) in toluene.

The crystal structure of **2a**, $[Zn_4O(BDC\text{-}NH_2)_{1.2}(BDC\text{-}NHEt)_{1.8}]\cdot 7Tol$ (60 % conversion), was successfully elucidated by single crystal X-ray diffraction, using a synchrotron X-ray source, and is summarised in Table 2.8. The overall framework topology has not changed significantly during the reaction, from IRMOF-3, in agreement with the PXRD data. It has the supertetrahedral $[Zn_4O(O_2CR)_6]$ SBU and has retained the cubic space group symmetry, *Fm*-3*m*. The unit cell length in **2a**, a = 25.9940(3) Å, is larger than the literature

value of a = 25.7786(7) Å, for IRMOF-3.[8] The higher collection temperature could account for some changes in the unit cell, (**2a** collected at 250 K and IRMOF-3 collected at 220 K). There is a significant loss of quality in diffraction data (increased diffuse scattering) below 220 K that may be caused by a phase change in the crystal, but diffraction experiments were unsuccessful in identifying any structural changes.

2a	$[Zn_4O(BDC\text{-}NH_2)_{1.2}(BDC\text{-}NHEt)_{1.8}]\cdot 7Tol$
Empirical formula	$C_{76.60}H_{78.20}N_3O_{13}Zn_4$
Formula weight / gmol^{-1}	1510.30
T / K	250(2)
λ / Å	0.6889
Crystal system	Cubic
Space group	*Fm*-3*m*
Unit cell dimensions ($a = b = c$) / Å	25.9940(3)
$\alpha = \beta = \gamma$ / ^{o}	90
Volume / Å^3	17563.8(4)
Z (no. molecules in the unit cell)	8
Density (calculated) / gcm^{-3}	1.142
Crystal size / mm	0.14 x 0.12 x 0.10
Pre-SQUEEZE R(int)	0.0734
Data Completeness	0.995
Data / restraints / parameters	1064 / 6 / 31
Final R indices [$I>2\sigma(I)$]	$R1$ = 0.0608 $wR2$ = 0.1937
R indices (all data)	$R1$ = 0.0761 $wR2$ = 0.2170
Largest diff. peak and hole / eÅ^{-3}	0.700 and -0.400

Table 2.8. Selected crystal data and structure refinement data for framework **2a**.

Very high crystallographic symmetry, coupled with disorder and a 60% PSM conversion, meant that only the nitrogen atom from the pendant group on the ligand could be located with any certainty (Figure 2.9). The increasing flexibility along the *N*-ethyl chain resulted in the α- and β-carbon atoms of the *N*-ethyl chain being observed as diffuse electron density over a large area. Seven toluene molecules along with 1.8 ethyl groups (per $[Zn_4O]$) disordered in the framework, further add to the diffuse electron density, making the task of assigning discrete atom positions impossible.

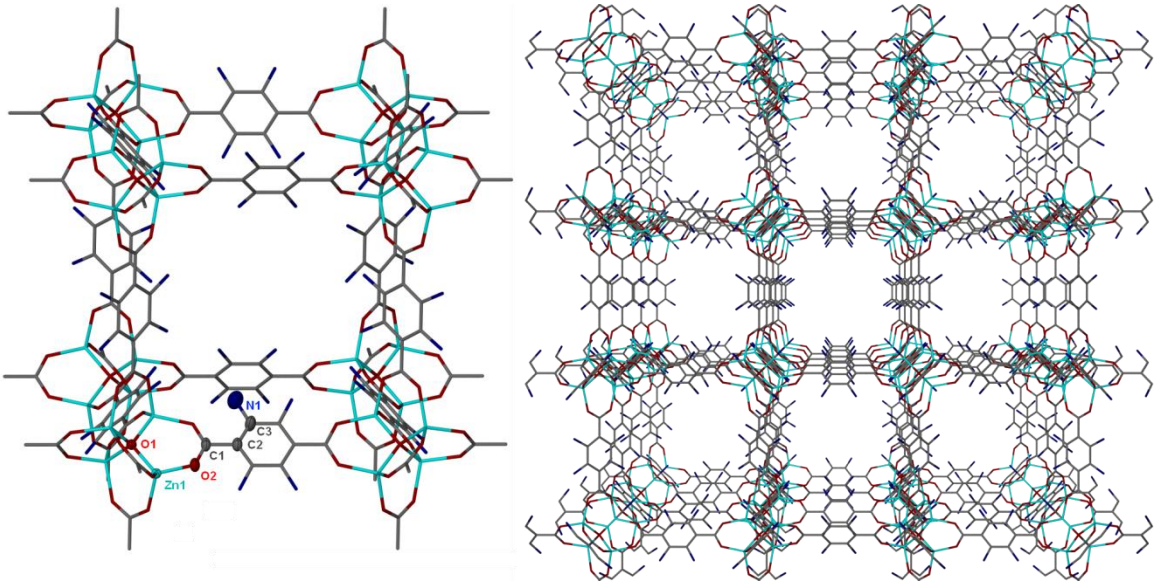

Figure 2.9. Structure of **2a** with 60% conversion of amino groups to ethylamino groups on pore surface modelled as disorder. **(left)** One enclosed pore, with atoms of the asymmetric unit shown at 30% ellipsoid probability. **(right)** View down the channels. *N*-ethyl chain α and β-carbon atoms could not be reliably located and are omitted. Solvent molecules are omitted.

The atom N1, (located at $x = 0.45$, $y = 0.32$, $z = 0.32$) is present at 12.5% occupancy, which means that the remainder of the functionalised group is subject to dynamic disorder, around all four carbon atoms of the dicarboxylate ligand. The thermal parameter of N1 was restrained and disorder precluded the addition of any hydrogen atoms to the model.

The residual electron density in the crystal structure was treated using Platon SQUEEZE,[12] which indicated a void volume of approximately 12,489 Å^3 per unit cell. This equates to a void space of 1561 Å^3 per 4 zinc centres. Based on TGA results, seven molecules of toluene have been included in the formula above, in addition to the appropriate ratio of the PSM derivatised ligand. The latter conversion rate was based on ^{1}H NMR digestion experiments on the crystalline material. Given a crude volume per non-hydrogen atom of 20 Å^3, the total volume of solvent and PSM tags is 1052 Å^3 per 4 zinc centres, which is below the value obtained from SQUEEZE.

Due to acid digestion of the MOF the ^{1}H NMR spectrum does not account for any imino tag groups on the framework, therefore extra imino tag groups may be present in the crystal, as it does have enough space to accommodate the extra atoms. SQUEEZE is less accurate when calculating over an area of >30 % unit cell volume and when the low-angle data is not of a high quality.

The calculated density of **2a**, ρ = 1.142 gcm^{-1} and for validation of this value, crystals were dropped into H_2O and DCM. They sank immediately in H_2O but floated for several seconds before absorbing DCM and sinking (ρ = 1.315 gcm^{-1}).

The pre-SQUEEZE difference electron density map, F_o-F_c, showed that the residual electron density is very diffuse, but given the nature of the samples and the well documented deficiencies in measuring diffraction data associated with MOFs of this type, the composition must be weighted in favour of chemical analysis.

The framework bond angle and distances (Table 2.9) have large errors associated with the values due to the poorer quality of the diffraction data than ideal (arising from the high symmetry, diffuse scattering and disorder from the guest solvent molecules and tag groups, the 3-D nature of the framework and the constraints and restraints put on the system during the solving and refining process).

Atoms	Bond length / Å	Atoms	Angles / °
Zn(1)-O(1)	1.9535(8)	O(2)-Zn(1)-O(1)	111.36(12)
Zn(1)-O(2)	1.948(3)	O(2)-Zn(1)-O(2)#1	107.51(13)
O(2)-C(1)	1.269(4)	O(2)-C(1)-O(2)#1	125.4(5)
N(1)-C(3)	1.46(3)	C(2)-C(3)-N(1)	121.9(15)

Table 2.9. Selected bond lengths and angles of **2a**. Symmetry transformation used to generate O2(#1) = x, ½-y, ½-z.

2.3.2. Tandem PSM of IRMOF-3 with Propanal

From the ^{1}H NMR spectrum of the digested product of **2b**, Figure 2.9, the presence of a sextet at δ 1.69 ppm (integral: 2H), from the hydrogen atoms on the β-carbon to the nitrogen of H_2BDC-NHPr, showed a CH_2 group next to neighbouring groups of CH_2 (α-carbon) and a CH_2 (γ-carbon) group from the secondary amino alkyl chain. Conversion was calculated by comparing the ratio of the Ar-H doublet at δ 7.64 to half the α-carbon sextet at 3.24 ppm for H_2BDC-NH_2 and H_2BDC-NHEt respectively to avoid peak overlap and increase accuracy. The average conversion was 69 % from two consistent, independent reactions and gave the formula for **2b** as $[Zn_4O(BDC\text{-}NH_2)_{0.93}(BDC\text{-}NHPr)_{2.07}]$.

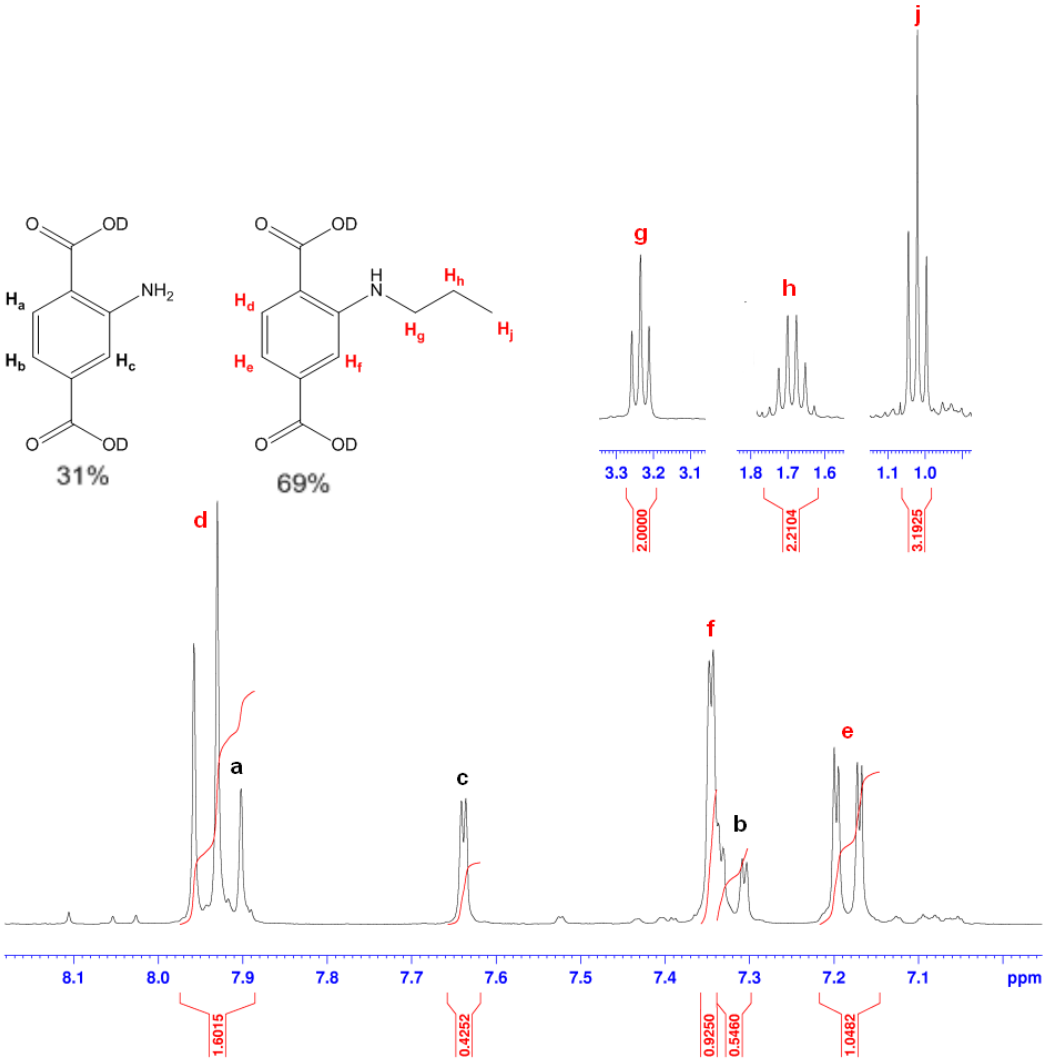

Figure 2.9. Aromatic and aliphatic (insert) regions of ^{1}H NMR spectrum of **2b** (inset). Digested product from reaction between IRMOF-3, MeCHO, $NaCNBH_3$ in THF:MeOH (15:1) at 50 °C.

The negative ESI mass spectrum of the digested solution confirms the presence of the singularly deprotonated anion of H_2BDC-NHPr at *m/z* = 222.0784 (predicted $[M\text{-}H]^-$ = 222.0766). The *in situ* FT-IR spectrum (experimental section 2.9.2, Figure 2.48) is very similar to the product from the reaction with ethanal, highlighting the difficulties in distinguishing PSM products from each other in the same series.

2.3.3. Tandem PSM of IRMOF-3 with Butanal

From the ^{1}H NMR spectrum of the digested product of **2c**, Figure 2.10, the presence of a quintet at δ 1.65 ppm (integral: 2H), from the β-carbon to the nitrogen of H_2BDC-NHBu, showed a CH_2 group next to neighbouring groups of CH_2 (α-carbon) and CH_2 (γ-carbon) from the secondary amino-alkyl chain. Conversion was calculated by comparing the ratio of Ar-H doublets at δ 7.54 and 7.32 ppm for H_2BDC-NH_2 and H_2BDC-NHBu respectively.

The average conversion was 65 % from two consistent, independent reactions and gave the formula for **2c** as $[Zn_4O(BDC\text{-}NH_2)_{1.05}(BDC\text{-}NHBu)_{1.95}]$.

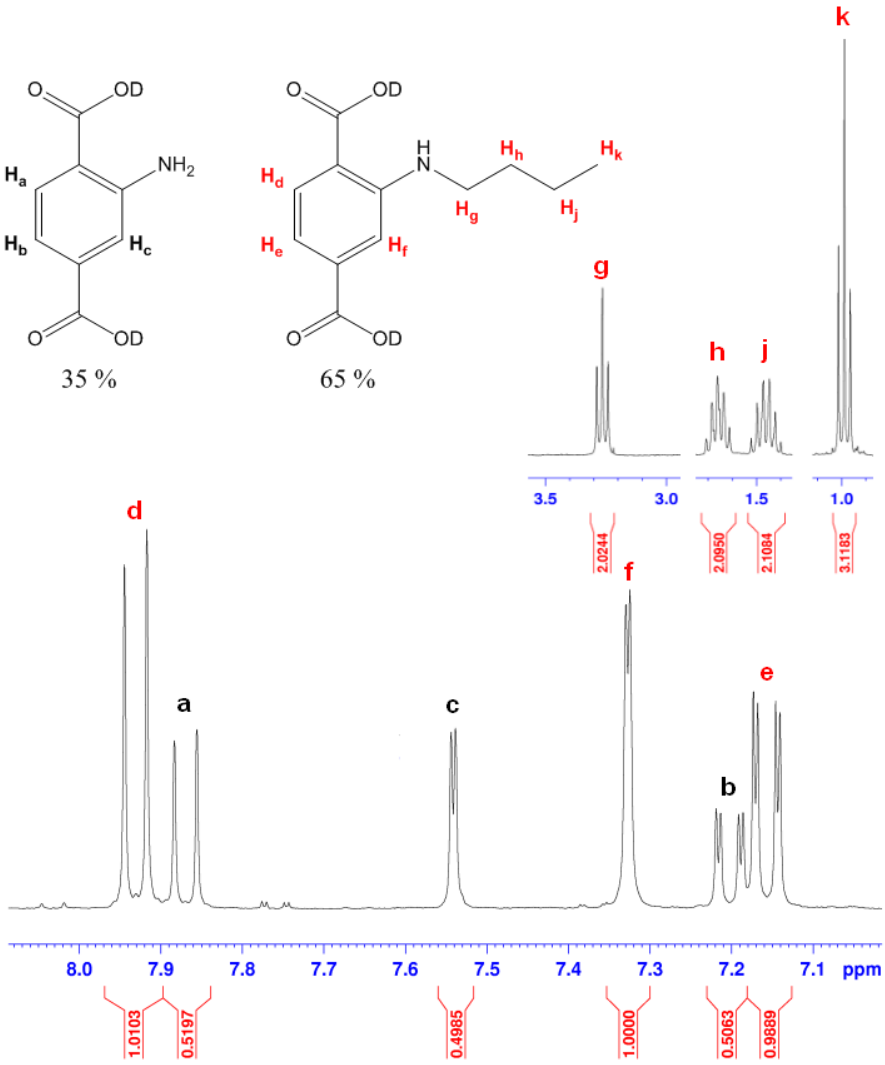

Figure 2.10. Aromatic and aliphatic (insert) regions of ^{1}H NMR spectrum of **2c** (inset). Digested product from reaction between IRMOF-3, PrCHO, $NaCNBH_3$ in THF:MeOH (15:1) at 50 °C.

The negative ESI mass spectrum of the digested solution confirms the presence of the singularly deprotonated anion of H_2BDC-NHBu at *m/z* 236.0934 (predicted $[M\text{-}H]^-$ = 236.0923).

2.3.4. Tandem PSM of IRMOF-3 with Octanal

During the PSM reaction, the $NaCNBH_3$ did not dissolve as well, when compared with the other aldehyde tandem PSM reactions. Octanal reduces the polarity of the solvent and hence reduces the solubility of the borohydride. This does not seem to affect the PSM

product tag group distributions as the conversion percentage follows the trend observed with the other alkyl chain aldehydes.

From the ^{1}H NMR spectrum of the digested product of **2d**, Figure 2.11, the presence of a triplet at δ 3.15 ppm (integral: 2H), from the α-carbon of $H_2BDC\text{-}NHC_8H_{17}$, showed a CH_2 group next to a neighbouring group of CH_2 (β-carbon). The terminal CH_3 group can be seen at δ 0.82 ppm. The multiplet in the range δ 1.2-1.4 ppm, represents 10 hydrogen atoms but is too overlapped to obtain an accurate integral. The ratio of the Ar-H doublets at δ 7.40 and 7.22 ppm for $H_2BDC\text{-}NH_2$ and $H_2BDC\text{-}NHC_8H_{17}$ were used to calculate conversion. The average conversion was 47 % from two consistent, independent reactions and gave the formula for **2d** as $[Zn_4O(BDC\text{-}NH_2)_{1.59}(BDC\text{-}NHC_8H_{17})_{1.41}]$.

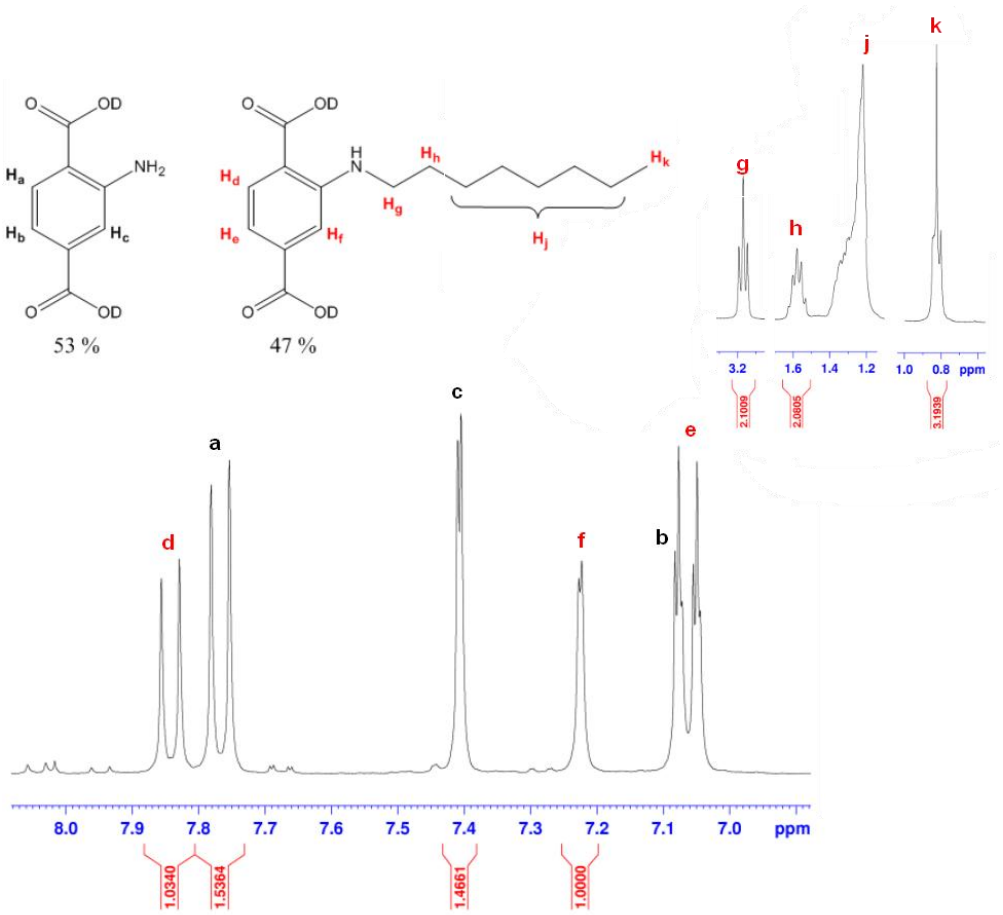

Figure 2.11. Aromatic and aliphatic (insert) regions of ^{1}H NMR spectrum of **2d** (inset). Digested product from reaction between IRMOF-3, $n\text{-}C_7H_{15}CHO$, $NaCNBH_3$ in THF:MeOH (15:1) at 50 °C.

The negative ESI mass spectrum of the digested solution confirms the presence of the mono-anionic linker of $H_2BDC\text{-}NHC_8H_{17}$, at m/z = 292.1558 (predicted $[M\text{-}H]^-$ =

292.1554). The *in situ* FT-IR spectrum is very similar to **2a**, **2b** and **2c** (experimental section 2.9.4, Figure 2.50).

2.3.5. Tandem PSM of IRMOF-3 with 1,2,3,6-Tetrahydrobenzadehyde

From the ^{1}H NMR spectrum of the digested product of **2e**, Figure 2.12, the presence of a doublet at δ 3.20 ppm (integral: 2H), from the α-carbon of H_2BDC-NHC_7H_{11}, showed a CH_2 group next to a neighbouring CH, of the cyclohexene ring. The ratio of the Ar-H doublets at δ 7.52 and 7.32 ppm were used to calculate conversion. The average conversion was 49 % from two consistent, independent reactions and gave the formula for **2e** as $[Zn_4O(BDC\text{-}NH_2)_{1.53}(BDC\text{-}NHCH_2C_6H_9)_{1.47}]$.

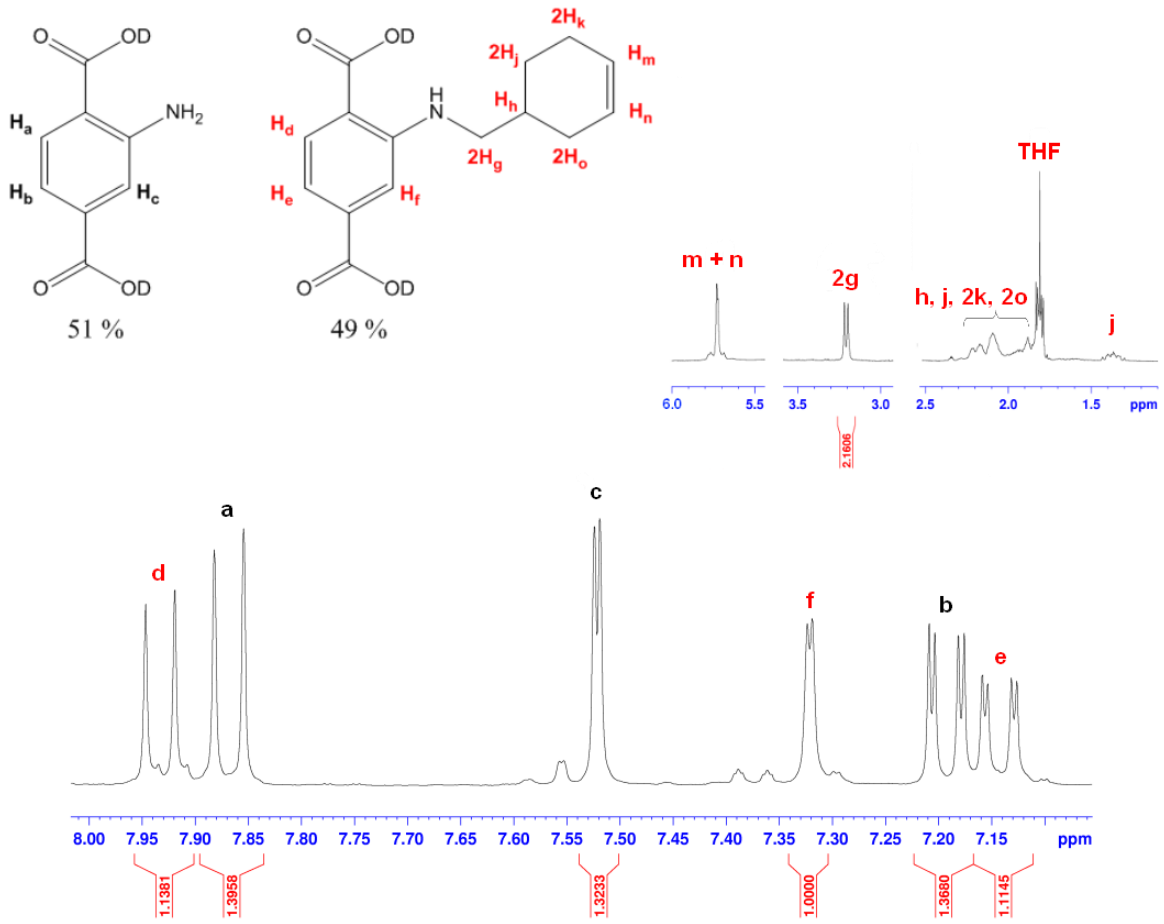

Figure 2.12. Aromatic and aliphatic (insert) regions of ^{1}H NMR spectrum of **2e** (inset). Digested product from reaction between IRMOF-3, C_6H_9CHO, $NaCNBH_3$ in THF:MeOH (15:1) at 50 °C.

The negative ESI mass spectrum of the digested solution confirms the presence of the deprotonated linker, H_2BDC-NHC_7H_{11}, at *m/z* = 247.1124 (predicted $[M\text{-}H]^-$ = 274.1085).

The *in situ* FT-IR spectrum was typical of these PSM products and closely resembles the compounds **2a-g** (experimental section 2.9.5, Figure 2.51).

2.3.6. Tandem PSM of IRMOF-3 with Ferrocenecarboxaldehyde

From the ^{1}H NMR spectrum of the digested product of **2f**, Figure 2.13, the signals at δ 4.15-4.31 ppm denotes the 11 hydrogen atoms in the H_2BDC-NHCH$_2$Fc in a 2:5:2:2 ratio consistent with a ferrocenyl methylamino group. The ratio of the Ar-H doublets (broad) at δ 7.61 and 7.29 ppm were used to calculate the extent of modification. The average conversion was 27 % from two consistent, independent reactions and gave the formula for **2f** as [Zn$_4$O(BDC-NH$_2$)$_{2.19}$(BDC-NHCH$_2$Fc)$_{0.81}$].

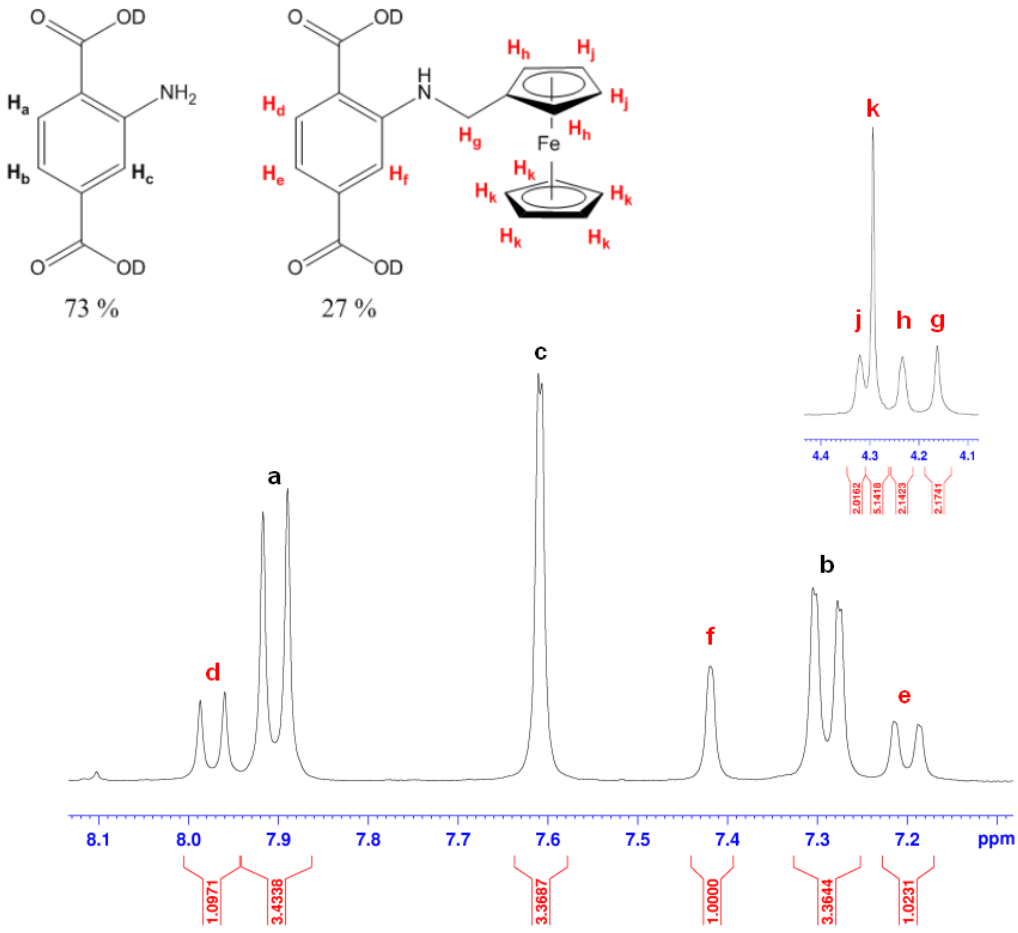

Figure 2.13. Aromatic and aliphatic (inset) regions of ^{1}H NMR spectrum of **2f** (inset). Digested product from reaction between IRMOF-3, FcCHO, NaCNBH$_3$ in THF:MeOH (15:1) at 50 °C.

Atomic adsorption spectroscopy on digested **2f** yielded an Fe:Zn ratio of 1:6.2, which corresponds to 23 % incorporation of ferrocenyl groups. This is in agreement with the ^{1}H NMR digestion experiments.

The negative ESI mass spectrum of the digested PSM product, **2f**, did not show up any presence of the deprotonated linker, H_2BDC-NHCH$_2$Fc, predicted $[M-H]^-$ = 378.0434. The reasoning is not fully understood for the lack of flight of the ligand ions, in the maldiTOF instrument as the free acid, **1f**, does show the correct fragment in the mass spectrum. The *in situ* FT-IR spectrum was typical of these PSM products and closely resembles the compounds **2a**-**g** (experimental section 2.9.6, Figure 2.52).

The crystal structure of **2f**, $[Zn_4O(BDC\text{-}NH_2)_{2.25}(BDC\text{-}NHCH_2Fc)_{0.75}]\cdot 2.5Tol$ (25 % conversion), was successfully elucidated by single crystal X-ray diffraction, using a synchrotron X-ray source, and is summarised in Table 2.10. This equates on average to 0.75 ferrocenyl methylamino groups per cubic pore [Zn_4O]. The framework has the [$Zn_4O(RCO_2)_6$], supertetrahedral SBU and has the same cubic space group symmetry, *Fm*-3*m*, as the stating material, IRMOF-3.

The unit cell length of **2f**, *a* = 26.0423(4) Å, is larger than the literature value for IRMOF-3, *a* = 25.7786(7) Å, possibly due to collection at 30 K warmer,[8] and significantly longer than **2a** (*a* = 25.9940(3) Å). Large ferrocenyl groups in the pores may have a steric effect on the unit cell length with expansion needed to accommodate the tag group.

2f	$[Zn_4O(BDC\text{-}NH_2)_{2.25}(BDC\text{-}NHCH_2Fc)_{0.75}]\cdot 2.5Tol$
Empirical formula	$C_{49.75}\,H_{42.50}\,Fe_{0.75}\,N_3\,O_{13}\,Zn_4$
Formula weight / $gmol^{-1}$	1193.74
T / K	250(2)
λ / Å	0.6889
Crystal system	cubic
Space group	*Fm*-3*m*
Unit cell dimensions ($a = b = c$) / Å	26.0423(4)
$\alpha = \beta = \gamma$ / °	90
Volume / $Å^3$	17661.9(5)
Z	8
Density (calculated) / gcm^{-3}	0.898
Crystal size / mm	0.15 x 0.15 x 0.10
Pre-SQUEEZE R(int)	0.0486
Independent reflections	1067 [R(int) = 0.0482]
Data Completeness	0.994
Data / restraints / parameters	1067 / 6 / 31
Final R indices [$I>2\sigma(I)$]	$R1$ = 0.0362 $wR2$ = 0.1150
R indices (all data)	$R1$ = 0.0387 $wR2$ = 0.1181
Largest diff. peak and hole / $eÅ^{-3}$	0.259 and -0.259

Table 2.10. Selected crystal data and structure refinement data for framework **2f**.

As is the case of **2a**, framework **2f** has very high crystallographic symmetry coupled with disorder and a 25% PSM conversion meant that only the nitrogen atom from the pendant group, on the ligand, could be located with any certainty (Figure 2.14). This is further hindered by the flexibility increasing along the chain, resulting in the α-carbon and the ferrocenyl group being observed as diffuse electron density over a large area. 2.5 toluene molecules and 0.75 ferrocenyl groups per $[Zn_4O]$, disordered in the pore, also adds to the total electron density, making the task of assigning discrete atoms impossible, yet it was still surprising not to observe any definite signs of an iron atom in the pores.

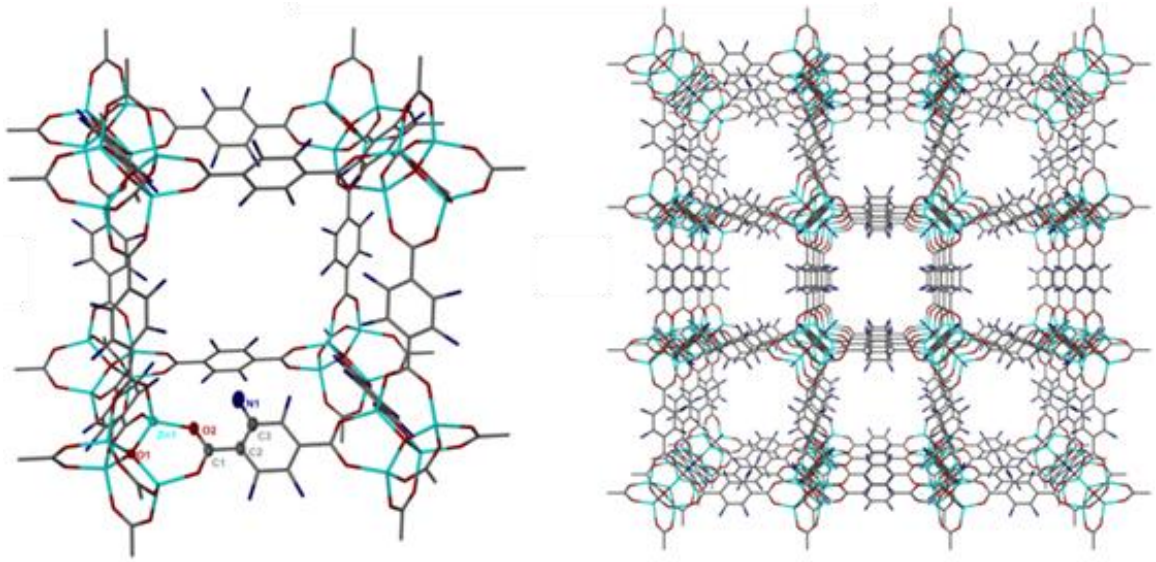

Figure 2.14. Structure of **2f** with 25% conversion of amino groups to ferrocenylmethylamino groups on pore surface. **(left)** One enclosed pore with atoms of the asymmetric unit shown at 30% probability. **(right)** View down the channels. The *α*-carbon atom to N1 and the ferrocenyl group could not be reliably located and are omitted. Solvent is omitted for clarity.

The atom N1 (located at x = 0.45, y = 0.32 and z = 0.68) is present at 12.5% occupancy, which means that the remainder of the functionalised group is subject to dynamic disorder, around all four carbons of the dicarboxylate ligand. The thermal parameter of N1 was restrained so it does not model the large area of electron density smearing. This disorder precluded the addition of any hydrogen atoms to the model. A low pre-SQEEZE $R_{(int)}$ of 4.9 % was obtained even though the tag group electron density (one ferrocenyl group per void) was not accounted for in the model. This is surprising and could be an artefact of surface modification (heterogeneous tag group distribution) as the bulk structure being measured would only be -NH_2 tagged IRMOF-3, however 25 % is larger than expected for only surface modification (5 % conversion reported by Burrows *et al.* with ferrocenyl anhydride on IRMOF-3).[13]

The residual electron density in the crystal structure was treated using Platon SQUEEZE, which indicated a void volume of approximately 12,531 $Å^3$ per unit cell. This equates to a void space of 1567 $Å^3$ per 4 zinc centres. Based on TGA results, 2.5 molecules of toluene have been included in the formula above, in addition to the appropriate ratio of the PSM derivatised ligand. The latter conversion rate was based on ^{1}H NMR digestion experiments of the crystalline material. Given a crude volume per non-hydrogen atom of 20 $Å^3$, the

total volume of solvent and PSM tags is 530 $Å^3$ per 4 zinc centres, which is well under the value calculated from SQUEEZE.

A possible explanation for the mismatch of predicted data with measured data may come from revisiting the assumption that all the imino groups are reduced by the $NaCNBH_3$. This may not be a correct one as the characterisation was not conclusive for determining extra imino groups. Solid-state techniques such as solid- state $^1H/^{13}C$ NMR spectroscopy, X-ray absorption/emission spectroscopy (XAS/XES), or Mössbauer spectroscopy may yield more insight into the extent of the incorporation of these extra Fe^{II} based groups.

The framework's bond angles and distances are summarised in Table 2.11.

Atoms	**Bond length / Å**	**Atoms**	**Angles / °**
Zn(1)-O(1)	1.9545(4)	O(2)-Zn(1)-O(1)	111.18(6)
Zn(1)-O(2)	1.9493(16)	O(2)-Zn(1)-O(2)#1	107.71(6)
O(2)-C(1)	1.266(2)	O(2)-C(1)-O(2)#1	124.7(3)
N(1)-C(3)	1.430(14)	C(2)-C(3)-N(1)	127.2(6)

Table 2.11. Selected bond lengths and angles. Symmetry transformation used to generate O2(#1) = x, -y, -z.

2.3.7. Tandem PSM of IRMOF-3 with 4-Methylthiobenzaldehyde

From the ^1H NMR spectrum of the digested product of **2g**, Figure 2.15, the presence of the 4-methylthiobenzene group can be confirmed with a multiplet in the aromatic region between δ 7.28-7.37 ppm in a 4:1 ratio with the BDC Ar-H at δ 7.26 ppm. The signal attributed to the α-CH_2 was visible at δ 4.51 ppm but was overlapped by the H_2O broad singlet. The ratio of the Ar-H doublets, at δ 7.49 and 7.26 ppm, were used to calculate conversion. The average conversion was 25 % from two consistent, independent reactions and gave the formula for **2g** as $[Zn_4O(BDC\text{-}NH_2)_{2.25}(BDC\text{-}NHCH_2C_6H_4SMe)_{0.75}]$.

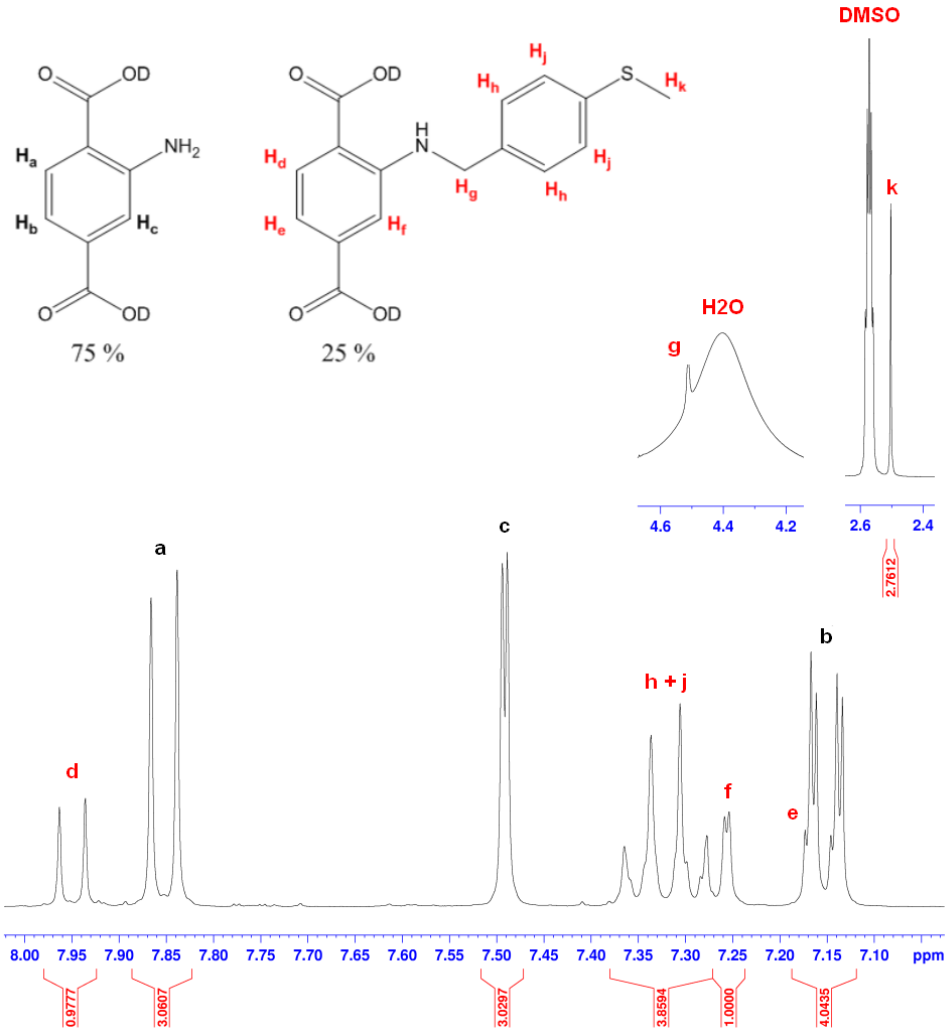

Figure 2.15. Aromatic and aliphatic (insert) regions of ^{1}H NMR spectrum of **2g** (inset). Digested product from reaction between IRMOF-3, $MeSC_6H_4$-CHO, $NaCNBH_3$ in THF:MeOH (15:1) at 50 °C.

The negative ESI mass spectrum of the digested solution confirms the presence of the deprotonated linker, $H_2BDC\text{-}NHC_7H_6SMe$, at *m/z* = 316.0757 (predicted $[M\text{-}H]^-$ = 316.0649). The *in situ* FT-IR spectrum is typical for these systems and specific functional differences cannot be distinguished between **2g** and **2a-f**.

2.3.8. Thermogravimetric analysis of *N*-alkyl PSM Products, 2a-d.

Thermogravimetric analysis (TGA) of **2a-d**, Figure 2.16, shows the mass change with respect to temperature. The initial mass loss stage (40-150 °C) represents the sum of the toluene that is in the pores and any excess toluene loosely bound to the MOFs. The plateau region in the range (150-300 °C) represents the activated MOF where the pores are free of

solvent. Decomposition of the organic ligand begins at 300 °C. These characteristics are common to all the alkyl chain tandem PSM reaction products.

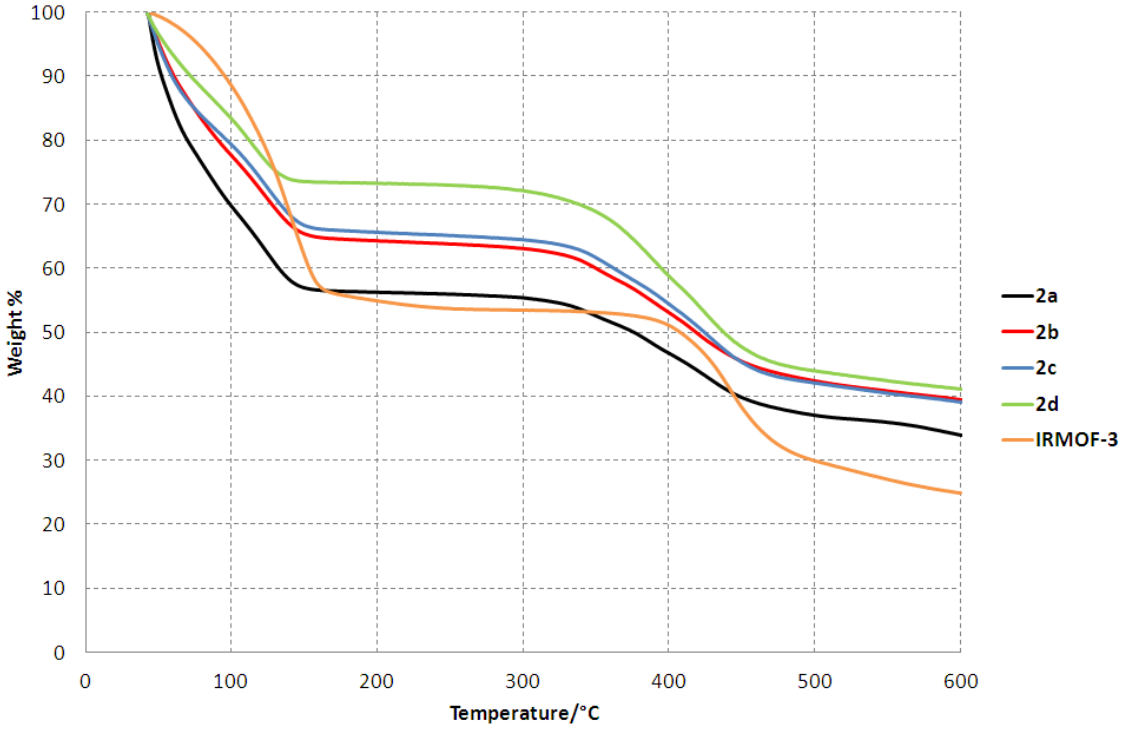

Figure 2.16. TGA of **2a-d** and IRMOF-3. Samples heated in $N_{2(g)}$ at 5 °Cmin^{-1}.

Compounds **2a-d** lose their toluene in the range 40-150 °C, 20 °C lower than IRMOF-3 and start to decompose 50 °C lower, at 320 °C. Per [Zn_4O] unit: **2a** has 7 toluene molecules, **2b** has 5.5, **2c** has 5.5 and **2d** has 4.0 toluene molecules per pore (or [Zn_4O]). In comparison to a report by Rosseinsky *et al.* in which there were 5 molecules of toluene per pore of IRMOF-3 and hence, is lower than observed here.[14] What remains after heating to 600 °C in $N_{2(g)}$, is a charred black solid and resembles ZnO, from PXRD (Figure 2.17).[15]

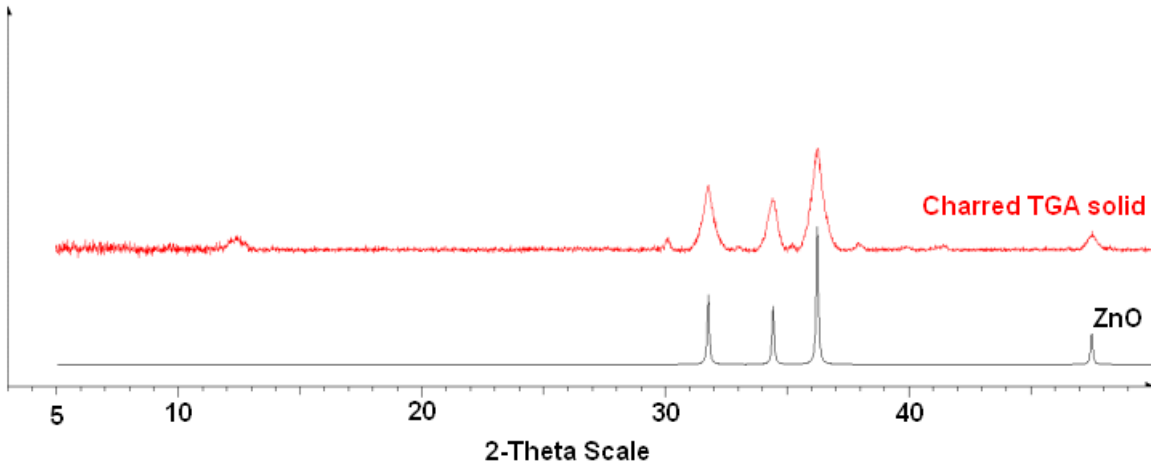

Figure 2.17. PXRD pattern of charred solid left over after a TGA experiment (red) and the literature pattern of ZnO, zincite (black).[15]

As the chain length of tag group increases in the pores, the percentage weight of toluene generally decreases. This is expected as increasing the steric demand of groups within the pores will reduce the space available for solvent. However, conversion decreases as chain length increases, hence a quantitative comparison is difficult.

2.3.9. Thermogravimetric Analysis of Functionalised PSM Products, 2e-g

The TGA of **2e-g**, Figure 2.18, shows the mass change as the sample is heated in $N_{2(g)}$. The initial mass loss stage (up to 150 °C) represents the total amount of toluene that is in the MOFs. The plateau region in the range 150-270 °C (**2e**) and 150-300 °C (**2f**, **2g**), represents the activated MOF where the pores are free of solvent. Decomposition of the organic ligand begins at 270 °C (**2e**) and 300 °C (**2f**, **2g**). The temperatures for activation and decomposition are similar with **2a-d**. Compared to IRMOF-3, **2e-g** lose their guest toluene molecules 20 °C lower and start to decompose at a temperature of 50-70 °C lower.

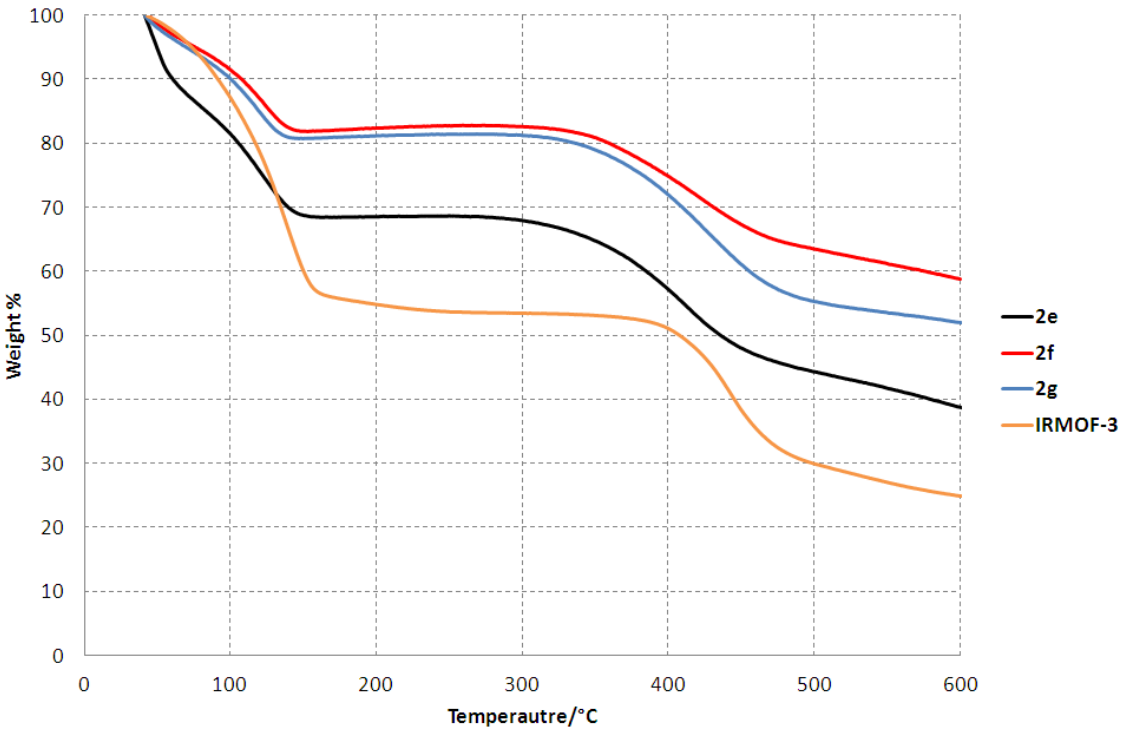

Figure 2.18. TGA of **2e-g** and IRMOF-3. Samples heated in $N_{2(g)}$ at 5 °Cmin^{-1}.

For each [Zn_4O] unit (one pore) **2e** has 3.5 toluene molecules, **2f** has 2.5 and **2g** has 4 toluene molecules per pore. Intuitively, as the number and size of tag groups increase the number of solvent molecules per pore decreases. MOF **2g** has 1.6 times more toluene in the pores than **2f** even though the modified tag incorporation and S_{BET} values are similar. This is unexpected and could be explained by more efficient packing of the toluene and flat phenyl rings in **2g** compared with the ferrocenyl group.

2.3.10. N_2 adsorption of *N*-alkyl Chain PSM Products, 2a-d

The TGA data above gives an insight into the activation temperatures of the MOFs, **2a-d**, and these in turn can be used as conditions for pre-treatment of the frameworks, for surface area measurements. In the series of MOFs **2a-d**, 150 °C for 3 hours under vacuum was used as the activating conditions. Results for IRMOF-3 with its pore guests exchanged with toluene, are also shown in Figure 2.19.

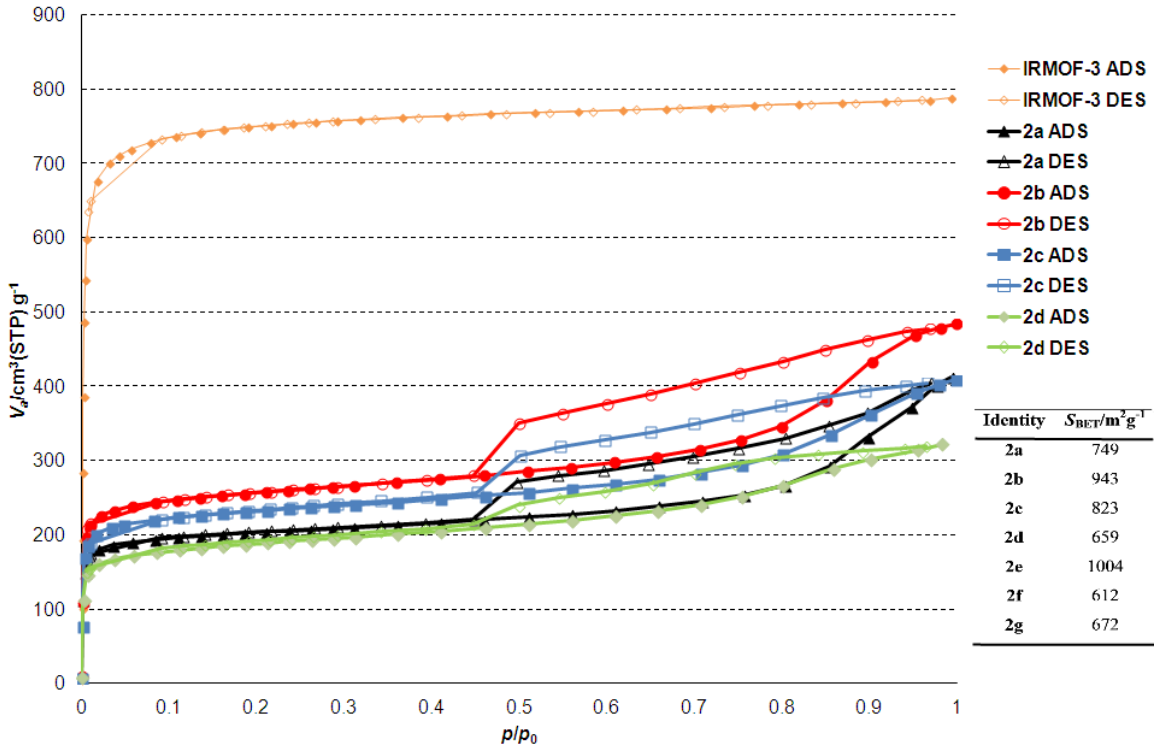

Figure 2.19. $N_{2(g)}$ adsorption (filled points) and desorption (open points) curves of IRMOF-3 and **2a-d** at 77K.

The lower BET surface areas (maximum S_{BET} = 1004 $m^2g^{-1}$for **2e**) and absolute $N_{2(g)}$ adsorption of **2a-d**, compared to IRMOF-3 (S_{BET} = 2613 m^2g^{-1}) may be partly rationalised by considering as the mass from the secondary amino tag group increases, the surface area (m^2g^{-1}) will decrease.

Higher numbers of tag groups in the pores of the MOF (e.g. a higher conversion) reduces space available for N_2 molecules to be adsorbed onto the pore surface. This could be coupled with blocking of favourable interaction sites for N_2 molecules in the pores *i.e.* proximate to the SBU. Non-reduced imino groups could be present and account for extra mass, decreasing S_{BET} further.

The activation conditions may not have been aggressive enough to completely empty all of the voids, in the framework, especially in the core of the crystals because of the presence of longer pendent groups. This could be regarded as a systematic error that only explains why the surface areas are consistently lower than expected compared with IRMOF-3 over the whole series of **2a-g**.

Further reductions in S_{BET} can occur from an inefficient washing process and may still leave unreacted organic reagents and trigonal boron by-products present from the THF:MeOH (15:1) solvent system utilised. Degradation of the crystals by solvent sheer forces, as toluene is forcibly removed by heating under vacuum can lead to non-porous mass present in the sample.

The materials, **2a-d**, are still microporous and display the same diameter pores as IRMOF-3 but only with a reduction in the absolute number of pores (pore size distribution ≡ $\delta V_p/\delta d_p \equiv dV_p/dd_p$). The pores sizes were calculated by a micropore analysis (MP) plot, and resulted in two maxima at 0.655 nm and 0.715 nm, Figure 2.20. When the PSM reaction was carried out with no aldehyde, *i.e.* IRMOF-3 only exposed to $NaCNBH_3$ in THF/MeOH at 50 °C for 72 h, the numbers of open pores decrease to a lesser extent (two-fold rather than five-fold decrease) than when they are exposed to aldehyde. This may be caused by a sterical pore blocking from the amino groups that are introduced into the pores of the MOF.

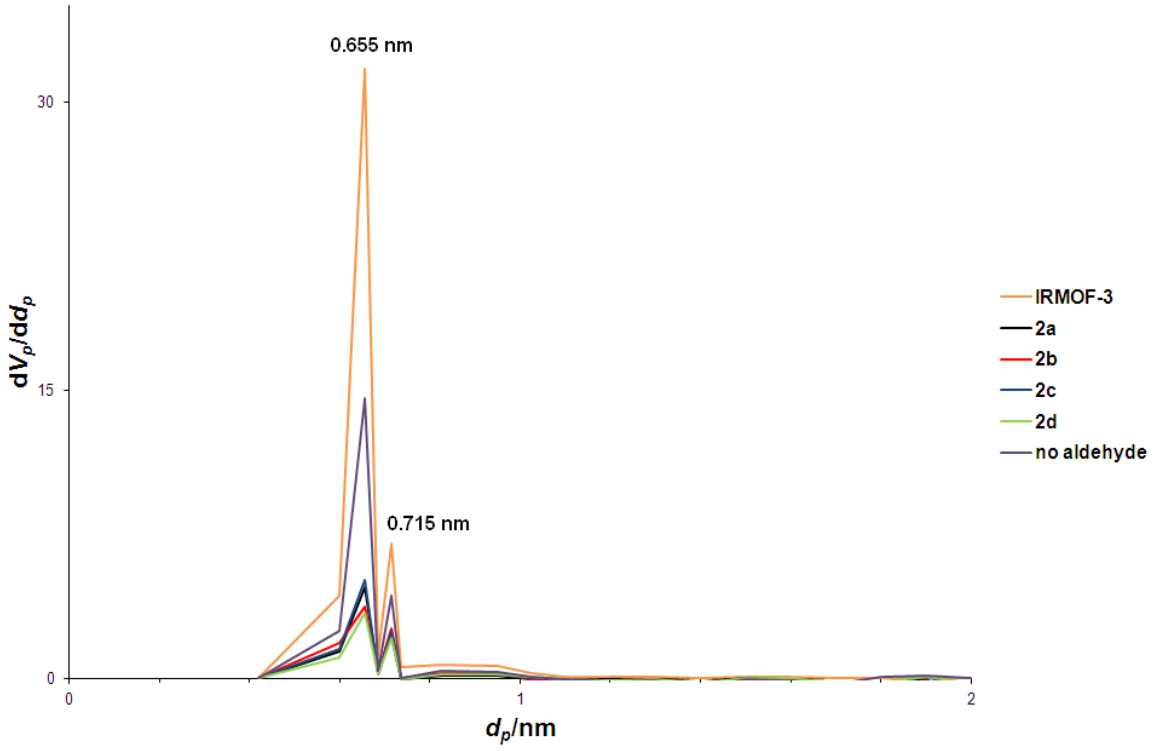

Figure 2.20. MP plot of IRMOF-3, **2a-d** and IRMOF-3 after treatment with $NaCNBH_3$ in THF/MeOH (15:1) only.

Notably, from the type IV nitrogen adsorption/desorption curves of **2a-d**, hysteresis is observed. As the length of the secondary amino chain in the MOF decreases, hysteresis

increases. The hysteresis closes at a partial pressure of 0.45 p/p_o. One reason could be the presence of non-uniformity in tag group modification. Another cause of this hysteresis may be observed from the peak Barret-Joyner-Halenda (BJH) pore diameter plot showing mesopore size distributions, Figure 2.21, in the crystalline MOFs. A mesopore is observed at 4-40 nm and can explain the hysteresis observed, by capillary condensation, in meso/macroporous materials, as demonstrated in the report by Jeong and co-workers.[2]

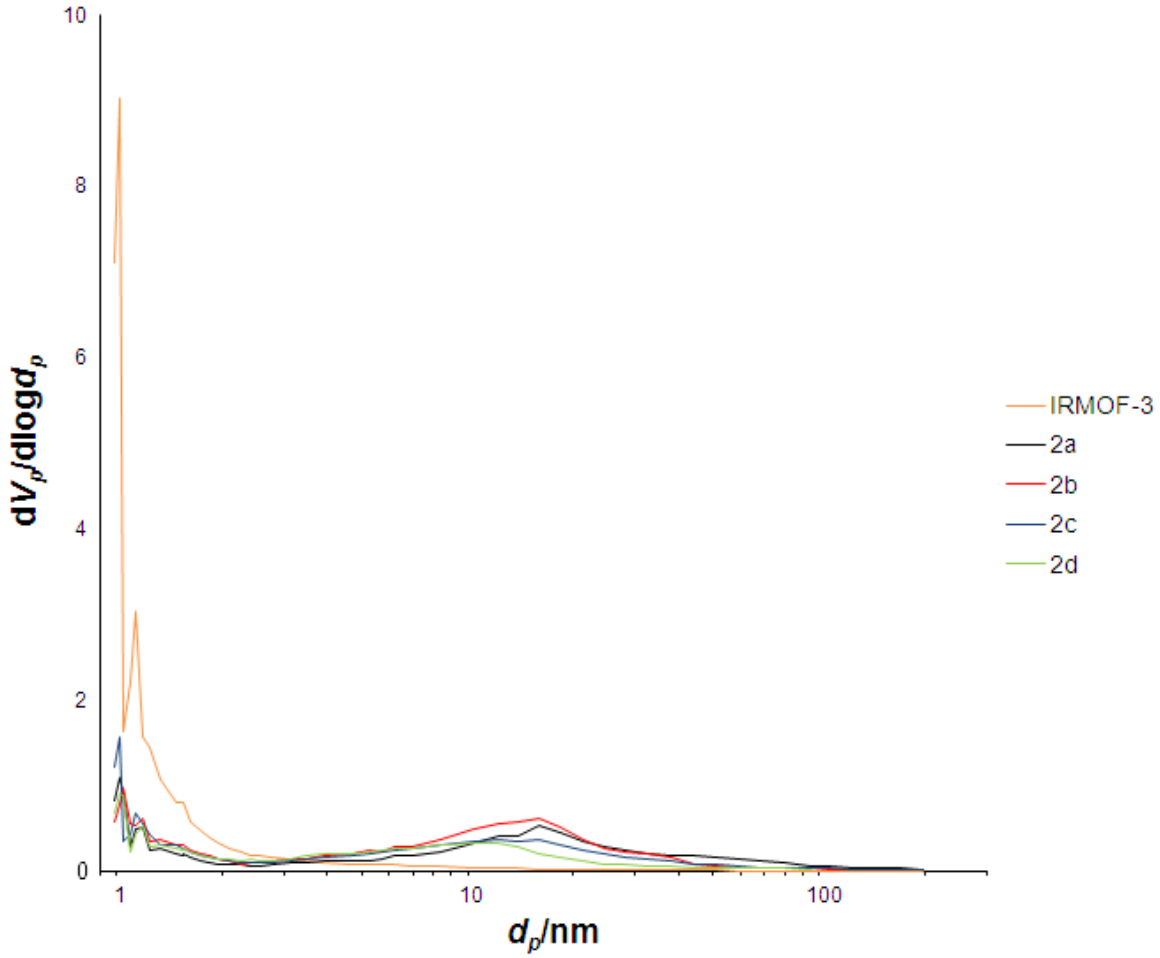

Figure 2.21. BJH plot of IRMOF-3 and compounds **2a-d**.

Generally the number of open pores decreases as aldehyde chain length increases. As the diameter of the pores tend from 4 to 40 nm, the chain length decreases and the number of larger voids increase. BJH mesopore sizes are generally underestimated due to errors using $N_{2(g)}$ as the probe gas (ideally use argon) therefore 40 nm is a soft limit to the mesopore diameters found herein.

To test if reducing the conversion by half would double the BET and half the hysteresis, IRMOF-3 was reacted under the optimised PSM conditions with propanal and $NaCNBH_3$

for 48 h in total (24 h exposure to $NaCNBH_3$, instead of 48 h). The conversion of BDC-NH_2 to BDC-NHPr was 33 %. The BET surface area slightly more than doubled, from 943 to 2074 m^2g^{-1} (2.2 fold increase) and due to halved exposure time to hydride general crystal quality did not decrease compared to longer times. This may allow a microwave PSM to be the next step to increase conversion whilst keeping crystal quality high.

2.3.11. N_2 adsorption of PSM Products, 2e-g

In the series of MOFs **2e-g**, 150 °C for 3 hours under vacuum was used as the activating conditions. The result for IRMOF-3 (guest exchanged with toluene) is also shown, Figure 2.22.

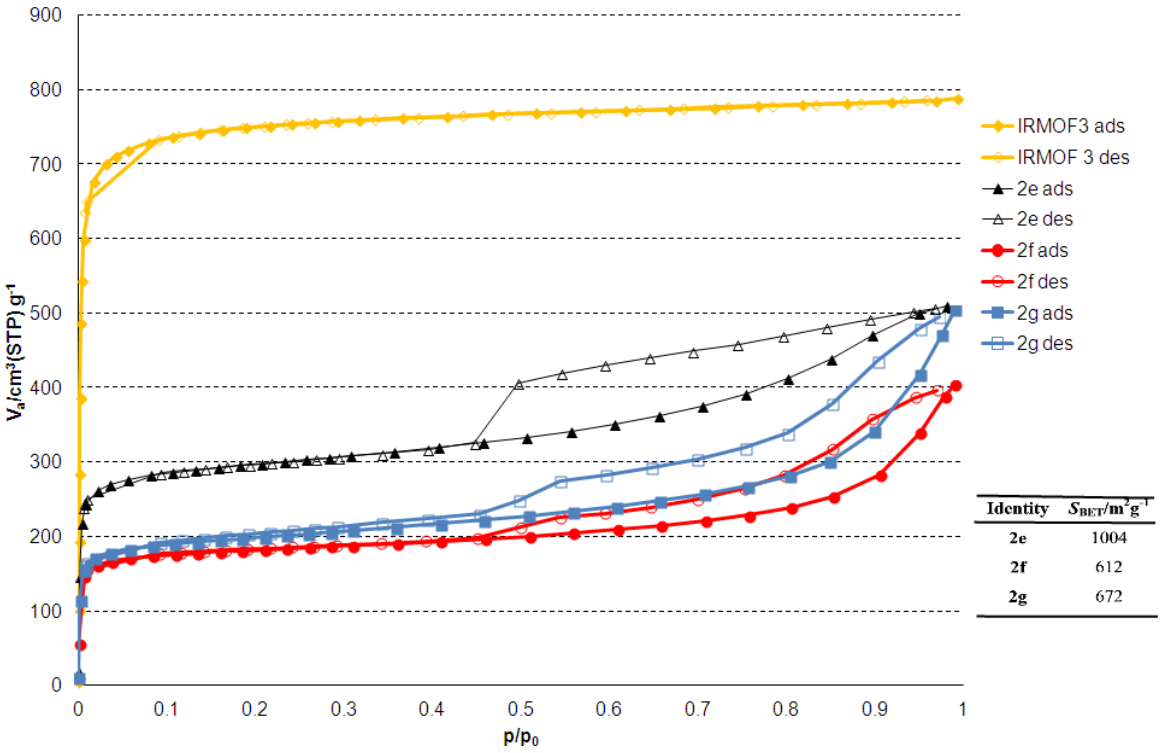

Figure 2.22. $N_{2(g)}$ adsorption (filled points) and desorption (open points) curves of IRMOF-3 (orange), **2e** (black), **2f** (red) and **2g** (blue) at 77K.

As in the case for the materials **2a-d** the nitrogen absorption curves of **2e-g** show hysteresis probably due to mesopore behaviour. The hysteresis closes at a partial pressure of 0.45 p/p_o: identical to compounds **2a-d**. This is not observed with the starting material, and may be explained by pit etching caused by the borohydride reducing agent. A control result with just sodium cyanoborohydride showed the same behaviour: IRMOF-3 treated with $NaCNBH_3$ in THF:MeOH (15:1) demonstrated a BET surface area of 1351 m^2g^{-1} also displaying the same type of hysteresis as the tandem PSM reaction products.

Washing IRMOF-3 with methanol only, gave material that did not display hysteresis in the N_2 adsorption curves, but had increased surface area (S_{BET} = 2886 m^2g^{-1}) compared with IRMOF-3 treated only with toluene (S_{BET} = 2613 m^2g^{-1}), perhaps due to more highly efficient washing conditions. The *in situ* PXRD patterns of **2e-g** matched the starting material and showed no reduction in crystallinity initially feared. Therefore, synergistic crystal degradation with the hydride source is probably responsible for the decrease in crystallinity and lower BET surface areas.

The MP plot shows the same reduced pore density for IRMOF-3, Figure 2.23. There is no difference between the pore sizes of materials **2e-g**, apart from a reduction in the number of these pores.

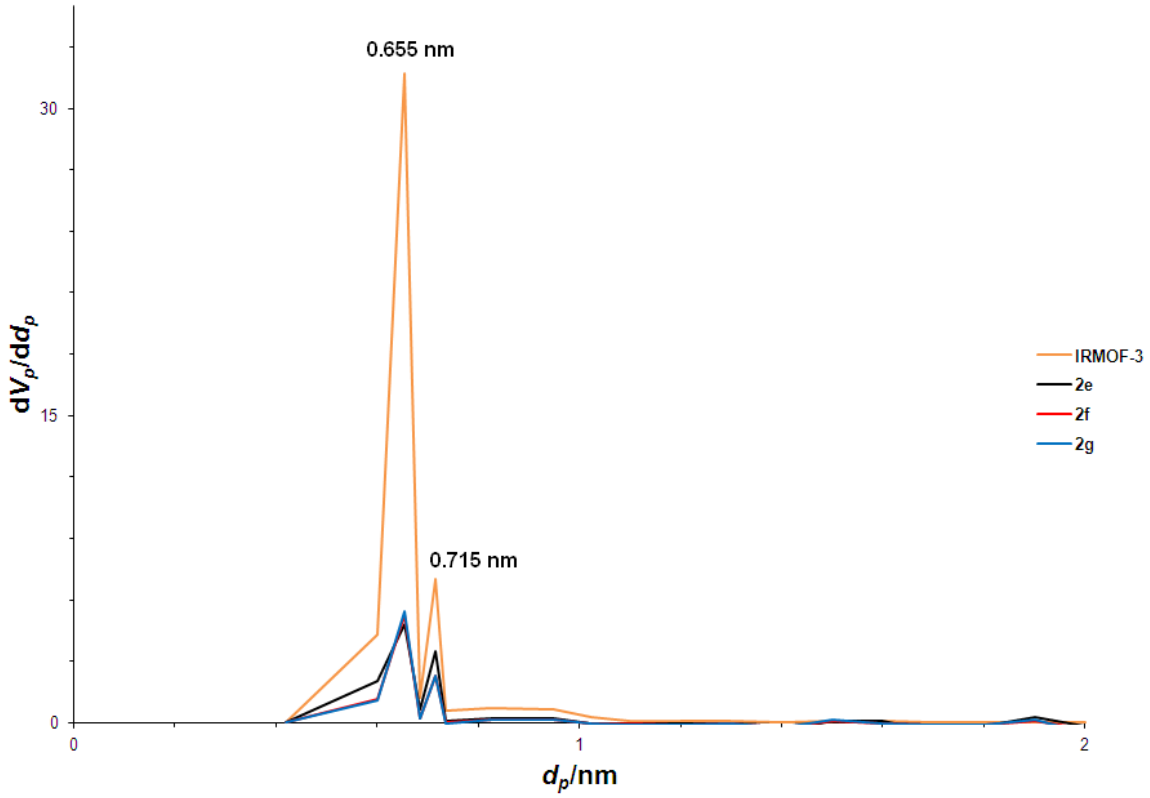

Figure 2.23. MP plot of functional PSM products **2e-g**. **2f** and **2g** traces are overlapped closely.

The BJH plot shows mesopore distributions similar to compounds **2a-d**. Tandem PSM product **2e** had a smaller diameter pores of 3-30 nm compared with **2f** and **2g** which pores were ~3-200 nm, Figure 2.24.

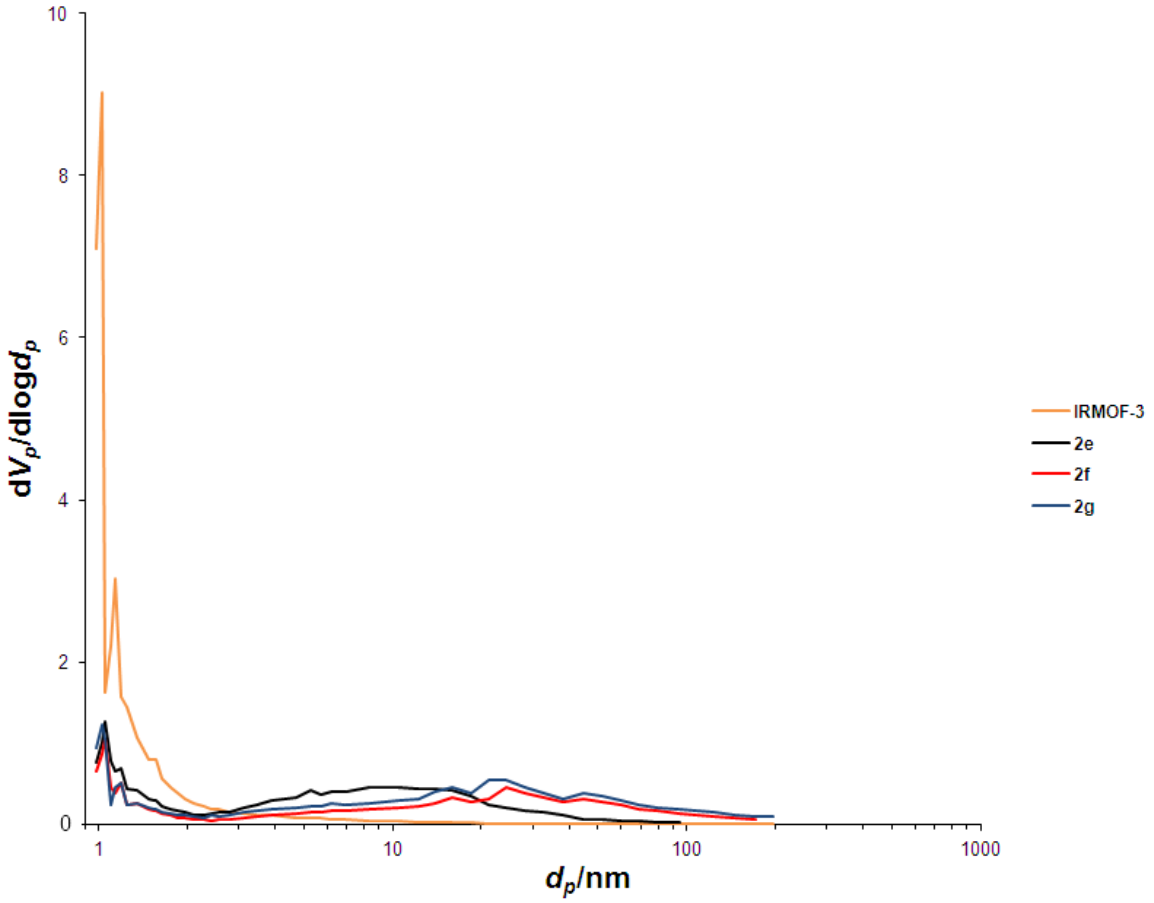

Figure 2.24. BJH plot of functional PSM products **2e-g**.

2.4. Pre-synthetic Functionalisation of H_2BDC-NH_2 and Direct synthesis of IRMOF-3-NHR.

To be able to synthesise MOFs with functionalised BDC linkers, without the tandem PSM reaction conditions, tagged H_2BDC-NHR ligands were prepared and the characterisation is given in Section 2.10. The general reaction scheme is summarised in Scheme 2.6. The pre-functionalised ligands were made following a modified procedure from the preliminary investigations of the tandem PSM reactions, on IRMOF-3. Attempts at isolating compounds **3a-g**, with imino functionality, were unsuccessful.

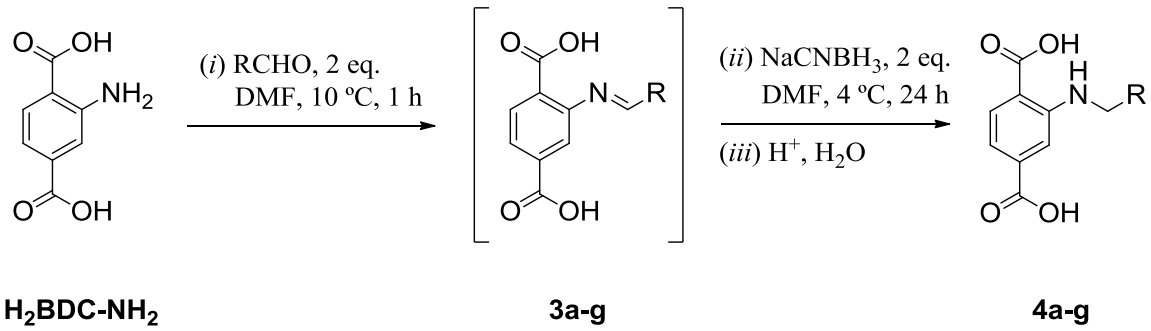

Scheme 2.6. Synthetic route to tagged H_2BDC-NHR. R = Me (**3a**, **4a**), Et (**3b**, **4b**), Pr (**3c**, **4c**), *n*-C_7H_{15} (**3d**, **4d**), C_6H_9 (**3e**, **4e**), Fc (**3f**, **4f**), C_6H_4SMe (**3g**, **4g**).

In contrast to the tandem PSM of IRMOF-3, alkylation of the free dicarboxylic acid with MeCHO, in DMF, gave an increased isolated yield (67 %) compared with THF (18 %). This may be caused by the lower solubility of the dicarboxylic acids in THF than DMF. Full characterisation can be found in experimental section 2.10 (summarised in Table 2.12).

Compound	R	H_2BDC-NH_2/%	H_2BDC-$NHCH_2R$/%	Yield/%
4a	Me	<1	>99	63
4b	Et	<1	>99	92
4c	Pr	<1	>99	45
4d	*n*-C_7H_{15}	<1	>99	97
4e	C_6H_9	<1	>99	97
4f	Fc	1	99	77
4g	C_6H_4SMe	1	99	50

Table 2.12. Product distribution of **4a**-**g** syntheses: yields of secondary amine products from the reaction between H_2BDC-NH_2, RCHO and $NaCNBH_3$.

The optimised reaction scheme for the direct synthesis of IRMOF-3-NHR is summarised in Scheme 2.7. The reaction proceeds in the same way as the synthesis of IRMOF-3, *i.e.* the ligand was dissolved in DMF and reacted with $Zn(NO_3)_2{\cdot}6H_2O$. The crystalline product was washed and stored in toluene with the PXRD matching IRMOF-3 (Appendix A, Figure 5.5 and 5.6).

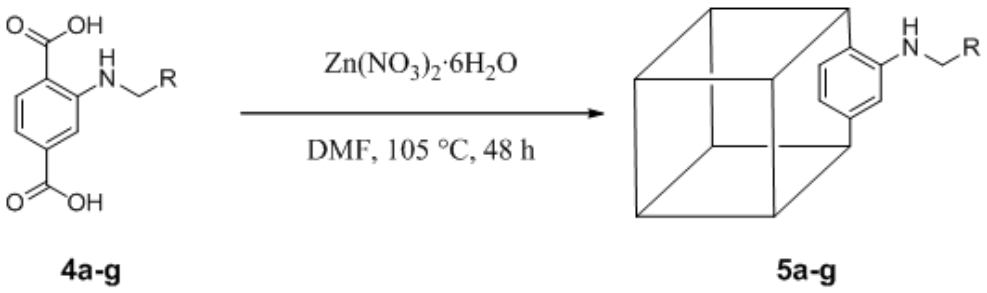

4a-g **5a-g**

Scheme 2.7. Direct Synthesis of IRMOF-3-NHCH$_2$R compounds **5a**-**g**. R = Me (**4a**, **5a**), Et (**4b**, **5b**), Pr (**4c**, **5c**), *n*-C_7H_{15} (**4d**, **5d**), C_6H_9 (**4e**, **5e**), Fc (**4f**, **5f**), C_6H_4SMe (**4g**, **5g**).

Interestingly the ^{1}H NMR digestion experiments showed that the percentage of ligand put into the MOF reaction did not match the tag group percentage distribution in the PSM products **5a**-**g**. These results are summarised in Table 2.13. Frameworks **5a**-**d** had the least deviation from the starting material and although all the characterisation data indicated > 99% purity of ligand, this was not translated to the MOF. The materials **5e**-**g** had a significant contamination of H_2BDC-NH_2 in, which could have been present in the starting material that was not included in the NMR tube or a decomposition pathway that may have occurred during MOF formation. Further experiments would need to be carried out to ascertain the reason for this H_2BDC-NH_2 incorporation.

Compound	R	BDC-NH_2/%	BDC-$NHCH_2R$/%	S_{BET}/m^2g^{-1}
5a	Me	4	96	2238
5b	Et	7	93	1914
5c	Pr	8	92	1862
5d	*n*-C_7H_{15}	7	93	1233
5e	C_6H_9	12	88	1335
5f	Fc	80	20	1742
5g	C_6H_4SMe	35	65	1076

Table 2.13. IRMOF-3-CH_2R direct syntheses: percentage ligand incorporation and BET surface areas of **5a**-**g**.

Although the ligand, **4f** (methylferrocenyl tag group), was synthesised with 99 % purity, using this in the direct MOF synthesis affords no crystalline product (the reaction yielded an orange/yellow non-crystalline solid). To gain access to the MOF, **5f**, the reaction with zinc(II) nitrate proceeded when a mix of 88 % ligand purity and 12 % H_2BDC-NH_2 was used in the MOF formation reaction. In this case the reaction produces crystals with an

average of 20% ferrocenyl incorporation shown by ^{1}H NMR spectroscopy and 29 % by atomic absorption spectroscopy. These results gave the molecular formula of **5f** as $[Zn_4O(BDC\text{-}NH_2)_{2.4}(BDC\text{-}NHCH_2Fc)_{0.6}]$.

One possible explanation for this phenomenon could be a non-random distribution of ferrocenyl groups in the MOF, for example a 77 % IRMOF-3 core and a 23 % ferrocenyl shell. However that would suggest that 100% Fe MOF could be made, which is not the case shown under a microscope where the samples were homogenous in colour and shape. The colours of the crystals were dark red throughout. Inaccuracies in the ^{1}H NMR overlapping of peaks can lead to making overestimates of ligand tag group percentages.

The digested material **5g** gave an unexpected ^{1}H NMR spectrum, suggesting another ligand was present, other than deuterated **3g** and $D_2BDC\text{-}NH_2$, Figure 2.25. This is probably due to an oxidation of the ligand, $BDC\text{-}NHCH_2C_6H_4SMe$, to the sulphoxide, $BDC\text{-}NHCH_2C_6H_4S(O)Me$, during the digestion experiment, as evidenced in the mass spectrum (*m/z* = 332.0643, predicted *m/z* = 332.0569), however this did not occur during the tandem PSM reaction, when forming product **2g**. A repeat spectrum taken of the digestion ^{1}H NMR solution, of **5g**, seven months later, showed the percentage of $H_2BDC\text{-}NHCH_2C_6H_4S(O)Me$ to have doubled, implying the oxidised ligand is produced from the digestion experiment and not the MOF formation reaction. The tandem PSM conversion from $BDC\text{-}NH_2$ to $BDC\text{-}NHCH_2C_6H_4SMe$ is therefore the sum of both ligands (oxidised and non-oxidised) in the ^{1}H NMR spectrum.

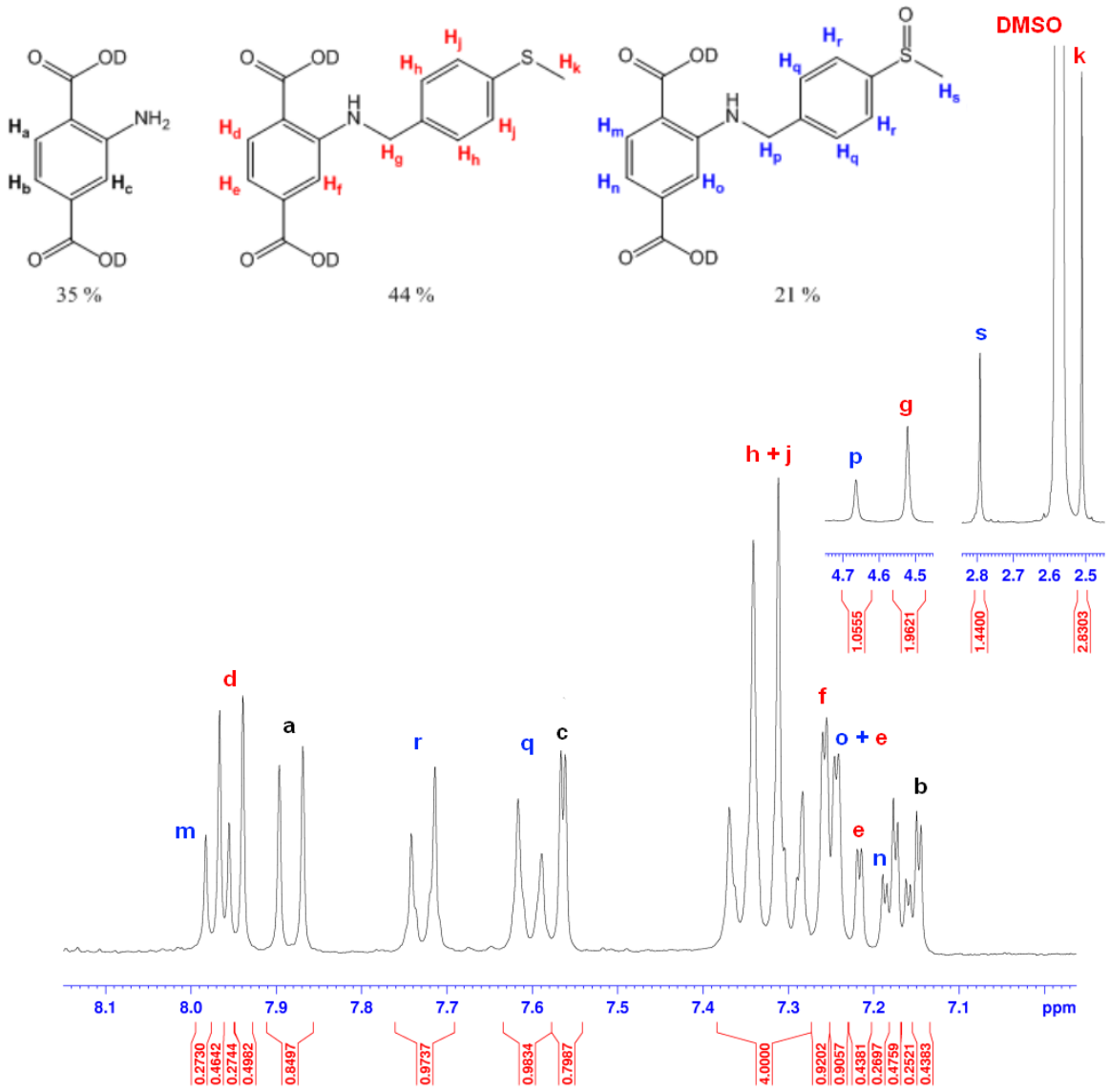

Figure 2.25. Aromatic and aliphatic (insert) regions of ^{1}H NMR spectrum of digested **5g** (inset).

2.4.1. Thermogravimetric analysis of *N*-alkyl MOF Products, 5a-d.

Compounds **5a-d** behave in a similar way to MOFs **2a-d** with regards to TGA, because the percentage of space available for solvent is proportional to the size of the tag group in the MOF. The TGA of **5a-d**, Figure 2.26, shows the mass change with respect to temperature. The initial mass loss stage (40-170 °C) represents the sum of the toluene that is in the pores and any excess toluene loosely bound to the MOFs. The plateau region, in the range: **5a** = 170-420 °C; **5b** and **5c** = 170-400 °C; **5d** = 170-360 °C, represents the activated MOF, where the pores are free of solvent. Decomposition of the organic ligand begins at a lower temperature as the chain length of tag group increases. These characteristics are similar to all the *N*-alkyl chain tandem PSM reaction products.

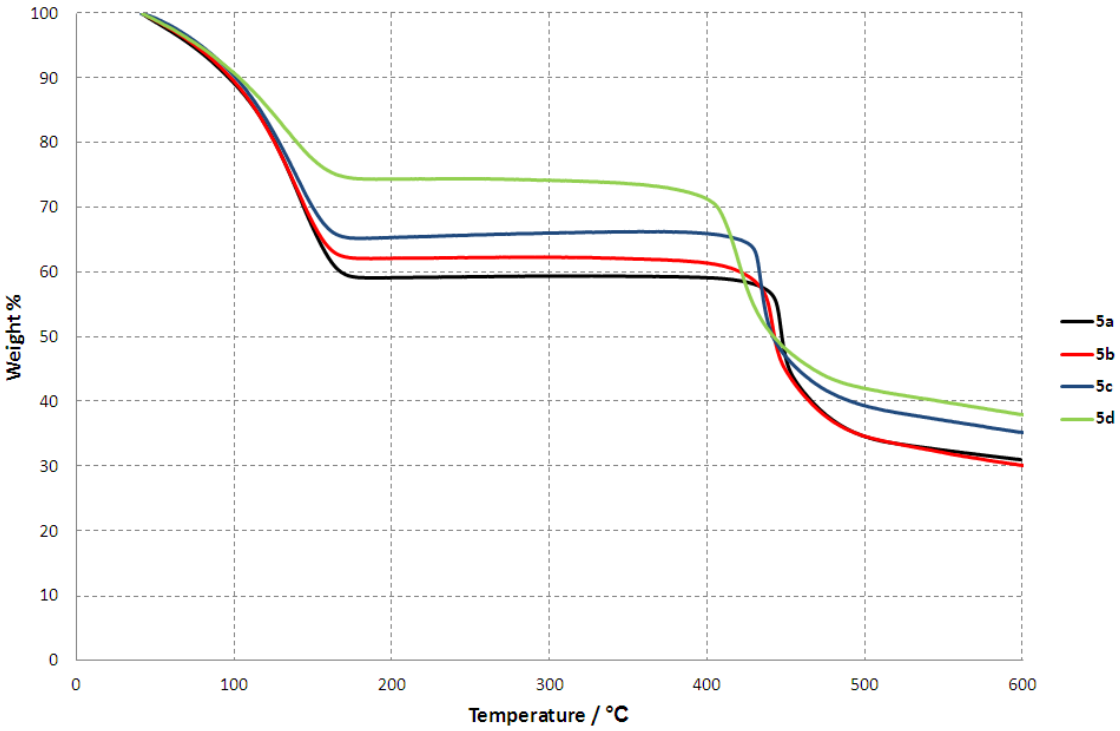

Figure 2.26. TGA of **5a-d**. Samples heated in $N_{2(g)}$ at 5 °Cmin^{-1}.

Compounds **5a-d** lose their toluene guests between 40-170 °C, the same as IRMOF-3 and retain the solvent molecules for 20 °C higher than MOFs **2a-d**. Framework **5a** starts to decompose at 420 °C, 100 °C higher than **2a** and 50 °C higher than IRMOF-3. For each [Zn_4O] unit: **5a** had 7 toluene molecules, **5b** had 6.3, **5c** had 5.5 and **5d** had 4.5 toluene molecules per pore (or [Zn_4O]). Although the number of tag groups is higher in the pre-modified MOFs **5a-d**, the amount of solvent, after drying under a flow of $N_{2(g)}$, is higher compared with **2a-d** because more toluene may be present in the mesopores and trenches of frameworks **2a-d**.

2.4.2. Thermogravimetric Analysis of Functionalised MOF Products, 5e-g

The TGA of **5e-g**, Figure 2.27, show the mass change as the sample is heated in a flow of $N_{2(g)}$. The initial mass loss stage represents the sum of the toluene that is associated with the MOFs. The plateau region, in the range: **5e** = 165-330 °C; **5f** = 150-270 °C; **5g** = 190-310 °C, represents the activated MOF where the pores are free of solvent. All three compounds have a different range of temperatures where a stable activated MOF exists highlighting the different ligand distributions observed in the ^{1}H NMR digestion experiments. Following the plateau region, decomposition of the organic ligands occur, all

of which are lower than IRMOF-3 (350 °C) and differ from their analogous PSM reaction counterparts, **2e-d**, because of the differing percentage incorporations of ligands.

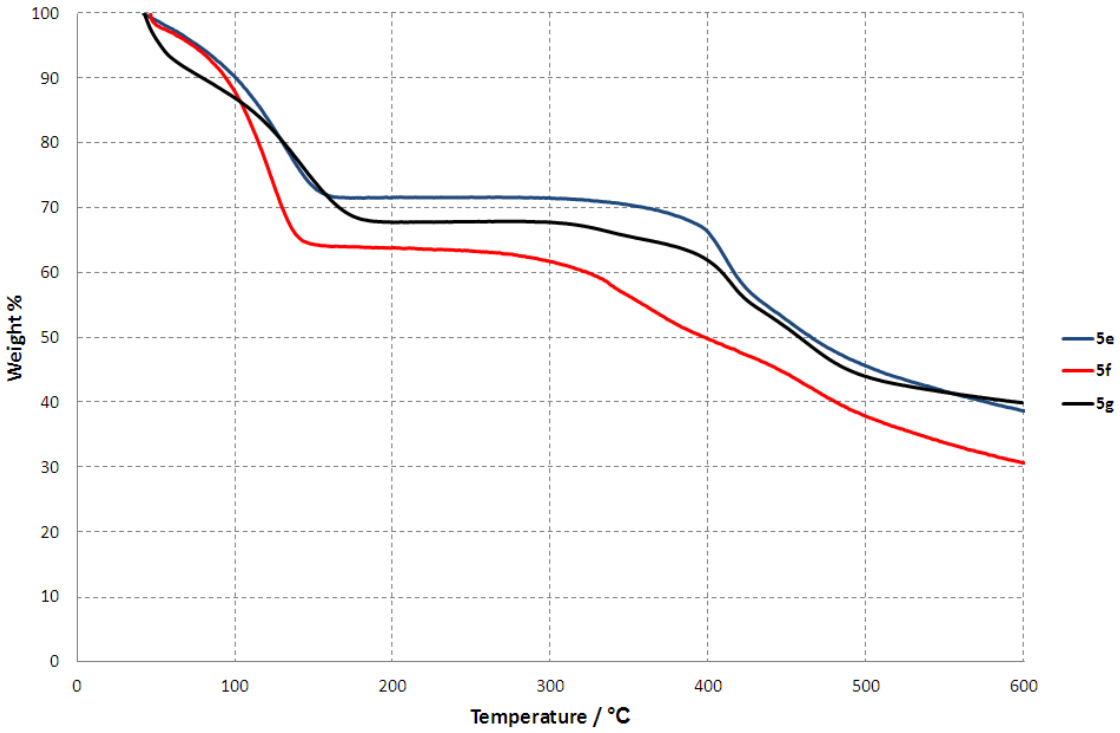

Figure 2.27. TGA of **5e-g**. Samples heated in $N_{2(g)}$ at 5 °Cmin^{-1}.

For each pore or [Zn_4O] unit: **5e** has 4.5 toluene molecules, **5f** has 6 and **5g** has 5.5. There is slightly less toluene in the voids of **5e**, compared with **2e**, which is expected as there are more cyclohexenyl groups in the pores of **5e**. In the voids of **5f** there was 2.4 times as much toluene as there was in **2f**, which was more than expected, considering **5f** had three quarters of the ferrocenyl tag groups present in **2f**, despite any effects of mesopore availability. MOF **5g** has 1.4 times more toluene guest molecules per [Zn_4O] than **2g**, despite more tag group incorporation and no exposure to tandem PSM reaction conditions (*i.e.* no etching reagent).

2.4.3. N_2 adsorption of Pre-Modified MOFs, 5a-d

The BET surface areas were measured *via* the N_2 isotherms of compound **5a-d**, Figure 2.28. They generally had lower surface areas than the value obtained for IRMOF-3, which is expected because of the additional mass of the incorporated tag groups. In the series of MOFs **5a-g**, the conditions for activation were 150 °C for 3 hours, under vacuum.

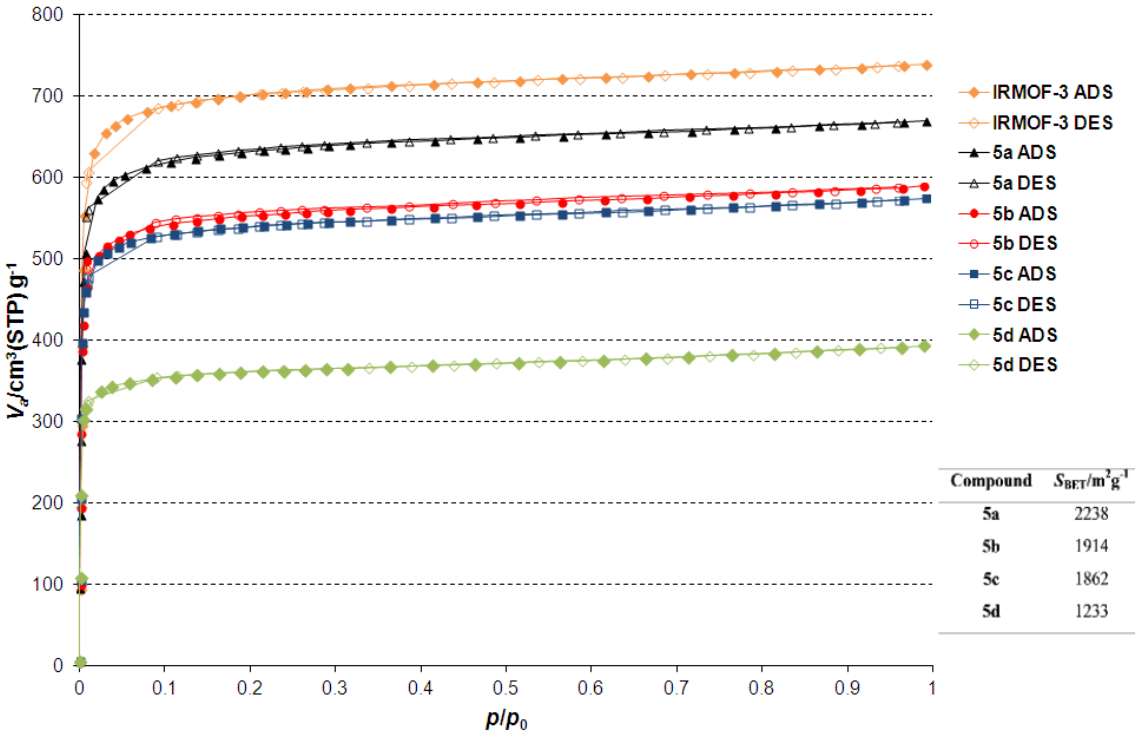

Compound	S_{BET}/m²g⁻¹
5a	2238
5b	1914
5c	1862
5d	1233

Figure 2.28. $N_{2(g)}$ adsorption (filled points) and desorption (open points) isotherms of **5a-d** (at 77 K) and IRMOF-3 as made

The BET surface areas decreased as chain length (or molecular weight) of the tag group increased, from 2238 m^2g^{-1} (**5a**, n = 2) to 1233 m^2g^{-1} (**5d**, n = 8).

The feature that stands out is the absence of hysteresis, which is due to a lack of mesopores in the materials, absent from the BJH plot, Figure 2.29. The MP plot is similar to frameworks **2a-d** and shows a decrease in the number of pores of diameter 0.655 nm and 0.715 nm, Figure 2.30, signifying lower availability pore due to blockage.

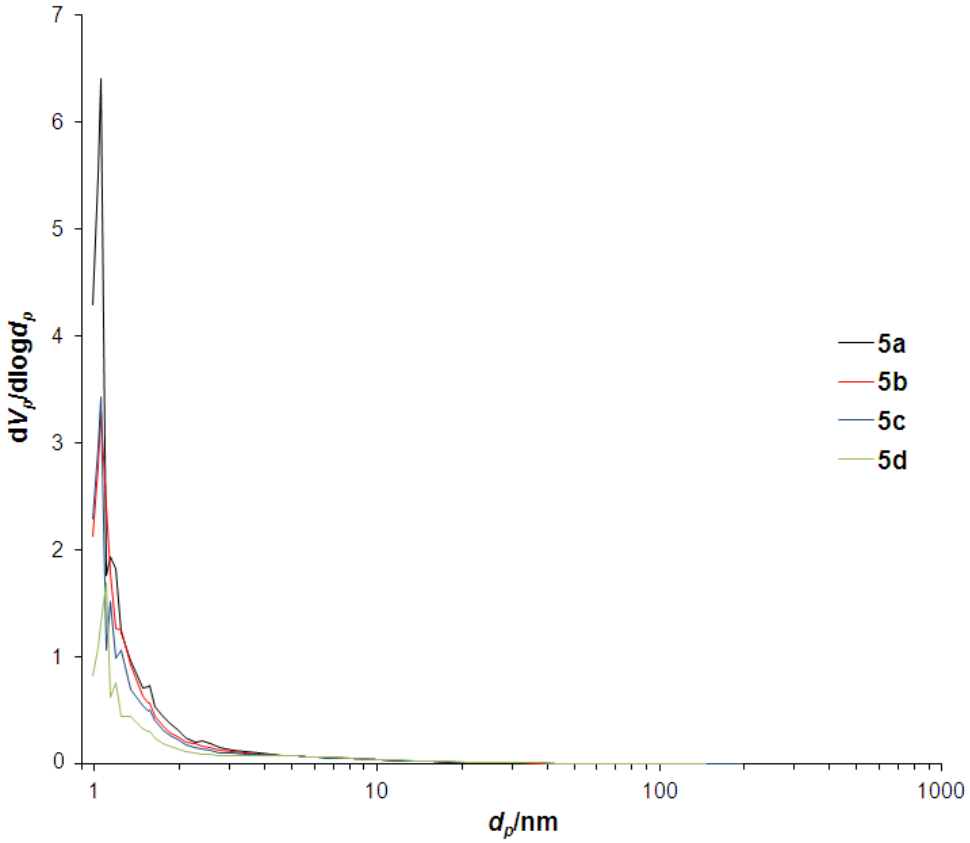

Figure 2.29. BJH plot of **5a-d**.

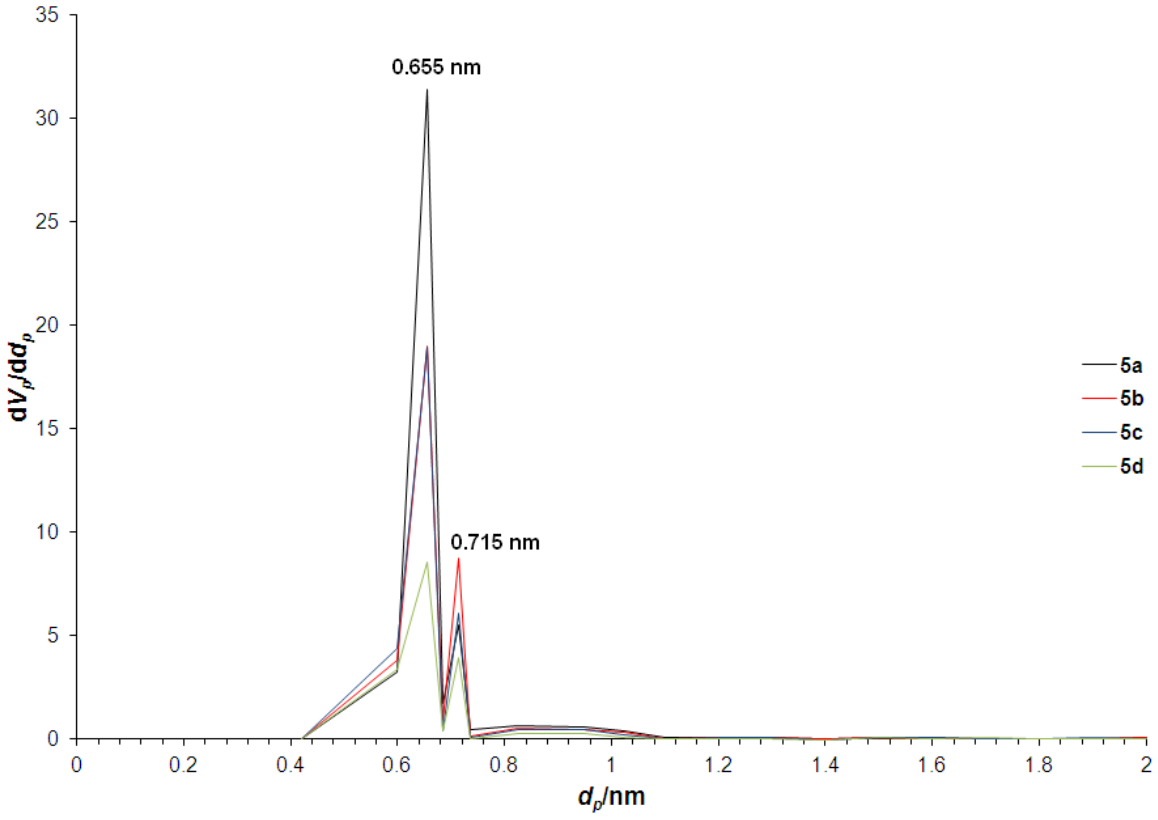

Figure 2.30. MP plot of **5a-d**.

2.4.4. N_2 adsorption of Pre-Modified MOFs, 5e-g

The BET surface areas were measured *via* the N_2 isotherms of compound **5e-g**, Figure 2.31. The BET surface areas were 1335 m^2g^{-1} (**5e**, 2.64 cyclohexenyl groups per pore), 1742 m^2g^{-1} (**5f**, 0.6 ferrocenyl groups per pore) and 1076 m^2g^{-1} (**5g**, 1.95 4-methylthiophenyl groups per pore).

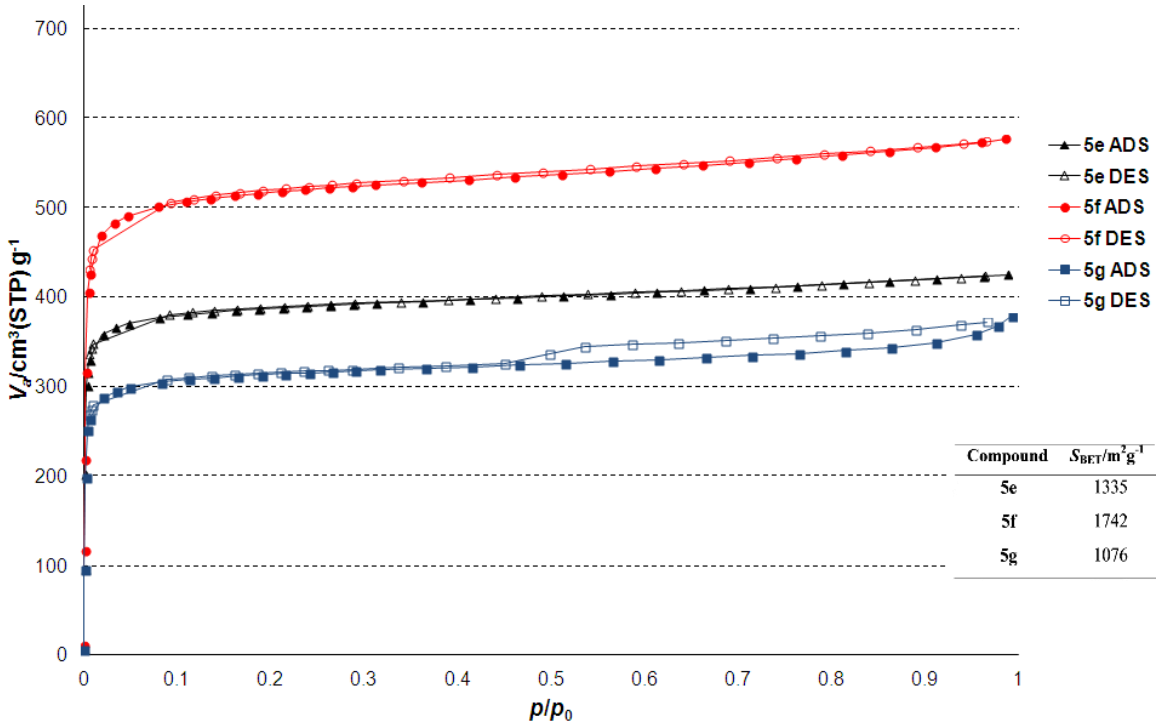

Figure 2.31. $N_{2(g)}$ adsorption (filled points) and desorption (open points) isotherms of **5e-g**.

Compound **5f** has a larger surface area than **5e** and **5g** because of less tag groups per pore and exhibits no hysteresis, which is seen in **5g** interestingly. Inclusion of 20 % of tag groups mean that in frameworks **5e** and **5f** have more amino functionalised pore surfaces present. Hysteresis is not expected if the tag groups are uniformly spread throughout the crystals and no mesopore are present, which should be the case in the synthetic conditions used to make these MOFs.

Material **5g** is anomalous because the nitrogen isotherm exhibits hysteresis. The BJH plot shows a small number of mesopores at 20-200 nm, and explains the small hysteresis gap (Figure 2.32). The reason for the presence of the mesopores in **5g** is unknown. This is not a consequence of etching, as the material has not been exposed to tandem PSM conditions, water, acid or base.

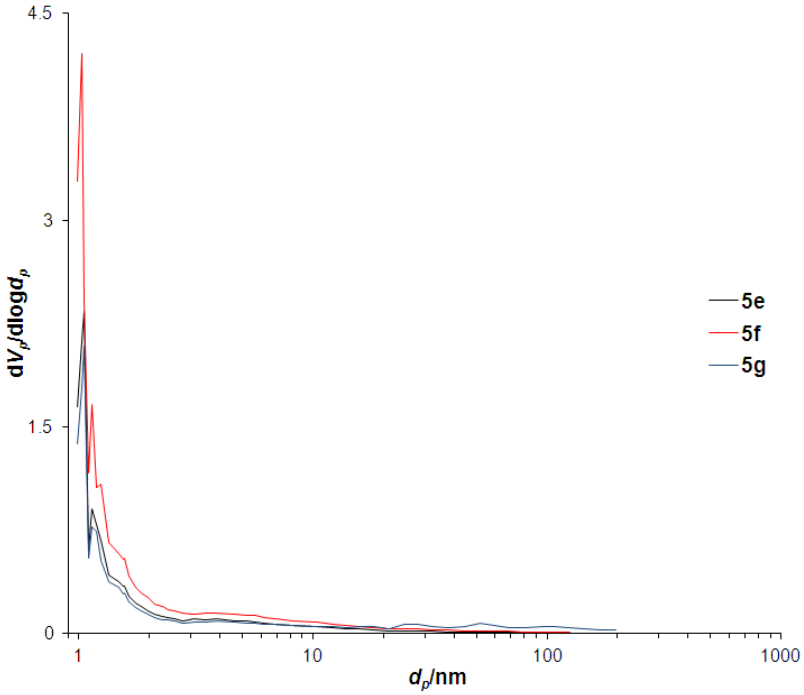

Figure 2.32. BJH plot of **5e-g**.

The MP plot of **5e-g** is similar to frameworks formed from the tandem PSM reaction, **2e-g**, and IRMOF-3 and shows a decrease in the availability, of pores, of diameter 0.655 nm and 0.715 nm (Figure 2.33).

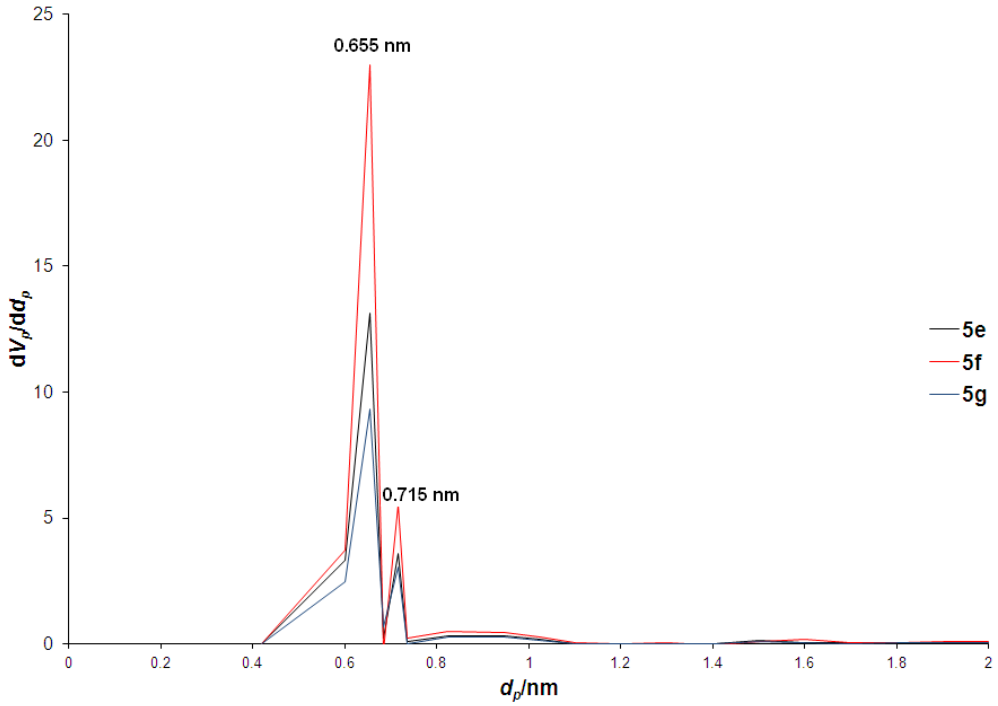

Figure 2.33. MP plot of **5e-g**.

The relative molecular mass of a modified MOF is a measure of its conversion and the steric, electronic and magnetic behaviour of incorporated ligands may make the functional groups non-comparable with the MOFs containing linkers with alkyl chain groups. Activation may also not be complete and the pores not completely empty, particularly in the core of the crystals. This could be regarded as a systematic error that only explains why the BET surface areas are generally lower than expected.

A plot of the predicted BET surface areas, as a function of percentage molecular mass of IRMOF-3, is shown in Figure 2.34. With respect to the functionalised MOFs made by direct synthesis; this plot suggests an extra underlying reason for the loss in BET surface area because as the molecular mass increases, a steeper negative gradient is observed than is predicted. However the error of both slopes is difficult to calculate as inaccuracies and overlaps in the ^{1}H NMR spectra can cause conversion estimate errors therefore it cannot be said that extra interactions with $N_{2(g)}$ are occurring or that sites for gas adsorption are being blocked.

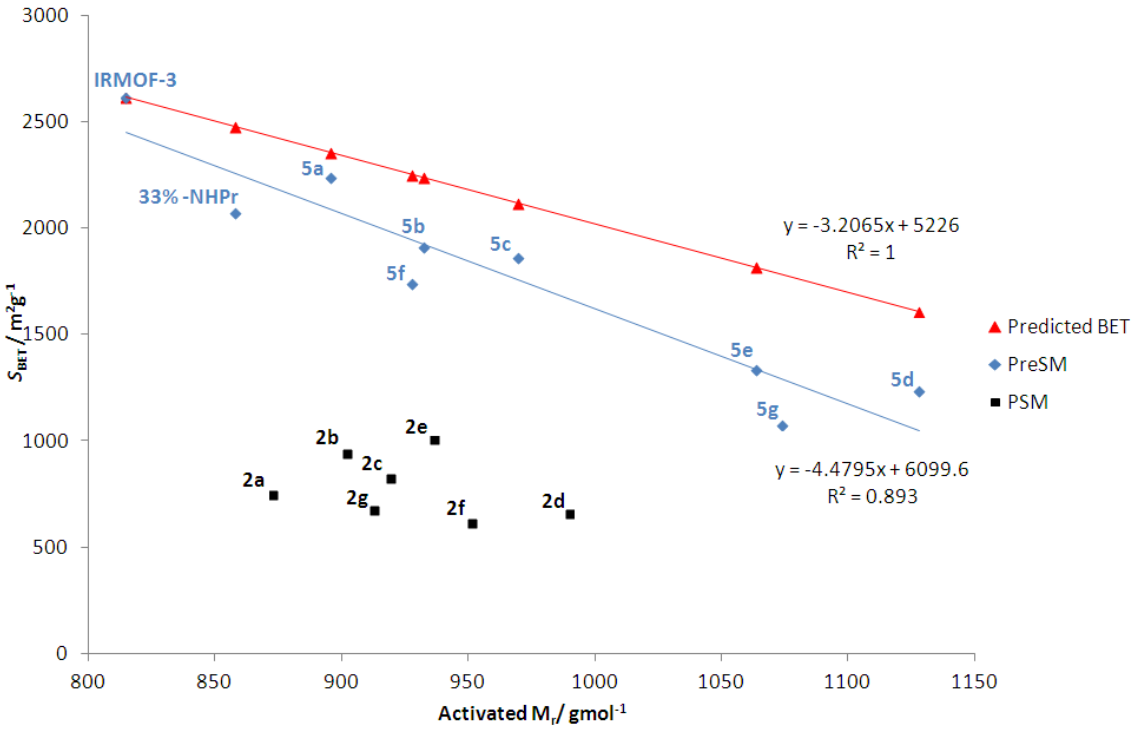

Figure 2.34. A plot to show the predicted S_{BET} as a function of percentage increase of molecular mass of activated MOF (red) compared with experimental results obtained for direct synthesis (blue) and PSM reaction products (black).

The MOFs formed from PSM reactions have much lower BET surface areas and display a smaller spread, due to nitrogen isotherm measurements being significantly dependent on the condition of the crystals after the PSM reaction. These effects were impossible to predict.

2.4.5. Single Crystal X-ray Diffraction studies on 5a, 5b, 5e and 5g.

The crystal structures of **5a**, **5b**, **5e** and **5g** were successfully elucidated by single crystal X-ray diffraction, using a synchrotron X-ray source, shown in Figure 2.35. The overall framework topologies match IRMOF-3, in agreement with the PXRD data. They had the $[Zn_4O(O_2CR)_6]$, supertetrahedral SBU and the same space group symmetry, *Fm*-3*m*.

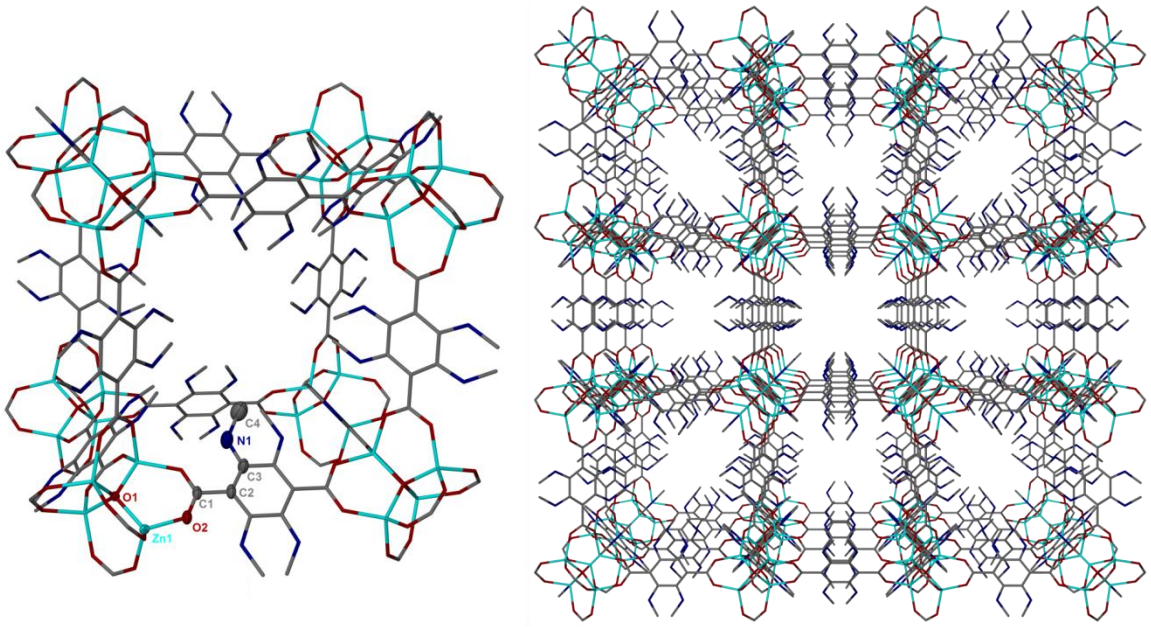

Figure 2.35. Summary of one pore of the pre-synthetically modified frameworks **(left)** including the successfully located α-carbon (C4) of the secondary amine group, **5b** and **5e** only. **(right)** view down the channels of the extended structures.

The single crystal diffraction experiments are summarised in Table 2.14 (**5a** and **5b**) and Table 2.15 (**5e** and **5g**). The unit cell lengths increase and thus the volume of the unit cell increases when the length of the groups increases in the range: **5a**, a = 25.7627(2) Å to **5e**, a = 25.8577(2), (IRMOF-3: a = 25.7786(7) Å).[8]

As with all the MOFs in this cubic system there was significant diffuse scattering and resulted in significant loss of quality of diffraction data (discrete spots joined by lines of diffuse scattering) coupled with a phase change in the crystal below 220 K (experiments to

identify what structural changes occurred were unsuccessful) made collecting the structures only possible with high flux X-rays from a synchrotron radiation source.

Compound No.	**5a**	**5b**
Formula	$[Zn_4O(BDC\text{-}NHEt)_3]\cdot 7Tol$	$[Zn_4O(BDC\text{-}NHPr)_3]\cdot 6.3Tol$
Empirical formula	$C_{79}\ H_{83}\ N_3\ O_{13}\ Zn_4$	$C_{77.10}\ H_{83.40}\ N_3\ O_{13}\ Zn_4$
Formula weight / $gmol^{-1}$	1543.96	1521.55
T / K	250(2)	250(2)
λ / Å	0.6889	0.6889
Crystal system	Cubic	Cubic
Space group	*Fm*-3*m*	*Fm*-3*m*
Unit cell dimensions ($a = b = c$) / Å	25.7627(2)	25.7702(1)
$\alpha = \beta = \gamma$ / °	90	90
Volume / $Å^3$	17099.1(2)	17114.07(12)
Z (no. molecules in the unit cell)	8	8
Density (calculated) / gcm^{-3}	1.200	1.181
Crystal size / mm	0.10 x 0.10 x 0.05	0.12 x 0.10 x 0.07
Pre-SQUEEZE R(int)	0.030	0.045
Data Completeness	0.975	0.996
Data / restraints / parameters	803 / 6 / 31	1163 / 12 / 37
Final R indices [$I>2\sigma(I)$]	$R1$ = 0.0434 $wR2$ = 0.1420	$R1$ = 0.0395 $wR2$ = 0.1357
R indices (all data)	$R1$ = 0.0465 $wR2$ = 0.1485	$R1$ = 0.0427 $wR2$ = 0.1387
Largest diff. peak and hole / $eÅ^{-3}$	0.405 and -0.327	0.731 and -0.319

Table 2.14. Selected crystal data and structure refinement data for frameworks **5a** and **5b**.

Frameworks **5a** and **5b** had 4 % and 7 % inclusion of BDC-NH_2 respectively, from ^1H NMR analysis of the digested products. This percentage was not accounted for in the models. The inclusion of BDC-NH_2, in frameworks **5e** and **5g,** was too great to ignore and was incorporated into the diffraction analysis. The atom N1 was located in all cases and modelled as 12.5% occupancy, which means that the remainder of the functionalised groups were subject to dynamic disorder, around the four carbon atoms of the dicarboxylate ligands, contributing to the diffuse scattering.

Compound No.	**5e**	**5g**
Formula	$[Zn_4O(BDC\text{-}NH_2)_{0.36}(BDC\text{-}NHCH_2C_6H_9)_{2.64}]\cdot 4.5Tol$	$[Zn_4O(BDC\text{-}NH_2)_{1.05}(BDC\text{-}NHCH_2C_6H_4SMe)_{1.95}]\cdot 5.5Tol$
Empirical formula	$C_{73.98}H_{77.40}N_3O_{13}Zn_4$	$C_{78.1}H_{74.6}N_3O_{13}S_{1.95}Zn_4$
Formula weight / $gmol^{-1}$	1478.12	1587.31
T / K	250(2)	250(2)
λ / Å	0.6889	0.6889
Crystal system	Cubic	Cubic
Space group	*Fm*-3*m*	*Fm*-3*m*
Unit cell dimensions ($a = b = c$) / Å	25.7752(2)	25.8577(2)
$\alpha = \beta = \gamma$ / °	90	90
Volume / $Å^3$	17124.0(2)	17289.0(2)
Z (no. molecules in the unit cell)	8	8
Density (calculated) / gcm^{-3}	1.147	1.220
Crystal size / mm	0.12 x 0.12 x 0.10	0.12 x 0.10 x 0.05
Pre-SQUEEZE R(int)	0.026	0.090
Data Completeness	0.986	0.993
Data / restraints / parameters	1028 / 12 / 37	818 / 0 / 31
Final R indices [$I>2\sigma(I)$]	$R1 = 0.0427$ $wR2 = 0.1464$	$R1 = 0.0543$ $wR2 = 0.1831$
R indices (all data)	$R1 = 0.0442$ $wR2 = 0.1486$	$R1 = 0.0563$ $wR2 = 0.1866$
Largest diff. peak and hole / $eÅ^{-3}$	0.514 and -0.277	0.529 and -0.94

Table 2.15. Selected crystal data and structure refinement data for frameworks **5e** and **5g**.

The void volume per unit cell was calculated using Platon SQUEEZE the results of which are summarised in Table 2.16. The accessible void volumes were similar for the four structures. The atom C4 was located in frameworks **5b** and **5e** and is reflected in a reduction of approximately 1300 $Å^3$ solvent accessible void volume per unit cell (per pore ~190 $Å^3$) from the SQUEEZE analysis. The pre-SQUEEZE difference electron density, F_o-F_c, maps are shown in Figures 2.36 and 2.37. These show the evidence for the electron density associated with atom C4. The other atoms of the tag group and toluene guest molecules were impossible to identify.

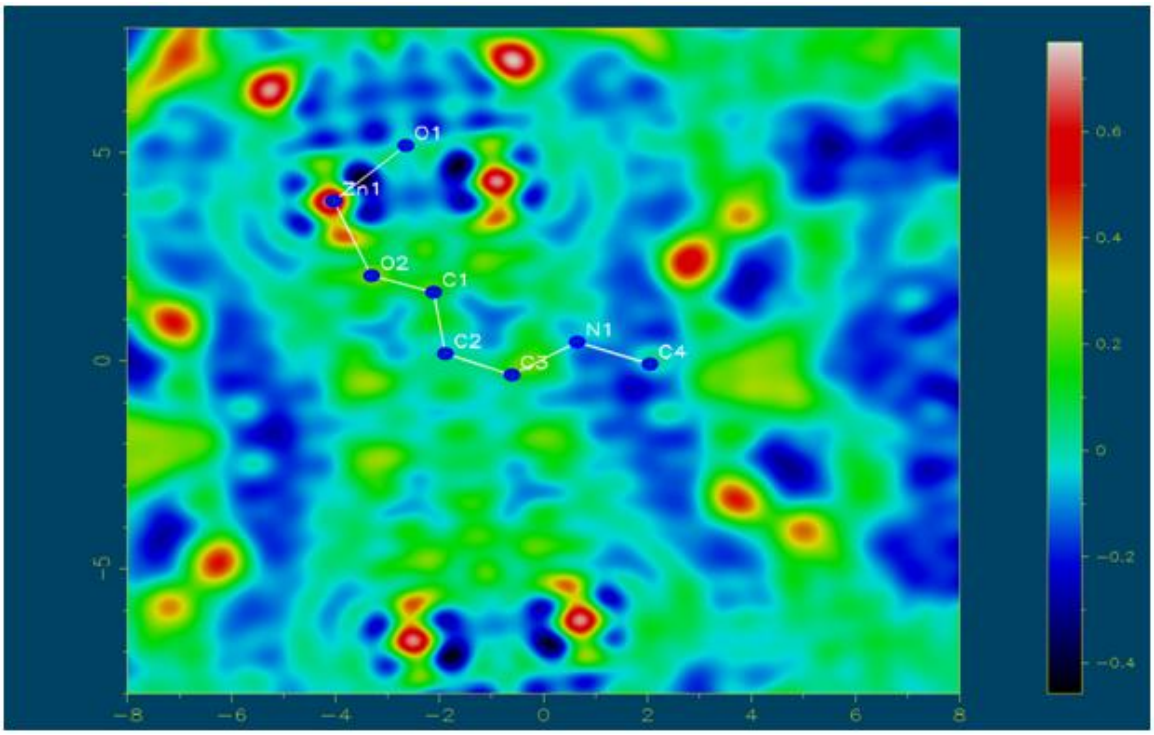

Figure 2.36. The pre-SQUEEZE F_o-F_c map of **5e** showing evidence for the methyl cyclohexenyl groups on the BDC linker.

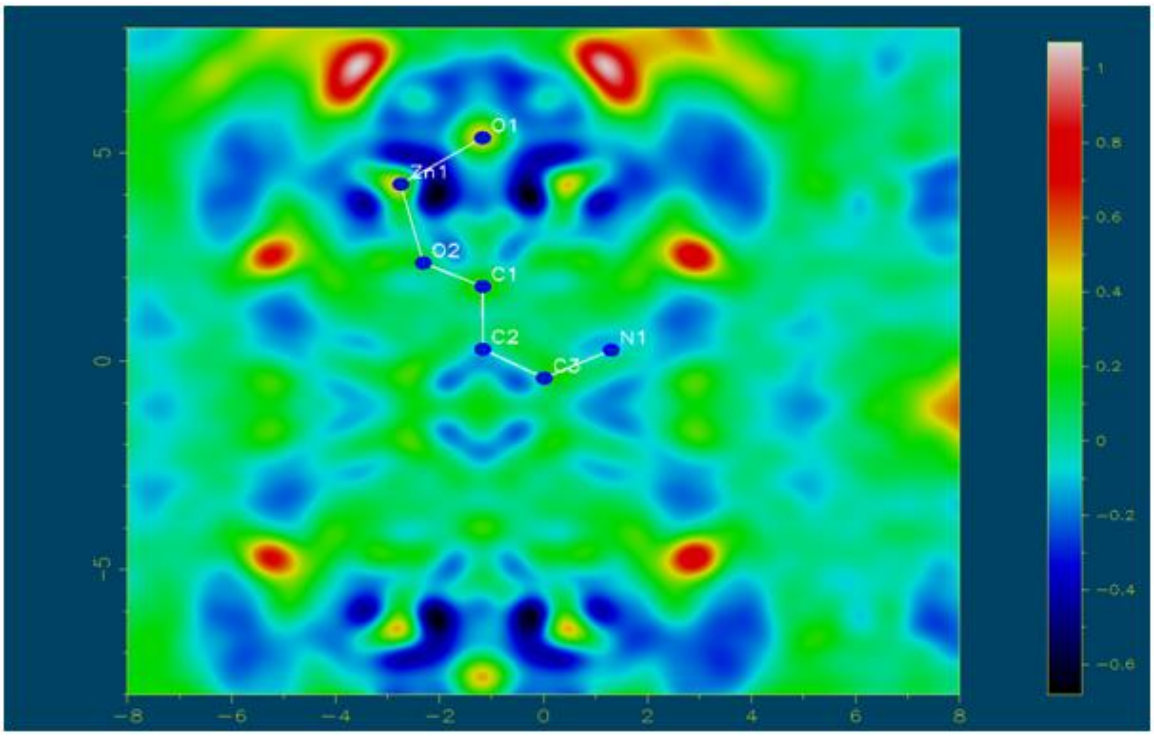

Figure 2.37. The pre-SQUEEZE F_o-F_c map of **5g** showing evidence for the tag groups on the BDC linkers.

Compound	Tag groups modelled per pore	Void volume per unit cell /Å^3	Void volume per [Zn_4O] /Å^3	Predicted Volume of Guests /Å^3
5a	3	12066	1508	1100
5b	3	10706[a]	1338[a]	1002[a]
5e	2.64	10734[a]	1217[a]	947[a]
5g	1.95	12145	1520	1191

Table 2.16. Platon SQEEZE analysis of accessible volume in the pores of frameworks **5a**, **5b**, **5e** and **5g**. [a] C4 was located and modelled in this case.

From the TGA results, toluene content was included in the volume above, in addition to the appropriate ratio of the PSM derivatised ligand. The inclusion percentages of **5e** and **5g** were based on ^{1}H NMR digestion experiments on the digested crystalline material. Given a crude volume per non-hydrogen atom of 20 Å^3, the total volume of the guest solvent and PSM tags is also shown above. These values are below the values obtained from the SQUEEZE analysis which are expected factoring in packing efficiency considerations. Due to acid digestion of the MOFs, the ^{1}H NMR analyses do not account for any imino tag groups on the frameworks, therefore extra imino groups may be present in the crystals, which could account for the extra electron density present. All of these deficiencies are coupled with the quality of the diffraction data, especially for **5g** 9 % pre-SQUEEZE *R*(int), and reduced the accuracy of the analysis.

The calculated density of **5a**, **5b**, **5e**, and **5g** were 1.1-1.2 gcm^{-3} and for validation of these values, crystals were dropped into water (ρ = 1.0 gcm^{-3}) and sank immediately, but floated for several seconds when in dichloromethane, DCM, before presumably absorbing the new solvent and then sinking (ρ = 1.315 gcm^{-3}).

2.5. Post-Synthetic N-alkylation of MIL-101(Cr)-NH_2

To investigate the *N*-alkylation tandem PSM reaction, as carried out with IRMOF-3, on a different MOF topology, MIL-101(Cr)-NH_2 was chosen. Reasons for this choice include more tolerance to variation of pH, atmospheric exposure and a high stability in MeOH. The MIL-101(Cr)-NH_2 framework has larger pores than IRMOF-3, consisting of mesopores with diameters of 29 and 34 Å.[5] Smaller pore MOFs such as DMOF-1-NH_2[16] and MOFs more sensitive to water such as UMCM-1-NH_2[7] failed to show any conversion under the tandem PSM reaction conditions employed and are not discussed further. Interestingly this

tandem PSM did not significantly convert the amino groups of MIL-68(In)-NH_2 or MIL-101(Al)-NH_2 into secondary amines with propanal and a hydride source.

MIL-101(Cr)-NH_2 was reacted with the aldehyde RCHO (R= Me, Et, Pr, *n*-C_7H_{15}) in MeOH, at 50 °C, for 1 hour, before adding $NaCNBH_3$ to the reaction mixture. The mixture was then sealed and heated to 50 °C for 72 hours, with no stirring. The reaction proceeds through an assumed imine intermediate, **6a-d**, but attempts at isolating these materials were unsuccessful. The products formed are the secondary amino tagged MOFs, with general formula MIL-101(Cr)-$NHCH_2R$, **7a-d**. The reaction scheme is summarised in Scheme 2.7.

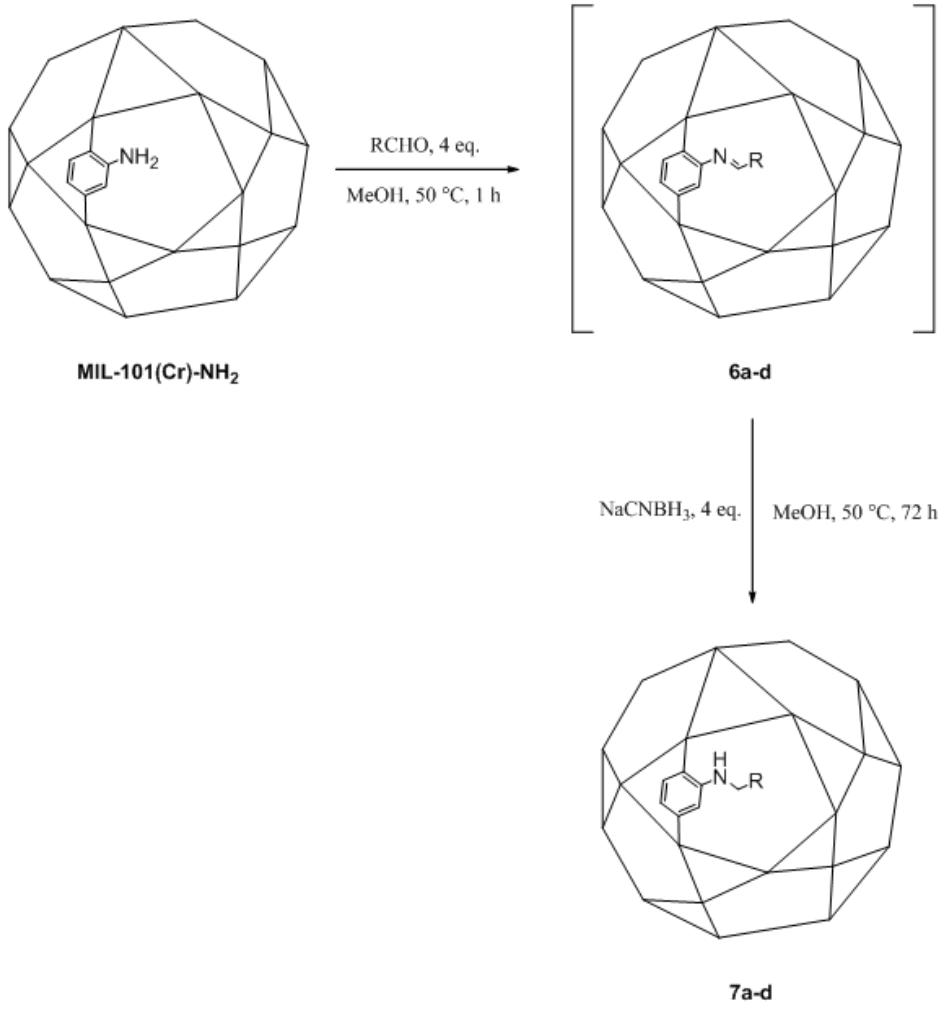

Scheme 2.7. General PSM procedure for reaction between MIL-101(Cr)-NH_2 and RCHO with $NaCNBH_3$. R = Me (**6a**, **7a**), Et (**6b**, **7b**), Pr (**6c**, **7c**), *n*-C_7H_{15} (**6d**, **7d**).

Under these tandem PSM reaction conditions, the higher molecular weight aldehydes with additional functional groups, RCHO (R = C_6H_9, R = Fc and R = C_6H_4SMe) did not give the

target *N*-alkylated products, of the MIL-101(Cr)-NH_2 framework. The products yielded from these investigations were green/yellow amorphous powders, with flat PXRD traces and are not discussed further. The tandem PSM reaction product linker distributions of MIL-101(Cr)-$NHCH_2R$, **7a-d**, are summarised in Table 2.17.

Compound	**R**	**MIL-101(Cr)-NH_2/%**	**MIL-101(Cr)-$NHCH_2R$/%**	**S_{BET}/ m^2g^{-1}**
7a	Me	49	51	1396
7b	Et	51	49	1237
7c	Pr	55	45	1013
7d	*n*-C_7H_{15}	65	35	841

Table 2.17. Ligand distribution in the PSM products, **7a-d**, from the reaction between MIL-101(Cr)-NH_2, RCHO and $NaCNBH_3$. S_{BET} MIL-101(Cr)-NH_2 = 1604m^2g^{-1} (in house).

Generally the percentage alkylation of amino tag groups is lower in the MIL-101(Cr)-NH_2 topology and all aldehyde cases, compared with IRMOF-3. This may be indicative of partially optimised reaction conditions, as the only change from the IRMOF-3 system has been to carry out the reaction in pure MeOH. PSM conversions could be increased with more optimisation experiments e.g. solvent screening, temperature and pH.

The PXRD peak intensities are generally weak for this MOF system with low flux X-ray sources. There is significant peak broadening due to the small particles synonymous with the MIL series, (bulk material average particle size is 50 nm from SEM)[17] and as the chain length of the tag groups increase, the relative intensity of the measured powder diffraction peaks decrease, as seen in Figure 2.38.

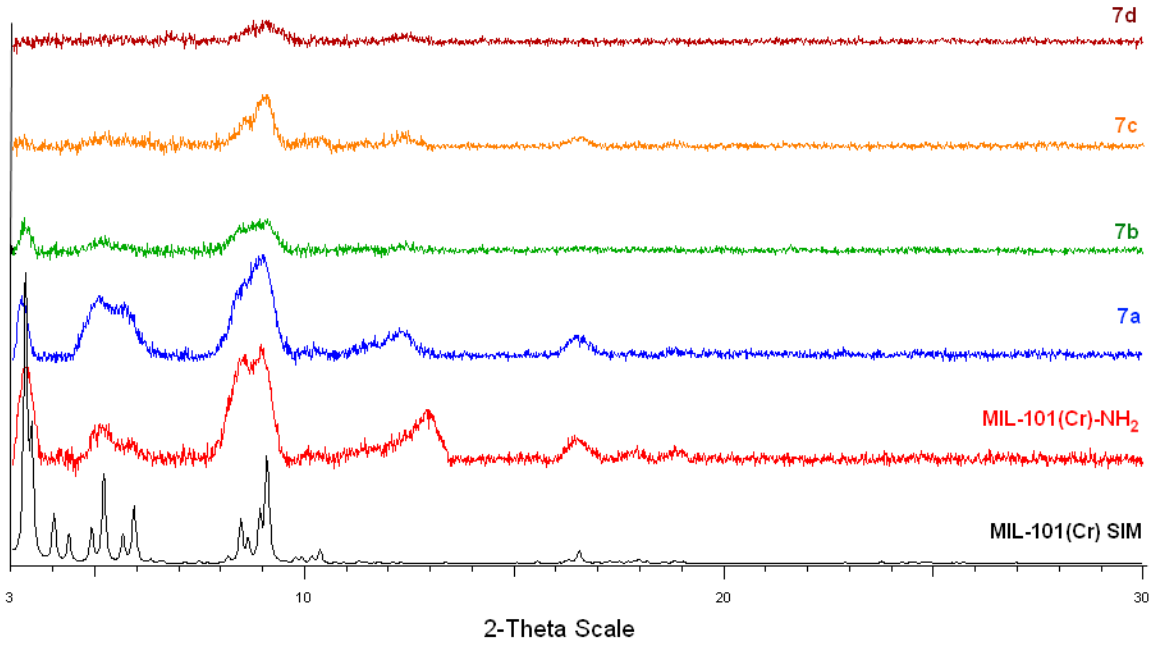

Figure 2.38. PXRD diffractograms for **7a-d** and MIL-101(Cr)-NH_2 as made (red) and simulated from literature data, CCDC refcode = OCUNAC (black).[4]

2.5.1. Tandem PSM of MIL-101(Cr)-NH_2 with Ethanal

The molecular formula of **7a**, $[Cr_3O(OH)(OH_2)_2(BDC\text{-}NH_2)_{1.47}(BDC\text{-}NHEt)_{1.53}]\cdot 3EtOH$, was garnered from ^1H NMR digestion experiments and TGA analysis. The digestion was carried out in $NaOD/D_2O$ and $Cr(OH)_3$ allowed to precipitate out of the solution, to reduce the paramagnetic Cr^{3+} concentration, to obtain sharper lines in the ^1H NMR spectrum.

From the ^1H NMR spectrum of the digested product of **7a**, Figure 2.39, the presence of a triplet at δ 1.01 ppm (integral: 3H), from the β-carbon to the nitrogen of $H_2BDC\text{-}NHEt$ shows a CH_3 group next to a neighbouring group of CH_2 (α-carbon) from the secondary amino alkyl chain. Conversion is calculated by comparing the ratio of Ar-H doublets at δ 7.03 and 7.01 ppm for $H_2BDC\text{-}NH_2$ and $H_2BDC\text{-}NHEt$ respectively. The average conversion was 51 % determined from two consistent, independent reactions.

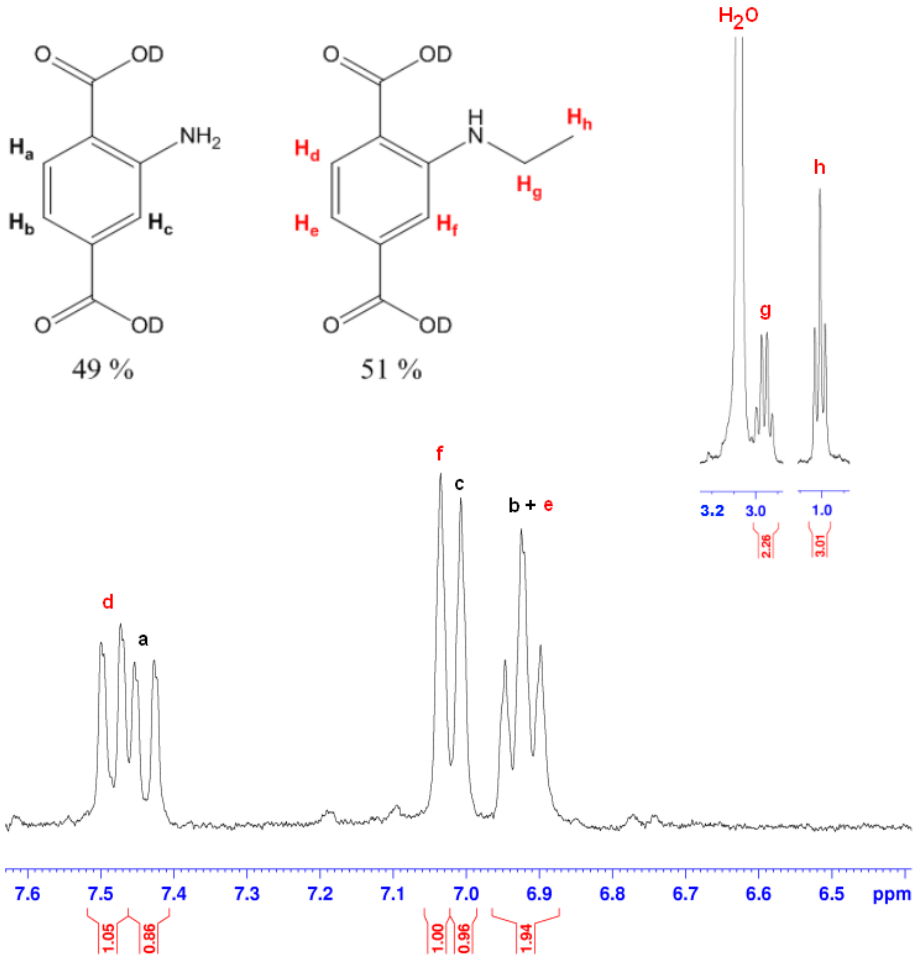

Figure 2.39. Aromatic and aliphatic (insert) regions of ^{1}H NMR spectrum of digested **7a**. PSM product from the reaction between MIL-101(Cr)-NH_2, MeCHO, $NaCNBH_3$ in MeOH at 50 °C.

2.5.2. Tandem PSM of MIL-101(Cr)-NH_2 with Propanal

From the ^{1}H NMR spectrum of the digested product of **7b**, Figure 2.40, the presence of a sextet at δ 1.41 ppm (integral: 2H), from the hydrogen atoms on the β-carbon to the nitrogen of H_2BDC-NHPr, show a CH_2 group next to neighbouring groups of CH_2 (α-carbon) and a CH_2 (γ-carbon) group from the secondary amino alkyl chain. Conversion was calculated by comparing the ratio of Ar-H doublets at δ 7.04 and 7.00 ppm for H_2BDC-NH_2 and H_2BDC-NHEt respectively. The average conversion was 49 % from two consistent, independent reactions and combining with TGA data gave the formula for **7b** as $[Cr_3O(OH)(OH_2)_2(BDC\text{-}NH_2)_{1.53}(BDC\text{-}NHPr)_{1.47}]\cdot 1.5EtOH$.

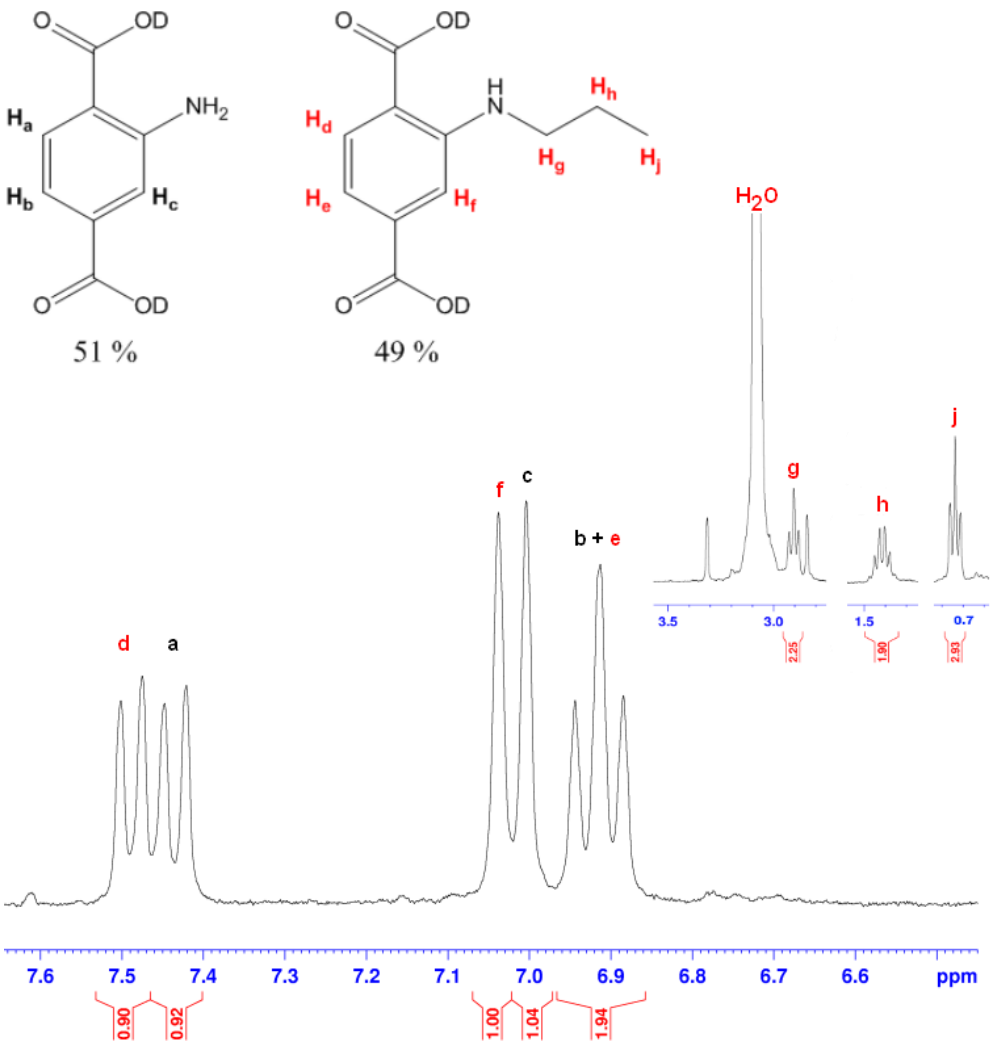

Figure 2.40. Aromatic and aliphatic (insert) regions of the ^{1}H NMR spectrum of digested **7b**. PSM product from the reaction between MIL-101(Cr)-NH_2, EtCHO, $NaCNBH_3$ in MeOH at 50 °C.

2.5.3. Tandem PSM of MIL-101(Cr)-NH_2 with Butanal

The molecular formula of **7c**, $[Cr_3O(OH)(OH_2)_2(BDC\text{-}NH_2)_{1.65}(BDC\text{-}NHBu)_{1.35}]\cdot 3EtOH$, was elucidated from NMR experiments and TGA analysis. From the ^{1}H NMR spectrum of the digested product of **7c**, Figure 2.41, the presence of a sextet at δ 1.21 ppm (integral: 2H), from the γ-carbon to the nitrogen of H_2BDC-NHBu shows a CH_2 group next to neighbouring groups of CH_2 (β-carbon) and CH_3 (δ-carbon) from the secondary amino alkyl chain. A quintet at δ 1.41 ppm represents the CH_2 group adjacent to four protons: a CH_2 group on the α-carbon and a CH_2 on the γ-carbon. Conversion was calculated by comparing the ratio of Ar-H doublets at δ 7.03 and 7.07 ppm for H_2BDC-NH_2 and H_2BDC-NHBu respectively. The average conversion was 45 % from two consistent, independent reactions.

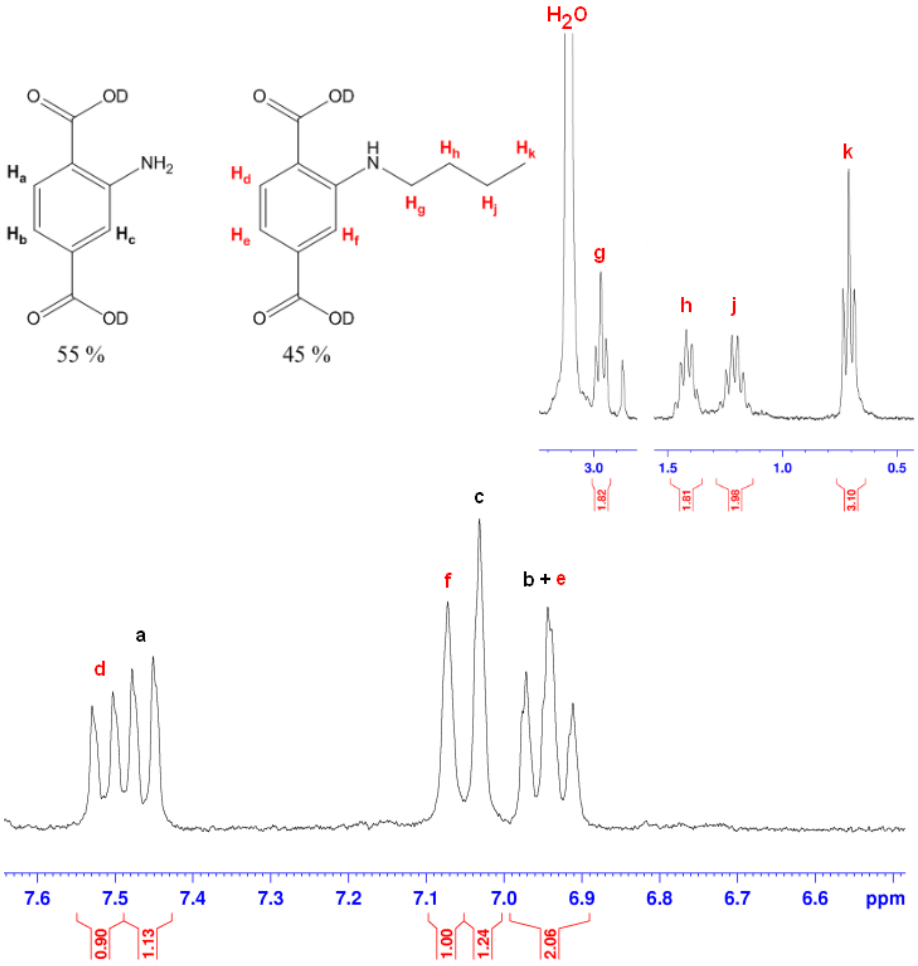

Figure 2.41. Aromatic and aliphatic (insert) regions of the ^{1}H NMR spectrum of digested **7c**. PSM product from the reaction between IRMOF-3, BuCHO, $NaCNBH_3$ in MeOH at 50 °C.

2.5.4. Tandem PSM of MIL-101(Cr)-NH_2 with Octanal

From the ^{1}H NMR spectrum of the digested product of **7d**, Figure 2.42, the presence of a triplet at δ 3.23 ppm (integral: 2H), from the α-carbon of H_2BDC-NHC_8H_{17} shows a CH_2 group next to a neighbouring CH_2 group (β-carbon). The terminal CH_3 group can be seen at δ 0.89 ppm. The multiplet in the range δ 1.2-1.6 ppm represents 10 hydrogen atoms, but is too broad and overlapped to obtain an accurate integral. The ratio of the Ar-H peaks at δ 7.30 and 7.34 ppm for H_2BDC-NH_2 and H_2BDC-NHC_8H_{17} are used to calculate conversion. The average conversion was 35 % from two independent reactions and with TGA data, gave the formula for **7d** as $[Cr_3O(OH)(OH_2)_2(BDC\text{-}NH_2)_{1.95}(BDC\text{-}NHC_8H_{17})_{1.05}]\cdot 2EtOH$.

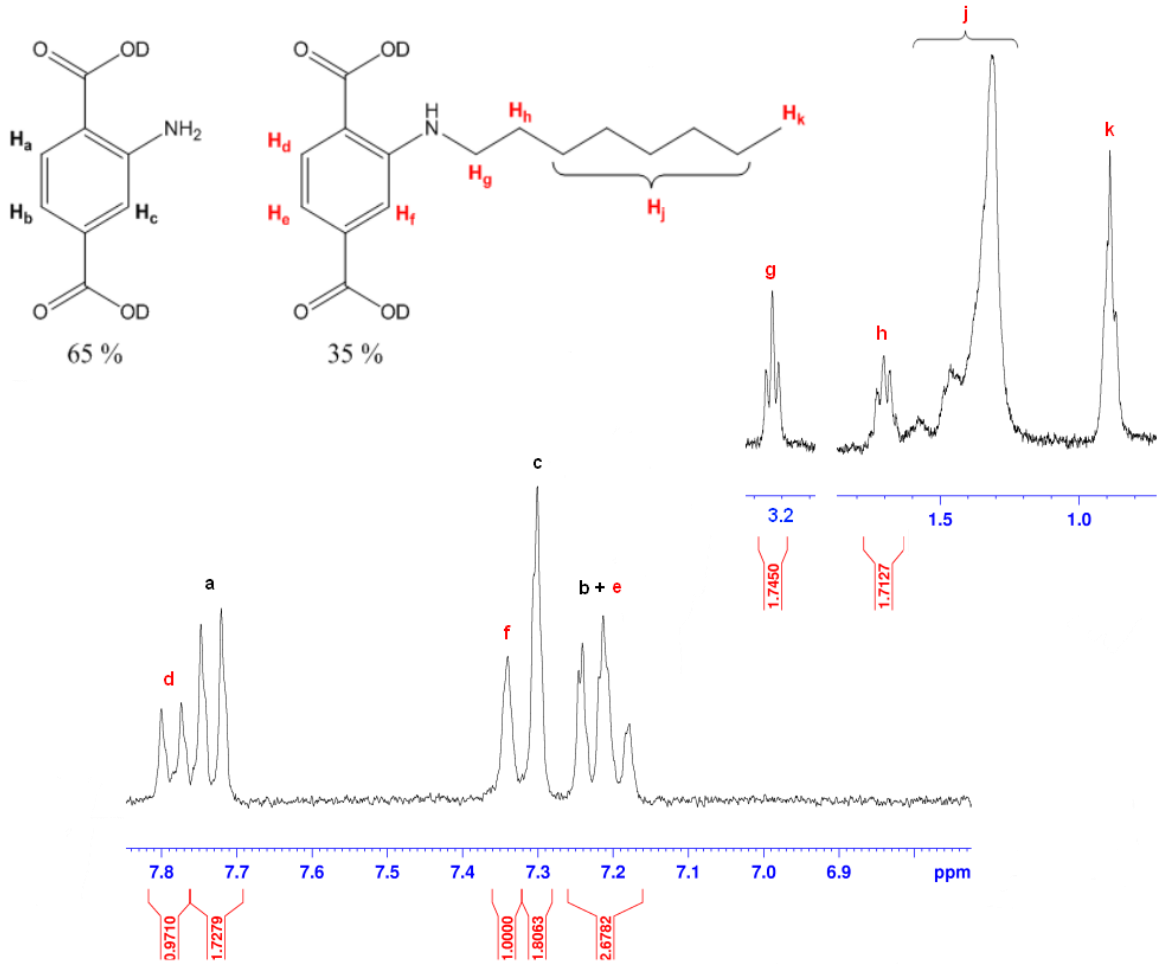

Figure 2.42. Aromatic and aliphatic (insert) regions of ^{1}H NMR spectrum of digested **7d**. PSM product from the reaction between IRMOF-3, *n*-$C_7H_{15}CHO$, $NaCNBH_3$ in MeOH at 50 °C.

2.5.5. FT-IR analysis of 7a-d

The FT-IR spectra of materials **7a-d**, Figure 2.43, had few differences to distinguish them from each other, but did differ from the starting material, MIL-101(Cr)-NH_2. Frameworks **7a-d** did not have the peak at 1049 cm^{-1} but gained a broad peak at 1570-1580 cm^{-1}, attributed to a secondary amino N-H bend. Both products **7a-d** and the starting MOF, had a C-N stretch at ~1260 cm^{-1}, but no C=N stretch at 1690 cm^{-1} from imino C-N groups.[18] This suggests the reduction of the imino group is going to completion and the addition of the aldehyde is the percentage conversion determining variable.

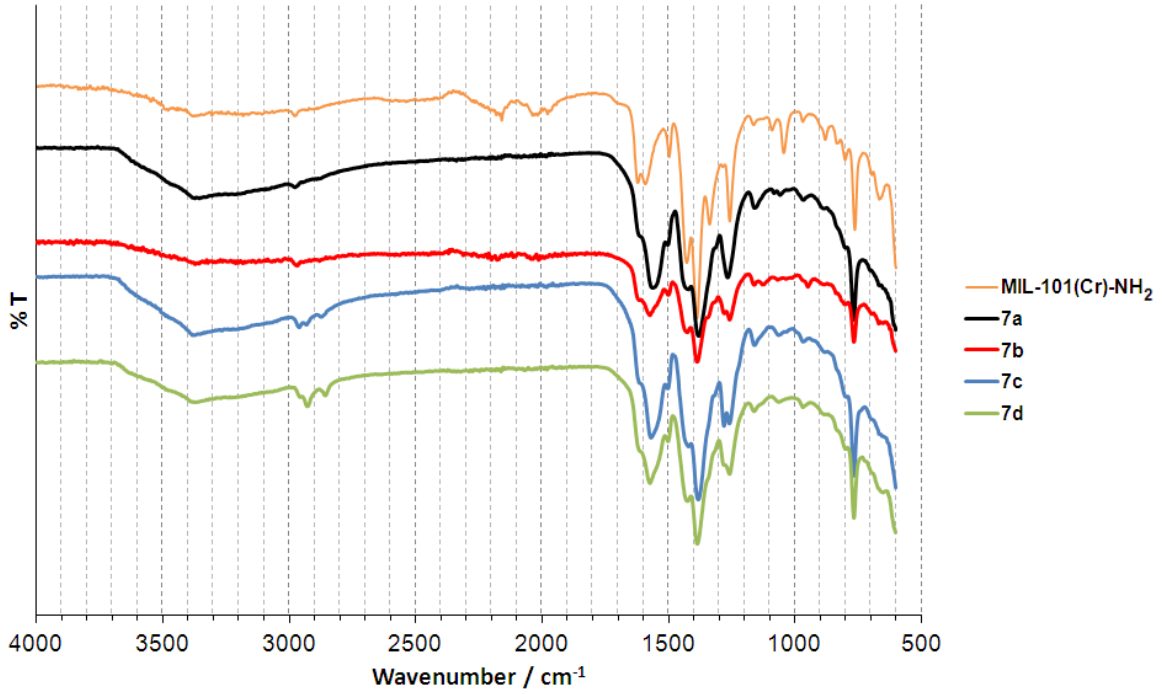

Figure 2.43. FT-IR spectrum of **7a-d**.

2.5.6. Thermogravimetric analysis of *N*-alkyl PSM Products, 7a-d.

Thermogravimetric analysis (TGA) of **7a-d** is shown in Figure 2.44, The initial mass loss stage (40-200 °C) represents the sum of the ethanol that is in the pores. There was a small plateau temperature range of 200-220 °C, representing the activated MOF, where the pores are free of solvent. Decomposition of the organic ligand begins at 220 °C for MIL-101(Cr)NH_2 and was similar to compounds **7a-d**.

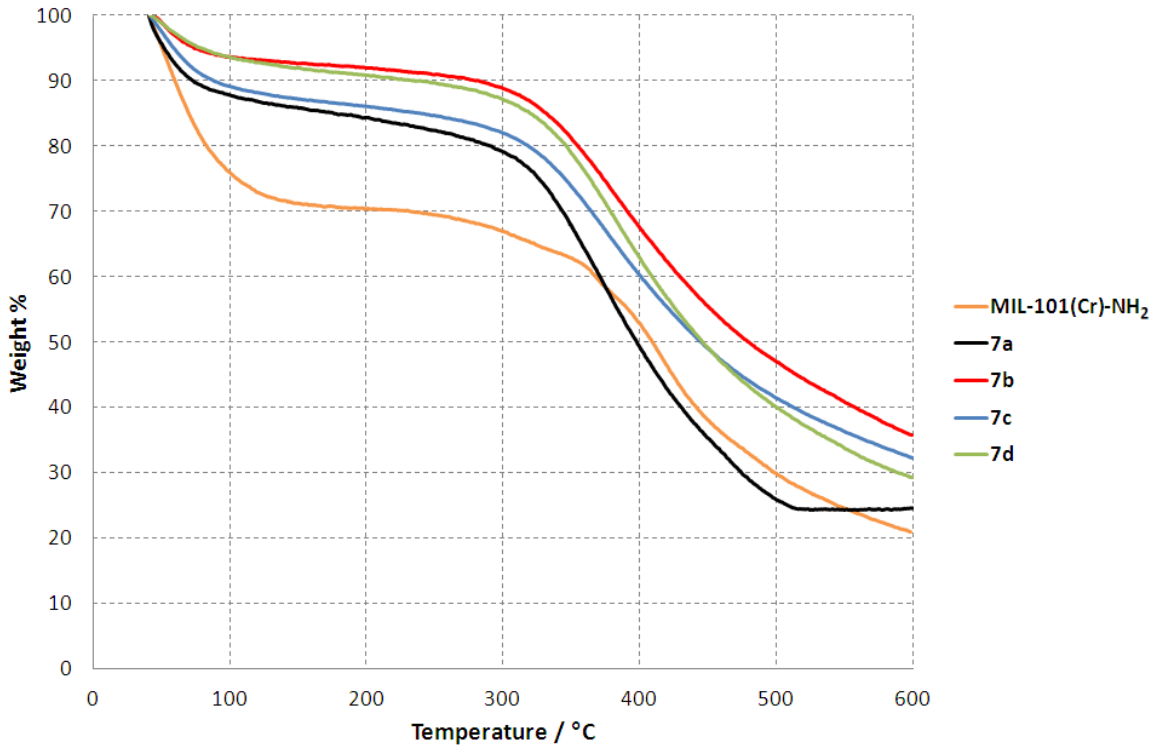

Figure 2.44. TGA of **7a-d**. Samples heated in $N_{2(g)}$ at 5 °Cmin^{-1}.

Compounds **7a-d** lose their ethanol between 40-200 °C. For each [Cr_3O] unit (or pore): **7a** had 3 EtOH molecules, **7b** had 1.5, **7c** had 3 and **7d** had 2 ethanol molecules. Even considering the number of tag groups was lower, the amount of solvent in **7b**, after drying under a flow of $N_{2(g)}$, was anomalously low.

2.5.7. Gas adsorption of *N*-alkyl Chain PSM Products, 7a-d

The BET surface areas were measured *via* the nitrogen isotherms of compounds **7a-d**, Figure 2.45. Generally the materials had lower BET surface areas than MIL-101(Cr)-NH_2 which was expected because of the additional mass of the incorporated tag groups. In the series of MOFs **7a-d**, the activating conditions used were 150 °C, for 4 hours, under vacuum. This is an important tool for MIL frameworks as PXRD peaks are very broad so the loss of porosity is garnered from the nitrogen adsorption experiments not PXRD. A higher flux of X-rays to get good PXRD data needs to be used as small particles broaden the peaks in the diffractogram.

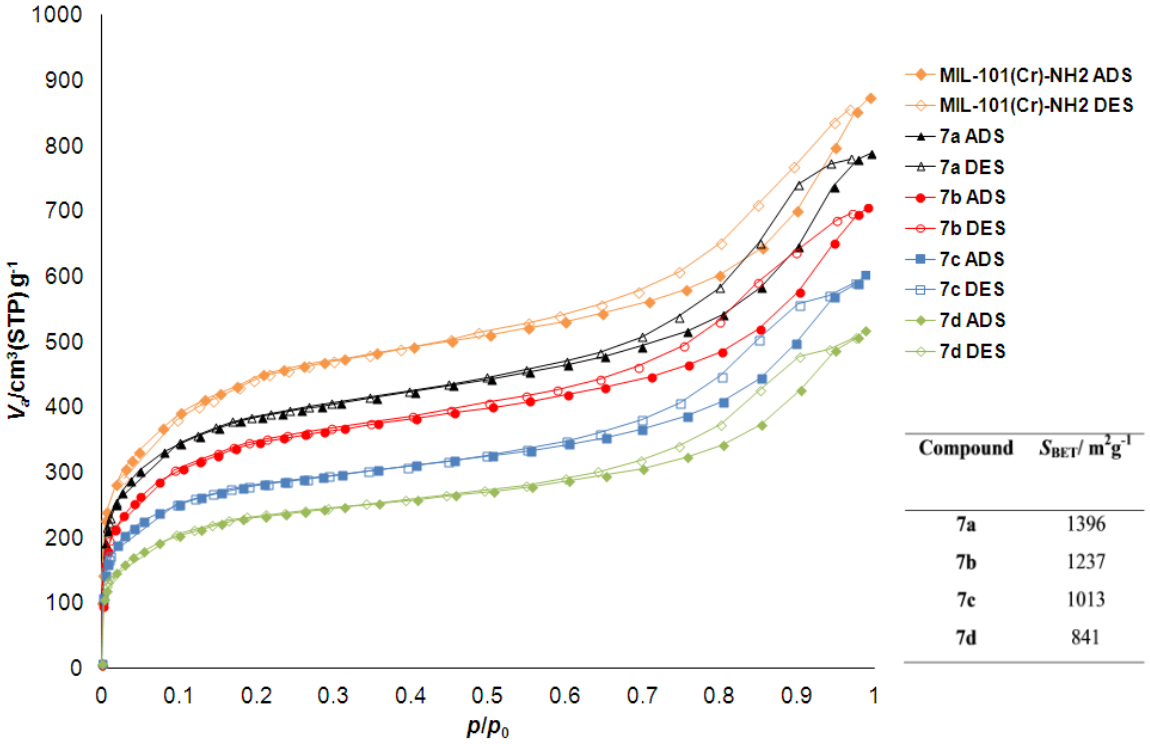

Compound	S_{BET}/ m^2g^{-1}
7a	1396
7b	1237
7c	1013
7d	841

Figure 2.45. $N_{2(g)}$ adsorption (filled points) and desorption (open points) isotherms of **7a-d** at 77 K. MIL-101(Cr)-NH_2 S_{BET} = 1604 m^2g^{-1}.

The BET surface area of the starting material, MIL-101(Cr)-NH_2 (S_{BET} = 1604 m^2g^{-1}) was lower than the reported values from the syntheses by Férey *et al.* carried out with an F^- source and reduction from a nitro tagged MIL-101(Cr)-NO_2 (S_{BET} = 1850 cm^{-1}) report by Stock.[18] This was attributed to the direct synthesis, in neat water, used herein.

The BET surface areas decreased as chain length (or molecular weight) of the tag group increased, from 1396 m^2g^{-1} (n = 2, **7a**) down to 841 m^2g^{-1} (n = 8, **7d**). The porosity was maintained even though the PXRD peaks were very weak. Material **7d** had a higher BET surface area than expected perhaps as a consequence of a lower conversion of amino groups (**7d** = 35 %, **7a** = 51 %).

The nitrogen adsorption isotherms can be described as type IV, with hysteresis that closes at 0.50 p/p_0 and was different to the hysteresis displayed in the IRMOF-3 systems. Rather than macro-trenches, in this case the hysteresis was attributed to large voids between aggregated particles, seen in the BJH plot at 20 nm, Figure 2.46. This plot also shows the mesopore distribution, with two pore sizes at 1.97 nm and 1.55 nm, in the starting material, but in the PSM products these are not monodisperse but broad up to 2.4 nm. Void sizes (in nm) vary with varying tag group size: **7a** (1.19, 1.75), **7b** (1.24, 1.56, 1.86), **7c** (1.14, 1.24,

1.55), **7d** (1.14, 1.55). Frameworks **7a** and **7b** are similar because of a small difference in chain length and conversion percentage. Materials **7c** and **7d** are similar to each other but not to the other materials suggesting a definite change when transitioning from n = 3 to n = 4.

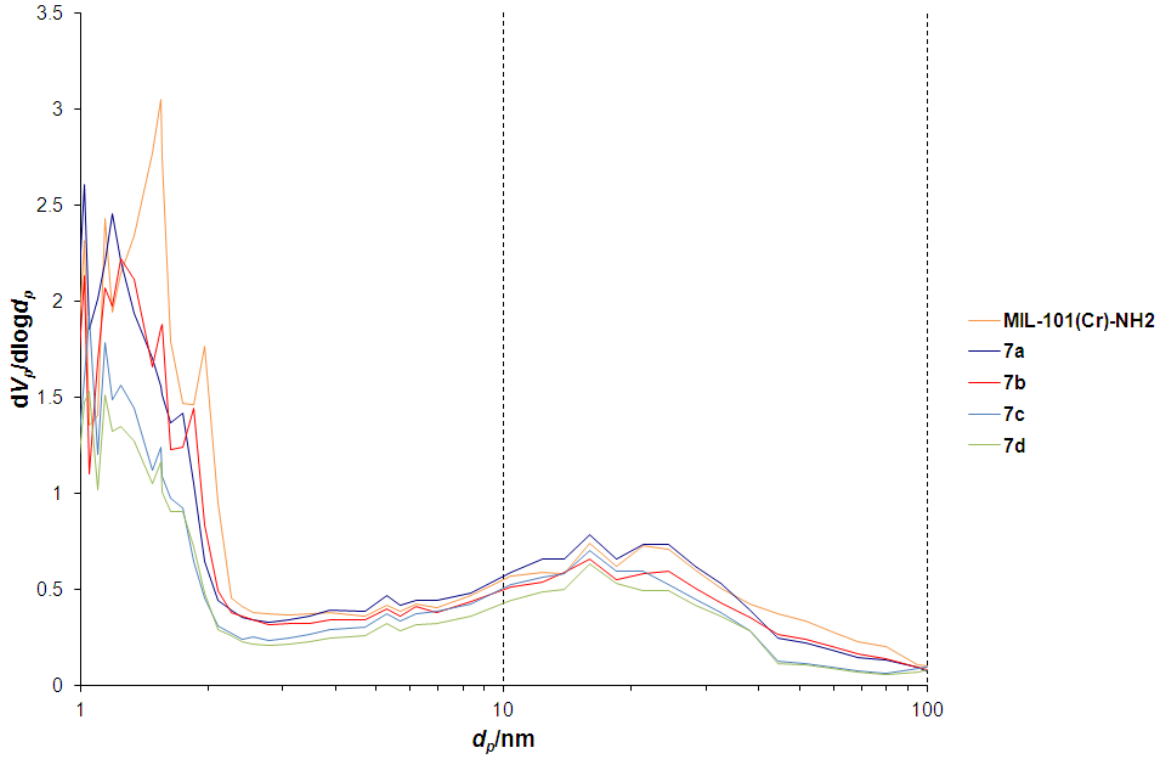

Figure 2.46. BJH plot of **7a-d**.

Carbon dioxide adsorption was studied at 273 K for compounds **7a-d** (Table 2.18 and Figure 2.47). MIL-101(Cr)-NH_2 showed a higher $CO_{2(g)}$ uptake (2.99 mmol g^{-1}) than the PSM reaction products. This was caused by the reduction in average pore size, by blocking from the tag groups and a lower number of amino groups, reducing favourable interactions with the CO_2 molecules. Somewhat surprisingly sample **7b** has a higher $CO_{2(g)}$ capacity (2.74 $mmolg^{-1}$) than **7a** (1.96 $mmolg^{-1}$), at 273 K and 1 atm, which is suspected to be due to a higher crystallinity of **7b**.

Compound	CO_2/mmol g^{-1}	N_2/mmol g^{-1}
MIL-101(Cr)-NH_2	2.99	0.12
7a	1.96	0.02
7b	2.74	0.04
7c	1.75	0.14
7d	1.73	0.09

Table 2.18. $CO_{2(g)}$ and $N_{2(g)}$ adsorption data for materials **7a-d** at 273 K and 1 atm.

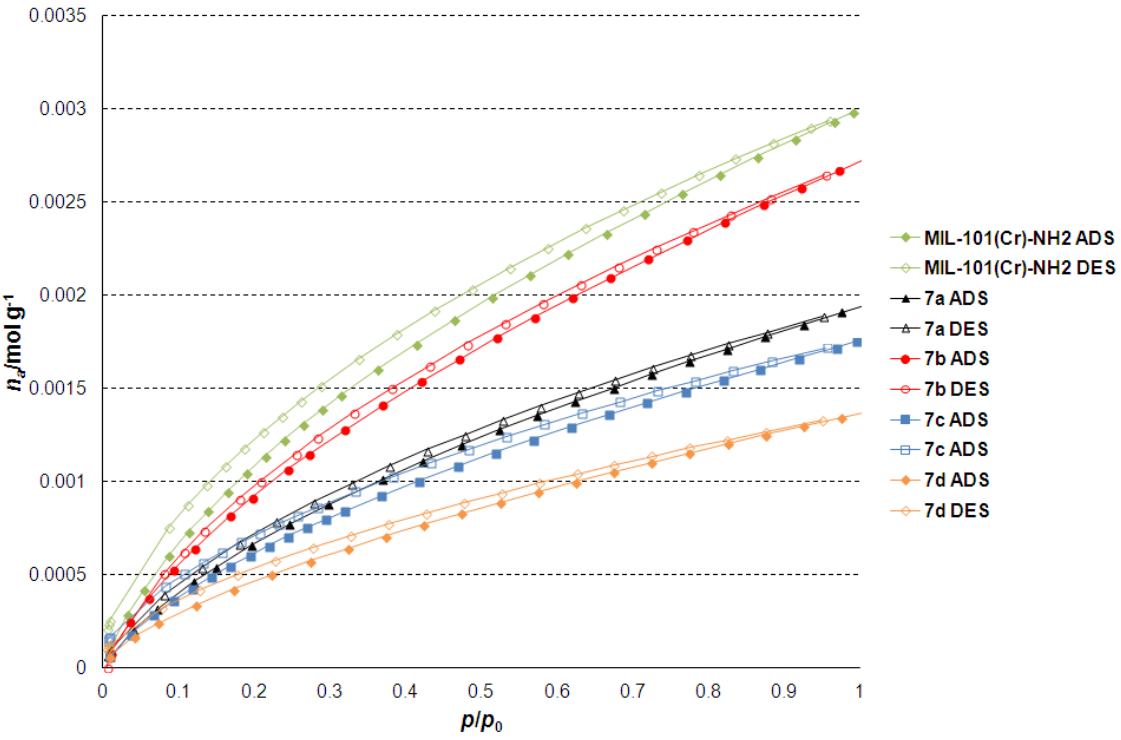

Figure 2.47. CO_2 adsorption and desorption isotherms of **7a-d** at 273 K.

2.6. Summary

The results presented herein demonstrate that a condensation-reduction tandem PSM of IRMOF-3 and MIL-101(Cr)-NH_2 systems can be used to convert the primary amine on the pore surface to a range of secondary amines of conversions up to 74 % and 51 % respectively. This is an example of an irreversible PSM reaction on the organic linkers of MOFs forming a more chemically stable group than an acid labile, imino group, formed in the first condensation step. Conversion percentages are consistent with the literature values of MOFs with similar length tag group incorporations reported by Cohen *et al.* with anhydrides.[8]

Reaction conditions were optimised, for maximising product crystallinity and percentage conversion, with respect to the solvent system used. The addition of MeOH to the reaction mixture is crucial for removing boron containing by-products from the pores and minimising the yield of PSM by-products. The borohydride is the major crystal degradation agent and as more MeOH is added, the synergistic effect increases and more SBUs can be attacked by hydride anions. It is surprising that DMF did not allow for higher conversions, in the MOF, which suggests the solubility of reactants was only one of many factors affecting conversion.

As the alkyl chain length in the aldehydes employed increases, PSM conversion decreases. Ethanal demonstrates higher crystal degradation as a consequence of higher relative volatility and visibly degrades the crystals more than longer chain aldehydes. This was confirmed by PXRD with an increase in noise and decrease in the absolute counts per second, of the diffraction peaks. Flexibility of a cyclohexenyl group in MOF pores can allow more guest molecules into the framework voids, compared to linkers with extra rigid groups such as ferrocenyl and phenyl groups.

The direct syntheses of functionalised IRMOF-3-NHR frameworks were successfully carried out with pre-synthetic modification of the linkers, followed by reaction with a metal salt. This method does not form the analogous MIL-101(Cr)-NHR pre modified system. This method still did not give access to the 100 % incorporated BDC-NHR MOF with lower yields than the PSM reaction pathway.

Several other ligands that did not give any PSM products from all MOF topologies studied herein including the acrolein modified linker H_2BDC-NHC_3H_5. 2,5-Dihydroxy- and carboxyphenyl tagged BDC ligands also did not form a MOF when reacted with a metal salt, perhaps due to the chelation of the metal ions acting in competition with the carboxylate groups.

The tandem PSM strategy was successful for *N*-alkylation of the amino groups of MIL-101(Cr)-NH_2 with up to a maximum of 51 % conversion being reported herein. Only alkyl chain aldehydes were successfully grafted on to the void surface as the larger, more functionalised, aldehydes failed to result in a crystalline product. The PSM products showed high CO_2 uptake and high selectivity over N_2 with good BET surface area retention after hydride and MeOH exposure.

The direct synthesis of functionalised MIL-101(Cr)-NHR was unsuccessful for all ligands, suggesting the tandem PSM pathway may be the only way to access these materials. However, a limitation of all tandem PSM reactions is the homogeneity of the MOF crystals. It is unclear whether the extremities are more concentrated with modified tag groups compared to the interiors of the crystals in this study.

2.7. Future Work

Decomposition pathways may exist for the direct synthesis of IRMOF-3-NHR. More investigation of the fundamentals of the MOF formation reaction would be needed to gain insight into any possible problems.

The first limitation of the tandem PSM reaction, detailed within this report, to overcome is be the long reaction times. Investigations using microwave assisted PSM could save crystallinity and increase conversion, for all MOF topologies, in a shorter time.

An increase in the scope of the tandem PSM reaction could be examined by trying it on other MOF topologies. The UiO-66(Zr)-NH_2[19] framework would be a good candidate with larger pores and hence, the space to accommodate large amines. The stability of UiO-66(Zr)-NH_2 makes it a good candidate for harsher PSM conditions at a very low or very high pH.

There is scope to extend the range of aldehydes such as implementing asymmetric ketones, as this could yield chiral secondary amino groups in a MOF for heterogeneous chiral catalytic applications. Aldehydes with additional boronic acids and esters on could be a useful anchor on MOF pore surfaces for a Suzuki coupling reaction.

Further PSMs on the functional groups incorporated in this study could yield more complex and specialised MOFs. For example, a tandem bromonation PSM could very simply be carried out on the double bond, of the cyclohexenyl group, of compound **5e** with Br_2.

In regards to the single crystal diffraction experiments, removal of some diffuse scattering, by annealing of the toluene in the pores, may help to remove the long range order and increase the quality of the diffraction pattern for easier collections and solving of structures, but time at a synchrotron is precious for such experiments.

Solid-state techniques such as SSNMR spectroscopy or soft XAS would confirm the incorporation of any extra imine groups that could be present from this PSM method. These investigations could give a truer representation of the ligand distributions in the PSM products and explain the lower BET surface areas than expected. High sensitivity ^{13}C NMR spectroscopy would show C=N formation in the intermediate species as a distinct peak and could show when the imine formation step had gone to completion.

A regular stumbling block in this investigation was the water sensitivity of IRMOF-3. Even in atmospheric humidity of 50 % the crystallinity would degrade (evidenced by PXRD). Methods for increasing the stability would be very welcome in the MOF community and perhaps hydrophobic monobenzoic acid modulators in the synthesis of IRMOF-3 (*e.g.* C_6F_5COOH) may give the crystals a water resistant surface that repels enough water to be able to characterise the materials more easily and reliably.

2.8. Experimental General Procedures

2.8.1. Powder X-ray Diffraction

Powder X-ray diffraction (PXRD) data was collected for each compound on a Bruker axs D8 Advance diffractometer with copper K_α radiation, with wavelength, λ = 1.5406 Å, at 298 K and with a beam slit set to 1 mm, detector slit set to 0.2 mm and anti-scattering slit set to 1 mm. Samples were either dried in ambient conditions and ground to a powder (MILs), using a pestle and mortar, or lightly ground in a solution they are stable in or crystallised from (IRMOF-3 = THF/DMF). Then the samples are packed into capillary tubes, of diameter 0.3, 0.5 or 0.7 mm depending on the size of the crystals, and mounted and centred using a graduated microscope (smallest division = 0.025 mm) to an error of +/- 0.025 mm in each axis. The scan speed was set to 0.5 s per step and the step size was 0.02 2θ scanning from 3-50 for IRMOF-3 and 1 s per step, 0.02 step size and 3-30 range for the MILs.

2.8.2. Single-Crystal X-ray Diffraction

Crystal size and shapes were observed under a light microscope (magnification up to 1000x) and a high resolution camera (with a graduated ruler on screen with smallest divisions of 0.025 mm).

Single-crystal X-ray diffraction analysis IRMOF-3-NHR was carried out at 250 K using synchrotron radiation of wavelength 0.6889 nm, obtained at Diamond Light Source at

beamline I19, on a Crystal Logic 4-circle diffractometer with a Rigaku Saturn CCD detector. The optimal data collection strategy with crystals from this family is to use large samples, a extensive beam attenuation (3.75mm of aluminium in this instance) and a speedy data collection. This minimises the influence of the (extensive) diffuse scattering during integration of the intensities and, more importantly, provides the best means of ensuring that the data collection completes without catastrophic degradation of the sample by the X-ray beam.

PSM reaction product crystals were generally of a poor diffraction quality even using a synchrotron source. Generally the MOF crystals were stored in toluene before being selected for the measurement and quickly mounted in Fomblin® oil, at 250 K. Etching and a high collection temperature increases disorder in the crystals, therefore decreasing the quality of the diffraction. There was also a phase change, below 220 K, that changes the diffraction to a wavy, amorphous like pattern and the same happens if the crystals are exposed for too long in the beam (radiation damage).

The solutions of structures were carried out using the software SHELX-97 and refinements were done with the software SHELXL-97 part of the programs XSeed and PLATON.[12]

2.8.3. NMR Spectroscopy

^{1}H NMR spectra were carried out on digested samples of the MOFs and were recorded at 298 K on a Bruker Avance 300 MHz Ultrashield NMR spectrometer. ^{1}H NMR spectra were referenced to the residual protio peaks at δ 7.26 ppm ($CDCl_3$) and δ 2.50 ppm for DMSO-d_6. ^{13}C NMR spectra were referenced to the residual solvent peaks at δ 77.2 ppm for $CDCl_3$ and δ 39.5 ppm for DMSO-d_6 and carried out at 75 MHz. ^{11}B NMR spectra were carried out at 160 MHz and referenced to $BF_3{\cdot}OEt_2$ at δ 0.0 ppm.

MOF digestion was carried out with approximately 5 mg of crystalline sample in 0.4 mL of DMSO and 0.2 mL of a stock solution of 0.1 mL of 35 % DCl/D_2O in 3 mL DMSO. This mixture was sonicated for three hours or until the solids had completely dissolved.

2.8.4. Mass Spectrometry

Mass spectra were carried out on digested MOF solutions, diluted in EtOH, using a Bruker micrOTOF electrospray ionization time-of-flight (ESI-TOF) machine. The method used was: confirm formula positive 50 to 500 loop injection.

2.8.5. FT-IR Spectroscopy

FT-IR analysis was carried out on solid, ground, dried samples (oven 90 ºC overnight) for the MILs using a PerkinElmer Spectrum 100 spectrometer mounted on a diamond/gem platform. Spectra on IRMOF-3-NHR were carried *in situ* in toluene removing the excess toluene dabbing with tissue.

2.8.6. Thermogravimetric Analysis

TGA data acquisitions were carried out on a PerkinElmer TGA 4000 thermogravametric analyzer from a temperature range of 40 ºC to 600 ºC at a rate of 5 ºC/min under a flow of N_2 gas (20 mL/min). The samples of IRMOF-3-NHR were dried under a $N_{2(g)}$ flow (293 K), evaporating toluene until constant weight, before measuring the TGA.

2.8.7. Nitrogen and Carbon Dioxide Adsorption Measurements

The sorption isotherms of N_2 at 77 K and 273 K, and of CO_2 at 273 K were carried out on a BELSORP Mini-II (BEL Japan) instrument. N_2 (77 K). Standard range $0.05<P/P_0<0.3$ (I have used 0.2 as upper limit, with R linear > 0.99) the range must be linear, with c (= y-intercept) a positive value. CO_2 and N_2 selectivity was assessed at 273 K.

Activation conditions for IRMOF-3-CH_2R were to use toluene and a flow of $N_{2(g)}$ because it reduces exposure to atmospheric humidity before activating at 150 °C for 3 h, under vacuum (~0.1 bar) on the instrument. MIL-101(Cr)-NHR samples were activated at 150 °C for 4 h, under vacuum.

2.8.8. Atomic adsorption Spectrometry

AAS was carried out by Mr. Alan Carver on a Perkin Elmer Model 3100 on aqueous solutions of digested MOFs.

2.8.9. Elemental Analysis

Microanalysis was carried out by Mr. Alan Carver, in house on an Exeter analytical inc. CE-440 elemental analyzer, on dried samples unless stated otherwise. Porous materials are notoriously difficult to analyse using elemental analysis because they absorb small molecules so readily.

2.9. Experimental: PSM procedures

General optimised PSM procedure: IRMOF-3 was washed with solvent (THF: 5 mL per 50 mg MOF) for 3 days with fresh solvent and exchanged once per day by decantation. The

aldehyde reagent (2-4 eq.) is then added to the solution. After 1 hour MeOH (THF:MeOH ratio 15:1) was added to the IRMOF-3 samples and then $NaCNBH_3$ (2-4 eq.). Hydrolysis of the borohydride occured with evolution of $H_{2(g)}$, so under a flow of $N_{2(g)}$ the mixture was left for 30 minutes to allow for $H_{2(g)}$ production to cease. The reaction vessel was sealed and heated to 50 °C for 48 hours with no stirring. After this the vessel was allowed to cool to ambient temperature. The crystal were rinsed with THF/MeOH 15:1 solution for 3 days replacing with fresh solvent once per 24 h by decantation and the solvent was exchanged with toluene, for storage and characterisation of IRMOF-3-NHR, by washing with toluene over 3 days replacing fresh solvent once per 24 h by decantation.

2.9.1. IRMOF-3-Et (74%), $[Zn_4O(BDC\text{-}NH_2)_{0.78}(BDC\text{-}NHEt)_{2.22}]\cdot 7Tol$, 2a

IRMOF-3 was synthesised according to a modified preparation by Cohen *et al.*[8] washed with solvent (THF) for 3 days with fresh solvent every 24 h. In a 6 mL Biotage microwave vial, ~100 mg IRMOF-3 (0.23 mmol NH_2eq) was added to a solvent system of 5.625 mL THF:0.375 mL MeOH (15:1). This was cooled in an ice bath to less than 5 °C. Ethanal (51 µL, 0.92 mmol, 4 eq.) and then $NaCNBH_3$ (58 mg, 0.92 mmol, 4 eq.) were added to this mixture. After 30 minutes, to allow for effervescence, the mixture was sealed and heated to 50 °C for 48 hours, no stirring, before being removed from the oven and cooled to ambient temperature. The crystalline product was rinsed with THF:MeOH 15:1. The resulting yellow-orange crystals were washed with 3 x 5 mL toluene over 3 days, by decantation and replacing with fresh toluene once every 24 h, and stored in fresh toluene.

m/z = 208.0646 (predicted $[C_{10}H_{10}NO_4]^-$, $[M\text{-}H]^-$ = 208.0615).

2.9.2. IRMOF-3-Pr (69 %), $[Zn_4O(BDC\text{-}NH_2)_{0.93}(BDC\text{-}NHPr)_{2.07}]\cdot 5.5Tol$, 2b

IRMOF-3 was washed with solvent (THF) for 3 days with fresh solvent every 24 h. In a 6 mL Biotage microwave vial, ~100 mg IRMOF-3 (0.23 mmol NH_2eq) was added to a solvent system of 5.625 mL THF:0.375 mL MeOH (15:1). Propanal (67 µL, 0.92 mmol, 4 eq.) and then $NaCNBH_3$ (58 mg, 0.92 mmol, 4 eq.) were added to this mixture. After 30 minute effervescence the mixture was sealed and heated to 50 °C for 48 hours, no stirring, before being removed from the oven and cooled to ambient temperature. The crystalline product was rinsed with THF:MeOH 15:1. The resulting yellow-orange crystals were washed with 3 x 5 mL toluene over 3 days, by decantation and replacing with fresh toluene once every 24 h, and stored in fresh toluene.

m/z = 222.0784 (predicted$[C_{11}H_{12}NO_4]^-$, $[M\text{-}H]^-$ = 222.0766).

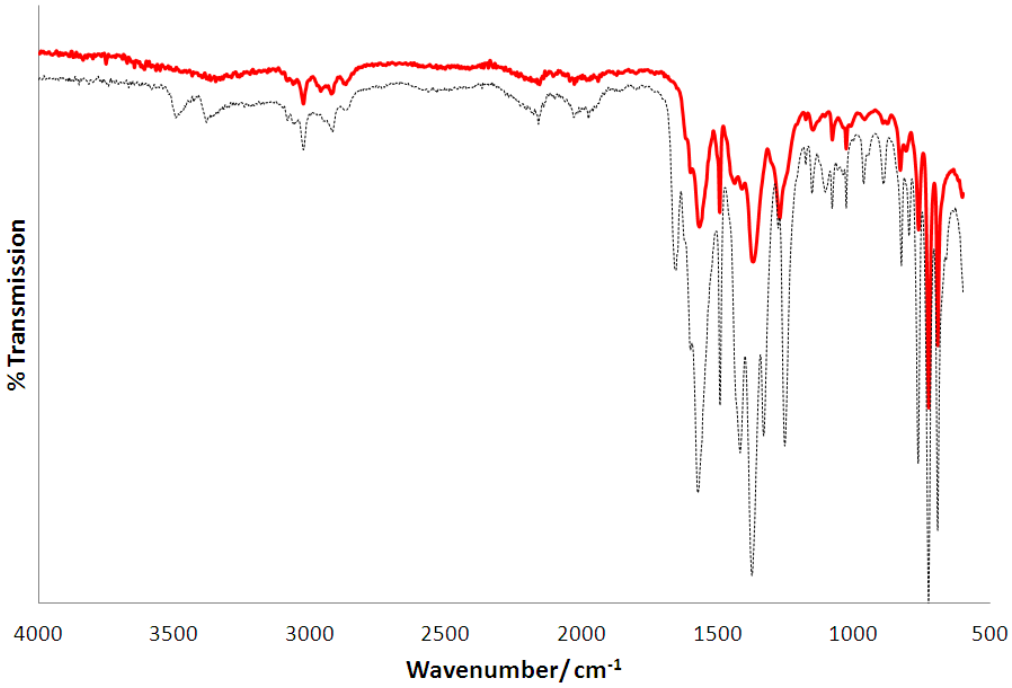

Figure 2.48. *In situ* FT-IR spectrum of **2b** (red) and IRMOF-3 (black).

2.9.3. IRMOF-3-Bu (65 %), $[Zn_4O(BDC\text{-}NH_2)_{1.05}(BDC\text{-}NHBu)_{1.95}]\cdot 5.5Tol$, 2c

IRMOF-3 was washed with solvent (THF) for 3 days with fresh solvent every 24 h. In a 6 mL Biotage microwave vial, ~100 mg IRMOF-3 (0.23 mmol NH_2eq) was added to a solvent system of 5.625 mL THF:0.375 mL MeOH (15:1). Butanal (81 µL, 0.92 mmol, 4 eq.) and then $NaCNBH_3$ (58 mg, 0.92 mmol, 4 eq.) were added to this mixture. After 30 minute effervescence the mixture was sealed and heated to 50 °C for 48 hours, no stirring, before being removed from the oven and cooled to ambient temperature. The crystalline product was rinsed with THF:MeOH 15:1. The resulting yellow-orange crystals were washed with 3 x 5 mL toluene over 3 days, by decantation and replacing with fresh toluene once every 24 h, and stored in fresh toluene.

m/z = 236.0934 (predicted $[C_{12}H_{14}NO_4]^-$, $[M\text{-}H]^-$ = 236.0923).

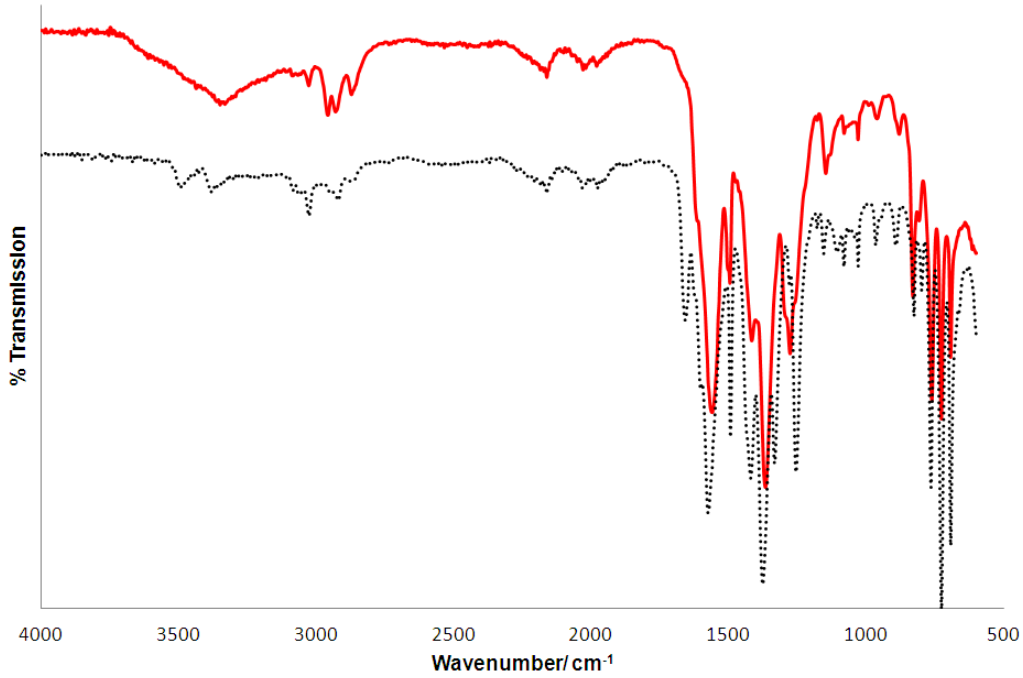

Figure 2.49. *In situ* FT-IR spectrum of **2c** (red) and IRMOF-3(black) in toluene.

2.9.4. IRMOF-3-C_8H_{17} (47 %), $[Zn_4O(BDC\text{-}NH_2)_{1.59}(BDC\text{-}NHC_8H_{17})_{1.41}]\cdot 4Tol$, 2d

IRMOF-3 was washed with solvent (THF) for 3 days with fresh solvent every 24 h. In a 6 mL Biotage microwave vial, ~100 mg IRMOF-3 (0.23 mmol NH_2eq) was added to a solvent system of 5.625 mL THF:0.375 mL MeOH (15:1). Octanal (144 µL, 0.92 mmol, 4 eq.) and then $NaCNBH_3$ (58 mg, 0.92 mmol, 4 eq.) were added to this mixture. After 30 minute effervescence the mixture was sealed and heated to 50 °C for 48 hours, no stirring, before being removed from the oven and cooled to ambient temperature. The crystalline product was rinsed with THF:MeOH 15:1. The resulting yellow-orange crystals were washed with 3 x 5 mL toluene over 3 days, by decantation and replacing with fresh toluene once every 24 h, and stored in fresh toluene.

m/z = 292.1558 (predicted $[C_{16}H_{22}NO_4]^-$, $[M\text{-}H]^-$ = 292.1554).

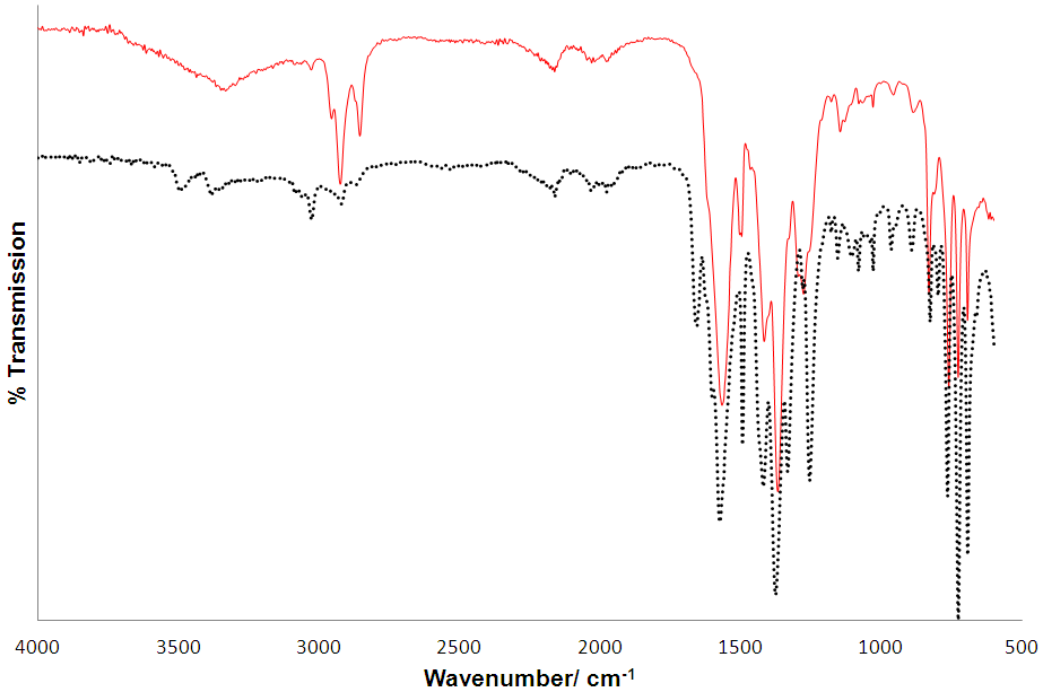

Figure 2.50. *In situ* FT-IR spectrum of **2d** (red) and IRMOF-3 (black).

2.9.5. IRMOF-3-C_7H_{11} (49 %), $[Zn_4O(BDC\text{-}NH_2)_{1.53}(BDC\text{-}NHCH_2C_6H_9)_{1.47}]\cdot 5Tol$, 2e

IRMOF-3 was washed with solvent (THF) for 3 days with fresh solvent every 24 h. In a 6 mL Biotage microwave vial, ~100 mg IRMOF-3 (0.23 mmol NH_2eq) was added to a solvent system of 5.625 mL THF:0.375 mL MeOH (15:1). 1,2,3,6-Tetrahydrobenzaldehyde (104 µL, 0.92 mmol, 4 eq.) and then $NaCNBH_3$ (58 mg, 0.92 mmol, 4 eq.) were added to this mixture. After 30 minute effervescence the mixture was sealed and heated to 50 °C for 48 hours, no stirring, before being removed from the oven and cooled to ambient temperature. The crystalline product was rinsed with THF:MeOH 15:1. The resulting yellow-orange crystals were washed with 3 x 5 mL toluene over 3 days, by decantation and replacing with fresh toluene once every 24 h, and stored in fresh toluene. Analysis found: C 42.0, H 3.44, N 4.83. Predicted activated sample: C 42.37 H 3.00 N 4.49 (43 % conversion batch).

m/z = 247.1124 (predicted $[C_{15}H_{16}O_4N]^-$, $[M\text{-}H]^-$ = 274.1085)

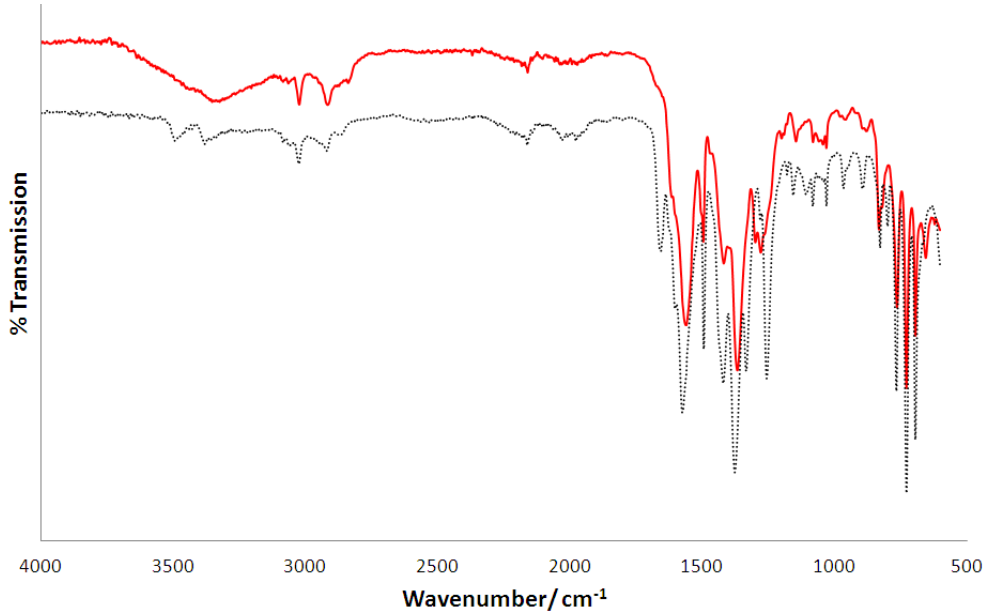

Figure 2.51. *In situ* FT-IR spectrum of **2e** (red) and IRMOF-3 (black).

2.9.6. IRMOF-3-CH_2Fc (27 %), $[Zn_4O(BDC\text{-}NH_2)_{2.19}(BDC\text{-}NHCH_2Fc)_{0.81}]\cdot 2.5Tol$, 2f

IRMOF-3 was washed with solvent (THF) for 3 days with fresh solvent every 24 h. In a 6 mL Biotage microwave vial, ~100 mg IRMOF-3 (0.23 mmol NH_2eq) was added to a solvent system of 5.625 mL THF:0.375 mL MeOH (15:1). Ferrocenecarboxaldehyde (197 mg, 0.92 mmol, 4 eq.) and then $NaCNBH_3$ (58 mg, 0.92 mmol, 4 eq.) were added to this mixture. After 30 minute effervescence the mixture was sealed and heated to 50 °C for 48 hours, no stirring, before being removed from the oven and cooled to ambient temperature. The crystalline product was rinsed with THF:MeOH 15:1. The resulting yellow-orange crystals were washed with 3 x 5 mL toluene over 3 days, by decantation and replacing with fresh toluene once every 24 h, and stored in fresh toluene. Atomic absorption spectrometry: Fe:Zn 1:6.2 (predicted 1:6.8).

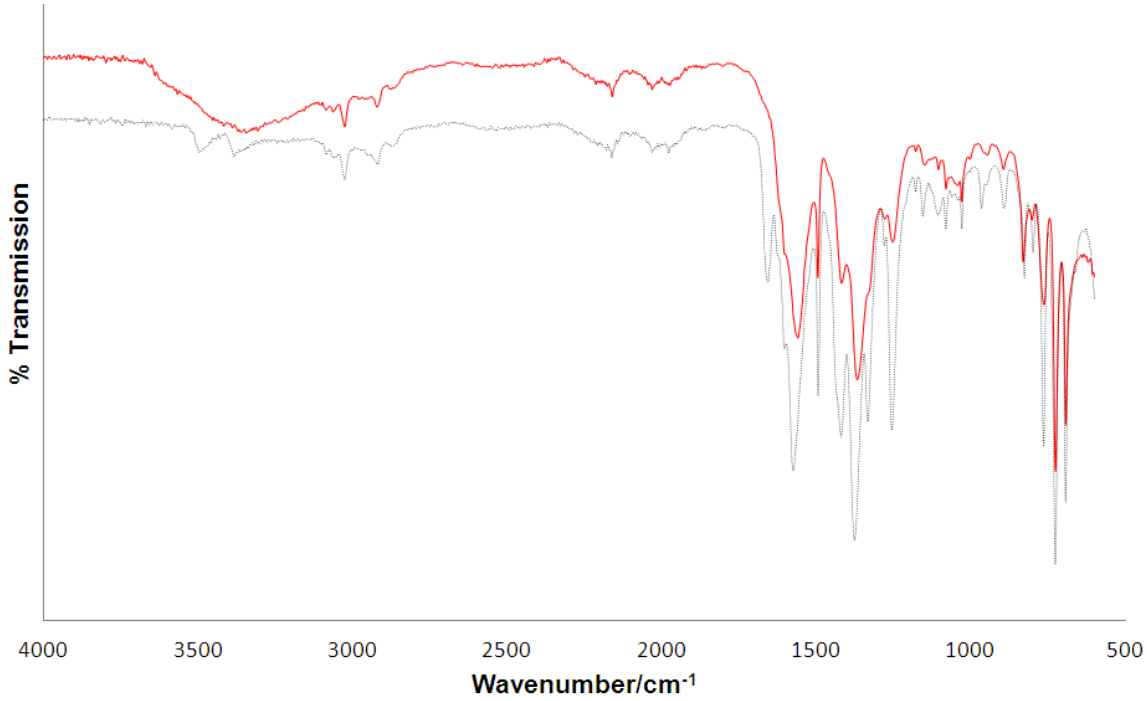

Figure 2.52. *In situ* FT-IR spectrum of **2f** (red) and IRMOF-3 (balck).

2.9.7. IRMOF-3-C_6H_4SMe (25 %), $[Zn_4O(BDC\text{-}NH_2)_{2.25}(BDC\text{-}NHCH_2C_6H_4SMe)_{0.75}]\cdot 4Tol$, 2g

IRMOF-3 was washed with solvent (THF) for 3 days with fresh solvent every 24 h. In a 6 mL Biotage microwave vial, ~100 mg IRMOF-3 (0.23 mmol NH_2eq) was added to a solvent system of 5.625 mL THF:0.375 mL MeOH (15:1). 4-Methylthiobenzaldehyde (122 µL, 0.92 mmol, 4 eq.) and then $NaCNBH_3$ (58 mg, 0.92 mmol, 4 eq.) were added to this mixture. After 30 minute effervescence the mixture was sealed and heated to 50 °C for 48 hours, no stirring, before being removed from the oven and cooled to ambient temperature. The crystalline product was rinsed with THF:MeOH 15:1. The resulting yellow-orange crystals were washed with 3 x 5 mL toluene over 3 days, by decantation and replacing with fresh toluene once every 24 h, and stored in fresh toluene.

m/z = 316.0757 (predicted $[C_{16}H_{14}O_4NS]^-$, $[M\text{-}H]^-$ = 316.0649).

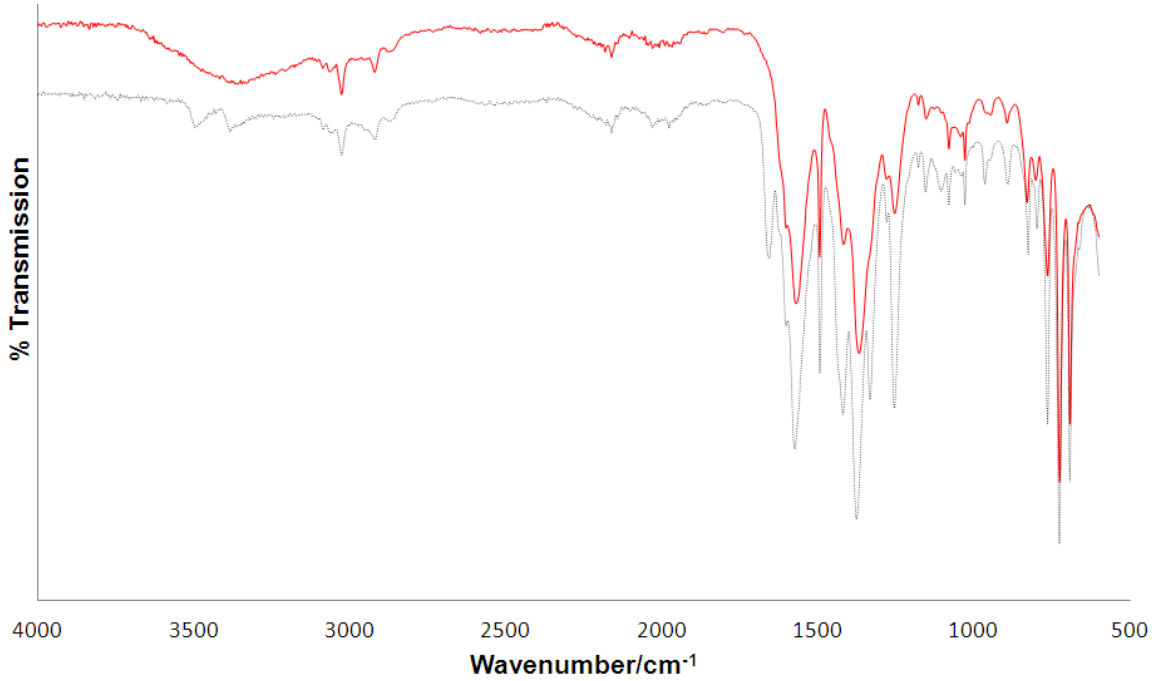

Figure 2.53. *In situ* FT-IR spectrum of **2g** (red) and IRMOF-3 (black).

2.10. Experimental: Dicarboxylic acid Syntheses

2.10.1. 2-(Ethylamino)benzene-1,4-dicarboxylic acid, H_2BDC-NHEt, 4a

2-Aminobenzene-1,4-dicarboxylic acid (H_2BDC-NH_2) (0.200 g, 1.104 mmol) was dissolved in *N*,*N*'-dimethylformamide (DMF) (10 cm^3), then ethanal (0.124 cm^3, 2.208 mmol) was added at 10 °C and the solution stirred at this temperature for 1 h. The solution was then cooled in an ice bath and $NaCNBH_3$ (0.139 g, 2.204 mmol) was added. The resulting reaction mixture was stirred at room temperature for 24 h. The mixture was acidified with 1 M HCl, and water was added until a yellow solid precipitated. Yield: 0.146 g (63 %). ^{1}H NMR (300 MHz, DMSO-d_6) δ/ppm: 7.79 (d, 1H, J = 7.8 Hz), 7.05 (s (br), 1H), 6.97 (dd, 1H, J = 7.8, 1.5 Hz), 3.11 (q, 2H, J = 7.0 Hz), 1.21 (t, 3H, J = 7.0 Hz). ^{13}C NMR (75 MHz, DMSO-d_6) δ/ppm: 169.9, 167.5, 150.7, 136.1, 132.3, 114.7, 113.3, 112.1, 37.05, 14.6. *m/z* (ESI) 208.0598 ($[M - H]^-$. $[C_{10}H_{10}O_4N]^-$ requires 208.0610). Found C: 57.15, H: 5.41, N: 7.01 %. $C_{10}H_{11}O_4N$ requires C: 57.41, H: 5.30, N: 6.70 %.

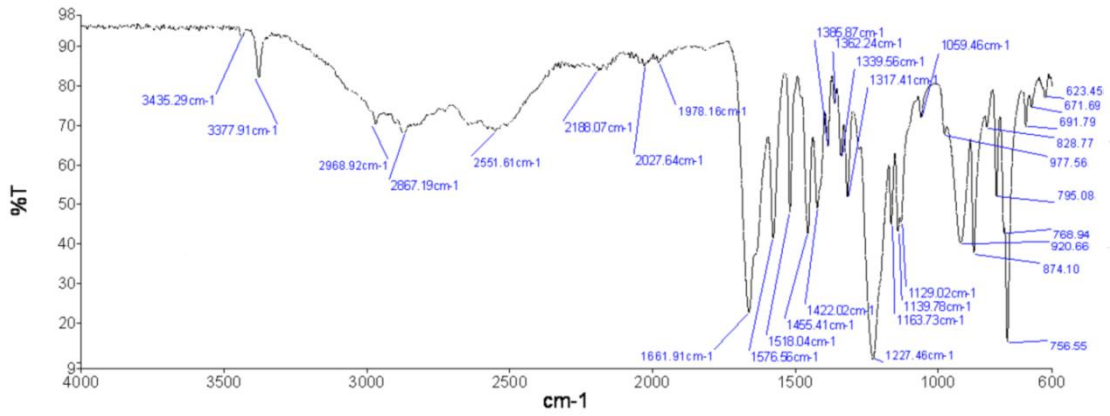

Figure 2.54. FT-IR spectrum of H_2BDC-NHEt, **4a**.

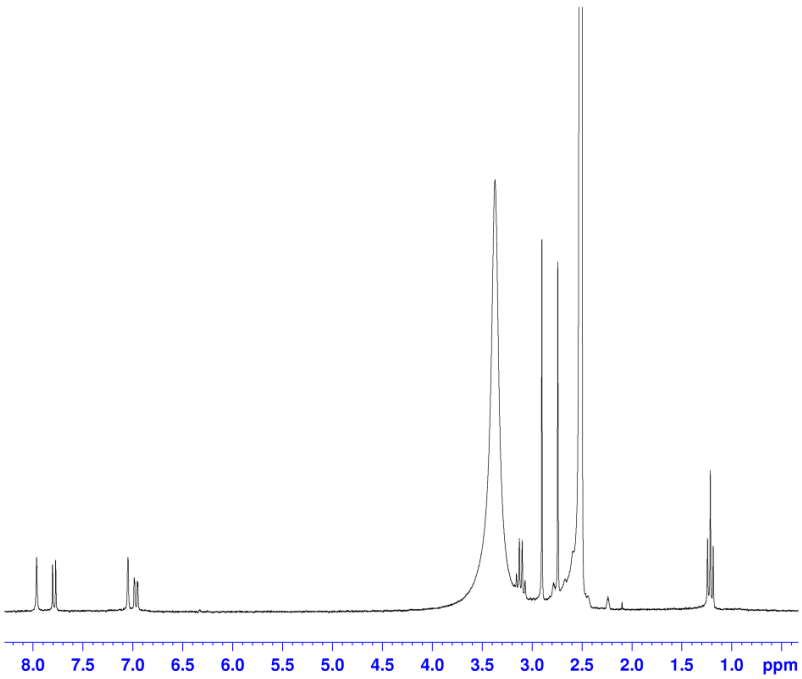

Figure 2.55. ^{1}H NMR spectrum of **4a** in DMSO-d_6.

2.10.2. 2-(Propylamino)benzene-1,4-dicarboxylic acid, H_2BDC-NHPr, 4b

2-Aminobenzene-1,4-dicarboxylic acid (H_2BDC-NH_2) (0.200 g, 1.104 mmol) was dissolved in DMF (10 cm^3), then propanal (0.161 cm^3, 2.208 mmol) was added and the solution stirred for 1 h. The solution was then cooled in an ice bath and $NaCNBH_3$ (0.139 g, 2.204 mmol) added. The resulting reaction mixture was stirred at room temperature for 24 h. The mixture was acidified with 1 M HCl, and water was added until a yellow solid precipitated. Yield: 0.227 g (92 %). ^{1}H NMR (300 MHz, DMSO-d_6) δ/ppm: 7.85 (d, 1H, J = 8.0 Hz), 7.22 (d, 1H, J = 1.6 Hz), 7.05 (dd, 1H, J = 8.0 Hz, 1.4 Hz), 3.15 (t, 2H, J = 7.2 Hz), 1.61 (sextet, 2H, J = 7.2 Hz), 0.95 (t, 3H, J = 7.2 Hz). ^{13}C NMR (75 MHz, DMSO-d_6)

δ/ppm: 169.9, 167.5, 150.9, 136.1, 132.3, 114.6, 113.3, 112.1, 44.2, 22.1, 11.8. *m/z* (ESI) 222.0807 ($[M - H]^-$. $[C_{11}H_{12}O_4N]^-$ requires 222.0766). Found C: 59.00, H: 5.95, N: 6.50 %. $C_{11}H_{13}O_4N$ requires C: 59.45, H: 5.44, N: 6.30 %.

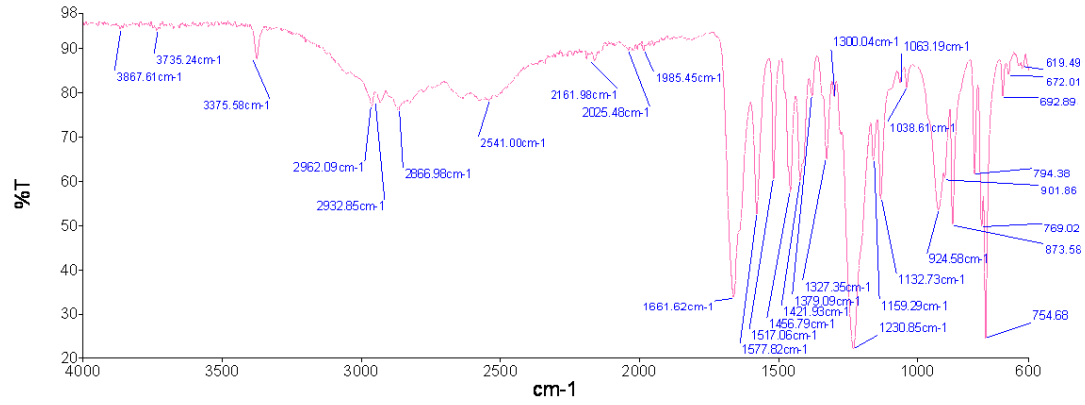

Figure 2.56. FT-IR spectrum of H_2BDC-NHPr, **4b**.

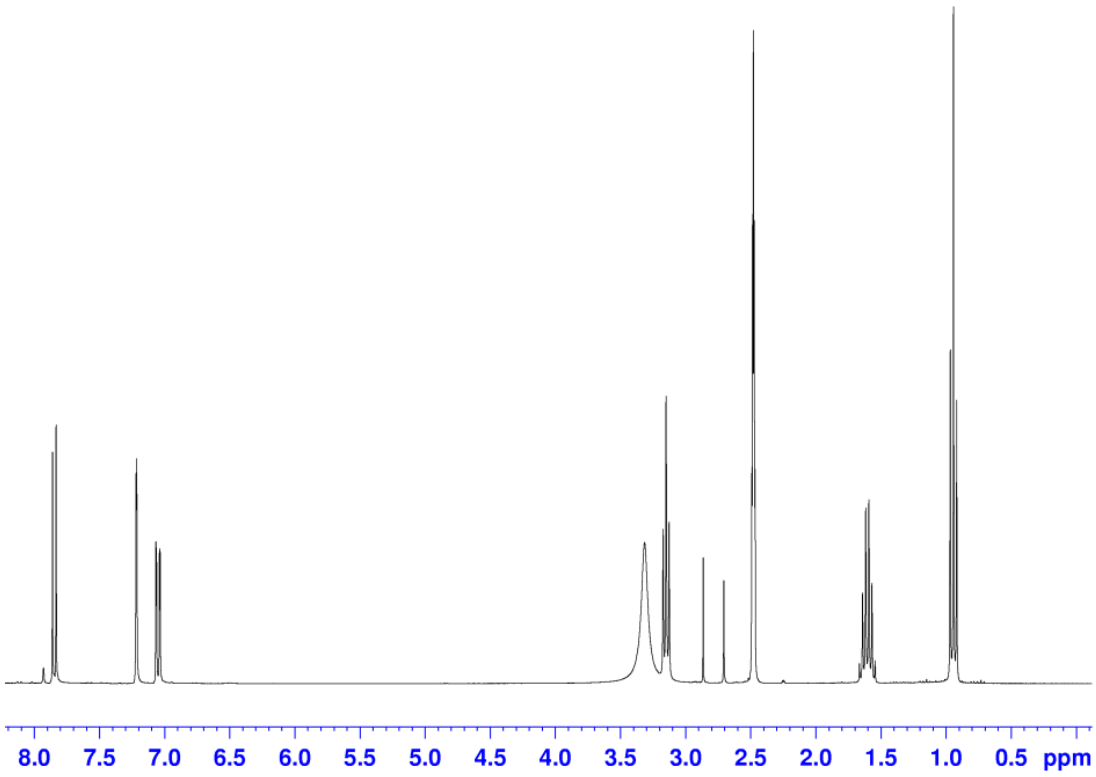

Figure 2.57. ^{1}H NMR spectrum for **4b** in DMSO-d_6.

2.10.3. 2-(Butylamino)benzene-1,4-dicarboxylic acid, H_2BDC-NHBu, 4c

2-Aminobenzene-1,4-dicarboxylic acid (H_2BDC-NH_2) (0.200 g, 1.104 mmol) was dissolved in DMF (10 cm^3), then butanal (0.195 cm^3, 2.208 mmol) was added and the solution stirred for 1 h. The solution was then cooled in an ice bath and $NaCNBH_3$ (0.139

g, 2.204 mmol) was added. The resulting reaction mixture was stirred at room temperature for 24 h. The mixture was acidified with 1 M HCl, and water was added until a yellow solid precipitated. Yield: 0.117 g (45 %). ^{1}H NMR (300 MHz, DMSO-d_6) δ/ppm: 7.84 (d, 1H, J = 8.2 Hz), 7.22 (d, 1H, J = 1.5 Hz), 7.05 (dd, 1H, J = 7.8 Hz, 1.5 Hz), 3.18 (t, 2H, J = 7.5 Hz), 1.58 (quintet, 2H, J = 6.7 Hz), 1.38 (sextet, 2H, J = 7.5 Hz), 0.91 (t, 3H, J = 6.7 Hz). ^{13}C NMR (75 MHz, DMSO-d_6) δ/ppm: 169.9, 167.5, 150.9, 136.1, 132.3, 114.6, 113.3, 112.1, 42.1, 30.9, 20.1, 14.0. *m/z* (ESI) 236.0948 ([M – H]$^-$. [$C_{12}H_{14}O_4N$]$^-$ requires 236.0923). Found C: 60.80, H: 6.49, N: 6.06 %. $C_{12}H_{15}O_4N$ requires C: 60.75, H: 6.37, N: 5.90 %.

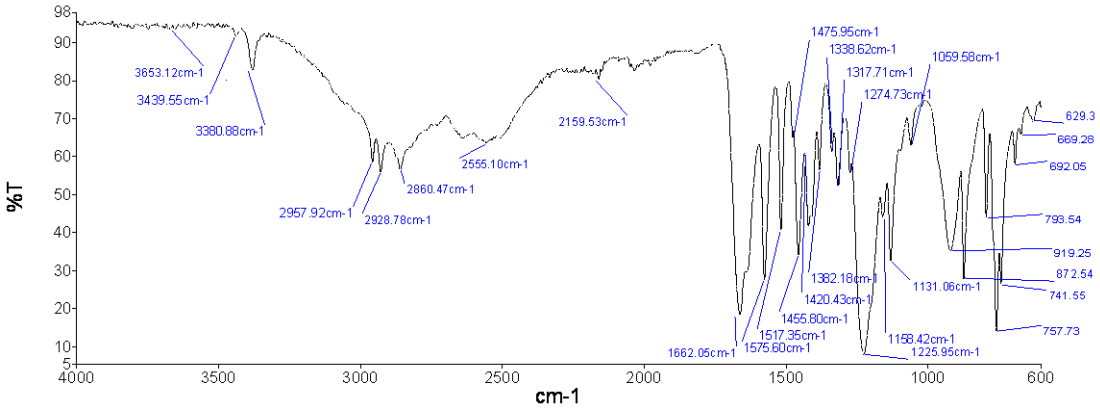

Figure 2.58. Infrared spectrum for H_2BDC-NHBu, **4c**.

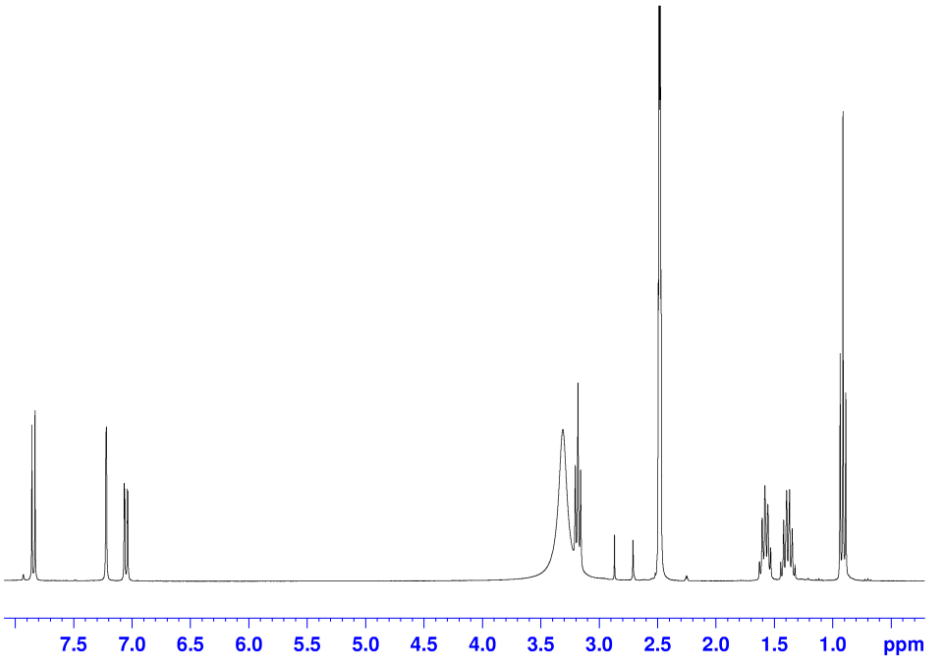

Figure 2.59. ^{1}H NMR spectrum for H_2bdc-NHBu in DMSO-d_6.

2.10.4. 2-(Octylamino)benzene-1,4-dicarboxylic acid, $H_2BDC\text{-}NHC_8H_{17}$, 4d

2-Aminobenzene-1,4-dicarboxylic acid ($H_2BDC\text{-}NH_2$) (0.200 g, 1.104 mmol) was dissolved in DMF (10 cm^3), then octanal (0.345 cm^3, 2.208 mmol) was added and the solution stirred for 1 h. The solution was then cooled in an ice bath and $NaCNBH_3$ (0.139 g, 2.204 mmol) added. The resulting reaction mixture was stirred at room temperature for 24 h. The mixture was acidified with 1 M HCl, and water was added until a yellow solid precipitated. Yield: 0.313 g (97 %). ^{1}H NMR (300 MHz, DMSO-d_6) δ/ppm: 7.84 (d, 1H, J = 8.2 Hz), 7.21 (d, 1H, J = 1.4 Hz), 7.05 (dd, 1H, J = 8.2 Hz, 1.4 Hz), 3.17 (t, 2H, J = 7.0 Hz), 1.58 (quintet, 2H, J = 6.3 Hz), 1.40-1.15 (m, 10H), 0.83 (t, 3H, J = 6.9 Hz). ^{13}C NMR (75 MHz, DMSO-d_6) δ/ppm: 169.9, 167.6, 150.9, 136.1, 132.3, 114.6, 113.3, 112.1, 42.4, 31.5, 29.01, 28.98, 28.8, 26.8, 22.4, 14.3. *m/z* (ESI) 292.1574 ($[M - H]^-$. $[C_{16}H_{22}O_4N]^-$ requires 292.1549). Found C: 66.20, H: 8.75, N: 4.26 %. $C_{16}H_{23}O_4N$ requires C: 65.51, H: 7.90, N: 4.77 %. (matches with 0.3 eq octanal and 0.1 eq H_2O added).

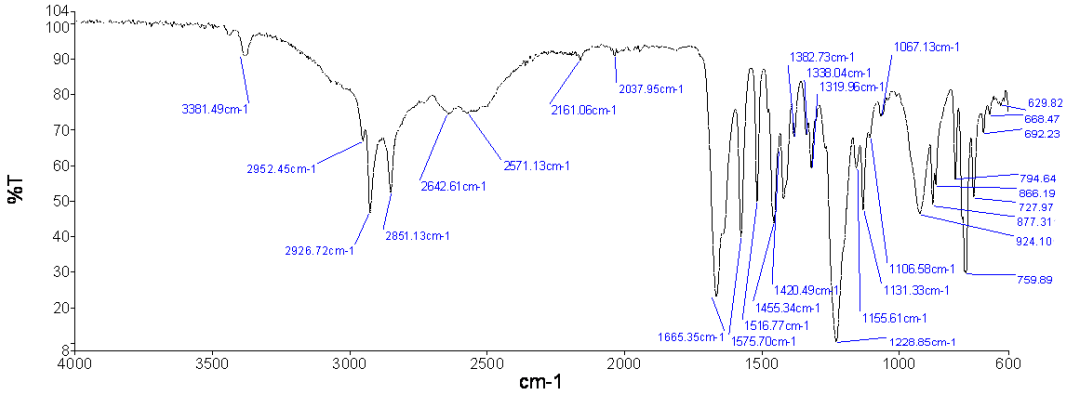

Figure 2.60. FT-IR spectrum for $H_2BDC\text{-}NHC_8H_{17}$, **4d**.

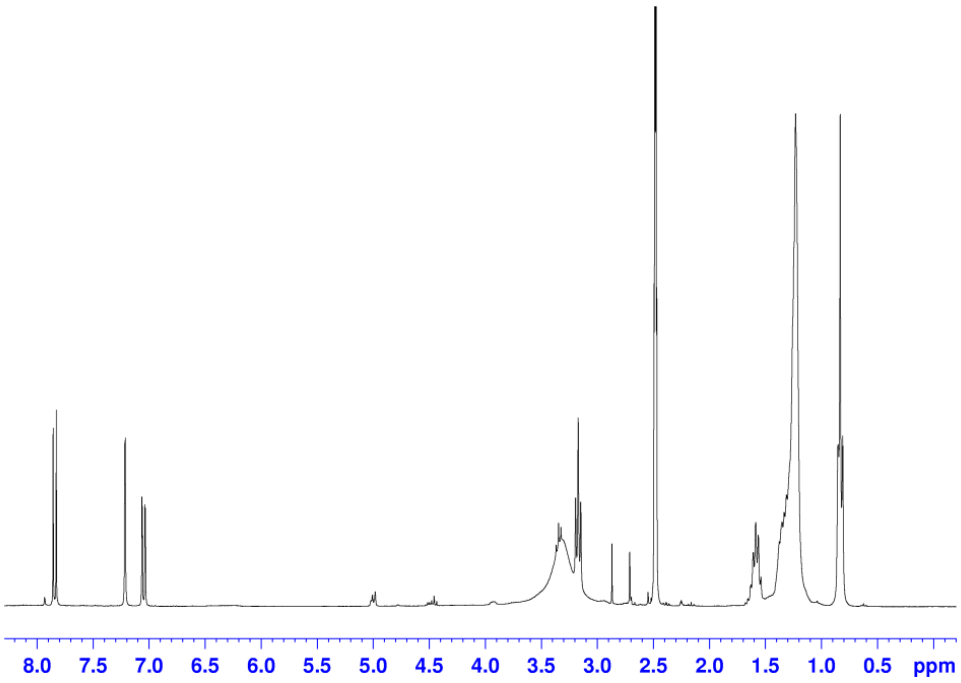

Figure 2.61. ^{1}H NMR spectrum for $H_2BDC\text{-}NHC_8H_{17}$ in DMSO-d_6.

2.10.5. 2-((Cyclohex-3-en-1-ylmethyl)amino)terephthalic acid, $H_2BDC\text{-}NHC_7H_{11}$, 4e

2-Aminobenzene-1,4-dicarboxylic acid ($H_2BDC\text{-}NH_2$) (0.200 g, 1.104 mmol) was dissolved in DMF (10 cm^3), then 1,2,3,6-tetrahydrobenzaldehyde (0.251 cm^3, 2.208 mmol) was added and the solution stirred at room temperature for 1 h. The solution was then cooled in an ice bath and $NaCNBH_3$ (0.139 g, 2.204 mmol) was added. The resulting reaction mixture was stirred at room temperature for 24 h. The mixture was acidified with 1 M HCl, and water was added until a yellow solid precipitated which was filtered, washed with 3 x 5 cm^3 H_2O and dried in an oven at 80 °C for 1 h. The compound was recrystallised from DMF/H_2O. Yield: 0.296 g (97 %). ^{1}H NMR (300 MHz, DMSO-d_6) δ/ppm: 7.93 (d, 1H, J = 8.2 Hz), 7.31 (d, 1H, J = 1.4 Hz), 7.13 (dd, 1H, J = 8.2, 1.5 Hz), 5.72 (m, 2H), 3.21(d, 2H, J = 6.4 Hz) 2.14 (m, 3H) 1.88 (m, 3H) 1.37 (m, 1H). ^{13}C NMR (75 MHz, DMSO-d_6) δ/ppm: 170.0, 167.5, 151.1, 136.1, 132.4, 127.3, 126.1, 114.7, 113.3, 112.2, 48.0, 33.1, 29.4, 26.5, 24.6. *m/z* (ESI) 274.1079 ([M – H]$^-$. $[C_{15}H_{16}O_4N]^-$ requires 274.1085). Found C: 65.70, H: 6.66, N: 5.25 %. $C_{15}H_{17}O_4N$ requires C: 65.44, H: 6.22, N: 5.09 %.

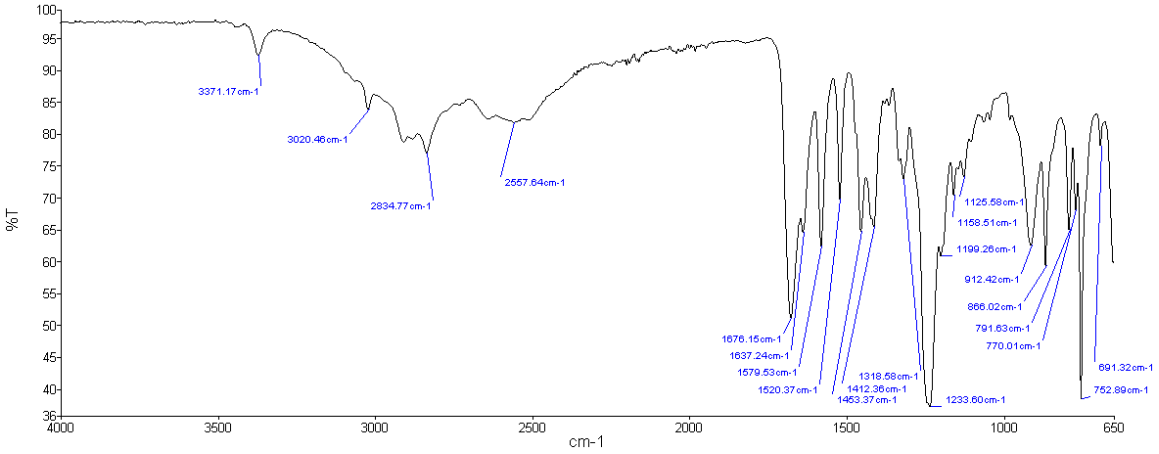

Figure 2.62. Infrared spectrum for $H_2BDC\text{-}NHC_7H_{11}$, **4e**.

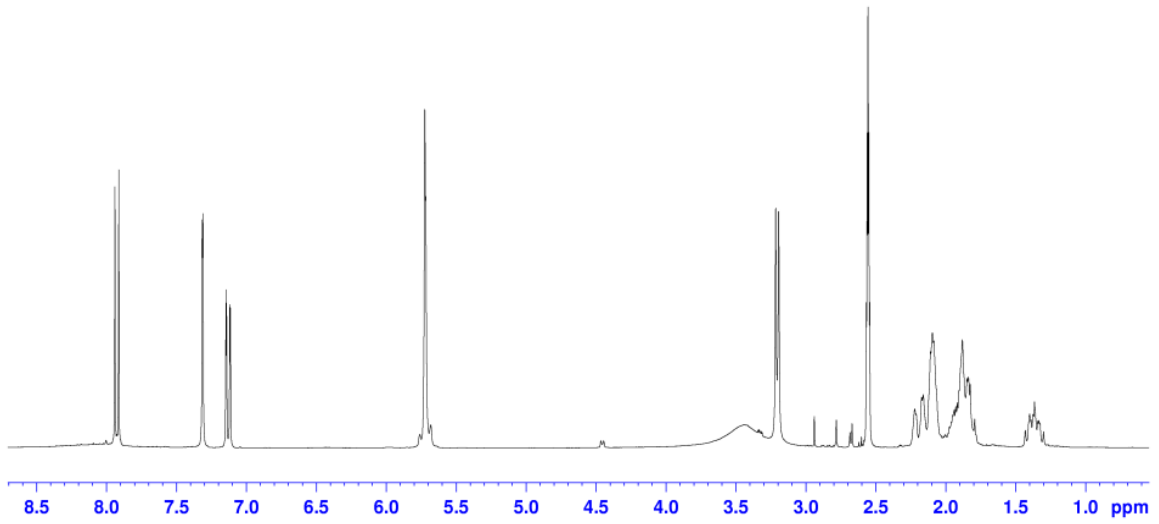

Figure 2.63. ^{1}H NMR spectrum for $H_2BDC\text{-}NHC_7H_{11}$ in DMSO-d_6.

2.10.6. 2-((Ferrocenylmethyl)amino)terephthalic acid, $H_2BDC\text{-}NHCH_2fc$, 4f

2-Aminobenzene-1,4-dicarboxylic acid ($H_2BDC\text{-}NH_2$) (0.200 g, 1.104 mmol) was dissolved in DMF (10 cm^3), then ferrocenecarboxaldehyde (0.473 g, 2.208 mmol) was added and the solution stirred at room temperature for 1 h under N_2. The solution was then cooled in an ice bath and $NaCNBH_3$ (0.139 g, 2.204 mmol) was added. The resulting reaction mixture was stirred at room temperature for 24 h. Water was added until a yellow/brown solid precipitated which was filtered, washed with 3 x 5 cm^3 H_2O and dried in an oven at 80 °C for 1 h. The compound was recrystallised from DMF/H_2O. Yield: 0.323 g (77 %). ^{1}H NMR (300 MHz, DMSO-d_6) δ/ppm: 7.88 (d (br), 1H), 7.31 (s (br), 1H), 7.08 (d (br), 1H), 4.25 (br, 2H), 4.23 (br, 5H) 4.16 (br, 2H), 4.07 (br, 2H). ^{13}C NMR (75 MHz, DMSO-d_6) δ/ppm: 170.0, 167.5, 136.2, 132.4, 114.9, 113.4, 112.4, 85.9, 83.7, 69.6,

69.2, 68.9, 68.7, 67.9, 67.7, 67.2, 41.7, 15.0. *m/z* (ESI) 378.0432 ([M – H]$^-$. $[C_{19}H_{16}O_4NFe]^-$ requires 378.0434). Found C: 61.10, H: 4.88, N: 3.06 %. $C_{19}H_{17}O_4NFe$ requires C: 60.18, H: 4.52, N: 3.69 %.

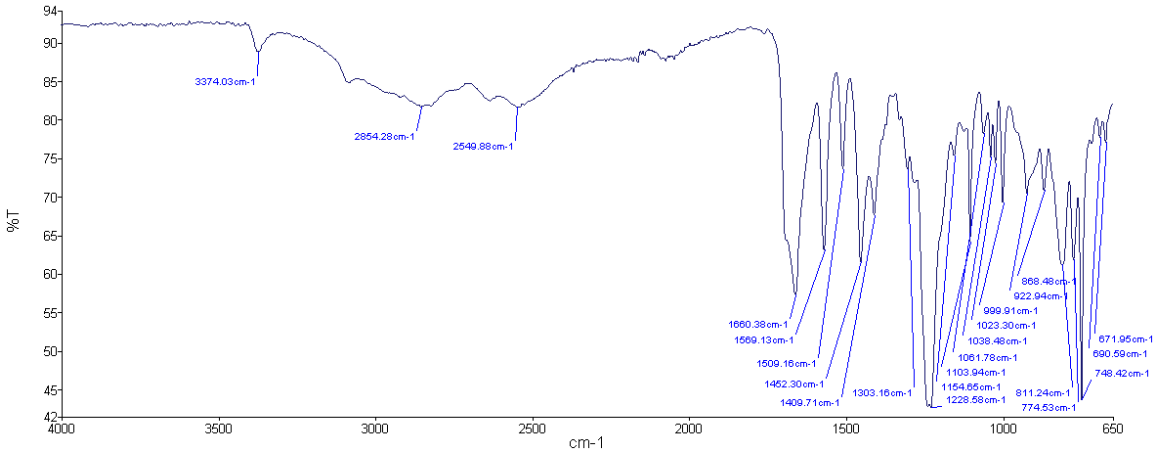

Figure 2.64. Infrared spectrum for H_2BDC-NHCH$_2$Fc, **4f**.

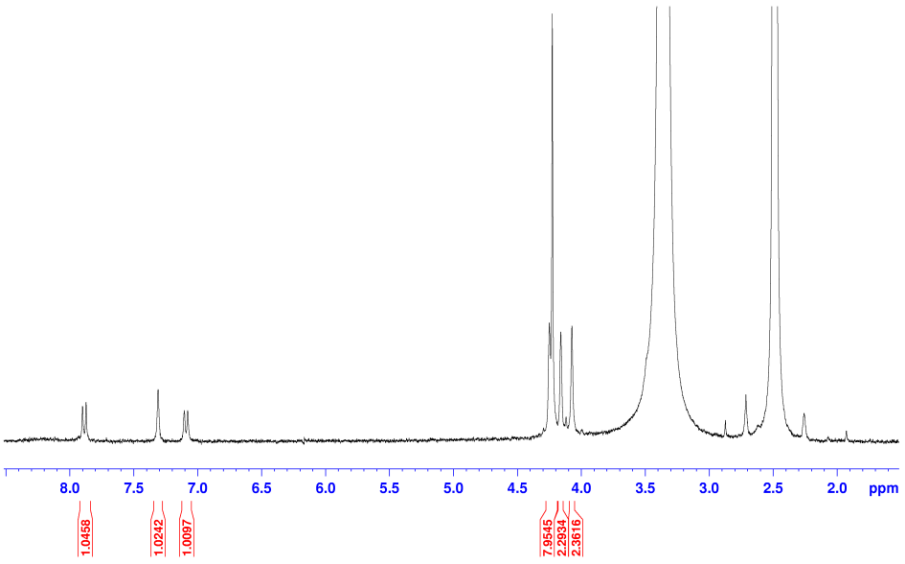

Figure 2.65. ^{1}H NMR spectrum for H_2BDC-NHCH$_2$Fc in DMSO-d_6.

2.10.7. 2-((4-(Methylthio)benzyl)amino)terephthalic acid, H_2BDC-NHCH$_2$C$_6$H$_4$SMe, 4g

2-Aminobenzene-1,4-dicarboxylic acid (H_2bdc-NH_2) (0.200 g, 1.104 mmol) was dissolved in *N*,*N*'-dimethylformamide (DMF) (10 cm^3), then 4-methylthiobenzaldehyde (0.294 cm^3, 2.208 mmol) was added and the solution stirred at room temperature for 1 h. The solution was then cooled in an ice bath and $NaCNBH_3$ (0.139 g, 2.204 mmol) was added. The resulting reaction mixture was stirred at room temperature for 24 h. The mixture was

acidified with 1 M HCl, and water was added until a yellow solid precipitated which was filtered, washed with 3 x 5 cm^3 H_2O and dried in an oven at 80 °C for 1 h. The compound was recrystallised from DMF/H_2O. Yield: 0.174 g (50 %). ^{1}H NMR (300 MHz, DMSO-d_6) δ/ppm: 7.87 (d, 1H, J = 8.2 Hz), 7.25 (m, 4H), 7.17 (d, 1H, J = 1.4 Hz), 7.07 (dd, 1H, J = 8.2, 1.5 Hz), 4.44 (s(br) 2H), 2.43 (s, 3H). ^{13}C NMR (75 MHz, DMSO-d_6) δ/ppm: 169.8, 167.4, 150.6, 136.9, 136.0 (2C), 132.3, 128.0 (2C), 126.5 (2C), 115.2, 113.9, 112.7, 45.7, 15.0. *m/z* (ESI) 316.0644 ([M – H]$^-$. $[C_{16}H_{14}O_4NS]^-$ requires 316.0649). Found C: 60.10, H: 4.76, N: 4.50 %. $C_{16}H_{15}O_4NS$ requires C: 60.55, H: 4.76, N: 4.41 %.

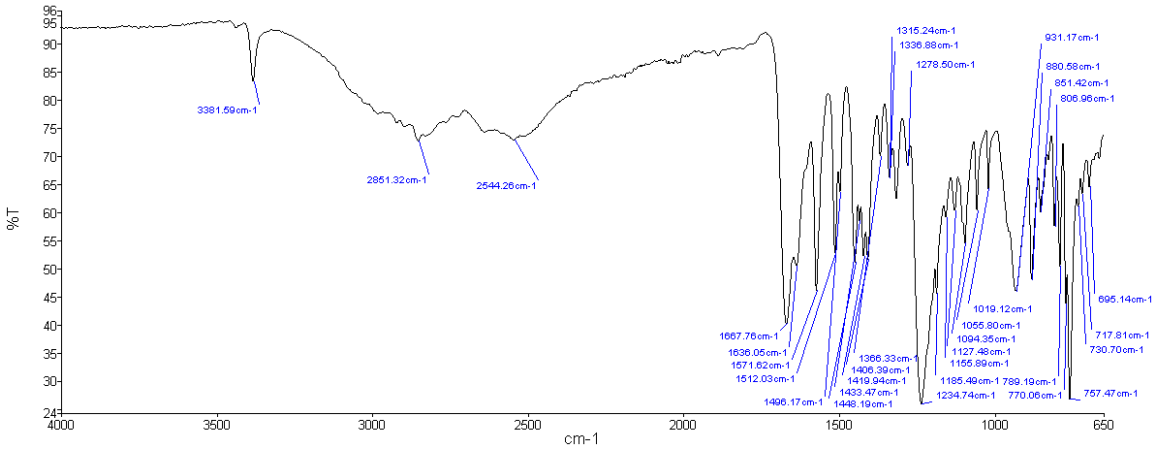

Figure 2.66. Infrared spectrum for H_2BDC-NHCH$_2$C$_6$H$_4$SMe, **4g**.

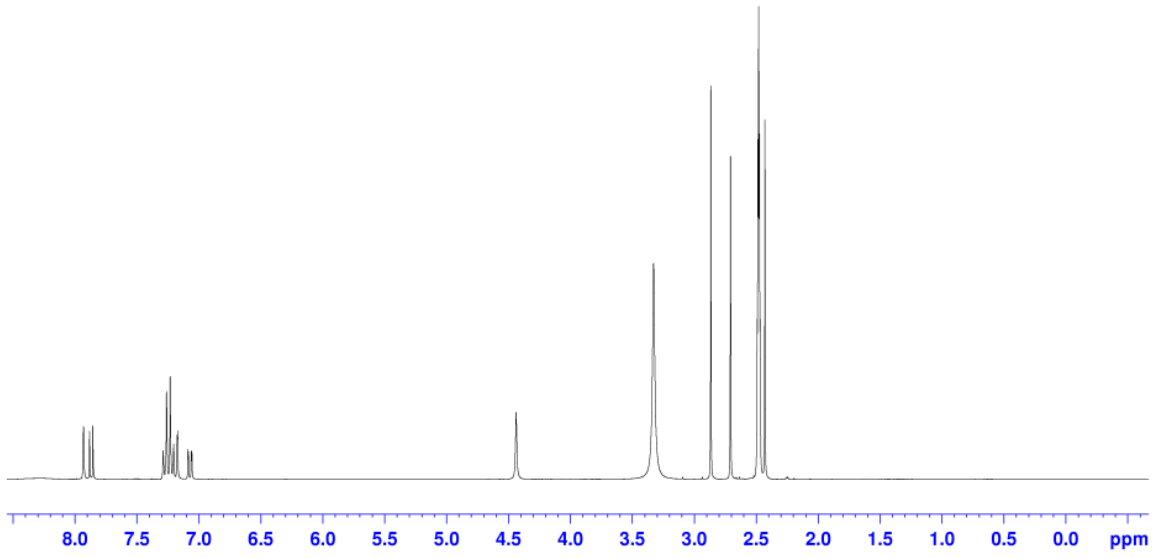

Figure 2.67. ^{1}H NMR spectrum for H_2BDC-NHCH$_2$C$_6$H$_4$SMe in DMSO-d_6.

2.11. Experimental: Direct IRMOF-3-CH_2R Synthesis

PXRD data for **5a-g** is located in Appendix A.

2.11.1. IRMOF-3-Et (93%), $[Zn_4O(BDC\text{-}NH_2)_{0.12}(BDC\text{-}NHEt)_{2.88}]\cdot 7Tol$, 5a

Ligand **4a**, (46.2 mg, 0.224 mmol, 1 eq.) was dissolved in 5 mL DMF and to this was added $Zn(NO_3)_2\cdot 6H_2O$ (200 mg, 0.672 mmol, 3 eq.). After the mixture was stirred for 30 minutes, the stirrer is removed and the vessel sealed and placed in an oven set at 105 °C for 48 h. The resulting yellow-orange crystalline product was washed once per day for three days with DMF and a further once per day for three days with toluene and finally stored in toluene. Yield = 28.8 mg.

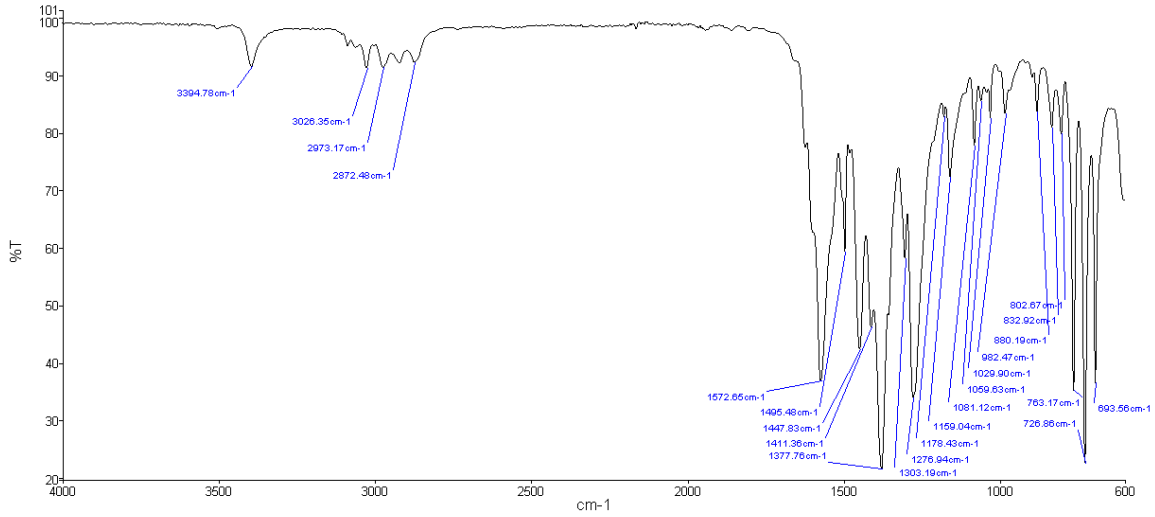

Figure 2.68. *In situ* FT-IR spectrum for **5a**.

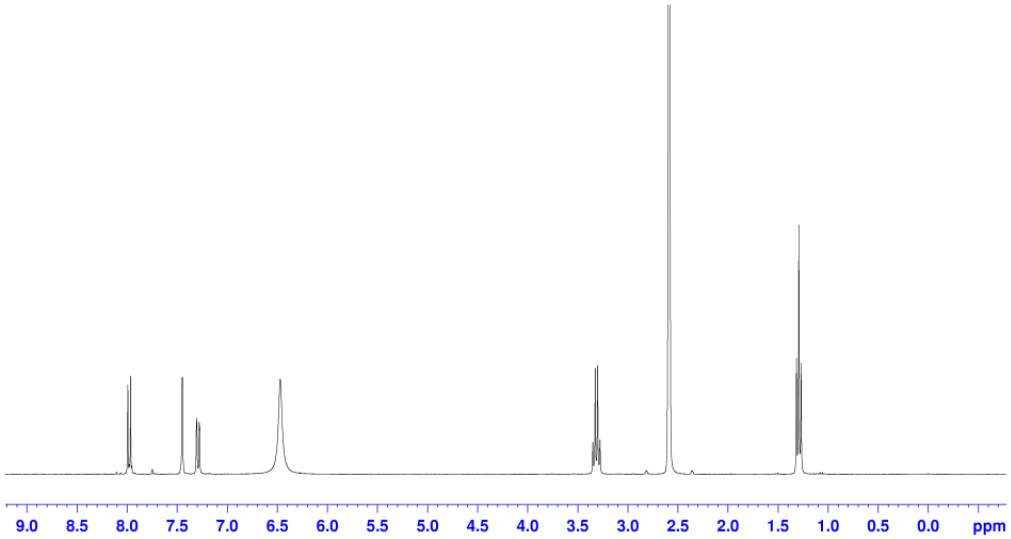

Figure 2.69. ^{1}H NMR spectrum for digested **5a** in DMSO-d_6.

2.11.2. IRMOF-3-Pr (92 %), $[Zn_4O(BDC\text{-}NH_2)_{0.21}(BDC\text{-}NHPr)_{2.79}]\cdot 6.3Tol$, 5b

Ligand **4b**, (30 mg, 0.134 mmol, 1 eq.) was dissolved in 5 mL DMF and to this was added $Zn(NO_3)_2\cdot 6H_2O$ (120 mg, 0.402 mmol, 3 eq.). After the mixture was stirred for 30 minutes, the stirrer is removed and the vessel sealed and placed in an oven set at 105 °C for 48 h. The resulting yellow-orange crystalline product, **5b**, was washed once per day for three days with DMF and a further once per day for three days with toluene and finally stored in toluene. Yield = 26.8 mg.

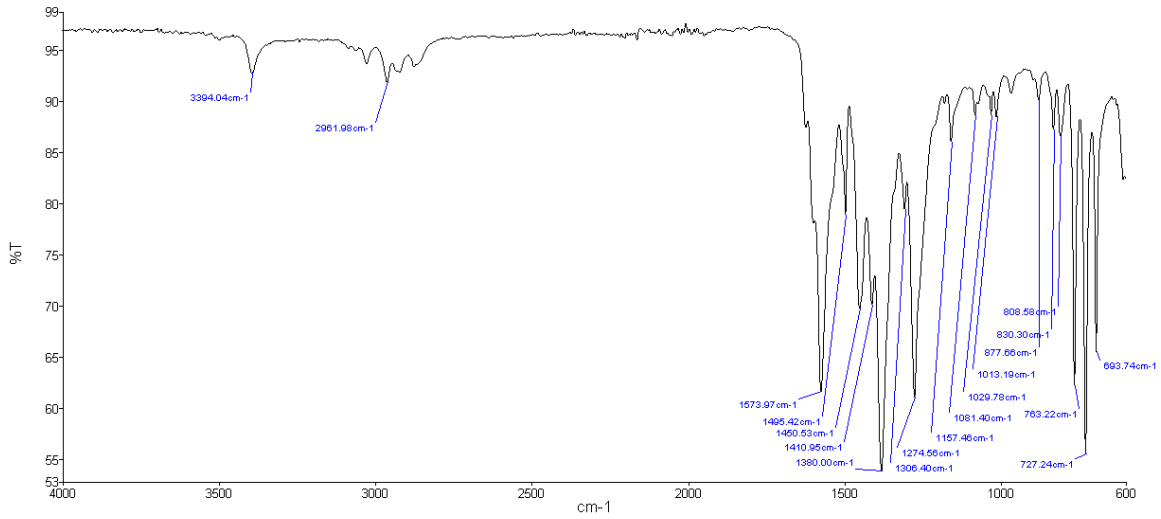

Figure 2.70. *In situ* FT-IR spectrum for **5b**.

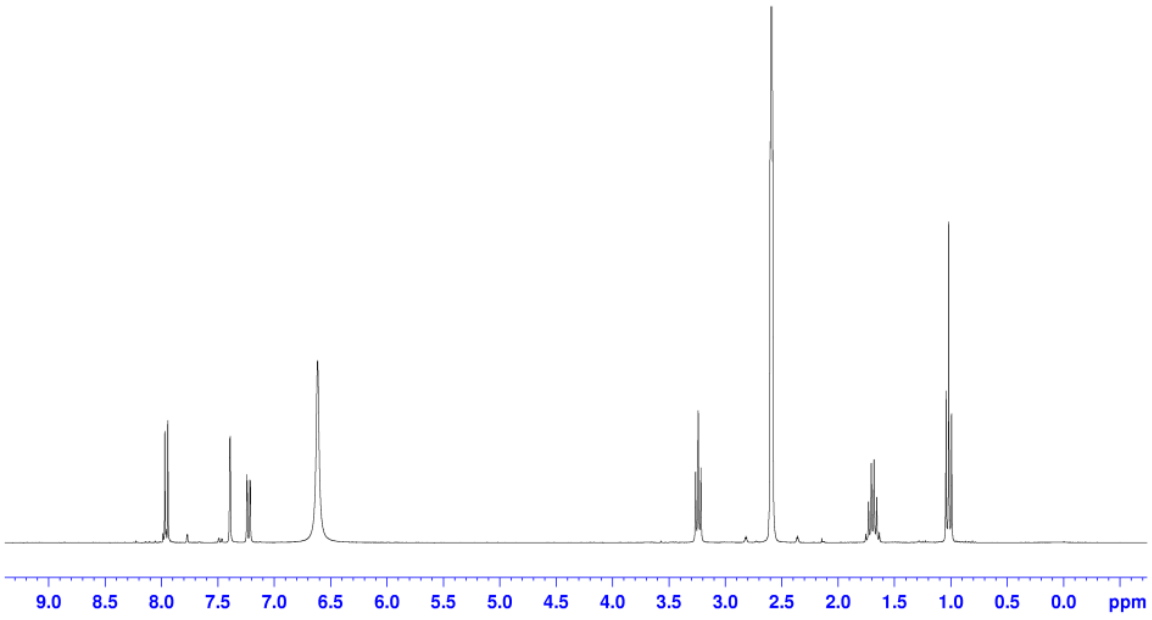

Figure 2.71. ^{1}H NMR spectrum for digested **5b** in DMSO-d_6.

2.11.3. IRMOF-3-Bu (93 %), $[Zn_4O(BDC\text{-}NH_2)_{0.24}(BDC\text{-}NHBu)_{2.76}]\cdot 5.5Tol$, 5c

Ligand **4c**, (30 mg, 0.126 mmol, 1 eq.) was dissolved in 5 mL DMF and to this was added $Zn(NO_3)_2\cdot 6H_2O$ (112 mg, 0.378 mmol, 3 eq.). After the mixture was stirred for 30 minutes, the stirrer is removed and the vessel sealed and placed in an oven set at 105 °C for 48 h. The resulting yellow-orange crystalline product was washed once per day for three days with DMF and a further once per day for three days with toluene and finally stored in toluene. Yield = 28.6 mg.

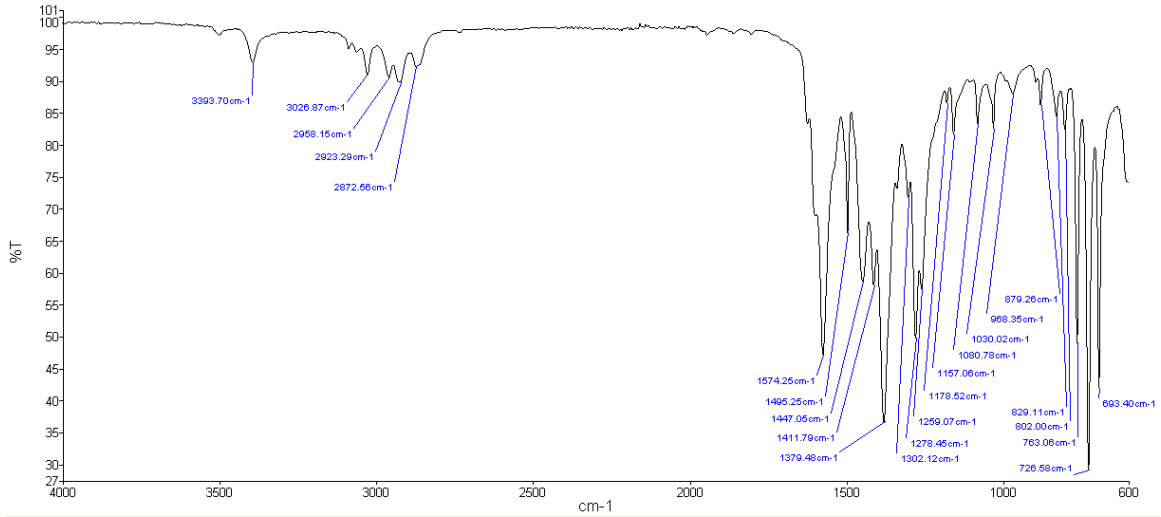

Figure 2.72. *In situ* FT-IR spectrum for **5c**.

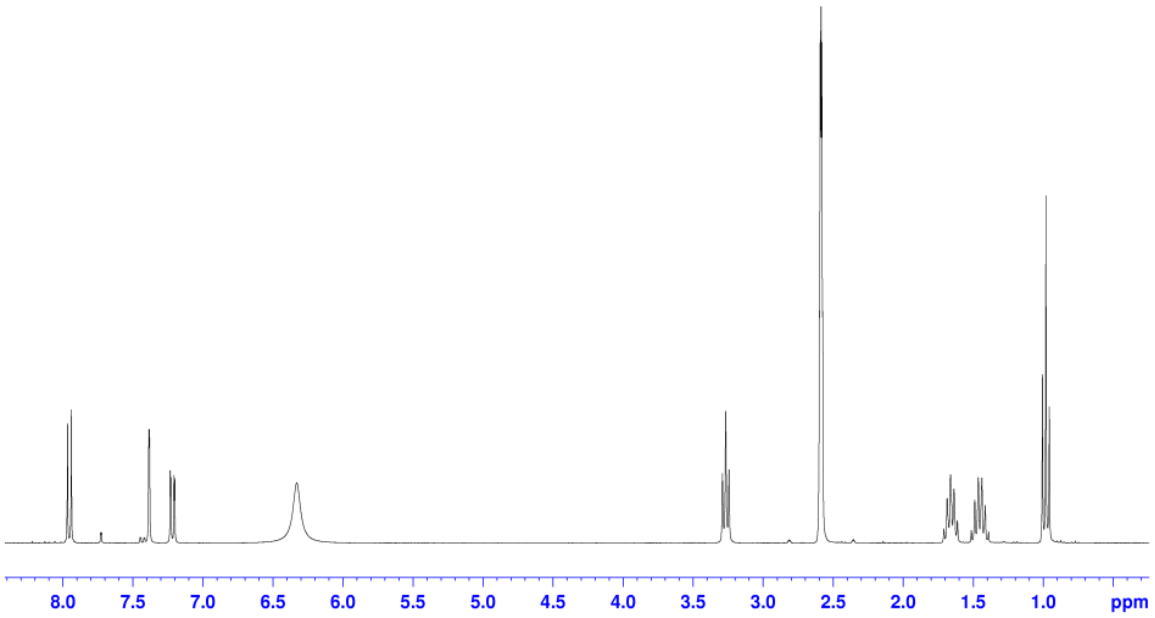

Figure 2.73. ^{1}H NMR spectrum for digested **5c** in DMSO-d_6.

2.11.4. IRMOF-3-C_8H_{17} (93 %), $[Zn_4O(BDC\text{-}NH_2)_{0.21}(BDC\text{-}NHC_8H_{17})_{2.79}]\cdot 4.5Tol$, 5d

Ligand **4d**, (30 mg, 0.102 mmol, 1 eq.) was dissolved in 5 mL DMF and to this was added $Zn(NO_3)_2\cdot 6H_2O$ (91 mg, 0.306 mmol, 3 eq.). After the mixture was stirred for 30 minutes, the stirrer is removed and the vessel sealed and placed in an oven set at 105 °C for 48 h. The resulting yellow-orange crystalline product was washed once per day for three days with DMF and a further once per day for three days with toluene and finally stored in toluene. Yield = 19.4 mg.

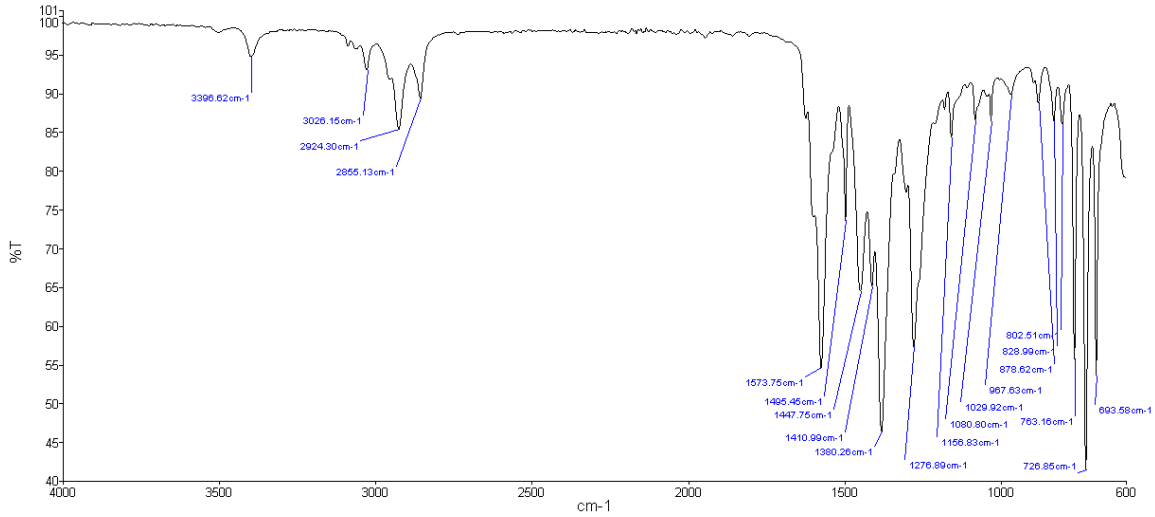

Figure 2.74. *In situ* FT-IR spectrum for **5d**.

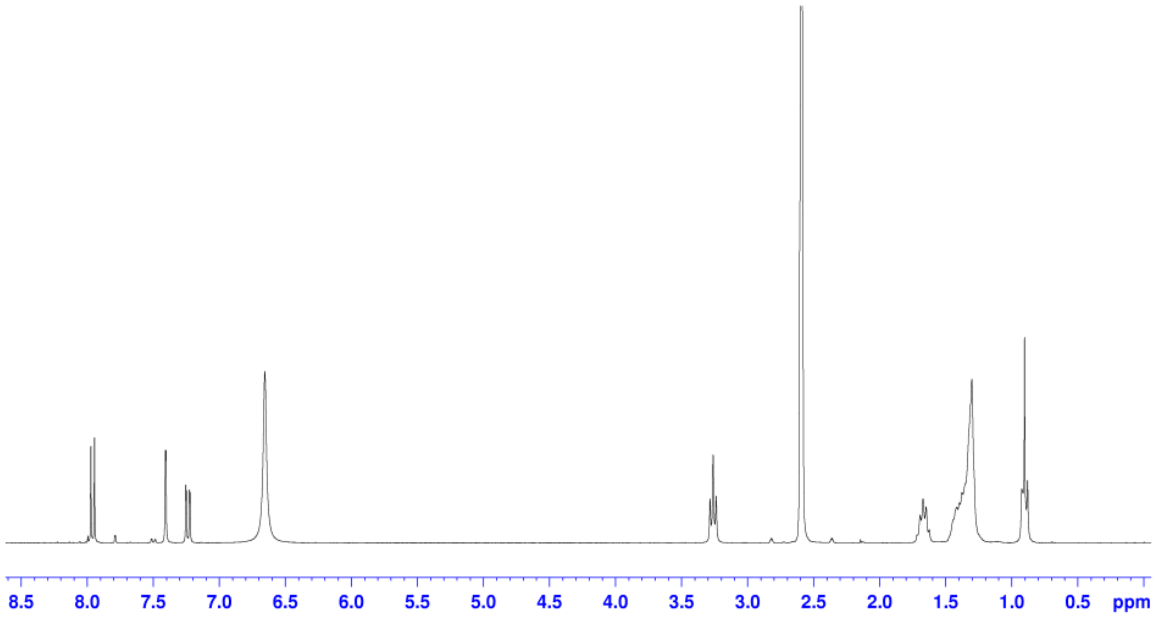

Figure 2.75. ^{1}H NMR spectrum for digested **5d** in DMSO-d_6.

2.11.5. IRMOF-3-C_7H_{11} (88 %), $[Zn_4O(BDC\text{-}NH_2)_{0.36}(BDC\text{-}NHCH_2C_6H_9)_{2.64}]\cdot 4.5Tol$, 5e

Ligand **4e**, (30 mg, 0.109 mmol, 1 eq.) was dissolved in 5 mL DMF and to this was added $Zn(NO_3)_2\cdot 6H_2O$ (97 mg, 0.327 mmol, 3 eq.). After the mixture was stirred for 30 minutes, the stirrer is removed and the vessel sealed and placed in an oven set at 105 °C for 48 h. The resulting yellow-orange crystalline product was washed once per day for three days with DMF and a further once per day for three days with toluene and finally stored in toluene. Yield = 19.7 mg.

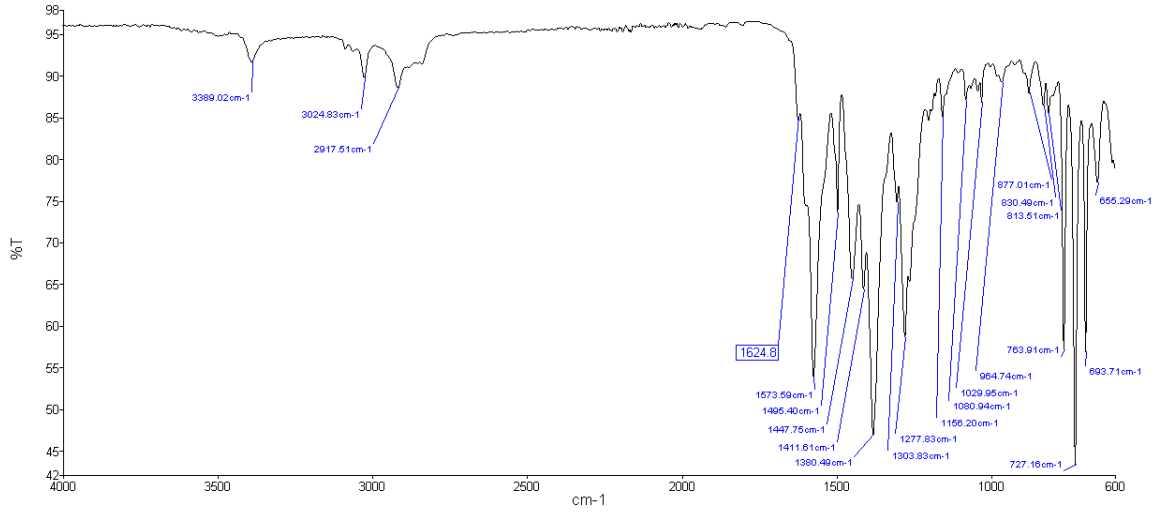

Figure 2.76. *In situ* FT-IR spectrum for **5e**.

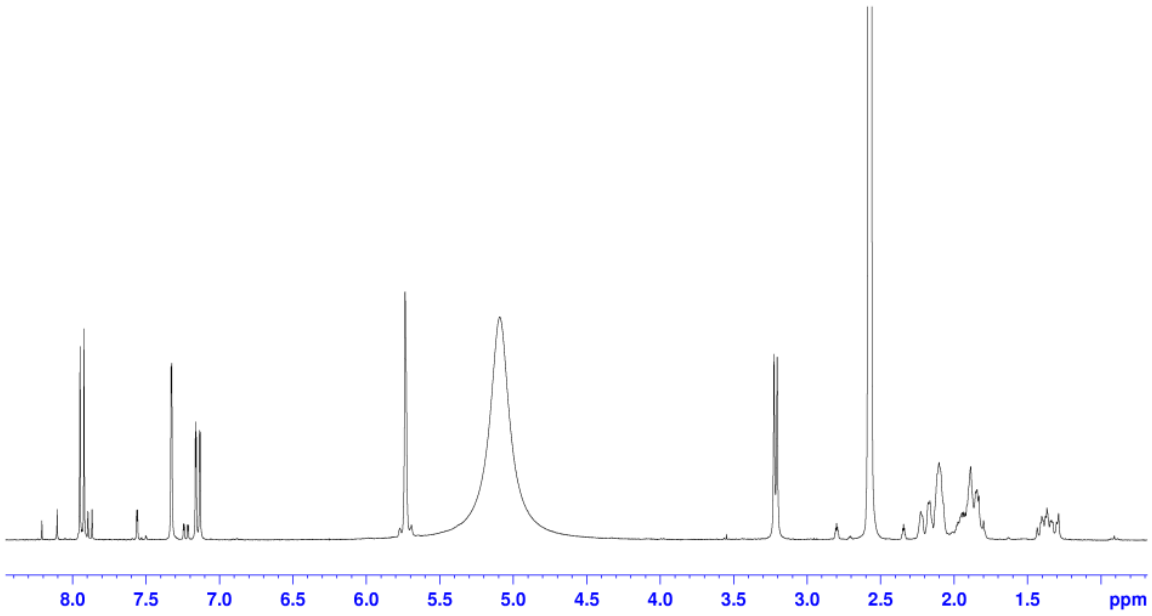

Figure 2.77. ^{1}H NMR spectrum for digested **5e** in DMSO-d_6.

2.11.6. IRMOF-3-CH_2Fc (20 %), $[Zn_4O(BDC\text{-}NH_2)_{2.4}(BDC\text{-}NHCH_2Fc)_{0.6}]\cdot 6Tol$, 5f

Ligand **4f** (75 mg, 0.197 mmol, 3.5 eq.) and $H_2BDC\text{-}NH_2$ 12 %, (10 mg, 0.056 mmol, 1 eq.) was dissolved in 5 mL DMF and to this was added $Zn(NO_3)_2\cdot 6H_2O$ (200 mg, 0.672 mmol, 12 eq.). After the mixture was stirred for 30 minutes, the stirrer is removed and the vessel sealed and placed in an oven set at 105 °C for 48 h. The resulting yellow-orange crystalline product was washed once per day for three days with DMF and a further once per day for three days with toluene and finally stored in toluene. Atomic absorption spectrometry = Fe:Zn 1:5.4 (predicted 1:7.8) . Yield = 14.6 mg.

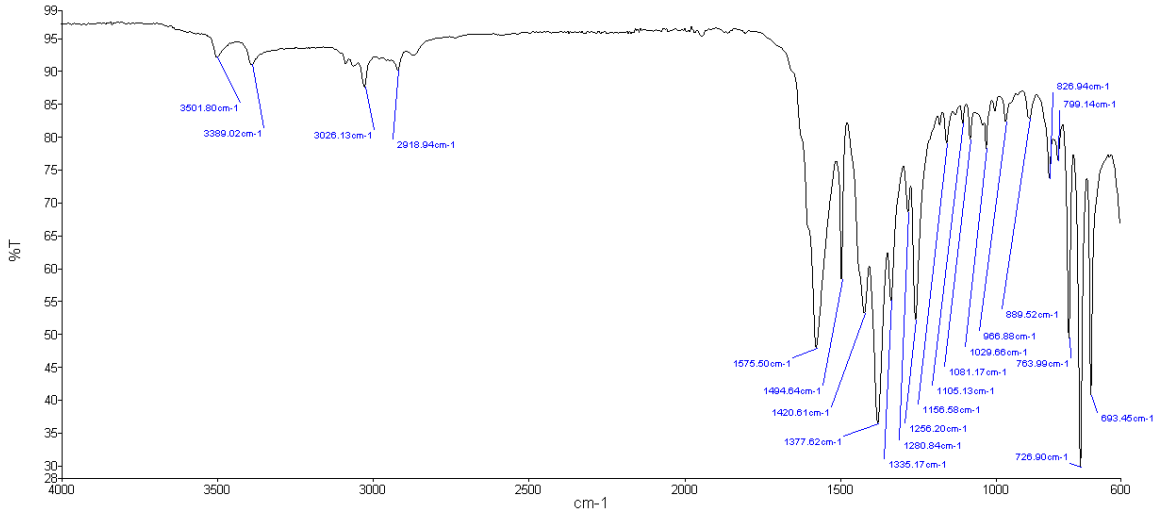

Figure 2.78. *In situ* FT-IR spectrum for **5f**.

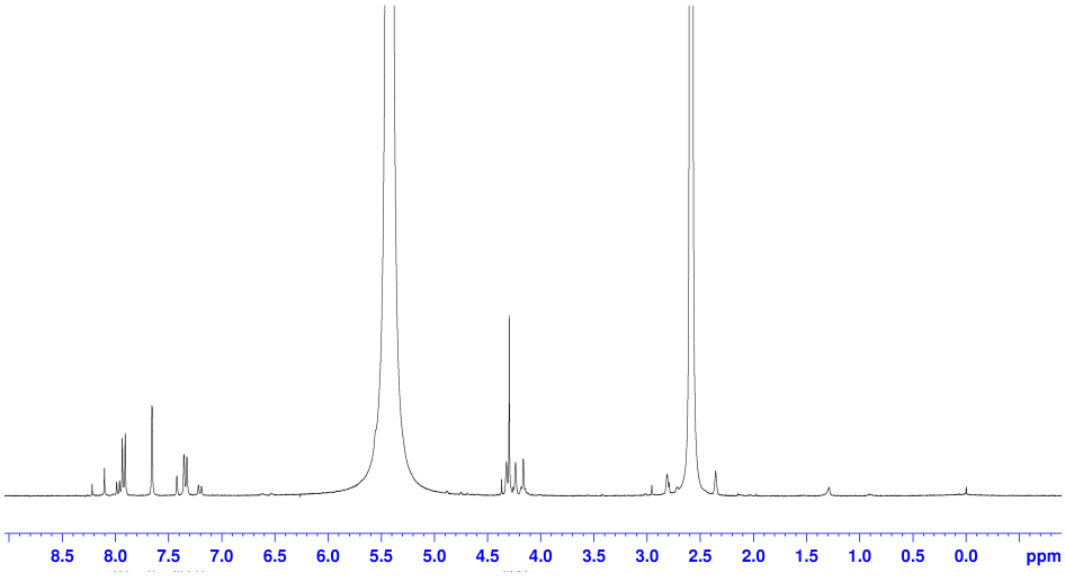

Figure 2.79. ^{1}H NMR spectrum for digested **5f** in DMSO-d_6.

2.11.7. IRMOF-3-C_6H_4SMe (65 %), $[Zn_4O(BDC\text{-}NH_2)_{1.05}(BDC\text{-}NHCH_2C_6H_4SMe)_{1.95}]\cdot 5.5Tol$, 5g

Ligand **4g**, (30 mg, 0.095 mmol, 1 eq.) was dissolved in 5 mL DMF and to this was added $Zn(NO_3)_2\cdot 6H_2O$ (84.4 mg, 0.284 mmol, 3 eq.). After the mixture was stirred for 30 minutes, the stirrer is removed and the vessel sealed and placed in an oven set at 105 °C for 48 h. The resulting yellow-orange crystalline product was washed once per day for three days with DMF and a further once per day for three days with toluene and finally stored in toluene. Yield = 24.6 mg.

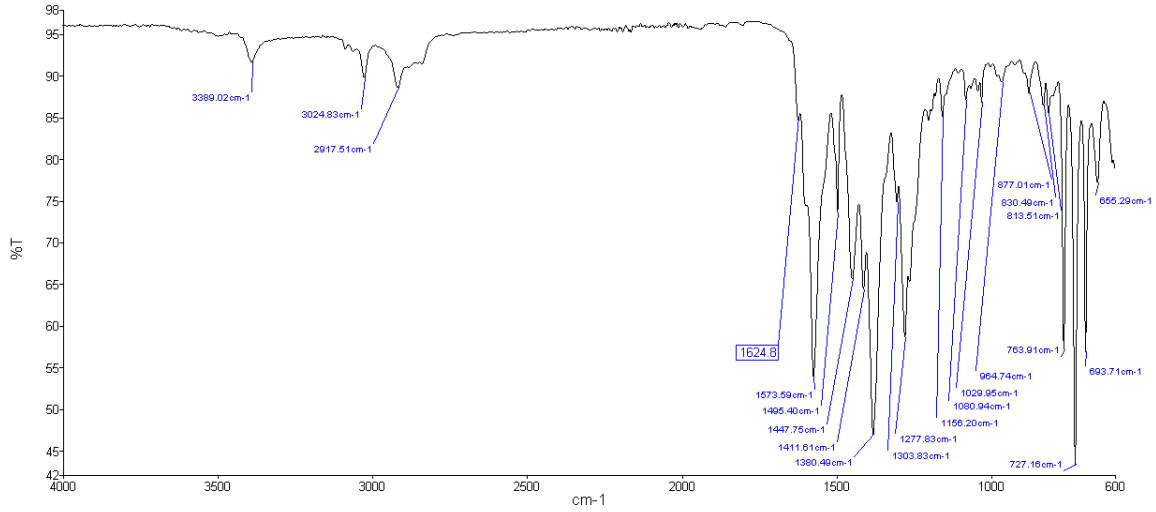

Figure 2.80. *In situ* FT-IR spectrum for **5g**.

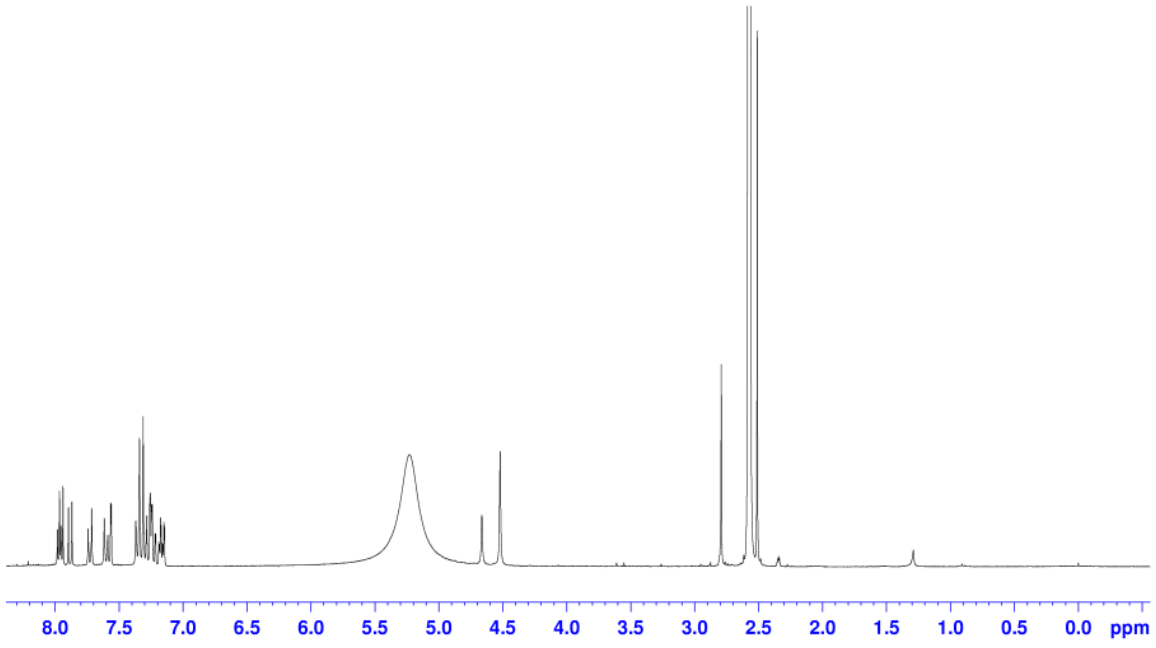

Figure 2.81. ^{1}H NMR spectrum for digested **5g** in DMSO-d_6.

2.12. Experimental: tandem PSM reaction of MIL-101(Cr)-$NHCH_2R$

The general PSM procedure requires MeOH exchanged MIL-101(Cr)-NH_2 and is synthesised according to a modified preparation by Burrows *et al.*[17] Under 5 mL MeOH add aldehyde (4 equiv.) and $NaCNBH_3$ (4 equiv.). Hydrolysis of the borohydride occurs with evolution of $H_{2(g)}$ therefore leave for 30 minutes to allow for $H_{2(g)}$ production to cease under a flow of $N_{2(g)}$. Heat to 50 °C for 72 hours with no stirring. Remove and cool to ambient temperature. Rinse with MeOH and then EtOH for 3 days by centrifuge at 11000 rpm replacing with fresh EtOH every 24 h. Dry MIL-101(Cr)-NHR in a flow of $N_{2(g)}$ at room temperature.

2.12.1. MIL-101(Cr)-NHEt (51 %), $[Cr_3O(OH)(OH_2)_2(BDC\text{-}NH_2)_{1.47}(BDC\text{-}NHEt)_{1.53}]\cdot 3EtOH$, 7a

MIL-101(Cr)-NH_2·7EtOH was washed with solvent (MeOH) for 3 days with fresh solvent every 24 h. In a 6 mL Biotage microwave vial, ~75 mg MIL-101(Cr)-NH_2 (0.295 mmol NH_2eq) was added to 5 mL MeOH. This was cooled in an ice bath to less than 5 °C. Ethanal (66 µL, 1.18 mmol, 4 eq.) and then $NaCNBH_3$ (74 mg, 1.18 mmol, 4 eq.) were added to this mixture. After 30 minute effervescence the mixture was sealed and heated to 50 °C for 72 hours, no stirring, before being removed from the oven and cooled to ambient temperature. The product was rinsed with MeOH. The resulting green micro-crystals were then washed in EtOH once per day for three days and dried under a flow of $N_{2(g)}$.

m/z = 208.0618 (predicted $[C_{10}H_{10}NO_4]^-$, $[M\text{-}H]^-$ = 208.0615).

2.12.2. MIL-101(Cr)-NHPr (49 %), $[Cr_3O(OH)(OH_2)_2(BDC\text{-}NH_2)_{1.53}(BDC\text{-}NHPr)_{1.47}]\cdot 1.5EtOH$, 7b

MIL-101(Cr)-NH_2·7EtOH was washed with solvent (MeOH) for 3 days with fresh solvent every 24 h. In a 6 mL Biotage microwave vial, ~75 mg MIL-101(Cr)-NH_2 (0.295 mmol NH_2eq) was added to 5 mL MeOH. Propanal (86 µL, 1.18 mmol, 4 eq.) and then $NaCNBH_3$ (74 mg, 1.18 mmol, 4 eq.) were added to this mixture. After 30 minute effervescence the mixture was sealed and heated to 50 °C for 72 hours, no stirring, before being removed from the oven and cooled to ambient temperature. The product was rinsed with MeOH. The resulting green micro-crystals were then washed in EtOH once per day for three days and dried under a flow of $N_{2(g)}$.

m/z = 222.0768 (predicted $[C_{11}H_{12}NO_4]^-$, $[M\text{-}H]^-$ = 222.0766).

2.12.3. MIL-101(Cr)-NHBu (45 %), $[Cr_3O(OH)(OH_2)_2(BDC\text{-}NH_2)_{1.65}(BDC\text{-}NHBu)_{1.35}]\cdot 3EtOH$, 7c

MIL-101(Cr)-NH_2·7EtOH was washed with solvent (MeOH) for 3 days with fresh solvent every 24 h. In a 6 mL Biotage microwave vial, ~75 mg MIL-101(Cr)-NH_2 (0.295 mmol NH_2eq) was added to 5 mL MeOH. Butanal (104 µL, 1.18 mmol, 4 eq.) and then $NaCNBH_3$ (74 mg, 1.18 mmol, 4 eq.) were added to this mixture. After 30 minute effervescence the mixture was sealed and heated to 50 °C for 72 hours, no stirring, before being removed from the oven and cooled to ambient temperature. The product was rinsed with MeOH. The resulting green micro-crystals were then washed in EtOH once per day for three days and dried under a flow of $N_{2(g)}$.

m/z = 236.0916 (predicted $[C_{12}H_{14}NO_4]^-$, $[M\text{-}H]^-$ = 236.0923).

2.12.4. MIL-101(Cr)-NHC_8H_{17} (35 %), $[Cr_3O(OH)(OH_2)_2(BDC\text{-}NH_2)_{1.95}(BDC\text{-}NHC_8H_{17})_{1.05}]\cdot 2EtOH$, 7d

MIL-101(Cr)-NH_2·7EtOH was washed with solvent (MeOH) for 3 days with fresh solvent every 24 h. In a 6 mL Biotage microwave vial, ~75 mg MIL-101(Cr)-NH_2 (0.295 mmol NH_2eq) was added to 5 mL MeOH. Octanal (184 µL, 1.18 mmol, 4 eq.) and then $NaCNBH_3$ (74 mg, 1.18 mmol, 4 eq.) were added to this mixture. After 30 minute effervescence the mixture was sealed and heated to 50 °C for 48 hours, no stirring, before being removed from the oven and cooled to ambient temperature. The product was rinsed with MeOH. The resulting green micro-crystals were then washed in EtOH once per day for three days and dried under a flow of $N_{2(g)}$.

m/z = 292.1549 (predicted $[C_{16}H_{22}NO_4]^-$, $[M\text{-}H]^-$ = 292.1554).

2.13. References

[1] J. Canivet, S. Aguado, C. Daniel, D. Farrusseng, *ChemCatChem,* **2011**, *3*, 675.
[2] Y. Yoo, H. K. Jeong, *Chem. Eng. J.,* **2012**, *182*, 740.
[3] J. S. Seo, D. Whang, H. Lee, S. I. Jun, J. Oh, Y. J. Jeon, K. Kim, *Nature*, **2000**, *404*, 982.
[4] G. Férey, C. Mellot-Draznieks, C. Serre, F. Millange, J. Dutour, S. Surblé, I. Margiolaki, *Science*, **2005**, *309*, 2040.
[5] K. M. L. Taylor-Pashow, J. D. Rocca, Z. Xie, S. Tran, W. Lin, *J. Am. Chem. Soc.*, **2009**, *131*, 14261.
[6] W. Morris, C. J. Doonan, O. M. Yaghi, *Inorg. Chem.,* **2011**, *50*, 6853.
[7] S. M. Cohen, *Chem. Rev.*, **2012**, *112*, 970.
[8] K. K. Tanabe, Z. Wang, S. M. Cohen, *J. Am. Chem. Soc.*, **2008**, *130*, 8508.

[9] M. Servalli, M. Ranocchiari, J. A. Van Bokhoven, *Chem. Commun.*, **2012**, *48*, 1904.
[10] C. E. Housecroft, A. G. Sharpe, *Inorganic Chemistry*, 2nd ed., Pearson Education Limited, **2005**.
[11] W. Morris, C. J. Doonan, H. Furukawa, R. Banerjee, O. M. Yaghi, *J. Am. Chem. Soc.*, **2008**, *130*, 12626.
[12] A. L. Spek, *J. Appl. Cryst.*, **2003**, *36*, 7.
[13] J. E. Halls, A. Hernan-Gomez, A. D. Burrows, F. Marken, *Dalton Trans.*, **2012**, *41*, 1475.
[14] M. J. Ingleson, J. Perez Barrio, J.-B. Guilbaud, Y. Z. Khimyak, M. J. Rosseinsky, *Chem. Commun.*, **2008**, 2680.
[15] Y. N. Xu, W. Y. Ching, *Phys. Rev. B*, **1993**, *48*, 4335.
[16] D. N. Dybtsev, H. Chun, K. Kim, *Angew. Chem. Int. Ed.*, **2004**, *43*, 5033.
[17] D. Jiang, L. L. Keenan, A. D. Burrows, K. J. Edler, *Chem. Commun.*, **2012**, *48*, 12053.
[18] A. Modrow, D. Zargarani, R. Herges, N. Stock, *Dalton Trans.*, **2012**, *41*, 8690.
[19] S. J. Garibay, S. M. Cohen, *Chem. Commun.*, **2010**, *46*, 7700.

3. PSM of MIL-101(Cr)-NH_2 *via* a Diazonium Intermediate

3.1. Introduction

First reported by Ferey *et al.*, the chromium(III) MOF $[Cr_3O(F,OH)(OH_2)_2(BDC)_3]\cdot nH_2O$, (MIL-101(Cr), n ~ 25), demonstrates high chemical and hydrothermal robustness, even though it contains mesoporous cages, Figure 3.1.[1] Two types of cages are observed in MIL-101(Cr): dodecahedral cages formed by five-membered ring faces (void diameter of 29 Å) and hexadecahedral cages (void diameter of 34 Å) formed by five-membered and six-membered ring faces.[2]

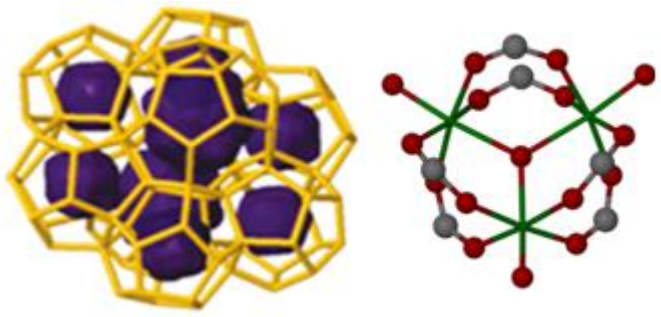

Figure 3.1. (left) Framework of MIL-101(Cr) shown with voids in purple. **(right)** SBU. C: gray, O: red, Cr: green. Refcode: OCUNAC.[1]

PSM reactions of MIL-101(Cr) with strong acids have been used to introduce nitro and sulfoxy acid groups as tags on the BDC ligands of the framework.[3, 4] Fe^{III} and Al^{III} metal based MIL-101 framework topologies are able to be synthesised by direct combination or by post-synthetic cation exchange.[5] The latter was reported by simply refluxing MIL-101(Cr) in an aqueous solution of $FeCl_3\cdot H_2O$ or $AlCl_3$, for three days, to exchange the chromium cations to various degrees of conversion.

Amino tag groups have already been shown to be very useful for a variety of transformations and through the use of $H_2BDC\text{-}NH_2$ they have been introduced into many structures as the linker in MOF synthesis. Stock and co-workers prepared MIL-101(Cr)-NH_2 by tandem post-synthetic modification involving nitration of MIL-101(Cr) followed by reduction from the nitro to the amino tag to give the highest quality crystalline MIL-101(Cr)-NH_2 sample to date.[3] Kong *et al.* have reported that MIL-101(Cr)-NH_2 can be

prepared by a hydroxide-assisted, hydrothermal synthesis in a one-step process, by direct combination of chromium(III) nitrate and H_2BDC-NH_2.[6]

Modification of the amino group in MIL-101(Cr)-NH_2 may lead to new functionalities not accessible from the direct combination, especially under some of the harsh synthetic conditions reported with HF. Focusing on the covalent modification of the amino tag groups of MIL-101(Cr)-NH_2 an example from the literature was the PSM reaction with salicylaldehyde and cobalt acetate. Sun *et al.* reported conversion to the imine tagged MOF MIL-101(Cr)-NH_2-Sal and complexation of cobalt(II) ions between tag groups therein, as summarised in Scheme 3.1.[7]

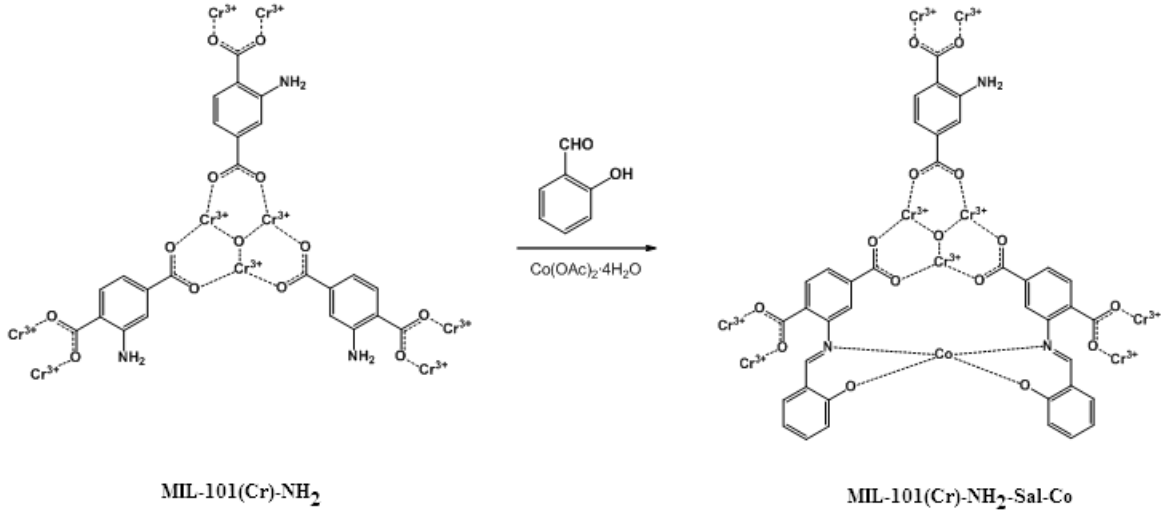

Scheme 3.1. Tandem PSM of MIL-101(Cr)-NH_2 to MIL-101(Cr)-NH_2-Sal-Co using the PSM reagents salicylaldehyde and cobalt acetate tetrahydrate.[7]

MIL-101(Cr)-NH_2-Sal-Co showed increased catalytic activity for the oxidation of cyclohexene to cyclohexanone *via* cyclohexanol (36.1 % over 6 h), with the cobalt(II) sites reported to be responsible for increasing activity.

3.2. A New Synthetic Route to MIL-101(Cr)-NH_2

MIL-101(Cr)-NH_2 was synthesised hydrothermally from an equimolar ratio of $Cr(NO_3)_3{\cdot}9H_2O$:H_2BDC-NH_2 at 130 °C for 24 h, Scheme 3.2.[8] This yields a green nanocrystalline compound and was characterised as $Cr_3O(OH)(OH_2)_2(BDC\text{-}NH_2)_3]{\cdot}nH_2O$, MIL-101(Cr)-$NH_2$ (**8**). The advantages of this synthetic pathway are a simple one-step process and HF not required.

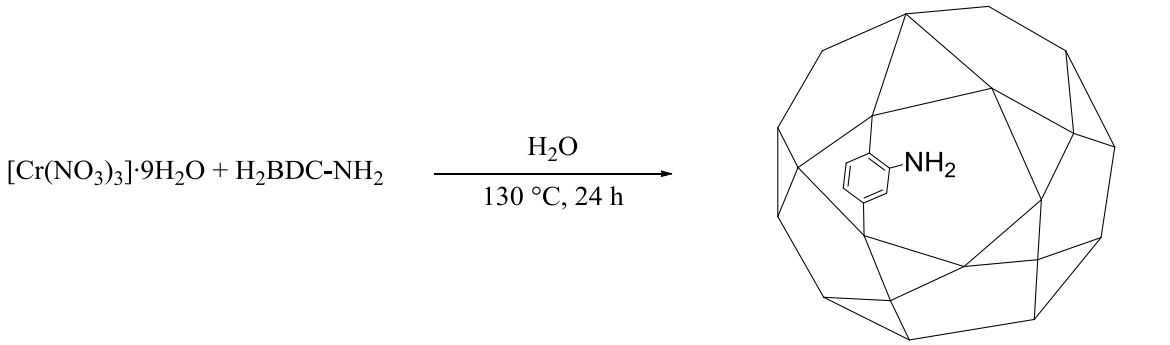

Scheme 3.2. Reaction conditions for the synthesis of MIL-101(Cr)-NH_2, **8**. Each vertex represents a $[Cr_3O(OH)(OH_2)_2(O_2CR)]$ SBU and each side denotes a BDC-NH_2 linker.

Powder X-ray diffraction was used to investigate the structure of this material, which confirmed the formation of the MOF topology. This was verified as the PXRD pattern is similar to the simulated pattern calculated from the MIL-101(Cr) crystal structure (Figure. 3.2). Broad peaks were seen in the PXRD as a consequence of a small particle size and not thought to be due to crystal strain issues. This is consistent with the results of Kong *et al*., and supported by TEM and SEM images (Figure 3.3). Analysis of the TEM images revealed that these samples of MIL-101(Cr)-NH_2 had an average particle size of 16 ± 4 nm.

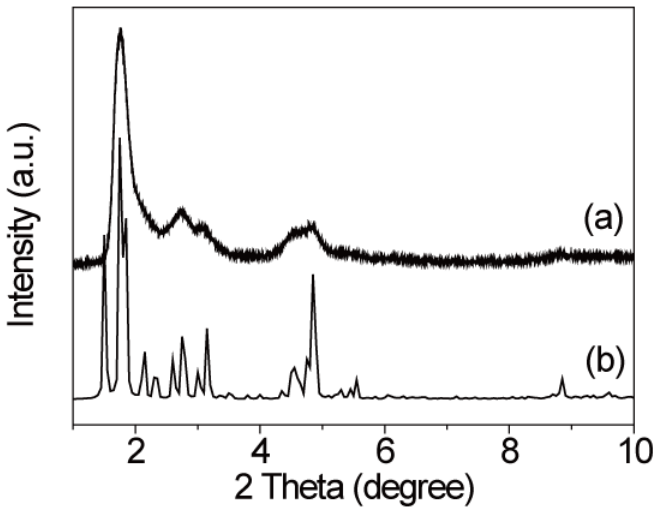

Figure 3.2. (a) High resolution PXRD pattern of **8**, **(b)** the simulated PXRD pattern calculated from the MIL-101(Cr) crystal structure.[8]

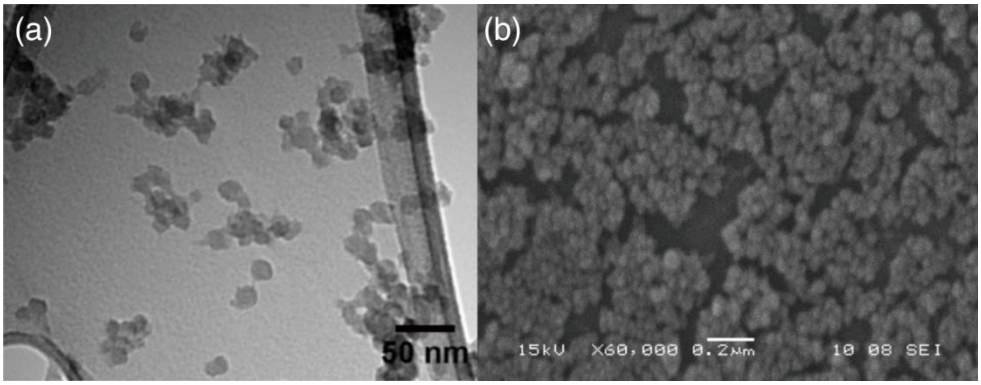

Figure 3.3. (a) TEM image and **(b)** SEM image of **8**.

3.3. The Synthesis of the functionalised MOFs MIL-101(Cr)-F, MIL-101(Cr)-I and MIL-101(Cr)-azo *via* MIL-101(Cr)-$N_2BF_4^-$ and MIL-101(Cr)-$N_2^+Cl^-$

Initially, framework **8** was suspended in an acidic aqueous solution of HBF_4, followed by slow addition of $NaNO_2$ and stirring the resulting mixture for 3 h at 0–5 °C to create a tetrafluoroborate salt pendent group *in situ*. The resultant MOF had the formula, MIL-101(Cr)-$N_2BF_4^-$, **9a**. This was heated at 100 °C for 18 h to eliminate nitrogen in a Balz–Schiemann reaction, yielding MIL-101(Cr)-F, **10a** (Scheme 3.3).

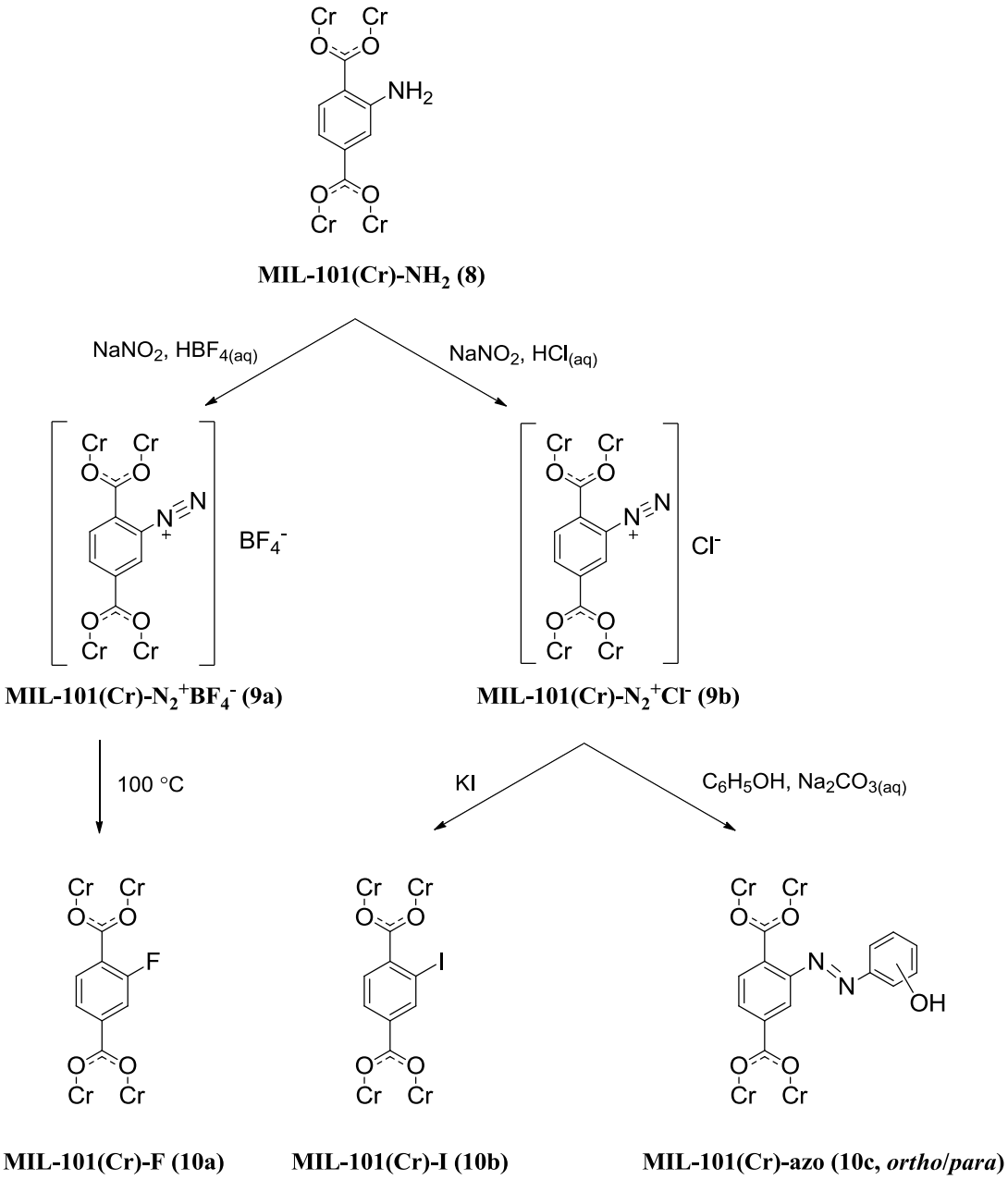

MIL-101(Cr)-NH_2 (8)

MIL-101(Cr)-$N_2^+BF_4^-$ (9a) **MIL-101(Cr)-$N_2^+Cl^-$ (9b)**

MIL-101(Cr)-F (10a) **MIL-101(Cr)-I (10b)** **MIL-101(Cr)-azo (10c, *ortho*/*para*)**

Scheme 3.3. General reaction scheme for the tandem PSM reaction of MIL-101(Cr)-NH_2 *via* a diazotisation pathway.

Compound **8** was treated with $NaNO_2$ and HCl to generate the arenediazonium chloride salt, **9b**. An aqueous solution of KI was added into the reaction mixture which was then stirred for 72 h at room temperature, in order to prepare the iodo-functionalised material, MIL-101(Cr)-I, **10b**. To prepare the azo dye-functionalised MIL-101(Cr), an aqueous phenol solution was added to the diazonium chloride, followed by adjustment of the pH to 7.0 by addition of Na_2CO_3. The mixture was stirred for 72 h at room temperature to yield MIL-101(Cr)-azo **10c**, summarised in Table 3.1. All PSM products were separated by

centrifugation with the exception of the diazonium chloride, MIL-101(Cr)-$N_2^+Cl^-$, which was used *in situ* and not isolated, whereas the tetrafluoroborate salt, MIL-101(Cr)-$N_2^+BF_4^-$, was digested in alkaline solution (NaOD/ D2O) and characterised by ^{1}H NMR spectroscopy.

Material	BDC-NH_2/%	BDC-X/%
10a	<1	>99
10b	<1	>99
10c	<1	>99

Table 3.1. Summary of conversion percentages for PSM products **10a**-**c**.

3.4. NMR spectroscopy of MIL-101(Cr)-F (10a)

The ^{1}H NMR spectrum for **10a** is 2nd order, Figure 3.4, but consistent with an ABCX spin system. This occurs because the difference in chemical shift of the protons is similar to the value of the coupling constants of approximately δ 7.4-7.5 ppm.

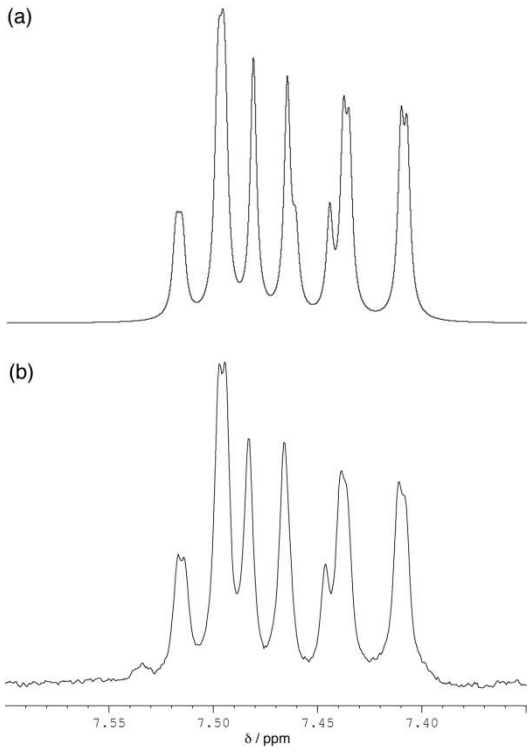

Figure 3.4. (a) Simulated[9] and **(b)** experimental ^{1}H NMR spectra of MIL-101(Cr)-F (**10a**) digested in basic aqueous solution (NaOD/D_2O).

The ^{19}F NMR spectrum of digested **10a** contains a doublet of doublets at δ -116 ppm for H_2BDC-F, plus two other signals that can be attributed to tetrafluoroborate (δ -151 ppm) and a decomposition product.

3.5. NMR spectroscopy of MIL-101(Cr)-I (10b)

In the case of **10b** (Figure 3.5), there are three proton resonances, two doublets and a singlet, in the aromatic region of the ^1H NMR spectrum, which is similar to the spectrum observed for H_2BDC-I. These resonances appear at different chemical shifts from the resonances observed in the spectra of H_2BDC-NH_2 and H_2BDC-$N_2^+BF_4^-$.

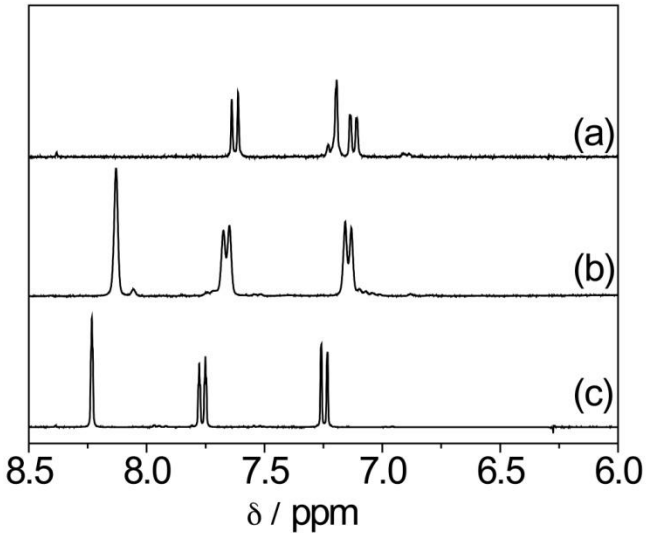

Figure 3.5. ^1H NMR spectra of the samples digested in the basic aqueous solution ($NaOD/D_2O$): **(a)** MIL-101(Cr)-NH_2, **(b)** MIL-101(Cr)-I, **(c)** H_2BDC-I.[8]

3.6. Characterisation of the azo dye functionalised MOF, MIL-101(Cr)-azo

The digested solution of MIL-101(Cr)-azo (**10c**) showed a more complicated ^1H NMR spectrum than those for the iodo- and amino- compounds, which is expected given the greater number of aromatic protons present. Analysis of the spectrum revealed the presence of two isomers, with the most intense peaks from the *para*-azo dye functional groups (denoted P#) and the weaker peaks from the *ortho*-azo dye functional groups (denoted O#), Figure 3.6. These features were compared with the functionalised dicarboxylic acid, H_2BDC-N_2-C_6H_4OH (**11**), synthesised in the same manner as the MOF and confirmed by mass spectrometry.

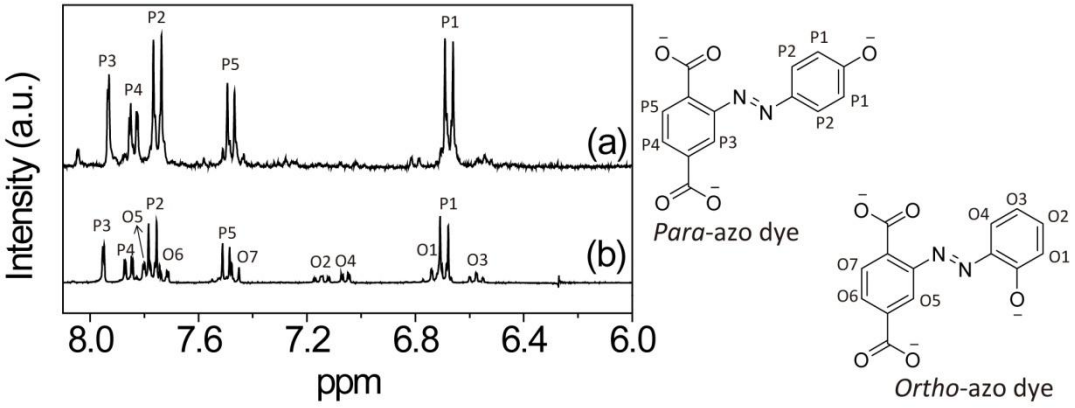

Figure 3.6. ^{1}H NMR spectra of the samples digested in basic aqueous solution (NaOD/D_2O): **(a)** MIL-101(Cr)-azo **10c** synthesised at pH 7, and **(b)** H_2BDC-N=N-C_6H_4OH, **11**.

The UV-visible spectrum of MIL-101(Cr)-azo digested in an aqueous basic solution (Figure 3.7) gave a strong adsorption peak at 400 nm deriving from the –N=N– group in the compound, whereas the absorption peak at 329 nm, observed in **8**, was absent. These results show the successful quantitative conversion from amino to azo dye-functional groups in **10c**, and demonstrate that the *para*-isomer is the major product because of the similarities in peak position λ_{max} at 400 nm compared with the free ligand **11,** dissolved in water. The solvent the measurement is carried out in is important, as **11** dissolved in ethanol gives a λ_{max} at 350 nm whereas in water it is at a longer wavelength of 400 nm. The digested stating material has λ_{max} at 325 nm. Charge transfer bands are present below 300 nm and there no significant peaks above 600 nm were observed.

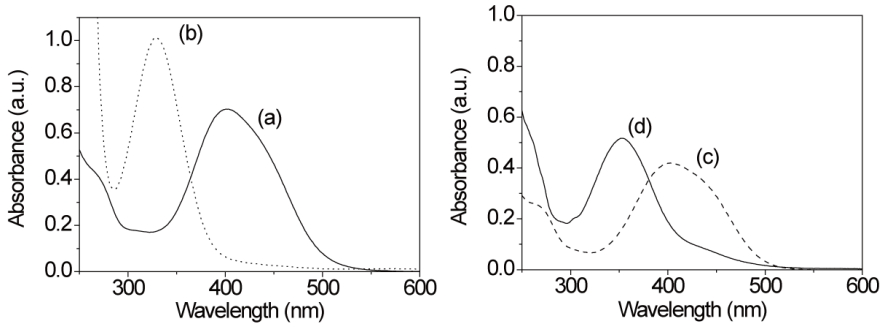

Figure 3.7. UV-visible spectra of **(a) 10c** digested in water at pH 10, **(b) 8** digested in water at pH 10, **(c) 11** dissolved in water with pH 10, and **(d) 11** dissolved in ethanol.[8]

The pH of the reaction mixture in the synthesis of MIL-101(Cr)-azo has a significant influence on the distribution of isomers in the product **10c**, with pH 7 optimum for maximising the *para*:*ortho* ratio. On reducing the pH to 1, ^{1}H NMR analysis showed that

the proportion of the *ortho*-isomer is increased in **10c**, compared with the *para*-isomer with a ratio of *ortho*:*para* of 7:3. A different mechanism or reaction pathway may be available with H^+ to form the *para*- isomer and is hitherto unknown. Above pH 7 digests the MOF breaking down the framework.

3.7. Powder X-ray Diffraction of 10a-c

The PXRD patterns for the modified materials **10a-c** are similar to those for MIL-101(Cr)-NH_2, confirming that diazotisation followed by substitution or coupling does not alter the framework structure (Figure 3.8).

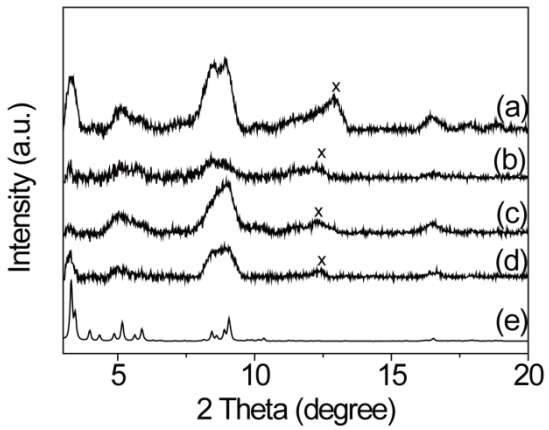

Figure 3.8. PXRD patterns of **(a)** MIL-101(Cr)-NH_2 **8**, **(b)** MIL-101(Cr)-I **10b**, **(c)** MIL-101(Cr)-F **10a**, **(d)** MIL-101(Cr)-azo **10c** and **(e)** the simulated PXRD pattern derived from the crystal structure of MIL-101(Cr) (λ = 1.542 Å). x highlights the peak due to the borosilicate glass capillary.[8]

A PXRD diffractogram usually gives information of phase concentrations (from the relative heights), the phases present (position of peaks), amorphous content (presence of a background hump) and crystallite size/strain (widths of peaks from micro strain giving variations in d-spacings). In the case of the MIL-101(Cr)-X samples even with synchrotron radiation it is only possible to gain information on phases present and that the crystallites are extremely small (broad peaks). The results suggest all of the MOF samples were phase pure.

3.8. Thermogravimetric analysis of 10a-c

Thermogravimetric analysis (Figure 3.9) showed that the materials decompose after 350 °C under a N_2 atmosphere. The first mass loss region for **8** occurs up to 200 °C and account for the loss of 7 molecules of ethanol per formula unit that has been solvent exchanged in the system. The MOFs **10a-c** show less % weight of solvent in their frameworks and display a steady mass loss up to the decomposition temperature.

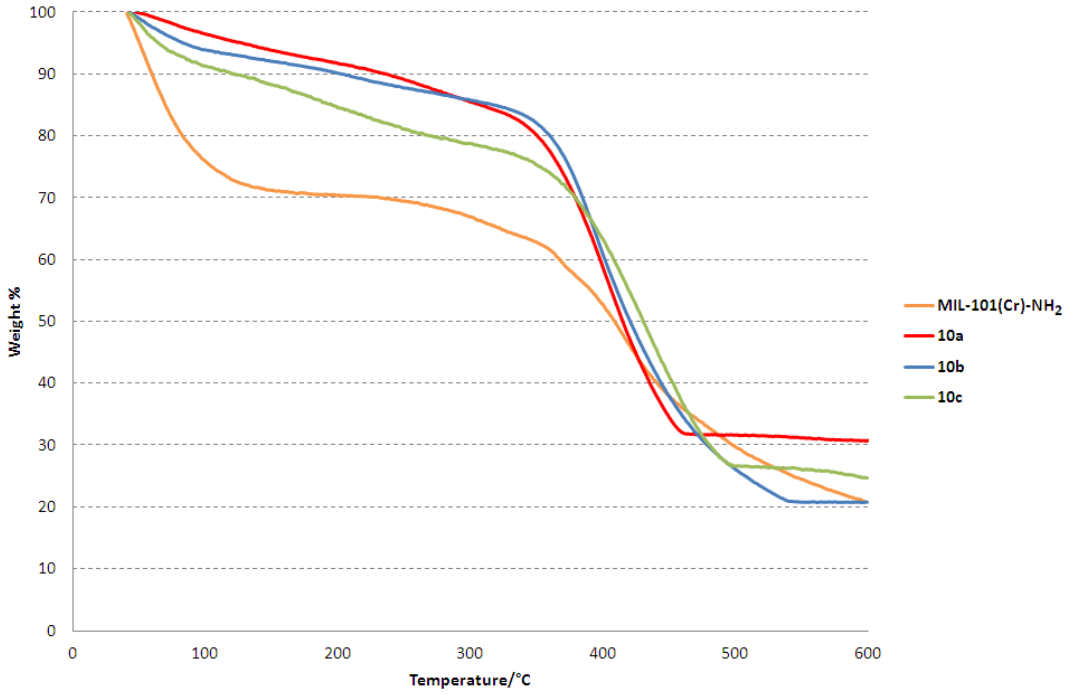

Figure 3.9. TGA curves for MIL-101(Cr)-NH_2 and PSM reaction products **10a-c**.

These results suggest no stable activated species is accessible for gas storage and selectivity applications. This is in contradiction to the BET surface area measurements that show activation at 150 °C for 4 h does give an activated species. This could possibly be due to the temperature ramp rate being too fast for the TGA experiment or solvent loss is slowed by the presence of tag groups in the pores and potentially blocking the pore windows. The gradient of decomposition is steeper in the PSM products compared to the starting material perhaps lending some evidence to this hypothesis.

3.9. ATR-IR spectroscopy of MIL-101(Cr)-NH_2, 10a-c and 11

The ATR-IR spectra of MIL-101(Cr)-NH_2 **8**, PSM products **10a-c** and the modified free diacid **11**, are shown in Figure 3.10. The two N-H bonds from the amino tag group of 8 can be seen as peaks at 3300 and 3350 cm^{-1} and are absent from all the PSM products which is consistent with full conversion of the amino groups in all cases.

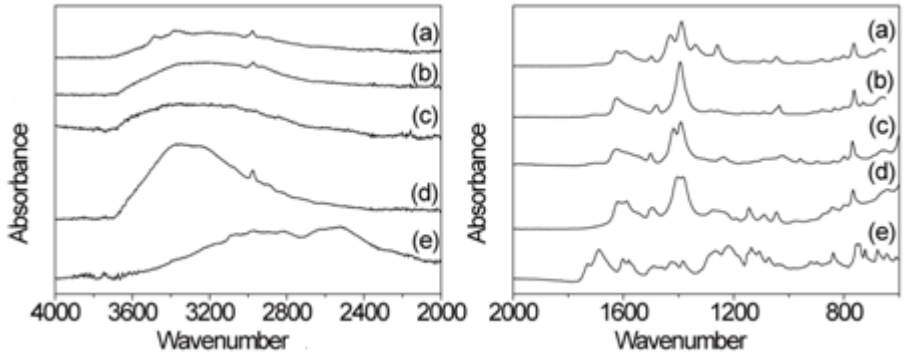

Figure 3.10. ATR-IR spectra of **(a)** MIL-101(Cr)-NH_2, **8**, **(b)** MIL-101(Cr)-I, **10b**, **(c)** MIL-101(Cr)-F, **10a**, **(d)** MIL-101(Cr)-azo, **10c** and **(e)** H_2BDC-N=N-C_6H_4OH, **11**.

Peaks at 1650-1700 cm^{-1} are absent in all of the MOF samples compared to the free diacid attributed to the carboxylate (C=O) stretches of the uncoordinated –COOH groups.

MOFs **10a** and **10b** have no substituent groups with C-N bonds in and this is reflected in an absence of peaks in the range 1200-1300 cm^{-1} in the ATR-IR spectra. However, there is a peak at 1250 cm^{-1} for **8** (Ar-N) and at least two peaks in the 1200-1300 cm^{-1} region, attributed to the multiple types of C-N bonds in the sample of **10c**. This is more clearly pronounced in the free diacid **11**. N=N stretch is not observed in the IR spectrum only the Raman spectrum (not recorded).

The fluoro tagged MOF has an extra peak at 1533 cm^{-1} not present in the iodo tagged MOF. The C-I bond would only be observed as a strong peak below 600 cm^{-1} not capable with this experimental set-up. The C-F stretching frequency can be present over a wide range 1000 – 1360 cm^{-1} but does not account for the peak at 1533 cm^{-1} and as such is un-characterised in this study.

10c shows a significant peak at 3300 cm^{-1} arising from the OH group on the phenol ring of the azo tag. The broad peaks in this region for the other samples were probably from

ethanol still present in the pores from synthesis or water adsorbed from the atmosphere during the experiment.

3.10. Nitrogen adsorption isotherms

Activation of the samples was carried out at 150 °C for 4 h. Figure 3.11 shows the N_2 adsorption–desorption isotherm of MIL-101(Cr)-NH_2 at 77 K following activation. The two uptake steps near P/P_0 = 0.1 and P/P_0 = 0.2 reflect the presence of the two kinds of pore in the crystal structure, whilst the increased nitrogen uptake under high relative pressure and the presence of a hysteresis loop derive from the inter-particulate voids created by the aggregated nanoparticles. The pore size distribution curve shows two pore sizes of 1.54 and 1.99 nm in MIL-101(Cr)-NH_2, which are smaller than those in MIL-101(Cr) (1.71 and 2.22 nm) due to the presence of amino groups projecting into the pores. The broad pore size distribution ranging from 10 nm to 50 nm reflects the existence of textural mesopores in the particle aggregates. MIL-101(Cr)-NH_2 has a high specific surface area of 2070 m^2g^{-1} and high total pore volume of 2.26 cm^3g^{-1}, which are comparable with those of the previous reported nanoMIL-101(Cr) (2944 m^2g^{-1}; 2.57 cm^3g^{-1}).[10]

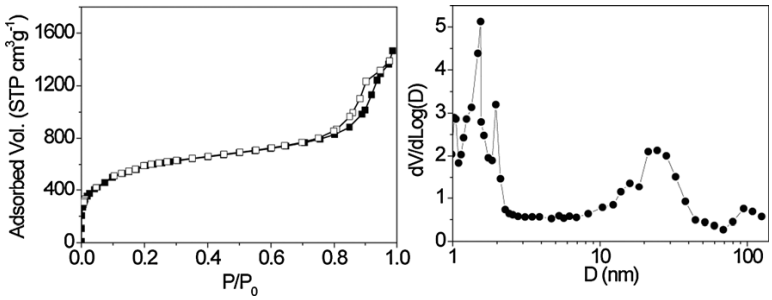

Figure 3.11. N_2 adsorption-desorption isotherms (left) and pore size distributions (right) for MIL-101(Cr)-NH_2.[8]

The tandem PSM products **10a-c** were characterised by N_2 sorption at 77 K (Figure 3.12). MIL-101(Cr)-I and MIL-101(Cr)-F show reduced BET surface areas and total pore volumes from those observed for MIL-101(Cr)-NH_2, but the pore size distribution curves are similar. MIL-101(Cr)-azo also showed a decreased BET surface area as well as a decreased pore volume. The larger molecular volume of the azo tag group compared with the iodo tag group leads to dramatically decreased pore sizes for MIL-101(Cr)-azo.

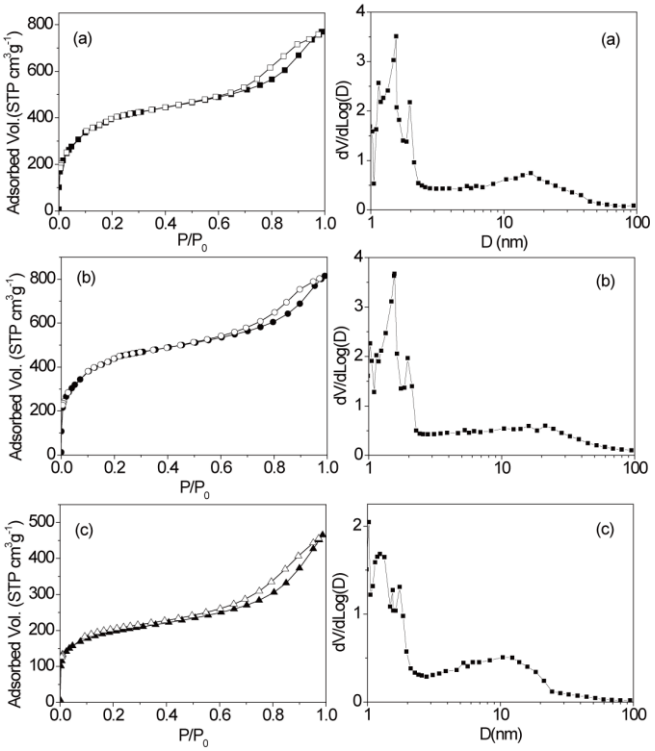

Figure 3.12. N_2 adsorption-desorption isotherms (left) and pore size distributions (right) for **(a)** MIL-101(Cr)-I, **(b)** MIL-101(Cr)-F, and **(c)** MIL-101(Cr)-azo.[8]

Carbon dioxide sorption properties of the **10a-c** were studied at 273 K (Figure 3.13). MIL-101(Cr)-NH_2 gave a CO_2 capacity of 3.02 mmol g^{-1} and a selectivity of 25 for CO_2 over N_2 at 1 atm, which is greater than that previously reported for MIL-101(Cr).[10] This may be attributed to the reduced interaction of the tag group with N_2 and little difference in CO_2 absolute sorption suggesting a more favourable interaction with CO_2. Frameworks **10a-c** show decreased CO_2 capacities over MIL-101(Cr)-NH_2. The incorporation of iodo-, fluoro- and azo-groups onto the pore surface of the MIL-101(Cr) framework also leads to increases in the selectivity for CO_2 over N_2, with the selectivity between 15 and 21. The selectivities at low partial pressures (0.1 atm) are in some cases even greater, with **10a** and **10c** showing selectivities at 273 K of 30 and 73 respectively.

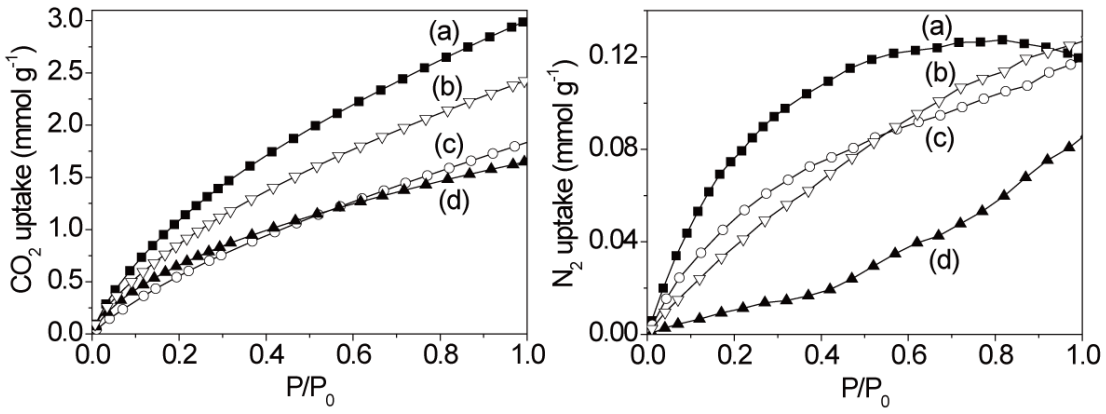

Figure 3.13. CO_2 (left) and N_2 (right) sorption for **(a)** MIL-101(Cr)-NH_2, **(b)** MIL-101(Cr)-F, **(c)** MIL-101(Cr)-I and **(d)** MIL-101(Cr)-azo.[8]

3.11. Summary

A new one step process for the synthesis of MIL-101(Cr)-NH_2 has been carried out. It is a hydrothermal pathway and affords a nano particulate (50 nm) MOF.

MIL-101(Cr)-NH_2 is stable to acids. Quantitative conversion of the amino groups therein to the chloro- and tetrafluoroboro- diazonium salts was achieved, with sodium nitrite and the corresponding strong acid. A second conversion step was also carried out with > 99 % conversion to the fluoro-, iodo- and azo dye- functionalised MIL-101(Cr) on those same materials, showing increased selectivity of CO_2 over N_2 at low partial pressures.

3.12. Experimental

Chemicals: Chromium nitrate nonahydrate [$Cr(NO_3)_3{\cdot}9H_2O$, 99%], absolute ethanol (AR) and potassium iodide were bought from Fisher Scientific, whereas 2-aminobenzene-1,4-dicarboxylic acid (H_2BDC-NH_2, 99%), phenol (99%) and HCl (32%) and HBF_4 (48%) were purchased from Sigma-Aldrich Chemical Co.

Safety: Care must be taken with diazonium halides as they are potentially explosive. Although no indications of this were observed in the work reported herein, it is vital to be aware of the potential hazards.

Characterisation: The high resolution powder X-ray diffraction (PXRD) experiment was carried out on Beamline I11 at the Diamond Light Source, UK. A high brightness monochromatic beam of E = 15 keV (calibrated λ = 0.825028 Å) was used to collect the diffraction pattern. The PXRD measurements of the samples were also carried out on a

Bruker AXS D8 Advance X-ray diffractometer with Cu Kα radiation (λ = 1.542 Å). Scanning Electron Microscopy (SEM) measurements were carried on a JEOL JSM6480LV instrument.

The transmission electron microscope (TEM) images of the materials were taken on a JEOL IEM1200EXII instrument with an operating voltage of 120 kV. The particle sizes were manually analysed using ImageJ software, with more than 50 particles taken for analysis.

The sorption isotherms of N_2 at 77 K and 273 K, and of CO_2 at 273 K were carried out on a BELSORP Mini-II (BEL Japan) instrument. The sample was degassed at 150 °C for 4 h prior to sorption. The specific surface areas of the samples were calculated by the Brunauer-Emmett-Teller method in the P/P_0 range of 0.05-0.1. The total volume was obtained by calculating the data at the relative pressure of 0.99. The selectivities of the materials for CO_2 were calculated from the single gas isotherms by dividing the CO_2 adsorption capacity by that of N_2 at the relative pressure of 1 or 0.1.

Infrared spectra of the samples were measured using a PerkinElmer Spectrum 100 spectrometer equipped with an ATR sampling accessory. Before measurement, the samples were dried under N_2 flowing gas at room temperature for 24 h.

UV-visible spectra of the digested samples in basic aqueous solution ($NaOH/H_2O$) were carried out on a Varian 50 Probe UV-visible spectrophotometer.

^{1}H NMR spectra were recorded on a Bruker AV 300 spectrometer operating at 300 MHz or a Bruker Avance 400 spectrometer operating at 400 MHz. ^{19}F NMR spectra were recorded on a Bruker Avance 400 spectrometer operating at 376 MHz. The second order ^{1}H NMR spectrum for base-digested MIL-101(Cr)-F was analysed using the NMR simulator at nmrdb.org.[9]

This basic digestion procedure for NMR measurements used <5 mg MOF, 0.1 mL NaOD (35 % in D_2O), 0.4 mL D_2O. This was sonicated until fully digested and dissolved with no visible precipitate left. NaOD was kept to the minimum amount to just digest all of the MOF, so as to keep the peak widths to a minimum. To remove the Cr^{III} from solution let the mixture stand for 1-2 weeks and a precipitate, of presumably, $Cr(OH)_3/Cr(OD)_3$ can be separated by decanting, after centrifuge at 11000 rpm for 30 minutes.

Mass spectra were recorded on a Bruker microTOF (ESI-TOF) spectrometer.

3.12.1. MIL-101(Cr)-NH_2, $[Cr_3O(OH)(OH_2)_2(BDC\text{-}NH_2)_3]\cdot x$EtOH, 8

In a typical experiment, $H_2BDC\text{-}NH_2$ (0.23 g, 1.26 mmol) and $Cr(NO_3)_3\cdot 9H_2O$ (0.50 g, 1.25 mmol) were added to water (7 cm^3). The resulting suspension was stirred for 3 h at room temperature then heated under autogenous pressure at 130 °C for 24 h in a Teflon-lined autoclave. After cooling to room temperature, the solid product was isolated as a green powder by centrifugation and washed five times with ethanol before drying under N_2 flowing gas at room temperature. The resulting material, yield of 75 mg, was denoted as MIL-101(Cr)-NH_2. ^{1}H NMR ($NaOD/D_2O$, 300 MHz): δ 7.24 (dd, J = 8.1, 1.3 Hz, 1H), 7.31 (d, J = 1.3 Hz, 1H), 7.74 (d, J = 8.1 Hz, 1H).

3.12.2. MIL-101(Cr)-$N_2^+BF_4^-$, 9a

MIL-101(Cr)-NH_2 (0.075 g, 0.261 mmol NH_2 eq.) was suspended in 1:1 mixture of water and 48% conc. HBF_4 (6 cm^3). The suspension was cooled to below 5 °C in an ice bath, diazotised by addition of an aqueous solution of $NaNO_2$ (0.045 g) in water (1.6 cm^3), and further stirred for 2 h at 0-5 °C. This mixture was centrifuged at 11000 rpm for 30 minutes and then the excess liquid decanted. Fresh deionised water was added and the centrifugation repeated two more times with fresh water each time. The green solid was stored in H_2O. ^{1}H NMR ($NaOD/D_2O$, 300 MHz): 7.29 (s, 1H), 7.58 (d, J = 8.0 Hz, 1H), 7.68 (d, J = 8.0 Hz, 1H).

3.12.3. MIL-101(Cr)-$N_2^+Cl^-$, 9b

The synthesis was modified from a procedure reported by Vinod and co-workers.[11] MIL-101(Cr)-NH_2 (0.075 g, 0.26 mmol NH_2 eq.) was suspended in 1:1 mixture of water and 32% conc. HCl (6 cm^3). The suspension was cooled to below 5 °C in an ice bath, diazotised by addition of an aqueous solution of $NaNO_2$ (0.045 g) in water (1.6 cm^3), and further stirred for 3 h at 0-5 °C. This was stored in water until needed.

3.12.4. MIL-101(Cr)-F, $[Cr_3O(OH)(OH_2)_2(BDC\text{-}F)_3]\cdot x$EtOH, 10a

9a was heated at 100 °C for 18 h. The solid product was washed with 3 × 5 cm^3 MeOH over 72 h, with fresh MeOH added every 24 h. The solid sample obtained was separated by centrifugation before drying under a flow of N_2 at room temperature (> 99% conversion). The resulting sample was denoted as MIL-101(Cr)-F. ESI (negative ion): *m/z* 183.0113 (calc. 183.0099 for $[HBDC\text{-}F]^-$, $C_8H_4FO_4^-$).^{1}H NMR ($NaOD/D_2O$, 400 MHz): δ 7.43 (m,

J_{HH} = 1.2 Hz, J_{HF} 10.9 Hz, 1H), 7.46 (m, J_{HH} = 8.0 Hz, J_{HF} = 6.8 Hz, 1H), 7.51 (m, J_{HH} = 8.0 Hz, J_{HH} = 1.2 Hz, 1H). ^{19}F NMR (NaOD/D_2O, 376 MHz): δ –116.4 (dd, J_{FH} 6.8, 10.9 Hz). *m/z*: 183.0113, calcd. $[HBDC\text{-}F]^-$ *m/z*: 183.0099.

3.12.5. MIL-101(Cr)-I, $[Cr_3O(OH)(OH_2)_2(BDC\text{-}I)_3]\cdot x$EtOH, 10b

To a suspension of **9b** in water: KI (0.260 g) in H_2O (9 cm^3) was slowly added and the reaction mixture was stirred at room temperature for 72 h. After this time, $NaHSO_3$ were added until the dark colour of the solution dissipated. The solid product was separated, washed with 3 × 5 cm^3 water over 72 h, with fresh water added every 24 h, and triturated in a 10 cm^3 mixture of CH_2Cl_2:H_2O (1:1). The solid sample obtained was separated by centrifugation and washed with ethanol before drying under a flow of N_2 at room temperature (> 99% conversion). The resulting product was denoted as MIL-101(Cr)-I. ESI (negative ion): *m/z* 290.9161 (calc. 290.9154 for $[HBDC\text{-}I]^-$, $C_8H_4IO_4^-$). ^{1}H NMR (NaOD/D_2O): δ 7.35 (d, *J* = 8.0 Hz, 1H), 7.87 (d, *J* = 8.0 Hz, 1H), 8.34 (s, 1H).

3.12.6. MIL-101(Cr)-azo, $[Cr_3O(OH)(OH_2)_2(BDC\text{-}azo)_3]\cdot x$EtOH, 10c

To a suspension of **9b** in water: an aqueous solution of phenol (0.087 g, 0.92 mmol) and Na_2CO_3 (1.0 g) was added, the pH of which was adjusted to 7 by addition of further Na_2CO_3 (0.9 g). The resultant dark red mixture was stirred for 72 h at room temperature, after which the solid product was separated by centrifuge and washed with H_2O then EtOH. The resulting solid material was dried under a flow of N_2 at room temperature and denoted MIL-101(Cr)-azo, **10c**. ^{1}H NMR (NaOD/D_2O, 400 MHz): δ 6.74 (d, *J* = 8.9 Hz, 2H, P1), 7.54 (d, *J* = 7.9 Hz, 1H, P5), 7.81 (d, *J* = 8.9 Hz, 2H, P2), 7.90 (dd, *J* = 1.6, 7.9 Hz, 1H, P4), 7.99 (d, *J* = 1.6 Hz, 1H, P3. *m/z*: 285.0522, $[HBDC\text{-}N_2\text{-}C_6H_4OH]^-$ (calc. 285.0517).

3.12.7. H_2BDC-azo, 11

$H_2BDC\text{-}NH_2$ (1.000 g, 5.52 mmol) was suspended in 1:1 mixture of water and 32% conc. HCl (6 cm^3). The suspension was cooled to below 5 °C in an ice bath, diazotised by addition of an aqueous solution of $NaNO_2$ (0.74 g) in water (1.6 cm^3), and further stirred for 10 minutes at 0-5 °C. To this an aqueous solution of phenol (1.000 g, 10.63 mmol) and Na_2CO_3 (425 mg) was added, the pH of which was adjusted to 7 by addition of further Na_2CO_3 (0.9 g). The resultant mixture was stirred for 72 h at room temperature, after which the brown solid product, **11**, was separated by filtration and washed with water. Yield: 1.58 g (95 %). ^{1}H NMR (NaOD/D_2O, 400 MHz): δ 6.74 (d, *J* = 8.9 Hz, 2H, P1),

7.54 (d, *J* = 7.9 Hz, 1H, P5), 7.81 (d, *J* = 8.9 Hz, 2H, P2), 7.90 (dd, *J* = 1.6, 7.9 Hz, 1H, P4), 7.99 (d, *J* = 1.6 Hz, 1H, P3).

3.13. Acknowledgements

Thanks to Dr. Dongmei Jiang who prepared the starting material of 16 nm particulate MIL-101(Cr)-NH_2, carried out the UV-Vis measurements, AT-IR measurements, TEM/SEM and producing the figures herein where referenced. Diamond Light Source beamline I11 who carried out the powder X-ray diffraction of framework **8**. John Lowe for help with NMR experiments.

3.14. References

[1] G. Férey, C. Mellot-Draznieks, C. Serre, F. Millange, J. Dutour, S. Surblé, I. Margiolaki, *Science*, **2005**, *309*, 2040.
[2] M. Lammert, S. Bernt, F. Vermoortele, D. E. De Vos, N. Stock, *Inorg. Chem.*, **2013**, *52*, 8521.
[3] S. Bernt, V. Guillerm, C. Serre, N. Stock, *Chem. Commun.*, **2011**, *47*, 2838.
[4] B. Li, Y. Zhang, D. Ma, L. Li, G. Li, G. Li, Z. Shi, S. Feng, *Chem. Commun.*, **2012**, *48*, 6151.
[5] P. A. Szilagyi, P. Serra-Crespo, I. Dugulan, J. Gascon, H. Geerlings, B. Dam, *CrystEngComm*, **2013**, *15*, 10175.
[6] Y. Lin, C. Kong, L. Chen, *RSC Advances*, **2012**, *2*, 6417.
[7] Z. Sun, G. Li, H.-o. Liu, L. Liu, *Applied Catalysis A: General*, **2013**, *466*, 98.
[8] D. Jiang, L. L. Keenan, A. D. Burrows, K. J. Edler, *Chem. Commun.*, **2012**, *48*, 12053.
[9] A. M. Castillo, L. Patiny, J. Wist, *J. Magn. Reson.*, **2011**, *209*, 123.
[10] D. Jiang, A. D. Burrows, K. J. Edler, *CrystEngComm*, **2011**, *13*, 6916.
[11] A. Kommreddy, M. S. Bowsher, M. R. Gunna, K. Botha, T. K. Vinod, *Tetrahedron Lett.*, **2008**, *49*, 4378.

4. Synthesis and Characterisation of MOFs as Potential PSM Candidates

4.1. Introduction

There are several reasons for investigating tagged isophthalate (IP) based MOFs. One compelling characteristic is the relatively small steric crowding around the tag group in the 5-position. This affords the possibility of access for a larger range of PSM reagents and thus transformations that could be possible. The single-crystal XRD data of potential PSM reaction products may have less structural disorder and one could measure conversion with diffraction analysis more confidently. This is due to more electron density available from the tag group on the 5-position of the aromatic ring, Figure 4.1. Many modified isophthalic acids have been synthesised and incorporated successfully in MOFs including those with amino,[1] pyridyl,[2] triazoyl,[2] tetrazoyl,[3] halo,[4] *tert*-butyl[5] and nitro[6] tag groups.

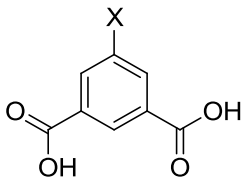

Figure 4.1. Isophthalic acid functionalised at the 5-position.

The simplest example of a MOF that incorporates a tagged isophthalate is [Mn(AIP)(DMF)] (AIP = 5-amino isophthalate) reported by Kongshaug *et al.* as CPO-9 (CPO = coordination polymer of Oslo).[1] They synthesised this MOF by solvothermal methods and the framework is shown in Figure 4.2. The amino tag groups are pointing into the channels and DMF molecules from the reaction are coordinated to the Mn(II) centres. This is the closest example of an isophthalate based MOF containing an open channel topology similar to the IRMOF series.[7]

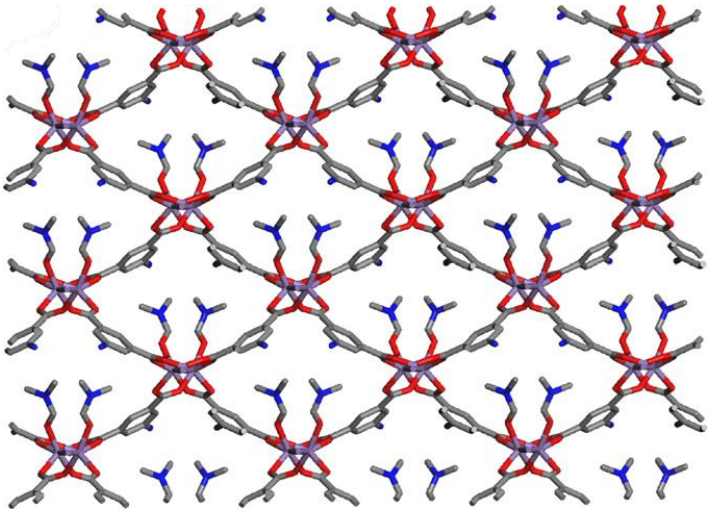

Figure 4.2. View down the channels of CPO-9. C: grey, O: red, N: blue, Mn: lilac. Hydrogen atoms omitted.[1]

A series of structures published by the Kitagawa group, including [Zn(IP)(bipy)] (CID-1, CID = coordination polymer with interdigitated structure) incorporates 4,4'-bipyridine (bipy) and an untagged isophthalate linker, Figure 4.3.[8] The aromatic rings of the IP moiety point into the pores of adjacent sheets in an interlocking fashion. This means that this 2-D interdigitated structure allows for reversible breathing when absorbing guest molecules. The framework expands at higher concentrations of guest molecules and demonstrates a two step MeOH adsorption isotherm.[9] Tagged interdigitated structures have since been reported by Kitagawa *et al.* with a 2,5-dihydroxy isophthalate linker.[10]

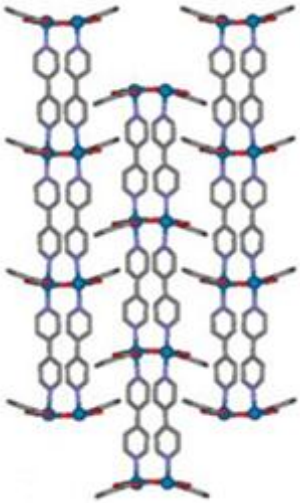

Figure 4.3. View of the interdigitated structure of CID-1. C: grey, O: red, N: dark blue, Zn: light blue. Hydrogen atoms omitted. [8]

Nitrogen pillaring ligands have repeatedly been used in conjunction with isophthalates to expand MOF networks with these long, rigid, non-carboxylate based linkers. Nickel(II) and cobalt(II) MOFs with coordinated amino tag groups were reported by Sarma *et al*. and utilise pyrazine in the spacer role, with formula $[M_2(AIP)_2(pyz)(H_2O)_2]\cdot 3H_2O$ (M = Co^{2+}, Ni^{2+}, pyz = pyrazine).[11] Unfortunately the amino tag group bonds to the metal centres and this is a common occurrence caused by the relatively open amino groups and their propensity for coordination to metal atoms (Figure 4.4). These 2-D sheets are pillared with bis-nitrogen bridging pyrazine linkers.

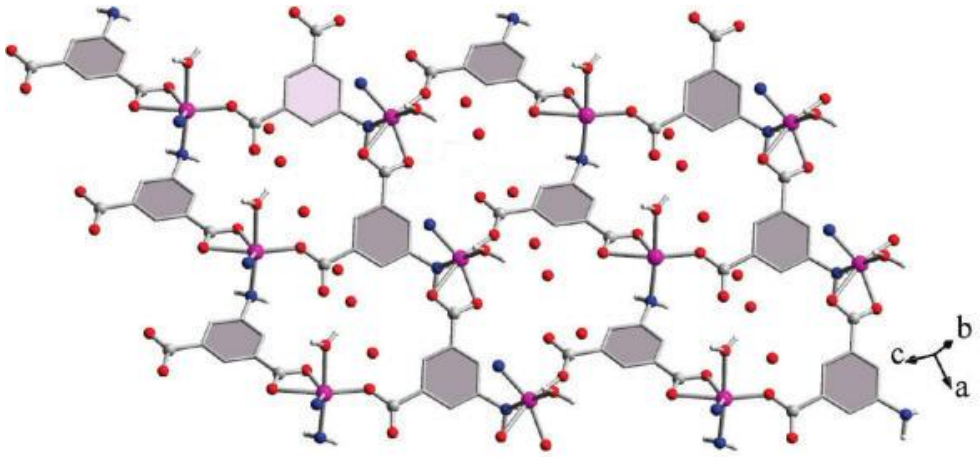

Figure 4.4. View of the 2-D carboxylate layers of $[M_2(AIP)_2(pyz)(H_2O)_2]\cdot 3H_2O$. C: grey, O: red, N:blue, M: purple. Hydrogen atoms omitted on aromatic rings.[11]

Another preventative approach when using amino groups to circumvent the propensity of participation in metal coordination in MOF synthesis is to use steric crowding, for example in 5-amino-2,4,6-triiodoisophthalic acid (H_2ATIIP). The neodymium based MOF, $[Nd(HCOO)(ATIIP)(DMF)_2]\cdot DMF\cdot H_2O$ is an example of a MOF incorporating ATIIP, reported by Sun *et al.*[4] The framework is an NbO type, consisting of neodymium cations bridged by formate anions and ATIIP linkers and exhibits uncoordinated amino groups. There are small channels with diameter 6.3 Å present (that possess chirality) and these surround a larger hexagonal channel with diameter of 15.9 Å in the gross structure seen in Figure 4.5.

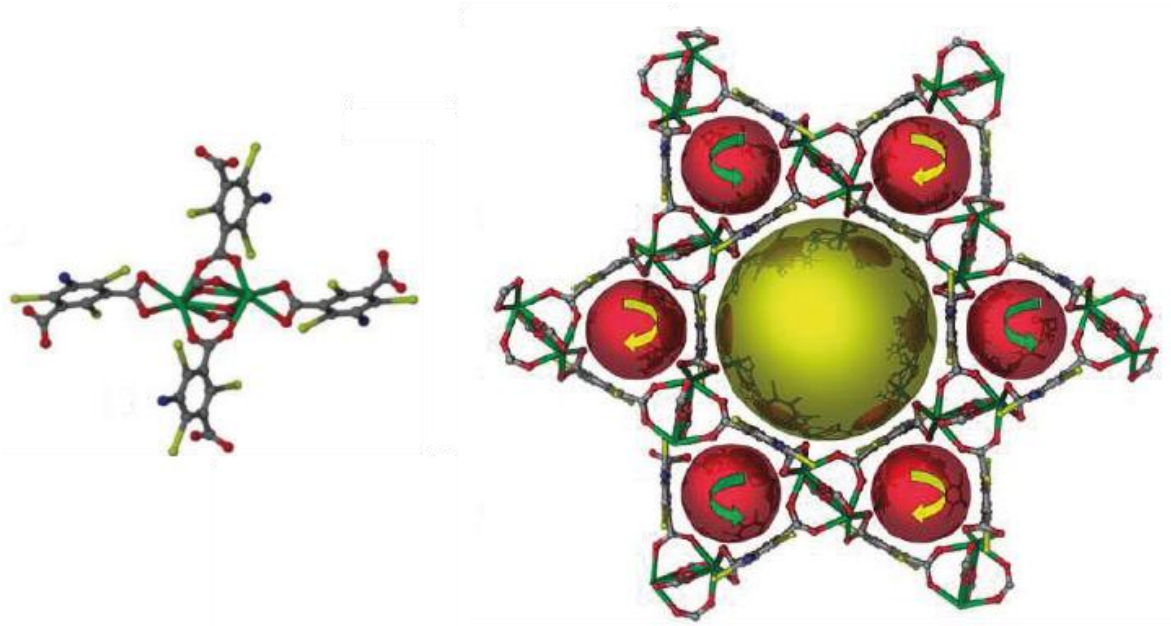

Figure 4.5. (left) SBU of $[Nd(HCOO)(ATIIP)(DMF)_2]\cdot DMF\cdot H_2O$ showing a Nd_2 node. **(right)** View down the channels showing the chiral 6.3 Å channels (red spheres) and the 15.9 Å channels (yellow spheres). C: grey, O: red, N: blue, I: yellow, Nd: green.[4]

In conclusion isophthalate based MOFs have a greater potential for the tag groups to be characterised by single-crystal X-ray diffraction than functionalised terephthalate containing MOFs. The more challenging aspect is to have tag groups accessible for PSM reagents in the case of covalent modifications.

4.2. PSM of [Mn(AIP)(DMF)] with Acetic Anhydride

To gauge the viability of 5-aminoisophthalate (AIP) containing MOFs for PSM studies, initially a porous framework was chosen from the literature that was thought to have sufficiently accessible amino groups. PSM studies were carried out on the chosen MOF, [Mn(AIP)(DMF)] (CPO-9),[1] by exposure to two equivalents of acetic anhydride (Ac_2O) in a solvent, such as DMF, with the goal of converting the free amino groups to acetamido groups, using a modified procedure of that reported by Cohen *et al.*[12]

Experiments in a range of solvents including $CHCl_3$ at room temperature and at 50 ºC, neat Ac_2O and DMF, all showed the correct fragment for 5-acetamido isophthalic acid (H_2AMIP) in their mass spectra, suggesting partial conversion in the solid state had occurred. The ^1H NMR spectra of the digested PSM products were consistent with the consistent with conversion of the starting material from [Mn(AIP)(DMF)] to $[Mn(AIP)_{1-j}(AMIP)_j(DMF)_x]$. Conversions for $CHCl_3$ at room temperature were 5 %; at 50 ºC, 40 %;

in neat Ac_2O 20 %; and in DMF, 60 % (j = 0.05, 0.40, 0.20 and 0.60 respectively). The amount of DMF per formula unit, x, was approximately 1-2 in all cases.

PXRD patterns of dried samples from the PSM reaction in DMF and neat Ac_2O were consistent with the retention of framework topology, Figure 4.6, with the PSM product from the reaction carried out in DMF displaying a higher quality diffraction pattern. In $CHCl_3$ the PSM reaction products are a mixture of crystalline products. These results, however, could be consistent with zero conversion from CPO-9 because the PXRD is the same in both cases, implying comparison of several complementary characterisation techniques is required to be fully confident with the degree of conversion.

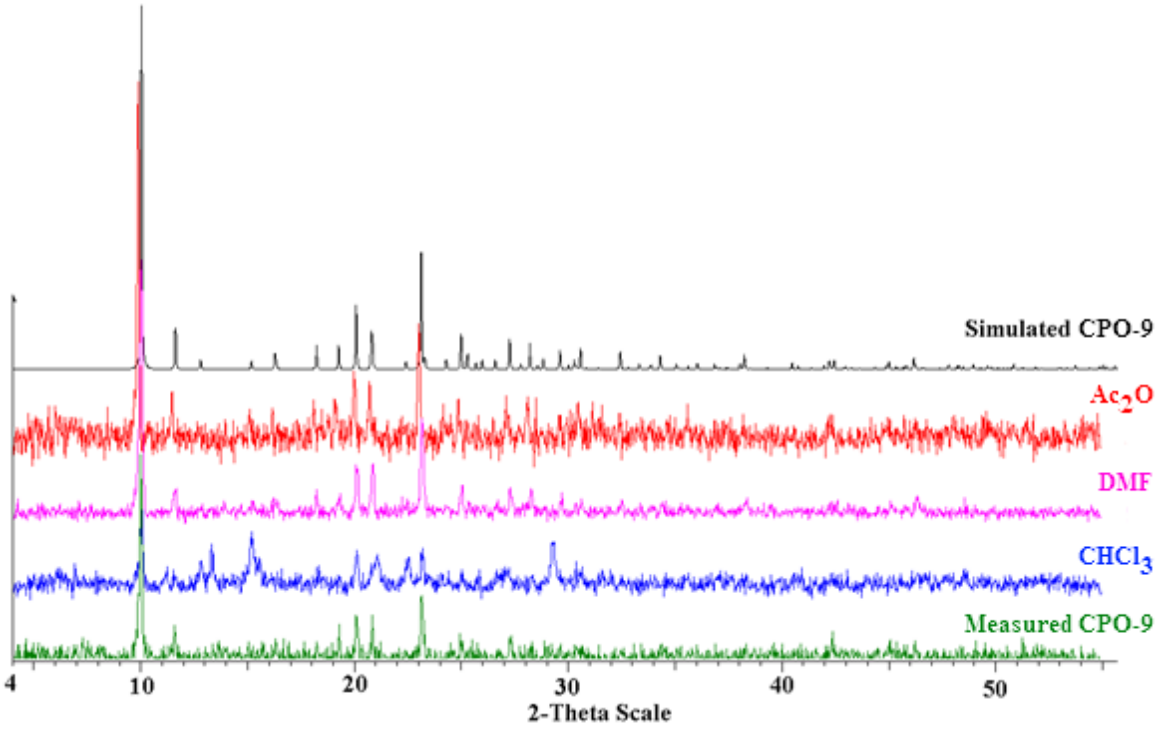

Figure 4.6. PXRD data comparison of dried samples the as made CPO-9 (green), PSM products from the reactions in $CHCl_3$ (blue), DMF (pink), Ac_2O (red) and the simulated data from the literature (refcode: VILXOE).[1]

The degree of conversion, j, cannot be accurately calculated from the ^{1}H NMR spectra due to broadening of the peaks by the presence of paramagnetic Mn(II), even when diluting the solutions that gave success in the ^{1}H NMR spectra of the Cr(III)-containing MIL frameworks. The mass spectrum was also inconclusive, due to differences in the degree of ionisation and fragmentation of H_2AIP and H_2AMIP. The FT-IR spectra showed the DMF carbonyl stretches overlap with the AMIP carbonyl stretches and no information was gleaned from this technique.

Figure 4.7 shows the TGA curve of [Mn(AIP)(DMF)], which is consistent with the TGA study reported in the literature.[1] Most of the DMF is lost up to 250 ºC (observed 21 wt%, calculated 23.8 wt%). Above 250 ºC the rest of the DMF is lost accompanied by framework decomposition. No plateau region is present in the TGA data suggesting an activated framework of CPO-9 cannot be obtained simply by heating.

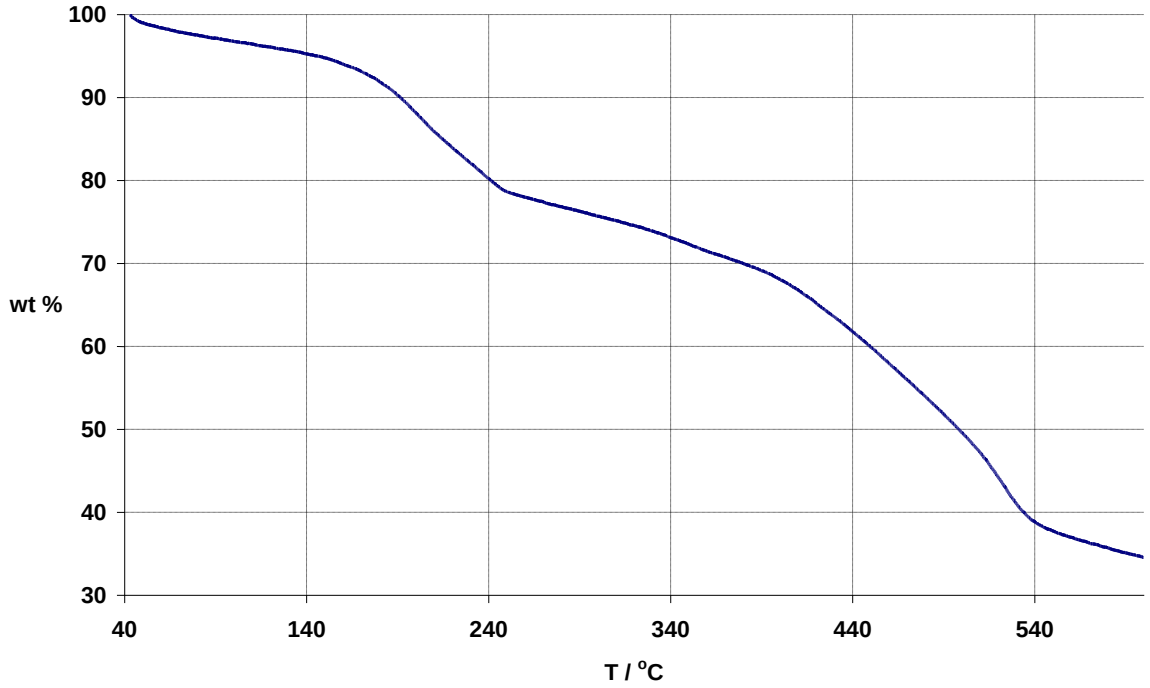

Figure 4.7. TGA of [Mn(AIP)(DMF)], heated in $N_{2(g)}$ at a rate of 5 ºCmin^{-1}.

In summary the DMF guest molecules of [Mn(AIP)(DMF)], cannot readily be removed to make the stable activated species evidenced by the TGA. Therefore with the limitations of this framework it was not taken forward for further PSM studies. AIP containing MOFs could still be viable but the difficulties in activation mean that CPO-9 is not the best choice of starting material.

4.3. Isophthalic Acid Based MOF Synthesis

4.3.1. MOF Synthesis with 5-Aminoisophthalic Acid

As there were few AIP containing MOFs suitable for PSM reaction in the literature, it was therefore necessary to synthesise a range of frameworks with different metal salts. New MOFs with free amino functionalised isophthalate linkers were pursued for potential PSM applications.

A preliminary experiment using $Co(NO_3)_2 \cdot xH_2O$ under standard MOF reaction conditions (metal:ligand ratio = 1:1.3, 120 ºC, DMF), yielded no precipitate during a 48 h period at

high temperature, or when left at low temperatures (4 ºC) for two weeks. The acetate salt tends to give crystalline products more readily in previously reported MOFs with AIP, therefore, $Co(OAc)_2{\cdot}4H_2O$ was chosen as the metal source. The solubility of $Co(OAc)_2{\cdot}4H_2O$ and H_2AIP in DMF was poor and in preliminary experiments the organic linker did not dissolve, even at higher temperatures (140 ºC). Therefore, another solvent system was investigated. After several, small scale trials, a 50:50 DMF:H_2O mixture was chosen.

Initially, three parallel reactions were carried out, to screen for the most promising reagent stoichiometry using the yield of crystalline products as a measure of success. It was found that an equal metal:ligand ratio gave the best results. The concentration was then doubled to 50 mg of ligand per 20 mL of solvent, which gave the highest yield of large crystals for characterisation studies. The reaction conditions that gave the best quality, crystalline, product are summarised in Scheme 4.1.

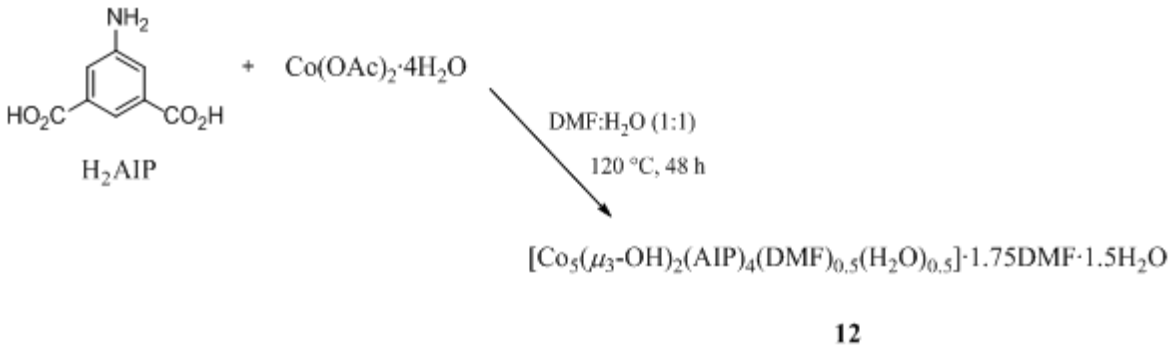

Scheme 4.1. Synthetic conditions for **12**.

This reaction gave thin, purple, plate-like crystals, which were characterised by single-crystal X-ray diffraction as $[Co_5(\mu_3\text{-}OH)_2(AIP)_4(DMF)_{0.5}(H_2O)_{0.5}]{\cdot}1.75DMF{\cdot}1.5H_2O$ (**12**). The crystallographic data are summarised in Table 4.1.

Formula	$[Co_5(\mu_3\text{-}OH)_2(AIP)_4(DMF)_{0.5}(H_2O)_{0.5}]\cdot 1.75DMF\cdot 1.5H_2O$
Empirical formula	$C_{38.75}H_{42.75}Co_5N_{6.25}O_{22.25}$
Formula weight / $gmol^{-1}$	1246.69
T / K	150(2)
λ / Å	0.71073
Crystal system	Monoclinic
Space group	$C2/c$
a / Å	35.6760(8)
b / Å	11.1920(2)
c / Å	22.2100(5)
$\alpha = \gamma$ / °	90
β / °	93.020(1)
Volume / $Å^3$	8855.8(3)
Z (no. molecules in unit cell)	8
Density (calculated) / gcm^{-3}	1.870
Crystal size / mm	0.28 x 0.15 x 0.05
Data Completeness	0.994
Final R indices [$I>2\sigma(I)$]	$R1$ = 0.0648, $wR2$ = 0.1530
R indices (all data)	$R1$ = 0.1178, $wR2$ = 0.1710
Largest diff. peak and hole / $eÅ^{-3}$	1.095 and -1.108

Table 4.1. Crystallographic data for **12**.

The node of framework **12** (Figure 4.8) consists of five cobalt(II) centres, three in octahedral environments and two in tetrahedral environments, four AIP dianions, two bridging μ_3-hydroxide anions (O8 and O9), a lattice DMF (based on O1) and a solvent ligated to Co3 which models optimally as 50 % occupancy DMF and 50 % occupancy water. Thus, O10 has 100 % occupancy, and additional electron density in this region has been treated as 1.5 partial waters (O21-23). In addition there is a region of diffuse solvent, in the unit cell, which was treated with PLATON SQUEEZE.[13] This diffuse region has been included as 0.75 of a DMF, but not modelled in the asymmetric unit.

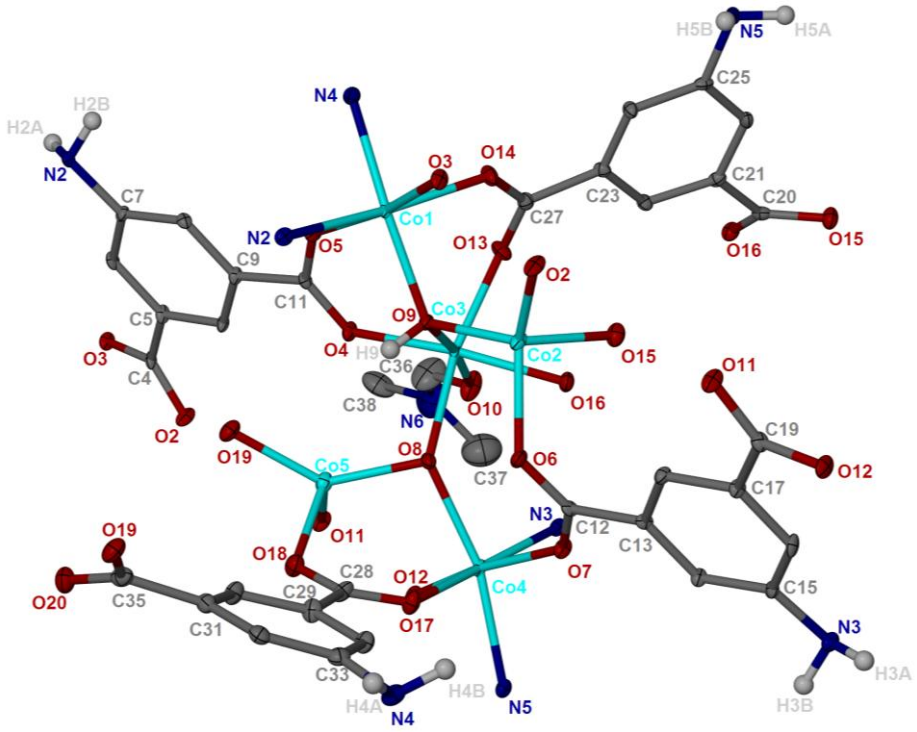

Figure 4.8. The metal-ligand interactions in the metal node of **12**. Atoms are represented as thermal ellipsoids at 30 % probability. C: gray, H: white, O: red, N:blue, Co: cyan. Aromatic hydrogen atoms omitted.

The hydroxide hydrogen atoms were readily located, but only that attached to O9 is included in the final least squares refinement, largely because that attached to O8 was not stable through least squares refinement. Partial water hydrogen atoms could not be reliably located and hence were omitted from the refinement. H9 was refined subject to being 0.89 Å from O9. Several other restraints were included for inter-atomic distances in the disordered solvent region.

The SBU of **12** contains five cobalt centres (Figure 4.9), and has not previously been reported in the literature. There are eight carboxylates, two hydroxides and four amino groups involved in this framework node arising from four independent AIP linkers. The SBU is a discrete unit only connected to other SBUs *via* AIP linkers. The closest analogous structure contains a four cobalt centre SBU, also incorporating a bridging hydroxide ligand, $[Co_2(H_2O)(\mu_3\text{-}OH)_2(AIP)]$, reported by Sarma *et al.*[11]

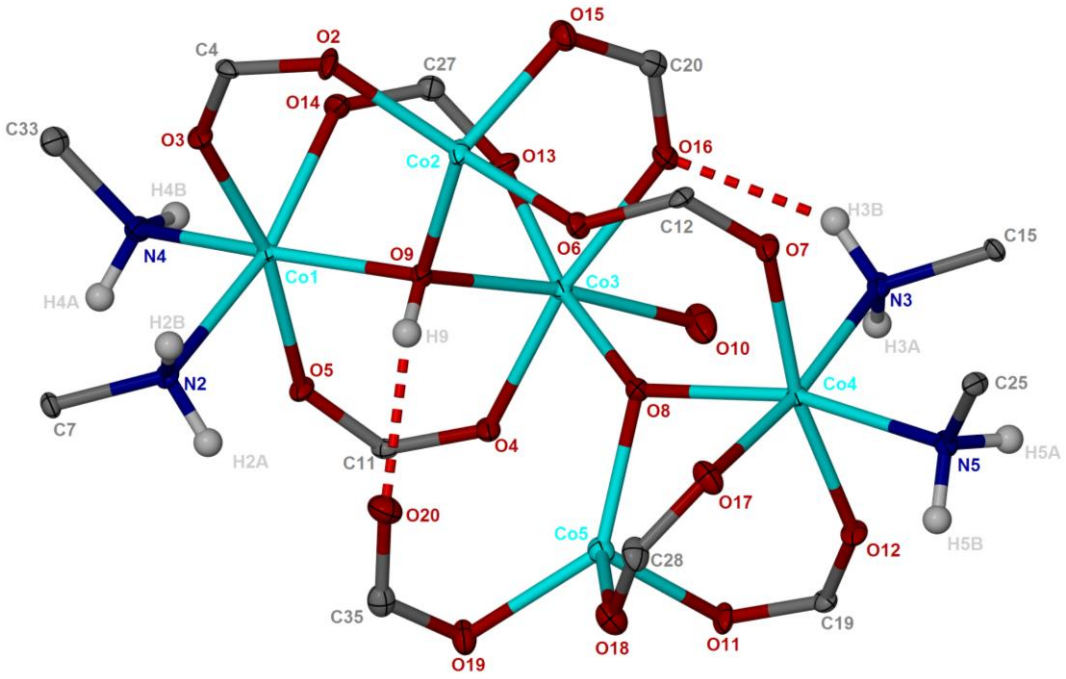

Figure 4.9. SBU of compound **12**. Thermal ellipsoids shown at 30 % probability. C: gray, H: white, O: red, N:blue, Co: cyan.

Co1 and Co4 are both in a pseudo-octahedral environment with similar donor atoms. Both are coordinated to two nitrogen atoms (from amino groups), three oxygen atoms (from bridging carboxylates) and a μ_3-OH oxygen. The ranges of bond lengths for both metal environments are not significantly different. Co1-O bond lengths are in the range 2.058(4)-2.103(4) Å, compared to Co4-O bonds of 2.056(4)-2.127(4) Å. Also Co1-N bond lengths are in the range 2.165(5)-2.290(5) Å, compared to Co4-N bonds of 2.191(5)-2.202(5) Å.

The bond angles are also not significantly different between Co1 and Co4. The *cis* angles for Co1 are between 78.88(16)-97.86(18)º and *trans* angles 163.08(17)-167.11(15)º, compared to Co4 *cis* angles 80.55(16)-101.37(16)º and *trans* angles 165.69(16)-171.80(16)º.

Atom Co3 is also pseudo-octahedral, coordinated to six oxygen atoms: three oxygen atoms (from bridging carboxylate groups, O13, O16 and O4), two μ_3-OH oxygen atoms (O9 and O8), and 50 % of the time O10 is from a H_2O oxygen and 50 % of the time from a DMF. Co3-O bond lengths are in the range 2.046(4)-2.185(4) Å. The *cis* angles are in the range 82.84(16)-99.31(14)º, and *trans* angles are 168.49(16)-173.03(18)º.

Co2 and Co5 are both in a tetrahedral coordination environment, but they differ by the origin of one donor group. Co2 has four oxygen atoms coordinated – O2, O6, and O15 are

from three bridging carboxylate groups, and O9 is from a μ_3 bridging hydroxide group. Co5 bonds to O18 and O11 from two bridging carboxylate groups, O8 is from a μ_3 bridging hydroxide group, and O19 is from a monodentate carboxylate moiety.

Co-O bond lengths are the same, within error, between Co2 and Co5, however there are deviations in the angles from a perfect tetrahedral environment. Co2-O bond lengths are in the range 1.943(4)-2.009(4) Å, which are similar to the Co5-O bonds, 1.943(4)-2.002(4) Å. Co2 has four O-Co-O angles in the range 102.14(16)-114.98(16)º, one small (O15-Co2-O6 = 95. 12(17)º) and one large (O2-Co2-O6 =126.19(17)º) tetrahedral angle.

Similarly, Co5 has four tetrahedral angles in the range 104.69(17)-108.48(18)º, but the remaining two angles are more distorted. The larger angle is distorted, O19-Co5-O8 = 135.29(17)º. This is due to the carboxylate involved in hydrogen bonding to N2 and O9, through O20, distorting the angle and this is compensated for by the smaller angle: O19-Co5-O18 (92.65(18)º).

Of the four AIP ligands in this structure those based on N2, N3 and N5 all exhibit bidentate bridging of the carboxylate groups therein. The fourth AIP ligand based on N4 has one bridging carboxylate group and one monodentate carboxylate group coordinated to Co5 through O19 and H-bonded to O9 (O20-O9 intermolecular distance, D···A = 2.883 Å, D-H···A angle = 147º) and N2 (O20-N2 intermolecular distance, D···A = 3.021 Å, D-H···A angle = 141º). All ligand nitrogen atoms are bound to one cobalt centre.

The gross packing of **12** gives a complex 3D MOF, with the SBU surrounded by twelve ligating AIP moieties. Each AIP moiety interacts with three distinct SBUs with all the amino tag groups coordinating to cobalt(II) centres. Figure 4.10 shows the densely packed framework (ρ = 1.870 gcm^{-3}).

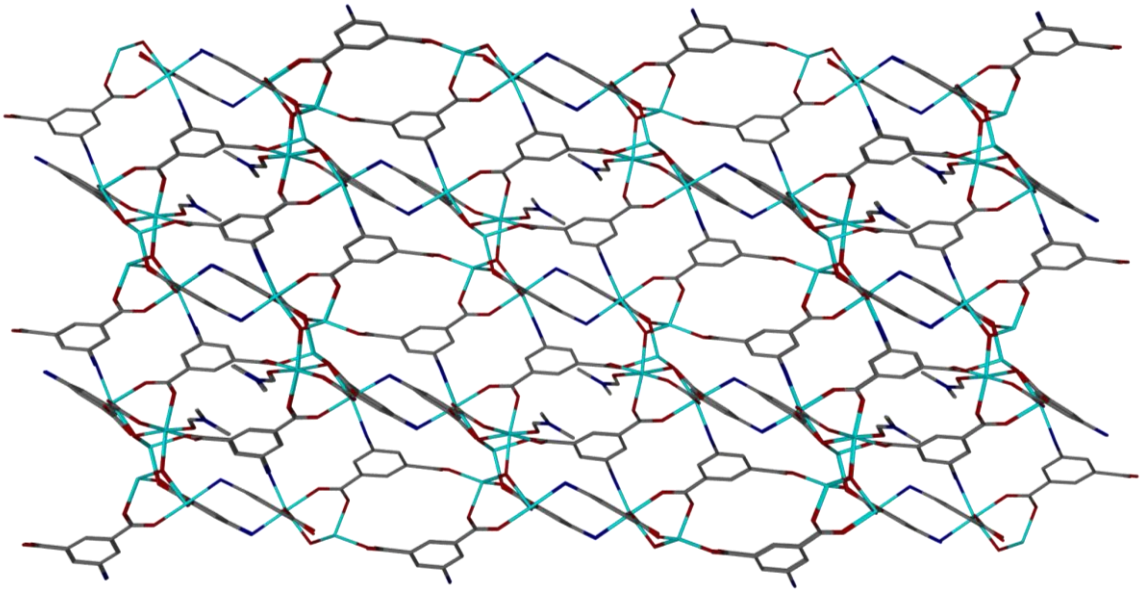

Figure 4.10. Gross packing of **12**, viewed along [010], shows a densely packed MOF. Lattice solvent and hydrogen atoms omitted. C: gray, O: red, N:blue, Co: cyan. Aromatic hydrogen atoms omitted.

The presence of free DMF in this structure suggests there may be a possibility of activating this material by removal of the solvent with heat under vacuum. In the as-prepared material there are eight pores per unit cell, each one with a volume of 104 $Å^3$, occupied by one DMF molecule (five non-hydrogen atoms ~100 $Å^3$). Therefore, the space occupied by guest DMF represents 9.4 % of the cell volume, or 832 $Å^3$ per unit cell.

A comparison of the PXRD pattern for the bulk material, with the predicted PXRD pattern from the single-crystal data is shown in Figure 4.11. The data show that the bulk material of **12** cannot be unambiguously identified as a pure sample of $[Co_5(\mu_3\text{-}OH)_2(AIP)_4(DMF)_{0.5}(H_2O)_{0.5}]\cdot 1.75DMF\cdot 1.5H_2O$. The weak peaks and very low signal:noise ratio could have arisen from the sample's degradation of crystallinity out of solution, or the degradation of the crystals in the X-ray beam. The PXRD quality can be increased by increasing the exposure time per step and a sample was ran overnight at 30 seconds per step. There was no noticeable increase in quality of the data. Also there was no noticeable improvement when a PXRD study was taken with the crystals still in solution (DMF).

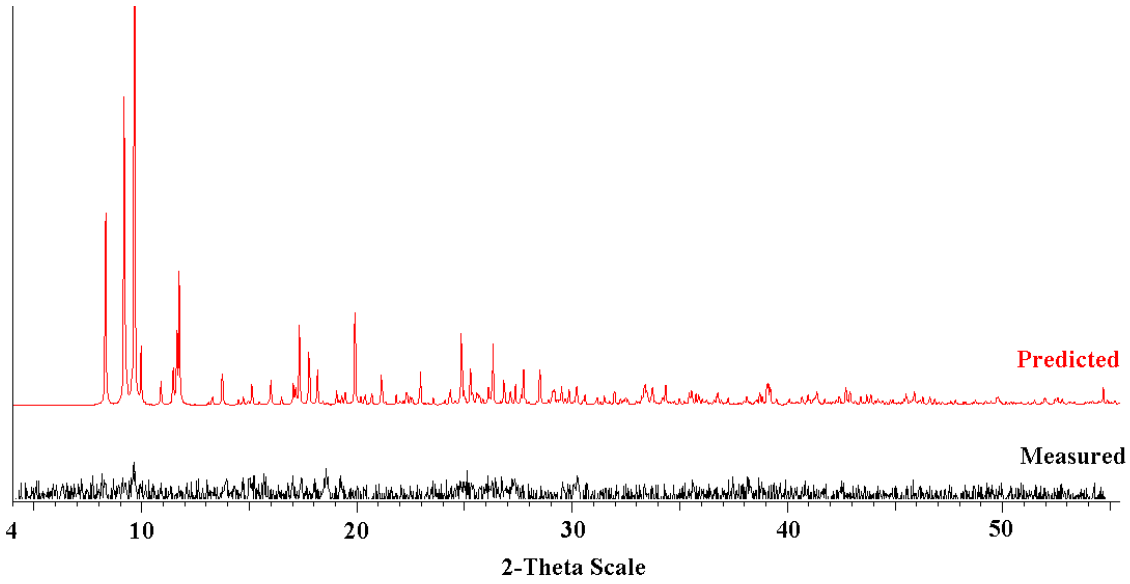

Figure 4.11. PXRD comparison of bulk and single crystal simulated data for compound **12**.

A TGA study of **12,** Figure 4.12, shows the stages of activation and decomposition of the bulk sample. Surprisingly this is more typical of an organic compound with no distinct regions separating solvent loss and sample decomposition at approximately 420 °C. The TGA does not show a distinct plateau, which suggests that no stable activated species can be accessed by heating.

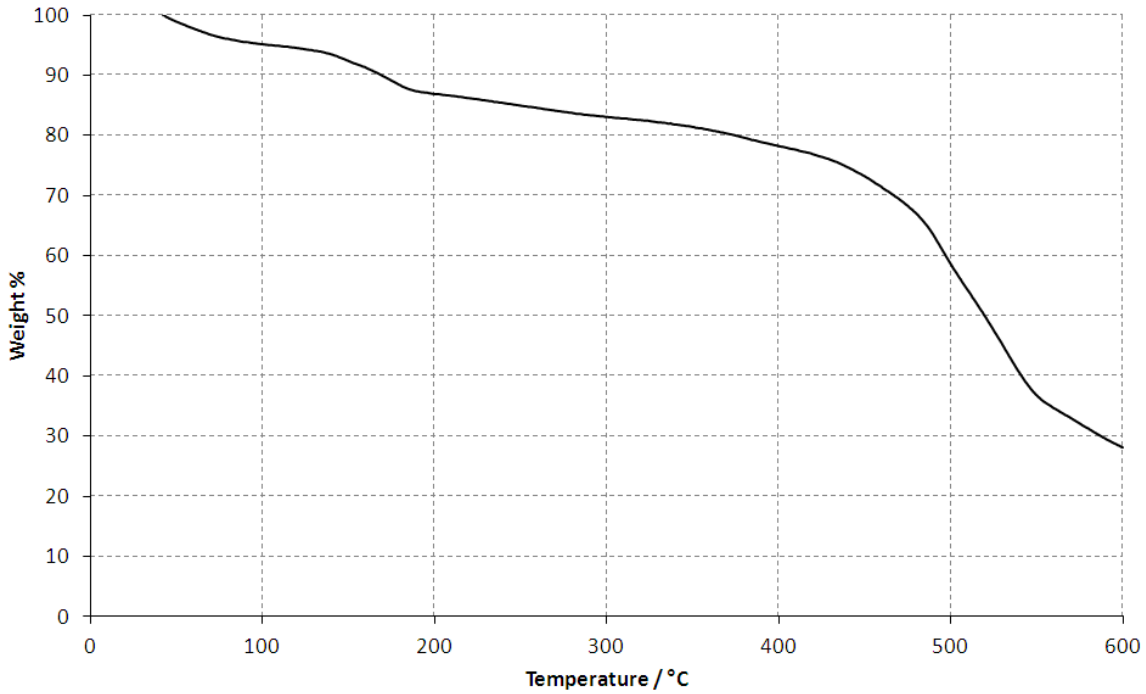

Figure 4.12. TGA of **12**.

Further work on activating this compound will need to be undertaken, if it is to be considered for gas storage. For example, heating a sample to 250 ºC under vacuum and

maintaining that temperature for a few hours, followed by a TGA study would show whether or not the solvent guest molecules could be removed without decomposition of the framework. PXRD data would confirm if the crystallinity of the sample is intact, because removing guest solvent will have little effect on the unit cell parameters and therefore would not shift major peak positions. Single-crystal X-ray diffraction data of the activated species could be obtained if the quality of the crystals were to remain high following activation. Nitrogen sorption studies would then reveal the effective surface area of this material. The relatively high density of **12**, 1.87 gcm^{-3}, means that % wt. gas uptake is more likely to be lower compared with similar structures of a lower density. Therefore the material is unlikely to be a sensible candidate for gas storage.

In summary the structure of **12** contains three AIP linkers that coordinate to five cobalt(II) ions and one AIP linker that coordinates to four cobalt(II) ions. There are no free NH_2 groups available for PSM studies, as they are all coordinated to cobalt(II) cations. Experiments run in tandem, with nickel(II) acetate, gave no crystalline products.

4.3.2. MOF Synthesis with 5-Acetamidoisophthalic Acid

The next strategy to obtain accessible amino groups in a MOF based on AIP was to protect the amino group before the MOF formation reaction and then deprotect by PSM. H_2AMIP was synthesised from H_2AIP, Scheme 4.2. This followed the procedure reported by Slusher *et al.*[10] This reaction gave good yield (66 %) and conversion (>99 %) for the conversion of H_2AIP to H_2AMIP. The protected compound H_2AMIP was soluble in common organic solvents and dissolved under standard MOF reaction conditions, above 100 ºC, but the compound had a low solubility in water at room temperature. This as-synthesised compound was of high enough purity (evaluated by ^{1}H, ^{13}C NMR and FT-IR to be >99 % pure) to take forward for MOF synthesis.

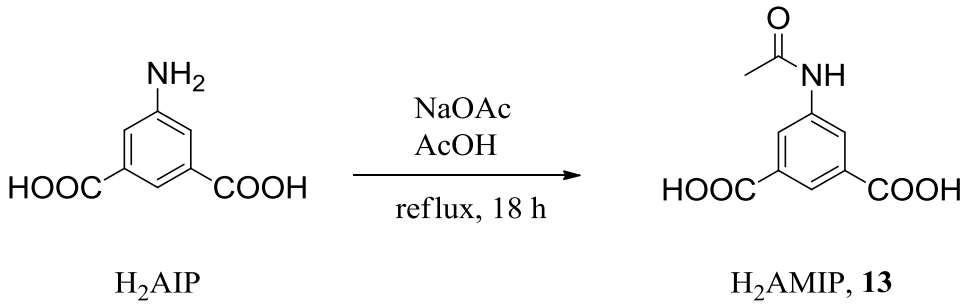

H_2AIP H_2AMIP, **13**

Scheme 4.2. One step synthesis of H_2AMIP, **13**.

4.3.3. Hydrolysis of the Amide Group of H_2AMIP Forming a Zwitterionic Organic Compound, $H_2AIP{\cdot}0.5H_2O$

The lability of the amido tag group was observed in the products of several hydrothermal reactions between H_2AMIP (**13**), zinc nitrate hexahydrate and benzoic acid, yielding colourless crystals. The synthetic conditions are summarised in Scheme 4.3.

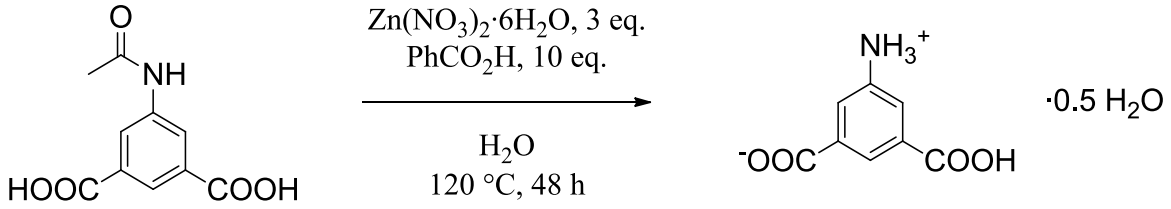

H_2AMIP, **13** $H_2AIP{\cdot}0.5H_2O$, **14**

Scheme 4.3. Synthetic conditions for **14**.

These crystals were characterised by small molecule X-ray diffraction as the zwitterionic, organic, extended framework, 3-ammonio-5-carboxybenzoate hemihydrate, $H_2AIP{\cdot}0.5H_2O$ (**14**). The crystallographic data is summarised in Table 4.2.

Formula	$H_2AIP{\cdot}0.5H_2O$
Empirical formula	$C_8\ H_8\ N\ O_{4.5}$
Formula weight / $gmol^{-1}$	190.16
T / K	150(2)
λ / Å	0.68890
Crystal system	Monoclinic
Space group	$C2/c$
a / Å	8.1317(2)
b / Å	17.4495(3)
c / Å	11.1643(2)
$\alpha = \gamma$ / °	90
β / °	94.123(3)
Volume / $Å^3$	1580.05(6)
Z (no. molecules in unit cell)	8
Density (calculated) / gcm^{-3}	1.599
Crystal size / mm	0.050 x 0.050 x 0.005
Data Completeness	0.972
Final R indices [$I>2\sigma(I)$]	$R1$ = 0.0510 $wR2$ = 0.1499
R indices (all data)	$R1$ = 0.0550 $wR2$ = 0.1573
Largest diff. peak and hole / $eÅ^{-3}$	0.355 and -0.329

Table 4.2. Crystallographic data for **14**.

The crystal structure, of **14**, comprises of one molecule of the zwitterionic ligand plus half of a molecule of water, shown in Figure 4.13. The oxygen atom from the latter is coincident with a crystallographic 2-fold rotation axis and therefore is assigned as 50 % occupancy. The associated hydrogen atom was located and refined at a distance of 0.98 Å from O5. This oxygen atom is bonded to two hydrogen atoms (H5) and is in a tetrahedral coordination with the other two positions taken up by two hydrogen bonds (with two H1C atoms from separate amino groups).

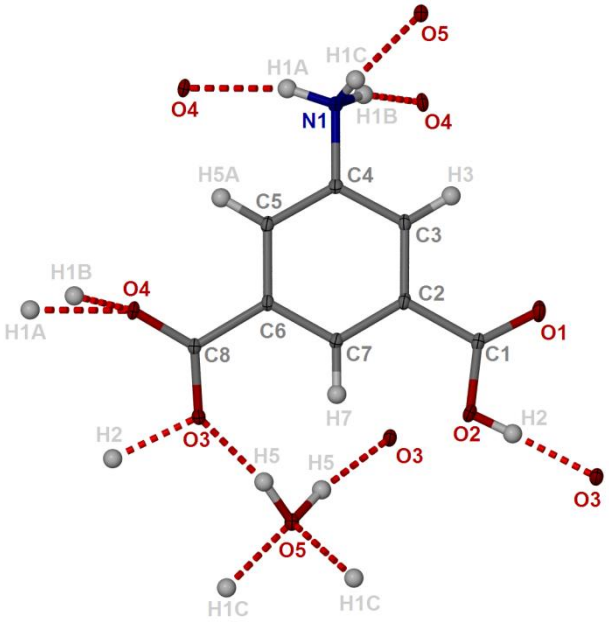

Figure 4.13. Compound **14** including hydrogen bonding. Ellipsoids shown for non-hydrogen atoms at 30 % probability. C: grey, H: white, O: red, N: blue.

A free carbonyl group is present on the zwitterionic H_2AMIP (C1-O1, bond length = 1.2221(16) Å) and demonstrates a carboxylic acid group double bond. Comparing this with the other C-O bond length, C1-O2 is significantly longer *i.e.* 1.3112(16) Å. The carboxylate group O3-C8-O4 shows delocalised single and double bonds as reflected in the similar bond lengths, within error [C8-O4, 1.2612(15) Å: C8-O3, 1.2565(15) Å].

The gross structure reveals off-centre π-stacking of aromatic rings in a layer arrangement. These are at an intercentroid distance of 3.77 Å and a C7-centroid-centroid angle of 110° (20° from a perfect eclipse of 90°). Aromatic molecules alternate along the sheets and form a hydrogen bond ring motif of graph set $R_2^2(14)$ shown in Figure 4.14.

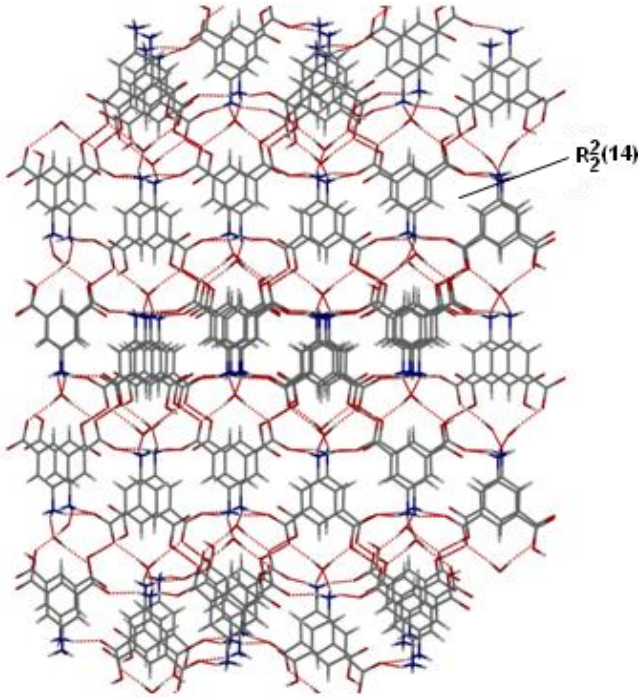

Figure 4.14. Wireframe diagram of **14** showing the view down the crystallographic *a*-axis. Alternating molecule orientations along the 2-D sheets can be seen. C: grey, H: white, O: red, N: blue.

The layers that pack on top of each other are held together by a dense hydrogen-bonding network involving all of the hetero atoms contained in the structure. The hydrogen bonds are summarised in Table 4.3, the shortest donor-acceptor, D···A, distance is O2-H2···O3 (2.538 Å) and the longest is N1-H1A···O4 (2.895 Å).

D-H	d(D-H)/Å	d(H···A) /Å	<DHA/°	d(D···A)/Å	A
O2-H2	0.84	1.70	173	2.54	O3
N1-H1A	0.91	2.04	155	2.90	O4
N1-H1B	0.91	1.88	164	2.77	O4
N1-H1C	0.91	1.92	159	2.78	O5
O5-H5	0.98	1.77	170	2.74	O3

Table 4.3. Hydrogen bonds with H···A < r(A) + 2.000 Å and <DHA > 110 °.

Hydrogen bonding occurs only between the organic molecules and the water molecules, not between adjacent water molecules, as shown in Figure 4.15. The distance between the sheets was measured at 3.54 Å, and hydrogen bonding between the sheets can be denoted by the graph set $R_4^3(18)$.

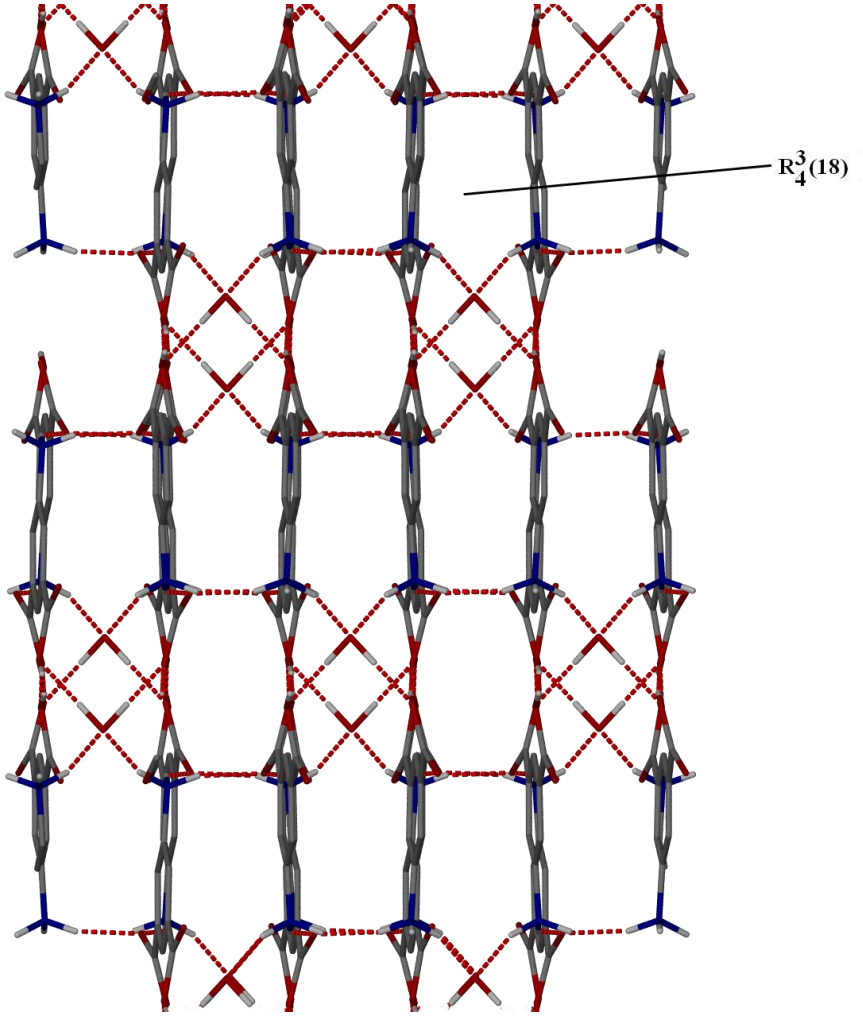

Figure 4.15. View along the *a*-*c* plane illustrating layered 2-D sheets 3.54 Å apart, held together by hydrogen bonding. C: dark grey, H: light grey, O: red, N: blue.

A comparison of the PXRD pattern for the bulk material, with the predicted PXRD pattern from the single-crystal data is shown in Figure 4.16. The data shows that the bulk material of **14** has crystalline phase purity in agreement with the single crystal diffraction experiment. The crystals were washed with acetone and air dried and, surprisingly for a purely organic crystal, the powder diffraction data was still of high quality.

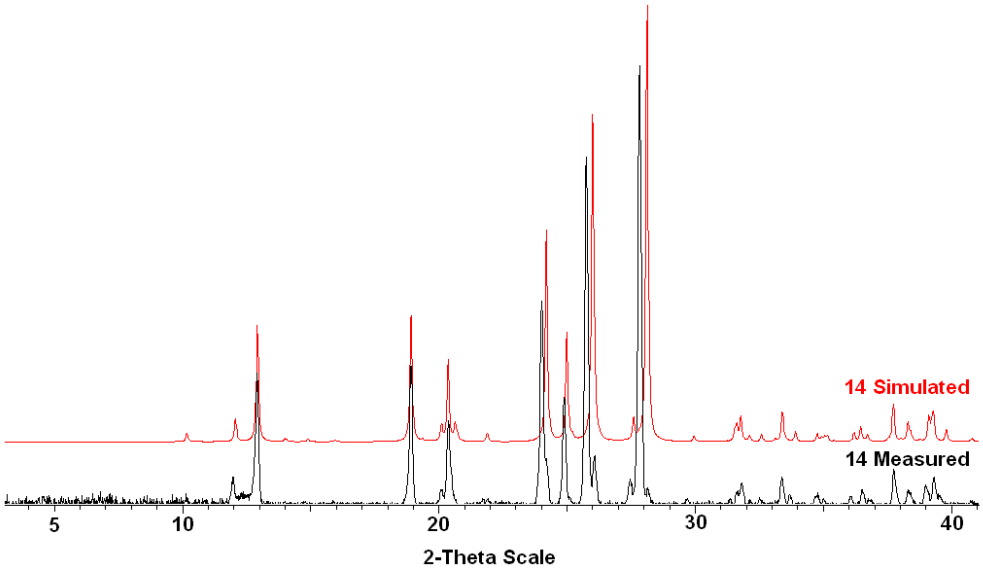

Figure 4.16. PXRD of measured **14** (black) and the simulated pattern (red) from the single crystal X-ray diffraction data.

Interestingly the hydrolysis of the amino group only proceeded in the presence of Zn(II) nitrate hexahydrate and not with Ni(II) acetate, Co(II) acetate, Mn(II) acetate or Cu(II) nitrate in water. Also the reaction only gave the crystalline product, **14**, in water and was not observed when DMF or DMSO was used as the reaction solvent.

The synthesis is an example of an amide C-N bond cleavage. There have been few examples of this reported in the literature the most recent example was a general reduction with a SmI_2 catalyst, amine and water, in THF at room temperature, reported by Szostak *et al*.[14]

4.3.4. A Cobalt(II) MOF Incorporating the AMIP Linker

To obtain the first example of a cobalt MOF containing the H_2AMIP linker, cobalt(II) acetate was chosen as the metal source. This decision was helped by preliminary experiments with cobalt(II) nitrate that gave no crystalline products, under standard MOF reaction conditions.

The reaction solvent was varied and the systems that were trialled were based on solubility of the ligand. Solutions that were clear, after stirring, were DMF:H_2O (1:1) and DMSO. All other solvent systems gave reaction mixtures that were cloudy with undissolved reagents. All reactions mixtures had a metal:ligand ratio of 1:1, and were run at 120 ºC for 48 h. Only the reaction in DMSO yielded a crystalline product, summarised in Scheme 4.4. This was characterised by diffraction techniques as [Co(AMIP)$(DMSO)_2$]·DMSO, **15**.

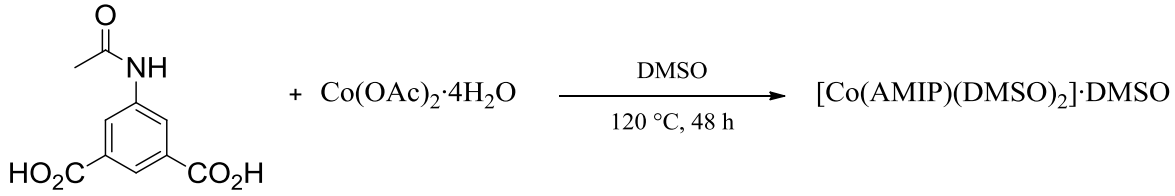

13 **15**

Scheme 4.4. Reaction conditions for the synthesis of **15**.

Framework **15** consisted of very thin (<0.025 mm) purple, plate-like crystals that were weakly diffracting. The sample was very difficult to characterise by single crystal X-ray diffraction in house due to weak diffraction, therefore a synchrotron source was used. The temperature of the experiment was kept at 240 K to reduce the risk of unwanted phase changes in the crystals at lower temperatures. The crystallographic data is summarised in Table 4.4.

Formula	$[Co(AMIP)(DMSO)_2]\cdot DMSO$
Empirical formula	$C_{16}\ H_{25}\ Co\ N\ O_8\ S_3$
Formula weight / $gmol^{-1}$	514.48
T / K	240(2)
λ / Å	0.68890
Crystal system	Triclinic
Space group	*P*-1
a / Å	8.410(3)
b / Å	9.303(4)
c / Å	16.311(5)
α / °	98.892(3)
β / °	99.943(1)
γ / °	110.819(8)
Volume / $Å^3$	1142.1(7)
Z (no. molecules in unit cell)	2
Density (calculated) / gcm^{-3}	1.496
Crystal size / mm	0.005 x 0.004 x 0.004
Data Completeness	0.937
Final R indices [$I>2\sigma(I)$]	$R1$ = 0.0556 $wR2$ = 0.1469
R indices (all data)	$R1$ = 0.0639 $wR2$ = 0.1515
Largest diff. peak and hole / $eÅ^{-3}$	1.178 and -0.879

Table 4.4. Crystallographic data for **15**.

The SBU and surrounding linkers are shown in Figure 4.17 and consist of two pseudo-octahedral cobalt(II) centres (Co1). These are related by an inversion centre, and covalently bound by two AMIP linkers through two bridging carboxylate linkers, Co1-O3-C8-O4-Co1. Axially ligated DMSO molecules complete the last two places in the coordination sphere. The DMSO molecule based on O7, exhibited disorder over two sites (50:50) of the sulphur (S2/S2A) and carbon (C13/13A, C14/14A) atoms therein. Anisotropic displacement parameter (ADP) restraints were applied to fractional occupancy carbon moieties in the disordered DMSO molecules, to assist convergence.

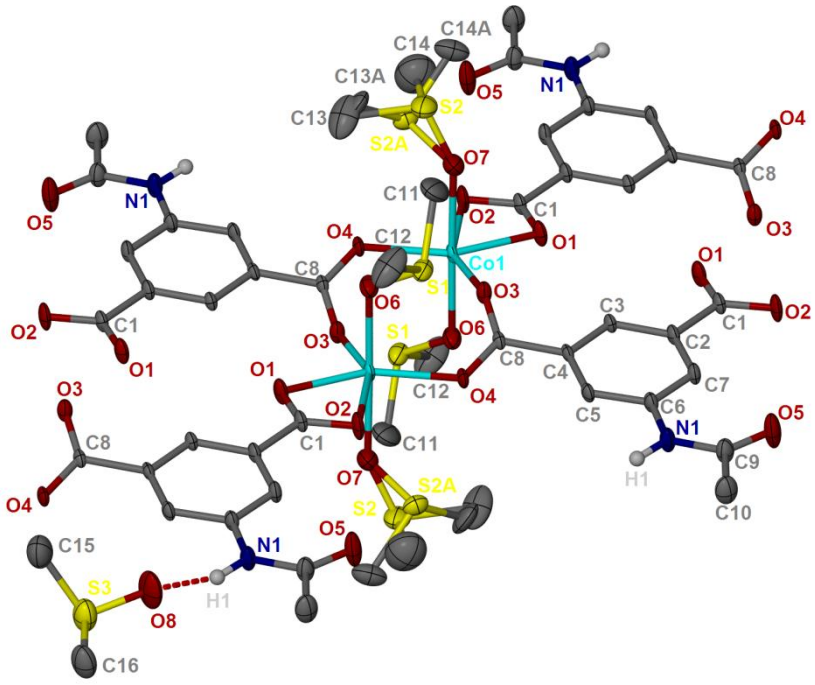

Figure 4.17. SBU and surrounding linkers of **15**. Ellipsoids shown for non-hydrogen atoms at 30 % probability. C: grey, H: white, O: red, N: blue, S: yellow, Co: cyan. Aromatic hydrogen atoms and methyl hydrogen atoms are omitted.

The metal centre, Co1, is coordinated to four oxygen atoms (of carboxylates): Co1-O1 bond length = 2.093(2) Å, Co1-O2 = 2.299(2) Å, Co1-O3 = 2.015(2) Å and Co1-O4 = 2.0253(18) Å. The equatorial angles are in two groupings: O1-Co1-O2 = 59.79(8)° and the opposite is 111.81(9)°, the other two are 94.14(8)° and 93.88(9)°. The axial *trans* angle O6-Co1-O7 is 178.29(10)° showing that there is no significant shortening of the distance between the axial solvent ligands but there is significant distortion of the equatorial atoms from octahedral. The two oxygen atoms from the DMSO molecules O6 and O7 have M-O

bond lengths in the same range as the carboxylate-metal bonds with Co1-O6 (2.107(2) Å), slightly shorter than Co1-O7 (2.172(3) Å) of the disordered DMSO site.

The carboxylate group based on C1 caps one cobalt(II) centre equatorially, whereas carboxylate groups based on C8 bridge two cobalt(II) centres. There are no free carbonyl groups in this framework. This results in the Co_2 SBU linking through bridges, *via* AMIP moieties, to form infinite 1-D chains, as shown in Figure 4.18.

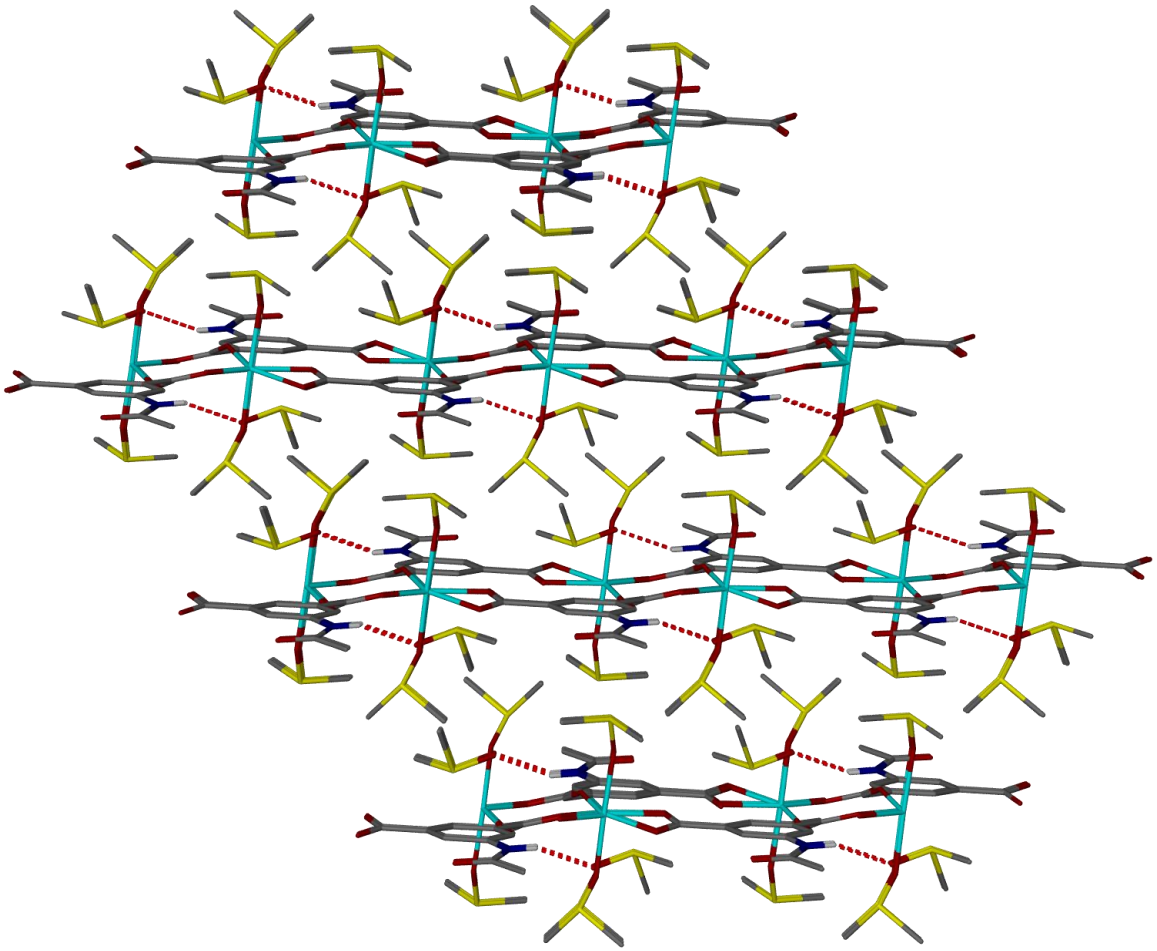

Figure 4.18. Cross section of channels of **15**, showing DMSO ligation and DMSO structural disorder. C: grey, H: white, O: red, N: blue, S: yellow, Co: cyan. Hydrogen atoms omitted.

A solvent dominated DMSO region is present in between the cobalt-AMIP ladders and the large number of DMSO methyl groups participate in van der Waals interactions, holding the ladders together and this packing is shown in Figure 4.19. Adjacent ladders are interdigitated side to side and from above and below. The density of the MOF (ρ = 1.496 gcm^{-3}) is indicative of a closely packed material. This would be significantly different if the DMSO could be removed without framework collapse.

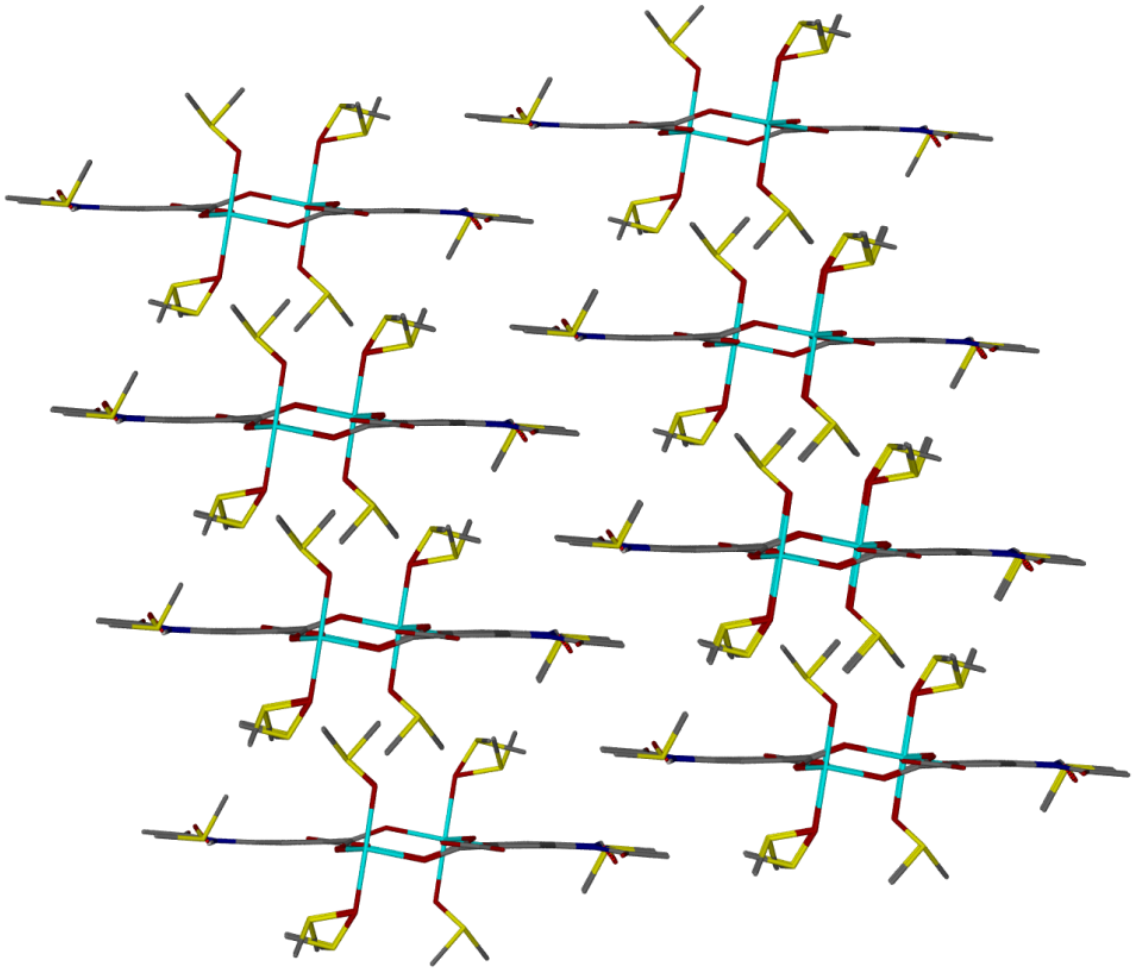

Figure 4.19. View of the interaction between adjacent chains of **15** illustrating interdigitation. C: grey, H: white, O: red, N: blue, S: yellow, Co: pink. Hydrogen atoms omitted.

Channels of diameter 8.3 Å are formed by interdigitated amido tag groups along the crystallographic *a*-axis (Figure 4.20). These channels are occupied by DMSO molecules bound to the framework by the hydrogen bonding of O8 to the H1-N1 amido tag group of AMIP, (O8-N1 intermolecular distance, D···A = 2.809 Å, D-H···A angle = 157º). This is an example of the simplest graph set *i.e.* D.

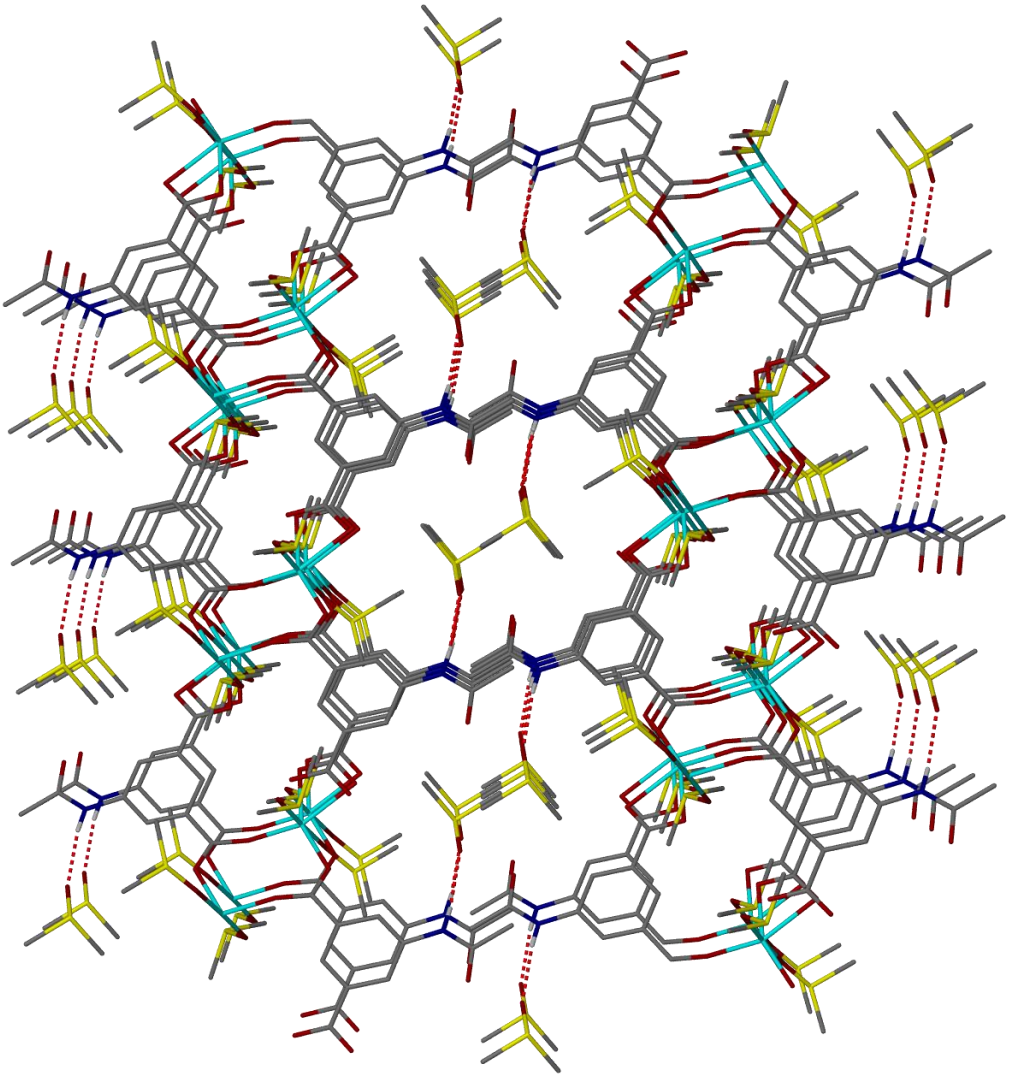

Figure 4.20. View down channels of **15** with DMSO hydrogen bonding to amide N-H (dashed red lines). C: grey, H: white, O: red, N: blue, S: yellow, Co: cyan. Hydrogen atoms omitted.

The PXRD pattern, given in Figure 4.21, shows the material gives a weak diffraction pattern *in-situ* in DMSO. In comparison with the simulated data from the single-crystal X-ray diffraction data, the highest intensity peaks are coincident and under an optical microscope the sample appears homogeneous. Therefore, it is reasonable to assume (but not certain) that the bulk material matches the structure obtained from the single crystal diffraction experiment and represents the whole sample. The low signal:noise ratio may be due to the difficulty in performing the experiment. There could have been some degradation of the crystals in the capillary prior to and during the experiment due to the instability of **15** to atmospheric moisture.

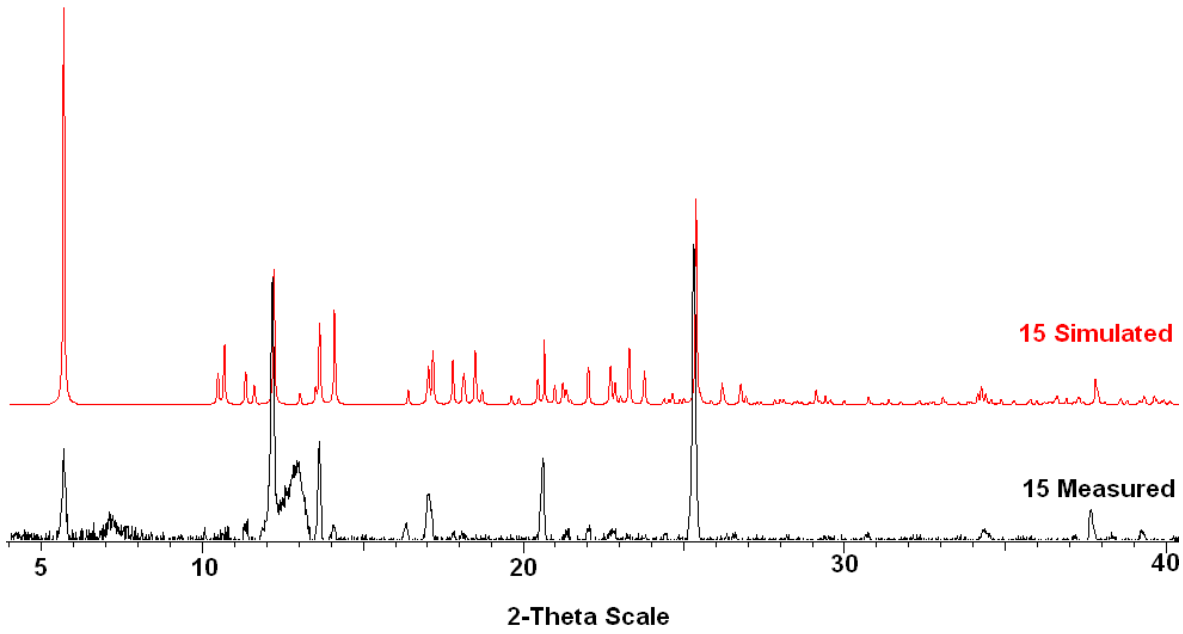

Figure 4.21. PXRD patterns of measured **15**, in DMSO, and the simulated pattern from the single crystal X-ray diffraction data. The peak at 13° (2θ) is attributed to the glass capillary.

The presence of DMSO in the channels suggests there may be a possibility of activating this material by removal of the solvent with heat under vacuum. The TGA, in Figure 4.22, shows solvent loss, up to 370 °C, in four stages before a plateau region. The first stage could be attributed to water introduced due to the highly hygroscopic nature of **15** and DMSO, with the following three steps representing the loss of three DMSO molecules per formula unit. This accounts for 61 % of the total mass of the compound and hence the sample has absorbed a significant amount of water. Three DMSO molecules account for 46 % per formula unit of **15** located in two different environments in the framework. The framework starts to decompose above 400 °C.

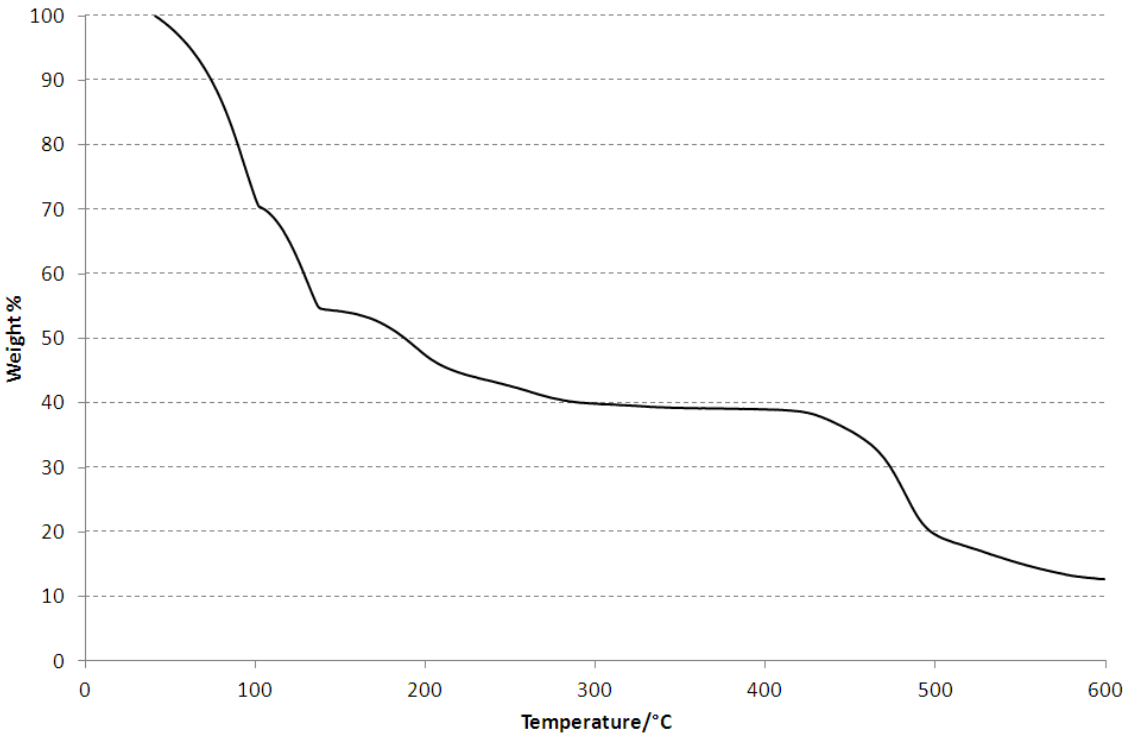

Figure 4.22. TGA of **15**.

It was impossible to characterise the framework topology of **15**, at the plateau region, by PXRD because of the sample instability during the experiment. Therefore it is difficult to know the precisely if a change in topology has occurred leading to a skewed TGA measurement. Activating a crystal of **15** whilst mounted in an X-ray beam and recording the structure as a function of increasing temperature may be one way of investigating this potential phase change.

The reaction gave no crystalline solids with many other solvents: H_2O, DMF, MeOH, Acetone, MeCN, Et_2O and THF. The product from the reaction in DMSO, **15**, was unstable on exposure to atmosphere, was readily soluble in water and attempts at activation or solvent exchange were met with framework collapse. Therefore potential applications, such as gas storage and selectivity are limited with this MOF system and framework **15** was not exposed to further PSM reactions.

4.3.5. Addition of 4,4'-Bipyridine to the MOF Formation Reaction Between Zinc(II) and H_2AMIP

For the purpose of gaining solvent accessible voids, a spacer was added to the MOF reaction mixtures. The linker that was selected was 4,4'-bipyridine (bipy) and was chosen because of the relationship of the N-donor atoms on two rigid aromatic rings. All the possibilities of π-stacking would remain, as well as metal coordination through the nitrogen atom lone electron pairs. This linker had also been successful with MOF formation in many structures in the literature, for example in the CID frameworks mentioned in Section 4.1.[8]

The first crystalline product obtained was from the reaction between zinc acetate tetrahydrate, H_2AMIP and bipy, under hydrothermal conditions, as summarised in Scheme 4.5.

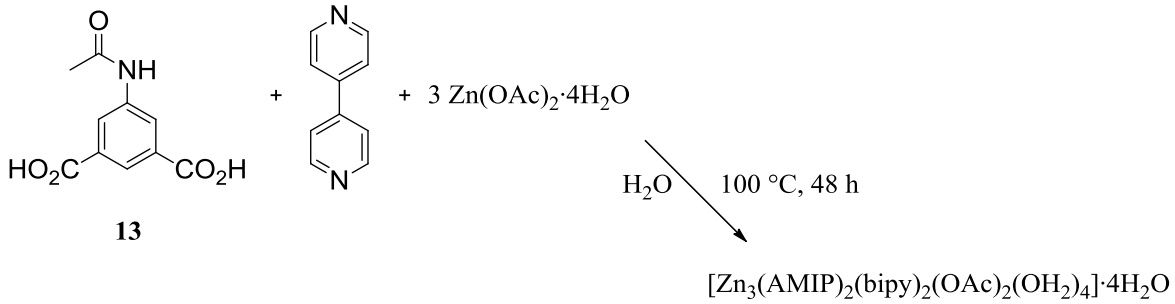

13 **16**

Scheme 4.5. Synthetic conditions for **16**.

The product obtained from this reaction was characterised by X-ray single crystal analysis as $[Zn_3(AMIP)_2(bipy)_2(OAc)_2(OH_2)_4]\cdot 4H_2O$, **16**. The diffraction data was recorded in-house and the relevant details are summarised in Table 4.5.

Hydrogen atoms in all water molecules were located and refined, subject to being a distance of 0.98 Å from the parent oxygen atoms; this is possible because of extensive hydrogen bonding making them easier to pinpoint.

Formula	$[Zn_3(AMIP)_2(bipy)_2(OAc)_2(OH_2)_4]\cdot 4H_2O$
Empirical formula	$C_{22}\ H_{26}\ N_3\ O_{11}\ Zn_{1.50}$
Formula weight / $gmol^{-1}$	606.51
T / K	150(2)
λ / Å	0.71073
Crystal system	Triclinic
Space group	P-1
a / Å	8.0390(1)
b / Å	8.5180(1)
c / Å	17.6830(3)
α / °	97.820(1)
β / °	91.631(1)
γ / °	97.306(1)
Volume / $Å^3$	1188.57(3)
Z (no. molecules in unit cell)	2
Density (calculated) / gcm^{-3}	1.695
Crystal size / mm	0.22 x 0.20 x 0.13
Data Completeness	0.990
Final R indices [$I>2\sigma(I)$]	$R1$ = 0.0282 $wR2$ = 0.0664
R indices (all data)	$R1$ = 0.0336 $wR2$ = 0.0695
Largest diff. peak and hole / $eÅ^{-3}$	0.442 and -0.431

Table 4.5. Crystallographic data for **16**.

There are two different metal nodes linked by bipy molecules, displayed in Figure 4.23. The first consists of a zinc(II) paddle wheel (based on Zn1). Two bridging AMIP molecules, two acetate ligands and two bipy spacers connect the two zinc(II) ions with inversion symmetry in the centre of the paddle wheel. Atom Zn1 has a coordination number of 5 consisting of four oxygen atoms, O1 and O2, from different carboxylate groups (Zn1-O1 = 2.0205(13) Å and Zn1-O2 = 2.0329(14) Å) and one ligated nitrogen atom, N1, from a bipy molecule (Zn1-N1 = 2.0352(14) Å). Zn1 is in a square based pyramidal geometry with a τ value (degree of trigonality)[15] of 0.03 (< 0.5 = square based pyramid).

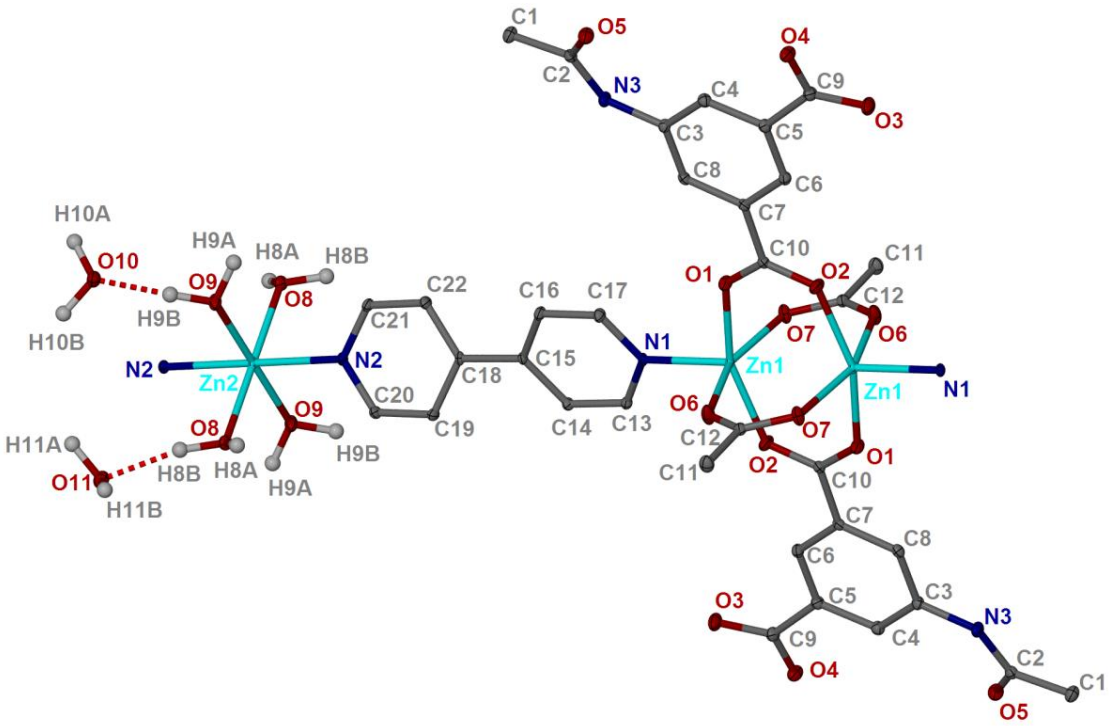

Figure 4.23. The two metal environments of compound **16** with surrounding linkers. Ellipsoids shown for non-hydrogen atoms at 30 % probability. C: grey, H: light grey, O: red, N: blue, Zn: cyan. Aromatic hydrogen atoms omitted.

Atom Zn2 is in a pseudo-octahedral environment and is located on a special position (inversion centre) and is therefore at 50 % occupancy. It is coordinated to four oxygen atoms of water ligands, of which two are symmetry equivalent, 2 x O8 and 2 x O9 related by the inversion centre. The Zn2-O8 bond length is 2.0932(14) Å and Zn2-O9 bond length is 2.1139(14) Å. It also has two bipy linkers in the axial positions, coordinated by N2 (Zn2-N2 = 2.1678 (14) Å) also related by the inversion centre located on Zn2. The *cis* angles are 88.84(6)º and 90.86(5)º, and *trans* angles are the same 180.00(5)º between bipy moieties as is between the water ligands (180.00(5)º).

The $(Zn1)_2$ paddle wheel and Zn2 octahedra are linked by rigid bipy molecules and alternate positions extending along an infinite 1-D chain. These 1-D chains are held together by hydrogen bonding (distance between the chains, 5.816 Å) *via* ligated water, amido N-H of an AMIP and the carboxylate group of an adjacent chain, listed in Table 4.6. Lattice water molecules are present in between the chains and aid in a complex 3-D hydrogen bonding network.

D-H	d(D-H)/Å	d(H···A)/Å	<DHA/°	d(D···A)/Å	A
O8-H8A	0.98	1.74	164	2.69	O4
O8-H8B	0.98	1.78	168	2.75	O11
O9-H9A	0.98	1.78	166	2.74	O5
O9-H9B	0.98	1.68	177	2.66	O10
O10-H10A	0.98	1.76	171	2.73	O4
O10-H10B	0.98	1.70	169	2.67	O3
O11-H11B	0.98	1.80	165	2.76	O10
O11-H11A	0.98	1.74	173	2.71	O3
N3-H2	0.88	2.10	168	2.96	O7

Table 4.6. Hydrogen bonds with H···A < r(A) + 2.000 Å and <DHA > 110 °.

The carboxylate group (O3-C9-O4) of AMIP in the framework is not involved in metal coordination but is part of the complex hydrogen bonding. Atom O3 participates in two hydrogen bonds with the lattice water molecules based on O10 and O11, through H10B and H11A respectively. Atom O4 also participates in two hydrogen bonds with the coordinated water molecule based on O8 and the lattice water based on O10, through H8A and H10A respectively. The AMIP tag group (N3-H2) and one uncoordinated carboxylate group (O5) form hydrogen bonds with lattice and coordinated water molecules (O9 and O7 respectively) making a 3-D network. Figure 4.24 shows this hydrogen bonding.

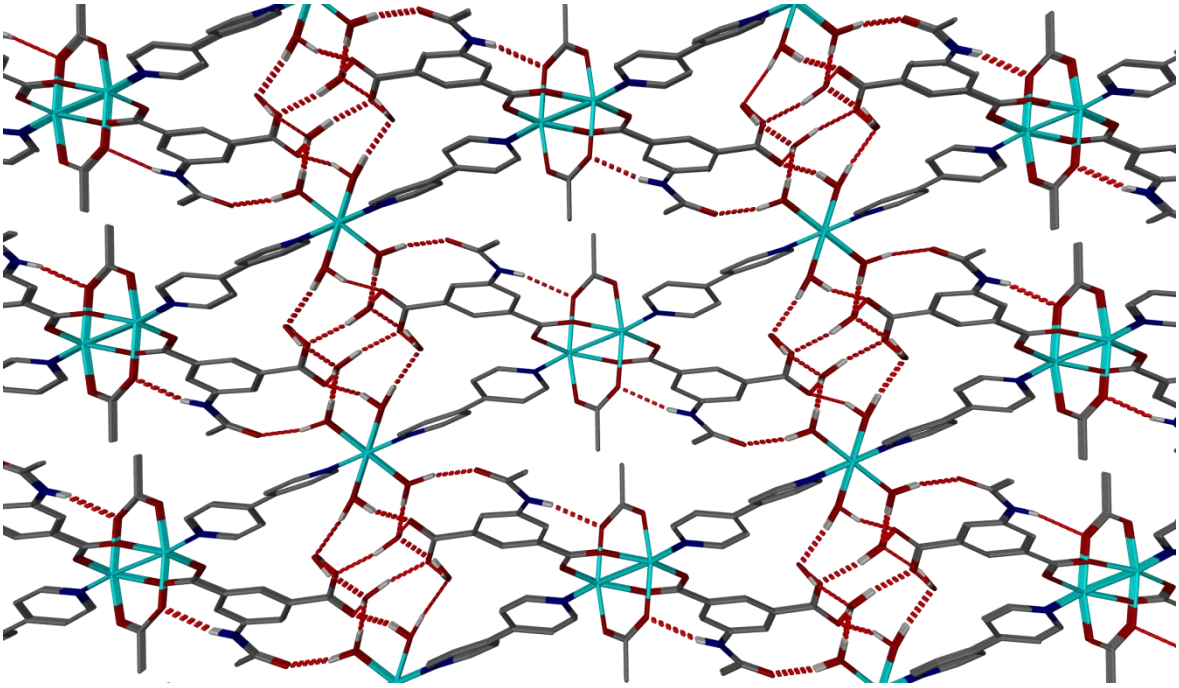

Figure 4.24. View down *a*-axis showing hydrogen bonded 1-D chains of **16**. AMIP tag group and one uncoordinated carboxylate group are forming hydrogen bonds with lattice and coordinated water molecules. C: grey, H: light grey, O: red, N: blue, Zn: cyan. Aromatic hydrogen atoms omitted.

The presence of face to face π-stacking between staggered rings of AMIP and bipy moieties (inter-centroid distance = 3.554 Å) and three dimensional hydrogen bonding hold the chains together in a densely packed network (ρ = 1.69 gcm^{-3}).

Substituting the acetate salt of zinc(II) for a nitrate salt in the synthetic conditions of **16**, afforded a completely new, more symmetrical topology, (a monoclinic instead of a triclinic crystal system). This is because the acetate ligands play a key structural role in **16**. The reaction carried out between zinc(II) nitrate, bipy and H_2AMIP is summarised in Scheme 4.6.

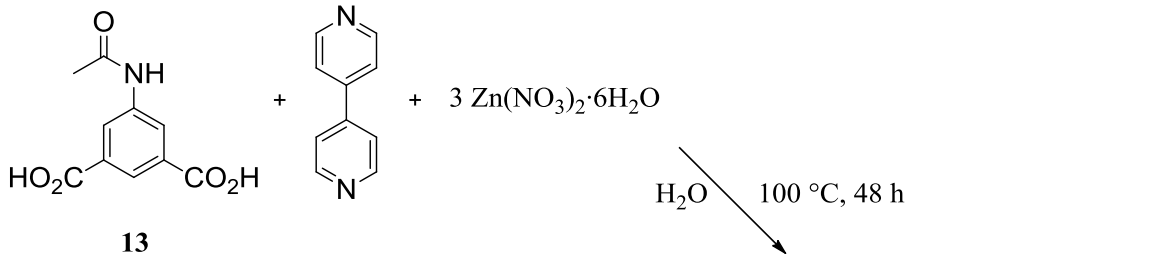

13 **17**

Scheme 4.6. Synthetic conditions for 17.

The resulting crystalline product was characterised as $[Zn_2(AMIP)_2(bipy)(OH_2)]\cdot 1.5H_2O$, **17**, and the single crystal diffraction results are summarised in Table 4.7.

Formula	$[Zn_2(AMIP)_2(bipy)(H_2O)]\cdot 1.5H_2O$
Empirical formula	$C_{30}\,H_{27}\,N_4\,O_{12.50}\,Zn_2$
Formula weight / $gmol^{-1}$	774.30
T / K	150(2)
λ / Å	0.71073
Crystal system	Monoclinic
Space group	$P2_1/a$
a / Å	17.3410(3)
b / Å	8.3900(2)
c / Å	22.2320(4)
$\alpha = \gamma$ / °	90
β / °	112.576(1)
Volume / $Å^3$	2986.69(10)
Z (no. molecules in unit cell)	4
Density (calculated) / gcm^{-3}	1.722
Crystal size / mm	0.25 x 0.20 x 0.10
Data Completeness	0.996
Final R indices [$I>2\sigma(I)$]	$R1$ = 0.0366 $wR2$ = 0.0719
R indices (all data)	$R1$ = 0.0632 $wR2$ = 0.0810
Largest diff. peak and hole / $eÅ^{-3}$	0.523 and -0.612

Table 4.7. Crystallographic data for **17**.

There are two distinct metal nodes in **17** (as in **16**) but these are five coordinate zinc(II) centres rather than octahedral seen in the acetate containing structure **16**. The framework of

17 contains 1.5 lattice water guest molecules, split between sites O12, O12A, O12B and O12C in a 40:30:40:40 ratio. The hydrogen atoms in the ligated water were refined at a distance of 0.98 Å from O11.

The atom Zn1 is coordinated to five atoms (Figure 4.25): four oxygen atoms from two carboxylate groups of two AMIP linkers based on N4, and one nitrogen atom from a bipy linker. Zn1-O bond lengths are in the range 1.956(2)-2.462(2) Å and the Zn1-N3 bond length is 2.074(2) Å. The atom Zn2 is also 5-coordinate: three coordinated oxygen atoms originate from carboxylate groups of AMIP linker based on N1, one oxygen atom from a ligated water molecule and one nitrogen atom from a bipy linker. Zn2-O bond lengths are in the range 1.967(2)-2.297(2) Å and the Zn2-N2 bond length is 2.037(2) Å. The degree of trigonality was calculated for Zn1, τ = 0.41, and hence is in a square based pyramidal environment. The metal centre Zn2 is in a trigonal bipyramidal coordination environment, τ = 0.87.

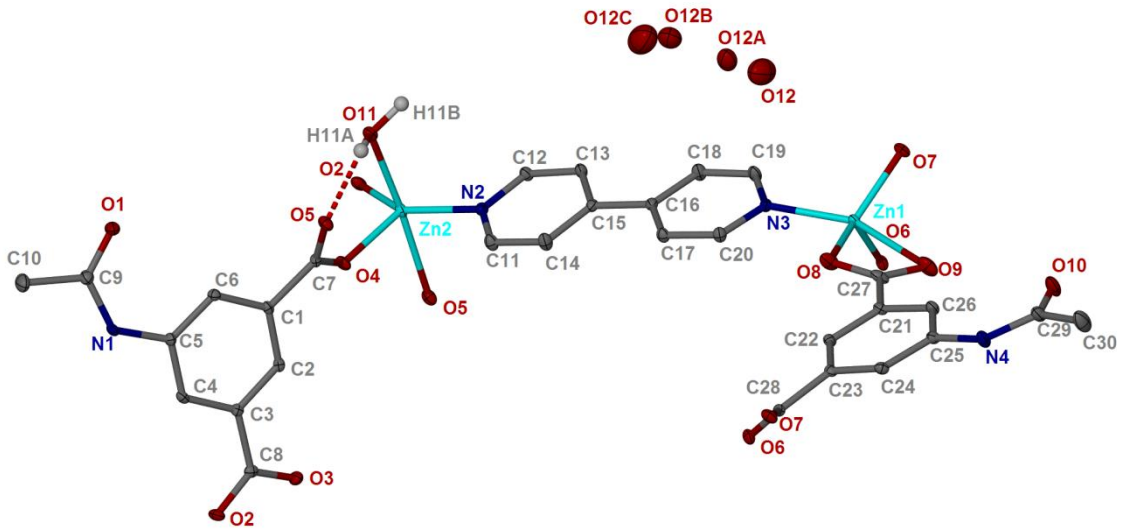

Figure 4.25. Metal coordination environments of **17**. Ellipsoids shown for non-hydrogen atoms at 30 % probability. C: grey, H: light grey, O: red, N: blue, Zn: cyan. Aromatic hydrogen atoms omitted.

The coordination modes of the linkers in **17** can be described in relation to the zinc(II) ions. The AMIP anion, based on N4, links two Zn1 atoms together through its two carboxylate groups: that based on C27 is bidentate chelating to Zn1 and that based on C28 is bridging two Zn1 atoms only. The AMIP based on N1 links two Zn2 atoms together with its two carboxylate groups. The free carboxylate oxygen atom O5 (C7-O5 = 1.256 Å) is involved in an intramolecular hydrogen bond to the coordinated water molecule (O11)

on Zn2. This interaction forms a six membered ring and is of graph set S(6) (O11···O5 = 2.822 Å, <DHA = 141°). The carboxylate group based on C7 and C8 is monodentate coordinate (differing from C27). The hydrogen bonds are listed in Table 4.8.

D-H	d(D-H)/Å	d(H..A)/Å	<DHA/°	d(D..A)/Å	A
O11-H11A	0.98	1.99	141	2.82	O5
O11-H11B	0.98	1.86	166	2.82	O3
N1-H1	0.88	2.04	160	2.88	O10
N4-H4	0.88	2.04	158	2.87	O1

Table 4.8. Hydrogen bonds in **17** with H···A < r(A) + 2.000 Å and <DHA > 110 °.

The two metal-AMIP chains are held together by bipy struts: N2 coordinated to Zn2 and N3 of the same bipy molecule coordinated to Zn1 forming an infinite 3-D network (perhaps described as a 3-D ladder), with metal carboxylate rungs extending in one dimension and organic struts in the other two dimensions, shown in Figure 4.26. This also shows Zn1 chains alternating with Zn2 chains and demonstrates a high density framework (ρ = 1.722 gcm^{-3})

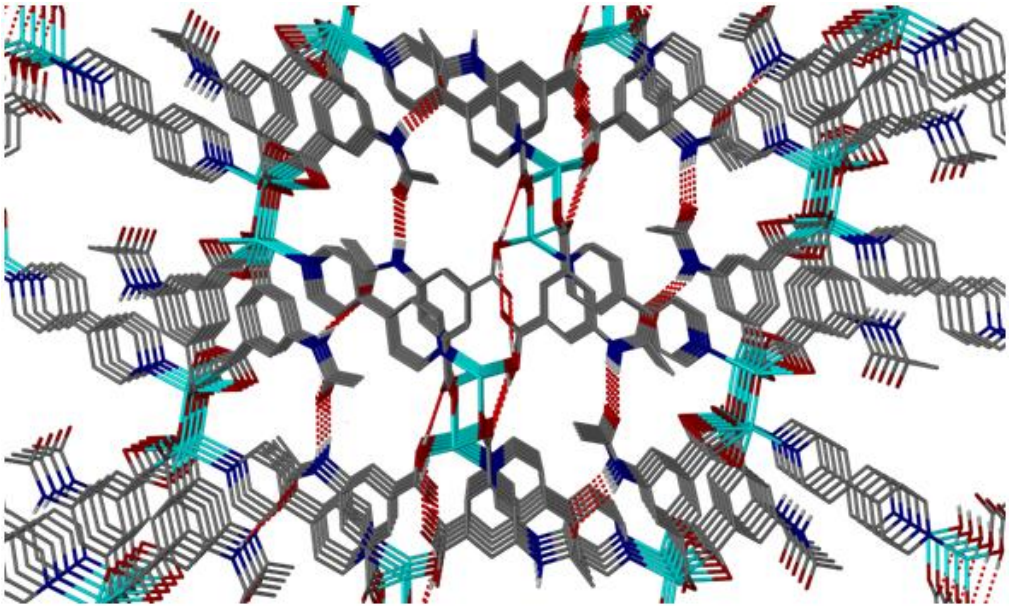

Figure 4.26. Amido tag in channels of dimensions 5.11 Å x 6.97 Å of **17**. $C_1^1(30)$ hydrogen bond chains extend parallel to the metal runs. Lattice water omitted. C: grey, H: light grey, O: red, N: blue, Zn: cyan. Hydrogen atoms omitted.

There is π-stacking present between aromatic rings of AMIP and bipy, along the metal chains (centroid distance measured 3.74 Å) with the ring planes parallel but slightly offset.

The aromatic rings border channels of dimensions 5.11 Å x 6.97 Å, which are similar to the dimensions of a bipy and AMIP moiety and house the AMIP amido tag groups.

Tag groups link together through hydrogen bonds of the amido groups connecting N4-H4···O1 and N1-H1···O10, with a pseudo-syndiotactic orientation of the corresponding rings, in a chain of graph set C(4) along [100] (Figure 4.27).

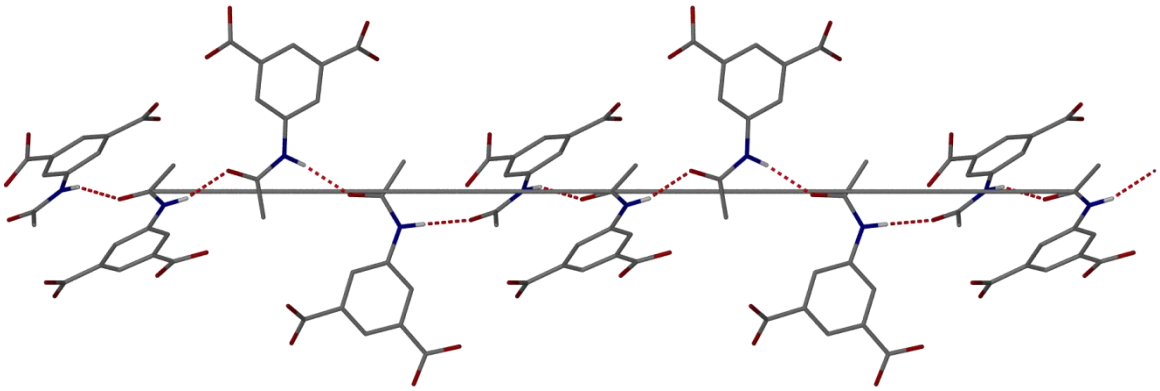

Figure 4.27. View of AMIP acetamido groups of **17** displaying an infinite hydrogen bond chain (dashed red lines) around a central rocking axis depicted by the light grey line. C: grey, H: light grey, O: red, N: blue. Hydrogen atoms omitted.

A comparison of the PXRD pattern for the bulk material, with the predicted PXRD pattern from the single-crystal diffraction data for **16** and **17** is shown in Figure 4.28. The data show that the bulk materials of **16** and **17** have crystalline phase purity in good agreement with the single crystal diffraction experiments. The crystals were stable in air and this is reflected in the high signal:noise ratio. The patterns are significantly different as expected for different crystal systems.

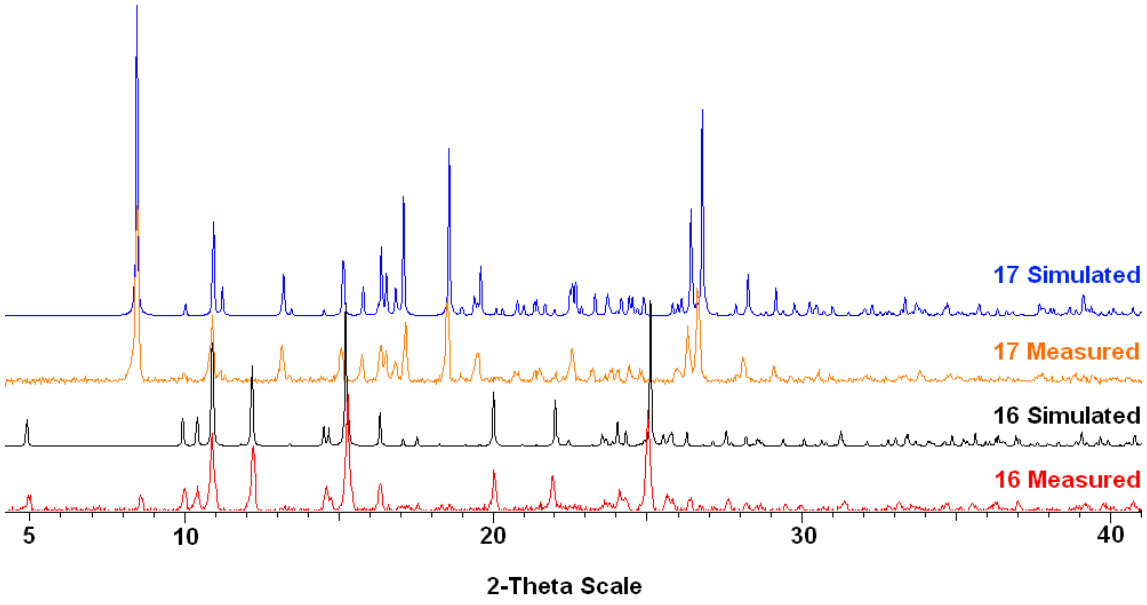

Figure 4.28. PXRD patterns of measured **16** and **17** compared with the simulated patterns from the single crystal X-ray diffraction data.

The TGA plots of **16** and **17** are shown in Figure 4.29. The data, for compound **16**, show the first mass loss region up to 110 °C (of 12 % loss) and represents the total of eight H_2O molecules per formula unit, hydrogen bonded between the 1-D metal-bipy chains and coordinated to Zn2. There is a small step where approximately one third of the water is more tightly held. A plateau region is present from 110 °C to 210 °C but it cannot be attributed to the activated crystalline framework, as the PXRD showed an amorphous compound after a similar *ex-situ* heat treatment. The framework decomposes above 210 °C which is relatively low, compared with **17**, and may be caused by the breakdown of the more labile acetate ligands on Zn1. It may also reflect the thermal stability of a 1-D topology (**16**) compared with a 3-D extended network (**17**), with a 1-D structure having only weak packing forces holding the lattice together.

In the case of framework **17**, the first mass loss region represents 6 % of the total and occurs up to 310 °C. This is accounted for by the 2.5 H_2O molecules per formula unit in the small channels of the 3-D network and coordinated to the zinc(II) ions (calculated 6.0 %). There is a plateau region from 310 °C to 390 °C, which could represent the activated framework but PXRD would need to be recorded to confirm this. The decomposition, starting at 390 °C, occurs in two steps and caused by the decomposition of the 4,4'-bipyridine (16 % mass loss observed between 390 °C and 420 °C, 20 % calculated) and finally the dicarboxylate linker.

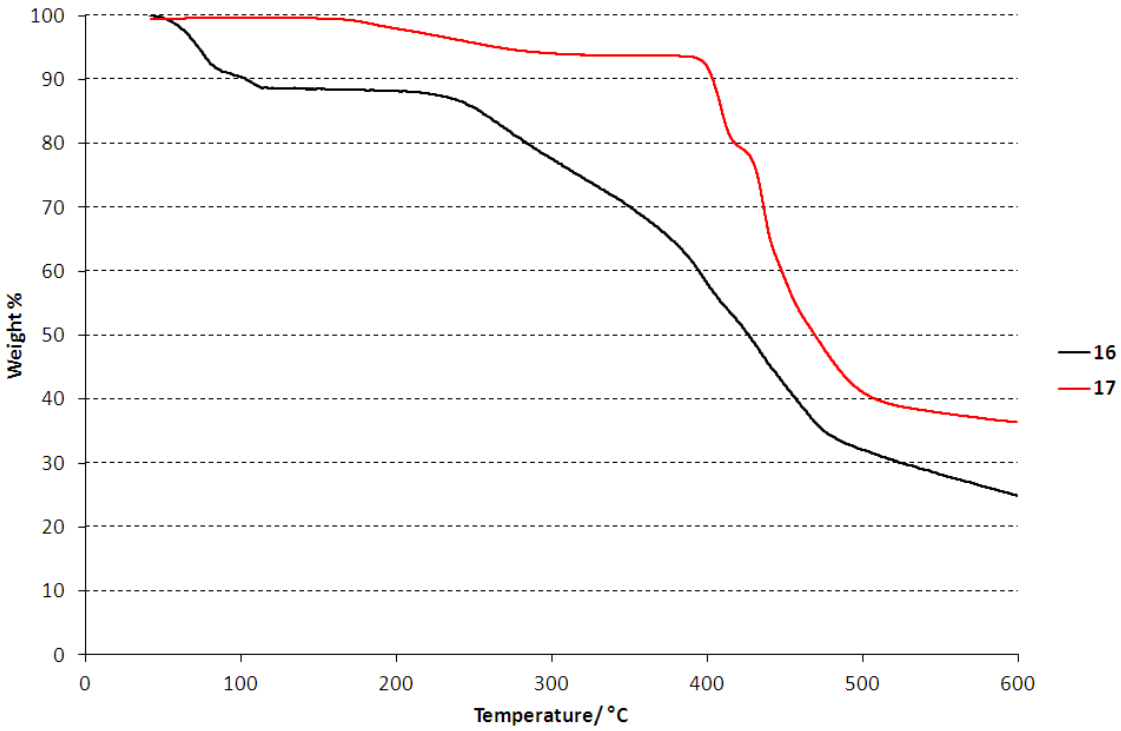

Figure 4.29. TGA of **16** and **17**.

Crystals of **16** and **17** were stable after washing with acetone and the reaction was successfully scaled up by a factor of three, however this increased the reaction time (2 weeks) as bipy is insoluble in this reaction mixture at the reaction temperatures used (100 °C).

There are no accessible voids in the frameworks but the tag groups may be thermally labile. Further experiments were carried out on framework **17** to activate by thermal deprotection. The results were that no amido cleavage was seen by ^{1}H NMR (when treated with H_2O at 130 °C for three days) except in the case of the zwitterionic structure, **14**, when in the presence of benzoic acid and zinc(II). This was corroborated by the PXRD patterns that were amorphous for the products. Boc protecting groups may have been more effective as protecting groups as reported by Telfer *et al.*[16]

4.3.6. AMIP in the Role of Counter Ion

Varying the metal from zinc(II) in the previous reactions, to nickel(II) and cobalt(II) yields crystals with AMIP in an interesting non-coordinating role. Two crystalline products were obtained from the hydrothermal reactions between nickel(II) acetate and cobalt(II) acetate with bipy and H_2AMIP. The reactions are summarised in Scheme 4.7. Similarly to the

synthetic reaction of **16** and **17**, bipy did not dissolve at room temperature in water, but in contrast it did dissolve at high temperature in this case.

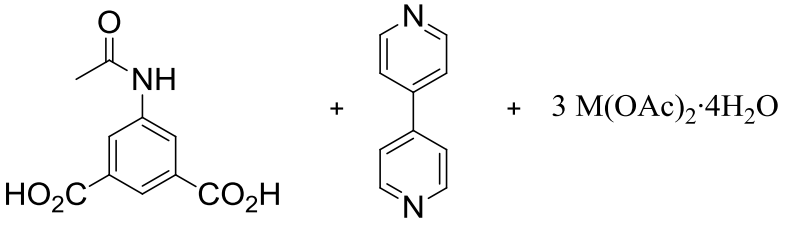

13

H_2O | 95 °C, 24 h

$[M(bipy)(OH_2)_4]^{2+}[AMIP]^{2-}$

18, M = Ni
19, M = Co

Scheme 4.7. Synthetic conditions for **18** and **19**.

Two analogous frameworks were obtained with the formula $[M(bipy)(OH_2)_4]^{2+}[AMIP]^{2-}$ (M = Ni(II), **18**, M = Co(II), **19**). The pale green-blue crystalline product of the nickel(II) based framework, **18**, was characterised by single-crystal X-ray diffraction experiments, the results of which are summarised in Table 4.9. Framework **19** was not fully refined crystallographically, as the data completeness was too low. However, the unit cell parameters and space group matched and the preliminary structural model that emerged was sufficient to deduce that **19** was isostructural to **18**. This conclusion was also reflected in the matching powder X-ray diffraction data from both MOFs.

Numerous attempts were made at picking a single crystal however the best data achieved was obtained from a crystal that was twinned, and a 2-fold rotation axis of -179.83° around the [100] reciprocal space vector, taken into account during refinement.

Formula	$[Ni(bipy)(OH_2)_4]^{2+}[AMIP]^{2-}$
Empirical formula	$C_{20}\ H_{23}\ N_3\ Ni\ O_9$
Formula weight / $gmol^{-1}$	508.12
T / K	150(2)
λ / Å	0.6889
Crystal system	Monoclinic
Space group	$P2_1/c$
a / Å	7.4362(5)
b / Å	11.4082(8)
c / Å	24.1577(18)
$\alpha = \gamma$ / º	90
β / º	90.801(6)
Volume / $Å^3$	2049.2(3)
Z (no. molecules in unit cell)	4
Density (calculated) / gcm^{-3}	1.647
Crystal size / mm	0.05 x 0.015 x 0.004
Data Completeness	0.980
Final *R* indices [$I>2\sigma(I)$]	$R1 = 0.0697$ $wR2 = 0.1853$
R indices (all data)	$R1 = 0.0926$ $wR2 = 0.2021$
Largest diff. peak and hole / $eÅ^{-3}$	1.255 and -0.962

Table 4.9. Crystallographic data for **18**.

The SBU of framework **18** is a solitary Ni^{II} ion, Ni1, and it is in a pseudo-octahedral environment. Atom Ni1 is coordinated to four oxygen atoms from ligated water molecules, O1-4. Ni1-O bond lengths are in the range 2.053(3)-2.100(3) Å. There are two bipy linkers coordinated in the axial positions through N1 and N2: Ni1-N1 = 2.149 (3) Å and Ni1-N2 = 2.113 (3) Å. The *cis* angles between the equatorial ligands are 88.84(6)º and 90.86(5)º, and *trans* angles <O1-O3 = 173.59(11)º and <O2-O4 = 176.01(11)º. The angle of the bipy moieties *trans* to each other (<N1-Ni1-N2 is 177.01(13)º). Therefore, the Ni1 coordination sphere is close to perfect octahedral symmetry (Figure 4.30).

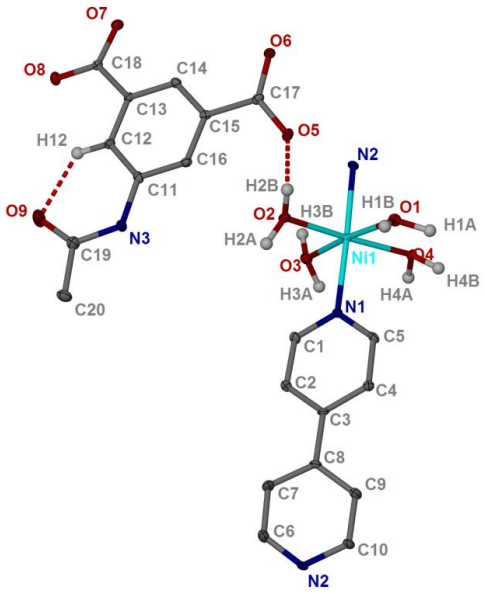

Figure 4.30. Metal coordination and surrounding linkers of **18**. Ellipsoids shown for non-hydrogen atoms at 30 % probability. C: grey, H: light grey, O: red, N: blue, Ni: cyan. Aromatic hydrogen atoms omitted.

The hydrogen atoms of the water molecules were located and refined subject to being equidistant from the nickel centre, 0.98 Å from the parent oxygens and 1.55 Å from each other within the individual water ligands. Due to extensive hydrogen bonding, no disorder needed to be modelled in the unit cell.

Metal centres are linked together by bipy linkers in 1-D chains and the substantial hydrogen bonding extends infinitely in three dimensions. These metal-bipy chains carry a formal charge of +2 that originates from the metal ions. To balance this charge, $[AMIP]^{2-}$ counter ions are present throughout the framework (Figure 4.31).

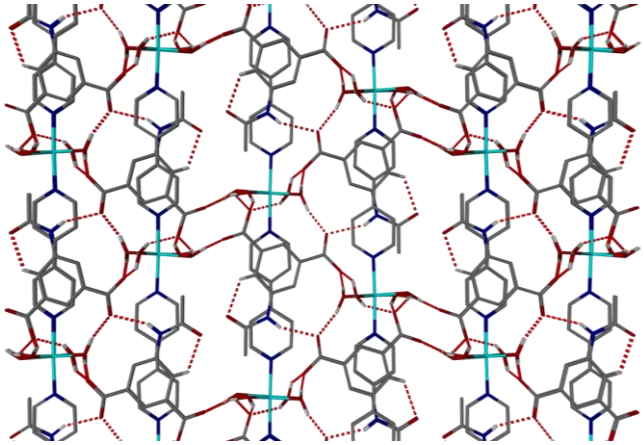

Figure 4.31. View down the *a*-axis of **18**. 1-D chains held together by hydrogen bonding. C: grey, H: light grey, O: red, N: blue, Ni: cyan. Aromatic hydrogen atoms omitted.

AMIP dianions are not directly coordinated to Ni^{II} ions but effectively bridge these metal cations *via* coordinated water molecules and form an extensive 3-D hydrogen bond network. The DH···A distances and DH···A angles are listed in Table 4.10. Of the free carbonyl groups based on C18, O7 is in a tetrahedral environment with hydrogen bonds to H1B, H3A, H4A from three water molecules and O8 is three-coordinate engaging in hydrogen bonding with H1A, H4A and H4B from two water molecules. The two oxygen acceptor atoms form a bifurcated hydrogen bond with H4A.

The carboxylate group based on C17 accepts four hydrogen bonds, two on each oxygen atom O5 and O6. The atom O5 accepts a hydrogen bond with H2B and H3B from two water molecules and O6 accepts two intermolecular hydrogen bonds from the amido group (H3) of an adjacent AMIP and from a water hydrogen atom (H2A). Two intramolecular hydrogen bonds, graph set S(6), are observed from C12-H12 to O9 of the carbonyl group within the amido tag of the same ring.

D-H	d(D-H)/Å	d(H···A)/Å	<DHA/°	d(D···A)/Å	A
N3-H3	0.88	2.19	153	3.00	O6
O1-H1A	0.98	1.82	154	2.74	O8
O1-H1B	0.98	1.78	153	2.69	O7
O2-H2A	0.98	1.78	165	2.73	O6
O2-H2B	0.98	1.76	174	2.76	O5
O3-H3A	0.98	1.86	144	2.72	O7
O3-H3B	0.98	1.99	134	2.76	O5
O4-H4A	0.98	1.73	152	2.64	O7
O4-H4A	0.98	2.64	128	3.33	O8
O4-H4B	0.98	1.84	156	2.76	O8

Table 4.10. Hydrogen bonds in **18** with H···A < r(A) + 2.000 Å and <DHA > 110 °.

Metal-bipy chains are orientated side on with each other, but face to face with AMIP moieties and this is depicted in Figure 4.32. This leads to $\pi\cdots\pi$ interactions of the aromatic rings of AMIP and bipy rings. The distance between centroids is 3.606 Å, staggered and very close to parallel (1.1° between ring planes). This results in relatively dense hydrogen bonding and close packing due high packing efficiency of straight chains (ρ = 1.647 gcm^{-3}).

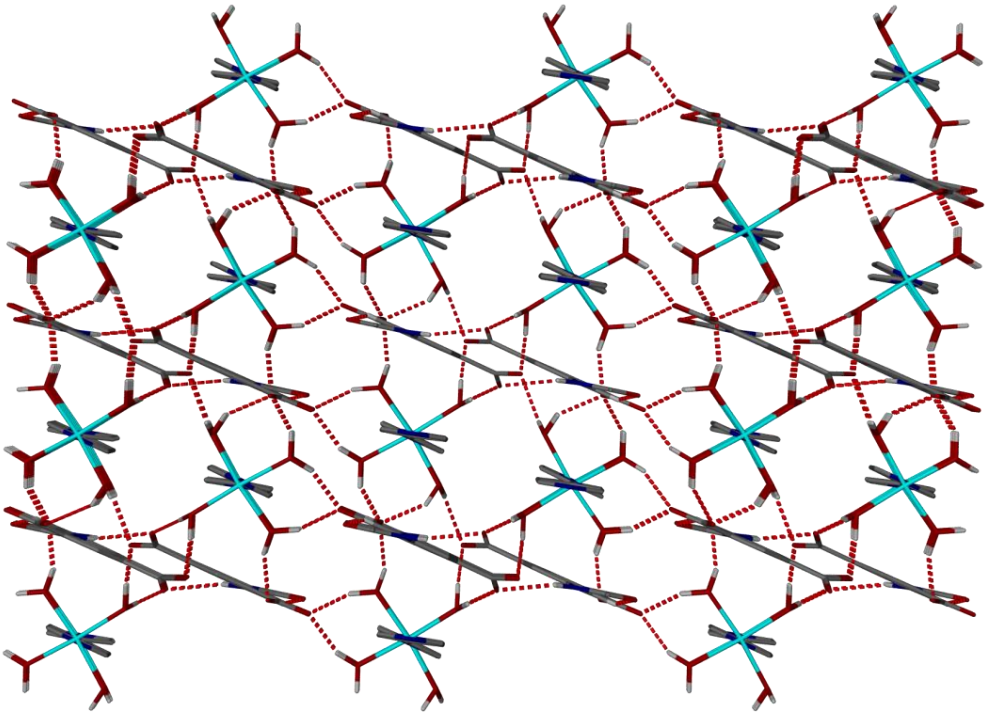

Figure 4.32. View down the metal-bipy chains of **18**. C: grey, H: light grey, O: red, N: blue, Ni: cyan. Aromatic hydrogen atoms omitted.

A comparison of the PXRD pattern for the bulk material with the predicted PXRD pattern from the single-crystal diffraction experiment is shown in Figure 4.33. The data shows that the bulk materials of **18** and **19** are phase pure and the two MOFs are isostructural matching the simulated data from the single-crystal X-ray diffraction experiments.

The quality of the powder diffraction was high after the crystals were washed with deionised water and air dried. The trace for framework **18** exhibits the higher signal:noise ratio which may be indicative of better crystal quality and less degradation from the washing and drying conditions.

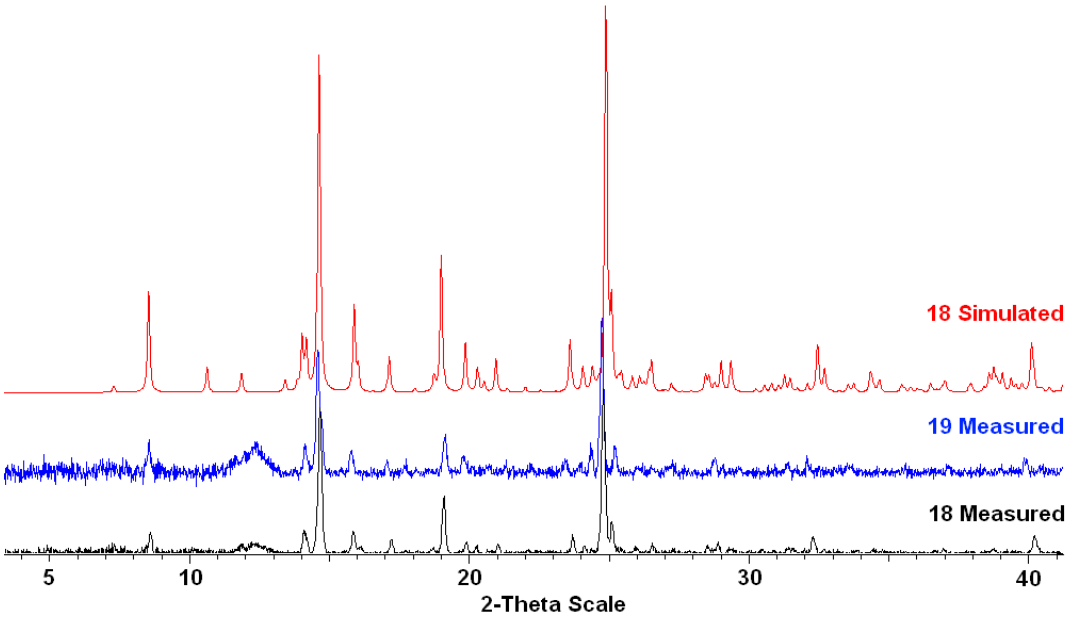

Figure 4.33. Measured PXRD patterns of **18** and **19** and simulated data from the single crystal diffraction experiment of **18**.

A TGA study of **18** and **19**, Figure 4.34, shows the stages of activation and decomposition of the bulk samples in nitrogen. In the first significant mass loss stage of **18**, between 40-100 ºC, there is a 3 % weight loss, most likely due to the samples not being thoroughly dried before the experiment. Framework **19** shows 1 % weight loss probably due to uncoordinated water from ineffective drying.

Both networks show 14 % mass loss from the coordinated water molecules (total coordinated solvent calculated = 14 %). In the case of **18** this loss of coordinated water molecules occurs between 100-180 ºC. For **19**, this mass loss region is between 100-140 ºC. Decomposition occurs immediately for both compounds with no plateau region observed. There is a 40 ºC difference of decomposition temperatures for the same topology and this may be explained by Ni(II) being more oxophilic than Co(II). The 1-D networks of **18** and **19** have relatively low thermal stabilities, similarly to the zinc(II), bipy, and acetate based framework of compound **16**. Distinct plateaus are absent from both sets of TGA data, which suggest that no stable activated species exists in either case. Any removal of guests may leave a charged framework, which would then collapse and could explain the relatively low decomposition temperature.

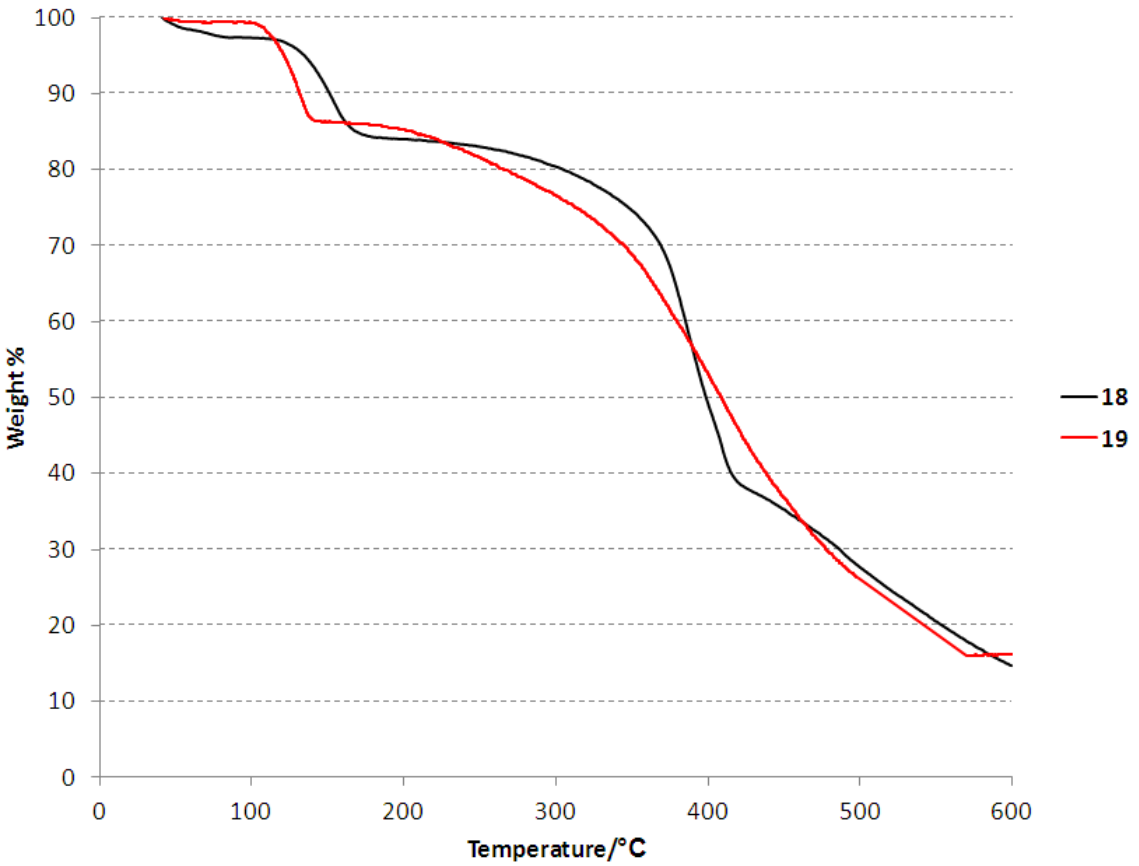

Figure 4.34. TGA of **18** and **19**.

Magnetic studies were carried out to determine the effective magnetic moment, μ_{eff}, of compounds **18** and **19**. A diamagnetic correction of -122.629 x 10^{-6} cm^3mol^{-1} was measured for the AMIP linker at the same time as **18** and **19**. The resulting magnetic moment, $\mu_{eff,}$ was 3.41 BM for compound **18** (calculated for Ni(II) d^8: μ_{so} = 2.83 BM). The measured magnetic moment, μ_{eff}, was 4.98 BM for **19** (calculated for high spin Co(II) d^7: μ_{so} = 3.87 BM and low spin μ_{so} = 1.73 BM). This suggests that Co(II) is high spin d^7 in this framework.

4.4. Mixed ligand MOF Synthesis with BPDC and tagged BDC linkers

Isophthalic acid based MOFs were not yielding frameworks with tag groups protruding into accessible pores, therefore a different line of investigation was followed returning to 1,4-benzenedicarboxylates functionalised at the 2-position. The bis-phenyl linker [1,1'-biphenyl]-4,4'-dicarboxylate, BPDC, was employed as an untagged spacer in an attempt to gain void volume and reduce the potential for steric crowding of tag groups in a hypothetical cubic net topology.

Pre-synthetic modification reactions were carried out, firstly synthesising the propylamino tagged BDC, H_2BDC-NHPr (**4b**), by treating H_2BDC-NH_2 with propanal, and exposing this dicarboxylic acid to MOF formation conditions with zinc(II) nitrate and H_2BPDC in DMF. Subsequent optimisation of ligand stoichiometries was carried out to increase the length of the unit to a proposed topology of SUMOF-4,[17] and gain extra space in the pores. As the secondary amine is chemically stable, the reaction would then be repeated with H_2BDC-NH_2 instead. Four different crystalline products were obtained, from this investigation, in varying ratios: the interpenetrated cubic structure of $[Zn_4O(BPDC)_3]$ (IRMOF-9), $[Zn_4O(BDC\text{-}NHPr)_{0.6}(BDC\text{-}NH_2)_{0.4}(BPDC)_2(DMF)]\cdot 1.5DMF$ (**20**), and two hexagonal honeycomb networks of $[Zn_4(BDC\text{-}NHPr)_3(NO_3)_2(H_2O)_2]\cdot xDMF\cdot y H_2O\cdot z$BPDC (PNMOF-3-NHPr, **21**) and $[Zn_4(BDC\text{-}NH_2)_3(NO_3)_2(H_2O)_2]\cdot xDMF\cdot y H_2O\cdot z$BPDC (PNMOF-3, **22**). Compounds **20** and **21** are new and the synthetic conditions are summarised in Scheme 4.8.

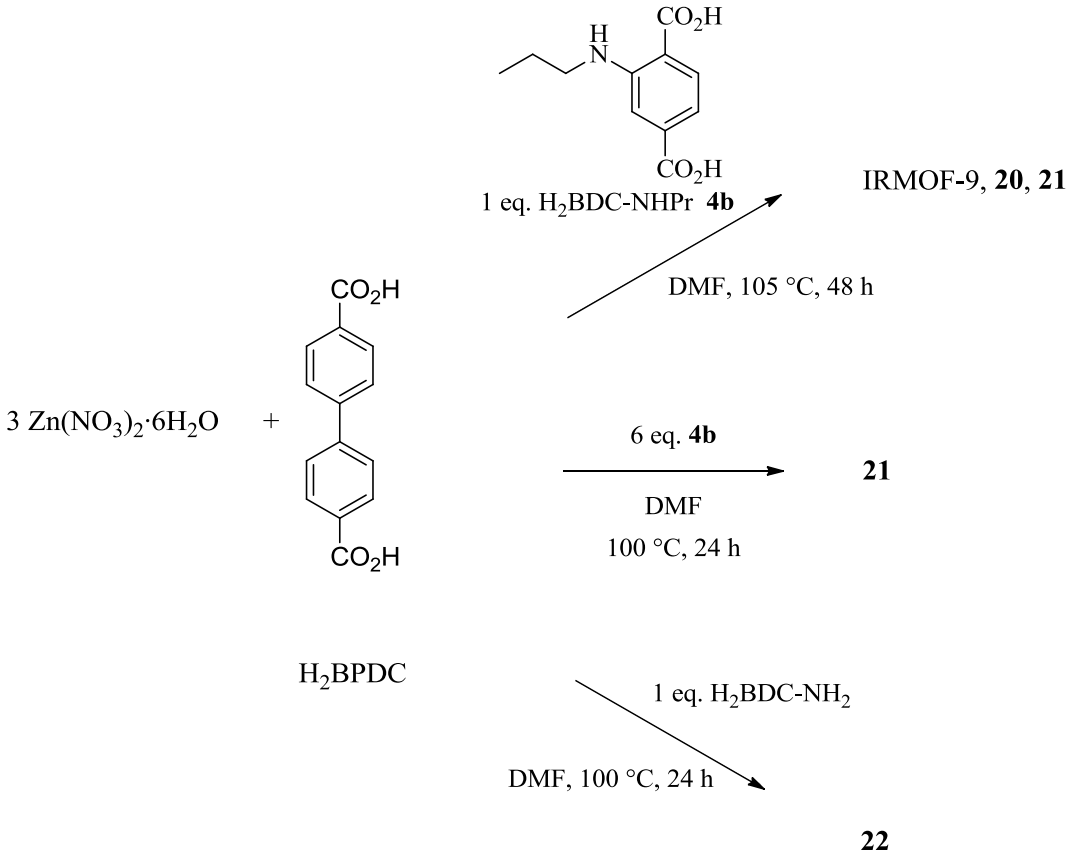

Scheme 4.8. Synthetic conditions for **20**-**22**.

4.4.1. A New Interpenetrated Framework Incorporating the Zn_4O Supertetrahedral Node.

From the reaction of a 3:1:1 ratio of zinc(II) nitrate:H_2BDC-NHPr:H_2BPDC three crystalline products were obtained with different habits. IRMOF-9 ($[Zn_4O(BPDC)_3]$) and framework **21** were the major compounds accompanied by small, high quality, crystals which were picked out and characterised by single crystal X-ray diffraction, at a synchrotron source. These were crystallographically characterised as $[Zn_4O(BDC\text{-}NHPr)_{0.6}(BDC\text{-}NH_2)_{0.4}(BPDC)_2(DMF)]\cdot 1.5DMF$ (**20**).

Refinement of this structural model was compromised by the limitations of the data collected and the decay of the sample as the experiment proceeded. Of the 4 scan strategy contributing to a hemisphere, only the first was useable due to degradation of the crystal in the synchrotron beam. Hence, the completeness of the data registers at 87%. Nevertheless, the overall interpenetrated MOF topology is unambiguous. Table 4.11 summarises the experimental results.

Formula	$[Zn_4O(BDC\text{-}NHPr)_{0.6}(BDC\text{-}NHPr)_{0.4}(BPDC)_2(DMF)]\cdot 1.5DMF$
Empirical formula	$C_{45.30}H_{42.10}N_{3.55}O_{15.50}Zn_4$
Formula weight / $gmol^{-1}$	1145.71
T / K	150(2)
λ / Å	0.68890
Crystal system	Monoclinic
Space group	$P2_1/n$
a / Å	16.6088(11)
b / Å	17.2666(5)
c / Å	24.8088(13)
$\alpha = \gamma$ / °	90
β / °	108.479(7)
Volume / $Å^3$	6747.8(6)
Z (no. molecules in unit cell)	4
Density (calculated) / gcm^{-3}	1.128
Crystal size / mm	0.03 x 0.03 x 0.02
Data Completeness	0.869
Final R indices [$I>2\sigma(I)$]	$R1$ = 0.1086 $wR2$ = 0.3093
R indices (all data)	$R1$ = 0.1368 $wR2$ = 0.3380
Largest diff. peak and hole / $eÅ^{-3}$	1.140 and -0.762

Table 4.11. Crystallographic data for **20**.

The asymmetric unit of **20** contains four zinc(II) ions in a Zn_4O supertetrahedron (with one vertex opened) consisting of three tetrahedral zinc(II) atoms, Zn1, Zn2 and Zn4 and an octahedral Zn3. These surround a tetrahedral μ_4-O^{2-} anion, O1. Large atomic displacement parameters are evident in the model, due in part to a low completeness and the large amount of disorder in the structure.

The SBU extends in three dimensions through two BPDC ligands, one derivatised BDC linker and one DMF ligand. The latter is attached to Zn3 and only the disordered, 50% occupancy, fractional oxygen atoms (O14, O14A) therein could be reliably located, added to the model and refined (Figure 4.35).

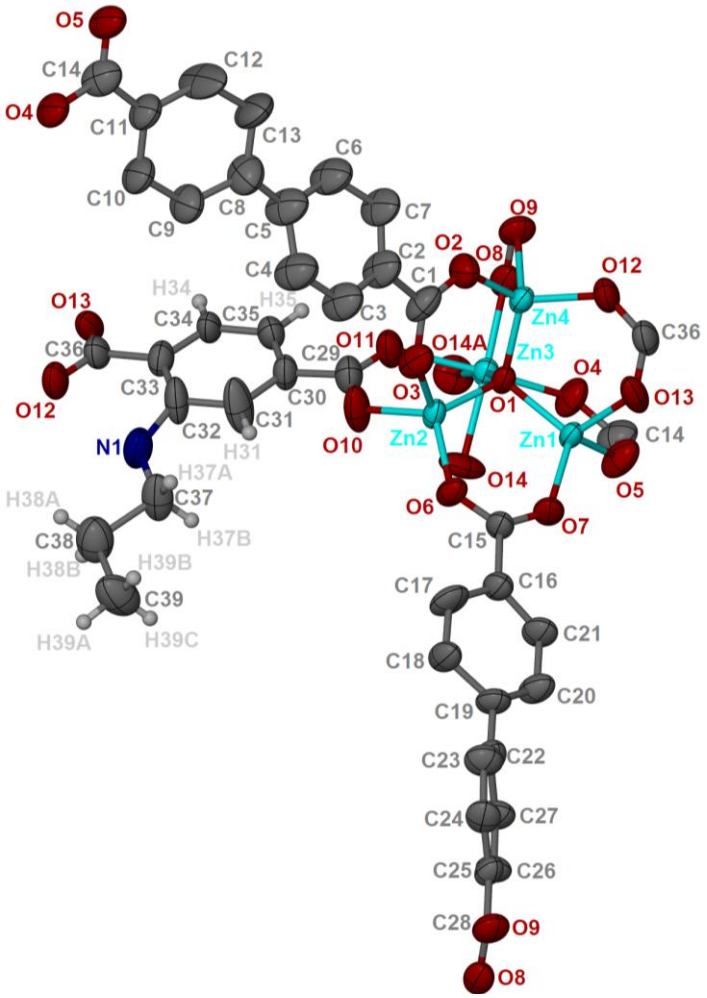

Figure 4.35. Node and linkers of **20**. BPDC hydrogen atoms omitted. C: grey, H: white, O: red, N: blue, Zn: cyan. Bipyridyl hydrogen atoms omitted.

The BDC based linker represents 60 % of a BDC-NHPr (100 % purity of the corresponding acid used in the synthesis) and it is probable that the remaining 40 % fractional occupancy linker is BDC-NH_2, in which the NH_2 group is disordered equally

over carbons C31, C32 C34 and C35. Additional alternative analysis would be needed to confirm this as either a decomposition product or a contaminant, of the reagent **4b**, used in the MOF synthesis (which may account for the very low yield).

It is unsurprising that the fractional nitrogen atoms (from the BDC-NH_2) attached to C31, C34 and C35 could not be readily resolved, from hydrogen atoms, at 10 % occupancy. Thus, N1 is present at 70 % occupancy, while carbons C37-C39 are included at 60% occupancy. The C-N and C-C distances were restrained to the same length in the -NHPr pendant functionality. The C-C distances were also subjected to restraints in the phenyl rings based on C2 and C16. ADPs were restrained for atoms N1, C2-C7, C8-C11 and C37-C39. The hydrogen atom attached to N1 could not be reliably located and hence was omitted from the model.

The guest solvent present in this structure was assessed with the SQUEEZE routine of the PLATON crystallographic software.[13] Hence, 1.5 molecules of DMF were included in the asymmetric unit. [*R*(int) pre-SQUEEZE = 9.61 %].

The gross packing is shown in Figure 4.36, with the orientation of the pendent groups into channels 8.8 x 4.7 Å in framework **20**. BPDC rigid linkers make up two of the sides of the channels and alternate with two BDC-X linkers. This leads to the distorted channels (off-square) that the tag groups protrude into. To see the functional tag group is rare (and a welcome benefit) in the refined structure and is a consequence of the constrained tag groups and ordered channel shape. This is another check that the pre-synthetic modification reaction has worked.

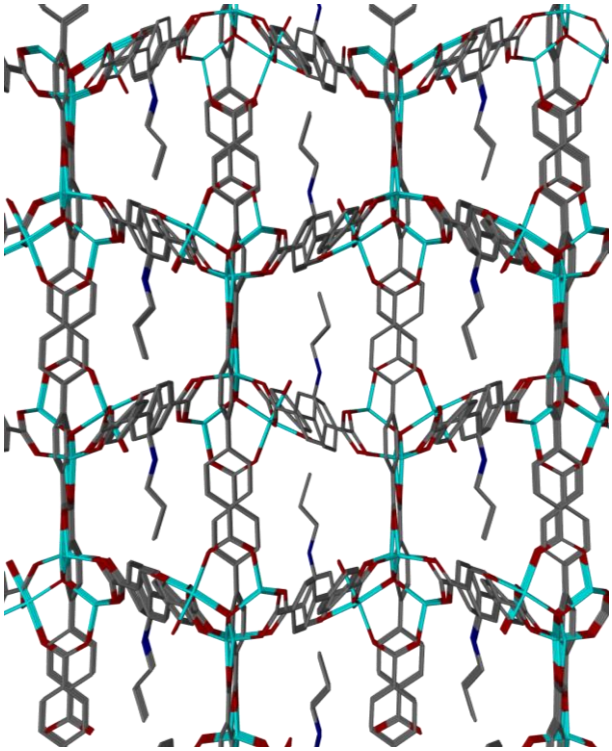

Figure 4.36. View down the channels of **20** with tag groups protruding into infinite channels. Hydrogen atoms omitted. C: gray, O:red, N:blue, Zn: cyan. Hydrogen atoms omitted.

The structure is doubly interpenetrated (Figure 4.37) with one 3-D network forming inside the other with no formal bonding between them. The size of the potential channels is therefore reduced and measures 7.3 x 11.5 Å.

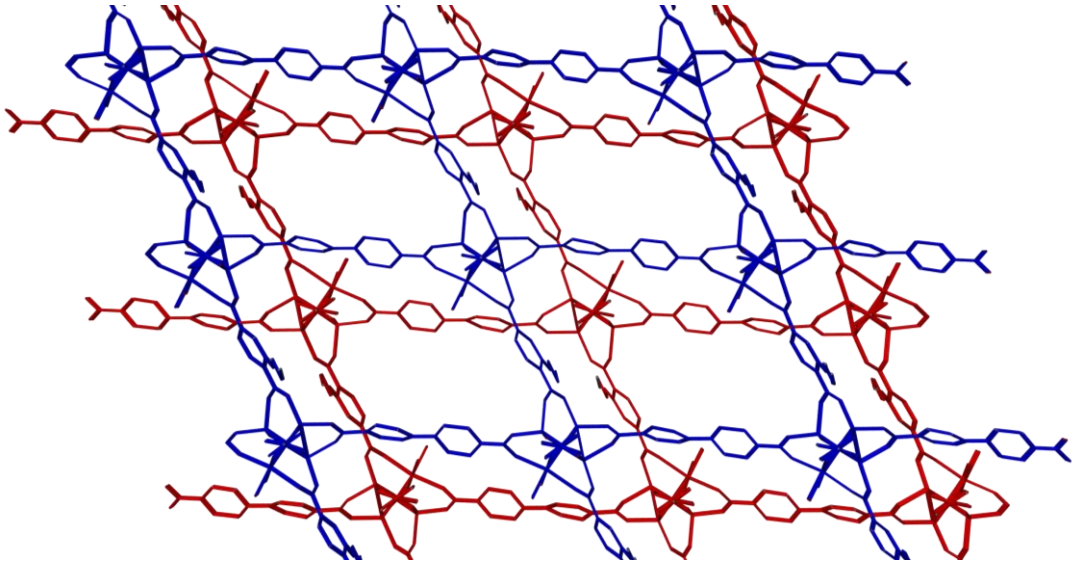

Figure 4.37. View of the doubly interpenetrated framework, **20**, separately highlighted. Note one open vertex of the Zn_4O supertetrahedra. Hydrogen atoms and guest solvent omitted.

There were several difficulties with this synthesis. A bulk sample could not be isolated after many optimisations and the 100 % BDC-NH_2 analogue was never observed after many attempts. As only a few crystals were available, bulk analyses by NMR, IR, mass spectrometry and elemental analysis were not collected for **20**. Rational linker stoichiometric investigation is needed in the future with 60% NHPr and 40% NH_2 as a starting point to yield an isolated sample.

4.4.2. Functionalised Honeycomb MOFs

The major product from the MOF formation reaction between H_2BDC-NHPr, BPDC and zinc nitrate hexahydrate were large (~5 mm) hexagonal crystals. Optimisation of the reaction stoichiometry and subsequent characterisation, yielded the structure as $[Zn_4(BDC\text{-}NHPr)_3(NO_3)_j(H_2O)_2]\cdot x DMF\cdot y H_2O\cdot z BPDC$ (PNMOF-3-NHPr), where *j*, *x*, *y* and *z* are unknowns and a match was found for the topology within the literature of a framework of the amino tagged $[Zn_4(BDC\text{-}NHPr)_3(NO_3)_2(H_2O)_2]$, PNMOF-3, (polymer-nucleated metal-organic framework, Hexagonal space group *P*6/*mmm*).[18]

Single-crystal X-ray diffraction experiments produced less than optimal quality data, which is reflected in the global equivalent isotropic displacement factors, U_{eq}, of approximately 0.2 $Å^2$. Resolution was low at 0.84 Å but the data had a high completeness 99.8 %. It was therefore impossible to assign a number of nitrates or locate the BPDC in the framework voids.

The framework is cationic with nitrate and/or BPDC anions balancing the charge. It is unclear from the single crystal diffraction experiments whether there are nitrate anions capping the zinc atoms. The structure could potentially contain no nitrate anions and one BPDC per formula unit, or zero BPDC and two nitrate anions. There is BPDC in the channels as seen in the ^1H NMR spectrum of the digested product which also shows retention of 100 % of the NHPr pendant group.

The TGA of **21**, Figure 4.38, shows a large amount of solvent, 55 %, (of probably DMF and H_2O) is lost from 40-320 °C, above which decomposition of the framework occurs. There may be a plateau region that has a small range from 300 to 320 °C but it is difficult to get that accuracy in such a small range in this TGA experiment.

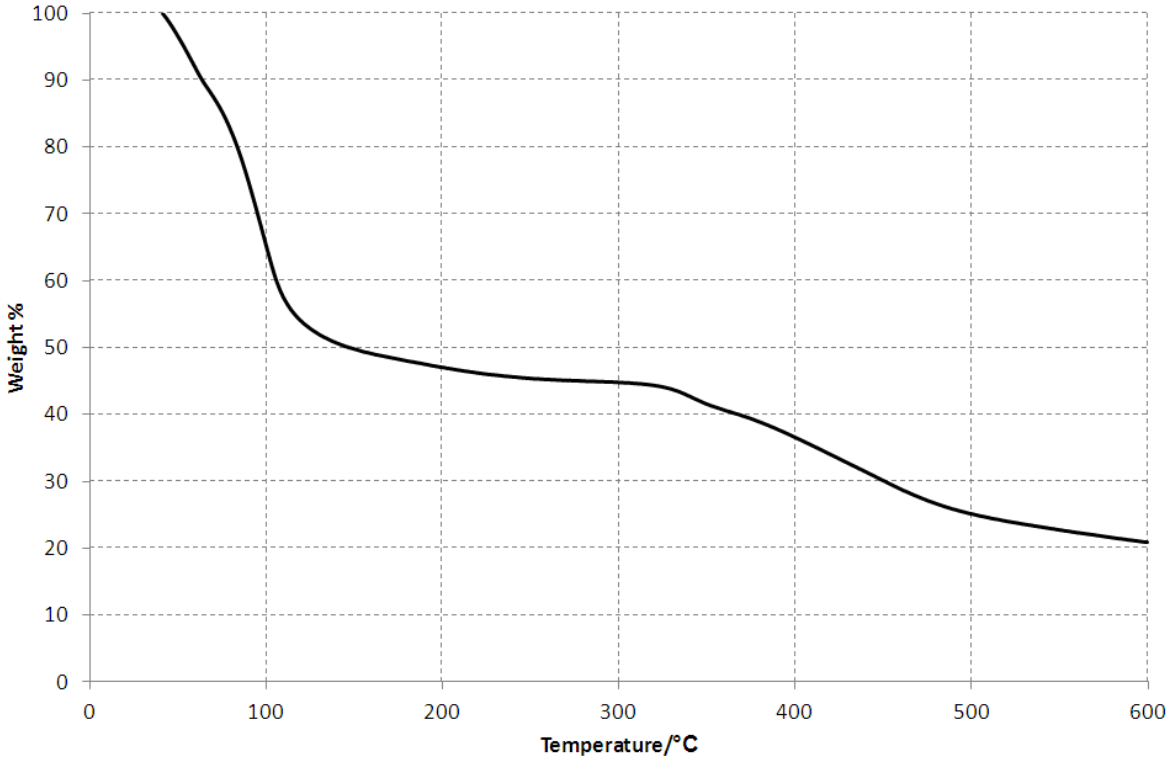

Figure 4.38. TGA of **21**.

Estimation of the total solvent in the framework of **21** by TGA was difficult. This was due to an unknown amount of water and BPDC in the pores coupled with the measurement carried out with the material being only dabbed dry from DMF. Attempts at activating **29** by heating to near 200 °C under vacuum were unsuccessful, as was solvent exchange with $CHCl_3$ or THF. The crystals collapse after solvent exchange or removal of BPDC from pores observed in the low nitrogen sorption at 77 K (BET = 10 m^2g^{-1}).

Based on this previous work with the propylamino tagged BDC-NHPr, a new question arose: was it possible to make the amino tagged MOF, PNMOF-3, using just BPDC? The originally prepared PNMOF-3 was synthesised with a complicated template consisting of a cross-linked copolymer of methacrylic acid and divinylbenzene, MAA/DVB, reported in 2006 by Yaghi *et al.*[18] Experimentally they report 20 % MAA/80 % DVB cross-linked copolymer was added to the reaction mixture of zinc(II) nitrate and H_2BDC-NH_2 in DEF at 100 °C for 24 h, to obtain PNMOF-3, the gross structure of which is shown in Figure 4.39.

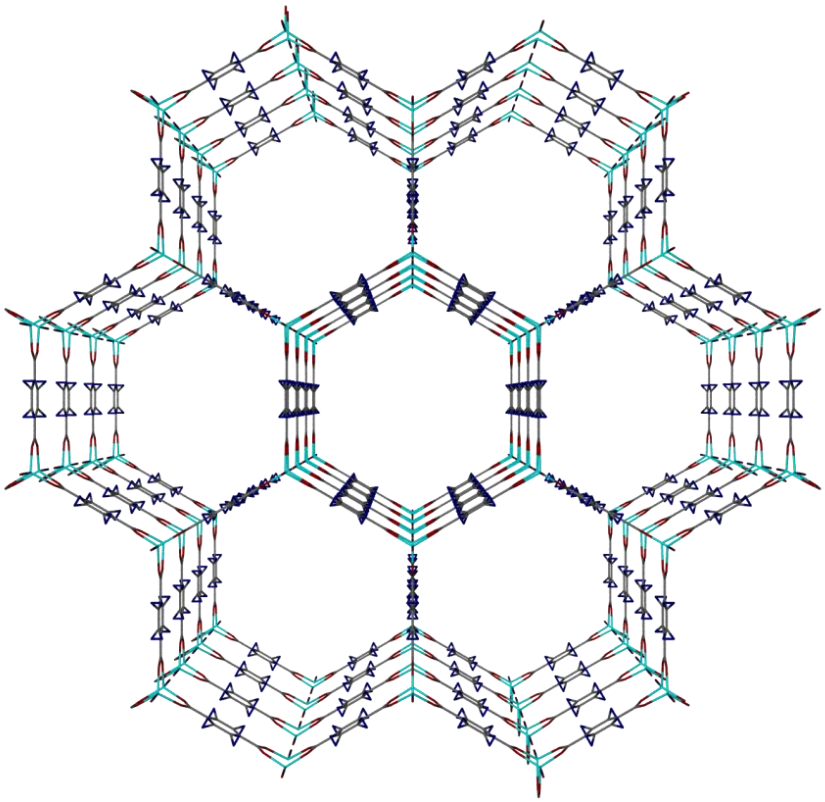

Figure 4.39. View down the 14 .9 Å channels of PNMOF-3 (measured between ring faces). Amino pendent groups disordered in four positions around ring and in two positions per carbon atom. Hydrogen atoms and guest molecules omitted. C: grey, O: red, N: blue, Zn: cyan.[18]

PNMOF-3, $[Zn_4(BDC\text{-}NH_2)_3(NO_3)_j(H_2O)_2]\cdot xDMF\cdot y H_2O\cdot z$BPDC, could indeed be made by substituting BDC-NHPr with BDC-NH_2 in the synthetic conditions of **21**: zinc(II) nitrate, H_2BDC-NH_2, H_2BPDC, DMF and 100 °C for 24 h. The identities of the crystalline products were confirmed by PXRD, Figure 4.40. During optimisation reactions, a mixture of products was obtained including IRMOF-9 and PNMOF-3 accompanied by the original three component mixed PXRD trace (green line), the major component of which is IRMOF-9.

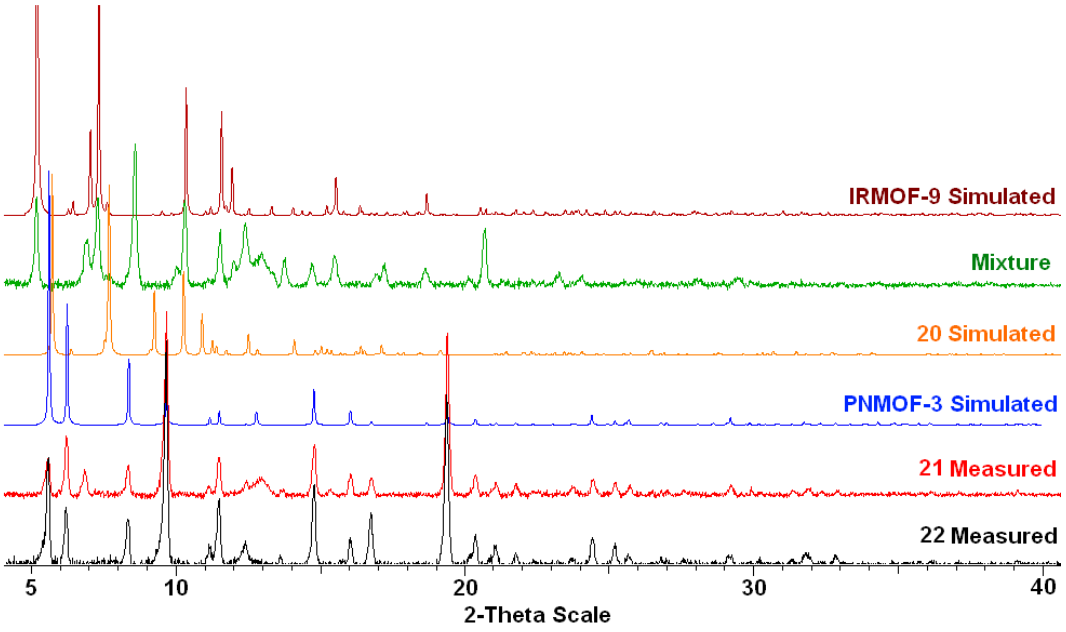

Figure 4.40. Measured PXRD patterns of **21** and **22** along with the simulated data from single crystal diffraction experiments. IRMOF-9 refcode= EDUVAA,[7] PNMOF-3 refcode = ICITOE.[18]

The powder diffraction pattern of **21** displays an extra peak at 2θ 6.8° perhaps associated with the NHPr tag group when compared with the simulated pattern of the amino tagged PNMOF-3. The PXRD pattern of **22** matches the literature simulated data of PNMOF-3 implying a phase pure sample. The majority of the peaks are coincident and under an optical microscope the sample looked homogeneous. The crystals of PNMOF-3 topology (**21** and **22**) degraded quickly out of solution so all the PXRD experiments were done *in-situ* in DMF with any loss of solvent causing framework collapse due to the large open channels.

4.5. Summary

One new crystalline MOF was synthesised containing the AIP linker, however the amino group was not accessible. Protecting this amino group with an acetamido group led to five new MOFs through pre-synthetic modification but the deprotection step (H_2O at 130 °C for three days) did not cleave the acetamido groups of frameworks **15-19**. The tag groups were too well integrated into the structure to be removed and no analogous amino tagged frameworks were synthesised. In the presence of zinc(II) and benzoic acid, the acetamido bond of H_2AMIP did cleave but formed an organic hydrate rather than a MOF.

Hydrogen bonding was extensive in the frameworks containing AMIP. This was integral to framework stability and complex chains, rings and a bifurcated hydrogen bond were observed.

Where cationic metal-bipy struts (frameworks **18**-**19**) were formed in reaction mixtures, counter anions of AMIP were present in non-coordinating role.

MOF synthesised with BPDC yielded a mixture of crystals and three topologies were characterised by X-ray diffraction with **22** (PNMOF-3 with an unknown amount of BPDC in the channels) was synthesised in a fewer step procedure than reported in the literature.[18] Framework **20** was a new BPDC spaced compound as was **21** (PNMOF-3-NHPr) as the alkylated framework of **22**.

4.6. Conclusions

Reaction conditions are critical for the topology of MOF produced. Zinc(II), nickel(II), manganese(II) and cobalt(II) yielded the best results regarding MOF formation reactions. Stoichiometry was optimised to the same metal:ligand ratio as in a target product or the metal was kept in excess if aiming for the supertetrahedral SBU of the IRMOF series. Generally DMF worked well as a reaction solvent in terms of reagent solubility with concentration tending to affect the crystallite size rather than product identity. Modulators were very useful (benzoic acid) to slow the crystal growth by competition with the dicarboxylate linkers. Replacing the mother liquor with fresh DMF was essential to prevent hydrolysed DMF causing problems with degradation of crystals after a few days storage.

With all the large surface area and highly disordered MOFs the systems are now large enough to need characterisation in the same way as biological crystals *i.e.* to use protein crystallography techniques. This will help to overcome the low completeness of the X-ray diffraction, data of MOFs displaying disorder, affecting every position of the electron density in the unit cell because it is the sum of all the squared structure factors, F^2. The reflection intensities (I_{hkl}) contain information for all locations in the unit cell from the Patterson or Fourier synthesis equations. Good quality low angle data as well as information from the diffuse scattering is needed to confidently characterise disordered molecules in these crystal structures.

4.7. Experimental

4.7.1. Equipment and characterisation techniques

Crystal size and shapes were observed under a light microscope (magnification up to 1000x) and a high resolution camera (with a graduated ruler on screen with smallest divisions of 0.025 mm).

Single crystal structures for materials were obtained in house, on a Nonius Kappa CCD diffractometer using X-rays with molybdenum K_α radiation, with wavelength, $\lambda = 0.71073$ Å, at 150 K. Samples are selected by eye, under microscope using polarized light, and mounted in Fomblin® oil (highly inert perfluoropolyether oil that does not diffract) on a glass fibre (~ 0.175 mm diameter) and centred in the x-ray beam to within +/-0.025 mm in each axis.

Single crystal structures for materials were obtained at Diamond Light Source at station I19, on a Crystal Logic 4-circle diffractometer with a Rigaku Saturn CCD detector, using X-rays with synchrotron radiation wavelength, $\lambda = 0.6889$ Å, at 150 K.

The solutions of structures were carried out using the software SHELX-97 and refinements were done with the software SHELXL-97 part of the programs XSeed and PLATON.

Powder X-ray diffraction (PXRD) was collected for each compound on a Bruker axs D8 Advance diffractometer with copper K_α radiation, with wavelength, $\lambda = 1.5406$ Å, at 298 K and with a beam slit set to 1 mm, detector slit set to 0.2 mm and anti-scattering slit set to 1 mm. Samples were either dried in ambient conditions and ground to a powder, using a pestle and mortar, or lightly ground in a solution they are stable in or crystallised from. Then the samples are packed into capillary tubes, of diameter 0.3, 0.5 or 0.7 mm depending on the size of the crystals, and mounted and centred using a graduated microscope (smallest division = 0.025 mm) to an error of +/- 0.025 mm in each axis. The scan speed was set to 2 s per step and the step size was 0.02 2θ unless stated otherwise.

Thermogravimetric analysis (TGA) was carried out on a PerkinElmer TGA 4000 thermogravimetric analyzer from a temperature range of 40 ºC to 600 ºC at a rate of 5 ºC/min under a flow of N_2 gas (20 mL/min).

FT-IR analysis was carried out on solid, ground, dried samples (oven 90 ºC overnight) using a PerkinElmer Spectrum 100 spectrometer mounted on a diamond/gem platform.

Microanalysis was carried out by Mr. Alan Carver, in house on an Exeter analytical inc. CE-440 elemental analyzer, on dried samples unless stated otherwise.

Magnetic Susceptibility Measurements were carried out on a Johnson Matthey Mk1 MSB.

MOF digestion was carried out with approximately 5 mg of crystalline sample in 0.4 mL of DMSO and 0.2 mL of a stock solution of 0.1 mL of 35 % DCl/D_2O in 3 mL DMSO. This mixture was sonicated for three hours or until the solids had completely dissolved.

Mass spectra were carried out on digested MOFs dissolved in MeOH, using a Bruker micrOTOF electrospray ionization time-of-flight (ESI-TOF) machine. The method used to confirm formula positive 50 to 500 by loop injection.

NMR spectra were recorded at 298 K on a Bruker Avance 300 MHz Ultrashield NMR spectrometer. ^{1}H NMR spectra were referenced to the residual protio peaks at δ 7.26 ppm ($CDCl_3$) and δ 2.50 ppm for DMSO-d_6. ^{13}C NMR spectra were referenced to the residual solvent peaks at δ 77.2 ppm for $CDCl_3$ and δ 39.5 ppm for DMSO-d_6 and carried out at 75 MHz.

4.7.2. Synthesis

Unless otherwise described, all organic and inorganic reagents, chemicals and solvents were commercially available (Sigma-Aldrich, Fisher Scientific or Acros Organics) and of reagent grade (>98% purity). They were used without further purification.

The general procedure for MOF synthesis is as follows. The metal salt and organic ligand were weighed out into the reaction vessel, (either a 10 mL oven vial, 15 mL autoclave or a pressure tube). Then the solvent was added, (the volume affects the size of vessel chosen, among other variables), and the reaction mixture stirred until completely dissolved or a homogenised suspension is formed at RTP. The stirrer is removed and the vessel sealed. It is then placed in on oven between 90-140 ºC depending on the desired temperature (heating rate ~5 ºC/min). The reaction is left for between 3 h and 1 week depending on the system with most reactions complete in 24 h. The reaction mixture is allowed to cool to room temperature in a fume hood (cooling rate ~1-2 ºC/min). The reaction mixture is then filtered immediately if crystals are present or left to stand (in the fridge or on the bench top), unagitated, until a precipitate/crystals form, or after 8 weeks, if no precipitate or crystals form, it is disposed of.

This is a common procedure that has many variables, which all have an effect on the crystals that are formed (if any). Therefore, this leads to a large range of conditions to screen, between a metal ion and a ligand, before crystals, suitable for analysis, are obtained.

4.7.3. $[Co_5(\mu_3\text{-}OH)_2(AIP)_4(DMF)_{0.5}(OH_2)_{0.5}]\cdot 1.75DMF\cdot 1.5H_2O$, (12)

H_2AIP (0.28 mmol, 50 mg) and $[Co(OAc)_2]\cdot 4H_2O$ (0.28 mmol, 69 mg), were dissolved in 10 mL DMF:10 mL H_2O and stirred till homogeneous, in a 10 mL pressure tube. This reaction mixture was put in an oven at 120 ºC for 48 h. The resultant purple crystals were isolated by filtration and washed with 3 x 10 mL DMF and stored in fresh DMF. Yield: 20 mg. Characterised by single-crystal X-ray diffraction as $[Co_5(\mu_3\text{-}OH)_2(AIP)_4(DMF)_{0.5}(OH_2)_{0.5}]\cdot 1.75DMF\cdot 1.5H_2O$, **12**.

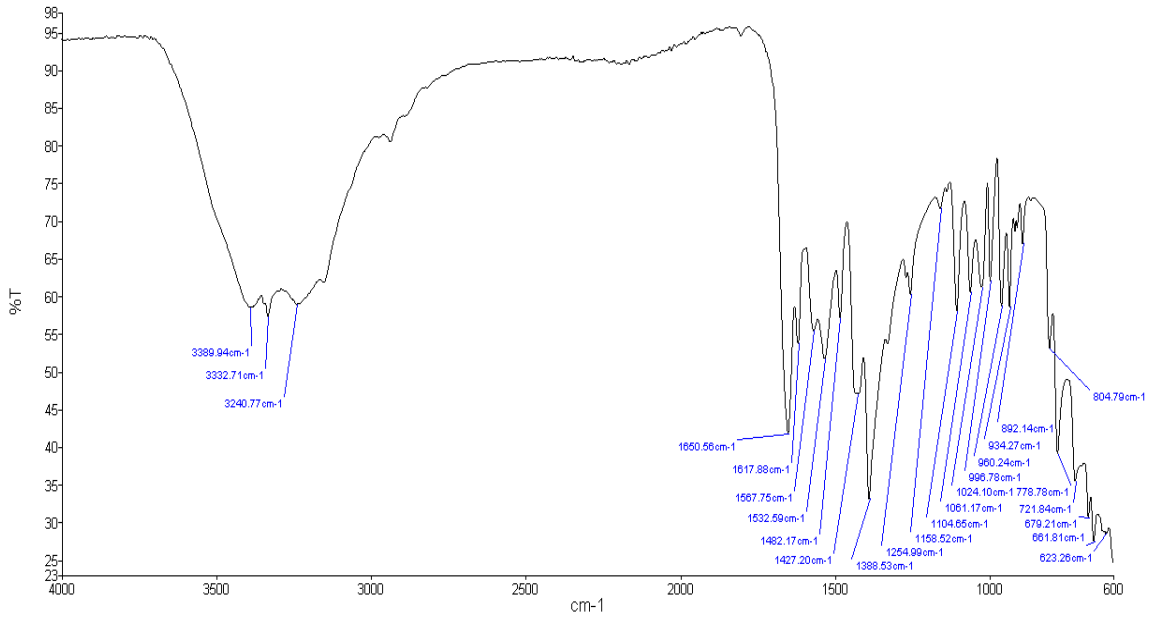

Figure 4.41. *In situ* FT-IR spectrum of **12** in H_2O/DMF.

4.7.4. 5-Acetamidoisophthalic acid, H_2AMIP (13)

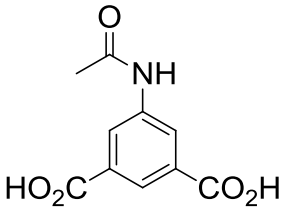

Figure 4.42. H_2AMIP. **13**

Prepared in the same way as reported by Slusher *et al.*[19] 25.4 mmol scale, yield = 3.71 g, 66 %. ^1H NMR (DMSO-d_6, 250 MHz, δ): 13.25 (br, 2H), 10.33 (s, 1H), 8.43 (d, J = 1.4

Hz, 2H), 8.15 (t, *J* = 1.4 Hz, 1H), 2.09 (s, 3H) ppm. ^{13}C NMR (DMSO-d_6, 75 MHz, δ): 169.3, 166.9, 140.2, 132.0, 124.7, 123.7, 24.3 ppm. FT-IR (diamond/gem, $\upsilon_{(max)}$, cm^{-1}): 3533, 3447, 3103 (br), 2526, 1714 (s), 1667 (s), 1613 (s), 1567 (s), 1440, 1405, 1369, 1336, 1303, 1249, 1200 (s), 1107, 1029. The spectroscopic data are consistent with the structure and the literature data.[19]

4.7.5. 3-ammonio-5-carboxybenzoate hemihydrate, $H_2AIP{\cdot}0.5H_2O$, (14)

To H_2AMIP (30 mg, 0.134 mmol), $Zn(NO_3)_2{\cdot}6H_2O$ (120 mg, 0.403 mmol) and PhCOOH (136 mg, 1.11 mmol): 5 mL H_2O was added in a 10 mL pressure tube and the resultant mixture stirred till homogeneous. This mixture was sealed and put in an oven at 120 ºC for 24 h. The resultant colourless block crystals were isolated by filtration and washed with 3 x 10 mL acetone and air dried. Yield: 17 mg. Single crystal X-ray diffraction studies confirmed the structure as $H_2AIP{\cdot}0.5H_2O$, **14**.

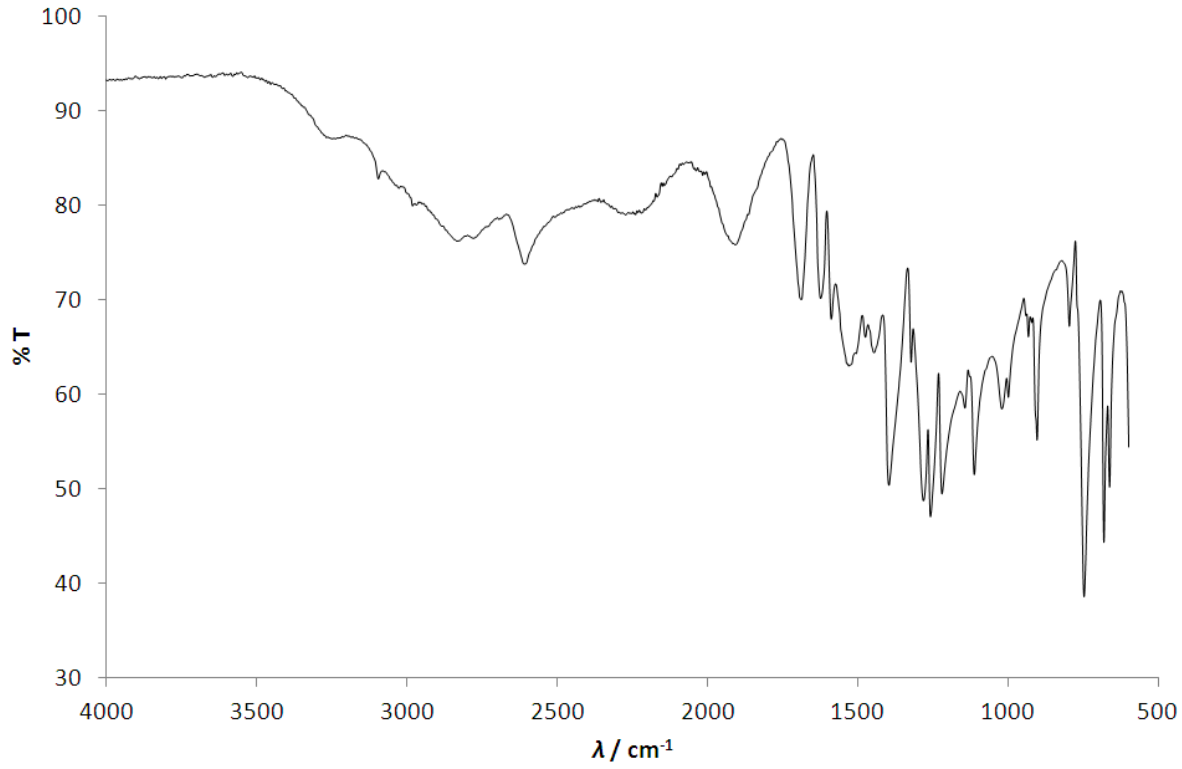

Figure 4.43. FT-IR spectrum of **14**.

4.7.6. $[Co(AMIP)(DMSO)_2]{\cdot}DMSO$, (15)

H_2AMIP (0.224 mmol, 50 mg) and $Co(OAc)_2{\cdot}4H_2O$ (0.224 mmol, 56 mg) were dissolved in 5 mL DMSO and stirred till homogeneous, in a 10 mL oven vial. This reaction mixture was sealed and put in an oven at 120 ºC for 48 h. Purple plate-like crystals, present at the end of

the reaction, were washed with 3 x 10 mL DMSO by decantation and stored in fresh DMSO. Yield: 30 mg. Single crystal X-ray diffraction studies confirmed the structure as $[Co(AMIP)(DMSO)_2]\cdot DMSO$, **15**. PXRD studies of dry and of DMSO wetted samples were inconclusive.

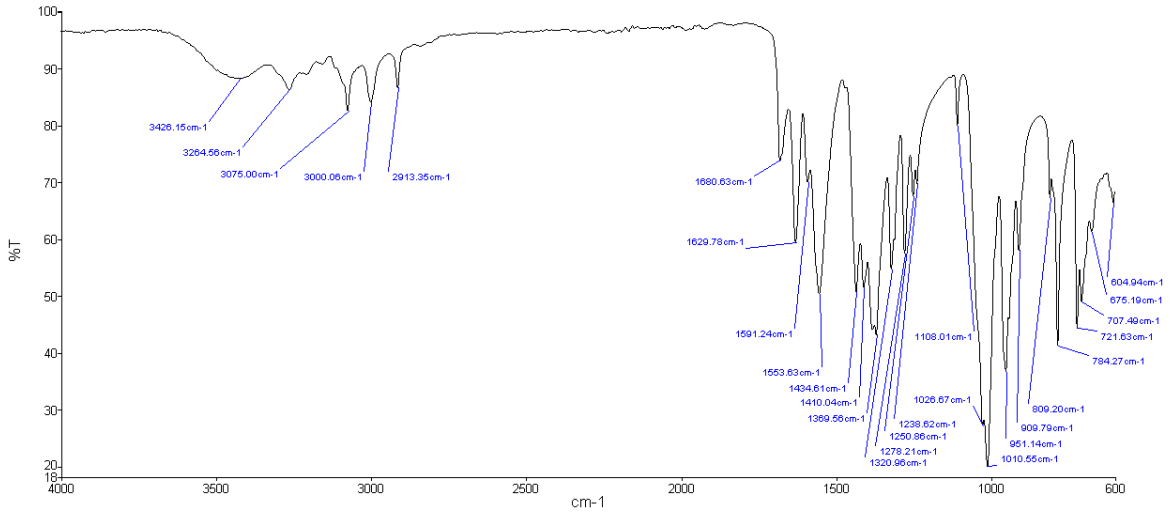

Figure 4.44. *In situ* FT-IR spectrum of **15** in DMSO.

4.7.7. $[Zn_3(AMIP)_2(bipy)_2(OAc)_2(OH_2)_4]\cdot 4H_2O$, (16)

H_2AMIP (0.134 mmol, 30 mg), $Zn(OAc)_2\cdot 2H_2O$ (0.401 mmol, 88 mg) and 4,4'-bipy (0.134 mmol, 21 mg) were dissolved in 5 mL H_2O and stirred until a homogeneous suspension was formed, in a 10 mL oven vial. This reaction mixture was sealed and put in an oven at 100 ºC for 48 h. Off-white crystals, present at the end of the reaction, were isolated by filtration, washed with 3 x 10 mL H_2O and air dried. Yield: 63 mg. Single crystal X-ray diffraction studies confirmed the structure as $[Zn_3(AMIP)_2(bipy)_2(OAc)_2(OH_2)_4]\cdot 4H_2O$, **16**.

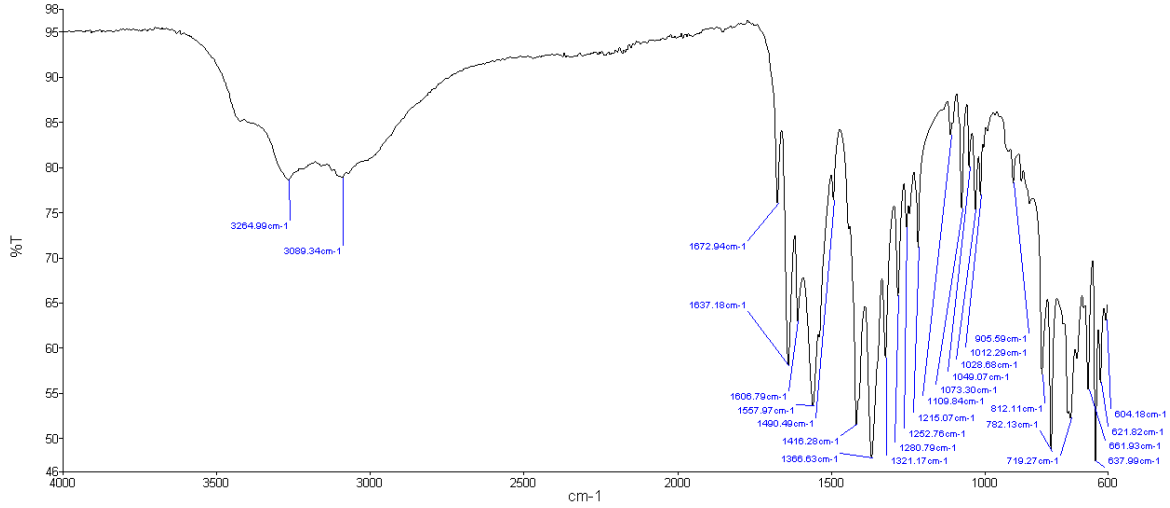

Figure 4.45. FT-IR spectrum of **16**.

4.7.8. $[Zn_2(AMIP)_2(bipy)(OH_2)]\cdot 1.5H_2O$, (17)

H_2AMIP (0.134 mmol, 30 mg), $Zn(NO_3)_2\cdot 6H_2O$ (0.402 mmol, 120 mg) and 4,4'-bipy (0.134 mmol, 21 mg) were dissolved in 5 mL H_2O and stirred until a homogeneous suspension was formed, in a 10 mL oven vial. This reaction mixture was sealed and put in an oven at 100 ºC for 48 h. Yellow block crystals, present at the end of the reaction, were isolated by filtration, washed with 3 x 10 mL H_2O and oven dried at 80 °C for 3 h. Yield: 45 mg. Single crystal X-ray diffraction studies confirmed the structure as $[Zn_2(AMIP)_2(bipy)(OH_2)]\cdot 1.5H_2O$, **17**.

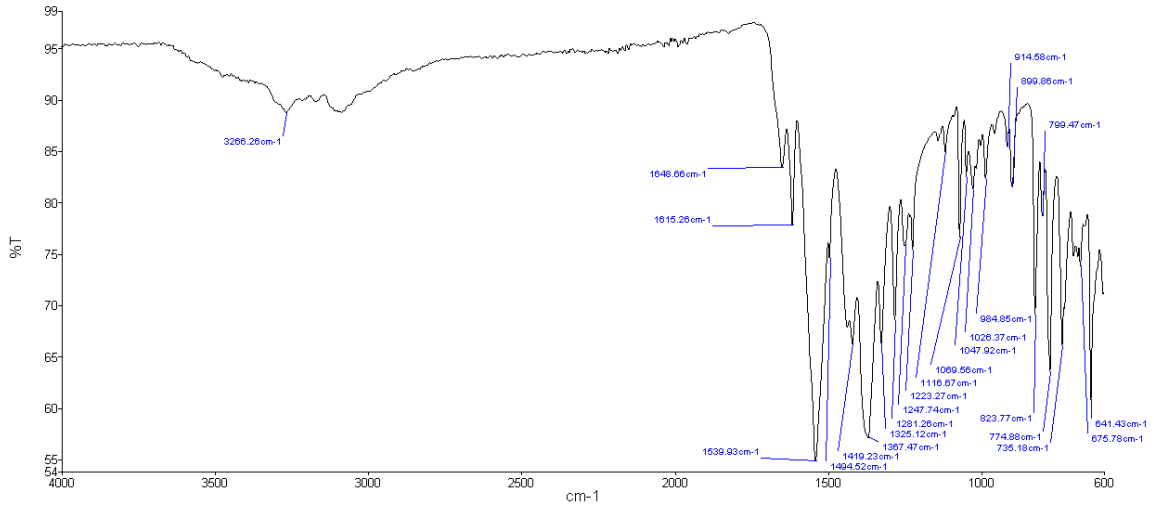

Figure 4.46. FT-IR spectrum of **17**.

4.7.9. $[Ni(bipy)(OH_2)_4]^{2+}[AMIP]^{2-}$, (18)

H_2AMIP (0.134 mmol, 30 mg), $Ni(OAc)_2\cdot 4H_2O$ (0.402 mmol, 100 mg) and 4,4'-bipy (0.134 mmol, 21 mg) were dissolved in 5 mL H_2O and stirred and stirred until a homogeneous suspension was formed, in a 10 mL oven vial. This reaction mixture was sealed and put in an oven at 95 ºC for 24 h. Pale green-blue plate-like crystals, present at the end of the reaction, were isolated by filtration, washed with 3 x 10 mL H_2O and air dried. Yield: 64 mg. Single crystal X-ray diffraction studies confirmed the structure as $[Ni(bipy)(OH_2)_4]^{2+}[AMIP]^{2-}$, **18**.

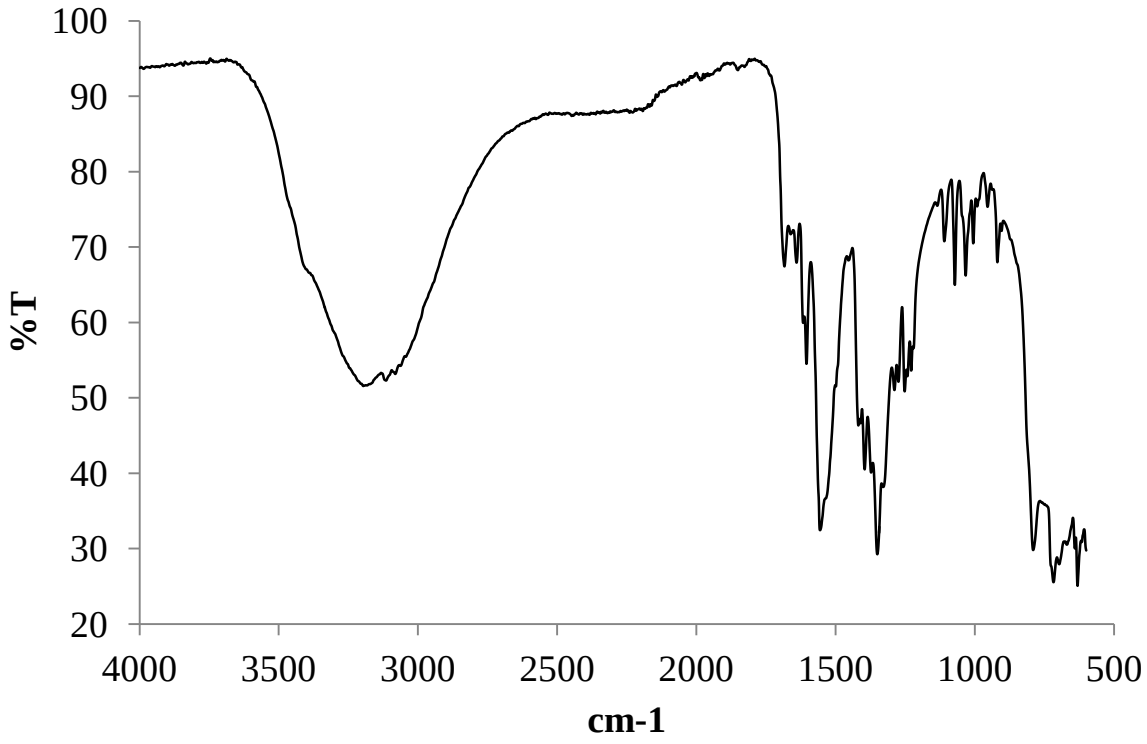

Figure 4.47. FT-IR spectrum of **18**.

4.7.10. $[Co(bipy)(H_2O)_4]^{2+}[AMIP]^{2-}$, (19)

H_2AMIP (0.134 mmol, 30 mg), $Co(OAc)_2 \cdot 4H_2O$ (0.402 mmol, 100 mg) and 4,4'-bipy (0.134 mmol, 21 mg) were dissolved in 5 mL H_2O and stirred until a homogeneous suspension was formed, in a 10 mL oven vial. The reaction mixture was sealed and put in an oven at 95 ºC for 24 h. Pale pink plate-like crystals, present at the end of the reaction, were isolated by filtration, washed with 3 x 10 mL H_2O and air dried. Yield: 53 mg. Single crystal X-ray diffraction studies suggests the structure as $[Co(bipy)(OH_2)_4]^{2+}[AMIP]^{2-}$, **19**.

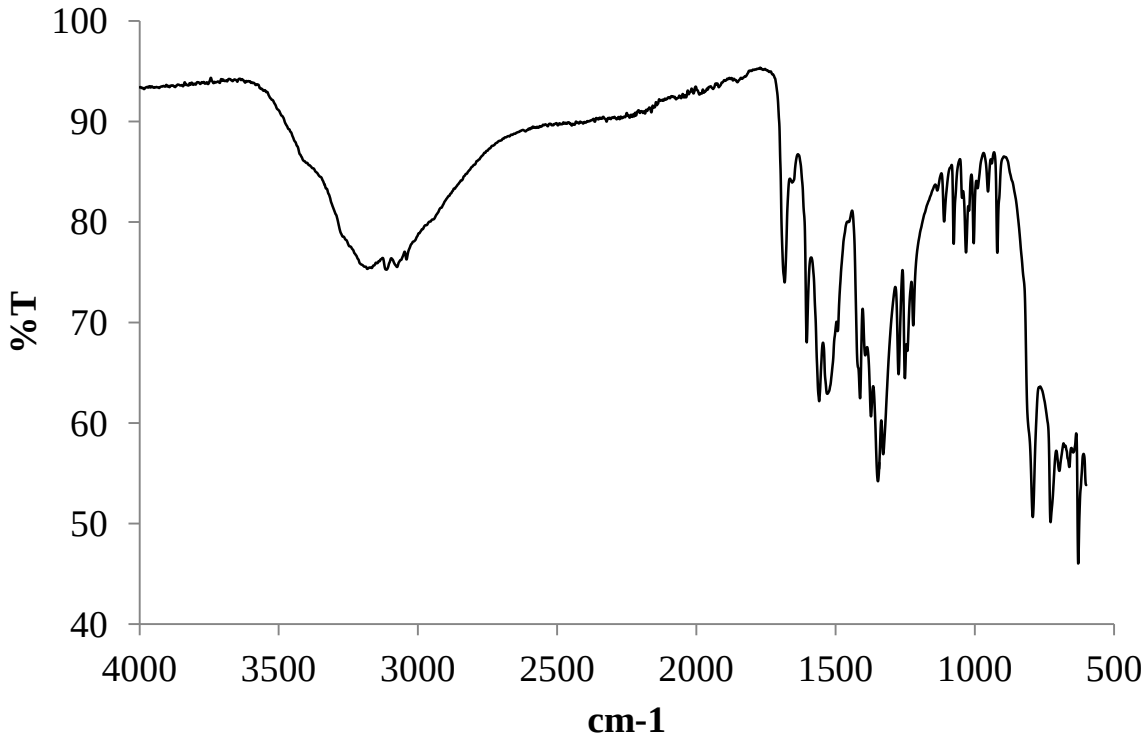

Figure 4.48. FT-IR spectrum of **19**.

4.7.11. $[Zn_4O(BDC\text{-}NHPr)_{0.6}(BDC\text{-}NH_2)_{0.4}(BPDC)_2(DMF)]\cdot 1.5DMF$, (20)

To $Zn(NO_3)_2\cdot 6H_2O$ (0.402 mmol, 120 mg), H_2BDC-NHPr (0.134 mmol, 34 mg) and H_2BPDC (0.134 mmol, 33 mg), was added 5 mL DMF in a 10 mL oven vial. This mixture was stirred for 30 minutes before sealing and placing in an oven at 105 °C for 48 h. Golden yellow block crystals were present at the end of the reaction. The structure was determined by single crystal X-ray diffraction only, as a minor side product $[Zn_4O(BDC\text{-}NHPr)_{0.6}(BDC\text{-}NH_2)_{0.4}(BPDC)_2(DMF)]\cdot 1.5DMF$, **20**.

4.7.12. $[Zn_4(BDC\text{-}NHPr)_3(NO_3)_2(H_2O)_2]\cdot x DMF\cdot y H_2O\cdot z BPDC$, PNMOF-3-NHPr, (21)

To $Zn(NO_3)\cdot 6H_2O$ (0.402 mmol, 120 mg), H_2BDC-NHPr (0.804 mmol, 179 mg) and H_2BPDC (0.134 mmol, 33 mg), was added 5 mL DMF in a 10 mL oven vial. This mixture was stirred for 30 minutes before sealing and placing in an oven at 100 °C for 24 h. Golden yellow hexagonal crystals were present at the end of the reaction, which were washed with 3 x 5 mL DMF over 3 days, by decantation and replacing with fresh DMF once every 24 h, and stored in fresh DMF. The structure was characterised as, $[Zn_4(BDC\text{-}NHPr)_3(NO_3)_2(H_2O)_2]\cdot x DMF\cdot y H_2O\cdot z BPDC$, **21**.

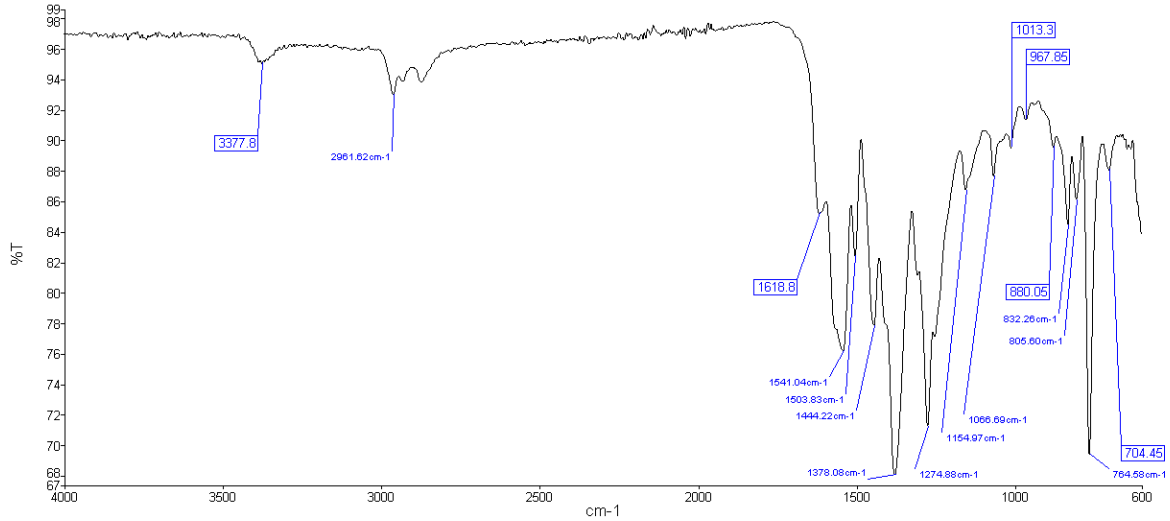

Figure 4.49. *In situ* FT-IR spectrum of **21** in THF.

4.7.13. $[Zn_4(BDC\text{-}NH_2)_3(NO_3)_2(H_2O)_2]\cdot x DMF\cdot y H_2O\cdot z BPDC$, PNMOF-3, (22)

To $Zn(NO_3)\cdot 6H_2O$ (0.402 mmol, 120 mg), $H_2BDC\text{-}NH_2$ (0.134 mmol, 34 mg) and H_2BPDC (0.134 mmol, 32 mg), was added 5 mL DMF in a 10 mL oven vial. The reaction mixture was stirred for 30 minutes before sealing and placing in an oven at 100 °C for 24 h. Golden yellow block crystals were present at the end of the reaction, which were washed with 3 x 5 mL DMF over 3 days, by decantation and replacing with fresh DMF once every 24 h, and stored in fresh DMF. The structure was characterised as $[Zn_4(BDC\text{-}NH_2)_3(NO_3)_2(H_2O)_2]\cdot x DMF\cdot y H_2O\cdot z BPDC$, **22**.

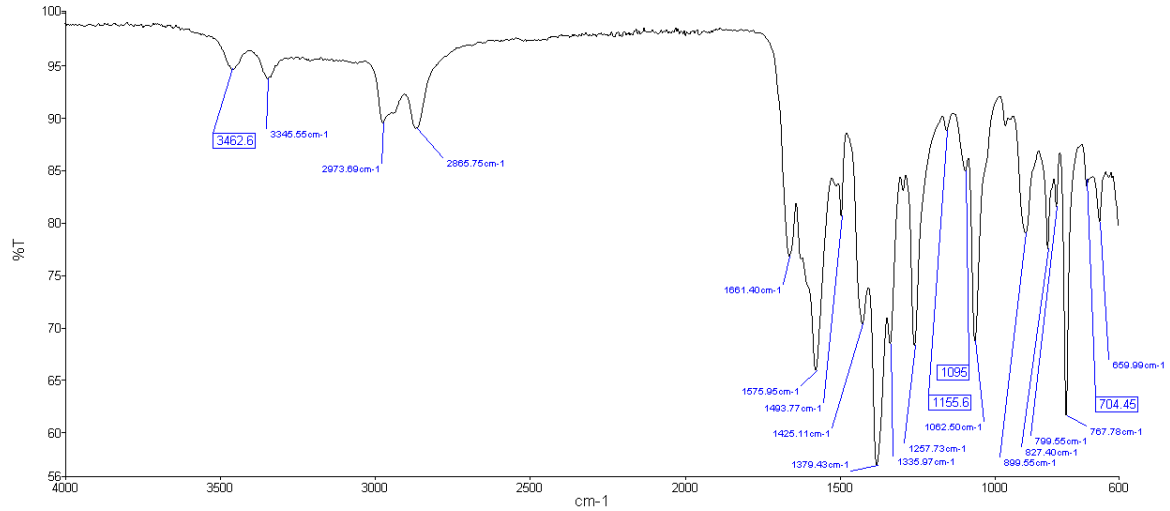

Figure 4.50. *In situ* FT-IR spectrum of **22** in THF.

4.8. References

[1] K. O. Kongshaug, H. Fjellvåg, *Polyhedron*, **2007**, *26*, 5113.
[2] J. F. Eubank, L. Wojtas, M. R. Hight, T. Bousquet, V. C. Kravtsov, M. Eddaoudi, *J. Am. Chem. Soc.*, **2011**, *133*, 17532.
[3] S.-M. Zhang, Z. Chang, T.-L. Hu, X.-H. Bu, *Inorg. Chem.*, **2010**, *49*, 11581.
[4] F. Dai, P. Cui, F. Ye, D. Sun, *Cryst. Growth Des.*, **2010**, *10*, 1474.
[5] L. Pan, B. Parker, X. Huang, D. H. Olson, Lee, J. Li, *J. Am. Chem. Soc.*, **2006**, *128*, 4180.
[6] L. Rajput, K. Biradha, *Polyhedron*, **2008**, *27*, 1248.
[7] M. Eddaoudi, J. Kim, N. Rosi, D. Vodak, J. Wachter, M. O'Keeffe, O. M. Yaghi, *Science*, **2002**, *295*, 469.
[8] S. Horike, D. Tanaka, K. Nakagawa, S. Kitagawa, *Chem. Commun.*, **2007**, 3395.
[9] D. Tanaka, A. Henke, K. Albrecht, M. Moeller, K. Nakagawa, S. Kitagawa, J. Groll, *Nat. Chem.*, **2010**, *2*, 410.
[10] Y. Inubushi, S. Horike, T. Fukushima, G. Akiyama, R. Matsuda, S. Kitagawa, *Chem. Commun.*, **2010**, *46*, 9229.
[11] D. Sarma, K. V. Ramanujachary, S. E. Lofland, T. Magdaleno, S. Natarajan, *Inorg. Chem.*, **2009**, *48*, 11660.
[12] K. K. Tanabe, Z. Wang, S. M. Cohen, *J. Am. Chem. Soc.*, **2008**, *130*, 8508.
[13] A. L. Spek, *J. Appl. Cryst.*, **2003**, *36*, 7.
[14] M. Szostak, M. Spain, A. J. Eberhart, D. J. Procter, *J. Am. Chem. Soc.*, **2014**, *136*, 2268.
[15] A. A. Addison, T. N. Rao, J. Reedijk, J. v. Rijn, G. C. Verschoor, *J. Chem. Soc., Dalton Trans.*, **1984**, 1349.
[16] R. K. Deshpande, J. L. Minnaar, S. G. Telfer, *Angew. Chem. Int. Ed.*, **2010**, *49*, 4598.
[17] Q. Yao, J. Su, O. Cheung, Q. Liu, N. Hedin, X. Zou, *J. Mater. Chem.*, **2012**, *22*, 10345.
[18] A. L. Grzesiak, F. J. Uribe, N. W. Ockwig, O. M. Yaghi, A. J. Matzger, *Angew. Chem. Int. Ed.*, **2006**, *45*, 2553.
[19] S. B. Slusher, K. Wozniak, *Patent: US2003/36534 A1*, **2003**.

5. Appendix

5.1. Appendix A: PXRD traces for Chapter 2

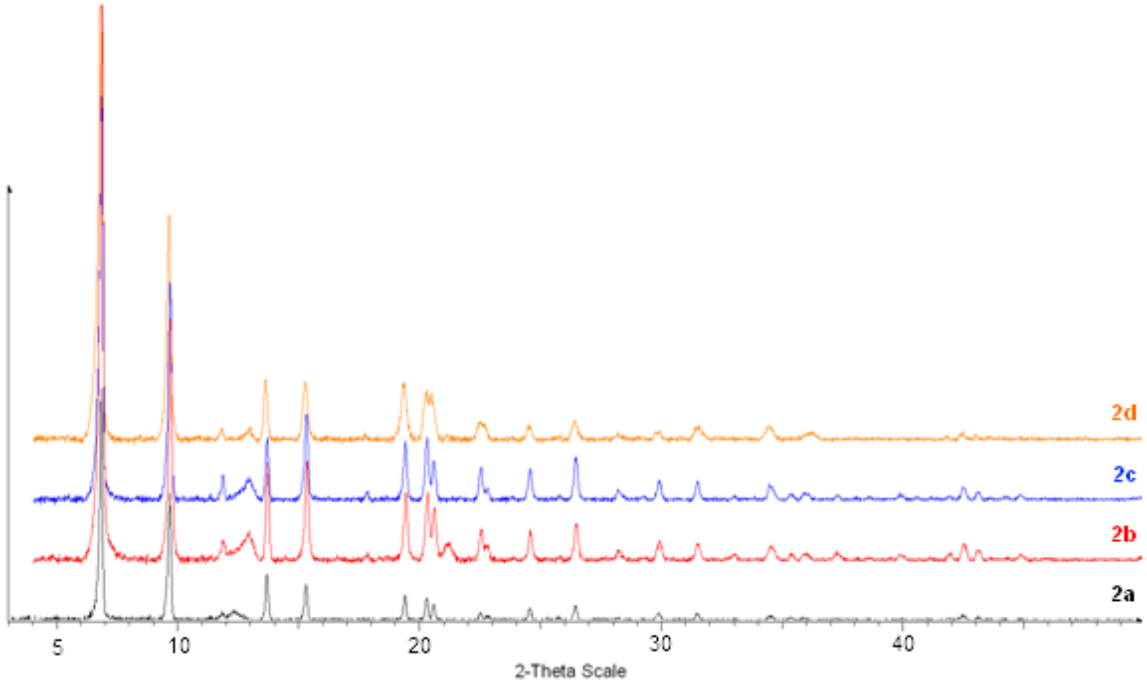

Figure 5.1. PXRD data of the conversion of IRMOF-3 to IRMOF-NHR, at room temperature, in THF after 72 h. **2a** (black), **2b** (red), **2c** (blue), **2d** (orange).

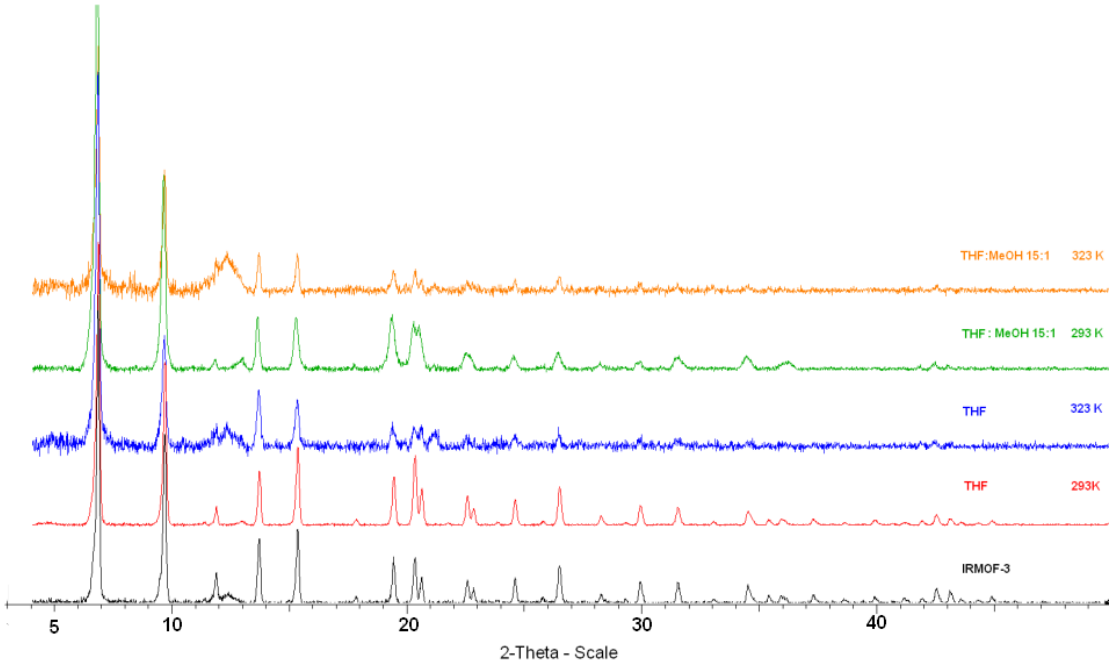

Figure 5.2. PXRD patterns of reaction between IRMOF-3, EtCHO and $NaCNBH_3$ in THF and THF:MeOH (15:1), at room temperature (293 K) and 50 °C (323 K).

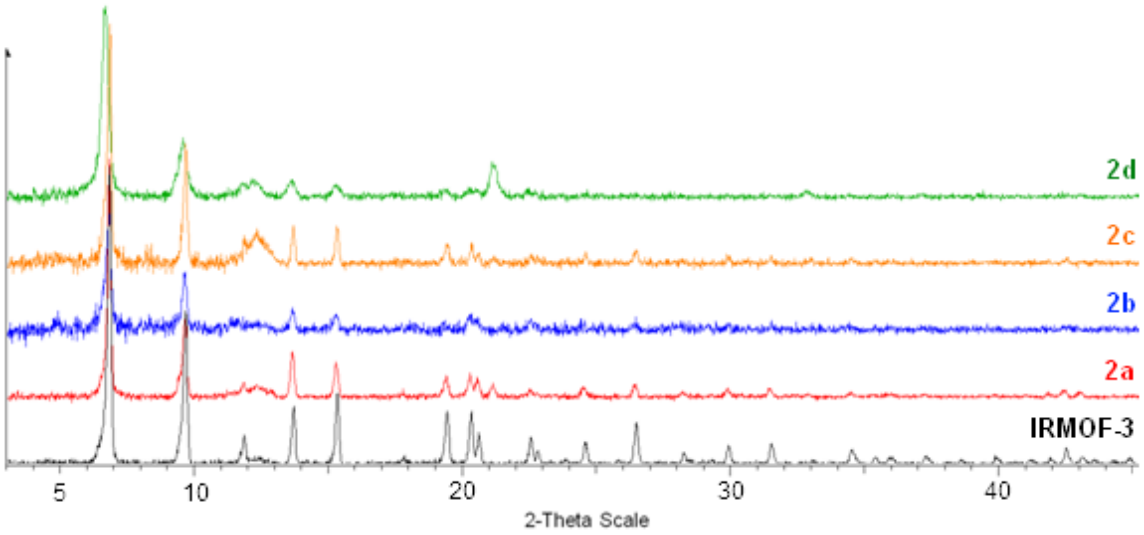

Figure 5.3. PXRD patterns of PSM products, **2a-d**, from the reaction between IRMOF-3 and $NaCNBH_3$ in THF:MeOH (15:1), at 50 °C (323 K) varying aldehydes.

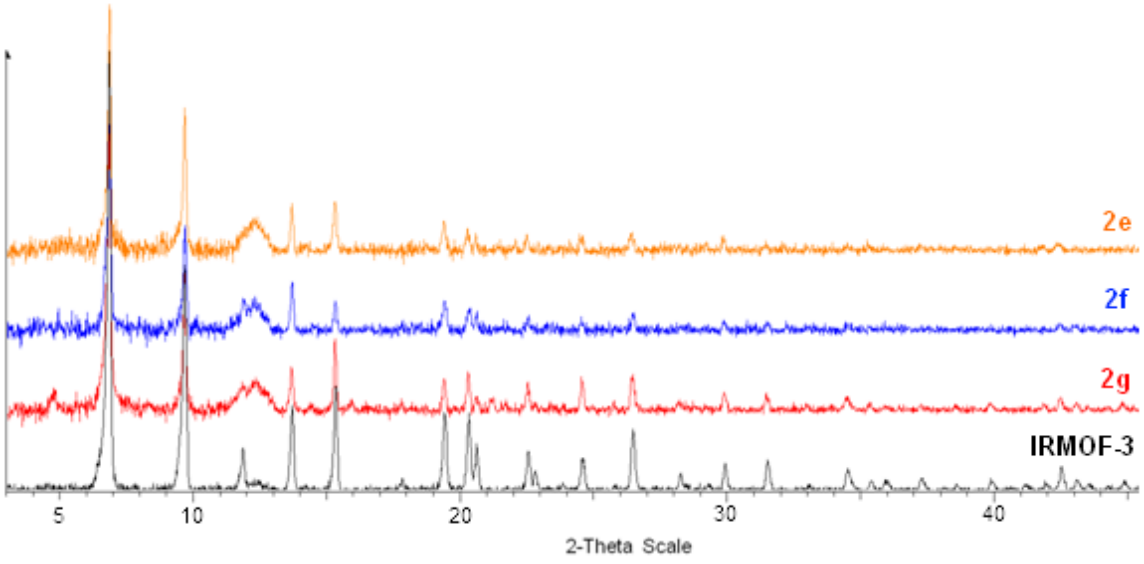

Figure 5.4. PXRD patterns of the PSM products, **2e-g**, from the reaction between IRMOF-3 and $NaCNBH_3$ in THF:MeOH (15:1), at 50 °C (323 K) varying aldehydes.

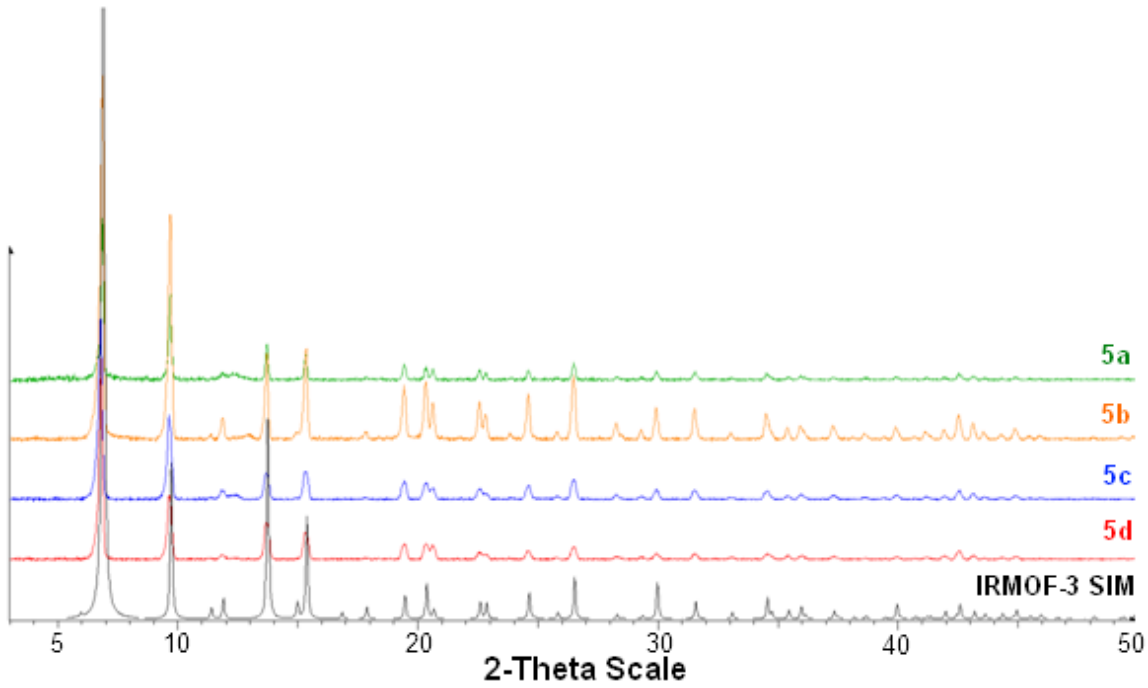

Figure 5.5. Powder X-ray diffraction data of **5a-d** and IRMOF-3 simulated from the literature single crystal data.[1]

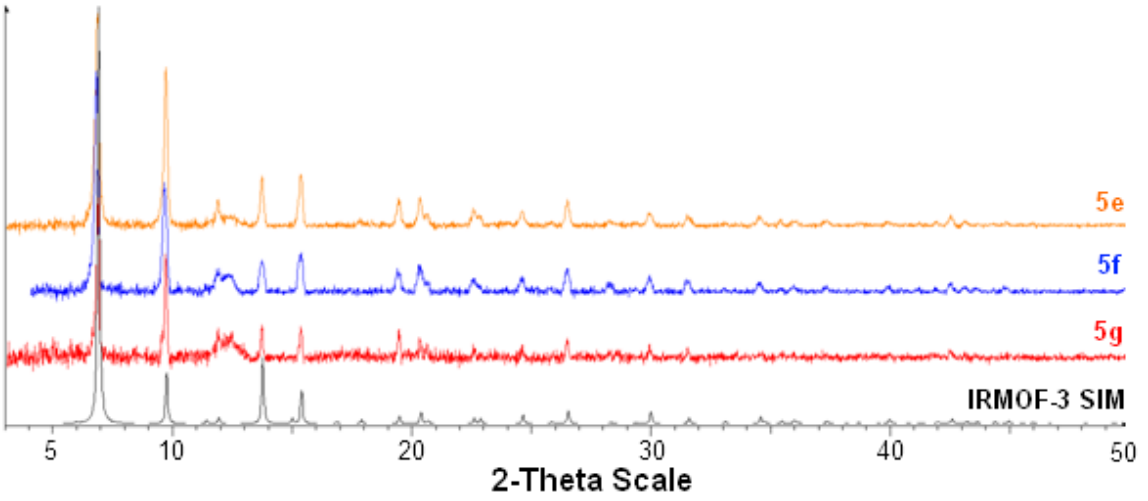

Figure 5.6. Powder X-ray diffraction data of **5e-g** and IRMOF-3 simulated from the literature single crystal data (black).[1]

5.2. Appendix B: Single Crystal X-ray Diffraction Full Tables

5.2.1. 2a

Table 5.1. Crystal data and structure refinement for **2a**.

Identification code	**2a** IRMOF-3 + PSM using ethanal (60% conversion) +7 toluenes
Empirical formula	C76.60 H78.20 N3 O13 Zn4
Formula weight	1510.30
Temperature	250(2) K
Wavelength	0.6889 Å
Crystal system	Cubic
Space group	*Fm*-3*m*
Unit cell dimensions	*a* = 25.9940(3)Å alpha = 90°
	b = 25.9940(3)Å beta = 90°
	c = 25.9940(3)Å gamma = 90°
Volume	17563.8(4) $Å^3$
Z	8
Density (calculated)	1.142 Mg/m^3
Absorption coefficient	1.132 mm^{-1}
F(000)	6262
Crystal size	0.14 x 0.12 x 0.10 mm
Theta range for data collection	2.52 to 26.57°
Index ranges	0<=h<=19; 0<=k<=23; 2<=l<=33
Reflections collected	1064
Independent reflections	1064 [*R*(int) = 0.0000]
R_σ	0.0143
Reflections observed (>2sigma)	758
Data Completeness	0.995
Absorption correction	Semi-empirical from equivalents
Max. and min. transmission	1.00 and 0.32
Refinement method	Full-matrix least-squares on F^2
Data / restraints / parameters	1064 / 6 / 31
Goodness-of-fit on F^2	1.040
Final R indices [I>2sigma(I)]	*R*1 = 0.0608 *wR*2 = 0.1937
R indices (all data)	*R*1 = 0.0761 *wR*2 = 0.2170
Largest diff. peak and hole	0.700 and -0.400 $eÅ^{-3}$

5.2.2. 2f

Table 5.2. Crystal data and structure refinement for **2f**.

Identification code	**2f**. IRMOF-3 + PSM using ferrocenecarboxaldehyde (25% conversion) + 2.5 toluene
Habit	Block (cuboid)
Colour	Brown
Empirical formula	$C_{76.6}$ $H_{78.2}$ N_3 O_{13} Zn_4
Formula weight	1510.30
Temperature	250(2) K
Wavelength	0.6889 Å
Crystal system	Cubic
Space group	*Fm*-3*m*
Unit cell dimensions	*a* = 25.9940(3)Å alpha = 90°
	b = 25.9940(3)Å beta = 90°
	c = 25.9940(3)Å gamma = 90°
Volume	17563.8(4) $Å^3$
Z	8
Density (calculated)	1.142 Mg/m^3
Absorption coefficient	1.132 mm^{-1}
F(000)	6262
Crystal size	0.14 x 0.12 x 0.10 mm
Theta range for data collection	2.52 to 26.57°
Index ranges	0<=*h*<=19; 0<=*k*<=23; 2<=*l*<=33
Reflections collected	1064
Independent reflections	1064 [*R*(int) = 0.0000]
Reflections observed (>2sigma)	758
Data Completeness	0.995
Absorption correction	Semi-empirical from equivalents
Max. and min. transmission	1.00 and 0.32
Refinement method	Full-matrix least-squares on F^2
Data / restraints / parameters	1064 / 6 / 31
Goodness-of-fit on F^2	1.040
Final *R* indices [I>2sigma(I)]	*R*1 = 0.0608 *wR*2 = 0.1937
R indices (all data)	*R*1 = 0.0761 *wR*2 = 0.2170
Largest diff. peak and hole	0.700 and -0.400 $eÅ^{-3}$

5.2.3. 5a

Table 5.3. Crystal data and structure refinement for **5a**.

Formula	$[Zn_4O(BDC\text{-}NHEt)_3]\cdot 7Tol$
Habit	Block (cuboid)
Colour	Yellow-orange
Empirical formula	$C_{79}\ H_{83}\ N_3\ O_{13}\ Zn_4$
Formula weight	1543.96
Temperature	250(2) K
Wavelength	0.6889 Å
Crystal system	Cubic
Space group	*Fm*-3*m*
Unit cell dimensions	*a* = 25.7627(2)Å alpha = 90°
	b = 25.7627(2)Å beta = 90°
	c = 25.7627(2)Å gamma = 90°
Volume	17099.1(2) $Å^3$
Z	8
Density (calculated)	1.200 Mg/m^3
Absorption coefficient	1.164 mm^{-1}
F(000)	6416
Crystal size	0.10 x 0.10 x 0.05 mm
Theta range for data collection	2.54 to 24.20°
Index ranges	0<=*h*<=17; 0<=*k*<=21; 3<=*l*<=30
Reflections collected	803
Independent reflections	803 [*R*(int) = 0.0000]
Reflections observed (>2sigma)	721
Data Completeness	0.975
Absorption correction	Semi-empirical from equivalents
Max. and min. transmission	1.00000 and 0.55537
Refinement method	Full-matrix least-squares on F^2
Data / restraints / parameters	803 / 6 / 31
Goodness-of-fit on F^2	1.162
Final R indices [I>2sigma(I)]	*R*1 = 0.0434 *wR*2 = 0.1420
R indices (all data)	*R*1 = 0.0465 *wR*2 = 0.1485
Largest diff. peak and hole	0.405 and -0.327 $eÅ^{-3}$

5.2.4. 5b

Table 5.4. Crystal data and structure refinement for **5b**.

Formula	$[Zn_4O(BDC\text{-}NHPr)_3]\cdot 6.3Tol$
Empirical formula	C77.10 H83.40 N3 O13 Zn4
Formula weight	1521.55
Temperature	250(2) K
Wavelength	0.6889 Å
Crystal system	Cubic
Space group	Fm-3m
Unit cell dimensions	a = 25.7702(1)Å alpha = 90^o
	b = 25.7702(1)Å beta = 90^o
	c = 25.7702(1)Å gamma = 90^o
Volume	17114.07(12) $Å^3$
Z	8
Density (calculated)	1.181 Mg/m^3
Absorption coefficient	1.162 mm^{-1}
F(000)	6328
Crystal size	0.12 x 0.10 x 0.07 mm
Theta range for data collection	2.54 to 27.72 ^{o}.
Index ranges	0<=h<=20; 0<=k<=24; 2<=l<=34
Reflections collected	1163
Independent reflections	1163 [R(int) = 0.0000]
Reflections observed (>2sigma)	1000
Data Completeness	0.996
Absorption correction	Semi-empirical from equivalents
Max. and min. transmission	1.00000 and 0.81944
Refinement method	Full-matrix least-squares on F^2
Data / restraints / parameters	1163 / 12 / 37
Goodness-of-fit on F^2	1.141
Final R indices [I>2sigma(I)]	R1 = 0.0395 *wR*2 = 0.1357
R indices (all data)	R1 = 0.0427 *wR*2 = 0.1387
Largest diff. peak and hole	0.731 and -0.319 $eÅ^{-3}$

5.2.5. 5e

Table 5.5. Crystal data and structure refinement for **5e**.

Identification code	$[Zn_4O(BDC\text{-}NH_2)_{0.36}(BDC\text{-}NHCH_2C_6H_9)_{2.64}]\cdot 4.5Tol$
Empirical formula	$C_{73.98}\,H_{77.40}\,N_3\,O_{13}\,Zn_4$
Formula weight	1478.12
Temperature	250(2) K
Wavelength	0.6889 Å
Crystal system	Cubic
Space group	Fm-3m
Unit cell dimensions	a = 25.7752(2)Å alpha = 90^o
	b = 25.7752(2)Å beta = 90^o
	c = 25.7752(2)Å gamma = 90^o
Volume	17124.0(2) $Å^3$
Z	8
Density (calculated)	1.147Mg/m^3
Absorption coefficient	1.161 mm^{-1}
F(000)	6280
Crystal size	0.12 x 0.12 x 0.10 mm
Theta range for data collection	3.75 to 26.57^o
Index ranges	-33<=h<=33; -31<=k<=33; -33<=l<=33
Reflections collected	42796
Independent reflections	1028 [R(int) = 0.0258]
Reflections observed (>2sigma)	972
Data Completeness	0.986
Absorption correction	Semi-empirical from equivalents
Max. and min. transmission	1.00000 and 0.76121
Refinement method	Full-matrix least-squares on F^2
Data / restraints / parameters	1028 / 12 / 37
Goodness-of-fit on F^2	1.123
Final R indices [I>2sigma(I)]	R1 = 0.0427 *wR*2 = 0.1464
R indices (all data)	R1 = 0.0442 *wR*2 = 0.1486
Largest diff. peak and hole	0.514 and -0.277 e$Å^{-3}$

5.2.6. 5g

Table 5.6. Crystal data and structure refinement for **5g**.

Formula	$[Zn_4O(BDC\text{-}NH_2)_{1.05}(BDC\text{-}NHCH_2C_6H_4SMe)_{1.95}]\cdot 5.5Tol$
Empirical formula	$C_{78.1}H_{74.6}N_3O_{13}S_{1.95}Zn_4$
Formula weight	1587.31
Temperature	250(2) K
Wavelength	0.6889 Å
Crystal system	Cubic
Space group	Fm-3m
Unit cell dimensions	a = 25.8577(2)Å a = 90°
	b = 25.8577(2)Å b = 90°
	c = 25.8577(2)Å g = 90°
Volume	17289.0(2) $Å^3$
Z	8
Density (calculated)	1.220 Mg/m^3
Absorption coefficient	1.207 mm^{-1}
F(000)	7360
Crystal size	0.12 x 0.10 x 0.05 mm
Theta range for data collection	2.53 to 24.11°
Index ranges	0<=h<=17; 0<=k<=21; 3<=l<=30
Reflections collected	818
Independent reflections	818 [R(int) = 0.0000]
Reflections observed (>2s)	746
Data Completeness	0.993
Absorption correction	Semi-empirical from equivalents
Max. and min. transmission	1.000 and 0.794
Refinement method	Full-matrix least-squares on F^2
Data / restraints / parameters	818 / 0 / 31
Goodness-of-fit on F^2	1.188
Final R indices [I>2s(I)]	R1 = 0.0543 *wR*2 = 0.1831
R indices (all data)	R1 = 0.0563 *wR*2 = 0.1866
Largest diff. peak and hole	0.529 and -0.94 $eÅ^{-3}$

5.3. Appendix C: List of publications arising from this report

D. Jiang, L. L. Keenan, A. D. Burrows and K. J. Edler, 'Synthesis and post-synthetic modification of MIL-101(Cr)-NH2 *via* a tandem diazotisation process,' *Chem. Commun.*, **2012**, 48, 12053-12055.

A. D. Burrows and L. L. Keenan, 'Conversion of primary amines into secondary amines on a metal–organic framework using a tandem post-synthetic modification,' *CrystEngComm*, **2012**, 14, (12), 4112.

5.4. References

[1] K. K. Tanabe, Z. Wang, S. M. Cohen, *J. Am. Chem. Soc.*, **2008**, *130*, 8508.